Beyond Hydrophobicity:

Aqueous Interfaces, Interactions, and Reactions

By

Russell James Perkins

B.A., University of Colorado Boulder, 2011

A thesis submitted to the

Faculty of the Graduate School of the

University of Colorado in partial fulfillment

of the requirement for the degree of

Doctor of Philosophy

Department of Chemistry and Biochemistry

2017

This thesis entitled:

Beyond Hydrophobicity: Aqueous Interfaces, Interactions and Reactions

written by Russell James Perkins

has been approved for the Department of Chemistry

_____

(Veronica Vaida)

_____

(Joel Eaves)

Date_____

The final copy of this thesis has been examined by the signatories, and we

find that both the content and the form meet acceptable presentation standards

of scholarly work in the above mentioned discipline.

Perkins, Russell James (Ph.D., Physical Chemistry, Department of Chemistry and Biochemistry)

Beyond Hydrophobicity: Aqueous Interfaces, Interactions and Reactions

Thesis Directed by Professor Veronica Vaida

Abstract

Many important chemical reactions from all branches of chemistry occur with water as a solvent. Furthermore, in environmental chemistry, biochemistry, and synthetic chemistry, key reactions occur in heterogeneous aqueous systems, where interfacial effects are particularly important. Despite the importance of aqueous environments and the tremendous amount of work done to study them, there are aspects that require further explanation and remain controversial. I have performed experimental studies to help elucidate the fundamental characteristics of aqueous systems, while examining specific phenomena across several fields.

The genetic disorder phenylketonuria (PKU) can result in increased levels of the aromatic amino acid phenylalanine in human serum. Much of my work has focused on the driving forces behind partitioning of aromatic small molecules, including phenylalanine, into air-water or membrane-water interfacial regions, and the consequences of partitioning on interfacial properties. Drastically different behaviors for structurally similar aromatic molecules are observed, differences that cannot be explained by hydrophobic effects. These observations can be explained, however, through the development of a more detailed picture of interactions and partitioning, including the formation of interfacial aggregates. For phenylalanine, this partitioning appears to result in drastic changes in membrane morphology and permeability. This is a likely molecular-level cause for the damage associated with the disease state of PKU.

Aqueous systems are further complicated by the reactivity of water. It often serves not only the role of a solvent, but also a reactant, a product, and/or a catalyst. I explore this reactivity using an organic molecule with relevance to environmental chemistry, zymonic acid. Zymonic acid forms spontaneously from pyruvic acid, an important atmospheric species. While zymonic acid exists as a single species in

solid form when dissolved in DMSO, once in aqueous solution it quickly reacts with water and equilibrates with at least four other forms. I studied the details and kinetics of these equilibria via time-dependent NMR. Several surprising mechanistic details were uncovered, including a direct enol to geminal diol conversion and base-catalyzed lactone ring formation. The consequences of zymonic acid's behavior are investigated in the context of environmental and prebiotic chemistry.

Acknowledgments

Works of this nature never happen in a vacuum. I had a tremendous amount of support getting here, from family, friends, teachers, colleagues, and acquaintances. There are so many people that made this journey possible, and while there is not enough room to list them all, I am eternally grateful for all of their help, both in big and small ways. There are several people that deserve special thanks, however.

First, I would like to thank my amazing wife, C.May Nickel, for always believing in me, pushing me to be the best version of myself, and helping me compensate for my shortcomings. I would like to thank all of my family for their endless support and encouragement throughout the years.

My sincerest gratitude goes to Prof. Veronica Vaida, for her continuous support and advocacy of my doctoral research, and life in general. I am especially thankful for her patience, knowledge and advice throughout my graduate career. I could not have chosen a better advisor.

I would like to thank the people I have worked the closest with in my research career: The rest of the Vaida Group for their camaraderie, guidance, and friendship. Rich Shoemaker, for his friendship, and for always making time for me, even when there weren't enough hours left in the day. Gordana Dukovic, Bryan Tienes, and the rest of the Dukovic group, for setting me up for success before my graduate career even started.

Contents

Tables

Schemes

Figures

Chapter 1: Thesis Introduction

Water is essential to many aspects of life as it evolved on earth. It comprises ~60% of the human body, and covers ~71% of the Earth's surface. It is thought to be so critical to life that NASA's search for habitable worlds is constrained by conditions where liquid water could exist.[1] Many important chemical reactions from all branches of chemistry occur with water as a solvent. A great deal of scientific thought and research has been focused on the study of water. Despite these efforts, there are facets of aqueous chemistry that require further exploration. Water remains a difficult solvent to model, due to its complex hydrogen bonding network.[2–4] There is strife in recent literature about both the phase diagram of water, and the state of water at a pure air-water interface.[5–7] In this work, I, with the help of many collaborators, examine the interactions between water and chemical systems. While the focus is fundamental in nature, the chemistry that is investigated is particularly relevant to biological systems, environmental systems, and chemical assemblies that prelude the origin of life.

The theory most commonly applied to explain aqueous interactions is that of hydrophobicity and hydrophilicity.[8–10] While this view of aqueous interactions is useful in some settings, it is often inconsistent or incorrect in fundamental ways. By examining the details of the systems under study, I hope to have contributed to a deeper insight into the real interactions at work in aqueous processes, and emphasize important and transferable concepts. This dissertation begins, in Chapter 2, with a discussion of experimental techniques that are used throughout this work. There is an emphasis on measurements of the properties of water interfaces, and some discussion of the thermodynamics of interfacial systems. Several technical points are emphasized here that I believe are important, or often overlooked. Chapters 3-10 discuss experimental work that was often the product of collaborations. Because of this, I describe the contributions of myself, and collaborators below. For all the work described in this manuscript, Veronica Vaida provided indispensable advice, direction, and discussion.

Chapter 3 through 7 detail a series of studies examining aqueous interfaces, and the molecular interactions responsible for the partitioning of material to those interfaces. Chapter 3 investigates the

interactions of the amino acid phenylalanine with a model cell membrane at an air-water interface.[11] This investigation involved simulations that were performed collaboratively between Elizabeth Griffith (CU Boulder) and Martina Roeselovà and Lukasz Cwiklik (Academy of Sciences of the Czech Republic, Prague). I contributed to Langmuir trough measurements alongside Elizabeth Griffith, Brewster Angle Microscope measurement with Ellen Adams and Dana-Marie Telesford (The Allen Group, The Ohio State University, Columbus, OH), and independently performed fluorescence confocal microscopy measurements. Elizabeth Griffith wrote the initial draft of the paper, which I revised to include contributions of collaborators and in response to comments during review. Chapter 4 describes unpublished work attempting to quantify surface hydrolysis in the model membrane system. This study was motivated by changes that were observed in the experimental work from Chapter 3. I am the sole contributor to this work. In Chapter 5, a series of aromatic compounds is investigated theoretically and experimentally, to uncover and explain the molecular level details behind the phenomena reported in Chapter 3.[12] Molecular dynamics simulations were performed by Alexandra Kukharchuk, Pauline Delcroix, Martina Roeselová, and Lukasz Cwiklik (Academy of Sciences of the Czech Republic, Prague). I contributed the bulk of the experimental work, aside from the NMR analysis which was performed by Rich Shoemaker (CU Boulder), and lead the analysis and writing of the manuscript. Chapter 6 describes studies of phenylalanine with a model cell membrane, although under significantly different conditions. These studies are in preparation for publication, but currently unpublished. Vesicles are synthesized with encapsulated dye, which allows for the performance of fluorescence permeability assays. Changes in vesicle permeability that are observed are consistent with the findings of Chapter 5. I am the sole contributor to this work. Chapter 7 details ongoing work in surface reflection spectroscopy in order to further study this system. I am the sole contributor to this work at this time.

Chapters 8 through 10 discuss a different line of study. A compound known as zymonic acid is investigated initially due to its role in aqueous heterogeneous chemistry.[13] Rich chemical reactions are discovered in aqueous solution, however, and investigated via NMR.[14] Chapter 8 discusses these

investigations. Rich Shoemaker (CU Boulder) provided a great deal of direction and oversight in the NMR work, and performed the solid state NMR analysis independently. Barry Carpenter (Cardiff University, United Kingdom) contributed to the formulation of the reaction mechanisms that are suggested. I performed the remainder of the NMR work, analysis, and wrote the resulting manuscript. Chapter 9 utilizes some of the new-found information about zymonic acid to expand previous mechanisms for the photochemistry of pyruvic acid.[15] The new mechanism utilizes zymonic acid as a photochemical intermediate, and helps identify and explain previously unidentified pyruvic acid photoproducts. In this section I contributed some initial mechanistic direction, which was verified and expanded by Barry Carpenter (Cardiff University, United Kingdom) and Rebecca Rapf (CU Boulder). The vast majority of the experimental work and analysis was performed by Rebecca Rapf, as well as the writing of the manuscript. I performed the NMR experiments for this work. Chapter 10 concludes the zymonic acid related section with a discussion of the spontaneous polymerization of zymonic and pyruvic acids, and their ability to act as prebiotically plausible sugar analogues. This work is in preparation for publications, and I am the sole contributor.

The two lines of study that are described in this thesis illustrate different aspects of the chemistry that occurs in aqueous solutions, and at the interface between aqueous solutions and other materials. Often times this chemistry is complex and counterintuitive, despite the prevalence of aqueous systems in biology and the natural environment. It is my hope that this work contributes to a deeper understanding of the complexities involved in aqueous systems, and that understanding of these systems eventually leads to more accurate simple and intuitive descriptions, which can then be more easily utilized across fields and disciplines.

Bibliography

(1)   Domagal-Goldman, S. D.; Wright, K. E.; Adamala, K.; Arina de la Rubia, L.; Bond, J.; Dartnell, L. R.; Goldman, A. D.; Lynch, K.; Naud, M.-E.; Paulino-Lima, I. G.; et al. The Astrobiology Primer v2.0. *Astrobiology* **2016**, *16* (8), 561–653.

(2)   Matsumoto, M.; Saito, S.; Ohmine, I. Molecular Dynamics Simulation of the Ice Nucleation and Growth Process Leading to Water Freezing. *Nature* **2002**, *416* (6879), 409–413.

(3)   Eaves, J. D.; Tokmakoff, A.; Geissler, P. L. Electric Field Fluctuations Drive Vibrational Dephasing in Water. *J. Phys. Chem. A* **2005**, *109* (42), 9424–9436.

(4)   Shultz, M. J.; Bisson, P.; Vu, T. H. Insights into Hydrogen Bonding via Ice Interfaces and Isolated Water. *J. Chem. Phys.* **2014**, *141* (18), 18C521.

(5)   Gallo, P.; Amann-Winkel, K.; Angell, C. A.; Anisimov, M. A.; Caupin, F.; Chakravarty, C.; Lascaris, E.; Loerting, T.; Panagiotopoulos, A. Z.; Russo, J.; et al. Water: A Tale of Two Liquids. *Chem. Rev.* **2016**, *116* (13), 7463–7500.

(6)   Björneholm, O.; Hansen, M. H.; Hodgson, A.; Liu, L.-M.; Limmer, D. T.; Michaelides, A.; Pedevilla, P.; Rossmeisl, J.; Shen, H.; Tocci, G.; et al. Water at Interfaces. *Chem. Rev.* **2016**.

(7)   Geissler, P. L. Water Interfaces, Solvation, and Spectroscopy. *Annu. Rev. Phys. Chem.* **2013**, *64* (1), 317–337.

(8)   Chandler, D. Hydrophobicity: Two Faces of Water. *Nature* **2002**, *417* (6888), 491–491.

(9)   Maibaum, L.; Dinner, A. R.; Chandler, D. Micelle Formation and the Hydrophobic Effect†. *J. Phys. Chem. B* **2004**, *108* (21), 6778–6781.

(10)   Wilce, M. C. J.; Aguilar, M.-I.; Hearn, M. T. W. Physicochemical Basis of Amino Acid Hydrophobicity Scales: Evaluation of Four New Scales of Amino Acid Hydrophobicity Coefficients Derived from RP-HPLC of Peptides. *Anal. Chem.* **1995**, *67* (7), 1210–1219.

(11)   Griffith, E. C.; Perkins, R. J.; Telesford, D.-M.; Adams, E. M.; Cwiklik, L.; Allen, H. C.; Roeselová, M.; Vaida, V. Interaction of L-Phenylalanine with a Phospholipid Monolayer at the Water–Air Interface. *J. Phys. Chem. B* **2015**, *119* (29), 9038–9048.

(12)   Perkins, R. J.; Kukharchuk, A.; Delcroix, P.; Shoemaker, R. K.; Roeselová, M.; Cwiklik, L.; Vaida, V. The Partitioning of Small Aromatic Molecules to Air–Water and Phospholipid Interfaces Mediated by Non-Hydrophobic Interactions. *J. Phys. Chem. B* **2016**, *120* (30), 7408–7422.

(13)   Reed Harris, A. E.; Pajunoja, A.; Cazaunau, M.; Gratien, A.; Pangui, E.; Monod, A.; Griffith, E. C.; Virtanen, A.; Doussin, J.-F.; Vaida, V. Multiphase Photochemistry of Pyruvic Acid under Atmospheric Conditions. *J. Phys. Chem. A* **2017**.

(14)   Perkins, R. J.; Shoemaker, R. K.; Carpenter, B. K.; Vaida, V. Chemical Equilibria and Kinetics in Aqueous Solutions of Zymonic Acid. *J. Phys. Chem. A* **2016**, *120* (51), 10096–10107.

(15)   Rapf, R. J.; Perkins, R. J.; Carpenter, B. K.; Vaida, V. Mechanistic Description of Photochemical Oligomer Formation from Aqueous Pyruvic Acid. *J. Phys. Chem. A* **2017**, *121* (22), 4272–4282.

Chapter 2: Experimental Techniques

2.1 Introduction

Different complementary experimental techniques are presented in this thesis. While brief explanations and relevant experimental details can be found in the chapters that follow, background and in some cases detailed explanations of basic principles are presented here.

2.2 Langmuir Trough

Langmuir troughs are deceptively simple instruments that can, in theory, be used with any liquid material. They have their roots from instruments designed and utilized by Agnes Pockels,[1] which were improved upon by Irving Langmuir to take similar form as modern instruments.[2] Further adjustments to Langmuir troughs were made by Katharine Blodgett that allowed for effective transfer of films from the water surface to a solid support.[3] These modified troughs are known as Langmuir-Blodgett troughs, and they are commonly found as modern instruments, in addition to Langmuir troughs.

While Langmuir trough techniques can apply to a range of liquids, for the sake of this explanation, we will assume the solution filling the trough (the subphase) is water. Operation is essentially the same for other liquids, although it is likely that different materials will be required for at least some components. Langmuir troughs consist of a shallow dish with movable barriers designed to scrape across the surface of the liquid filling the dish, combined with a surface tension measuring device. The most common usage for Langmuir Troughs is the collection of compression isotherms, where a known amount of insoluble, surface active (surface partitioning) material is deposited, usually in a volatile, immiscible solvent. After the solvent has evaporated, the barriers are scraped across the water surface and the surface area and surface tension are monitored.

The trough dish is usually made of polytetrafluoroethylene (PTFE, Teflon) due to its chemical inertness, and ease of cleaning. Troughs made of stainless steel and glass both appear in the literature however, and there are no strict constraints on what materials are usable, as long as they can hold liquid and be cleaned effectively. The barriers are generally composed of either PTFE or polyoxymethylene

(POM, Delrin) plastic. PTFE has the advantage of being chemically resistant and easier to clean, while Delrin has the advantage of being hydrophilic, which can prevent the movement of material under the barriers during compression.

The most common surface tension probes are microbalances with Wilhelmey plates, rod probes, or Du Noüy rings.[4] All of these probes operate on the same principles. Surface tension can be conceptualized as the unit energy it takes to increase the unit surface area. The surface tension probes used rely on being extremely hydrophilic, which in this case means they have low contact angles with water, as shown in Figure 2.1.
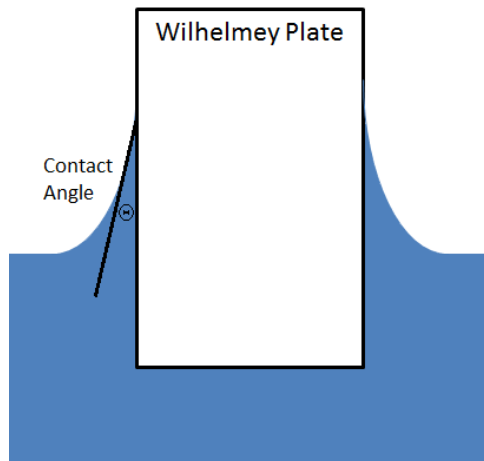
Figure 2.1: Illustration of the way water reacts to a hydrophilic surface tension probe. The contact angle is shown as Θ.

Because creating new surface costs energy, this results in a restoring force pulling the probe into the liquid. For a rod probe or Wilhelmy plate, the surface tension can be described as

$$\gamma = \left(\frac{\partial G}{\partial A}\right)_{T,P,n_i} \cong \frac{F * \Delta h}{\Delta h * p * \cos(\Theta)} = \frac{F}{p * \cos(\Theta)}$$

where G is gibbs free energy, A is surface area, T is temperature, P is pressure, n_i is number of moles of each substance, F is force, h is plate height above the liquid surface, p is plate perimeter, and Θ is contact angle. Surface tension measurements are often given in mN/m, but mJ/m^2 are equivalent units. In practice materials are usually chosen such that the contact angle is approximately zero, which simplifies the relationship between the force measured by the microbalance and the surface tension.

While this method works well, there are other effects that alter the force measured by the microbalance. The most common of these are buoyant forces, from the probes displacing water, and the accumulation of water on the probe, increasing its weight. These effects are particularly problematic with

probes made of porous filter paper (although they are advantageous due to their low cost and complete wetting). In order to correct for these effects, the tensiometer is usually zeroed using clean water as a reference. This results in measurements of surface pressure, i.e. the difference in surface tension from that of pure water, rather than surface tension. Measurement of absolute surface tension can still be carried out with this technique, even with filter paper plates, by taking care that the probe remains wet and at the same depth between samples.

The largest technical difficulty inherent to Langmuir Troughs is cleanliness. Because of the two dimensional nature of the surface, it takes very few molecules of contamination to cause noticeable differences in measurements. As discussed in Chapter 5, contamination can manifest over time, and can be due to impurities on the trough, balance, barriers, etc., in the subphase, in the surfactant, in the spreading solvent, or in the gas phase. Because of this, great care needs to be taken when cleaning the trough, and selecting cleaning supplies and reagents. Water quality is particularly important. We have found that pre-bottled reagent grade water is insufficiently pure, likely due to the packing materials. The best option is use of a high purity water generator, such as a MilliQ system used for this work, which generates 18.2 mΩ/cm resistivity and 3 ppb total oxidizable carbon (TOC) water, starting from house deionized water feed. It should also be noted that low TOC does not necessarily guarantee the cleanliness of the water for our purposes; many surface active molecules are not oxidizable, and will not increase the TOC levels. This appears to be particularly true of some polymeric materials that are released from new pipe installs, which have caused a great deal of experimental trouble in our work. Langmuir trough studies are utilized in Chapters 3, 4, 5, and 7 in experiments that either require controlled surface conditions, or seek to gather thermodynamic information.

2.3 Surface Thermodynamics

While the basic design and operation of a Langmuir trough is simple, but not easy, the thermodynamics behind interpreting the collected data are more complicated. So much so, that even the

most basic steps are often derived in ways that are not strictly correct. Good derivations of the basic thermodynamics of an interface appear in the seminal works of Gibbs[5] and Guggenheim.[6,7] A series of papers by Kinsi Motomura have detailed derivations of the thermodynamics of liquid interfaces,[8] mixed insoluble surfactant solutions,[9] and mixed soluble and insoluble surfactant solutions.[10] An attempt at complete thermodynamic derivations is not made here, but rather key conceptual points will be emphasized.

Surface tension is perhaps the most useful measured quantity, and is an inherently thermodynamic variable. Represented as γ, it is defined as

$$\gamma = \left(\frac{\partial G}{\partial A}\right)_{T,P,n_i}$$

where A is the surface area, and the integral is taken at constant temperature, pressure, and composition. While this is a thermodynamic variable, great care must be taken to use it in situations where the measurement of surface tension is done in a setting that is out of equilibrium. Certain surface tension measurements, especially utilizing moving drops or bubbles, will give measurements of dynamic, out of equilibrium surface tensions, which will often produce meaningless results when paired with equilibrium thermodynamic relationships.

There are many different ways to relate surface tension to other thermodynamic variables. A common starting point is the total differential for Gibbs free energy for a three phase system, including two bulk phases and an interface, and can be expressed as

$$dG = \sum_{phases}\left(VdP - SdT + \sum_i \mu_i dn_i + \sum_i n_i d\mu_i\right) + Ad\gamma + \gamma dA$$

where V is volume, P is pressure, S is entropy, T is temperature, μ_i is chemical potential of component i, n_i is the number of molecules of component i. The fundamental expression of Gibbs energy in a multicomponent system also holds, however, indicating that:

$$dG = VdP - SdT + \sum_i \mu_i dn_i$$

The combination of these two equations, along with the realization that the bulk phases at equilibrium do not contribute and the assumption that the surface area is constant, results in the expression

$$-Ad\gamma = \sum_i n_i^s \, d\mu_i$$

where n^s is the number of molecules in the surface phase. This expression is known as the Gibbs adsorption isotherm equation, and is more commonly expressed as

$$-d\gamma = \sum_i \Gamma_i \, d\mu_i$$

where Γ is the surface excess concentration. This equation can be used, generally by expressing the chemical potential in terms of an activity or concentration, to calculate a surface excess concentration based on a series of equilibrium surface tension measurements.

The surface excess concentration is a conceptually interesting quantity, as it is effectively a two dimensional concentration of (inherently three dimensional) molecules. This quirk arises because the surface phase does not have a volume associated with it, despite being occupied by material in the system. This is also the reason that it is referred to as a surface excess concentration, rather than a concentration. Generally, near the interface between two phases some molecules will have either higher or lower concentrations than the rest of the bulk phases. The surface excess concentration is simply the extra material near the interface compared to the bulk concentration. In the case of lower concentrations near the interface, this results in a negative surface excess concentration.

The choice of the dividing surface between the two phases is in some sense arbitrary, because the thermodynamics will hold regardless of this choice (although the relative amounts of material in each phase will change). For the sake of simplicity, the dividing surface is usually chosen such that one of the

bulk components has a surface excess concentration of zero. This is shown in Figure 2.2. In this example there is some depletion of material below (to the left) of the dividing surface, but an equal amount of excess material above (to the right of) the dividing surface, both in comparison to the bulk phases further from the dividing surface.
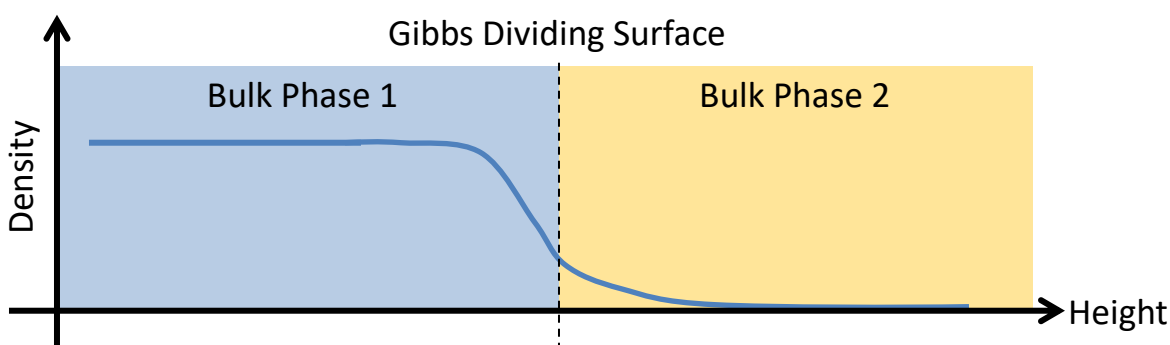
Figure 2.2: Example of a Gibbs dividing surface such that the surface excess concentration of the depicted component is zero.

With this description of the surface phase, it is possible for surface excess concentration to manifest in many different ways. It is important to keep this in mind, as experimental determinations of material at the surface will not always relate to the thermodynamic definition of material that is in the surface phase. This is illustrated in Figure 2.3, where the red, orange, and green traces all exhibit surface excess concentrations, but with very different distributions of material throughout both the bulk and near-interface regions.
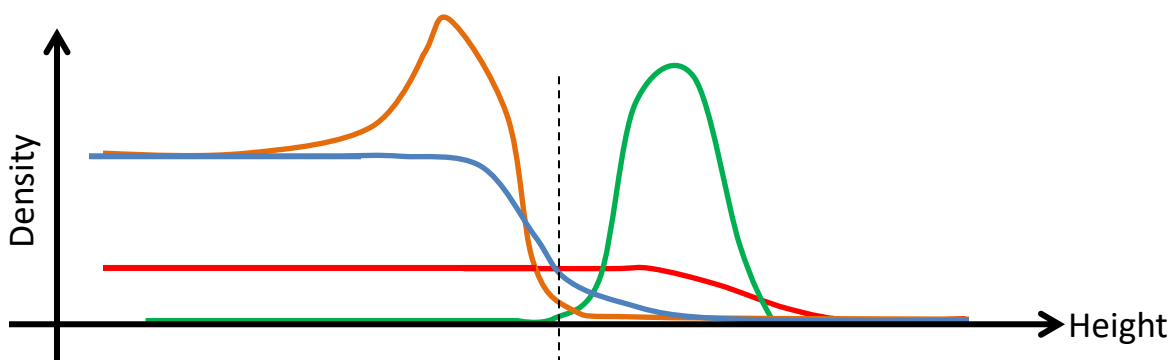
Figure 2.3: Example of different density profiles of materials. The dividing surface is chosen such that the blue trace has no surface excess concentration, however the orange, red and green traces all have positive surface excess concentrations.

Having an understanding of surface thermodynamics is essential to much of the work presented in this dissertation. It is particularly important in Chapters 3-7 for interpreting experimental data.

2.4 Brewster Angle Microscopy

Brewster Angle Microscopy (BAM) is a useful technique that is complementary to other surface sensitive measurements. It is a relatively new technique, first reported in 1991 by two groups.[11,12] The Brewster angle is the angle at which incident light to a uniform dielectric will produce no p-polarized reflection. The Fresnel equations predict this angle as

$$\theta_B = Tan^{-1}\left(\frac{n_2}{n_1}\right)$$

where Θ_B is the Brewster angle, n_2 is the refractive index of the reflecting medium, and n_1 is the refractive index of the initial medium. The Brewster angle of water has some wavelength (and temperature) dependence, but is approximately 53°.

The general design behind a BAM is to utilize a highly p-polarized laser to illuminate the water (or other liquid) surface, then image the reflected light. For a clean, instantaneous change in refractive index, there would be no reflected light. For a real interface, there is a minimum of reflectance. When any additional material is present at the water interface, however, the refractive index is altered slightly, and results in a large increase in reflected light compared to the clean interface. This allows, in many cases, for imaging of single-molecule thick films with relatively cheap and simple optics, and low exposure times (often milliseconds or seconds).

The simplest experimental configuration is shown in Figure 2.4, where a polarized laser illumination source is further polarized, and the reflected light is focused onto a CCD (or CMOS) detector to record the image. The advantage of these systems is that they are cheap and easy to build, requiring only a relatively stable laser, and a moderately sensitive CCD. A goniometer is generally used to match the angles of the two optical axes, and allows for fine tuning of the angle to minimize reflection from a

clean surface with relative ease. The optics used for focusing the light onto the CCD are generally microscope objectives, which work reasonably well for this purpose. The drawback to this system is that microscope objective lenses are designed to focus light in a plane perpendicular to the optical axis. This, combined with the tilt of the optical axis with respect to the imaging surface, results in images that have a narrow focused strip, with unfocused regions on either side. The area that is in focus generally decreases as the magnification of the objective increases.[13]
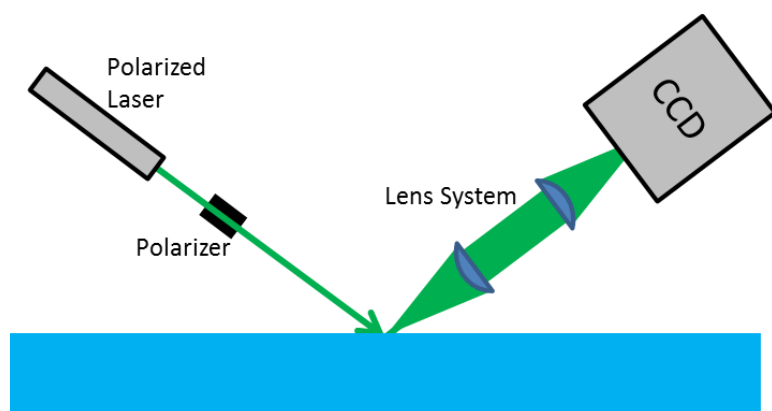
Figure 2.4: Schematic of a simple Brewster Angle Microscope design.

There are several ways to compensate for the tilted axis of the imaging surface relative to the optical axis. The first strategy is to build custom objective lenses, which is not simple, but can produce excellent results.[14,15] The second strategy is to correct the image prior to imaging, and this can be accomplished using a diffraction grating.[16] This strategy requires careful selection of the diffraction grating to match both the tilt angle and the wavelength of the light, but is cheap and relatively simple to do. It does, however, add another optical angle to adjust to the system, which can introduce more complexity to the design and alignment processes.

Several commercial BAM instruments exist that likely use one of these types of correction, but the majority of home-build BAM instruments are uncorrected. When analyzing data from uncorrected images, it is important to acknowledge the distortions that are present when analyzing domains, as the image is not only unfocused, but also stretched in one dimension. Software can be used to partially account for the distortion, but not the lack of focus. Even in these simple systems, BAMs remain useful instruments for monitoring changes to the domain morphologies under a variety of conditions, generally at the same time as other Langmuir trough experiments. BAM studies are described in Chapter 3.

2.5 Vesicle Formation

An in-depth discussion of vesicle formation procedures for DPPC appears in the introduction and methods subsections of Chapter 6.

2.6 Spectroscopy

Spectroscopy is the study of the interactions between light (of all wavelengths) and matter. Because it often relies of the microscopic details of molecules, the tools of quantum mechanics are necessary to accurately describe spectroscopic phenomena. Because of the dependence on the molecular details, spectroscopic studies can be used to learn about various aspects of molecules or mixtures of molecules under study. Absorption spectroscopies are among the more common variants, and rely on the simultaneous elimination of a photon and elevation of a molecule to an excited state. This process is isoergic, such that the energy of the eliminated photon equals the energy gained by the molecule. In order for an absorption process to occur, the transition moment must be non-zero. The transition moment, D, between states 2 and 1 is defined as

$$D_{21} = \int \Psi_2^* \vec{\mu} \Psi_1 d\tau$$

where Ψ_1 is the initial wavefunction, Ψ_2 is the excited wavefunction, and $\vec{\mu}$ is the transition moment operator and $d\tau$ indicates the integral is over all space. Analysis of this quantity is often difficult, but there are many situations where symmetry arguments can be made to identify the situations where this quantity is zero, and transitions are forbidden. To make these symmetry arguments, however, approximations often must be made. Because of this, classically forbidden transitions are often observed with low to moderate intensity, depending on the error induced by the approximation.

Absorption is not the only spectroscopic quantity of interest, but it also relates to emission processes through the Einstein coefficients. The Einstein coefficient for absorption, B_{12}, is proportional to the magnitude of the transition moment. Through thermodynamic and detail balance arguments, it can be shown that absorbing species must also be able to undergo stimulated emission. Stimulated emission

occurs when a photon of an energy that could be absorbed by a ground state molecule interacts with an excited state molecule and subsequently produces an identical photon and ground state molecule. The Einstein coefficients for absorption, B_{12}, and stimulated emission, B_{21}, are simply related by the number of degenerate excited, g_2, and ground, g_1, states, as:

$$\frac{B_{12}}{B_{21}} = \frac{g_2}{g_1}$$

As a consequence of stimulated emission, for systems with singly degenerate ground and excited states, it is impossible to place more than 50% of the molecules in the excited state by illumination. Additionally, if this system were at 50% excited state occupation, it would have no net absorption and appear transparent, due to absorption and stimulated emission occurring at the same rate.

These coefficients further relate to the rate of spontaneous emission by the equation

$$\frac{A_{21}}{B_{21}} = C\nu^3$$

where C is a constant and ν is the frequency of the emitted light. This necessitates that spontaneous emission occurs only for transitions where absorption can also occur (although sometimes it is not observed due to unpopulated states). It also shows that spontaneous emission occurs more quickly for higher energy states. These basic relationships hold for all types of spectroscopy discussed in the following sections, although the practical results are different for different regions of the electromagnetic spectrum due to the types of transitions that are involved.

2.6.1 Infrared Spectroscopy

Infrared (IR) spectroscopy has become a workhorse for chemical identification across many fields. It primarily examines molecular vibrational energy levels, which are often characteristic of certain molecules or functional groups within a molecule.[17] The vibrational states in a given molecule can be separated into orthogonal normal modes with distinct quantum energy levels available in each mode. In

addition to excitation of vibrational states, rotational states of much lower energy can be excited as well. Application of the transition moment equation, above, to vibrational and rotational initial and finals states yields several selection rules for allowed transitions, based on symmetry arguments. The first requirement for an allowed transition is that the vibrational level changes by ± 1. At room temperature, generally only the ground state vibrational mode is occupied, so typically the spectral signature is due to excitation of the first excited state. The second requirement is that the rotational quantum number changes by 0 or ± 1. Because rotational states are relatively low in energy, multiple rotational levels are generally occupied. This allows for transitions from each occupied rotational state, and produces characteristic branched shapes in IR spectra. Rotational levels are generally only observed for small gas phase molecules with permeant electric dipoles. Larger molecules have less energy difference between rotational states, and as a result the differences between rotations becomes smaller than the spectrometer resolution.

The most common type of IR spectroscopy utilizes light in the mid IR wavelength range of 4000-400 cm^{-1} (2,500-25,000 nm). Common laboratory instruments utilize an interferometer and a broadband lightsource to generate a beam of IR light in which the contained frequencies are modulated as a function of time. In order to convert this from the time domain to the frequency domain (and thereby wavelength or energy), a Fast Fourier Transform (FFT) computer algorithm is employed. This technique allows for higher signal to noise and faster acquisition of spectra compared to more intuitive single wavelength (dispersive) absorption methods. This instrument configuration is described as a Fourier Transform Infrared Spectrometer (FTIR). FTIR data is often reported as either percent transmittance (%T) or absorption (A), described as:

$$\%T = \frac{I}{I_0} \quad A = -Log(\%T)$$

Where I is the light intensity passing through the sample, and I_0 is the light intensity passing through a blank.

Because different molecules have different normal modes and rotational energy spacings, IR spectra are well suited to identifying many molecules. Identifications can be made by comparisons to spectra of pure substances. Additionally, some insight can be gained into unknown molecules based on the regions in which absorption occurs. In the local mode approximation, the normal modes responsible for vibrational signatures are approximated by the vibrations of a single functional group. For example, carbonyl functional groups generally produce strong, sharp absorption features in the 1700-1750 cm^{-1} region of the spectrum. This approach works reasonably well for some molecules and some functional groups, but is never fool-proof. In this dissertation, UV-visible spectroscopy is utilized several times, and is one of the main focuses of Chapter 7.

2.6.2 UV-Visible Spectroscopy

The visible and ultraviolet (UV) regions of the electromagnetic spectrum are higher in energy than the IR region. This allows for the excitation of electronic transitions. Electronic transitions can also be accompanied by changes in both vibrational and rotational states, which makes the selection rules significantly more complicated. The selection rules do require, however, that the total spin state is preserved, and that the total orbital angular momentum changes by 0 or ±1. The total angular momentum is difficult to analyze intuitively, but can be useful when combined with the symmetry arguments for individual molecules to gain insight into expected transitions.

Because of the relaxed selection rules, electronic transitions can result in changes or more than one quantum of vibrational energy. The probability of a given vibrational transition occurring alongside an electronic transition can be found based on Franck-Condon factors. These factors are simply the overlap between the vibrational wavefunctions in the ground and excited states, and can be expressed as:

$$C_{FC} = \int \Psi_{V2}^* \Psi_{V1} d\tau$$

Predicting excited states relies on having some knowledge of the underlying electronic structure of a molecule. For simple molecules, this can often be predicted from a simple molecular orbital framework.

For larger molecules, there are several trends that can be useful. Excited electronic states are often due to localized functional groups, such as n → π* or π → π* transitions in double bonded carbonyls or C=C bonds. They are also frequently due to conjugated systems, however, where π electrons are delocalized across many atoms. At higher UV energies even simple, single bonded systems begin to absorb, such as water which absorbs starting around 185 nm.[18]

UV-visible spectroscopy ultimately provides information about the electronic structure of a molecule. In some cases it also provides information about the vibrational and rotational properties as well. The observation that some functional groups often absorb light can be helpful in identifying and predicting absorption spectra of molecules. As an analytical tool, UV-visible spectroscopy is more limited in its applications, due to the fact that many molecules will not absorb across the used wavelength range, but this can be advantageous if it limits signals from contaminants and solvents. In this dissertation, UV-visible spectroscopy is utilized several times, and is one of the main focuses of Chapter 7.

2.6.3 Fluorescence Spectroscopy

Fluorescence is results when excited molecular state relaxes, and produces a photon in the process. In practice, fluorescence spectroscopies depend on the absorption of light to generate excited state molecules. Because of this, and considerations of excited state dynamics, fluorescence spectroscopies can become considerably more complex than absorption ones. A diagram of likely transitions in a fluorescent experiment is shown in Figure 2.5.

S₁

S_1

S_0

v=2

v=1

v=0

v=2

v=1

v=0

Energy

Q_{vib}
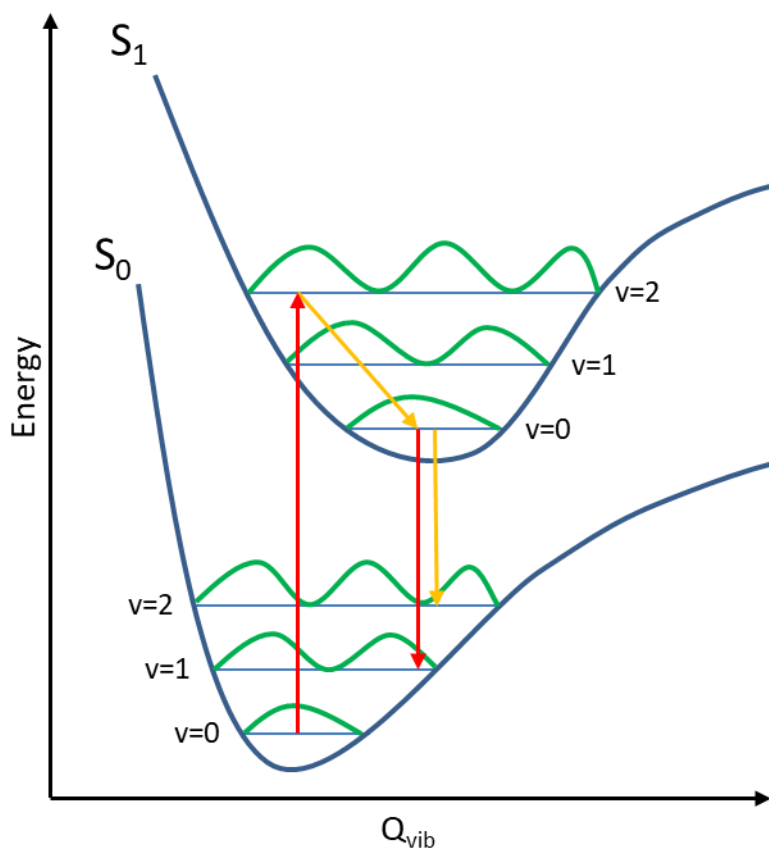
Figure 2.5: Diagram of molecular processes that lead to fluorescence. Blue curves indicate potential energy as a function of reaction coordinate for the ground (S_0) and excited (S_1) electronic states. Blue lines indicate vibrational states, and are labeled with their vibrational quantum numbers, v. Green curves indicate probability distributions for the underlying vibrational. Red lines indicate absorption (left) and emission (right) of light. Yellow lines indicate non-radiative process that release energy thermally to the surrounding bath.

The first process leading up to fluorescence is the creation of an excited state molecule, which is often accomplished by the absorption of light. The electronically excited molecule is generally created in an excited vibrational state, governed the Franck-Condon factors for the system. This initial excited state is capable of fluorescing (as shown by the Einstein coefficients), in many situations it will vibrationally relax on a timescale that is faster than fluorescence. This relaxation process, known as internal conversion (IC), transfers energy to surrounding molecules in the form of heat. The emission of light that occurs afterwards will also generally produce a ground electronic state molecule in an excited vibrational state, again due to Franck-Condon factors. The loss of vibrational energy on both sides of the emission transition results in emitted light being of lower energy (and higher wavelength) compared to the absorption transition. This is known as a Stokes shift. Relatively high Stokes shifts can be useful for fluorescence measurements, because the fluorescence signal has less overlap with the absorption spectrum of the fluorophore. This also allows for higher sensitivity measurements compared with absorption techniques; it is easier to detect a small increase over a small or zero baseline in fluorescence, compared to a small decrease from a large signal in absorption.

Molecules in excited states will not always produce fluorescence. Other processes occur from the excited state that lead to its relaxation, such as energy transfer or chemical reaction. One process that is very common is intersystem crossing (ISC), where the excited electronic state molecule transitions to a ground electronic state configuration that has a high level of vibrational energy. This is generally followed by IC to produce an equilibrium, ground state molecule. All of these processes will compete with fluorescence, and reduce the relative yield of fluorescence based on the relative rates between the processes. The relative yield of fluorescence is often expressed as a quantum yield, as

$$\Phi_R = \frac{k_R}{k_R + k_{NR}}$$

where Φ_R is the radiative (fluorescent) quantum yield, k_R is the radiative decay rate, and k_{NR} is the effective non-radiative decay rate. This is an internal quantum yield, contrasting an external quantum yield which would need to account for the absorption process as well.

High fluorescence quantum yields are desirable in fluorescent probes for several reasons. First, they are easier to detect, because more photons will be produced for a given intensity of excitation. Second, photochemistry is among the non-radiative processes, and will often alter the fluorescent molecule to the point it no longer fluoresces. This is known as photobleaching, and reduces the fluorescence intensity over time, dependent on the intensity of illumination.

Fluorescent assays that utilize the change in quantum yield as a function of conditions are described in Chapters 5 and 6. With proper calibration, they allow for probing the conditions of a fluorophore based on the fluorescent signal.

2.6.4 Nuclear Magnetic Resonance Spectroscopy

Nuclear Magnetic Resonance Spectroscopy (NMR) is an extremely powerful analytical tool for many different situations. It relies on fundamental interactions between magnetic fields and spin states of atomic nuclei. Protons and neutrons both have quantum spin states which describe the angular momentum

associated with them. This angular momentum combined with the fact that these particles are charged, or in the case of neutrons composite of charged sub-atomic particles, results in generation of magnetic moments. In the absence of external fields, these magnetic moments are degenerate in energy. NMR instruments utilize large magnetic fields to break the degeneracy in the spin states of atomic nuclei. This creates an energy difference between molecular spins oriented with or against the magnetic field of the instrument, and allows for the absorption and emission of low (radio) frequency light from these states.

The overall spin state of the atomic nucleus determines the reaction to the NMR field. So long as the overall spin is not zero, the nucleus will interact and absorb radiation. The region of the spectrum where absorption occurs will generally be nucleus dependent however, so signals from different nuclei are often probed separately. Most elements have NMR-active isotopes that can be used, including, but not limited to, ^{1}H, ^{2}H, ^{13}C, ^{14}N, ^{17}O, ^{19}F, ^{31}P, ^{33}S, etc. In all of these cases, the response is dictated by three things: the magnitude of the external magnetic field, the nucleus being probed, and the local chemical environment of that nucleus. In order to make NMR spectra comparable between instruments of different field strengths, data is usually presented in terms of intensity versus a quantity known as chemical shift. Chemical shift, δ, in units of parts per million (ppm) is defined as

$$\delta = \frac{\nu_{sample} - \nu_{ref}}{\nu_{ref}} \; x \; 10^6$$

where ν_{sample} is the observed frequency of the sample peak, and ν_{ref} is the observed frequency of the reference compound, with different reference compounds chosen for different nuclei.

The chemical shift of a given nucleus, then, will vary only with changes in the local chemical environment. A large part of the chemical shift comes from magnetic fields that are induced when electrons are exposed to a magnetic field. This results in larger (downfield) chemical shifts for atoms that have less electron density, and smaller (upfield) chemical shifts for atoms that have higher electron density. The amount of electron density in a given position can be predicted qualitatively based on the

electronegativity of nearby substituents. The other effect that gives rise to changes in chemical shift in NMR is coupling between different nuclei. This coupling comes in many different varieties, and can either occur through space, or through nearby chemical bonds. Through-bond couplings can be very useful in ^{1}H NMR for identifying molecules due to characteristic splitting patterns.

While it is simpler to explain the fundamentals of NMR as though absorption of light were detected, as conventional spectrometers often work, the actual detection process in modern instruments is more complicated, but more sensitive and specific. The energy differences between spin states are small, even in the high external field of the NMR. This means that for room temperature samples, many nuclei exist in excited spin states due to thermal energy. If a standard absorption experiment were attempted, the ground spin state nuclei would quickly be excited, and a 50% excited state composition would be reached, resulting in equal amounts of absorption and stimulated emission, and consequently transparent samples. In order to avoid this problem, pulsed experiments have been developed utilizing the advantages of Fourier transform detection, as described for IR spectrometers, and detection of emission, as described for fluorescence spectroscopy.

In modern instruments, broadband radio frequency pulses, of defined length and phase, are applied to the sample to induce an out-of-equilibrium magnetization of the sample. This magnetization then slowly decays back to equilibrium, and the decay of this induced magnetization is monitored by emission from the sample over time. The raw data is known as a free induction decay (FID). The FID has two components, resulting from different phases in the emitted radio frequency light. The FID can be processed via a Fourier Transform in order to generate a frequency domain spectrum, and referenced to create a spectrum in terms of chemical shift. This excitation/detection technique is advantageous due to higher sensitivity and faster acquisition, but also due to a much broader range of experimental control. Using different series of excitation pulses, modifying pulse frequency, phase, and timing, highly selective and multi-dimension experiments can be performed. This allows for techniques such as correlation

experiments monitoring coupling between specific nuclei, which is useful for identifying unknown molecules, or suppressing solvent peaks, which allows for detection of comparatively small signals.[19]

Water suppression is employed throughout this dissertation for all aqueous NMR spectra involving ^{1}H nuclei. Complete details for this technique are addressed elsewhere,[20] but in essence a series of pulses is used to place the ^{1}H nuclei associated with water out-of-equilibrium in a manner that is orthogonal to the rest of the sample, and subsequently remove >99% of the water signal from the collected spectra. Simpler one dimensional NMR spectra utilizing solvent suppression are described in Chapters 5 and 8-10. Solvent suppression pulse sequences are appended to other 2D experiments involving ^{1}H and aqueous samples as well. Correlation spectroscopies are described in Chapter 8 that allow for an unambiguous identification of a mixture of molecules in solution. The first of these correlation spectroscopies is gradient homonuclear correlation spectroscopy (gCOSY) which observes the transfer of excitations from one nucleus to another of the same time (e.x. ^{1}H). Because the excitation transfer generally occurs through chemical bonds in COSY, this allows for the assignment of nuclei to the same molecule. Similar techniques known as heteronuclear single quantum coherence spectroscopy (HSQC) and heteronuclear multiple bond coherence spectroscopy (HMBC) monitor excitation transfers between different nucleus types (often ^{1}H to ^{13}C) through only one, or one or more chemical bonds, respectively.

2.7 Mass Spectrometry

Mass spectrometry (MS) has become an increasingly powerful tool for the identification and analysis of a number of different samples. Several excellent reviews exist on the subject; the work of Cech and Enke[21] is particularly helpful due to the level of detail on electrospray ionization mass spec, one of the more commonly used variants. Mass spec relies on the movement and detection of charged particles under the effects of an electric field. First, analyte molecules are ionized, through one of an ever expanding list of ionization techniques. Next, analyte ions are separated based on their mass to charge ratio (M/Z) in a mass analyzer, before finally being detected.

Mass analyzers come in many different forms, but operate on similar principles. Once a charged, isolated analyte enters, an electric field is applied. The electric field accelerates the analyte in a way that is dependent on the M/Z ratio of the analyte. Because differences in acceleration under an applied force are the basis for mass analysis, analyte ions must undergo ballistic motion. Because of this, it is generally required that they are operated under relatively high vacuum conditions. In turn, this places the requirement that the ionization technique must produce analyte ions in the gas phase. There are many different schemes for achieving this, but one of the most common techniques for small molecules, and the technique used in the following chapters, is electrospray ionization (ESI). Electrospray ionization involves the ejection of fluid through a small, charged capillary. Ions of similar charge to the capillary walls are repelled. Near the tip of the capillary, this repulsion forces ions to the liquid surface, and subsequently lowers the surface tension. As the surface tension approaches zero, droplets are spontaneously formed and ejected from the surface. Because these droplets were formed in the surface region, where the species of like charge to the capillary wall were forced, they are enriched in charged ions and carry an overall charge. Under proper conditions the solvent will evaporate from the charged droplets to generate individual charged molecules that are passed into the mass analyzer of the MS.

There are several important properties of a molecule that will affect how well it is ionized in the ESI process. Perhaps the most important is the ionization energy of the analyte. This is particularly important in mixed solutions, where ions with higher ionization energies will often transfer charge to analytes that are more easily ionized. Another important property is surface activity. Because the droplets that go on to form free ions are created in the interfacial region, molecules with a propensity to accumulate at the interface tend to produce ions more readily. Exact ionization conditions can be very important as well, with some ionization conditions favoring a given analyte. Because of all of these complex, and difficult to predict, factors, ESI MS, and most other MS techniques, are not inherently quantitative. In order to properly quantify MS data, calibration curves must be constructed. Even then, response is very likely to change when analyzing mixtures of molecules.

MS measurements are particularly useful due to their high achievable mass resolutions. Ions of very similar masses can often be distinguished, based on the mass defect intrinsic to different elements and different isotopes. Because of this, it is often possible to uniquely identify chemical formulas for observed MS signals. This can be very helpful for making positive identifications of products in solution. However, the lack of MS signal of a given product generally does not prove it does not exist in solution. MS experiments appear in Chapter 5 briefly, and more extensively in Chapters 9 and 10.

Bibliography

(1)   Pockels, A. On the Relative Conamination of the Water-Surface by Equal Quantities of Different Substances. *Nature* **1892**, No. 46, 418–419.

(2)   Langmuir, I. THE CONSTITUTION AND FUNDAMENTAL PROPERTIES OF SOLIDS AND LIQUIDS. II. LIQUIDS.1. *J. Am. Chem. Soc.* **1917**, *39* (9), 1848–1906.

(3)   Blodgett, K. B. Films Built by Depositing Successive Monomolecular Layers on a Solid Surface. *J. Am. Chem. Soc.* **1935**, *57* (6), 1007–1022.

(4)   du Noüy, P. L. A NEW APPARATUS FOR MEASURING SURFACE TENSION. *J. Gen. Physiol.* **1919**, *1* (5), 521–524.

(5)   Gibbs, J. W.; Bumstead, H. A.; Name, R. G. V. *Thermodynamics*; Longmans, Green and Company, 1906.

(6)   Guggenheim, E. A. Statistical Thermodynamics of the Surface of a Regular Solution. *Trans. Faraday Soc.* **1945**, *41* (0), 150–156.

(7)   Guggenheim, E. A.; Adam, N. K. The Thermodynamics of Adsorption at the Surface of Solutions. *Proc. R. Soc. Lond. Math. Phys. Eng. Sci.* **1933**, *139* (837), 218–236.

(8)   Motomura, K. Thermodynamics of Multicomponent Monolayers. I. General Formulation. *J. Colloid Interface Sci.* **1974**, *48* (2), 307–318.

(9)   Motomura, K.; Yoshino, S.; Fujii, K.; Matuura, R. Thermodynamics of Multicomponent Monolayers. *J. Colloid Interface Sci.* **1977**, *60* (1), 87–95.

(10)   Motomura, K.; Hayami, Y.; Aratono, M.; Matuura, R. Thermodynamics of Multicomponent Monolayers: IV. Monolayer Penetration. *J. Colloid Interface Sci.* **1982**, *87* (2), 333–338.

(11)   Hénon, S.; Meunier, J. Microscope at the Brewster Angle: Direct Observation of First-order Phase Transitions in Monolayers. *Rev. Sci. Instrum.* **1991**, *62* (4), 936–939.

(12)   Hoenig, D.; Moebius, D. Direct Visualization of Monolayers at the Air-Water Interface by Brewster Angle Microscopy. *J. Phys. Chem.* **1991**, *95* (12), 4590–4592.

(13)   Cohen Stuart, M. A.; Wegh, R. A. J.; Kroon, J. M.; Sudhölter, E. J. R. Design and Testing of a Low-Cost and Compact Brewster Angle Microscope. *Langmuir* **1996**, *12* (11), 2863–2865.

(14)   Meunier, J. Why a Brewster Angle Microscope? *Colloids Surf. Physicochem. Eng. Asp.* **2000**, *171* (1–3), 33–40.

(15)   Lheveder, C.; Hénon, S.; Mercier, R.; Tissot, G.; Fournet, P.; Meunier, J. A New Brewster Angle Microscope. *Rev. Sci. Instrum.* **1998**, *69* (3), 1446–1450.

(16)   Chastang, J. C. Oblique Viewing Attachment For Microscope. *Proc. SPIE* **1983**, *399*, 239–245.

(17)   Wilson Jr., E. B.; Decius, J. C.; Cross, P. C. *Molecular Vibrations: The Theory of Infrared and Raman Vibrational Spectra*, Revised ed. edition.; Dover Publications: New York, 1980.

(18)   Gürtler, P.; Saile, V.; Koch, E. E. Rydberg Series in the Absorption Spectra of H2O and D2O in the Vacuum Ultraviolet. *Chem. Phys. Lett.* **1977**, *51* (2), 386–391.

(19)   Giraudeau, P.; Silvestre, V.; Akoka, S. Optimizing Water Suppression for Quantitative NMR-Based Metabolomics: A Tutorial Review. *Metabolomics* **2015**, *11* (5), 1041–1055.

(20)   Ogg, R. J.; Kingsley, P. B.; Taylor, J. S. WET, a T1- and B1-Insensitive Water-Suppression Method for in Vivo Localized 1H NMR Spectroscopy. *J. Magn. Reson. B* **1994**, *104* (1), 1–10.

(21)   Cech, N. B.; Enke, C. G. Practical Implications of Some Recent Studies in Electrospray Ionization Fundamentals. *Mass Spectrom. Rev.* **2001**, *20* (6), 362–387.

Chapter 3: Interaction of L-Phenylalanine with a Phospholipid Monolayer at the Water–Air Interface

This chapter is adapted with permission from: Griffith, E. C.; Perkins, R. J.; Telesford, D.-M.; Adams, E. M.; Cwiklik, L.; Allen, H. C.; Roeselová, M.; Vaida, V. Interaction of L-Phenylalanine with a Phospholipid Monolayer at the Water–Air Interface. *J. Phys. Chem. B* **2015**, *119* (29), 9038–9048. Copyright 2015 American Chemical Society. The original article can be accessed at http://pubs.acs.org/doi/abs/10.1021/jp508473w.

3.1 Introduction

Aromatic residues serve many purposes throughout modern biology[1-2] ranging from playing key roles in membrane channel gating functions[3-4] to the formation of deleterious amyloid structures[5-6]. Phenylalanine residues in particular have been identified as a key component in the formation of amyloid structures.[7] In general, phenylalanine (Phe) is a unique molecule in terms of its propensity for self-assembly. Short peptides solely composed of phenylalanine (e.g. Phe-Phe) are known to self-assemble into ordered nanostructures in water.[8] Further, the monomer amino acid has recently been suggested to self-assemble into amyloid-like fibrils that are proposed to play a role in cytotoxicity relevant to phenylketonuria (PKU) disease.[9-10] On the other hand, the process of polypeptide fibrillization was shown to be modulated by lipid-peptide interactions and to be able to disturb membrane function.[11-12]

Despite the vast knowledge currently being amassed on the many functions of aromatic residues, and even single aromatic amino acids, it is still quite difficult to obtain molecular-level information on the cause and mechanism of these functions. To aid in the molecular-level description of interactions involving biological lipid membranes, the simplified model system of a monolayer at the air-water interface is often used rather than the bilayer structure found in natural biological systems.[13-19] Despite being a model system (neglecting for instance, the presence of proteins, membrane asymmetry and curvature effects), monolayers have the same lipid – water interface present in bilayer systems and thus allow for exploration of perturbations to the membrane caused by changes in the aqueous phase

composition or penetration of various compounds into the lipid phase. In addition, using a monolayer rather than a bilayer has many advantages, allowing for a greater ease in control of both experimental and simulation conditions.[20-21] Here, a DPPC monolayer is used as a model system to explore the interactions of Phe with a phospholipid membrane, in order to gain molecular-level information not traditionally available to more phenomenological molecular biology studies. DPPC (1,2-Dipalmitoyl-*sn*-glycero-3-phosphocholine) was chosen as it is one of the best experimentally and computationally characterized lipids that is also biologically relevant (phosphatidylcholines are the major class of lipids found in mammalian cell membranes and DPPC itself is the main lipid component of lung surfactants).[21-26]

The interactions between interfacial molecules with varying hydrophobic structure are important in wide ranging fields, from atmospheric chemistry to biological and medicinal chemistry.[14-17, 19, 27-32] In previous work, aromatic soluble surfactants (L-phenylalanine (Phe), benzoic acid, and benzaldehyde) have been shown to affect surface morphology and even to disrupt the stability of a monolayer of insoluble fatty acid surfactant (stearic acid) at the water-air interface depending on the headgroup structure of the aromatic species.[28-29] Among the aromatic species explored, Phe caused complete destabilization of the fatty acid film,[28] whereas benzoic acid and benzaldehyde[29] exhibited only evidence of interaction and small modification of the fatty acid monolayer at the water surface. In this work, the interaction of Phe with a phospholipid (DPPC) monolayer at the air-water interface is explored with complementary information obtained through experiment, using Langmuir trough methods and Brewster Angle Microscopy (BAM), and through Molecular Dynamics (MD) simulations. In addition, the aggregation of L-phenylalanine in the bulk aqueous phase is studied using confocal microscopy.

The recent work by Adler-Abramovich et al.[9] is intriguing in this context. They reported the self-assembly of Phe monomers into long fibrils that were subsequently observed to be cytotoxic, even resulting in misshapen membranes for the remaining viable cells. This effect is very important in understanding the cause of the phenylketonuria disease (PKU), characterized by an inability to process ingested phenylalanine. However, no mechanistic insight into this cytotoxicity has been obtained to date

beyond the assertion of the apparent similarity to amyloid structures. Thus, the aim of this work is to gain insight into the molecular-level interactions of Phe with a model phospholipid – water interface, characteristic of cell membranes. This will aid in not only understanding the mechanism of the cytotoxicity of Phe in PKU disease, but also in the interactions of other Phe-rich aggregates found in biology with cell membranes.

3.2 Materials and Methods

All materials were purchased and used without further purification. L-phenylalanine was purchased from Alfa Aesar (99%) and was dissolved in DI water to a final concentration of 2.5 mM for the pre-equilibrated subphase experiments and 115 mM for the injection experiments (pre-equilibrated DPPC monolayer experiments, see below). The pH of DI water was measured at 5.5, indicating the zwitterionic state of Phe would dominate in bulk solution as well as near the air – water interface in the absence of DPPC.[33] The solution was prepared fresh for each experiment. It is important to note that there was a difference found in the purity of commercial L-phenylalanine that affected the rate of adsorption to the surface. However, the overall effects observed remained consistent. 1,2-Dipalmitoyl-*sn*-glycero-3-phosphocholine (DPPC, >99%, purchased from Sigma-Aldrich for Langmuir trough experiments and purchased from Avanti, Lot# 223938, for the BAM experiments) was dissolved in chloroform (ACS grade, Mallinckrodt Baker, Inc.) to a final concentration of 1.6 mg/ml, to be deposited dropwise onto the aqueous subphase in the Langmuir trough in the subsequent experiments.

Two different experiments were performed using the Langmuir trough and Brewster Angle Microscope (BAM): one with a pre-equilibrated subphase containing Phe and one with a pre-equilibrated DPPC monolayer. In the pre-equilibrated subphase experiment, a 2.5 mM solution of Phe was prepared and spread on the Langmuir trough. Then, DPPC was deposited at a molecular area of 70 Å^2/molecule on the equilibrated subphase. In the pre-equilibrated DPPC monolayer experiments, DPPC was deposited dropwise on a neat water surface to a molecular area of 70 Å^2/molecule, allowing DPPC to form a stable

monolayer. Then, 2 mL of the 115 mM solution of Phe (in the small Langmuir trough described in the BAM experiments) was slowly injected beneath the DPPC-covered water surface.

3.2.1 Langmuir Trough

Langmuir trough methods were used to monitor and characterize the phase behavior of the mixed film system. The Langmuir trough used was custom-built (52 x 7 x 0.5 cm), consisting of a PTFE trough as well as two PTFE barriers controlled by software purchased from NIMA (KSV-NIMA, Finland). This trough was coupled to a Wilhelmy balance used to measure surface pressure (π), i.e. decrease in surface tension. By moving the PTFE barriers, surface pressure – area ($\pi - A$) isotherms can be produced, or the barriers can be held stationary to record surface pressure – time adsorption isotherms. These isotherms yield surface thermodynamic information allowing for the monitoring of changes in the phase behavior of the surfactant of interest (DPPC) in the presence of a perturbant (Phe).

3.2.2 Brewster Angle Microscopy (BAM)

BAM is a useful tool to visualize morphological changes on a microscopic scale (approximately 500x500 μm^2 image size) at the water surface.[34-35] BAM images were collected by illuminating the water surface in the Langmuir trough (8.34 x 16.90 cm) at the Brewster angle of water (53°) and magnifying the reflected image before collection with a camera. The illumination source was a 5 mW polarized 543 nm laser (Research Electro-Optics), which passed through a half-wave plate and Glan-Thompson polarizer for attenuation and p-polarization relative to the water surface. The reflection was magnified using a Nikon 10x infinity corrected super long working distance objective, and corresponding tube lens. The camera was a back illuminated electron multiplying CCD (Andor iXon model DV887-BV, 512x512 pixels). BAM images were obtained every 5 minutes.

3.2.3 Microscopy

Confocal microscope images were taken of 120 mM Phe dyed with 0.2 mM Thioflavin T (ThT) using a Nikon A1R confocal microscope with a 100x (NA 1.45) Plan Apochromatic objective. The sample was prepared by adding 100 μL of 40 mM ThT dye to a 20 mL volume of Phe, then depositing a

10-20 μL drop on a pre-cleaned glass coverslip prior to illumination with a 457.9 nm laser. Emission from the sample was filtered with a 482/35 nm band pass filter prior to collection with an iXon X3 EMCCD.

3.2.4 Molecular Dynamics (MD) Simulations

Classical MD simulations were performed for three different systems, all of them composed of two monolayers of DPPC (64 molecules each), one on either side of an aqueous slab, placed in the middle of a 6.69 x 6.69 x 28 nm^3 simulation box. Periodic boundary conditions were used in all directions. The thickness of the entire slab system (including the two DPPC monolayers) was approximately 7 nm, leaving about 21 nm of vacuum between the periodic images in the z direction normal to the aqueous–DPPC interface. In the three systems simulated, the aqueous slab was composed of water, water containing zwitterionic Phe, and water containing neutral Phe molecules. Although Phe does exist in its zwitterionic form in aqueous solution at physiologically relevant pH values, it could transition to its neutral form in the relatively non-polar core of the phospholipid bilayer as has been seen with other membrane-perturbing molecules.[36-37] Phe itself has been seen to alter its ionization state at the air-water interface[33], allowing for the possibility of its alteration at the membrane interface. Thus, both situations (i.e., zwitterionic as well as neutral Phe) were simulated and subsequently analyzed. Each system is described in more detail below.

DPPC monolayer on water: The system consisted of two monolayers of DPPC (64 molecules each) solvated with a slab containing 6876 water molecules. Standard DPPC force field parameters were obtained from http://people.su.se/~jjm/Stockholm_Lipids/Downloads_files/DPPC.itp, with many parameters coming from CHARMM36. The system was created based on a previously equilibrated (50 ns, NPT ensemble, p=1 bar, T=310 K) lipid bilayer of 128 DPPC molecules (64 in each leaflet) applying the following procedure. The size of the periodic box used in the bilayer-water simulation was increased three-fold in the direction of the bilayer normal. Then, the two lipid leaflets with their hydrating water layers were rearranged by translating them along the bilayer normal to create two

monolayers, each at one surface of a water slab. The resulting system was equilibrated for 10 ns in the NVT ensemble at T=310 K. Then the negative lateral pressure (-25 bar) was employed in the NPT ensemble in a short (below 1 ns) simulation in order to laterally decompress the system and hence to obtain the desired area per lipid of 70 $Å^2$/molecule. The resulting simulation box had the dimensions of 6.69 x 6.69 x 28.0 nm^3. The system was further equilibrated in the NVT ensemble for 50 ns at T=310 K. This was followed by a 50 ns-long trajectory that was used for analysis.

Zwitterionic Phe/DPPC system: The initial DPPC monolayer configuration was taken from the equilibrated configuration described in the previous section. The aqueous slab containing 20 zwitterionic Phe molecules distributed randomly and solvated with water molecules was then inserted between the two hydrated DPPC monolayers (insertion procedure described in more detail in Appendix 1), resulting in the total of 5531 water molecules in the system. This corresponds to the initial Phe concentration of 200 mM in the aqueous solution slab separating the two DPPC monolayers. A short energy minimization was first run, after which the newly created system was equilibrated for 10 ns in the NVT ensemble at T=310 K and then propagated for 100 ns (see below). After completion of the 100ns production run, most Phe molecules had partitioned into the interfacial regions, depleting the bulk aqueous phase only leaving approximately 5-10% of the initial Phe molecules in the aqueous phase. Thus, a second simulation (100 ns) was performed with 15 additional molecules of zwitterionic Phe added to the interior of the aqueous slab (following the same insertion procedure described for the initial insertion of Phe) to more closely mimic the experimental conditions in which a near continuous supply of monomers to the interfacial region is provided from the macroscopic bulk phase. The last 50 ns of each of the two simulations (with 20 Phe and 35 Phe molecules) was used for analysis.

Neutral Phe/DPPC system: The system was prepared following the same procedure as for the zwitterionic Phe/DPPC system, with the initial DPPC monolayer configuration again taken from the equilibrated configuration described above. The final composition of the aqueous portion of the system was 20 neutral Phe molecules distributed randomly and solvated with 5613 water molecules between the

DPPC monolayers. This corresponds to an initial concentration of 198 mM Phe in the aqueous phase of the system. As in the previous case, a short energy minimization was first run followed by a 10ns equilibration period. Then a 100ns production run was completed of which the last 50 ns were used for analysis.

All simulations were performed in the isochoric-isothermal (NVT) ensemble at the temperature of 310 K. The Nosé-Hoover thermostat[38-39] with a time constant of 0.5 ps was used for temperature control. Equations of motion were integrated utilizing the leap-frog algorithm[40] with a timestep of 2 fs, with snapshots saved every 10ps. A cut-off distance of 1 nm was used for the Lennard-Jones and the short-range part of the electrostatic interactions, the long-range part of the electrostatic interaction was treated using the particle-mesh Ewald scheme.[41]. All bond lengths were constrained using the LINCS algorithm[42]. Simulations were run and analyzed using GROMACS version 4.6.3[43] and were visualized using VMD[44].

The SLipids force field[45-46] was used for the DPPC molecules, while the TIP3P model was employed for water molecules (TIP3P is the default water model for SLipids). Phe molecules were modeled using the Amber ff03[47-48] force field. The atomic partial charges of both zwitterionic and neutral form of Phe were calculated by geometry optimization at the B3LYP/cc-pVTZ level of theory followed by RESP (restrained electrostatic potential) fitting.[49] For zwitterionic Phe, the geometry optimization was carried out including implicit solvation using the PCM (polarizable continuum model).[50] All ab initio calculations were conducted using the Gaussian09 package,[51] and the RESP calculations were performed by Antechamber.[52] The atomic types and charges of both zwitterionic and neutral Phe are given in Tables A1.1 and A1.2 of the Appendix 1. Molecular structures of Phe and DPPC with numbering of atoms are shown in Figure 3.1. The topology files containing all force field parameters used in this work are also available in the Appendix 1.
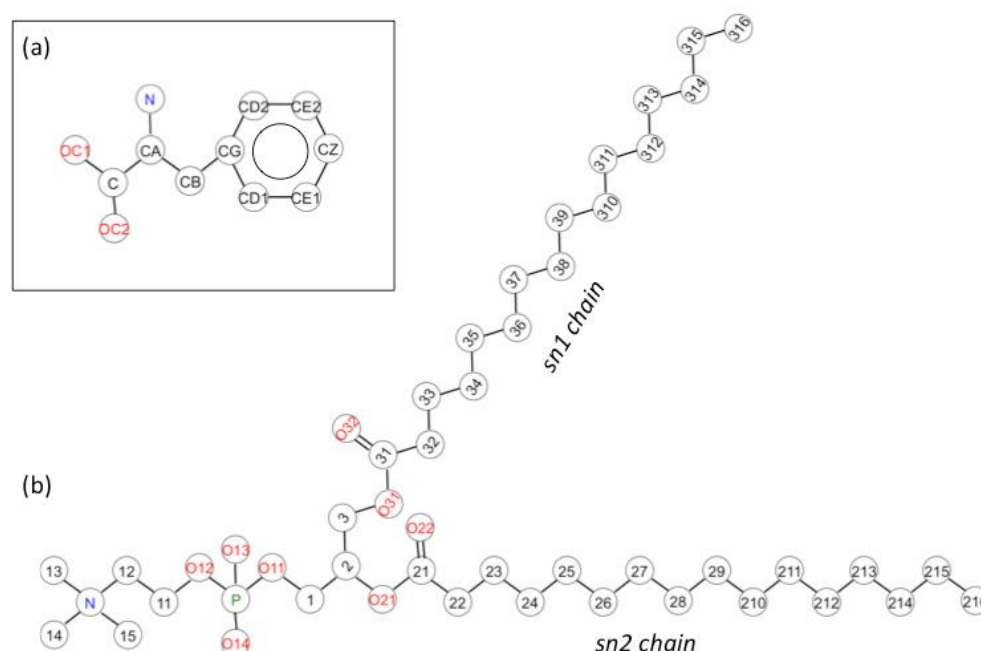
Figure 3.1: Molecular structure with numbering of atoms of (a) L-phenylalanine and (b) DPPC used in the MD simulation and analysis. The carbon atoms in the DPPC molecule are shown with numbers only, all hydrogen atoms are removed for clarity.

3.3 Results and Discussion

In the following, both experimental and MD simulation results are presented for the system composed of L-phenylalanine (Phe) dissolved in water in the presence of a DPPC monomolecular surface film. In classical PKU, blood Phe concentrations exceed 1.2 mM and prolonged exposure is associated with growth defects, seizures, and intellectual impairment.[53] The concentrations of Phe used in the following experiments were 2.5 mM in order to mimic the damaging disease state, or higher when no effect was observed at low concentration. Langmuir trough methods and Brewster Angle Microscopy (BAM) were used to explore the effect of Phe on the phase behavior of DPPC at a molecular area representative of cell membranes (70 Å^2/molecule).[54] Confocal microscopy was then used to explore the aggregation state of Phe in solution. In addition, MD simulations were used to gain insight into the interactions between the Phe molecules and the DPPC film, as well as the effect of the intercalation of Phe on the DPPC film itself.

3.3.1 Influence of L-Phenylalanine on Surface Tension

The red curve in the inset of Figure 2 shows the adsorption of Phe to a bare aqueous – air interface manifested as a mild increase of surface pressure over time measured for 2.5 mM Phe solution. In contrast, when DPPC was deposited on a subphase of aqueous Phe (2.5 mM) at the molecular area of 70 Å^2/molecule, there was a significant rise in surface pressure over time (black curve, inset of Figure 3.2), indicative of a much stronger adsorption of Phe to the DPPC-covered interfacial region.[28] Of some interest is the long timescale observed for the saturation of the interface, suggesting that a process other than simple diffusive equilibration is important. Once saturation of the interfacial region was reached for the DPPC coated interface (indicated by a constant surface pressure), a pressure-area (π – A) compression isotherm was obtained (black curve, Figure 3.2). When compared with a π – A isotherm of DPPC deposited on a neat water subphase (blue curve, Figure 3.2), exhibiting the well-known phase changes of DPPC monolayers at the water surface[26], it is apparent that there is a change in the phase behavior of DPPC due to the presence of Phe. In the case of the DPPC film on pure water, the π – A isotherm was measured starting from large molecular area corresponding to the liquid expanded – gas coexistence region of the DPPC monolayer. Upon compression, the film transitions to a liquid expanded (LE) phase around 100 Å^2/molecule. Then, the plateau between 80 and 60 Å^2/molecule indicates the liquid expanded – liquid condensed (LE – LC) coexistence region, the region representative of the phase experienced by phospholipids in cell membranes.[54] Finally, the film transitions to a pure liquid condensed (LC) phase around 55 Å^2/molecule. For the DPPC film on the Phe solution subphase, however, an increased equilibrium surface pressure is measured (~25 mN/m (after Phe adsorption) compared to ~6 mN/m for DPPC on the water subphase), indicating perturbation to the LE – LC coexistence region of the DPPC film. This is followed by transition to the LC phase at ~48 Å^2/molecule. The increase in surface pressure of the DPPC film on Phe solution subphase with respect to water subphase in the region between 70 and 48 Å^2/molecule is attributed to the presence of Phe in the interfacial region.
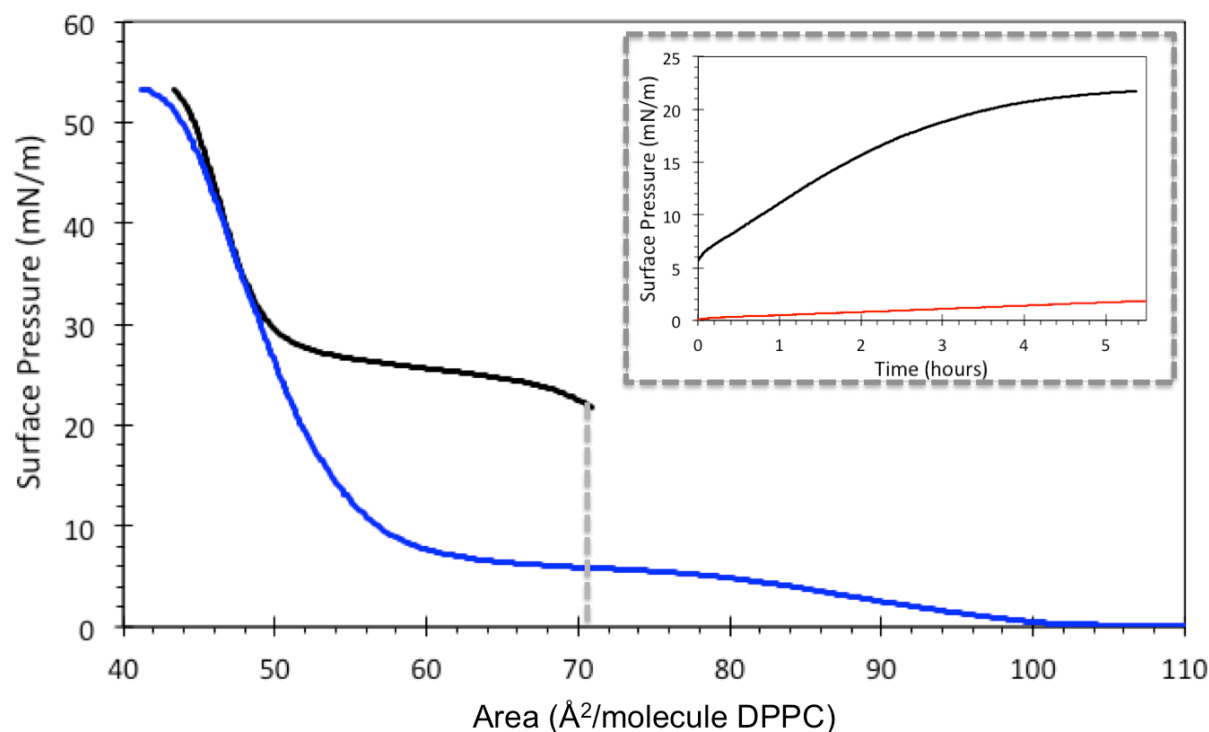
Figure 3.2: π – A isotherms of DPPC deposited on neat water surface (blue) and DPPC deposited on a 2.5 mM aqueous solution of Phe (black). Inset shows adsorption of Phe to the DPPC-covered interface over time at mean molecular area of 70 Å²/molecule (in the region indicated by the gray dotted line in the π – A isotherms), prior to surface compression (black) as well as adsorption of Phe to a bare aqueous interface over time at the same concentration (2.5 mM) for comparison (red).

The change in surface tension illustrated in Figure 3.2 due to the presence of Phe can have significant consequences on the stability and morphology of a cell membrane. For example, regions of differing surface tension on the cell membrane surface can induce changes in the cell shape and even can cause the membrane to rupture.[55-56] The results presented here in conjunction with those of Adler-Abramovich et al.[9] suggest that this decrease in surface tension induced by the presence of Phe in the interfacial region contributes to the cytotoxicity as well as the change in cell morphology observed.

3.3.2 Partitioning of L-Phenylalanine at the Aqueous/DPPC Interface

The isotherms shown above (Figure 3.2) indicate the presence of Phe in the DPPC-covered interfacial region; however no information can be gained from the isotherms as to whether the Phe molecules are strictly partitioning to the lipid – water interface under the lipid film, or whether they are intercalating into the lipid film. To gain further insight into the details of Phe interactions with the DPPC

film, MD simulations of the mixed film system were used, beginning with Phe molecules solvated in the bulk aqueous phase in the presence of an interface coated with DPPC molecules at a mean molecular area of 70 Å^2/molecule (LE – LC coexistence region, representative of cell membranes[54]). Both zwitterionic and neutral Phe were simulated. Although Phe would exist in a zwitterionic state in pure water, transition to a neutral state would be possible within the phospholipid membrane. Both systems were examined in order to determine what changes would be expected if this transition were to occur.

Visual inspection of the trajectories reveals that both neutral and zwitterionic Phe diffuse within the aqueous phase at the start of the simulation, forming short-lived small clusters in the aqueous phase ranging from approximately two to five monomers in size (see Figure A1.2 in Appendix 1 for characteristic snapshots of both simulations during adsorption). As the trajectory progresses, molecules of both ionization states interact with the DPPC monolayers. The neutral Phe molecules quickly intercalate into the film and remain inside the film for the rest of the simulation, never returning to the aqueous phase, thus depleting the aqueous phase of all Phe molecules. The zwitterionic Phe molecules however are much more dynamic, interacting with and even intercalating into the DPPC film but subsequently returning back into the bulk aqueous phase. However, even in the case of the zwitterionic Phe molecules, as the trajectory progresses a majority of Phe molecules remain embedded within the DPPC monolayers. Molecules of both ionization states primarily intercalate as monomers, but dimer clusters were also observed within the film. With the addition of 15 zwitterionic Phe molecules to the original 20 Phe zwitterions after the initial 100ns simulation, the same behavior was observed in the following 100ns run as described above with the exception of larger clusters (reaching three and four monomers in size) observed within the film towards the end of the trajectory.

To ascertain the average positioning of the Phe molecules in the interfacial region, density profiles along the direction normal to the DPPC interface were calculated and are shown in Figure 3.3. Figure 3.3(a) and 3.3(b) show the density profiles of the zwitterionic Phe/DPPC system, and 3(c) and 3(d) show the density profiles of the neutral Phe/DPPC system. Both sets of density profiles were computed

from the simulations with 20 Phe molecules; density profiles of the zwitterionic Phe evaluated from the additional simulation with 35 Phe molecules yield the same result and are therefore not shown here. On the left-hand side of Figure 3.3 (panels (a) and (c)), the density profiles of the polar head groups are compared, and on the right-hand side (panels (b) and (d)), the density profile of the terminal ring carbon of Phe (CZ in the molecular scheme shown in Figure 1(a)) is matched with the closest of the density profiles of carbon atoms of the hydrocarbon tails of DPPC (shown in red).
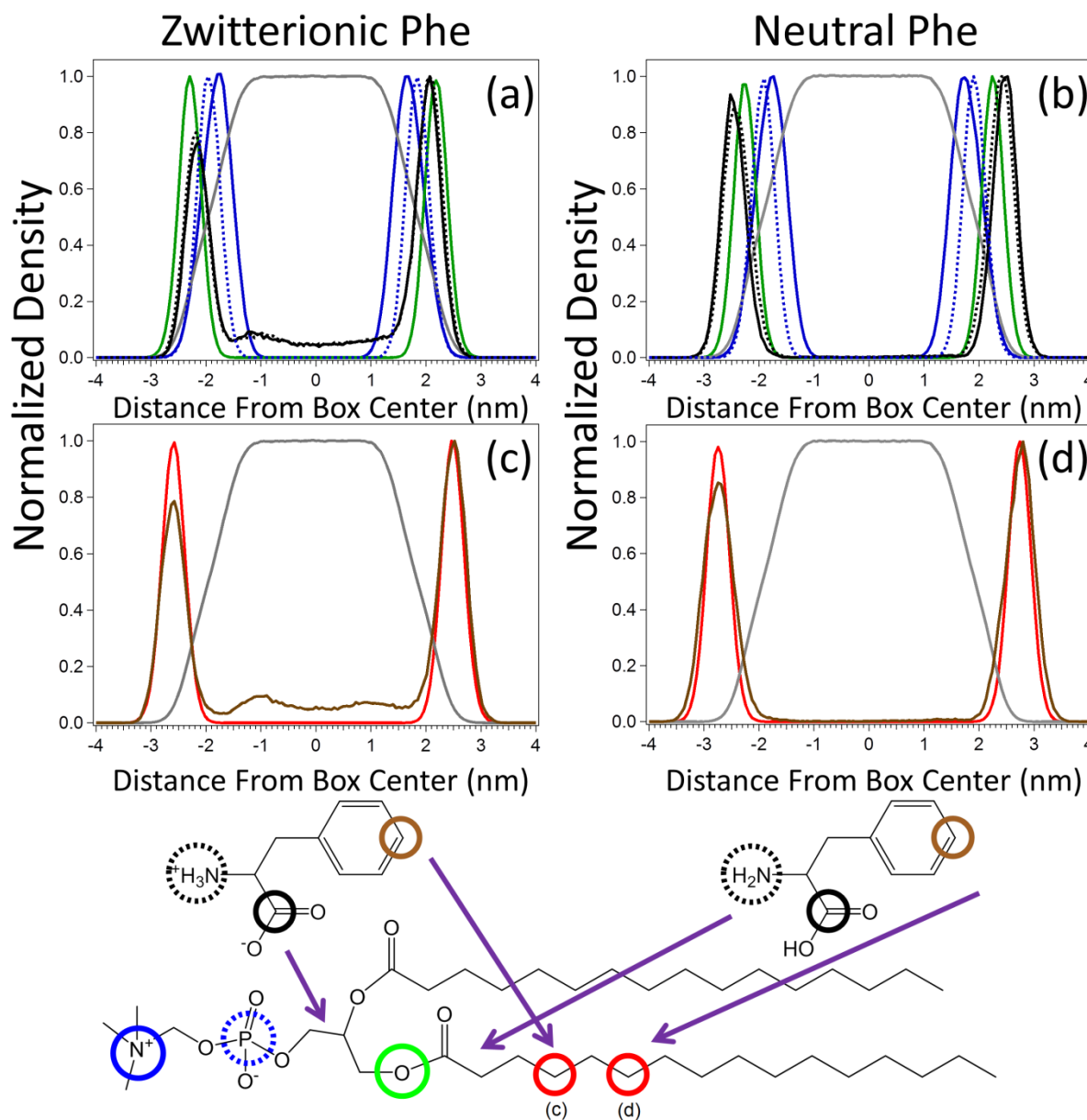
Figure 3.3: Density profiles illustrating average positioning of Phe (20 molecules) during the last 50 ns of simulation time (100 ns total) in comparison with DPPC density profiles. (a) and (c) are for the zwitterionic Phe and (b) and (d) are from the neutral Phe simulations (corresponding structures shown in the bottom). The grey curve in all panels corresponds to the density profile of water. The cartoon on the bottom highlights atoms graphed above in matching colors. Purple arrows indicate rough positions of labeled atoms based on the density profiles. Color coding: Phe: black solid line – C (carboxyl group), black dotted line – N (amine group), brown – CZ atom (aromatic ring); DPPC: blue solid line – N (choline group), blue dotted line – P (phosphate group), green – O21 (carbonyl groups), red – C24 in (c), C26 in (d).

From the density profiles it can be concluded that zwitterionic Phe is positioned, on average, with its head group between the phosphate group of DPPC (P) and O21/O31 on the sn2/sn1 chains. Density profiles for corresponding atoms on the two chains are nearly identical and thus only the atoms from the sn2 chain are shown here. The aromatic group of zwitterionic Phe does penetrate between the hydrocarbon tails of DPPC with the density profile of the CZ atom of Phe overlapping most closely with the density profile of the C24 atom in DPPC. Neutral Phe penetrates deeper into the DPPC film compared to the zwitterion, with the neutral head group positioned on average beyond O21/O31 region of DPPC, and the CZ atom as deep as the C26 atom of DPPC hydrocarbon tail.

The above findings inferred from the density profiles are further corroborated by visual inspection of the trajectories revealing that neutral Phe molecules can change their orientation within the film, dehydrating their polar groups and embedding deeper into the nonpolar phase (see Figure A1.3 of the Appendix 1). Zwitterionic Phe, however, remains with its polar groups hydrated and anchored in the aqueous region of the interface. This suggests that if Phe does transition to its neutral state upon entering the phospholipid film, it can penetrate rather deeply between the DPPC molecules, well into the hydrophobic region of the monolayer. Although this is a monolayer study and membrane crossing events are impossible here, the dehydration and deeper penetration of neutral Phe into the nonpolar region of the phospholipid monolayer opens the possibility for such crossing events in a bilayer system.

3.3.3 Aggregation State of Phe in Solution

It has been suggested in the literature that Phe forms large amyloid-like fibrils in solution, proposing that these fibrils are responsible for the cytotoxicity observed in PKU disease.[9-10] Throughout the simulations performed in this work, small clusters of Phe molecules (both in the neutral and zwitterionic simulations) were observed in the bulk and in the interfacial region in the presence of DPPC, but were rather short-lived, with no long fibril-like structures observed. The extent of aggregation of amino acids can be dependent upon the force field chosen for the simulations[57], thus the formation of fibrils was also explored experimentally here using confocal microscopy and staining with Thioflavin T

(ThT). As seen below in Figure 3.4(a), no fibrils were observed in solution, even at the high concentration of 120 mM. However, upon drying of the solution (presumably yielding supersaturated solution >153 mM[58]), crystallization occurred in the same viewpoint (Figure 3.4(b), see Figure A1.4 in Appendix 1 for the time evolution of crystallization with drying), yielding structures comparable to those in samples prepared under similar conditions and reported in the literature as amyloid-like fibrils.[9-10]
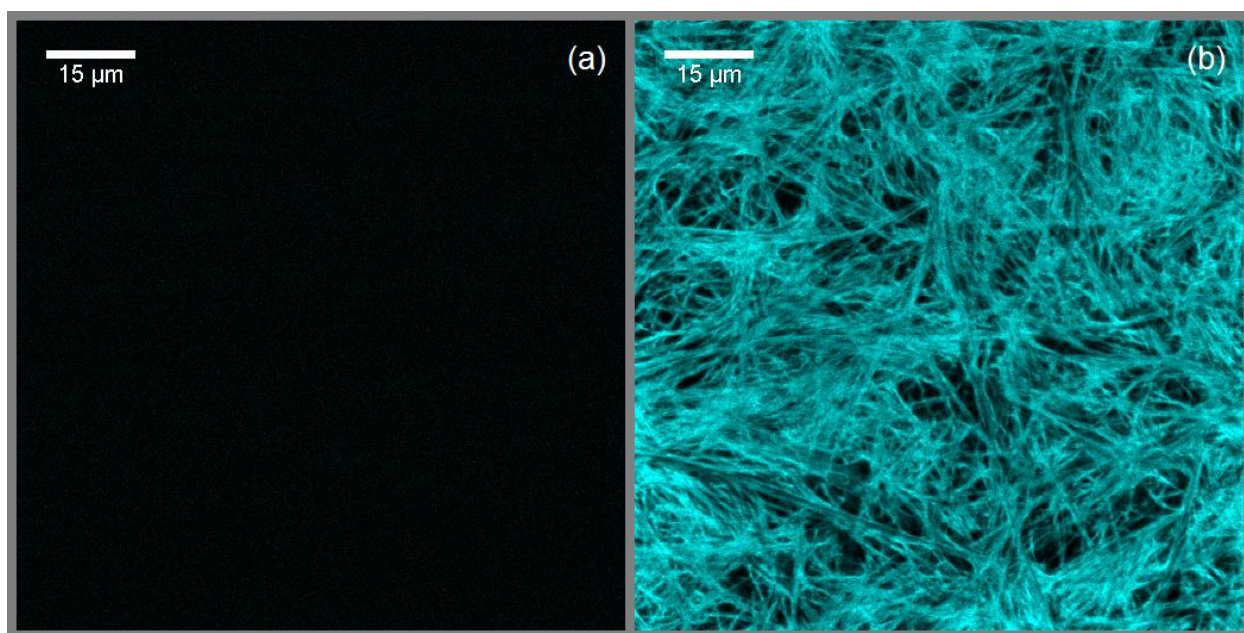
Figure 3.4: Confocal microscope images of 120 mM Phe stained with Thioflavin T (ThT). (a) image of Phe in aqueous solution (this panel is mostly black, with small dots corresponding to free dye but no structures), (b) refocused image of same spot after drying with the same imaging contrast. Scale bar represents 15 μm.

Further, at lower concentrations (2.5 mM Phe, Figure A1.5 in Appendix 1) the similar crystal formation occurs, and appears to begin at the periphery of the drop as it dries. In contrast with bulk solution images, some aggregates were also observed in BAM images of 2.5 – 20 mM Phe on a bare water surface (Figure A1.6 in Appendix 1). The experimental findings presented indicate that most of the Phe in pure bulk solution, even at the relatively high physiological concentrations present in a diseased state, does not exist as long fibril-like aggregates, but rather fibril formation occurs upon significantly

increased concentration or interactions with the interface. The special environment provided by an interface has been suggested to be important in many different contexts previously, ranging from its influence on ionization state of molecules to promoting chemistry not available in the bulk aqueous environment.[13, 33, 59-61] Here, the surface is implicated in promoting aggregation through increased local concentrations and interactions of Phe with the interface. It is important to note that in these studies no ions were present in solution as is the case in biological systems and as have been used in previous studies.[9] The addition of salt to the system could also influence the aggregation and interactions of Phe.

The absence of Phe aggregate formation in bulk solution is important in terms of the interaction of Phe with a biological membrane. Despite the fact that Phe is dilute in the bulk aqueous environment at biologically relevant concentrations, it does accumulate in the interfacial region, as evidenced here by the surface tension data as well as the MD simulations. Thus, in the interfacial region, much higher concentrations of Phe may be reached, increasing the likelihood of more extended aggregation in the specific, special environment provided by the phospholipid interface. Additionally, an interfacial aggregation phenomenon would be consistent with the long timescale saturation effects observed in Phe surface adsorption experiments (i.e. the non-diffusive process alluded to earlier), although it is possible that this long timescale saturation is due to another slow process, such as intercalation into the membrane or change in ionization state. Interestingly, phospholipid - water interfaces have been shown to promote aggregation of a variety of peptide sequences,[11-12, 62-64] through increased local concentration and two dimensional diffusion when bound to phospholipid membranes[65]. One specific example is the toxic misfolding of Human Islet Amyloid Polypeptide (hIAPP).[66] hIAPP is a naturally disordered protein that forms ordered structures through interaction with a membrane; in general, the misfolding of naturally disordered proteins is thought to be a contributing factor in diseases such as Alzheimer's, Parkinson's and type II diabetes.[67-69] It is possible that the membrane is playing a similar role here, and is indeed enhancing the aggregation of Phe and contributing to the cytotoxicity associated with PKU and observed in other studies.[9]

3.3.4 Morphological and Ordering Effect of Phe on the DPPC Film

Beyond understanding the intercalation of Phe into the DPPC monolayer, it is important in a biological context to understand the effect this intercalation has on the DPPC film itself. The domain morphology of a DPPC film is one good way to experimentally gain insight into the effect of additives such as Phe on a phospholipid membrane.[24] BAM images of DPPC deposited on water, an aqueous subphase of 2.5 mM Phe, and on water followed by injection of Phe beneath the surface layer are shown in Figure 3.5(a) – (c), respectively.
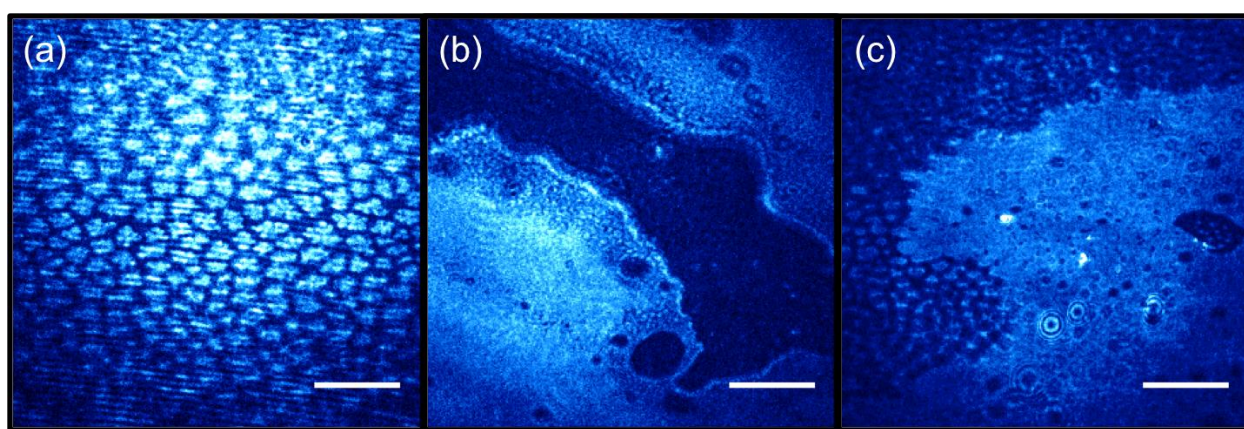
Figure 3.5: BAM images of DPPC deposited at 70 Å^2/molecule (a) on a neat water surface, (b) on an aqueous subphase composed of 2.5 mM Phe, and (c) on a neat water subphase followed by injection of Phe beneath the water surface. Scale bar represents 100 μm. Image (b) was collected approximately 5 minutes after deposition and image (c) was collected approximately 2 hours 51 minutes after injection.

On a bare water subphase (Figure 3.5(a)) DPPC exhibits the characteristic island structure formed in the LE-LC coexistence region of its π – A isotherm (BAM images of DPPC in various phases throughout its π – A isotherm are shown in Figure A1.7 of Appendix 1).[24] However, when deposited on a subphase containing Phe (Figure 3.5(b)), DPPC exhibits extended condensed domains, with ribbons and circular domains of lesser DPPC coverage. Deposition on a subphase containing Phe molecules resulted in immediate domain morphology changes that were stable over time. Despite this immediate perturbation, the initial surface tension recorded upon spreading of DPPC at the surface was identical in the presence and absence of Phe in the subphase (the initial surface pressure upon spreading at 70 Å^2/molecule both on a bare water surface and on an aqueous Phe solution was consistent at ~6 mN/m),

indicating that although the film was perturbed, it was still able to attain similar surface pressures. However, to confirm that the pre-existence of Phe in the subphase was not causing an artificial change in domain morphology due to different spreading behavior, an injection experiment was also performed. In this experiment, DPPC was deposited on a water surface, forming its characteristic domain structure as shown in Figure 3.5(a). Then, Phe was injected beneath the surface layer, the resulting BAM image shown in Figure 3.5(c). As in Figure 3.5(b), large condensed domains were also observed in the injection experiment as well as domains of less surfactant coverage. However, in both cases (Figure 3.5(b) and (c)), there were also still some domains observed with the characteristic island structure of DPPC in the LE-LC phase region. Thus, regardless as to whether the DPPC or the Phe solution is initially equilibrated, there is a similar perturbation observed due to Phe yielding a change of the DPPC film morphology. Due to the heterogeneity of the mixed films in regions larger than the images (approximately 500x500 μm^2) and morphological changes observed within minutes of Phe exposure, no useful information could be gathered about morphological changes over time. Because of this, images were chosen to be representative of observed morphologies rather than for temporal significance.

This experimental effect was supported by the simulation results in which small voids were periodically formed in the DPPC film in the presence of zwitterionic Phe. One snapshot showing this effect is presented in Figure 3.6 with the void in the film circled in white.
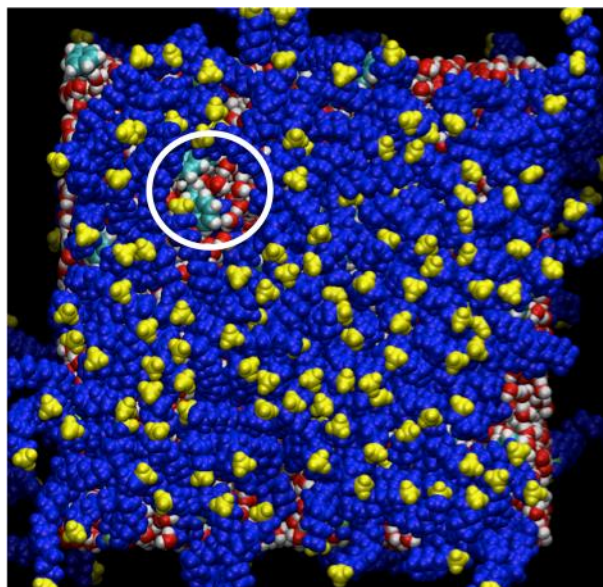
Figure 3.6: Top view snapshot of a small-scale defect in the DPPC film from MD simulation (defect circled in white). DPPC molecules are colored blue with terminal methyl groups colored yellow. Water molecules are red and white, and Phe molecules can be seen by their green aromatic rings.

The proximity and ordering of the terminal methyl groups of DPPC (colored in yellow in Figure 3.6) can be used as an indicator of condensed domains in the film.[70] In conjunction with periodic voids formed in the monolayer like the one shown in Figure 3.6, there were also regions of condensed film (seen as clusters of yellow terminal methyl groups) visually observed throughout the simulation.

To quantify the visual condensing effect of Phe on the DPPC monolayer observed in the MD simulations, deuterium order parameters were calculated[71] and are presented in Figure 3.7. Deuterium order parameter is typically used to characterize the order in acyl chains and can be also obtained experimentally from deuterium NMR quadrupole splittings. It is defined by the equation $S_{cd}=<3/2 \cos^2(\Theta_{cd})-1/2>$ where Θ_{cd} is the angle between the C-H bond vector and the normal of the bilayer.[72] Figure 3.7(a) and (b) are the order parameters calculated for the sn2 and sn1 chains of DPPC, respectively, and Figure 3.7(c) and (d) are the corresponding changes in order parameters for the mixed film systems in comparison with the pure DPPC values.
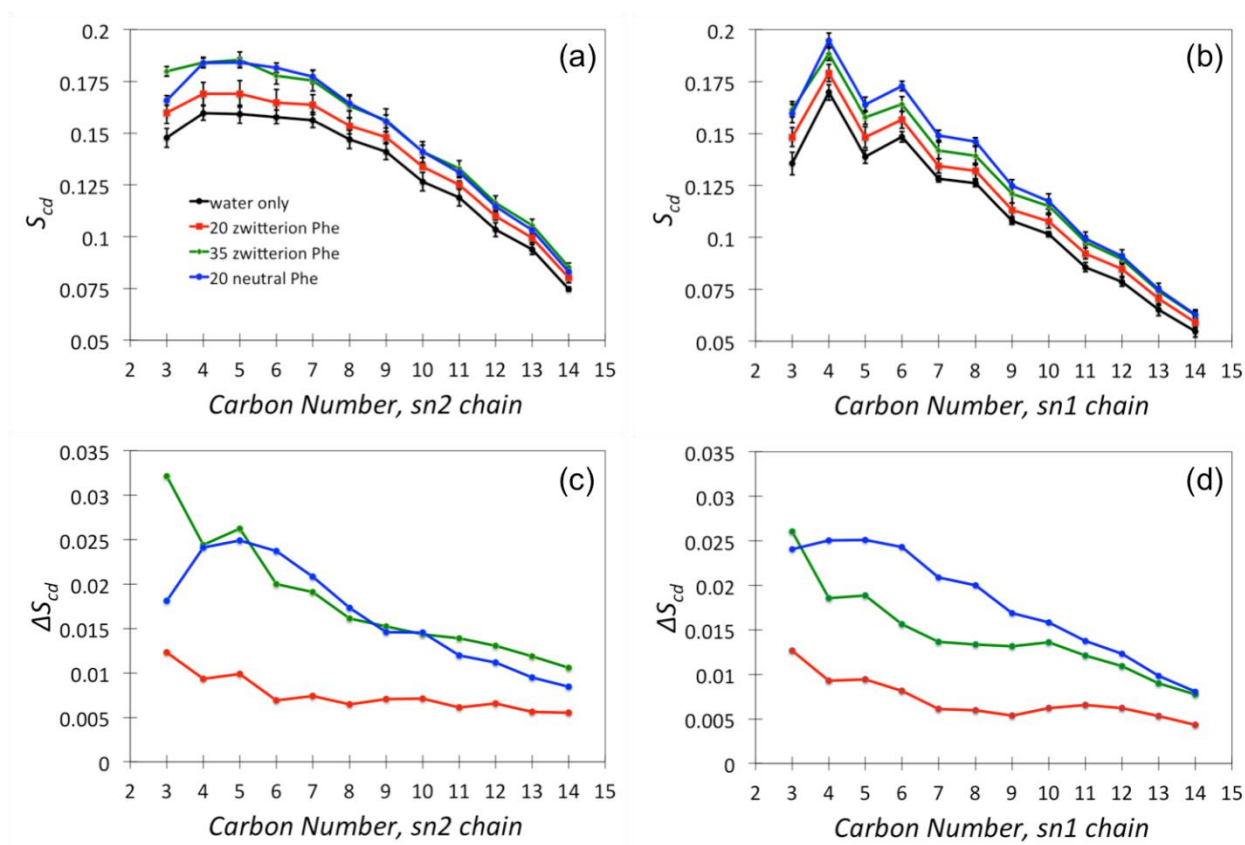
Figure 3.7: Deuterium order parameters of sn2 (a) and sn1 (b) chains of DPPC. Color coding: DPPC on a pure water slab (black), in the presence of 20 molecules of zwitterionic Phe (red), with 15 additional zwitterionic Phe molecules added (green), and in the presence of 20 molecules of neutral Phe (blue). Error bars correspond to one standard deviation. In panels (c) and (d), the relative change in order parameter from that of the DPPC monolayer on pure water subphase in shown for the sn2 and sn1 chains, respectively.

In the case of both zwitterionic and neutral Phe, the presence of Phe increases the microscopic order of the hydrocarbon chains of the DPPC molecules. In the presence of 20 molecules of zwitterionic Phe the perturbation to the tails of DPPC is fairly uniform, evidenced by the near constant change in order parameters (red line, Figure 3.7(c)), with a slightly more pronounced effect closest to the head group of DPPC. To simulate more realistically the experimental situation where the macroscopic bulk solution provides a near constant supply of Phe monomers to the interfacial region to replenish those that have already partitioned into the monolayer, a subsequent simulation was run with an additional 15 molecules of zwitterionic Phe added to the bulk underneath the DPPC film, yielding a total of 35 molecules of Phe in the simulation. After this addition, there is a much more pronounced effect on the order parameters,

with a more distinct perturbation near the head group of DPPC, but still with significant perturbation to the rest of the tail. Finally, in the presence of 20 neutral Phe molecules, there is also a significant increased microscopic ordering of the hydrocarbon tails of DPPC, but now with a maximum effect around carbons 5 and 6, and less of an effect closer to the head group. These results are consistent with the density profiles (Figure 3.3) that showed neutral Phe partitioning deeper into the DPPC film than zwitterionic Phe.

A similar condensing effect on a DPPC film was observed using BAM in the presence of dimethylsulfoxide (DMSO), a membrane penetration enhancer used in drug delivery applications by Chen et al.[15] In this study it was observed that DMSO condenses the phospholipid films, resulting in more condensed regions and likely lower surface coverage of phospholipid. This was then suggested to be a contributing factor in the enhanced penetration ability of cells treated with DMSO. Similarly here, the presence of Phe the DPPC film appears to become more microscopically condensed, yielding some areas of lower DPPC coverage such as the microscopic pore pictured in Figure 3.6. Additionally the domain morphology changes observed through BAM are consistent with the picture put forward by Chen et al. as well as the microscopic effects observed through MD simulations. Thus, an ordering of DPPC in the presence of Phe in the interfacial region may be contributing to the increased permeability, in a manner similar to DMSO, and destruction of cells observed in PKU studies.[9]

3.4 Conclusions

Using a combination of surface sensitive experimental techniques with MD simulations, it is shown here that L-phenylalanine does intercalate into a DPPC film at the air-water interface, thereby affecting the surface tension, phase morphology, and ordering of the DPPC film. Phe was not observed to form long fibrils in solution in the experiments or simulations presented here. Rather, Phe was seen to form dynamic small clusters in the simulations, and in the experiments was shown to have the ability to form needle like crystals upon drying and supersaturation. Combined with the observation of small aggregates of Phe at the bare water surface using BAM, the interfacial region is suggested to play a role in

enhancing the aggregation of Phe. Regardless of the extent of aggregation in the bulk, the effects of Phe on DPPC films, as observed in experiments and simulations, can have great influence on the permeability and stability of a cell membrane. The experimental Langmuir trough and BAM results illustrate the change in surface tension and phase behavior. The simulation results further characterize the molecular-level interactions and perturbation to the microscopic ordering of the hydrocarbon chains of DPPC illustrating these changes. In addition, if Phe transitions to its neutral state once within the hydrophobic part of the phospholipid phase, it is shown here to have the ability to penetrate deeper within the hydrocarbon core of the DPPC film compared to the zwitterionic form of Phe, enhancing the possibility for embedding into the membrane, membrane crossing events, and increasing local concentration to favor aggregation. In summary, Phe significantly perturbs the structure and morphology of a two-dimensional DPPC film used as a model for a cell membrane, through direct Phe - phospholipid interactions and/or membrane – mediated aggregation. This study indicates that it is likely that cytotoxicity in PKU arises from interactions between phenylalanine and the cell membrane. Our results illustrate how phenylalanine affects membrane structure and stability, which may be applied to many different biological systems.

Supporting Information Available in Appendix 1: Molecular dynamics simulation insertion procedure and snapshots of Phe adsorption into the DPPC film. Confocal microscopy images of Phe fibril formation during droplet drying. BAM images of Phe aggregates at bare water interface. BAM images of unperturbed DPPC film at various surface concentrations. Atomic names and charges for neutral and zwitterionic Phe used in MD simulations. Topology files are also available for DPPC, neutral Phe and zwitterionic Phe.

Bibliography

(1)   Krzysciak, W., Activity of Selected Aromatic Amino Acids in Biological Systems. *Acta Biochim Pol* **2011,** *58*, 461-466.

(2)   Hong, H. D.; Park, S.; Jimenez, R. H. F.; Rinehart, D.; Tamm, L. K., Role of Aromatic Side Chains in the Folding and Thermodynamic Stability of Integral Membrane Proteins. *J. Am. Chem. Soc.* **2007,** *129*, 8320-8327.

(3)   Domene, C.; Vemparala, S.; Klein, M. L.; Vénien-Bryan, C.; Doyle, D. A., Role of Aromatic Localization in the Gating Process of a Potassium Channel. *Biophys. J.* **2006,** *90*, L01-L03.

(4)   Kelkar, D.; Chattopadhyay, A., Membrane Interfacial Localization of Aromatic Amino Acids and Membrane Protein Function. *J. Biosci. (Bangalore)* **2006,** *31*, 297-302.

(5)   Gazit, E., A Possible Role for Π-Stacking in the Self-Assembly of Amyloid Fibrils. *FASEB J* **2002,** *16*, 77-83.

(6)   Makin, O. S.; Atkins, E.; Sikorski, P.; Johansson, J.; Serpell, L. C., Molecular Basis for Amyloid Fibril Formation and Stability. *Proc. Natl. Acad. Sci. U.S.A.* **2005,** *102*, 315-320.

(7)   Marshall, K. E.; Morris, K. L.; Charlton, D.; O'Reilly, N.; Lewis, L.; Walden, H.; Serpell, L. C., Hydrophobic, Aromatic, and Electrostatic Interactions Play a Central Role in Amyloid Fibril Formation and Stability. *Biochemistry* **2011,** *50*, 2061-2071.

(8)   Tamamis, P.; Adler-Abramovich, L.; Reches, M.; Marshall, K.; Sikorski, P.; Serpell, L.; Gazit, E.; Archontis, G., Self-Assembly of Phenylalanine Oligopeptides: Insights from Experiments and Simulations. *Biophys. J.* **2009,** *96*, 5020-5029.

(9)   Adler-Abramovich, L.; Vaks, L.; Carny, O.; Trudler, D.; Magno, A.; Caflisch, A.; Frenkel, D.; Gazit, E., Phenylalanine Assembly into Toxic Fibrils Suggests Amyloid Etiology in Phenylketonuria. *Nat. Chem. Biol.* **2012,** *8*, 701-706.

(10)   Singh, V.; Rai, R. K.; Arora, A.; Sinha, N.; Thakur, A. K., Therapeutic Implication of L-Phenylalanine Aggregation Mechanism and Its Modulation by D-Phenylalanine in Phenylketonuria. *Sci. Rep.* **2014,** *4*.

(11)   Gorbenko, G. P.; Kinnunen, P. K. J., The Role of Lipid–Protein Interactions in Amyloid-Type Protein Fibril Formation. *Chem. Phys. Lipids* **2006,** *141*, 72-82.

(12)   Coutinho, A.; Loura, L. M. S.; Prieto, M., Fret Studies of Lipid-Protein Aggregates Related to Amyloid-Like Fibers. *J. Neurochem.* **2011,** *116*, 696-701.

(13)   Griffith, E. C.; Vaida, V., In Situ Observation of Peptide Bond Formation at the Water-Air Interface. *Proc. Natl. Acad. Sci. USA* **2012,** *109*, 15697-15701.

(14)   Chen, X.; Allen, H. C., Interactions of Dimethylsulfoxide with a Dipalmitoylphosphatidylcholine Monolayer Studied by Vibrational Sum Frequency Generation. *J. Phys. Chem. A* **2009,** *113*, 12655-12662.

(15)   Chen, X. K.; Huang, Z. S.; Hua, W.; Castada, H.; Allen, H. C., Reorganization and Caging of Dppc, Dppe, Dppg, and Dpps Mono Layers Caused by Dimethylsulfoxide Observed Using Brewster Angle Microscopy. *Langmuir* **2010,** *26*, 18902-18908.

(16)   Yan, E. C. Y.; Fu, L.; Wang, Z.; Liu, W., Biological Macromolecules at Interfaces Probed by Chiral Vibrational Sum Frequency Generation Spectroscopy. *Chem. Rev.* **2014**, *114***,** 8471–8498.

(17)   Seoane, R.; Minones, J.; Conde, O.; Casas, M.; Iribarnegaray, E., Thermodynamic and Brewster Angle Microscopy Studies of Fatty Acid/Cholesterol Mixtures at the Air/Water Interface. *J. Phys. Chem. B* **2000,** *104*, 7735-7744.

(18)   Berkowitz, M. L.; Bostick, D. L.; Pandit, S., Aqueous Solutions Next to Phospholipid Membrane Surfaces: Insights from Simulations. *Chem. Rev.* **2006,** *106*, 1527-1539.

(19)   McConlogue, C. W.; Malamud, D.; Vanderlick, T. K., Interaction of Dppc Monolayers with Soluble Surfactants: Electrostatic Effects of Membrane Perturbants. *Biochim. Biophys. Acta* **1998,** *1372*, 124-134.

(20)   Brockman, H., Lipid Monolayers: Why Use Half a Membrane to Characterize Protein-Membrane Interactions? *Curr. Opin. Struct. Biol.* **1999,** *9*, 438-443.

(21)   Ma, G.; Allen, H. C., Dppc Langmuir Monolayer at the Air−Water Interface: Probing the Tail and Head Groups by Vibrational Sum Frequency Generation Spectroscopy. *Langmuir* **2006,** *22*, 5341-5349.

(22)   Sampaio, J. L.; Gerl, M. J.; Klose, C.; Ejsing, C. S.; Beug, H.; Simons, K.; Shevchenko, A., Membrane lipidome of an epithelial cell line. *Proc. Natl. Acad. Sci. USA* **2011**, *108*, 1903-1907.

(23)   Zuo, Y. Y.; Veldhuizen, R. A. W.; Neumann, A. W.; Petersen, N. O.; Possmayer, F., Current Perspectives in Pulmonary Surfactant — Inhibition, Enhancement and Evaluation. *Biochim. Biophys. Acta* **2008,** *1778*, 1947-1977.

(24)   McConlogue, C. W.; Vanderlick, T. K., A Close Look at Domain Formation in DPPC Monolayers. *Langmuir* **1997,** *13*, 7158-7164.

(25)   Creuwels, L.; vanGolde, L. M. G.; Haagsman, H. P., The Pulmonary Surfactant System: Biochemical and Clinical Aspects. *Lung* **1997,** *175*, 1-39.

(26)   Klopfer, K. J.; Vanderlick, T. K., Isotherms of Dipalmitoylphosphatidylcholine (Dppc) Monolayers: Features Revealed and Features Obscured. *J. Colloid Interface Sci.* **1996,** *182*, 220-229.

(27)   Gilman, J. B.; Tervahattu, H.; Vaida, V., Interfacial Properties of Mixed Films of Long-Chain Organics at the Air-Water Interface. *Atmos. Environ.* **2006,** *40*, 6606-6614.

(28)   Griffith, E. C.; Adams, E. M.; Allen, H. C.; Vaida, V., Hydrophobic Collapse of a Stearic Acid Film by Adsorbed L-Phenylalanine at the Air-Water Interface. *J. Phys. Chem. B* **2012**, *116*, 7849-7857.

(29)   Griffith, E. C.; Guizado, T. R. C.; Pimentel, A. S.; Tyndall, G. S.; Vaida, V., Oxidized Aromatic-Aliphatic Mixed Films at the Air-Aqueous Interface. *J. Phys. Chem. C* **2013**, *117*, 22341-22350.

(30)   Jubb, A. M., Hua, W. & Allen, H. C. Environmental Chemistry at Vapor/Water Interfaces: Insights from Vibrational Sum Frequency Generation Spectroscopy. *Annu. Rev. Phys. Chem.* **2012**, 63, 107–130.

(31)   Rontu, N.; Vaida, V., Surface Partitioning and Stability of Pure and Mixed Films of 8-2 Fluorotelomer Alcohol at the Air-Water Interface. *J. Phys. Chem. C* **2007**, *111*, 11612-11618.

(32)   Rontu, N.; Vaida, V., Miscibility of Perfluorododecanoic Acid with Organic Acids at the Air-Water Interface. *J. Phys. Chem. C* **2007**, *111*, 9975-9980.

(33)   Griffith, E. C.; Vaida, V., Ionization State of L-Phenylalanine at the Air-Water Interface. *J. Am. Chem. Soc.* **2013**, *135*, 710-716.

(34)   Henon, S.; Meunier, J., Microsope at the Brewster Angle - Direct Observation of 1st-Order Phase Tranisitions in Monolayers. *Rev. Sci. Instrum.* **1991**, *62*, 936-939.

(35)   Honig, D.; Mobius, D., Direct Visualization of Monolayers at the Air-Water Interface by Brewster Angle Microscopy. *J. Phys. Chem.* **1991**, *95*, 4590-4592.

(36)   Avdeef, A.; Box, K. J.; Comer, J. E. A.; Hibbert, C.; Tam, K. Y., Ph-Metric Logp 10. Determination of Liposomal Membrane-Water Partition Coefficients of Ionizable Drugs. *Pharm. Res.* **1998**, *15*, 209-215.

(37)   MacCallum, J. L.; Bennett, W. F. D.; Tieleman, D. P., Distribution of Amino Acids in a Lipid Bilayer from Computer Simulations. *Biophys. J.* **2008**, *94*, 3393-3404.

(38)   Nose, S., A Molecular-Dynamics Method for Simulations in the Canonical Ensemble. *Mol. Phys.* **1984**, *52*, 255-268.

(39)   Hoover, W. G., Canonical Dynamics: Equilibrium Phase-Space Distributions. *Phys. Rev. A* **1985**, *31*, 1695-1697.

(40)   Hockney, R. W.; Goel, S. P.; Eastwood, J. W., Quiet High-Resolution Computer Models of a Plasma. *J. Comp. Phys.* **1974**, *14*, 148-158.

(41)   Darden, T.; York, D.; Pedersen, L., Particle Mesh Ewald: An N·Log(N) Method for Ewald Sums in Large Systems. *J. Chem. Phys.* **1993**, *98*, 10089-10092.

(42)   Hess, B.; Bekker, H.; Berendsen, H. J. C.; Fraaije, J. G. E. M., Lincs: A Linear Constraint Solver for Molecular Simulations. *J. Comput. Chem.* **1997**, *18*, 1463-1472.

(43)   Hess, B.; Kutzner, C.; van der Spoel, D.; Lindahl, E., Gromacs 4: Algorithms for Highly Efficient, Load-Balanced, and Scalable Molecular Simulation. *J. Chem. Theory Comput.* **2008**, *4*, 435-447.

(44)   Humphrey, W.; Dalke, A.; Schulten, K., Vmd: Visual Molecular Dynamics. *J. Mol. Graphics* **1996**, *14*, 33-38.

(45)   Jämbeck, J. P. M.; Lyubartsev, A. P., Derivation and Systematic Validation of a Refined All-Atom Force Field for Phosphatidylcholine Lipids. *J. Phys. Chem. B* **2012,** *116*, 3164-3179.

(46)   Jämbeck, J. P. M.; Lyubartsev, A. P., An Extension and Further Validation of an All-Atomistic Force Field for Biological Membranes. *J. Chem. Theory Comput.* **2012,** *8*, 2938-2948.

(47)   Duan, Y.; Wu, C.; Chowdhury, S.; Lee, M. C.; Xiong, G.; Zhang, W.; Yang, R.; Cieplak, P.; Luo, R.; Lee, T., et al., A Point-Charge Force Field for Molecular Mechanics Simulations of Proteins Based on Condensed-Phase Quantum Mechanical Calculations. *J. Comput. Chem.* **2003,** *24*, 1999-2012.

(48)   Lee, M. C.; Duan, Y., Distinguish Protein Decoys by Using a Scoring Function Based on a New Amber Force Field, Short Molecular Dynamics Simulations, and the Generalized Born Solvent Model. *Proteins: Struct., Funct., and Bioinf.* **2004,** *55*, 620-634.

(49)   Bayly, C. I.; Cieplak, P.; Cornell, W. D.; Kollman, P. A., A Well-Behaved Electrostatic Potential Based Method Using Charge Restraints for Deriving Atomic Charges - the Resp Model. *J. Phys. Chem.* **1993,** *97*, 10269-10280.

(50)   Tomasi, J.; Mennucci, B.; Cancès, E., The Ief Version of the Pcm Solvation Method: An Overview of a New Method Addressed to Study Molecular Solutes at the Qm Ab Initio Level. *J. Mol. Struct.-THEOCHEM* **1999,** *464*, 211-226.

(51)   Frisch, M. J.; Trucks, G. W.; Schlegel, H. B.; Scuseria, G. E.; Robb, M. A.; Cheeseman, J. R.; Scalmani, G.; Barone, V.; Mennucci, B.; Petersson, G. A., et al. *Gaussian 09*, Gaussian, Inc.: Wallingford, CT, USA, 2009.

(52)   Wang, J. M.; Wang, W.; Kollman, P. A.; Case, D. A., Automatic Atom Type and Bond Type Perception in Molecular Mechanical Calculations. *J. Mol. Graphics Modell.* **2006,** *25*, 247-260.

(53)   Williams, R. A.; Mamotte, C. D. S.; Burnett, J. R., Phenylketonuria: An Inborn Error of Phenylalanine Metabolism. *Clin. Biochem. Rev.* **2008,** *29,* 31-41.

(54)   Petrache, H. I.; Dodd, S. W.; Brown, M. F., Area Per Lipid and Acyl Length Distributions in Fluid Phosphatidylcholines Determined by H-2 Nmr Spectroscopy. *Biophys. J.* **2000,** *79*, 3172-3192.

(55)   López-Montero, I.; Vélez, M.; Devaux, P. F., Surface Tension Induced by Sphingomyelin to Ceramide Conversion in Lipid Membranes. *Biochim. Biophys. Acta* **2007,** *1768*, 553-561.

(56)   Dolowy, K., 275 - Effect of Interfacial Tension and Curvature of Charged Lipid Bilayer-Polylysine Complexes. *Bioelectrochem. Bioenerg.* **1979,** *6*, 305-307.l

(57)   Andrews, C. T.; Elcock, A. H., Molecular Dynamics Simulations of Highly Crowded Amino Acid Solutions: Comparisons of Eight Different Force Field Combinations with Experiment and with Each Other. *J. Chem. Theory Comput.* **2013,** *9*, 4585-4602.

(58)   Zhou, X.; Fan, J.; Li, N.; Du, Z.; Ying, H.; Wu, J.; Xiong, J.; Bai, J., Solubility of L-Phenylalanine in Water and Different Binary Mixtures from 288.15 to 318.15 K. *Fluid Phase Equilib.* **2012,** *316*, 26-33.

(59)   Eisenthal, K. B., Liquid Interfaces Probed by Second-Harmonic and Sum-Frequency Spectroscopy. *Chem. Rev.* **1996,** *96*, 1343-1360.

(60)   Donaldson, D. J.; Vaida, V., The Influence of Organic Films at the Air-Aqueous Boundary on Atmospheric Processes. *Chem. Rev.* **2006,** *106*, 1445-1461.

(61)   Vaida, V., Perspective: Water Cluster Mediated Atmospheric Chemistry. *J. Chem. Phys.* **2011,** *135*, 8.

(62)   Lee, H. J.; Choi, C.; Lee, S. J., Membrane-Bound Alpha-Synuclein Has a High Aggregation Propensity and the Ability to Seed the Aggregation of the Cytosolic Form. *J. Biol. Chem.* **2002,** *277*, 671-678.

(63)   Knight, J. D.; Miranker, A. D., Phospholipid Catalysis of Diabetic Amyloid Assembly. *J. Mol. Biol.* **2004,** *341*, 1175-1187.

(64)   ChooSmith, L. P.; GarzonRodriguez, W.; Glabe, C. G.; Surewicz, W. K., Acceleration of Amyloid Fibril Formation by Specific Binding of a Beta-(1-40) Peptide to Ganglioside-Containing Membrane Vesicles. *J. Biol. Chem.* **1997,** *272*, 22987-22990.

(65)   Morriss-Andrews, A.; Brown, F. L. H.; Shea, J. E., A Coarse-Grained Model for Peptide Aggregation on a Membrane Surface. *J. Phys. Chem. B* **2014,** *118*, 8420-8432.

(66)   Fu, L.; Ma, G.; Yan, E. C. Y., In Situ Misfolding of Human Islet Amyloid Polypeptide at Interfaces Probed by Vibrational Sum Frequency Generation. *J. Am. Chem. Soc.* **2010,** *132*, 5405-5412.

(67)   Dyson, H. J.; Wright, P. E., Intrinsically Unstructured Proteins and Their Functions. *Nat. Rev. Mol. Cell Bio.* **2005,** *6*, 197-208.

(68)   Tompa, P., Intrinsically Unstructured Proteins. *Trends Biochem. Sci.* **2002,** *27*, 527-533.

(69)   Uversky, V. N., Natively Unfolded Proteins: A Point Where Biology Waits for Physics. *Protein Sci.* **2002,** *11*, 739-756.

(70)   Knecht, V.; Müller, M.; Bonn, M.; Marrink, S.-J.; Mark, A. E., Simulation Studies of Pore and Domain Formation in a Phospholipid Monolayer. *J. Chem. Phys.* **2005,** *122*, 024704.

(71)   Chau, P. L.; Hardwick, A. J., A New Order Parameter for Tetrahedral Configurations. *Mol. Phys.* **1998,** *93*, 511-518.

(72)   Schindler, H.; Seelig, J., Deuterium Order Parameters in Relation to Thermodynamic Properties of a Phospholipid Bilayer. Statistical Mechanical Interpretation. *Biochemistry* **1975,** *14*, 2283-2287.

Chapter 4: Phospholipid Hydrolysis Studies

4.1 Introduction

Phospholipids are a class of molecule of great interest due to their prevalence in biology, where they make up a large fraction of most biological membranes. Certain phospholipids also play important roles in modern cellular signaling processes. Phospholipids generally possess a number of chemical bonds that are susceptible to reaction with water, both in the form of ester and phosphoester linkages. Because these bonds are exposed to water during the course of their normal function, the rate of hydrolysis reactions is of great interest. Aside from biological applications, these reactions are also important in understanding experimental artifacts in any number of studies utilizing phospholipids. The study of phospholipid hydrolysis is complicated by the fact that relevant phospholipid species are relatively insoluble in aqueous solution. This leads to their partitioning to interfaces, or aggregation into structures such as vesicles, and potentially great sensitivity to the conditions that occur in these environments.[1] Here, I attempt to study the hydrolysis of dipalmitoylphosphatidylcholine (DPPC) monolayers at an air-water interface using Langmuir trough techniques.

Previous studies have examined hydrolysis rates of dipalmitoylphosphatidylcholine (DPPC) systems under several conditions using a variety of techniques. Kensil and Dennis[2] found hydrolysis rate constants of (13.2 ± 0.2) x 10^{-3} $s^{-1}M^{-1}$ for DPPC dispersed in Triton X-100 as micelles at pH 12.7 and 40 °C. This rate constant is a second order rate constant with dependence on hydroxide concentration. At a given pH, a first order rate constant can be calculated. Given a hydroxide activity of 0.05 M, a rate constant of (6.6 ± 0.1) x 10^{-4} s^{-1} is calculated, which yields a half-life of 1050 s, or about 17.5 minutes. This hydrolysis rate was found to increase as the mole ratio of Triton/Phospholipid increased, with a 30% increase in hydrolysis of egg phosphatidylcholine increasing the mole ration from 4.5 to 15. DPPC vesicles were found to hydrolyze at a significantly slower rate than DPPC detergent micelles, on the order of (0.9 ± 0.2) x 10^{-3} $s^{-1}M^{-1}$, approximately 15 times slower. In vesicles, the packing of surfactants is generally more ordered, and of higher density than in micelle systems. This higher density is likely to

result in less hydration at the hydrolysable ester bonds. This lowered availability of water is likely the reason that hydrolysis is slower in vesicular systems than micellar ones.

Under significantly different conditions, Ho, Schmetz, and Deamer[3] conducted studies at pH 1, 4, 7, and 10 using 1-palmitoyl 2-oleoyl phosphatidylcholine (POPC) vesicles (both small and large) and micelle dispersions, but they report only summed data across all systems. These studies presumably took place at room temperature. At pH 1, they found a reaction rate of 5.3×10^{-6}, neglecting to indicate units. They suggest the rate is 300 fold slower than a 1.4×10^{-3} $s^{-1}M^{-1}$ rate reported by Kensil and Dennis,[2] giving some indication they intended to use the same units. Assuming the rate constant is 5.3×10^{-6} s^{-1}, the half-life would be 130782 s, or 36.3 hours. Were the rate constant 5.3×10^{-6} $s^{-1}M(H^+)^{-1}$, at pH 1 the half-life would be 363 hours. Depending on which graphs are compared, either of these numbers could be consistent. Hydrolysis rates could not accurately be measured at pH 4, 7, or 10 using their techniques, with less than 1-2% hydrolysis after 6 days. This work is not terribly reliable, but does suggest that hydrolysis is slower when acid catalyzed than when base catalyzed.

Studies by Ickenstein et al.[4] utilized a system of vesicles made from DPPC and 1,2-distearoyl-sn-glycerol-3-phosphatidylethanolamine-N-[methoxy(polyethylene glycol)-2000] (DSPE-PEG$_{2000}$), a ~2000 dalton molecular weight polyethylene glycol polymer attached to a phospholipid. The DSPE-PEG$_{2000}$ is utilized to add relevance to vesicle delivered drug therapies, but is potentially problematic for other applications. They report observed reaction rates of 4.95×10^{-7} s^{-1} and 0.85×10^{-7} s^{-1} for pH 2 at 22 °C and 4 °C respectively, and 0.59×10^{-7} s^{-1} and 0.018×10^{-7} s^{-1} for pH 4 at 22 °C and 4 °C respectively. No hydrolysis was observed in pH 6.5 samples at either temperature over 27 weeks. Comparing to the $(6.6 \pm 0.1) \times 10^{-4}$ s^{-1} from Kensil and Dennis,[2] there is good confirmation that the hydrolysis occurs much slower under comparable concentrations of H^+ than of OH^-.

Despite the fact that hydrolysis is slow under mild pH's for these systems, it still could be significant in Langmuir monolayers at air-water interfaces. The packing conditions of DPPC were shown

to be relevant for the rate of hydrolysis under basic conditions in the studies of Kensil and Dennis,[2] and in both the micelle and vesicle systems DPPC will have significantly higher surface density than expanded Langmuir films. Additionally, the interfacial energy in an air-water interface may be much higher than at a water-micelle or water-vesicle interface, and could accordingly change the energetics and rate of the reaction.[5–8] These air-water interfaces are also particularly relevant for DPPC hydrolysis, due to DPPC's role as a lung surfactant.[9–12]

Using a Langmuir trough and performing compression isotherms, a calibration curve is constructed using known mixtures of DPPC and hydrolyzed DPPC. Compression isotherms of pure DPPC are then collected as a function of time. By comparing the isotherm shapes of the pure DPPC at various time points with the calibration isotherms, concentrations of hydrolyzed DPPC can be calculated, and hydrolysis rates determined. If successful, the density of DPPC films could be controlled, to get density dependent hydrolysis rates.

4.2 Results/Discussion

Using typical methods for monitoring chemical reactions is difficult in Langmuir films due to the very low amount of material present in a monolayer film. For example, a 35 Å^2/chain DPPC film on a 200 cm^2 surface that is 5 mm deep corresponds with a bulk concentration of ~0.5 µM. Because of this, I am interested in measuring hydrolysis rates through the use of surface-pressure surface-area compression isotherms obtained with a Langmuir trough. This first requires the construction of a calibration curve by measuring compression isotherms of various mixtures of DPPC and hydrolyzed DPPC products, 1-phosphatidyl-phosphatidylcholine (1-PPC) and palmitic acid, which can all be purchased in their pure forms. Averaged data over several runs is shown in Figure 4.1. Error bars are small, only slightly larger than the width of the lines.
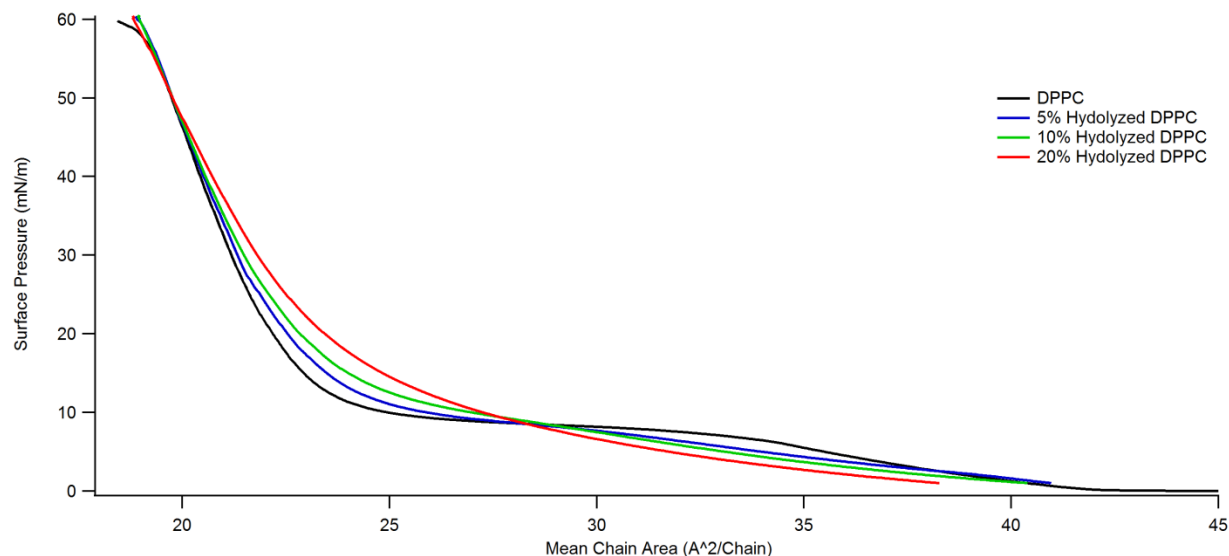
Figure 4.1: Hydrolyzed DPPC calibration isotherms averaged over several runs. Error bars are small, only slightly larger than the width of the lines. Calibrations were performed at ~22 °C.

With these calibrations, isotherms for mixed films can be constructed using the additivity rule. While the additivity rule normally assumes ideal behavior, in this case because I am not using only isotherms for pure compounds, it only assumes linear changes in ideality. This assumption is expected to hold well for the small changes in composition in this study.

The next step is determining the change in the shape of the DPPC isotherm as a function of time. This was accomplished by depositing DPPC solution in chloroform at the water surface, waiting at least 15 minutes for chloroform evaporation, then compressing the same film at regular intervals. An example of this is shown in Figure 4.2. Each isotherm was adjusted to match mean molecular areas at 45 mN/m, based on the know characteristic area of pure DPPC. This accounts for the fact that some DPPC is pushed under the barriers upon each compression. Because of this adjustment, it is not surprising that the isotherms overlap in the region around 45 mN/m (~20 $Å^2$/chain). However, the overlap in the relaxed region of the isotherm, around 45-35 $Å^2$/chain, is unexpected. This, unfortunately, disagrees with the changes observed in the calibration isotherms (Figure 4.1) which have a clear decrease in pressure at these same mean chain areas. This appears to indicate that hydrolysis is not the dominant mechanism for the change in isotherm shape under these conditions.
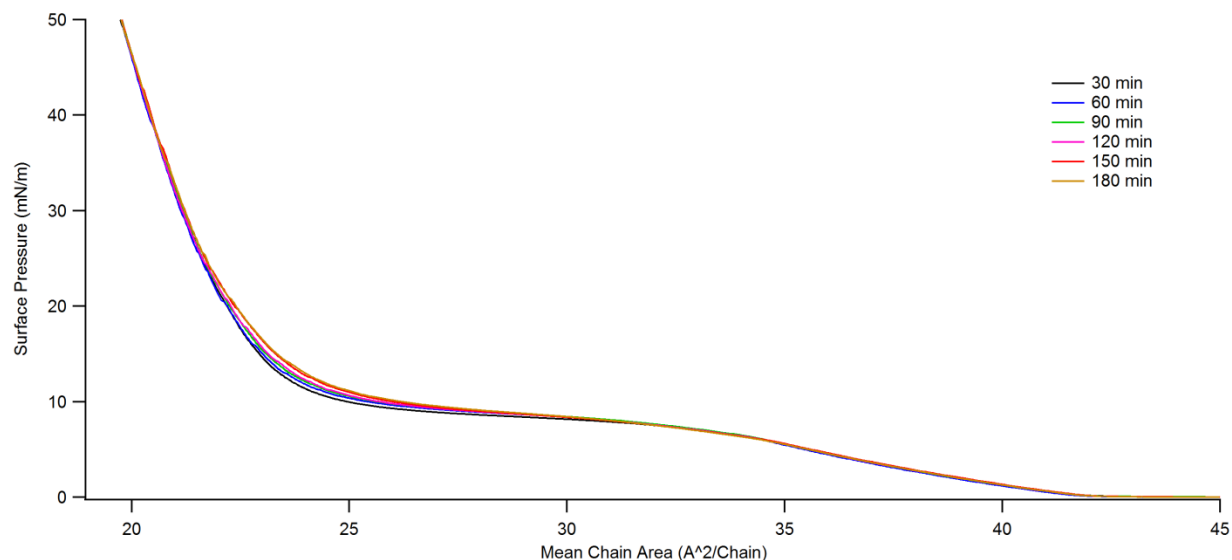
Figure 4.2: Change in DPPC isotherm over time. Experiment was performed using isotherm cycles, adjusting for DPPC loss under the barriers on each compression. Isotherms overlap well in the 45-35 Å^2/chain and the <22 Å^2/chain regions.

The question remains as to what causes the change in isotherm shape that is observed over time, however. Analyzing data from different runs of DPPC compression cycles over time shows significant differences between the early and more recent experiments examined in this study. As shown in Figure 4.3, there is good agreement between the two more recent sets of data, while the oldest set of data has significant deviations. There are two large differences between the new and old data sets. First, the old data set appears to be at a lower temperature (~2-5 °C) due to the lower surface pressure in the phase coexistence region of the DPPC isotherm. Second, the older set of data was take on the older KSV-NIMA Langmuir trough, with a Wilhelmey paper plate for measuring surface tension, while the newer sets of data was taken using the new Kibron Langmuir trough with an hydrophilic oxide needle for measuring surface tension. There are several plausible sources for the change in isotherm shape, and either of these differences could be relevant.
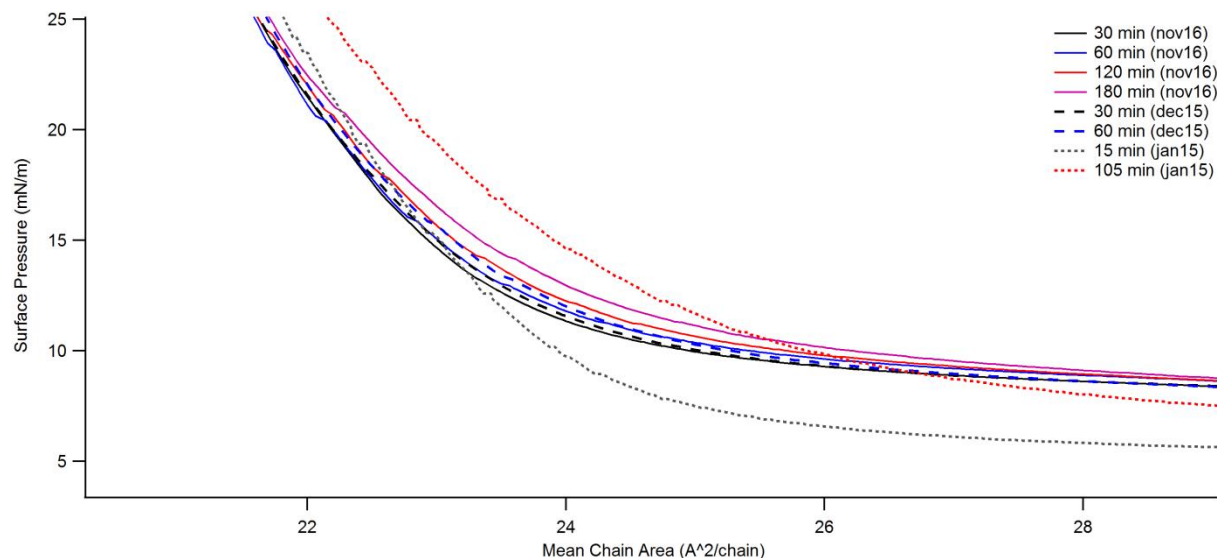
Figure 4.3: Differences in DPPC compression isotherms as a function of time for different sets of compression experiments (destinguished by time after deposition, and the month and year the experiment was performed in).

In the work of Klopfer and Vanderlick,[13] changes in the shape of the DPPC isotherm are also observed over time. In addition to the changes in isotherm shape, they also observe changes in the domain morphologies of DPPC films in the phase coexistence region. They analyze their isotherm data in a particularly strange way, however, which makes their conclusions suspect. They create a new variable $\hat{\pi}$ that is the average surface pressure for a given experiment, including the surface pressure during the hold time. This variable has no intrinsic significance, as it will change dramatically with different hold times and hold pressures, regardless of the isotherm shape. They then further obscure their isotherm data by presenting only $\hat{\pi}$ versus time data and a number representing the "magnitude of the surface pressure increase" with no units. Finally, they assume that their change in isotherm shape is due to contamination, and make up an equation with no thermodynamic relevance (despite their claims) to calculate a percentage of contaminant at their film surface. There are several details discussed in the text that may be useful, however. They observe that depositing films on water that has been aged on the trough and on fresh water does not result in any differences. I have reproduced these results, even on the KSV-NIMA trough where the change in isotherm shape is very rapid. They reason that this result indicates the contamination must come from the gas phase. This is particularly creative logic, as adsorption is often

dependent on the interfacial properties (including whether there is a film present), and the gas phase deposition of material seems equally likely to be affected as the solution phase adsorption. They discuss several other sources of impurities, such as the purchased DPPC or the spreading solvent, although neither of these would be expected to cause increased surface pressure as a function of time.

The changes that are observed between the two different trough systems suggest that trough cleanliness could be a very large contributing factor for the change in isotherm shape over time. The new Kibron trough had been used for fewer experiments, and was easier to clean due to the detachable nature of the Teflon sheet and flame cleaning of the surface tension probe. It does not seem unlikely that the changes in isotherm shape that are left with the new trough system are still dominated by contamination, probably through a combination of all the sources: trough, tension probe, solution, spreading solvent, lipid, and the atmosphere. It is also possible that a longer term relaxation is taking place in the DPPC film. It is even possible that a small amount of the change is due to the hydrolysis of DPPC. Unfortunately, due to the sensitivity of the system, it is very difficult to distinguish between the contributions to the shape of the compression isotherms of DPPC.

4.3 Conclusions

I successfully constructed a series of calibration isotherms for the hydrolysis of DPPC at a water surface. Closer examination of the changes to DPPC films over time, however, revealed that the shape change that is observed does not match the shape change due to hydrolysis. Relevant literature is discussed for this shape change, but it is difficult to draw definitive conclusions from the experiments or the available literature. It is likely that the shape change is due to adsorption of contaminants into the DPPC film, likely from a variety of the many possible sources. While long term relaxation or lipid hydrolysis are possible explanations of the changes to the compression isotherms, under these conditions they are likely overshadowed by contamination.

4.4 Materials and Methods

DPPC (≥99% semisynthetic), 1-PPC (>99%), palmitic acid (≥99%) and chloroform (≥99.8%) were purchased from Sigma-Aldrich and used without further purification. For cleaning, isopropyl alcohol (Fisher 99.9%) was used along with MilliQ water with at least 18.2 MΩ/cm resistivity and less than 3 ppb total oxidizable carbon (TOC).

Two separate Langmuir troughs were used. The first, for the older set of experiments, a custom built PTFE trough of dimensions 52 x 7 x 0.5 cm was used, as well as two PTFE barriers controlled by software purchased from NIMA (KSV-NIMA, Finland). This trough used a balance with a filter paper Wilhelmey plate sensor. The second trough, used for more recent experiments, including the construction of calibration isotherms, was purchased from Kibron Inc., Finland. This trough has a surface area of 431 x 106 mm, and utilizes a hydrophilic oxide needle sensor on a micobalance. The oxide needle was flame cleaned between all samples, and the troughs were cleaned with isopropanol several times, before being cleaned with water at least 3x to remove residual isopropanol. Blank compression isotherms of water were taken to detect contamination, and cleaning was repeated as necessary until the blank isotherms looked clean.

Bibliography

(1)   Gobrogge, C. A.; Blanchard, H. S.; Walker, R. A. Temperature-Dependent Partitioning of Coumarin 152 in Phosphatidylcholine Lipid Bilayers. *J. Phys. Chem. B* **2017**, *121* (16), 4061–4070.

(2)   Kensil, C. R.; Dennis, E. A. Alkaline Hydrolysis of Phospholipids in Model Membranes and the Dependence on Their State of Aggregation. *Biochemistry (Mosc.)* **1981**, *20* (21), 6079–6085.

(3)   Ho, R. J. Y.; Schmetz, M.; Deamer, D. W. Nonenzymatic Hydrolysis of Phosphatidylcholine Prepared as Liposomes and Mixed Micelles. *Lipids* **1987**, *22* (3), 156–158.

(4)   Ickenstein, L. M.; Sandström, M. C.; Mayer, L. D.; Edwards, K. Effects of Phospholipid Hydrolysis on the Aggregate Structure in DPPC/DSPE-PEG2000 Liposome Preparations after Gel to Liquid Crystalline Phase Transition. *Biochim. Biophys. Acta BBA - Biomembr.* **2006**, *1758* (2), 171–180.

(5)   Vaida, V. Atmospheric Radical Chemistry Revisited Sunlight May Directly Drive Previously Unknown Organic Reactions at Environmental Surfaces. *Science* **2016**, *353*, 650–650.

(6)   Tinel, L.; Rossignol, S.; Ciuraru, R.; Dumas, S.; George, C. Photosensitized Reactions Initiated by 6-Carboxypterin: Singlet and Triplet Reactivity. *Phys Chem Chem Phys* **2016**, *18* (25), 17105–17115.

(7)   Martins-Costa, M. T. C.; Anglada, J. M.; Francisco, J. S.; Ruiz-Lopez, M. F. Reactivity of Volatile Organic Compounds at the Surface of a Water Droplet. *J. Am. Chem. Soc.* **2012**, *134*, 11821–11827.

(8)   Griffith, E. C.; Vaida, V. In Situ Observation of Peptide Bond Formation at the Water–air Interface. *Proc. Natl. Acad. Sci.* **2012**, *109* (39), 15697–15701.

(9)   Creuwels, L. A.; van Golde, L. M.; Haagsman, H. P. The Pulmonary Surfactant System: Biochemical and Clinical Aspects. *Lung* **1997**, *175* (1), 1–39.

(10) D. Estrada-López, E.; Murce, E.; P. Franca, M. P.; S. Pimentel, A. Prednisolone Adsorption on Lung Surfactant Models: Insights on the Formation of Nanoaggregates, Monolayer Collapse and Prednisolone Spreading. *RSC Adv.* **2017**, *7* (9), 5272–5281.

(11) Ma, G.; Allen, H. C. New Insights into Lung Surfactant Monolayers Using Vibrational Sum Frequency Generation Spectroscopy. *Photochem. Photobiol.* **2006**, *82* (6), 1517–1529.

(12) Thompson, K. C.; Jones, S. H.; Rennie, A. R.; King, M. D.; Ward, A. D.; Hughes, B. R.; Lucas, C. O. M.; Campbell, R. A.; Hughes, A. V. Degradation and Rearrangement of a Lung Surfactant Lipid at the Air–Water Interface during Exposure to the Pollutant Gas Ozone. *Langmuir* **2013**, *29* (14), 4594–4602.

(13) Klopfer, K. J.; Vanderlick, T. K. Isotherms of Dipalmitoylphosphatidylcholine (DPPC) Monolayers: Features Revealed and Features Obscured. *J. Colloid Interface Sci.* **1996**, *182* (1), 220–229.

Chapter 5: The Partitioning of Small Aromatic Molecules to Air–Water and Phospholipid Interfaces Mediated by Non-Hydrophobic Interactions

5.1 Introduction

The interactions between aromatic molecules are important in a variety of biological contexts. Biological roles of aromatic species include DNA stacking, protein folding and function,[1,2] signaling,[3,4] metabolic electron transport,[5] and diseases such as phenylketonuria (PKU)[6] and amyloid fibril formation.[7,8] The most common biological aromatic molecules are the three aromatic amino acids, tyrosine (Tyr), phenylalanine (Phe) and tryptophan (Trp), the DNA/RNA bases, and a variety of hormones and signaling molecules. To emphasize the number of aromatic interactions, consider the following: about 20% of the human body is protein,[9] and about 8.6% of vertebrate protein is composed of Phe, Tyr or Trp,[10] meaning there are approximately 1.2 kg of aromatic amino acids in a 70 kg human! While most of these amino acids will be incorporated into polypeptides or proteins, examining free amino acids can be useful for gaining insight into the role of these amino acids in proteins,[11] as well as their behavior during their synthesis, transport, and subsequent incorporation into proteins. Some diseases can result in highly elevated concentrations of free amino acid in the body; in classical PKU serum Phe concentrations are greater than 1.2 mM.[12]

The human body is a largely inhomogeneous system even on small scales. Phospholipid membranes separate both cytoplasm from external environments and organelles from cell cytoplasm. These abundant phospholipid interfaces makes their interactions with aromatic species of particular interest. Indeed, interactions between biological membranes and aromatic species are important in understanding the folding of membrane proteins,[13] the function of membrane protein channels,[14] and the transport of metabolites in membranes.[5] These interactions have even been implicated as a likely mechanism of damage in PKU.[15] In these cases, the partitioning of a molecule into the lipid interfacial region, i.e. its interfacial activity or ability to act as a surfactant, is a key factor in understanding function.

It has been postulated that the hydrophobic effect is the main factor affecting the interfacial partitioning of Phe, where the behavior of Phe is attributed to the hydrophobicity of the aromatic group.[11] On the other hand, there is evidence that this picture is incomplete, where the DPPC-Phe interactions are stabilized by interaction between the Phe amine group and water.[16] In this study we will show that a simple hydrophobic picture of aromatic interactions cannot predict the behavior of the aromatic species under study in bulk water, at air-water interfaces, or in phospholipid monolayers.

A related, but not identical, prediction for the interfacial behavior of water soluble molecules is that more soluble, more polar molecules will be less surface active. Some trends have been established that are consistent with these general ideas, such as the increase in surface activity of fatty acids and alcohols as the aliphatic chain length increases and the molecules become less polar and less soluble.[17] It will be shown in this work, however, that the trend for less soluble molecules to be more surface active is also starkly contrasted for very similar aromatic molecules.

While utilizing biological membranes to study interactions with aromatic species would be the most directly relatable system to a variety of applications, these types of complex systems make it difficult to understand the molecular level details at work. Because of this, we have chosen to work with a much simpler model system consisting of a single monolayer of dipalmitoylphosphatidylcholine (DPPC)

at an air water interface as our membrane mimic. These types of model systems are often used to represent more complex ones.[18–25] DPPC in particular was chosen due to its prevalence in biological cell membranes,[26] and the fact it is exceptionally well characterized.[27–31] While the conditions under which a DPPC monolayer best represents a cell membrane are debated,[32–35] it is generally agreed that higher surface pressure (>30 mN/m) systems are most similar, although there is a mismatch between monolayer and liquid crystalline vesicle packing density under this conditions.[36] In this study, we chose to use a lower surface tension DPPC film in order to better characterize the differences between the aromatic molecules under study, at the expense of direct biological relevance.
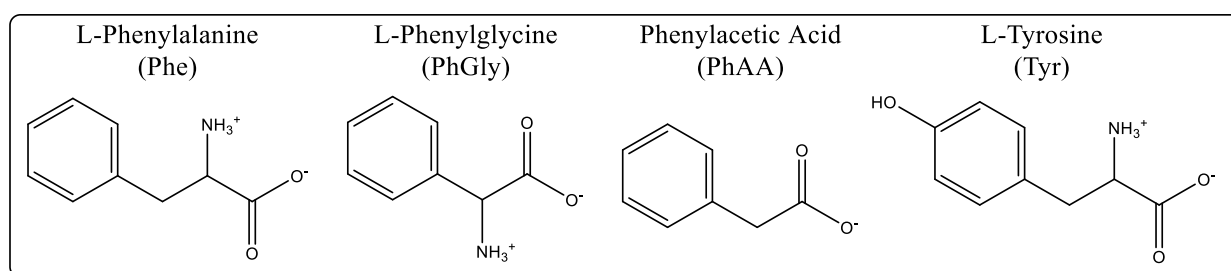
Figure 5.1: Structures of the series of similar compounds under investigation in this study.

In our previous work,[15] we investigated the ability of Phe to perturb model cell membranes, discovering significant changes to interfacial film morphology, ordering, and interfacial tension at relatively low Phe concentrations (2.5 mM). These results were also discussed in the context of PKU, and we suggested the membrane perturbations were drastic enough to contribute to the cytotoxicity associated with PKU. Here, a series of analogous compounds are investigated to understand the molecular interactions at work in heterogeneous aqueous environments. This series is shown in Figure 5.1. Surface partitioning and solubility are discussed for solutions of pure aromatic compounds, followed by a discussion their partitioning into DPPC films. Molecular dynamics simulations are discussed in the context of experimental results, and a study of clustering and aggregation concludes this work.

5.2 Materials and Methods

All materials were purchased and used without further purification unless noted. L-Phenylalanine (99%) was purchased from Alfa Aesar, L-phenylglycine (99%), L-tyrosine (>99%), L-alanine (99%) and

phenylacetic acid (99%) were purchased from Sigma Aldrich. Aqueous solutions of these compounds were prepared by mixing with 18.2 MΩ deionized water with less than 10 ppb total oxidizable carbon. Solutions were prepared fresh prior to each experiment. A bath sonicator (VWR aquasonic 75T) was used until solutions were clear and free from visible precipitate, followed by an additional 20 minutes to help ensure dissolution. Solutions were cooled to room temperature (22-23°C) prior to use. Solution pH was recorded with a pH meter at: 2.5 mM Phe: 7.0 ± 0.3, 2.5 mM PhGly: 6.6 ± 0.3, 2.5 mM PhAA: 4.0 ± 0.3, 2.4 mM Tyr: 7.0 ± 0.3. Large uncertainties in pH are attributed to low ion concentrations in solution.

5.2.1 Langmuir Trough:

The Langmuir Trough used was custom built from PTFE with dimensions of 52 cm x 7 cm x 0.5 cm with two PTFE barriers allowing for symmetrical compression, and it was controlled using software purchased from NIMA (KSV-NIMA, Finland). A Wilhelmy microbalance with a filter paper plate was used to measure the decrease in surface tension from that of pure water (i.e. surface pressure, π). Adsorption experiments were performed for L-phenylalanine, L-phenylglycine, L-tyrosine, and L-phenylacetic acid by depositing aqueous solution containing one of these molecules on the trough and recording surface pressure over time with barrier position, and therefore surface area, held constant. 1,2-Dipalmitoyl-sn-glycerol-3-phosphorylcholine (DPPC, >99% semisynthetic) was purchased from Sigma Aldrich and dissolved at a concentration of 1.6 mg/mL in chloroform (Sigma Aldrich >99.8% ACS grade). For adsorption experiments with a DPPC film present, aqueous aromatic solutions were deposited as subphase, followed by DPPC solution deposition dropwise to reach a DPPC mean molecular area (MMA) of approximately 70 $Å^2$/molecule. In both cases adsorption experiments were recorded overnight, and compression experiments performed the following morning by compressing the PTFE barriers to reduce surface area at a rate of 75 cm^2/minute. The compression experiments following adsorption were used to characterize the MMA of the DPPC film used (see Figures A2.7-A2.12 in Appendix 2).

An alternative method that could be used for performing these experiments would involve depositing pure water on the Langmuir trough, creating a DPPC monolayer, and then injecting a

concentrated solution under the monolayer. This method can be advantageous because it ensures that the DPPC monolayer has time to equilibrate prior to being perturbed by the soluble surfactant. However, the method can be problematic due to concentration gradients and incomplete subphase mixing. Additionally, low solubility limits for PhGly and Tyr would not allow for concentrated solutions to be used for injection, barring useful comparison between the molecules in our series. Because of these drawbacks, we opted not to perform injection experiments.

5.2.2 Fluorescence Experiments:

A QM-6 steady-state spectrofluorimeter from Photon Technology International (PTI) was used to acquire fluorescence spectra. A 160 µL cuvette was filled with amino acid solution was stirred continuously in a temperature controlled holder at 23°C while spectra were acquired using a 257 nm excitation with 2 nm entrance and exit slits, scanning over a 275-375 nm range with a 5 second integration time and 1 nm step. The emission intensities measured on the photomultiplier remained in the calibrated linear range for all measurements.

5.2.3 NMR Experiments:

NMR experiments were performed with a Varian INOVA-500 NMR spectrometer operating at 499.60 MHz for ^{1}H observation. Phe solutions were prepared in D_2O (Cambridge Isotope Laboratories, 99.9%). 2D DOSY NMR measurements of the diffusion coefficients (D) for Phe and HOD were performed with convection compensation using the gradient compensated stimulated echo pulse sequence.[37] In the calculation of the diffusion coefficient, calibrated pulsed field gradient strengths included non-uniform gradient compensation, with a maximum calibrated gradient strength of 55.5 Gauss/cm.[38] A constant diffusion delay Δ of 0.025 s and δ of 0.002 s was used in all experiments. The DOSY calculations were performed using the multi-component analysis in the VNMRJ 3.2A software package (Agilent Technologies, Inc.), allowing for 2 possible D values for each peak, using integrated intensities vs. gradient strength. The ratio of the diffusion constant of Phe to HOD was used for

comparison between solutions in order to account for changes in solution viscosity due to changes in Phe concentration.

5.2.4 Mass Spectrometry Experiments:

Mass spectrometry analysis was performed on a Waters Synapt G2 HDMS mass spectrometer using both 5 and 50 volt negative electrospray ionization. 1 mM aromatic samples dissolved in a 1:1 mixture of water and methanol were analyzed. Other instrument parameters remained constant, and were as follows: Analyzer: Resolution Mode, Capillary Voltage: 1.5000 kV, Source Temperature: 80 °C, Sampling Cone: 30.0000 deg, Extraction Cone: 5.0000 deg, Source Gas Flow: 0.00 mL/min, Desolvation Temperature: 150 °C, Cone Gas Flow: 0.0 L/Hr, Desolvation Gas Flow: 500.0 L/Hr.

5.2.5 Molecular Dynamics Simulations:

Classical MD simulations were performed for Phe, PhGly, PhAA, and Tyr at both water-air and water-DPPC-air interfaces. Amino acids were introduced to the water phase at a concentration of 150 mM with the exception of Tyr, where a concentration of 30 mM was used to account for the lower Tyr solubility. As a control, simulations with 150 mM Tyr concentration were also performed. The all-atom force field, Slipids, was employed for description of lipids.[39] The TIP3P model was used for water.[40] Amino acids were parametrized in-house, based on quantum chemical calculations and the GAFF force field that is compatible with Slipids.[41] Simulated systems consisted of approximately 7000 water molecules and 128 DPPC (64 at each interface) in the case of lipids-coated interfaces. A pre-equilibrated DPPC monolayer system was used and held at an area per lipid of 79 $Å^2$/lipid employing NVT ensemble. A slab of water, either pure or with the DPPC film at both surfaces was present in the middle of the box (see Figure A2.15 in Appendix 2). A simulation box of a rectangular prismatic shape was employed with periodic boundary conditions applied in all directions. The lateral dimensions of the interfaces were equal to 6×6 nm^2 in the case of the water-air system, and 6.69×6.69 nm^2 in the case of the water-DPPC-air system. In order to prevent interactions between periodic images, the box was elongated in the direction perpendicular to monolayers to a size of 16 nm and 28 nm for water-air and water-DPPC-air systems,

accordingly. This resulted in a vacuum region that was approximately three-fold thicker than that of the water-lipid system. The temperature was set to 310 K and controlled employing the velocity rescale algorithm.[42] Equations of motion were integrated with a 2 fs time step. A cut off of 1 nm was employed for both van der Waals and short-range coulomb interactions whereas long-range electrostatics were accounted for by employing the Particle Mesh Ewald method.[43] MD trajectories of 100 ns were calculated, with the final 50 ns used for analysis. In the case of PhAA and Tyr in the DPPC-containing systems, longer trajectories, of 200 and 300 ns respectively, were calculated in order to improve convergence. Simulation convergence was controlled by means of the number of amino acids adsorbed at the interfaces together with the standard convergence criteria for energy and temperature. All MD simulations were performed using the Gromacs 4.6.1 software suit and visualization was done employing the VMD package.[44,45]

5.3 Results/Discussion

5.3.1 Air-Water Interfacial Partitioning

The series under investigation consists of Phe, Tyr, phenylglycine (PhGly), and phenylacetic acid (PhAA). All of these can be thought of as structural derivatives of Phe, and their structures are shown in Figure 5.1. Tyr is equivalent to Phe with an extra hydroxyl group at the para position of the aromatic ring. PhGly is Phe without the linking methylene group between the phenyl ring and the amino acid. Phenylacetic acid is Phe with a simpler carboxylic acid headgroup, or it could also be thought of as PhGly without the amine group. Under the conditions of this study, Phe, PhGly, and Tyr are expected to exist in their zwitterionic forms, while PhAA will be partially ionized. The differences in behavior of this series of Phe molecules, as examined in this study, can give insight into the importance of these various structural changes to Phe.

The use of surface sensitive Langmuir trough techniques allows for direct measurement and manipulation of surface area and surface tension or surface pressure (i.e. the decrease in surface tension from that of bare water). The first series of experiments was carried out with aqueous solutions of

aromatic compound in the absence of other surfactants, in order to characterize the behavior of these molecules at bare air-water interfaces. Of the compounds under study, PhAA's behavior follows most closely that which would be expected for a simple soluble surfactant system and will, therefore, be used to exemplify the analysis of surface partitioning behavior and energetics. Koller and Washburn,[46] previously measured surface tension as a function of PhAA concentration, and note its quick surface tension equilibration times of less than 10 minutes. Surface pressure data collected via Langmuir trough experiments in this work agrees with these measurements (Figure A2.1 in Appendix 2), although Langmuir Trough/Wilhelmy Microbalance setups are less accurate for measuring the surface tension of quickly equilibrating systems than the capillary measurements previously carried out. Because of this, we will use their previously published data. Data from Koller and Washburn[46] is recreated approximately in Figure 5.2, using the fit and uncertainty in surface tension described, as well as the number of points they collected. The exact data points they used were not described, instead they report an equation that fit their data, along with an uncertainty. We spaced the data points evenly in concentration over the concentration region that was studied. Their data was recreated in order to get a more accurate uncertainty for determining the line slope, and therefor surface excess concentration, below.
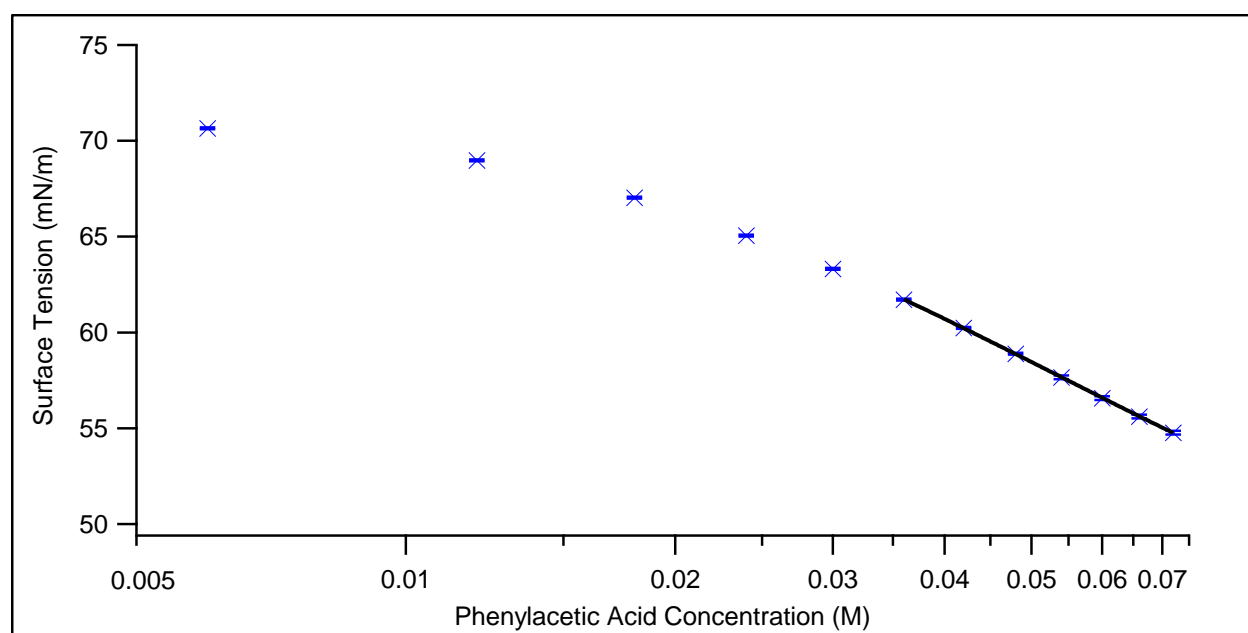
Figure 5.2: Phenylacetic Acid Concentration v. Surface Tension reproduced from Koller and

Washburn[46]. Error bars are shown but are relatively small. The fit to evaluate ∂γ/∂ln C is shown as a black line. The region where a linear fit is accurate for this data is known as the saturation regime.

For well-behaved soluble surfactant systems such as this, surface excess concentrations can be calculated by fitting to the Gibbs adsorption isotherm. In its most basic form, it states that:

$$-\partial\gamma = \sum_i \Gamma_i\, \partial\mu_i$$

Where γ is surface tension, Γ_i is the surface excess concentration of component i, and μ_i is the chemical potential of component i. For a single surfactant in solution, this can be simplified to:

$$\Gamma = \frac{-1}{n\mathrm{RT}}\left(\frac{\partial\gamma}{\partial \ln a}\right)$$

Where R is the gas constant, T is temperature, and a is the activity of the soluble surfactant. n is a factor that depends on the ionization of the soluble surfactant as well as additional electrolyte concentration. For completely dissociated monoionic surfactants in the absence of electrolytes, n approaches 2 to account for contributions from the surfactant as well as the counterion. In the limit of high electrolyte concentration or neutral surfactants n approaches 1. For low additional electrolyte concentration with a single acidic surfactant, n can be calculated as:

$$n = \left(1 + \frac{[\mathrm{A^-}]}{[\mathrm{A^-}] + [\mathrm{AH}]}\right)$$

Where $[\mathrm{A^-}]$ is the concentration of deprotonated acid and $[\mathrm{AH}]$ is the concentration of protonated acid. This further simplifies to:

$$n = \frac{2 + 10^{pKa-pH}}{1 + 10^{pKa-pH}}$$

At sufficiently low concentrations, the activity can be approximated by the concentration, yielding:

$$\Gamma = \frac{-1}{n\text{RT}}\left(\frac{\partial\gamma}{\partial\ln C}\right)$$

The derivative can be obtained by fitting the highest seven concentration values, shown in Figure 5.2, where the slope is approximately constant in $\partial\gamma/\partial\ln$ C. This region is often referred to as the saturation regime, where surface excess concentration no longer varries with increased concentration. This yields a slope of 10.1 ± 0.2 mN/m. The experimental pKa of PhAA is 4.31,[47] and the measured pH value of the solutions were 4.0 ± 0.3, yielding an n value of 1.3 ± 0.2. Using these derived values, the surface excess concentration is 54 ± 6 Å^2/molecule mean molecular area (MMA). The majority of the uncertainty in this value comes from the relatively large uncertainty in the measurement of pH, which is attributed to the low electrolyte concentration of the solutions.

The physical size of one PhAA molecule can be estimated from the solid density of 1.08 g/cm^3, yielding a size of 209 Å^3/molecule. Assuming each molecule to be a cube, the molecular area is estimated at 35 Å^2/molecule. This estimate is likely high for many orientations of the molecule, but it is still significantly smaller than the experimental mean molecular area of 54 ± 6 Å^2/molecule at surface saturation. This implies that a saturated surface film of PhAA is still somewhat compressible, which is important for the interpretation of mixed film results that will be presented below. This may seem counterintuitive because the surface saturation in the case of soluble surfactants refers to the regime in which surface excess concentration no longer increases with increasing bulk concentration. In the saturation regime, however, the surface is generally not completely covered. In fact, the total surface concentration must necessarily increase with increasing bulk concentration in order for the excess surface concentration to remain constant.

5.3.2 DPPC Interfacial Partitioning

Next, experiments were carried out in the presence of our model cell membrane, a DPPC monolayer at a mean molecular area (MMA) of ~70 Å^2/molecule. This MMA was chosen to induce easily observable changes in the monolayer and accurately characterize the differing behavior of the aromatic

molecules under study. For a mixed system consisting of aqueous PhAA solutions covered with a monolayer of insoluble DPPC, adsorption isotherms were measured (Figure 5.3). The surface pressure of the mixed system is significantly higher than that of either PhAA or DPPC individually under the same conditions, as is often the case for mixed soluble/insoluble surfactant films.[48–51]
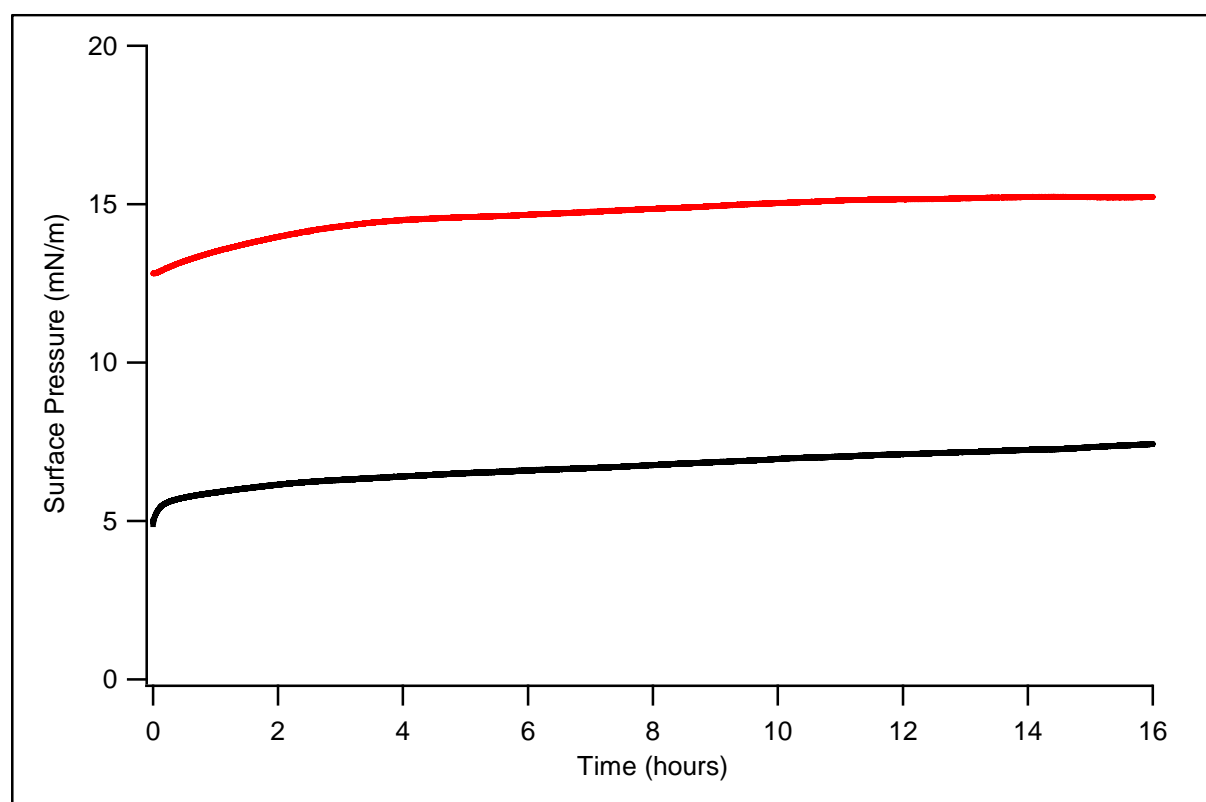
Figure 5.3: Average adsorption isotherms of 2.5 mM PhAA in the presence of a surface film of 70 Å²/molecule DPPC film (red, top) and a DPPC film in the absence of soluble surfactant (black, bottom).

In the case of adsorption of a soluble surfactant to an interface containing an insoluble surfactant, in-depth analysis becomes much more difficult than for single surfactant systems. The simple theoretical analysis using Gibbs adsorption isotherms, used above, no longer applies. The theories most often used to model mixed surfactant films describe either mixtures of soluble surfactants,[52–54] or mixtures of insoluble surfactants.[55–58] Either regime has inadequacies for soluble/insoluble mixed surfactant systems by failing to describe the two dimensional phase transitions of the insoluble surfactant, or the equilibrium between the surface and solution for the insoluble surfactant, respectively. There are also theories explaining the "penetration" of soluble surfactants into insoluble surfactant films.[59–63] While the

penetration theories are clearly the most relevant to the system at hand, they require the collection of data that cannot be obtained for any of the aromatic molecules studied here, aside from PhAA. For such analysis, the quantity most problematic to obtain is the change in surface tension as a function of bulk concentration in the presence of a DPPC film. It will be apparent that this quantity cannot be evaluated even in the absence of DPPC film in the following section, due to surface tensions that are invariant with concentration and equilibration time that are longer than experiment timescales. Because of this, we have chosen to employ a simpler, more approximate analysis of the mixed film systems, using ideas common to theories of mixed insoluble monolayers.

For insoluble mixed films, the Additivity Rule is based on the idea that an ideal mixture of surfactants will adopt the phase, and thereby the MMA, they would exist in as a pure film at any given surface pressure.[64] While the entirety of the Additivity Rule generally is only applicable to mixtures of insoluble surfactants, the basic idea behind it can be used to examine the more complicated mixed soluble-insoluble surfactant systems present in this work. This usage can give useful information and help analyze deviations from ideal behavior.
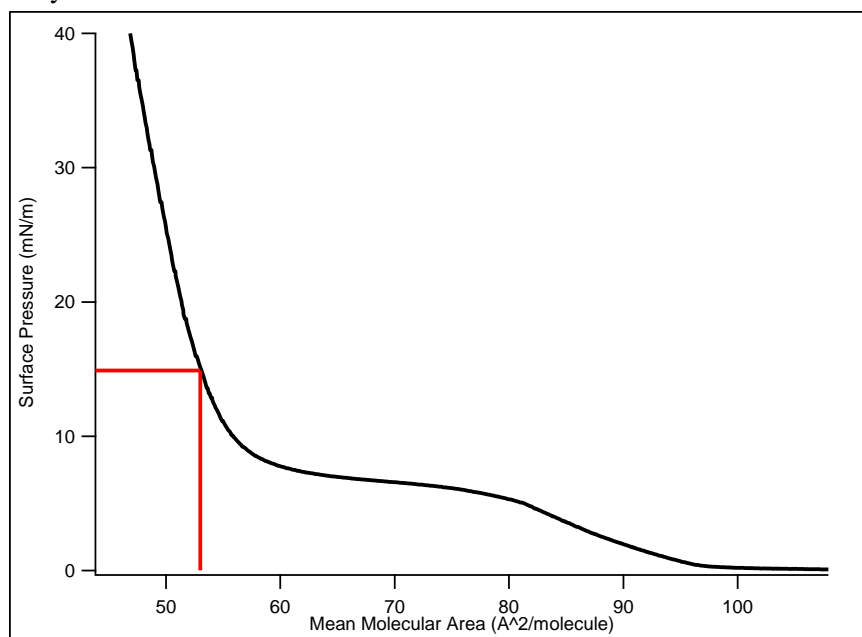
Figure 5.4: DPPC compression isotherm (black) on water, in the absence of soluble surfactants. Red lines illustrate the value of mean molecular area that would be expected for a pure DPPC film at the surface pressure that is observed in our mixed DPPC PhAA system.

In the case of the mixed PhAA and DPPC system, the average surface pressure attained at equilibrium (data from 40,000 – 50,000 seconds used, Figure A2.11) is 14.9 ± 0.5 mN/m. For an ideal system, this corresponds with MMA$_{DPPC}$ of 53 Å^2/molecule (found in a pure DPPC system), as illustrated

in Figure 5.4. For PhAA the ideal MMA can be estimated through the surface pressure v. concentration data discussed earlier for a pure PhAA solution. A 14.9 mN/m surface pressure is associated with a 55 mM PhAA solution, a concentration where the surface excess concentration has saturated, with the saturation MMA$_{PhAA}$ value of 54 ± 6 Å^2/molecule found in the preceding section. This analysis implies that even for ideal interactions between DPPC and PhAA, the DPPC film in the mixed system has been compressed from 70 to 53 Å^2/molecule, and the PhAA surface film in the mixed system is existing at surface pressures that are normally inaccessible for low concentration solutions, even with a surface saturated film. Both these changes, the compression of DPPC and the increased surface excess of PhAA, would require energy, however. The energy source would have to be, for lack of anything else, favorable interactions between the DPPC and PhAA. Because of this, the interaction energy between DPPC and PhAA under these conditions can be estimated from the combined free energy costs of bringing additional PhAA to the surface, compressing the DPPC film, and compressing the PhAA film.

The requirement PhAA be compressed is consistent with the simple dimensional argument given earlier. Even a surface with saturation coverage of PhAA is still compressible, meaning that there is space in the film for DPPC to occupy, as well as the possibility for additional PhAA molecules to partition to the surface, due to favorable interactions with DPPC. It is, unfortunately, difficult to quantify the amount of energy required to bring addition PhAA to the surface. However, a lower bound on the energetic interactions between DPPC and PhAA can be produced by estimating the energy required to compress the DPPC film. The surface pressure – surface area work required to compress the DPPC film can be calculated as:

$$\int_{A_1}^{A_2} \frac{1}{C_s} \, dA$$

Where A is the mean molecular area and C$_s$ is the surface compressibility, defined as:

$$C_s = \frac{1}{A}\frac{dA}{d\gamma} = \frac{-1}{A}\frac{dA}{d\pi}$$

The combination of these two equations yields:

$$\int_{A_1(\pi)}^{A_2(\pi)} A(\pi)d\pi$$

This is easily evaluated numerically using the compression isotherm of a pure DPPC film (Figure 5.4). To compress a DPPC film from 70 to 53 $\mathring{A}^2$/molecule, an energy of approximately 3 kJ/(mole DPPC) is required. This corresponds with the lower bound on the energy of interaction between DPPC and PhAA. When considering the interaction energy between PhAA and DPPC it is important to note that if, on average, there are multiple PhAA molecules interacting with each DPPC molecule the energetic value of any given interaction would be decreased accordingly. It should be reiterated, however, that this calculation provides only the minimum interaction energy, as an additional entropic costs are certainly required to bring additional PhAA molecules to the interface and compress them, if they are indeed compressed.

	Phenylalanine (2.5 mM)	Phenylglycine (20 mM)	Phenylacetic Acid (2.5 mM)	Tyrosine (2.4 mM)
Equilibrium Surface Pressure (mN/m)	0.9 ± 0.1	0.0 ± 0.2	0.95 See Ref[46]	0.1 ± 0.1
Surface Pressure with DPPC (mN/m)	22.7 ± 0.6	6.9 ± 0.3	14.9 ± 0.5	6.8 ± 0.3
Change in Surface Pressure with DPPC (mN/m)	15.8 ± 0.8	0.0 ± 0.6	8.1 ± 0.8	-0.1 ± 0.7

Table 5.1: Experimental surface pressures at equilibrium of aqueous solutions of aromatic species both with a bare air-water interface and with a 70 $\mathring{A}$2/molecule DPPC film. The change in surface pressure from a pure DPPC film is shown as well. The values are averaged over time periods where equilibrium appears to be established, i.e. surface pressure change over time is near zero. Times used were: hours 1-2 of adsorption for PhGly and Tyr, hours 13-15 for Phe, and hours 8-10 for all mixed aromatic/DPPC systems. The surface pressure measured for DPPC on pure water was 6.9 $\pm$ 1.1 averaged over the same time period as the DPPC data presented. Listed uncertainties are standard deviations of the mean values. See Appendix 2 for raw data and discussion of uncertainties (Figures A2.2-A2.12 in Appendix 2).

The equilibrium surface pressures reached for the entire series of molecules are shown in Table 5.1. Equilibrium surface pressure here is described as the surface pressure once it has stopped varying with time. There are several features of these data that are worth noting. First, there are no significant differences between either the PhGly or Tyr solutions and pure water, even near the solubility limits of these compounds, 25-35 mM[65] and 2.5 mM,[66] respectively. Second, the alteration to surface tension by Phe with a DPPC film is even greater than the effect observed with PhAA, despite its similar equilibrium surface pressure at 2.5 mM. The adsorption isotherms with DPPC used to create the data in Table 5.1 are shown in Figure 5.5.
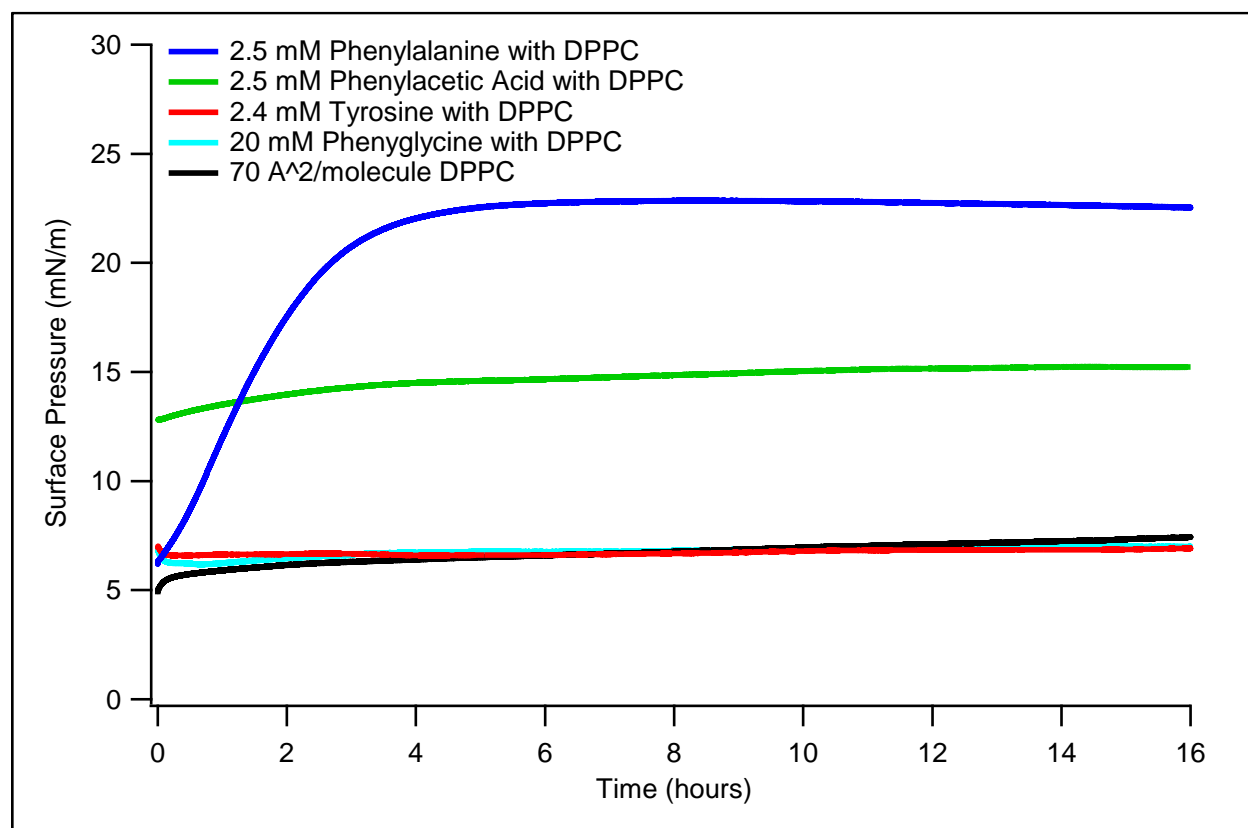
Figure 5.5: Average adsorption isotherms of (from top to bottom at time 0): 2.5 mM PhAA (green), 2.4 mM Tyr (red), and 20 mM PhGly (light blue), 2.5 mM Phe (blue) with 70 Å²/molecule DPPC film, and, finally, the unperturbed DPPC film (black).

Phe can be analyzed in a similar manner as PhAA, although with several additional difficulties that impede quantitative analysis. Namely, solutions of pure Phe take a very long time for surface pressure to equilibrate. For 7.5 mM Phe (with no DPPC) the equilibration time is approximately 10 hours.

This time increases to approximately 20 hours at 5 mM Phe and at 2.5 mM Phe the equilibration time is likely much longer. This makes measuring both the equilibration time and the surface pressure difficult due to competition from water evaporation and surface contamination. These slow equilibration times are associated with an activation barrier for moving surfactant from the bulk to the surface.[67] This activation barrier appears to exist for all soluble surfactants,[68] although the equilibration in the case of Phe is exceptionally slow. Additionally, equilibrium surface pressure no longer changes with bulk Phe concentrations above ~10 mM. In this region, commonly associated with micelle or soluble aggregate formation, use of the Gibbs adsorption equation becomes impossible. These two factors limit the concentration range that surface tension v. concentration measurement could be used for a Gibbs adsorption isotherm to approximately 2.5 to 10 mM. This concentration is not in the surface saturated region, so the Gibbs adsorption isotherm and more complicated penetration theories do not apply.

Despite these difficulties, the same analysis that was used for the PhAA and DPPC system can be employed for Phe and DPPC. The equilibrium surface pressure of Phe with DPPC is 22.6 ± 0.6 mN/m. This surface pressure corresponds to a 50.6 $Å^2$/molecule pure DPPC film. While, for the reasons described above, the surface excess concentration of Phe cannot be exactly determined, this experimental surface pressure corresponds to a degree of surface partitioning that would be expected for a Phe bulk concentration above ~10 mM, even though the experimental concentration of Phe was 2.5 mM, implying a significant increase in partitioning of Phe to the surface in the presence of a DPPC film. In the same way as for the PhAA and DPPC system, this implies favorable energetic interactions between DPPC and Phe of at least ~5 kJ/(mol DPPC) to offset the energy cost of compressing the DPPC film. In this case, however, it is unknown if it is required that the Phe at the surface is compressed beyond the equilibrium mean molecular area normally obtained for a pure Phe/water system, in order to account for the observed surface pressure, although compression is not unlikely. Our previous theoretical and experimental studies of Phe and DPPC systems are consistent with these results, showing condensing effects on the DPPC as well as drastic surface morphology changes.[15]

The remaining two molecules in our series, PhGly and Tyr, display no modification to surface pressure that is observable with our techniques, either in the presence or absence of DPPC. This indicates that neither of these species acts as a surfactant, and their concentration at the water surface is not in significant excess of their concentration in the bulk. Because there is no surface partitioning in either case, very little can be said about the interactions of PhGly and Tyr with DPPC. If the interactions are similar to those observed in Phe and PhAA, significant perturbations to the DPPC film would be expected by these molecules. This suggests that the interactions of DPPC with PhGly and Tyr are not strongly favorable, but range from either weakly favorable to strongly unfavorable. The results of the Langmuir trough data analysis are summarized in Figure 5.6.
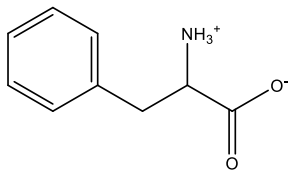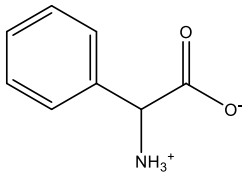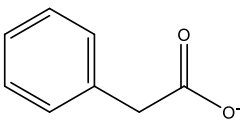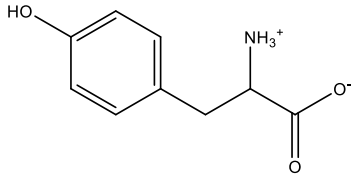
Figure 5.6: A summary of the target molecules of this study, with their approximate solubilities and the observed trends in surface activity and interactions with DPPC. Solubility data are for 25°C solutions and taken from references for Phe[69,70], PhGly (D enantiomer, solubility is pH dependent)[65] PhAA[71], and Tyr.[66]

An interesting feature of these data is the lack of correlation between their surface activity and the solubility of the compounds in this series. Less soluble molecules are generally expected to be more surface active, but here, instead, we observed that the least soluble molecules are also the least surface active. Further, the calculated polar surface area places the molecules in the order Tyr (83.6 Å^2) > Phe = PhGly (63.3 Å^2) > PhAA (37.3 Å^2),[72] which does not correlate with either the solubility or surface activity orderings to a significant extent. In fact, the molecules with the highest polar surface areas are the least soluble by a large margin. PhAA and Phe arguably have the lowest polar surface area per total surface

area while also being the most surface active. However, the ordering between Phe and PhAA is incorrect, and some surface activity for PhGly would still be expected considering the relatively insignificant change from Phe. There is clearly something more complex at work, which defies simplistic polarity or solubility predictions.

5.3.3 Molecular Dynamics Simulations

The extremely different behavior observed between Phe and PhGly, the two most similar molecules in the system, is particularly intriguing. In order to gain a better molecular level understanding of why the aromatic compounds under study behave in drastically different ways, classical molecular dynamics (MD) simulations were performed. There are several difficulties that arise when attempting to compare molecular dynamics simulations with experimental data of this type. Mainly, there is a mismatch between both the observable time and size scales (simulations: nanoseconds and nanometers; experiments: seconds to hours and centimeters) due to computational and experimental limitations. In simulations, restricted size scales can be problematic both for capturing DPPC phase behavior,[73] as well as reducing the usable range of soluble surfactant concentrations. Low concentration simulations are additionally problematic due to larger simulation sizes requirements as well as longer time averaging. Moreover, in classical MD simulations, the protonation state of considered molecules has to be fixed because during simulations there is no possibility of covalent bonds breaking or forming. Because of these constraints, full quantitative agreement is not expected between experiments and simulations, but qualitative agreement lends validity to the computational results and their molecular level description of phenomena observed in experiments.

Molecular dynamics simulations were performed for all four molecules under study, both in the presence of a DPPC film as well as with a bare water interface. The zwitterionic form of all surfactant molecules was assumed. To enhance sampling along the trajectories, concentration of Phe, PhAA and PhGly was set to 150 mM. In the case of Tyr, due to its relatively low solubility, concentration of 30 mM was considered. Simulations were performed for 150 mM Tyr as well, and density profiles are shown in

Figure A2.16 in Appendix 2. The qualitative behavior of Tyr was similar at both concentrations, although the magnitude of its surface partitioning decreased at lower concentrations as would be expected. Density profiles calculated for the case of bare air-water interfaces are presented in Figure 5.7.

Figure 5.7: Density profiles of amino acids at the water-air interface: a) 150 mM Phe, b) 150 mM PhGly, c) 150 mM PhAA and d) 30 mM Tyr. Profiles of water (red), the carbon atom of the carboxylic group of the aromatic species (green), and the para carbon atom of the aromatic ring (purple) are depicted. The profiles are calculated along the interface normal. In each system, the whole simulation box containing two interfaces was used for analysis.

Based on the information contained in the density profile data, the MD simulations appear to be in qualitative agreement with the experimental data for aromatic species in water with a bare surface. For the cases of Phe and PhAA, the density of amino acid is decreased in the bulk aqueous phase, and enriched near the interface. This suggests preferential surface partitioning of both PhAA and Phe, which corresponds with an increase in surface pressure. For PhGly, there is little depletion in the bulk phase, and, in turn, little enrichment at the interface. For all three of these species, however, moving through the para-carbon density profile from the center of the water slab outwards there is a decrease in density followed by an increase. The same shape is observed for the carboxylic acid carbon density, although the peak is closer to the center of the slab. This implies a preferential orientation of the molecule when it is near the air-water interface, with the aromatic group pointed away from the solution and the carboxylic acid toward it. This result is not surprising for these amphiphilic molecules, where the aromatic group is expected to be hydrophobic and partially excluded from the solvent while the hydrophilic groups remain solvated. However, In the case of Tyr the bulk density is enriched, while density is depleted near the air-water interface. This interfacial depletion would correspond to a negative surface excess concentration, as well as a small negative surface pressure (an increase in surface tension). Tyr near the interface is still preferentially oriented with the aromatic moiety away from the bulk water, despite the surface depletion, although there may be more orientational flexibility.

Qualitative agreement with experiments is observed. The simulations predict high surface partitioning of Phe and PhAA, combined with the lower surface partitioning of PhGly and the surface depletion of Tyr. This matches with experimentally observed surface pressure increases by Phe and PhAA, and negligible surface pressure changes by PhGly and Tyr.

Molecular dynamics simulations were also performed to mimic the mixed film experiments, where DPPC film was present at a MMA of approximately 70 Å^2/molecule initially, and the aromatic species begin in bulk solution. Density profiles are shown in Figure 5.8.
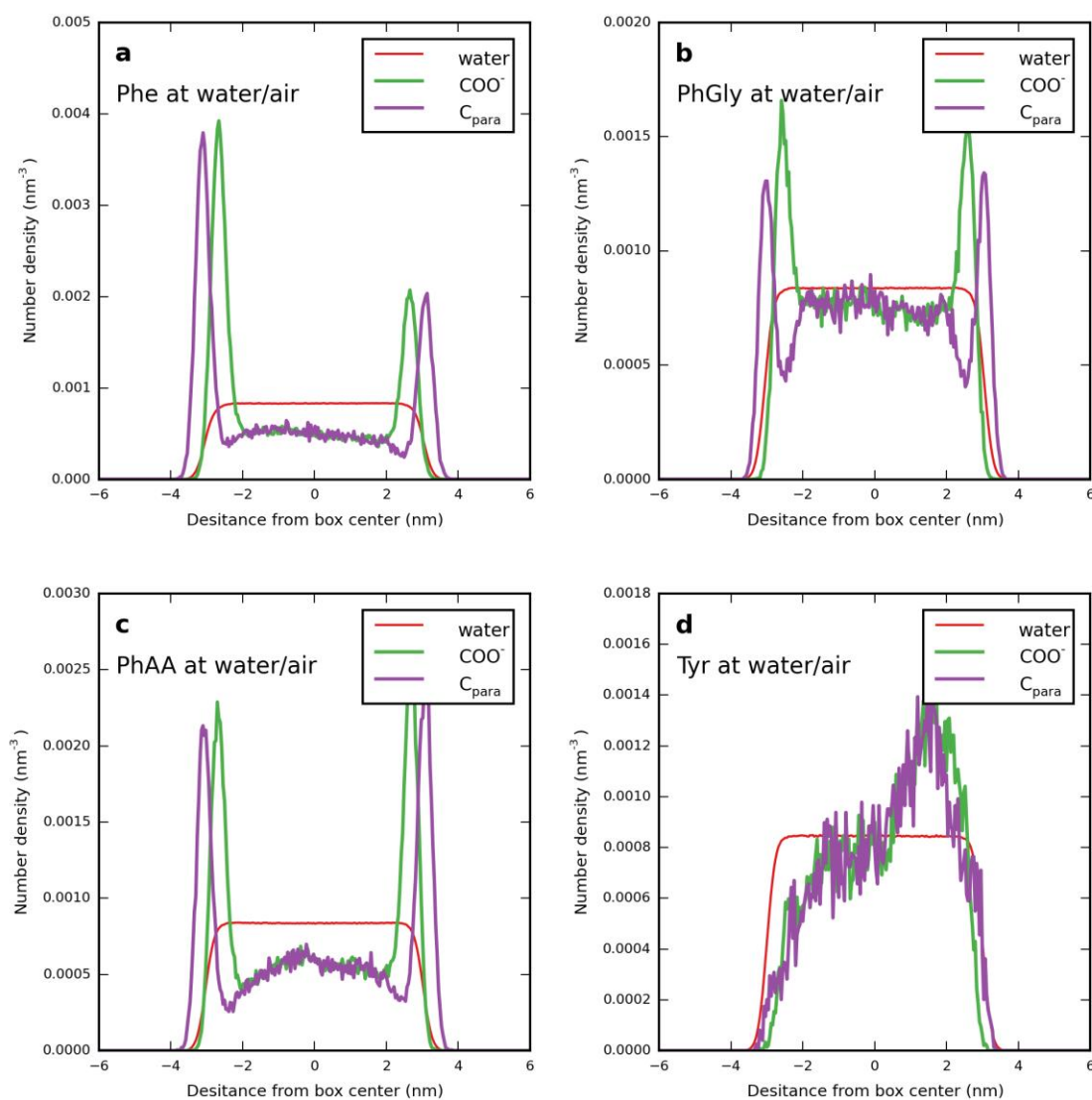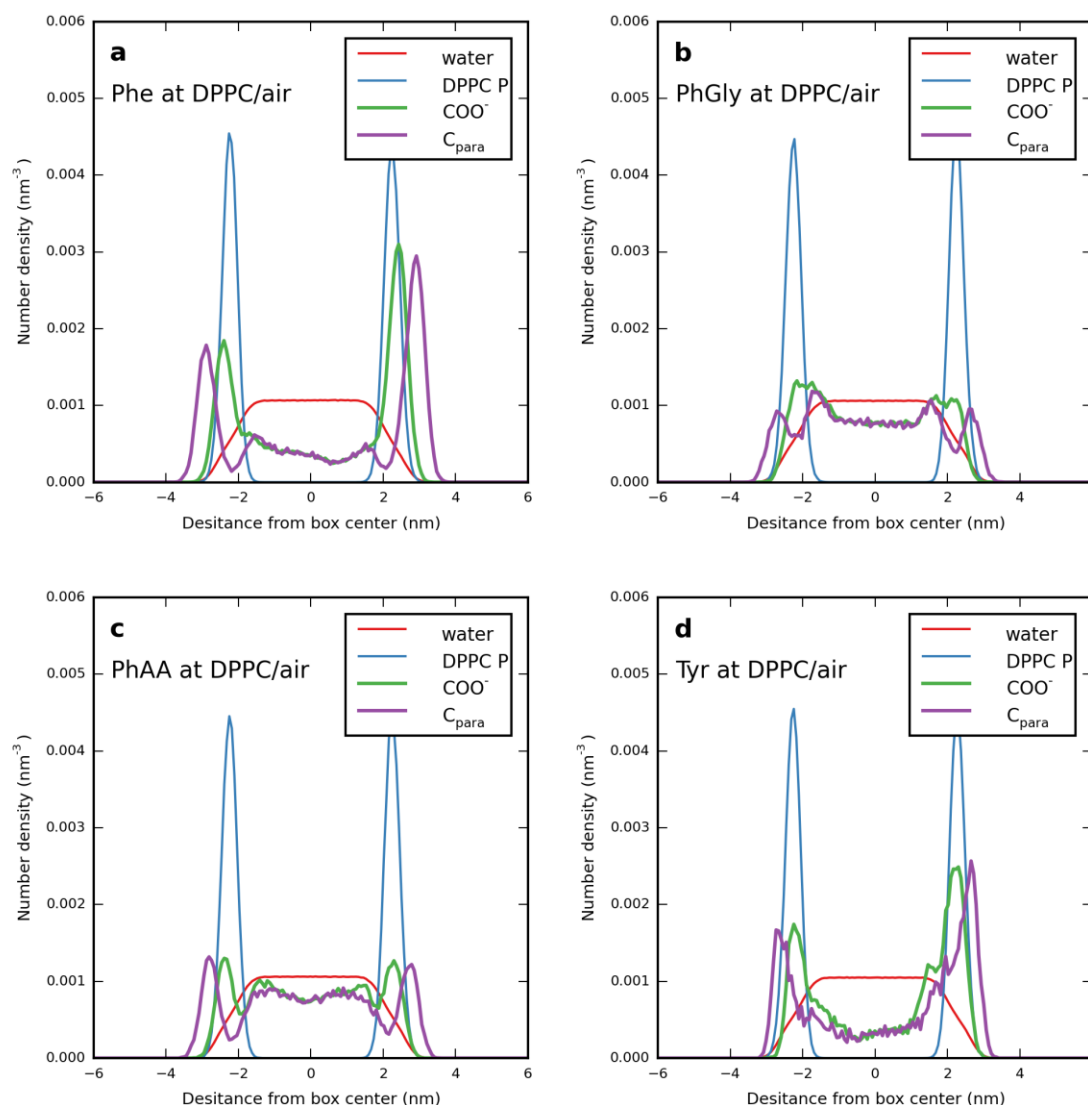
Figure 5.8: Density profiles of amino acids at the DPPC/air interface: a) 150 mM Phe, b) 150 mM PhGly, c) 150 mM PhAA, and d) 30 mM Tyr. Profiles of water (red), phosphorous atom of DPPC headgroup (blue), the carbon atom of the aromatic compound's carboxylic group (green), and para carbon atom of the aromatic ring (purple) are depicted. The profiles are calculated along the interface normal. In each system, the whole simulation box containing two interfaces was used for analysis.

The density profiles indicate that each aromatic species undergoes a degree of preferential partitioning into the DPPC film. This contrasts the experimental results where partitioning was observed only for Phe and PhAA into a DPPC film. Note, however, that because there are various orientations of the aromatic molecules, the density profiles have a complicated structure, and careful interpretation is

required. For instance, note that Phe is the only amino acid in which the COO⁻ moiety penetrates into the lipid monolayer further from the box center than the location of phosphate groups of DPPC. Also, when visually comparing Phe and Tyr trajectories, it is clear that while Phe predominantly orients its aromatic ring parallel to the non-polar lipid acyl chains of DPPC, the ring of Tyr has more flexible interfacial orientations. The latter is due to the presence of the hydroxyl group of Tyr, which can participate in hydrogen bonds with water. The differences in ring orientations between Phe and Tyr are also visible in the different shapes of the corresponding density profiles at the interface, where Phe has well-defined and separated peaks, but Tyr has wide and complicated peaks.

There is additional information about molecular orientation contained in the density profiles. For all the aromatic species, there are two peaks near the surface in both the para carbon and the carboxyl density profiles: one deeper into the DPPC film, and one closer to the water slab. For the case of the deeper peaks, there is a separation between the para carbon and the carboxyl peaks, corresponding to approximately the length of the aromatic molecule. This implies the same orientation that is observed without DPPC, where the molecules are perpendicular to the water surface with the aromatic groups pointing away from the water slab. The second peak, closer to the water slab, has overlap between the phenyl ring para carbon and carboxyl carbon, indicating an orientation parallel to the water surface for the population of molecules that is enriched near the DPPC headgroup region. To reiterate, two orientations are found: one deeper in the DPPC film perpendicular to the water surface, and one slightly below the DPPC film parallel to the water surface.

The partitioning can be evaluated more quantitatively through calculation of surface excess concentrations. Here, surface excess is defined as:

$$\Gamma = \frac{n_T - V_b C_b}{A}$$

Where n_T is the total number of molecules, V_b is the volume of the bulk phase and C_b is the concentration of the bulk phase. In order to do this calculation, dividing surfaces between phases are chosen such that the surface excess concentration of water is zero. Surface excess concentrations in the presence and absence of DPPC are calculated and shown in Figure 5.9. Among the considered aromatic species, Phe is the most surface active at both interfaces. PhGly is less surface active than Phe. PhAA behaves similarly to PhGly with somewhat higher presence at the water-air interface. The behavior of Tyr is complex: while strongly surface inactive at the water-air interface (negative surface excess concentration), it is adsorbed to the DPPC monolayer. However, the analysis of molecular orientations show that while Phe penetrates relatively deep into the DPPC film, Tyr to a large extent remains in the well-hydrated region due to the presence of the polar hydroxyl group in the Tyr aromatic system.
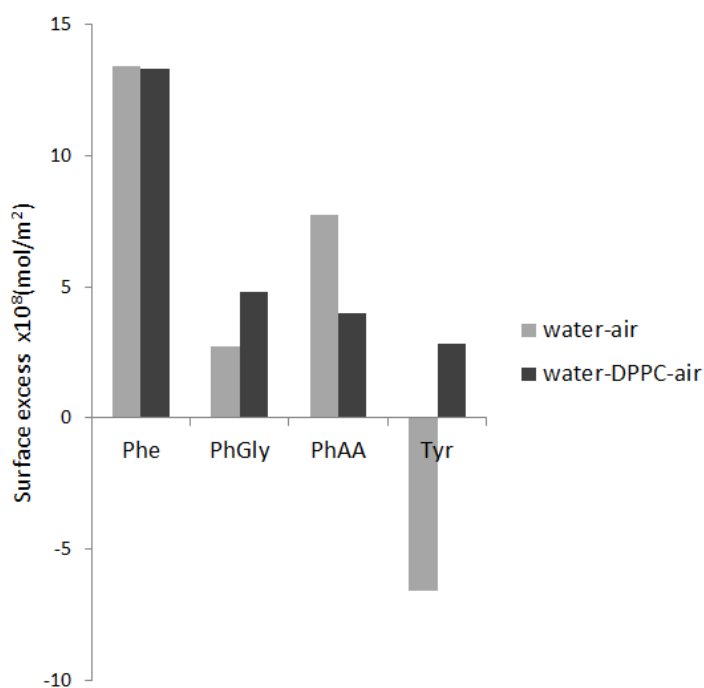
Figure 5.9: Surface excess concentrations of aromatic molecules adsorbed at water-air and water-DPPC-air interfaces. In each case, the center of mass of solute molecule was used for calculation. The Gibbs dividing surface was chosen such that the surface excess concentration of water is zero.

5.3.4 Clustering Analysis

Perhaps the most interesting observation from the simulations is evidence of cooperativity in the partitioning for several of the aromatic species to the surface. This was first noted through observation of simulation trajectories for Phe. Cases where one Phe molecule was already adsorbed allowed for somewhat easier penetration of another molecule into DPPC in its vicinity. To quantify the synergetic

effects, clustering of the considered aromatic molecules was analyzed along simulated trajectories (Figure 5.10). Note that in the clustering analysis all molecules present the simulation box were taken into account. In all cases, with the exception of Tyr in the water-air system, these populations are predominantly molecules adsorbed at the interface. The analysis clearly demonstrates that Phe is present in both systems mostly in the form of dimers (there were also ~5% of trimers and a negligible number of tetramers observed). Similar cluster distributions are observed for PhGly adsorbed at DPPC, while at the water-air interface PhGly forms dimers and monomers with almost equal probability. In the case of PhAA either with or without DPPC, some dimerization is observed. Tyr, however, exists mostly in the monomeric form regardless of DPPC coverage. Note that the observed molecular aggregates were dynamic with lifetimes in the range of tens of nanoseconds. However, in the case of aromatic molecules incorporated deep into the DPPC monolayer, the lifetimes were on the order of the simulation timescale (hundreds of nanoseconds).
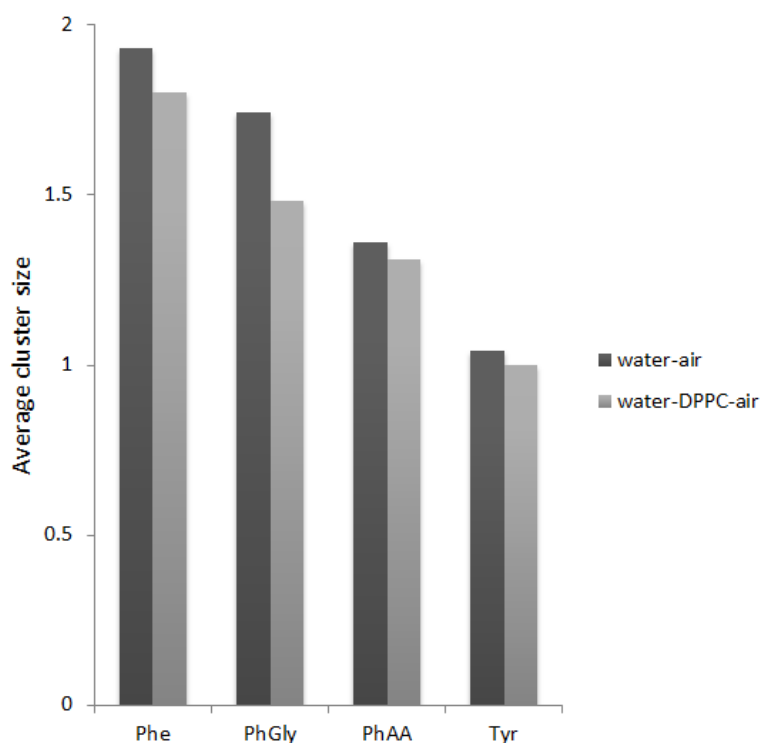
Figure 5.10. Average cluster size (number of molecules forming a cluster) of aromatic molecules in the presence of water-air and water-DPPC-air interfaces. The cutoff of 0.6 nm between centers of geometry of aromatic rings was used for definition of a cluster. Cluster size of 1 indicates monomers in solution.

In addition to these simulation results, there are several different pieces of experimental evidence that support the formation of clusters or aggregates of at least some of the aromatic molecules under study. First, the observed constant surface tension with increasing Phe concentration indicates soluble aggregate formation. Second, the kinetics of surface tension equilibration with Phe are slow, with higher order dependence on Phe concentration. Due to this, as well as previous reports of Phe clustering

or aggregation,[6,74,75] we investigated the aggregation behavior of our aromatic series using several different techniques.

In previous studies of Phe, we used light microscopy to determine that there were no large, long-lived Phe clusters present in solution at concentrations below the solubility limit of Phe, although molecular dynamics simulations suggested the presence of small transient clusters in solution.[15] In order to investigate smaller solution phase clusters that would be invisible to a confocal microscope, diffusion measurements were carried out through the use of diffusion ordered spectroscopy (DOSY) NMR. Solutions of Phe at both 0.1 mM and 100 mM were analyzed (Figure A2.14 in Appendix 2), and each solution was found to have a single diffusion constant. In order to account for viscosity changes as a function of Phe concentration, the ratio of the diffusion constant of Phe to HOD was found for each solution, and in both cases it was 0.30 ± 0.01. The identical, viscosity-corrected diffusion constants indicate that if there is clustering in Phe, the cluster lifetime has to be less than the 25-30 millisecond timescale that is measured via DOSY-NMR. It is also possible Phe is diffusing only as dimers over the entire concentration range, although concentration independent clustering of this nature would be surprising. This technique would also be insensitive to very large clusters, but these have already been ruled out via light microscopy.

In order to investigate the potential for even shorter timescale clustering or aggregation in solution, fluorescence spectroscopy was used, taking advantage of the phenomenon of self-quenching that is observed in many molecules. The peak fluorescence intensity was measured for pure solutions of Phe and PhGly as a function of concentration. Comparison was made between these two molecules because of their structural similarities and their contrasting surface behavior. Data is shown in Figure 5.11, and it is important to note that the relative fluorescence per molecule is directly proportional to the quantum yield of fluorescence.
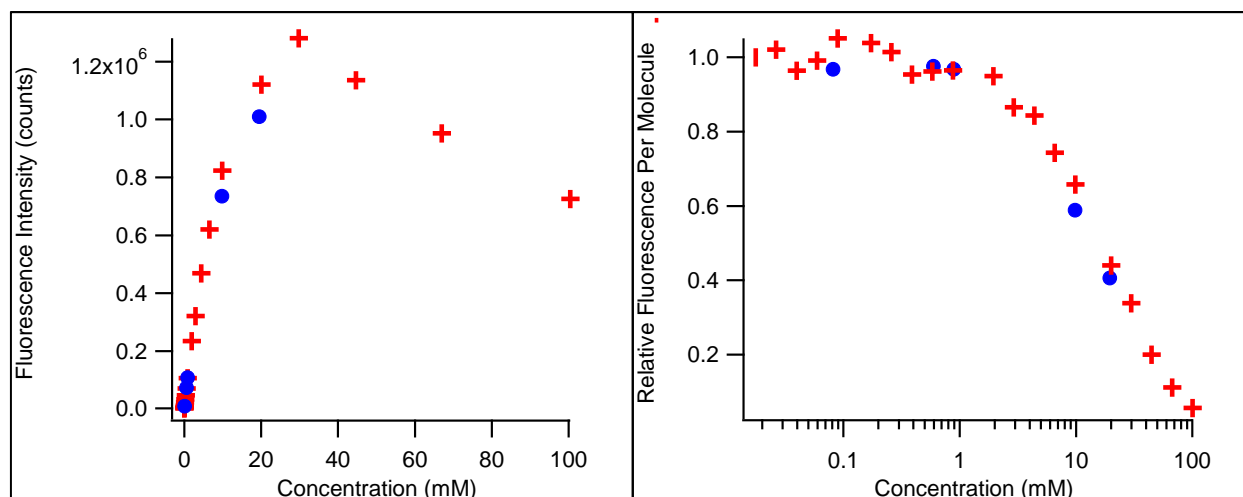
Figure 5.11: A) Peak fluorescence intensity, measured as an average of 282-283 nm fluorescence intensity, versus the concentration of Phe (blue circles) or PhGly (red crosses). B) Relative fluorescence intensity per molecule of Phe or PhGly versus concentration, directly proportional to the quantum yield of fluorescence.

The quantum yield of fluorescence appears to remain constant for both solutions below 1 mM, where, presumably, self-quenching does not occur. Above 1 mM, the fluorescence quantum yield steadily decreases with increasing concentration, as is characteristic of self-quenching. Both molecules display identical fluorescence yields and quenching characteristics. Although the mechanisms of self-quenching in these molecules are uncertain (and could be diverse), quenching mechanisms are generally strongly separation dependent.[76] While there is some evidence in the literature that Phe fluorescence quenching may occur through collisions with acid moieties,[77] no quenching was observed for solutions with low concentrations of Phe and a high concentration of the amino acid alanine. Because the characteristics of the acid groups with both amino acids are nearly identical, this suggests that the quenching is occurring through the aromatic group. Indeed, this is consistent with the fluorescence self-quenching observed in benzene, where the aromatic is clearly the only functional group.[78] Because of the strongly separation dependent nature of quenching, dynamic molecular clusters would be expected to quench very efficiently. Because the aromatic groups appear to be responsible for the quenching interactions, it is the dynamic ring-ring separation that is important. Above 1 mM concentrations, transient clustering may occur through ring-ring interactions, although it appears to be identical for Phe and PhGly. This may be an indication that transient clustering is occurring in both species, or neither.

If transient clustering in bulk solution is occurring the clustering lifetime in Phe is constrained to between 10^{-6} and 10^{-3} seconds, because the measured Phe fluorescent lifetime is 8 µs,[77] and the DOSY-NMR measurements take place on a millisecond timescale. Regardless of whether fluorescence data indicates transient clustering, Phe and PhGly behave identically, implying that solution phase clustering cannot be responsible for the differences in surface behavior that are observed. Because we have observed several effects in both the experimental studies and the molecular dynamics simulations that would be consistent with a clustering explanation but have strong evidence that bulk solution clustering for Phe and PhGly is identical and either transient or non-existent, we suggest that clustering at the air-water interface or within the DPPC film may be responsible for these effects. In this picture, Phe and PhGly would exist as free monomers (or potentially dimers) in solution, but once adsorbed to the interface Phe could form larger, more surface-active aggregates, while PhGly would not.

There have been several previous experimental investigations of Phe clustering in solution. Adler-Abromovich et al.[6] investigate pure Phe aggregate formation, nominally in the bulk, through the use of stained confocal microscopy and electron microscopy. In the case of both these experiments, long fibril structures are observed. In an attempt to repeat confocal microscopy experiments, however, it was observed that fibril formation occurred only upon sample drying, indicating crystallization rather than aggregation.[15] It should be noted, however, that the evidence of Phe aggregation in biological samples may not share the same experimental difficulty. Further, Phe aggregate formation in biological systems is not inconsistent with the results of our study, showing that aggregate formation may occur in interfacial regions. Singh et al.[74] have also utilized light scattering and solution phase stained fluorescence to examine Phe aggregation. Using these techniques, they see evidence for aggregation at concentrations above approximately 30 mM. These results appear contradictory to ours, but they were not performed in a quantitative way and give no indication of the extent of aggregation in solution concentrations below the solubility limit of Phe (180 mM). It is possible that our results are consistent with this study if aggregation is occurring to a very small extent under concentrations below the solubility limit of Phe.

Do et al.[75] utilized ion mobility electrospray ionization mass spectrometry (IM-ESI-MS) to examine Phe clusters. They observe the formation of large Phe clusters and investigate their structures and pH dependence. In the past, the clustering of other amino acids has also been investigated by mass spectrometry. Electrospray ionization (ESI) is almost always used,[79,80] as clustering is common in ESI,[81] although amino acid clusters have been reported using sonic spray ionization as well.[82] It is likely that the clustering of small molecules that is observed in these studies occurs during ionization, and that the structures that are identified may not exist in solution. We investigated the clustering characteristics of Phe, PhGly, PhAA and Tyr through simple ESI-MS experiments, to try to at least gain insight into the relative clustering propensities of these species. This investigation was performed both under high and low voltage ionization conditions; however, there was no consistent trend in clustering tendency of each aromatic species that was observed between the two sets of conditions (Table A2.1 in Appendix 2). This is a strong indication that the observed clustering is, in fact, occurring during ionization, and that these experiments do not probe solution phase structures. The structural data obtained by Do et al.[75] should not be discounted, however, as aggregates that are formed in phospholipid membranes or other water depleted environments may share structural characteristics.

5.4 Broader Implications

The interfacial partitioning behavior of Phe, PhGly, PhAA, and Tyr has been experimentally observed via Langmuir trough techniques. Phe and PhAA both preferentially partition to air-water interfaces as well as into DPPC films. The favorable energetic interactions between the aromatics and DPPC is estimated at >3 kJ/mole DPPC for PhAA and >5 kJ/mole DPPC for Phe. Despite their very similar structures to Phe and PhAA, PhGly and Tyr do not partition to air-water interfaces or into DPPC films. Molecular dynamics simulations match experimental data qualitatively for the partitioning to air-water interfaces for the series of molecules. They also add molecular level detail about the orientation of each molecule, with the aromatic group pointed out of the water surface. With DPPC present, a second

orientation is also observed, where a population of molecules lay parallel to the interface near the polar headgroup region of DPPC.

The molecular dynamics simulations also show evidence for a strong cooperative effect in the interfacial partitioning for Phe. PhGly and PhAA display a somewhat weaker cooperative effect, and virtually no cooperativity was observed in simulations of Tyr. Such cooperativity, in combination with the experimental measurements of surface tension and equilibration times as a function of concentration, suggested the occurrence of clustering or aggregation, especially for Phe. Solution phase aggregation behavior was investigated, and the only evidence consistent with aggregation was for small, transient clusters with a sub-millisecond lifetime. All of this, taken together, strongly suggests that clustering is not happening in solution, but may be happening at the air-water interface or inside a DPPC film.

We propose that the relationship between molecular structure, clustering, and surface activity has to do with the conformational flexibility of each molecule. The ability of conformational flexibility to allow for the exploration of more favorable binding and aggregation interactions is often observed for biopolymers.[83–91] This concept is perhaps less common for small molecules, although similar analysis has been performed for aromatic alcohols.[92] In some sense, the relationship between conformational flexibility and stability is a simple one: being able to explore more possible configurations increases the likelihood that an energetically favorable conformation is found. For any given system, however, the details of specific interactions will be important for fully characterizing the behavior, and could be the subject of further study.

Comparing Phe to PhGly, the only structural difference is the loss of a linking methylene group between the aromatic and polar regions of the molecule. This methylene adds flexibility for the Phe molecule, allowing for more freedom in the orientations between the aromatic ring and the polar amino acid. This appears to be important for accessing energetically favorable cluster states in an interfacial environment. The clustering of Phe in its zwitterionic form has been investigated previously through

molecular dynamics simulations in aqueous solution.[93] Stacked ring-like structures of Phe were observed with the zwitterionic headgroup regions at the core and aromatic moieties at the periphery.[93] Under the simulation conditions these structures did not form until high concentrations above the solubility limit of Phe (200-300 mM). In our work, under 150 mM concentration, Phe was present mostly in a dimeric form with a negligible number of larger aggregates. This result is consistent with our experimental findings that solution phase clustering does not occur. Similar structures may form, however, in the water-depleted interfacial region.

PhAA, while containing the same number of carbons as PhGly, appears to behave more like Phe. This could be explained again by the linking methylene between the aromatic and polar regions of the molecule. Tyr, on the other hand, does not show any experimental evidence of interfacial partitioning or hydrophobic cluster formation. The para-hydroxylation of the aromatic group, in conjunction with the conformational flexibility of Phe, may allow for significantly more stable aggregates to form for Tyr. The additional stability of Tyr clusters and/or solid would explain the notable decrease in water solubility in comparison with Phe, in spite of an increase in polar surface area. Additionally, it could explain the surface partitioning trend – rather than forming small, hydrophobic clusters, any aggregates of Tyr may not be thermodynamically stable compared to the solid, resulting in only crystallization. The melting point of Tyr and Phe could be useful in confirming this, but decomposition occurs prior to melting for both species. It is also possible that the aggregates of Tyr would not be surface active, although the molecular dynamics simulations performed are not in support of this.

Our results stress an important idea when considering partitioning between different phases: General trends in the literature suggest that lower solubility compounds should be more surface active. This idea can be useful, but in light of results presented here, it is important to realize that solubility is a measure of the relative free energy of a molecule existing in solution versus as a phase-separated solid or liquid, as a function of concentration. Likewise, surface partitioning is a comparison of the energy of a molecule in solution versus at the interface. Because of this, the solubility of a molecule should be

expected to correlate with its surface activity to the extent that the energy of this molecule at the surface is similar (but more favorable) than the energy in its solid or liquid phase. In the case where the solid is more energetically favorable than the surface film, surface partitioning competes with crystallization, and surface partitioning is not expected. This is likely the case with Tyr.

Trends relating polarity and solubility have a similar issue. Polarity is generally a reasonable indicator of the interactions a molecule has with water, but it has little relevance to the energetics of a pure compound. The hydrophobic effect in simple terms shares the same flaw; it considers only the interactions with water. In all cases, the considerations should be the same: for partitioning out of solution, the energies of the new phases must always be considered in addition to the energy of the dissolved species.

For the series of molecules used in this study, the fact that none of these trends hold is a good indication that the interfacial and crystal structures are dissimilar. If aggregation is occurring, as we suggest for Phe and possibly PhAA, this may indicate that the aggregate structure is dissimilar from the crystal structures of these molecules. This would support the type of aggregate structure found by German et al., which deviates from Phe's crystal structure.[93]

5.5 Conclusions

For this series of aromatic molecules, a variety of interactions are at play in dictating the molecular behavior of a heterogeneous system. Perhaps counterintuitively, their behavior is not dominated by water-aromatic interactions or even aromatic-phospholipid interactions, but seems controlled through interactions of aromatic species with themselves. In fact, the general trend that would be expected if considering only the hydrophobic effect is completely inconsistent with experimental data. Even the interactions between the phospholipid and the aromatic species do not appear to be important in capturing the coarse partitioning of molecules to the interface, as the same trend is observed with a bare water interface. That is not to say that these other interactions are unimportant, only that they are not

responsible for the extreme differences in behavior that are observed within the series of aromatic molecules.

Bibliography

(1)   Krzyściak, W. Activity of Selected Aromatic Amino Acids in Biological Systems. *Acta Biochim. Pol.* **2011**, *58* (4), 461–466.

(2)   van Kan, E. J. M.; Demel, R. A.; van der Bent, A.; de Kruijff, B. The Role of the Abundant Phenylalanines in the Mode of Action of the Antimicrobial Peptide Clavanin. *Biochim. Biophys. Acta BBA - Biomembr.* **2003**, *1615* (1–2), 84–92.

(3)   Pandey, R.; Swamy, K. V.; Pandey, Rachna; Swamy, K V; Khetmalas, M. B. Indole: A Novel Signaling Molecule and Its Applications. *Indian J. Biotechnol.* **2013**, *12* (3), 297–310.

(4)   Mandal, S. M.; Chakraborty, D.; Dey, S. Phenolic Acids Act as Signaling Molecules in Plant-Microbe Symbioses. *Plant Signal. Behav.* **2010**, *5* (4), 359–368.

(5)   Stroobant, P.; Kaback, H. R. Reconstitution of Ubiquinone-Linked Functions in Membrane Vesicles from a Double Quinone Mutant of Escherichia Coli. *Biochemistry (Mosc.)* **1979**, *18* (1), 226–231.

(6)   Adler-Abramovich, L.; Vaks, L.; Carny, O.; Trudler, D.; Magno, A.; Caflisch, A.; Frenkel, D.; Gazit, E. Phenylalanine Assembly into Toxic Fibrils Suggests Amyloid Etiology in Phenylketonuria. *Nat Chem Biol* **2012**, *8* (8), 701–706.

(7)   Gazit, E. A Possible Role for π-Stacking in the Self-Assembly of Amyloid Fibrils. *FASEB J.* **2002**, *16* (1), 77–83.

(8)   Makin, O. S.; Atkins, E.; Sikorski, P.; Johansson, J.; Serpell, L. C. Molecular Basis for Amyloid Fibril Formation and Stability. *Proc. Natl. Acad. Sci. U. S. A.* **2005**, *102* (2), 315–320.

(9)   Freitas, R. A. *Nanomedicine, Volume I: Basic Capabilities*, 1 edition.; CRC Press: Austin, TX, 1999.

(10)   King, J. L.; Jukes, T. H. Non-Darwinian Evolution. *Science* **1969**, *164* (3881), 788–798.

(11)   White, S. H.; Wimley, W. C. Hydrophobic Interactions of Peptides with Membrane Interfaces. *Biochim. Biophys. Acta BBA - Rev. Biomembr.* **1998**, *1376* (3), 339–352.

(12)   Hanley, W. B. Adult Phenylketonuria. *Am. J. Med.* **2004**, *117* (8), 590–595.

(13)   Hong, H.; Park, S.; Flores Jiménez, R. H.; Rinehart, D.; Tamm, L. K. Role of Aromatic Side Chains in the Folding and Thermodynamic Stability of Integral Membrane Proteins. *J. Am. Chem. Soc.* **2007**, *129* (26), 8320–8327.

(14)   Domene, C.; Vemparala, S.; Klein, M. L.; Vénien-Bryan, C.; Doyle, D. A. Role of Aromatic Localization in the Gating Process of a Potassium Channel. *Biophys. J.* **2006**, *90* (1), L01–L03.

(15)   Griffith, E. C.; Perkins, R. J.; Telesford, D.-M.; Adams, E. M.; Cwiklik, L.; Allen, H. C.; Roeselová, M.; Vaida, V. Interaction of L-Phenylalanine with a Phospholipid Monolayer at the Water–Air Interface. *J. Phys. Chem. B* **2014**.

(16)   Rosa, A. S.; Cutro, A. C.; Frías, M. A.; Disalvo, E. A. Interaction of Phenylalanine with DPPC Model Membranes: More Than a Hydrophobic Interaction. *J. Phys. Chem. B* **2015**.

(17)   Tuckermann, R. Surface Tension of Aqueous Solutions of Water-Soluble Organic and Inorganic Compounds. *Atmos. Environ.* **2007**, *41* (29), 6265–6275.

(18)   Griffith, E. C.; Vaida, V. In Situ Observation of Peptide Bond Formation at the Water–air Interface. *Proc. Natl. Acad. Sci.* **2012**, *109* (39), 15697–15701.

(19)   Chen, X.; Allen, H. C. Interactions of Dimethylsulfoxide with a Dipalmitoylphosphatidylcholine Monolayer Studied by Vibrational Sum Frequency Generation†. *J. Phys. Chem. A* **2009**, *113* (45), 12655–12662.

(20)   Chen, X.; Huang, Z.; Hua, W.; Castada, H.; Allen, H. C. Reorganization and Caging of DPPC, DPPE, DPPG, and DPPS Monolayers Caused by Dimethylsulfoxide Observed Using Brewster Angle Microscopy. *Langmuir* **2010**, *26* (24), 18902–18908.

(21)   Yan, E. C. Y.; Fu, L.; Wang, Z.; Liu, W. Biological Macromolecules at Interfaces Probed by Chiral Vibrational Sum Frequency Generation Spectroscopy. *Chem. Rev.* **2014**, *114* (17), 8471–8498.

(22)   Seoane, R.; Miñones, J.; Conde, O.; Miñones, J.; Casas, M.; Iribarnegaray, E. Thermodynamic and Brewster Angle Microscopy Studies of Fatty Acid/Cholesterol Mixtures at the Air/Water Interface. *J. Phys. Chem. B* **2000**, *104* (32), 7735–7744.

(23)   Berkowitz, M. L.; Bostick, D. L.; Pandit, S. Aqueous Solutions next to Phospholipid Membrane Surfaces: Insights from Simulations. *Chem. Rev.* **2006**, *106* (4), 1527–1539.

(24)   McConlogue, C. W.; Malamud, D.; Vanderlick, T. K. Interaction of DPPC Monolayers with Soluble Surfactants: Electrostatic Effects of Membrane Perturbants. *Biochim. Biophys. Acta BBA - Biomembr.* **1998**, *1372* (1), 124–134.

(25)   Brockman, H. Lipid Monolayers: Why Use Half a Membrane to Characterize Protein-Membrane Interactions? *Curr. Opin. Struct. Biol.* **1999**, *9* (4), 438–443.

(26)   Sampaio, J. L.; Gerl, M. J.; Klose, C.; Ejsing, C. S.; Beug, H.; Simons, K.; Shevchenko, A. Membrane Lipidome of an Epithelial Cell Line. *Proc. Natl. Acad. Sci.* **2011**, *108* (5), 1903–1907.

(27)   Ma, G.; Allen, H. C. DPPC Langmuir Monolayer at the Air−Water Interface: Probing the Tail and Head Groups by Vibrational Sum Frequency Generation Spectroscopy. *Langmuir* **2006**, *22* (12), 5341–5349.

(28)   Zuo, Y. Y.; Veldhuizen, R. A. W.; Neumann, A. W.; Petersen, N. O.; Possmayer, F. Current Perspectives in Pulmonary Surfactant — Inhibition, Enhancement and Evaluation. *Biochim. Biophys. Acta BBA - Biomembr.* **2008**, *1778* (10), 1947–1977.

(29)   McConlogue, C. W.; Vanderlick, T. K. A Close Look at Domain Formation in DPPC Monolayers. *Langmuir* **1997**, *13* (26), 7158–7164.

(30)   Creuwels, L. A.; van Golde, L. M.; Haagsman, H. P. The Pulmonary Surfactant System: Biochemical and Clinical Aspects. *Lung* **1997**, *175* (1), 1–39.

(31)   Klopfer, K. J.; Vanderlick, T. K. Isotherms of Dipalmitoylphosphatidylcholine (DPPC) Monolayers: Features Revealed and Features Obscured. *J. Colloid Interface Sci.* **1996**, *182* (1), 220–229.

(32)   Ohki, S.; Ohki, C. B. Monolayers at the Oil/water Interface as a Proper Model for Bilayer Membranes. *J. Theor. Biol.* **1976**, *62* (2), 389–407.

(33)   Maget-Dana, R. The Monolayer Technique: A Potent Tool for Studying the Interfacial Properties of Antimicrobial and Membrane-Lytic Peptides and Their Interactions with Lipid Membranes. *Biochim. Biophys. Acta BBA - Biomembr.* **1999**, *1462* (1–2), 109–140.

(34)   Peetla, C.; Stine, A.; Labhasetwar, V. Biophysical Interactions with Model Lipid Membranes: Applications in Drug Discovery and Drug Delivery. *Mol. Pharm.* **2009**, *6* (5), 1264–1276.

(35)   Hąc-Wydro, K.; Dynarowicz-Łątka, P. Biomedical Applications of the Langmuir Monolayer Technique. *Ann. UMCS Chem.* **2008**, *63*.

(36)   Petrache, H. I.; Dodd, S. W.; Brown, M. F. Area per Lipid and Acyl Length Distributions in Fluid Phosphatidylcholines Determined by (2)H NMR Spectroscopy. *Biophys. J.* **2000**, *79* (6), 3172–3192.

(37)   Jerschow, A.; Müller, N. Suppression of Convection Artifacts in Stimulated-Echo Diffusion Experiments. Double-Stimulated-Echo Experiments. *J. Magn. Reson.* **1997**, *125* (2), 372–375.

(38)   Connell, M. A.; Bowyer, P. J.; Adam Bone, P.; Davis, A. L.; Swanson, A. G.; Nilsson, M.; Morris, G. A. Improving the Accuracy of Pulsed Field Gradient NMR Diffusion Experiments: Correction for Gradient Non-Uniformity. *J. Magn. Reson.* **2009**, *198* (1), 121–131.

(39)   Jämbeck, J. P. M.; Lyubartsev, A. P. Derivation and Systematic Validation of a Refined All-Atom Force Field for Phosphatidylcholine Lipids. *J. Phys. Chem. B* **2012**, *116* (10), 3164–3179.

(40)   Vega, C.; Miguel, E. de. Surface Tension of the Most Popular Models of Water by Using the Test-Area Simulation Method. *J. Chem. Phys.* **2007**, *126* (15), 154707.

(41)   Wang, J.; Wolf, R. M.; Caldwell, J. W.; Kollman, P. A.; Case, D. A. Development and Testing of a General Amber Force Field. *J. Comput. Chem.* **2004**, *25* (9), 1157–1174.

(42)   Bussi, G.; Donadio, D.; Parrinello, M. Canonical Sampling through Velocity-Rescaling. *J. Chem. Phys.* **2007**, *126* (1), 14101.

(43)   Essmann, U.; Perera, L.; Berkowitz, M. L.; Darden, T.; Lee, H.; Pedersen, L. G. A Smooth Particle Mesh Ewald Method. *J. Chem. Phys.* **1995**, *103* (19), 8577–8593.

(44)   Hess, B.; Kutzner, C.; van der Spoel, D.; Lindahl, E. GROMACS 4: Algorithms for Highly Efficient, Load-Balanced, and Scalable Molecular Simulation. *J. Chem. Theory Comput.* **2008**, *4* (3), 435–447.

(45)   Humphrey, W.; Dalke, A.; Schulten, K. VMD: Visual Molecular Dynamics. *J. Mol. Graph.* **1996**, *14* (1), 33–38.

(46)   Koller, J. E.; Washburn, E. R. The Diffusion of Phenylacetic Acid in Water as Measured by Changes of Surface Tension. *J. Am. Chem. Soc.* **1954**, *76* (9), 2562–2565.

(47)   Albert, A. *The Determination of Ionization Constants : A Laboratory Manual*, 3rd ed.; Chapman and Hall: New York, 1984.

(48)   Griffith, E. C.; Guizado, T. R. C.; Pimentel, A. S.; Tyndall, G. S.; Vaida, V. Oxidized Aromatic–Aliphatic Mixed Films at the Air–Aqueous Solution Interface. *J. Phys. Chem. C* **2013**, *117* (43), 22341–22350.

(49)   Magalhães, N. S. S.; Benita, S.; Baszkin, A. Penetration of Poly(oxyethylene)—poly (Oxypropylene) Block Copolymer Surfactant into Soya Phospholipid Monolayers. *Colloids Surf.* **1991**, *52*, 195–206.

(50)   Tajima, K.; Koshinuma, M.; Nakamura, A. Equilibrium Penetration of N-Dodecyl-.beta.-Alanine into the Lecithin and Dilaurin Monolayers. 1. Interaction between Polar Head Groups. *Langmuir* **1991**, *7* (11), 2764–2773.

(51)   Sundaram, S.; Stebe, K. J. Dynamic Penetration of an Insoluble Monolayer by a Soluble Surfactant: Theory and Experiment. *Langmuir* **1997**, *13* (6), 1729–1736.

(52) Szymczyk, K. Composition of Multicomponent Surfactant Systems at the Water–Air Interface. *J. Surfactants Deterg.* **2012**, *15* (5), 647–656.

(53) Li, P. X.; Li, Z. X.; Shen, H.-H.; Thomas, R. K.; Penfold, J.; Lu, J. R. Application of the Gibbs Equation to the Adsorption of Nonionic Surfactants and Polymers at the Air–Water Interface: Comparison with Surface Excesses Determined Directly Using Neutron Reflectivity. *Langmuir* **2013**, *29* (30), 9324–9334.

(54) Xu, H.; Li, P. X.; Ma, K.; Thomas, R. K.; Penfold, J.; Lu, J. R. Limitations in the Application of the Gibbs Equation to Anionic Surfactants at the Air/Water Surface: Sodium Dodecylsulfate and Sodium Dodecylmonooxyethylenesulfate Above and Below the CMC. *Langmuir* **2013**, *29* (30), 9335–9351.

(55) Gaines, G. L. The Thermodynamic Equation of State for Insoluble Monolayers. *J. Colloid Interface Sci.* **1982**, *85* (1), 16–18.

(56) Panda, A. K.; Nag, K.; Harbottle, R. R.; Possmayer, F.; Petersen, N. O. Thermodynamic Studies on Mixed Molecular Langmuir Films: Part 2. Mutual Mixing of DPPC and Bovine Lung Surfactant Extract with Long-Chain Fatty Acids. *Colloids Surf. Physicochem. Eng. Asp.* **2004**, *247* (1–3), 9–17.

(57) Rontu, N.; Vaida, V. Miscibility of Perfluorododecanoic Acid with Organic Acids at the Air−Water Interface. *J. Phys. Chem. C* **2007**, *111* (27), 9975–9980.

(58) Adams, E. M.; Allen, H. C. Palmitic Acid on Salt Subphases and in Mixed Monolayers of Cerebrosides: Application to Atmospheric Aerosol Chemistry. *Atmosphere* **2013**, *4* (4), 315–336.

(59) Pethica, B. A. The Thermodynamics of Monolayer Penetration at Constant Area. Part 1. *Trans. Faraday Soc.* **1955**, *51* (0), 1402–1411.

(60) McGregor, M. A.; Barnes, G. T. The Equilibrium Penetration of Monolayers. *J. Colloid Interface Sci.* **1974**, *49* (3), 362–367.

(61) Motomura, K.; Hayami, Y.; Aratono, M.; Matuura, R. Thermodynamics of Multicomponent Monolayers: IV. Monolayer Penetration. *J. Colloid Interface Sci.* **1982**, *87* (2), 333–338.

(62) Barnes, G. T.; Lawrie, G. A.; Walker, K. Equilibrium Penetration of Monolayers. 9. A Comparison of Treatments for Analyzing Surface-Pressure−Area Data. *Langmuir* **1998**, *14* (8), 2148–2154.

(63) Magalhães, N. S. S.; de Oliveira, H. M.; Baszkin, A. Motomura's Modified Equation for Surfactant Penetration into Spread Monolayers. *Colloids Surf. Physicochem. Eng. Asp.* **1996**, *118* (1–2), 63–73.

(64) Gaines, G. L. Thermodynamic Relationships for Mixed Insoluble Monolayers. *J. Colloid Interface Sci.* **1966**, *21* (3), 315–319.

(65) Santana, M.; Ribeiro, M. P. A.; Leite, G. A.; Giordano, R. L. C.; Giordano, R. C.; Mattedi, S. Solid–liquid Equilibrium of Substrates and Products of the Enzymatic Synthesis of Ampicillin. *AIChE J.* **2010**, *56* (6), 1578–1583.

(66)   *CRC Handbook of Chemistry and Physics, 96th Edition*, 96 edition.; Haynes, W. M., Ed.; CRC Press, 2015.

(67)   Miura, T.; Seki, K. Diffusion Influenced Adsorption Kinetics. *J. Phys. Chem. B* **2015**, *119* (34), 10954–10961.

(68)   Ward, A. F. H.; Tordai, L. Time-Dependence of Boundary Tensions of Solutions I. The Role of Diffusion in Time-Effects. *J. Chem. Phys.* **1946**, *14* (7), 453–461.

(69)   Zhou, X.; Fan, J.; Li, N.; Du, Z.; Ying, H.; Wu, J.; Xiong, J.; Bai, J. Solubility of L-Phenylalanine in Water and Different Binary Mixtures from 288.15 to 318.15 K. *Fluid Phase Equilibria* **2012**, *316*, 26–33.

(70)   Needham, T. E.; Paruta, A. N.; Gerraughty, R. J. Solubility of Amino Acids in Pure Solvent Systems. *J. Pharm. Sci.* **1971**, *60* (4), 565–567.

(71)   Gracin, S.; Rasmuson, A. Solubility of Phenylacetic Acid,p-Hydroxyphenylacetic Acid, P-Aminophenylacetic Acid,p-Hydroxybenzoic Acid, and Ibuprofen in Pure Solvents. *J. Chem. Eng. Data* **2002**, *47* (6), 1379–1383.

(72)   *Advanced Chemistry Development (ACD/Labs) Software*.

(73)   Duncan, S. L.; Larson, R. G. Comparing Experimental and Simulated Pressure-Area Isotherms for DPPC. *Biophys. J.* **2008**, *94* (8), 2965–2986.

(74)   Singh, V.; Rai, R. K.; Arora, A.; Sinha, N.; Thakur, A. K. Therapeutic Implication of L-Phenylalanine Aggregation Mechanism and Its Modulation by D-Phenylalanine in Phenylketonuria. *Sci. Rep.* **2014**, *4*.

(75)   Do, T. D.; Kincannon, W. M.; Bowers, M. T. Phenylalanine Oligomers and Fibrils: The Mechanism of Assembly and the Importance of Tetramers and Counterions. *J. Am. Chem. Soc.* **2015**, *137* (32), 10080–10083.

(76)   Zhuang, X.; Ha, T.; Kim, H. D.; Centner, T.; Labeit, S.; Chu, S. Fluorescence Quenching: A Tool for Single-Molecule Protein-Folding Study. *Proc. Natl. Acad. Sci.* **2000**, *97* (26), 14241–14244.

(77)   Feitelson, J. On the Mechanism of Fluorescence Quenching. Tyrosine and Similar Compounds. *J. Phys. Chem.* **1964**, *68* (2), 391–397.

(78)   Luria, M. Fluorescence Quenching in Benzene Vapor. *Isr. J. Chem.* **1972**, *10* (3), 721–724.

(79)   Nemes, P.; Schlosser, G.; Vékey, K. Amino Acid Cluster Formation Studied by Electrospray Ionization Mass Spectrometry. *J. Mass Spectrom.* **2005**, *40* (1), 43–49.

(80)   Singh, A.; Kaur, S.; Kaur, J.; Singh, P. Transformation of Gas-Phase Amino Acid Clusters to Dipeptides: A Nice Approach to Demonstrate the Formation of Prebiotic Peptides. *Rapid Commun. Mass Spectrom.* **2014**, *28* (18), 2019–2023.

(81)   Cech, N. B.; Enke, C. G. Practical Implications of Some Recent Studies in Electrospray Ionization Fundamentals. *Mass Spectrom. Rev.* **2001**, *20* (6), 362–387.

(82)   Takats, Z.; Nanita, S. C.; Cooks, R. G.; Schlosser, G.; Vekey, K. Amino Acid Clusters Formed by Sonic Spray Ionization. *Anal. Chem.* **2003**, *75* (6), 1514–1523.

(83)   Kalimeri, M.; Rahaman, O.; Melchionna, S.; Sterpone, F. How Conformational Flexibility Stabilizes the Hyperthermophilic Elongation Factor G-Domain. *J. Phys. Chem. B* **2013**, *117* (44), 13775–13785.

(84)   Tsoneva, Y.; Jonker, H. R. A.; Wagner, M.; Tadjer, A.; Lelle, M.; Peneva, K.; Ivanova, A. Molecular Structure and Pronounced Conformational Flexibility of Doxorubicin in Free and Conjugated State within a Drug–Peptide Compound. *J. Phys. Chem. B* **2015**, *119* (7), 3001–3013.

(85)   Sobell, H. M.; Tsai, C.-C.; Jain, S. C.; Sakore, T. D. Conformational Flexibility in DNA Structure and Its Implications in Understanding the Organization of DNA in Chromatin. *Philos. Trans. R. Soc. Lond. B. Biol. Sci.* **1978**, *283* (997), 295–298.

(86)   Tu, P.; Yao, Y.; Li, Y.; Liu, B. Conformational Flexibility of Phycocyanobilin: Monte-Carlo and DFT Study. *J. Mol. Struct. THEOCHEM* **2009**, *894* (1–3), 9–13.

(87)   Ng, C. L.; Waterman, D. G.; Koonin, E. V.; Walters, A. D.; Chong, J. P.; Isupov, M. N.; Lebedev, A. A.; Bunka, D. H.; Stockley, P. G.; Ortiz-Lombardía, M.; et al. Conformational Flexibility and Molecular Interactions of an Archaeal Homologue of the Shwachman-Bodian-Diamond Syndrome Protein. *BMC Struct. Biol.* **2009**, *9*, 32.

(88)   Ariza, A.; Richard, D. J.; White, M. F.; Bond, C. S. Conformational Flexibility Revealed by the Crystal Structure of a Crenarchaeal RadA. *Nucleic Acids Res.* **2005**, *33* (5), 1465–1473.

(89)   Zhang, C.; Su, M.; He, Y.; Zhao, X.; Fang, P.; Ribbe, A. E.; Jiang, W.; Mao, C. Conformational Flexibility Facilitates Self-Assembly of Complex DNA Nanostructures. *Proc. Natl. Acad. Sci.* **2008**, *105* (31), 10665–10669.

(90)   Sterling, H. J.; Cassou, C. A.; Trnka, M. J.; Burlingame, A. L.; Krantz, B. A.; Williams, E. R. The Role of Conformational Flexibility on Protein Supercharging in Native Electrospray Ionization. *Phys. Chem. Chem. Phys.* **2011**, *13* (41), 18288–18296.

(91)   Huber, R. Conformational Flexibility and Its Functional Significance in Some Protein Molecules. *Trends Biochem. Sci.* **1979**, *4* (12), 271–276.

(92)   Varughese, S.; Hoser, A. A.; Jarzembska, K. N.; Pedireddi, V. R.; Woźniak, K. Positional Isomerism and Conformational Flexibility Directed Structural Variations in the Molecular Complexes of Dihydroxybenzoic Acids. *Cryst. Growth Des.* **2015**, *15* (8), 3832–3841.

(93)   German, H. W.; Uyaver, S.; Hansmann, U. H. E. Self-Assembly of Phenylalanine-Based Molecules. *J. Phys. Chem. A* **2015**, *119* (9), 1609–1615.

Chapter 6: Phenylalanine Increases Membrane Permeability

6.1 Introduction:

The interactions between amino acids and biological membranes are important for many systems. Interactions between the aromatic amino acids, phenylalanine (Phe), tyrosine (Tyr), and tryptophan (TRP), are particularly important for membrane-interacting proteins, such as membrane channel proteins.[1,2] The interactions between free aromatic amino acids and membranes can also be important in some biological cases. In the genetic disorder phenylketonuria (PKU), for example, phenylalanine cannot be processed correctly and human serum levels of Phe can exceed 1.2 mM if untreated.[3] This elevated Phe concentration often results in brain damage, and, in many parts of the world, infants are tested for PKU at birth.[3] Adler-Abramovich et al.[4] observed the formation of amyloid-like fibrils of Phe under biologically relevant conditions, as well as cytotoxic effects of high Phe concentration. In our previous studies,[5,6] interactions between Phe and air-water or model membrane systems were investigated. Our experiments indicated that Phe does not spontaneously aggregate in solution, as was previously claimed,[4] although we find indirect evidence that aggregation occurs at the interface.[5,6] Large changes to the morphology of a monolayer model membrane were observed both theoretically and experimentally and such changes could, potentially, result in changes to the permeability of a bilayered system.[5] In this work, we find that Phe does, in fact, increase the permeability of a bilayered vesicle model membrane. This has profound implications for PKU as well as the fundamental understanding of interactions between aromatic species and membrane systems.

Our previous experimental studies[5,6] utilized very simple model cell membranes composed of a monolayer of 1,2-dipalmitoyl-*sn*-glycero-3-phosphatidylcholine (DPPC). This system was advantageous due to its simplicity, which allowed for ease of interpretation but was lacking in its direct biological relevance. The bilayered membrane studies reported here serve to supplement our previous results by supplying properties that are unavailable in monolayered systems (i.e. permeability) and also serve to compare our previous results to a system that is a better proxy for biology. It should be stressed, however,

that real biological membranes are not simple surfactant systems but are, rather, complex, asymmetric bilayers containing mixtures of many lipids and proteins, generally supported by protein scaffolds. Because of this, using model systems as mimics of biological membranes can be difficult. Because of this complexity, models are often chosen to match a specific property of the natural system (such as interfacial tension, area per lipid, deuterium order parameter, etc.), but this can result in a mismatch of other properties between the model and reality. While some model systems have gained acceptance in the literature, and their relevance to biological membranes is supported to some extent, it isn't always clear that these are the best conditions to utilize for biological relevance in all cases. However, it is generally agreed that bilayered systems are advantageous in their biological relevance compared to monolayered membranes.

In vesicle systems, there are only a few parameters that can be experimentally controlled. Surfactant composition, vesicle size, temperature, pressure, and solution composition lend themselves to regulation. In this work, we again choose DPPC as the sole surfactant composing the vesicles in order to allow for comparison with previous monolayer studies.[5,6] Vesicle size is an interesting property to consider in theory, due to changes to surface curvature, and in turn, membrane asymmetry. In practice, however, vesicle size is generally chosen due to experimental limitations. It is generally assumed vesicles under 200 nm diameter form unilamellar structures, so vesicles in this size range are chosen. For single vesicle studies larger vesicles are generally desirable, if not required. Syntheses of unilamellar vesicles are carried out through a variety of techniques.[7–12] Temperature is perhaps the most important variable for a DPPC lipid system as there are several phase transitions for DPPC vesicles that occur near ambient temperature. The four DPPC vesicle phases are termed crystal, gel, ripple, and liquid crystal in order from lowest to highest temperature.[13,14] DPPC vesicles exist in a gel phase at room temperature, and transition to the ripple phase at ~38 °C before transitioning to the liquid crystal phase very shortly after (~41 °C).[13] DPPC vesicles in the gel phase are very impermeable, while the ripple phase is highly permeable.[15,16] The

liquid crystal phase is of an intermediate permeability, and is thought to be the most useful proxy for biological membranes.

In order to probe the permeability properties of DPPC vesicles, an indirect measurement using a fluorescent probe is employed. The basis of the measurement is using a membrane-impermeant, self-quenching dye. Perhaps the most commonly used dye for this purpose is the calcium binding dye, calcein. The dye is first encapsulated in the vesicles of interest, while residual dye is removed from the solution around the vesicles. When the vesicles are exposed to a change in osmotic pressure, water leaves the vesicle, effectively concentrating the encapsulated calcein. This in turn changes the fluorescence properties of the dye, which can be monitored and calibrated to vesicle size. At longer timescales, the added osmolyte may be able to diffuse inside the vesicle, returning water inside of the vesicle along with it. This change can again be monitored via a recovery in the fluorescence. This technique has been employed successfully for a number of different vesicle systems and osmolytes.[17–19]
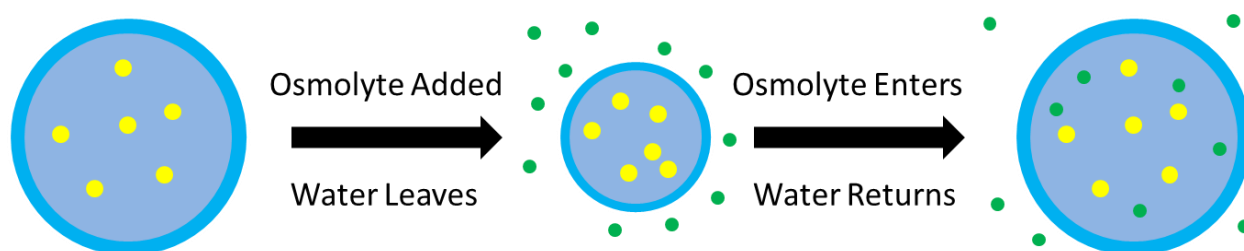
Figure 6.1: Schematic of changes to vesicle size and encapsulated concentrations after osmolyte is added. Yellow dots represent calcein dye, green dots represent added osmolyte.

In order to match previous experimental studies,[6] a series of analogous aromatic molecules is used. This series consists of Phe, phenylglycine (PhGly), phenylacetic acid (PhAA), and tyrosine (Tyr). This series is shown in Figure 6.2. All these molecule are structurally similar and contain both an aromatic and polar moiety but have considerable differences in their surface behavior both at a bare air-water interface and in the presence of a DPPC film.[6]
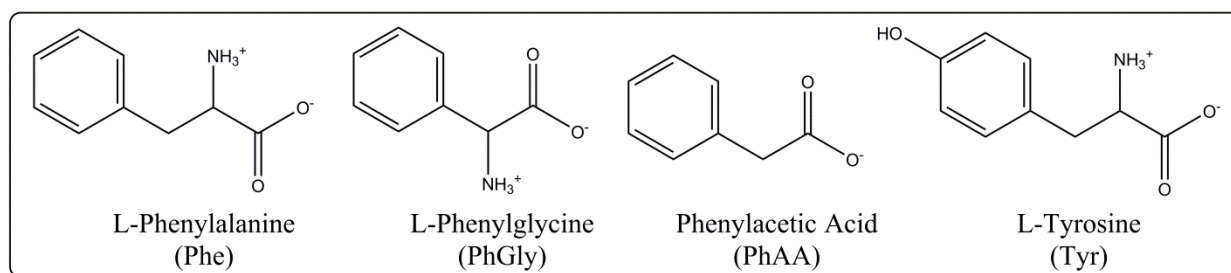
Figure 6.2: The series of aromatic molecules under study.

6.2 Methods:

Stock buffer solution was prepared using phosphate buffered saline powder (Sigma, 10 mM phosphate, 138 mM NaCl, 2.7 mM KCl) and 1 mM ethylenediaminetetraacetic acid (EDTA, Sigma >98.5%) to scavenge trace calcium that could otherwise bind the calcein dye. Buffer solution was pH adjusted to 7.25 using concentrated NaOH or HCl. This will be referred to as PBS buffer or solution. 5 mM calcein, 20 mM Phe, 2.5 mM Phe/PhGly/PhAA, 2.4 mM Tyr and 1 M ribose solutions were prepared by dissolving calcein dye (Sigma), L-phenylalanine (Alfa Aesar 99%), L-phenylglycine (Sigma 99%), phenylacetic acid (Sigma 99%), L-tyrosine (Sigma >99%), or ribose (Sigma >99%) in PBS buffer, then pH adjusted to 7.25 with 10 mg/mL and/or 1 mg/mL NaOH prepared in the buffer solution.

A schematic of the vesicle preparation method is shown in Figure 6.3. Vesicles were prepared by placing ~13 mg of DPPC powder in a smooth 50 mL round bottom flask. The DPPC powder was then dissolved in ~2 mL CHCl$_3$ before being subjected to rotary evaporation at <1 Torr until the liquid was removed, followed by an additional 30 minutes to remove residual CHCl$_3$. This produced a relatively thin film of DPPC on the bottom of the flask, which was then suspended in 1 mL of calcein solution via brief sonication at >42 °C. The suspension at this point consisted of a mix of aggregates and vesicles of disperse sizes. The suspension was then transformed to a more homogeneous solution of vesicles by extruding through a 80 nm track-etched membrane >20 times while the temperature of the mixture is held above 42 °C. Isolation of the dye-containing vesicles from the external dye was accomplished using size exclusion chromatography. A sepharose 4B column was stored in ethanol at 4 °C. Prior to use, the

column material was washed and equilibrated with PBS and was repacked in a 10 cm tall by 1 cm diameter tube. The vesicle solution was added to the column under constant flow of PBS buffer, being careful not to disturb the column packing. Separation was visible, with the faster moving fraction corresponding to the vesicle-encapsulated dye and the slower moving fraction corresponding to the free dye. There was generally ~1 mL of clear solution that eluted between the two colored fractions, so the entire vesicle fraction was collected and generally totaled ~1 mL. Vesicle solutions were diluted 1:20 with either PBS buffer or Phe solution for a final Phe concentration of 20 mM. Vesicles were stored at room temperature and used within 2 days of preparation.
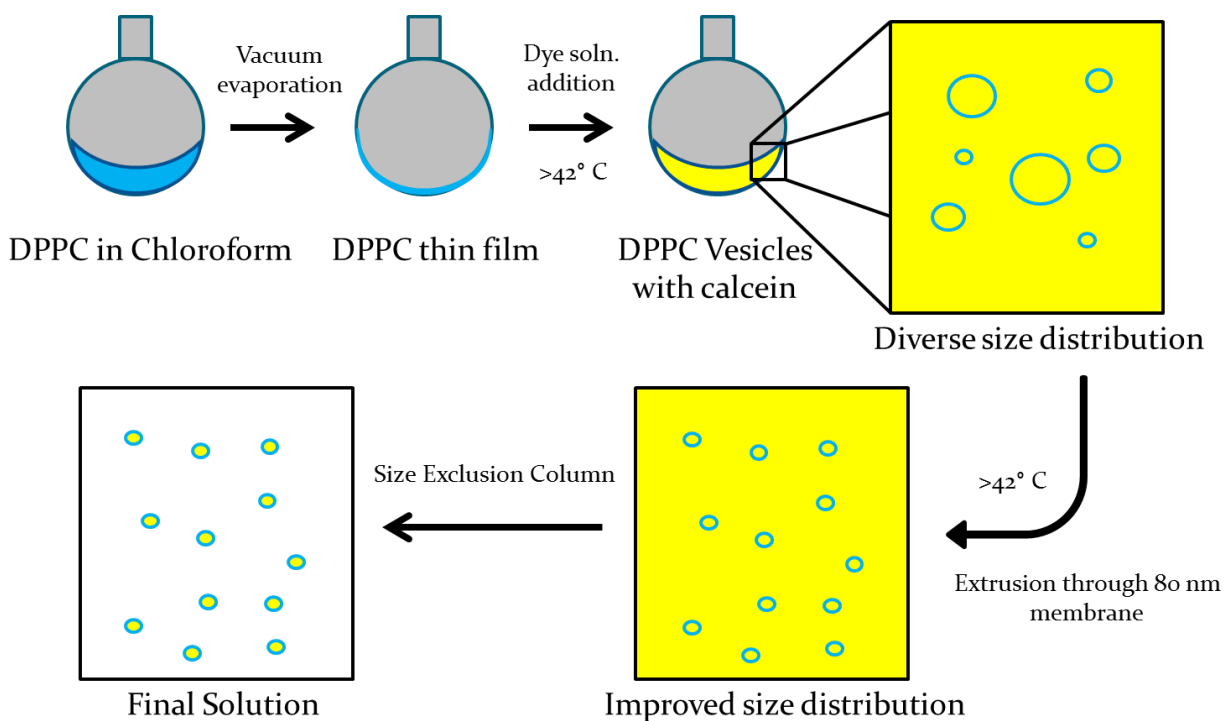
Figure 6.3: Representation of preparation process to generate DPPC vesicles with encapsulated calcein dye.

Fluorescence assays were performed on a Photon Technology International QM-6 steady state fluorimeter equipped with two emission channels and a sample holder with stirring and temperature control via a circulating water bath. The water bath temperature was set to 45 °C and at least 15 minutes was allowed for the sample holder to equilibrate once the water bath was up to temperature prior to any measurements. A 160 μL quartz fluorescence cuvette was used with a small stir bar. Fluorescence spectra

were taken using 1 nm entrance and exit slits, 75 W power supplied to the Xe arc lamp lightsource, 1000 V supplied to the photomultiplier tube detector, a 490 nm excitation wavelength, and a 500 nm long pass filter.

Permeability assays were performed using an Applied Photophysics Chirascan CS/SF with a stopped-flow accessory. 1:1 mixing was performed of ribose and vesicle solutions, while the entire stopped flow assembly was heated using a 45 °C circulating water bath. At least 150 µL total shot volume was used each run to ensure solution replacement in the fluorescence cell. Excitation wavelength was 490 nm, and emission wavelengths were controlled by the use of a band-pass filter with a center wavelength of 540 nm and absorbance values less than 5 in the range of 521-556 nm. The gain on the detector was held constant between runs.

6.3 Results:

Calcein fluorescence properties were first measured at the experimental temperature of 45 °C as a function of concentration and a calibration curve was constructed. Reference calcein/PBS/EDTA solutions were prepared in the same manner as the solutions used in vesicle synthesis, and then fluorescence measurements were taken for a series of serial dilutions of these free calcein samples (Figure 6.4). Scan parameters were held constant, but neutral density filters were used for highly fluorescent samples in order to avoid saturation of the detector. These filtered spectra were then scaled, using measured absorption spectra of the neutral density filters.
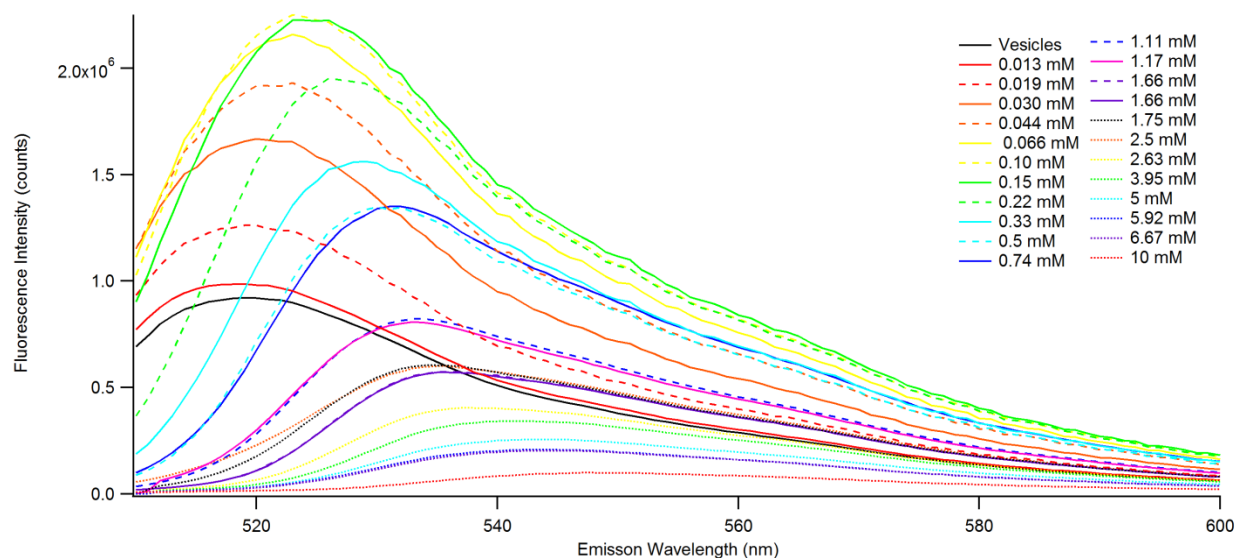
Figure 6.4: Calcein fluorescence intensity as a function of concentration and vesicles with encapsulated Calcein for reference (black). Step size was 1 nm and integration time was 1 second, with a 490 nm excitation wavelength.

A clear increase in fluorescence intensity is observed with increasing concentrations of calcein dye at low concentrations, followed by a sharp peak in intensity and subsequent decrease. While it is tempting to assume that the increasing region is before the onset of self-quenching, the behavior is, in fact, more complicated. In this case, the observed intensity increase is in the region where the addition of more chromophores by increasing concentration has a larger effect than the decrease of fluorescence quantum yield due to self-quenching. There are two convoluted effects, because both the number of fluorophores and the quantum yield of fluorescence are changing. In order to directly relate to the vesicle experiments, which have a fixed number of fluorophores but variable fluorescent yield, this calibration data needs to be further processed to account for both the emission range that is monitored and the number of dye molecules. The observed emission range is limited by a band-pass filter, so the emission intensity is weighed by the transmission of the filter and then integrated, before being normalized to produce the calibration curve shown in Figure 6.5. The normalization is not strictly a required step, but because different detectors were used for the two types of measurements (intensity v. wavelength and the fast-mixing of vesicles), it serves to simplify the analysis without loss of useful information.
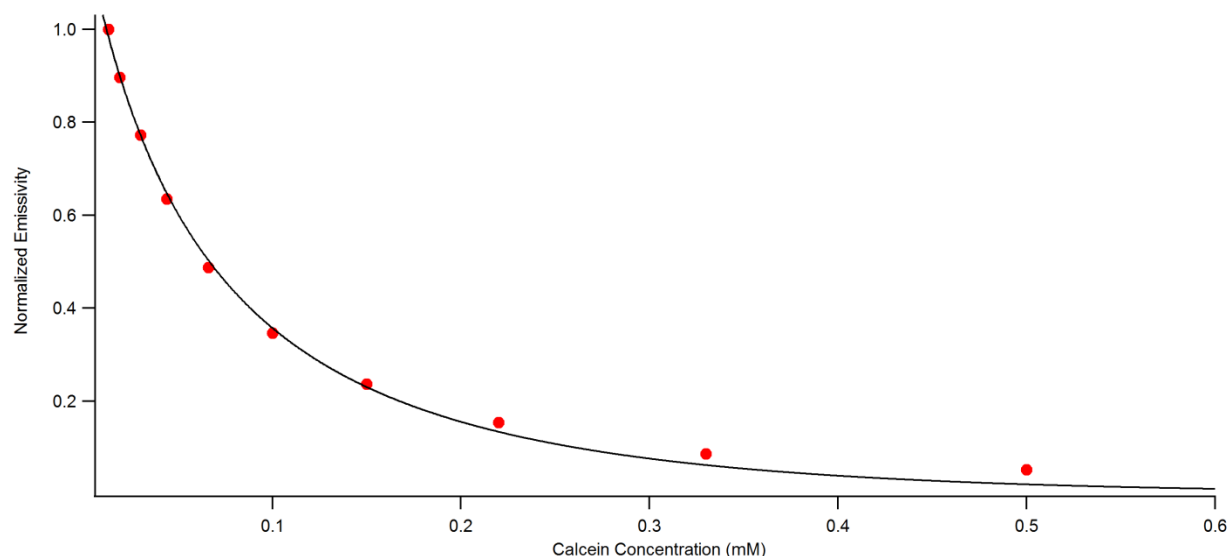
Figure 6.5: Filtered fluorescence intensity per mM of calcein dye, as a function of calcein concentration. The efficiency of self-quenching clearly changes across the entire concentration range that is probed. Red circles are experimental data, and the black line is the empirical fit to the data.

We are, for the most part, only concerned with the shape of the curve, not the exact value at any point. Because of this, the emissivity was normalized to the values from 0.013 mM concentration of free calcein in order to simplify the analysis. The normalized emissivity data can be fit to the empirical equation

$$E = \frac{1}{1.53 + e^{-6.08c}} - \frac{1}{1.53}$$

where c is concentration in mM. This fit appears to hold well for dye concentrations between 10 and 300 μM. This allows us to directly correlate emissivity with dye concentration, an important step toward examining volume changes due to osmotic pressure on a vesicle and the rates of diffusion of water and solutes through the bilayer membrane. In order to proceed further, however, it is important to quantify the initial concentration of calcein inside the vesicles. Fortunately, the shift in peak absorption wavelength can be used to estimate the interior calcein concentration (Figure 6.6).
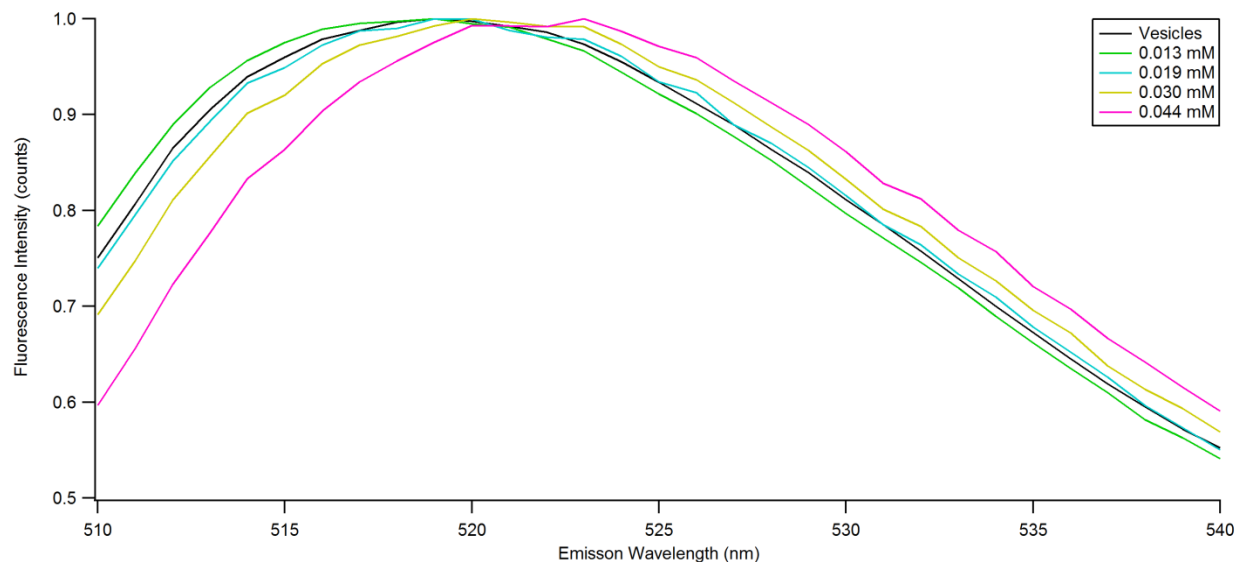
Figure 6.6: Calcein peak emission vs. concentration. This can be used to calibrate the initial concentration of calcein in the interior of the vesicles.

As seen in Figure 6.6, the shape of the vesicle emission spectrum most closely matches the 0.019 mM calcein dye solution. There is perhaps a slight blue shift, indicating a concentration less than 0.019 mM but greater than 0.013 mM. While it is, in principle, possible to fit the shape of the curve of the vesicle solution to extract a more precise calcein concentration, such a fit would rely on many variable parameters, making it unlikely that the resultant concentration would be more reliable than a simple estimate due to uncertainty in calcein concentration arising from the fit. Because of this, we simply estimate the internal calcein concentration of our vesicles at 0.018 ± 0.001 mM.

A noteworthy side point is the stark difference in calcein concentration between the inside and outside of the DPPC vesicles that is generated as the vesicles are formed. The solution in which vesicles are formed is 5 mM calcein, while the apparent interior calcein concentration is approximately 0.018 mM. This selective exclusion of solute during vesicle formation is surprising, but has been reported previously for relatively low concentration solutes,[20,21] and can be particularly low for fluorescein dies like calcein,[22] and smaller vesicles.[23] In order to verify the initial dye concentration, we can check several parameters using simple estimations. We can first estimate the total amount of fluorescence in the system. The approximate emissivity is known for a 0.018 mM solution, from our previous experiments. The total

emission, then, should be the emissivity times the volume fraction of the solution that is encapsulated in vesicles. This, in turn, depends on the radius and number of vesicles in solution. These quantities can be estimated based on the total amount of DPPC that has been added to the system. Letting vesicle size and number vary freely, the difference between the predicted and experimental solution fluorescence and DPPC concentration can be computationally minimized. Assuming spherical, bilayered vesicles with DPPC at 63 Å^2/molecule,[24] the estimated a vesicle radius is ~57 nm with a vesicle concentration of ~$1.4*10^{16}$ vesicles/liter. The estimated radius is reasonable because, experimentally, the vesicles were extruded through an 80 nm pore diameter membrane. These estimates assume no loss of DPPC during vesicle creation and the purification process. If any DPPC was lost, this estimation shifts to larger sizes and lower concentrations. Our assumptions, in effect, make the estimates a lower bound for the vesicle radius, and an upper bound on the vesicle concentration. For example, if 20% of the initial DPPC is lost, the estimated radius becomes 73 nm with a concentration of $6.5*10^{15}$ vesicles/L. The measurement of vesicle radius is important because it is an input in the fit equation for the permeability coefficient. Because of the details of the calculations, discussed below and in Appendix 3, errors in vesicle radius will not alter the relative permeability coefficients between measurements on identical vesicle solutions. This makes exact quantification less important for the purposes of this work. This calculation does show, however, that the encapsulated calcein concentration determined by fluorescence intensity is reasonable, given the observed fluorescence intensity and peak wavelength, the amount of DPPC used, and the calculated vesicle radius.

With reasonable certainty that vesicle-encapsulated dye concentration is ~0.018 mM, vesicle permeability assays were then performed. Fluorescence was recorded, filtered by a 540 nm band pass filter, following ribose addition to 500 mM final concentration to vesicle solution. Vesicle solutions were prepared with the addition of an aromatic species (Phe, PhAA, PhGly, and Tyr) and allowed to equilibrate overnight. In order to avoid changing the concentration of the aromatic species upon ribose addition, equimolar amounts were also added to the ribose solution to be mixed with these vesicles. Individual runs

were analyzed and fit separately. The fitting procedure is described in Appendix 3. Overlaid runs for each

of the different aromatic species are shown in Figure 6.7.
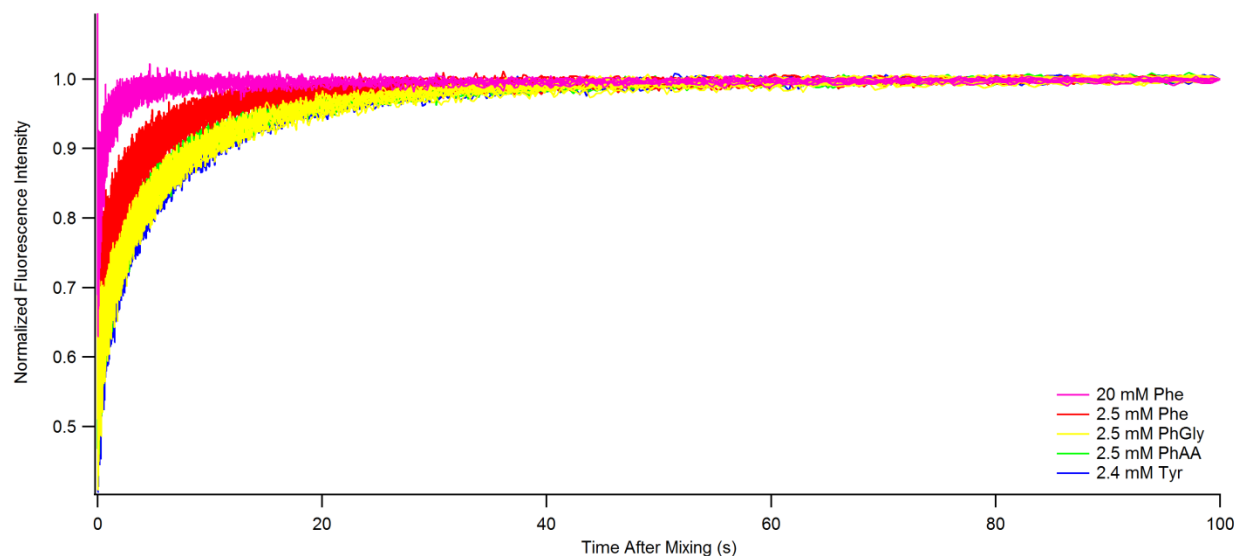
Figure 6.7: Normalized fluorescence data for all vesicle solutions spiked with aromatic species. Seven to eleven traces are overlaid for each aromatic species.

Even without the assistance of fitting procedures, it is apparent that Phe causes an increase in

vesicle permeability relative to the other aromatic molecules. This change is visible even at the relatively

low concentration of 2.5 mM. The permeability coefficients obtained by fitting this data generally

reinforces this result. The most reliable permeability coefficients obtained are listed in Table 6.1.

No Aromatic ($x10^{-9}$ m/s)	20 mM Phe ($x10^{-9}$ m/s)	2.5 mM Phe ($x10^{-9}$ m/s)	2.5 mM PhAA ($x10^{-9}$ m/s)	2.5 mM PhGly ($x10^{-9}$ m/s)	2.4 mM Tyr ($x10^{-9}$ m/s)
5.2 ± 0.7	33 ± 5	7.4 ± 0.4	5.2 ± 0.1	4.9 ± 0.1	5.0 ± 0.1

Table 6.1: Ribose permeability coefficients of DPPC vesicles in the presence of various aromatic species, with experimental uncertainties based on averaging the results of individual runs.

The measured permeability coefficient, P_s, for ribose is in the same range as previous

measurements for ribose permeation of 20:15:2 DPPC:Cholesterol:1,2-dipalmitoyl-glycero-3-phosphate,

with a P_s value of $0.9x10^{-9}$ m/s.[19] Again, our reported values may be high given the assumed vesicle

radius of 80 nm, but P_s values scale linearly with vesicle diameter, so 40 nm radius vesicles would

produce P_s values (and uncertainties) that are half of those that are reported in Table 6.1. It should be

noted, however, that this change in P_s values is due to the radius used in our calculations. In order to determine the rate that material moves through the vesicle surface, the permeability coefficient, surface area, and concentration difference must be know. Because the concentration change depends on the rate solute enters, but also the volume of the vesicle, the amount of time to reach equilibrium, which is measured experimentally, scales with the surface area to volume ratio. This is the root of the size dependence in the calculations. However, once P_s values are calculated appropriately, P_s is invariant with respect to vesicle size.

Interestingly, Phe appears to be able to modify membrane permeability, even at low concentrations, while the other aromatic molecules under study do not. This is consistent with our previous work,[6] where Phe was shown to be the most surface active molecule in the same series. While PhAA was also shown to be surface active in that study, it did not appear to undergo interfacial clustering to the same degree as Phe. This lack of clustering can be inferred from the absence of several behaviors indicative of interfacial clustering that were present for Phe, such as slow equilibration with high order concentration dependence and a leveling off of surface tension with increasing concentration. Cooperative effects were observed in molecular dynamics simulations for Phe, PhAA, and PhGly, although Phe displayed the highest magnitude of cooperativity. So while PhAA's ability to alter surface tension is similar to Phe's, it does not seem to have the ability to alter membrane permeability. This suggests that the change to permeability observed here is due to the aggregation of Phe, rather than simply the partitioning of aromatic material into the membrane.

In our previous studies, large changes were observed in the DPPC film morphology over large size scales.[5] In MD simulations, small clusters of Phe caused small pores to form in the DPPC film.[5] We have also reported indirect evidence that formation of larger Phe clusters occurs at the water-DPPC or water-air interface.[6] In the work of Adler-Abramovich et al.,[4] there is evidence of large Phe aggregate formation in neat solution as well as several membrane-containing solutions. We have published experimental evidence concluding that Phe does not aggregate in bulk solution, however the aggregation

of Phe in a membrane is supported by our work.[5,6] It is likely that the change in permeability is due to either a large-scale change in the morphology of the membrane and/or due to a small scale change immediately around a Phe cluster or aggregate. These two morphological changes are related, but the mechanism of increasing permeability could be distinct. Longer range morphological changes could result in permeability at sites where there is little or no Phe present, while this is not possible for more local changes.

There have been several studies of what molecular level structures Phe aggregates may adopt.[25–28] However, none of these investigations were performed or simulated under similar conditions to ours, that is, at low bulk concentration in an aqueous-DPPC interfacial region. However, they still may give hints as to the structure of Phe aggregates in this system. It seems likely that Phe would adopt a high aspect ratio, needle-like structure, as those have been found under a variety of theoretical aggregation conditions and contrast the crystal structure of solid Phe.[26] Phe-Phe dimers, [26,29] and larger peptides,[30] appear to adopt similar needle-like structures, with larger hollow cores. This may suggest that the mechanism altering permeability is more local around a Phe "needle" embedded in the membrane. This mechanism could be similar to the mechanism of modern membrane proteins, where a protein channel penetrates the bilayer.

Regardless of the exact details of aggregation and assembly, the ability of Phe to alter membrane permeability is a likely cause of the damage associated with untreated PKU. This is consistent with previous studies exposing cytotoxic effects of low concentration Phe,[4] as well as the detection of aggregates both immunologically and microscopically in cells cultured with Phe.[4] It also seems consistent with the symptoms of untreated PKU, such as intellectual impairment and seizures,[3] due to the stringent permeability requirements of nerve cells for proper function.[31] In particular, permeability changes observed here are consistent with the observation that brain abnormalities in adults[32] are reversed by decreasing Phe serum levels.[33,34]

The findings that relatively small concentrations of amino acid are capable of altering membrane permeability, while important to the study of PKU, also has applications in other areas. Research in the origins of life has many different approaches and has focused on many difficulties in transforming a non-living system into a living one, as well as the transformation of a very primitive "living" system into something more reminiscent of modern life. One key transformation is generation of proteins from amino acids. In modern biology, this is carried out by protein enzymes and mediated by RNA templates. Clearly the synthesis of proteins from enzymes that are themselves made of protein is not an acceptable source for the first proteins. Some RNA sequences have been shown to possess catalytic activity,[35] leading to a common theory that the first generation of protein was catalyzed by RNA.[36–40] While this view certainly has merits, it is not obvious why the generation of random sequences of polypeptide would be advantageous to any organism. Without some advantage to the system, there is an apparent lack of selective pressure that would lead to the synthesis of the first proteins.

In this work, however, we have shown that Phe is able to alter membrane permeability, likely because it is able aggregate within the membrane. Phe-Phe dimers have been shown to aggregate very efficiently into tubular structures, although they adopt additional structures depending on the conditions.[26,29,41,42] Larger phenylalanine peptides also appear to function as efficient membrane channels.[30] Given this behavior, it is not unreasonable to assume that useful interactions with membranes could set a direct path from amino acid monomers to functional proteins without the need for genetic encoding. Additionally, the water-restricted environment of the interfacial region has been shown to promote a variety of chemical reactions,[43–45] including peptide bond formation.[46] Although Phe is not thought to be a particularly primitive amino acid, based on its genomic coding,[47–50] these experiments provide a proof-of-concept that aggregates of amino acids can fill at least some of the same roles as proteins, in an environment that favors peptide bond formation without enzymatic assistance.

6.4 Conclusions:

In this work, we have shown that phenylalanine, unlike structurally similar aromatic molecules, has the ability to alter the permeability of bilayered vesicles, serving as model membranes. This ability appears to be unique to Phe due to its ability to assemble into aggregates within the interfacial region.[6] We propose that this permeability change drives the deleterious symptoms associated with elevated Phe serum levels in PKU. It is consistent both with the symptoms that are observed, as well as their reversible nature.[3]

The alteration of membrane permeability by Phe further relates to the origin of life. Membrane proteins are an essential component of modern biology, and the ability of a simple amino acid to perform some functions of a membrane protein helps bridge the gap between living and non-living systems. This system is particularly advantageous in that regard, due to the ability of the water limited interfacial region to promote non-enzymatic peptide bond formation. Intermediate systems even appear to be beneficial, due to the aggregation-prone nature of Phe dimers and small polymers.

Bibliography

(1)   Hong, H.; Park, S.; Flores Jiménez, R. H.; Rinehart, D.; Tamm, L. K. Role of Aromatic Side Chains in the Folding and Thermodynamic Stability of Integral Membrane Proteins. *J. Am. Chem. Soc.* **2007**, *129* (26), 8320–8327.

(2)   Domene, C.; Vemparala, S.; Klein, M. L.; Vénien-Bryan, C.; Doyle, D. A. Role of Aromatic Localization in the Gating Process of a Potassium Channel. *Biophys. J.* **2006**, *90* (1), L01–L03.

(3)   Hanley, W. B. Adult Phenylketonuria. *Am. J. Med.* **2004**, *117* (8), 590–595.

(4)   Adler-Abramovich, L.; Vaks, L.; Carny, O.; Trudler, D.; Magno, A.; Caflisch, A.; Frenkel, D.; Gazit, E. Phenylalanine Assembly into Toxic Fibrils Suggests Amyloid Etiology in Phenylketonuria. *Nat Chem Biol* **2012**, *8* (8), 701–706.

(5)   Griffith, E. C.; Perkins, R. J.; Telesford, D.-M.; Adams, E. M.; Cwiklik, L.; Allen, H. C.; Roeselová, M.; Vaida, V. Interaction of L-Phenylalanine with a Phospholipid Monolayer at the Water–Air Interface. *J. Phys. Chem. B* **2015**, *119* (29), 9038–9048.

(6)   Perkins, R. J.; Kukharchuk, A.; Delcroix, P.; Shoemaker, R. K.; Roeselová, M.; Cwiklik, L.; Vaida, V. The Partitioning of Small Aromatic Molecules to Air–Water and Phospholipid Interfaces Mediated by Non-Hydrophobic Interactions. *J. Phys. Chem. B* **2016**, *120* (30), 7408–7422.

(7)   De Kruijff, B.; Cullis, P. R.; Radda, G. K. Differential Scanning Calorimetry and 31P NMR Studies on Sonicated and Unsonicated Phosphatidylcholine Liposomes. *Biochim. Biophys. Acta BBA - Biomembr.* **1975**, *406* (1), 6–20.

(8)   Kaasgaard, T.; Mouritsen, O. G.; Jørgensen, K. Freeze/Thaw Effects on Lipid-Bilayer Vesicles Investigated by Differential Scanning Calorimetry. *Biochim. Biophys. Acta BBA - Biomembr.* **2003**, *1615* (1–2), 77–83.

(9)   Guida, V. Thermodynamics and Kinetics of Vesicles Formation Processes. *Adv. Colloid Interface Sci.* **2010**, *161* (1), 77–88.

(10)   Ho, J. C. S.; Rangamani, P.; Liedberg, B.; Parikh, A. N. Mixing Water, Transducing Energy, and Shaping Membranes: Autonomously Self-Regulating Giant Vesicles. *Langmuir* **2016**, *32* (9), 2151–2163.

(11)   Elani, Y.; Purushothaman, S.; Booth, P. J.; Seddon, J. M.; Brooks, N. J.; Law, R. V.; Ces, O. Measurements of the Effect of Membrane Asymmetry on the Mechanical Properties of Lipid Bilayers. *Chem. Commun.* **2015**, *51* (32), 6976–6979.

(12)   Ahumada, M.; Calderon, C.; Alvarez, C.; Lanio, M. E.; Lissi, E. A. Response of Unilamellar DPPC and DPPC:SM Vesicles to Hypo and Hyper Osmotic Shocks: A Comparison. *Chem. Phys. Lipids* **2015**, *188*, 54–60.

(13)   Nagarajan, S.; Schuler, E. E.; Ma, K.; Kindt, J. T.; Dyer, R. B. Dynamics of the Gel to Fluid Phase Transformation in Unilamellar DPPC Vesicles. *J. Phys. Chem. B* **2012**, *116* (46), 13749–13756.

(14)   Tierney, K. J.; Block, D. E.; Longo, M. L. Elasticity and Phase Behavior of DPPC Membrane Modulated by Cholesterol, Ergosterol, and Ethanol. *Biophys. J.* **2005**, *89* (4), 2481–2493.

(15)   Xiang, T.-X.; Anderson, B. D. Phase Structures of Binary Lipid Bilayers as Revealed by Permeability of Small Molecules. *Biochim. Biophys. Acta BBA - Biomembr.* **1998**, *1370* (1), 64–76.

(16)   Xiang, T.-X.; Xu, Y.-H.; Anderson, B. D. The Barrier Domain for Solute Permeation Varies With Lipid Bilayer Phase Structure. *J. Membr. Biol.* **1998**, *165* (1), 77–90.

(17)   Chen, P. Y.; Pearce, D.; Verkman, A. S. Membrane Water and Solute Permeability Determined Quantitatively by Self-Quenching of an Entrapped Fluorophore. *Biochemistry (Mosc.)* **1988**, *27* (15), 5713–5718.

(18)   Saito, H.; Shinoda, W. Cholesterol Effect on Water Permeability through DPPC and PSM Lipid Bilayers: A Molecular Dynamics Study. *J. Phys. Chem. B* **2011**, *115* (51), 15241–15250.

(19)   Sacerdote, M. G.; Szostak, J. W. Semipermeable Lipid Bilayers Exhibit Diastereoselectivity Favoring Ribose. *Proc. Natl. Acad. Sci.* **2005**, *102* (17), 6004–6008.

(20)   Gruner, S. M.; Lenk, R. P.; Janoff, A. S.; Ostro, N. J. Novel Multilayered Lipid Vesicles: Comparison of Physical Characteristics of Multilamellar Liposomes and Stable Plurilamellar Vesicles. *Biochemistry (Mosc.)* **1985**, *24* (12), 2833–2842.

(21) Reiner, J. E.; Jahn, A.; Stavis, S. M.; Culbertson, M. J.; Vreeland, W. N.; Burden, D. L.; Geist, J.; Gaitan, M. Accurate Optical Analysis of Single-Molecule Entrapment in Nanoscale Vesicles. *Anal. Chem.* **2010**, *82* (1), 180–188.

(22) Sun, B.; Chiu, D. T. Determination of the Encapsulation Efficiency of Individual Vesicles Using Single-Vesicle Photolysis and Confocal Single-Molecule Detection. *Anal. Chem.* **2005**, *77* (9), 2770–2776.

(23) Xu, X.; Costa, A.; Burgess, D. J. Protein Encapsulation in Unilamellar Liposomes: High Encapsulation Efficiency and A Novel Technique to Assess Lipid-Protein Interaction. *Pharm. Res.* **2012**, *29* (7), 1919–1931.

(24) Petrache, H. I.; Dodd, S. W.; Brown, M. F. Area per Lipid and Acyl Length Distributions in Fluid Phosphatidylcholines Determined by (2)H NMR Spectroscopy. *Biophys. J.* **2000**, *79* (6), 3172–3192.

(25) Do, T. D.; de Almeida, N. E. C.; LaPointe, N. E.; Chamas, A.; Feinstein, S. C.; Bowers, M. T. Amino Acid Metaclusters: Implications of Growth Trends on Peptide Self-Assembly and Structure. *Anal. Chem.* **2016**, *88* (1), 868–876.

(26) German, H. W.; Uyaver, S.; Hansmann, U. H. E. Self-Assembly of Phenylalanine-Based Molecules. *J. Phys. Chem. A* **2015**, *119* (9), 1609–1615.

(27) Singh, V.; Rai, R. K.; Arora, A.; Sinha, N.; Thakur, A. K. Therapeutic Implication of L-Phenylalanine Aggregation Mechanism and Its Modulation by D-Phenylalanine in Phenylketonuria. *Sci. Rep.* **2014**, *4*, 3875.

(28) Singh, P.; Brar, S. K.; Bajaj, M.; Narang, N.; Mithu, V. S.; Katare, O. P.; Wangoo, N.; Sharma, R. K. Self-Assembly of Aromatic α-Amino Acids into Amyloid Inspired Nano/Micro Scaled Architects. *Mater. Sci. Eng. C* **2017**, *72*, 590–600.

(29) Rissanou, A. N.; Georgilis, E.; Kasotakis, E.; Mitraki, A.; Harmandaris, V. Effect of Solvent on the Self-Assembly of Dialanine and Diphenylalanine Peptides. *J. Phys. Chem. B* **2013**, *117* (15), 3962–3975.

(30) Shen, Y.; Si, W.; Erbakan, M.; Decker, K.; Zorzi, R. D.; Saboe, P. O.; Kang, Y. J.; Majd, S.; Butler, P. J.; Walz, T.; et al. Highly Permeable Artificial Water Channels That Can Self-Assemble into Two-Dimensional Arrays. *Proc. Natl. Acad. Sci.* **2015**, *112* (32), 9810–9815.

(31) Voet, D.; Voet, J. G. *Biochemistry*, 4th Edition Binder Ready Version edition.; Wiley: Hoboken, NJ, 2010.

(32) Thompson, A. J.; Tillotson, S.; Smith, I.; Kendall, B.; Moore, S. G.; Brenton, D. P. Brain MRI Changes in Phenylketonuria. Associations with Dietary Status. *Brain J. Neurol.* **1993**, *116 (Pt 4),* 811–821.

(33) Cleary, M. A.; Walter, J. H.; Wraith, J. E.; White, F.; Tyler, K.; Jenkins, J. P. Magnetic Resonance Imaging in Phenylketonuria: Reversal of Cerebral White Matter Change. *J. Pediatr.* **1995**, *127* (2), 251–255.

(34) Walter, J. H.; White, F.; Wraith, J. E.; Jenkins, J. P.; Wilson, B. P. M. Complete Reversal of Moderate/Severe Brain MRI Abnormalities in a Patient with Classical Phenylketonuria. *J. Inherit. Metab. Dis.* **1997**, *20* (3), 367–369.

(35) Zaug, A. J.; Cech, T. R. The Intervening Sequence RNA of Tetrahymena Is an Enzyme. *Science* **1986**, *231* (4737), 470–475.

(36) Cech, T. R. A Model for the RNA-Catalyzed Replication of RNA. *Proc. Natl. Acad. Sci.* **1986**, *83* (12), 4360–4363.

(37) Kawamura, K.; Maurel, M.-C. Walking over 4 Gya: Chemical Evolution from Photochemistry to Mineral and Organic Chemistries Leading to an RNA World. *Orig. Life Evol. Biospheres* **2017**, 1–16.

(38) Lazcano, A.; Miller, S. L. The Origin and Early Evolution of Life: Prebiotic Chemistry, the Pre-RNA World, and Time. *Cell* **1996**, *85* (6), 793–798.

(39) Orgel, L. E. Prebiotic Chemistry and the Origin of the RNA World. *Crit. Rev. Biochem. Mol. Biol.* **2004**, *39* (2), 99–123.

(40) Robertson, M. P.; Joyce, G. F. The Origins of the RNA World. *Cold Spring Harb. Perspect. Biol.* **2012**, *4* (5).

(41) Görbitz, C. H. Nanotube Formation by Hydrophobic Dipeptides. *Chem. Weinh. Bergstr. Ger.* **2001**, *7* (23), 5153–5159.

(42) Guo, C.; Luo, Y.; Zhou, R.; Wei, G. Probing the Self-Assembly Mechanism of Diphenylalanine-Based Peptide Nanovesicles and Nanotubes. *ACS Nano* **2012**, *6* (5), 3907–3918.

(43) Vaida, V. Atmospheric Radical Chemistry Revisited Sunlight May Directly Drive Previously Unknown Organic Reactions at Environmental Surfaces. *Science* **2016**, *353*, 650–650.

(44) Tinel, L.; Rossignol, S.; Ciuraru, R.; Dumas, S.; George, C. Photosensitized Reactions Initiated by 6-Carboxypterin: Singlet and Triplet Reactivity. *Phys Chem Chem Phys* **2016**, *18* (25), 17105–17115.

(45) Martins-Costa, M. T. C.; Anglada, J. M.; Francisco, J. S.; Ruiz-Lopez, M. F. Reactivity of Volatile Organic Compounds at the Surface of a Water Droplet. *J. Am. Chem. Soc.* **2012**, *134*, 11821–11827.

(46) Griffith, E. C.; Vaida, V. In Situ Observation of Peptide Bond Formation at the Water–air Interface. *Proc. Natl. Acad. Sci.* **2012**, *109* (39), 15697–15701.

(47) Trifonov, E. N. Consensus Temporal Order of Amino Acids and Evolution of the Triplet Code. *Gene* **2000**, *261* (1), 139–151.

(48) Koonin, E. V.; Novozhilov, A. S. Origin and Evolution of the Genetic Code: The Universal Enigma. *IUBMB Life* **2009**, *61* (2), 99–111.

(49) Lu, Y.; Freeland, S. On the Evolution of the Standard Amino-Acid Alphabet. *Genome Biol.* **2006**, *7*, 102.

(50)   Wong, J. T.-F. Coevolution Theory of the Genetic Code at Age Thirty. *BioEssays* **2005**, *27* (4), 416–425.

Chapter 7: UV-Visible and Infrared Reflection-Absorption Spectroscopies

7.1 Introduction

Previous work, discussed in chapters three through six, and their associated publications,[1,2] has examined the interactions of phenylalanine (Phe) as well as analogous aromatic compounds, with water-air and water-phospholipid interfaces. This work was largely motivated by the disease phenylketonuria (PKU), which can cause Phe concentrations in human serum to exceed 1.2 mM,[3] and work suggesting that Phe aggregates may be responsible for the damage caused by PKU.[4] In our work, experimental evidence suggested that Phe does not aggregate in solution, but may aggregate in interfacial regions.[1,2] In order to compliment the indirect evidence of interfacial aggregate formation in our previous work, I set out to find direct, spectroscopic evidence.

Spectroscopy has remained a powerful tool for physical chemistry since its inception. A wide variety of spectroscopic tools now exist, and can probe electronic, vibrational, and rotational states of molecules, and often obtain information about their surroundings in the process. Among the plethora of spectroscopic techniques, there are several that allow for the collection of spectra from interfacial regions. Two similar techniques, Sum Frequency Generation (SFG) and Second Harmonic Generation (SHG) have attracted increasing attention in recent years. Both of these techniques rely on non-linear optical processes (they require interaction of a molecule with two photons). This produces the constraint that SFG/SHG signals will not be significant unless the illuminated molecules are anisotropic, and illumination intensities are very high.[5–8] Because bulk phase material is generally isotropic, these techniques will only be sensitive to material at interfaces. The trade-off for this selectivity, however, is that these systems are generally expensive and the resulting spectra can be difficult to interpret.[9–11]

An alternative surface sensitive technique is reflection absorption spectroscopy (RAS). These techniques are linear spectroscopies, the same as standard absorption experiments. Light is reflected off an interfacial region before being detected. The interfacial selectivity comes from the fact that light is

only reflected from the region where the refractive index is changing. The most common application for RAS spectroscopies is Infrared Reflection Absorption Spectroscopy (IRRAS, RAIRS). It is often performed with the addition of a photoelastic modulator (PM-IRRAS, PM-RAIRS), which adds the selection condition that the absorbing molecules are anisotropic. The most advantageous aspect of this increase in selectivity is the removal of gas-phase water signatures, which are unavoidable when examining aqueous interfaces. In exchange for this increase in selectivity, the sensitivity is generally decreased, due largely to a loss of photons upon polarization.

Because of the different criteria for interfacial selectively, RAS techniques may probe different surface regions than SFG or SHG techniques. Additionally, because the thermodynamic definition of interfacial species is based on surface excess concentrations, the interfacial region defined thermodynamically may differ from the region probed by RAS, SFG, and SHG. Several cases are presented in Figure 7.1 representing a soluble surfactant, a surface depleted solute, and a soluble surfactant (A, B, and C, respectively). The assumption that the refractive index changes as a function of density near the interface, while not exact, is expected to hold reasonably well for two component systems. For more complex systems, it may break down.
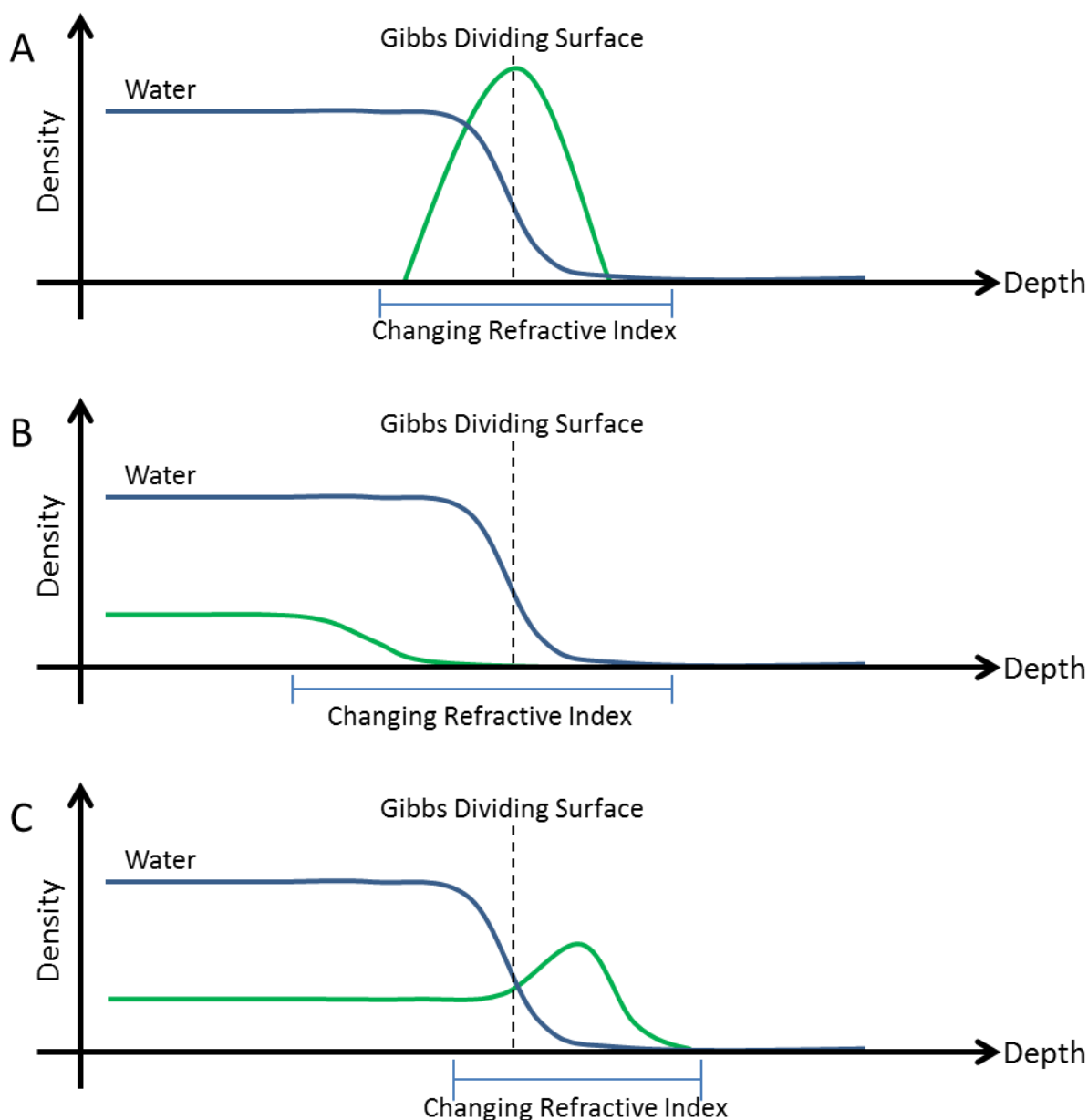
Figure 7.1: Density profiles near a water interface for three different cases. The curve in blue represents the density versus depth of water, while the curve in green represents the density versus depth for a surfactant or solute. Case A is representative of a classical insoluble surfactant. Case B is representative of a soluble, surface depleted molecule. Case C is representative of a soluble, surface partitioning molecule. The Gibbs dividing surface is defined such that the surface excess concentration of water is zero. The region of refractive index change is estimated based on the total density as a function of depth. Anisotropic regions are only loosely related to regions where density is changing.

In case A, the region of changing refractive index overlaps well with the region where excess concentration of the second component exists. Insoluble surfactants also tend to be anisotropic at an interface, so for this case A, SFG/SHG, RAS, and thermodynamic interfacial definitions overlap well.

The region of refractive index change is also similar with and without surfactant present. In case B, the refractive index changes over a larger region due to a change in solute density further from the Gibbs dividing surface. This change will result in greater depth of water probed, and ultimately a change in water signal, for RAS techniques. The solute will also be probed to some extent, determined by the refractive index changes where the solute concentration is changing. For SFG/SHG, in this situation it is likely that the depleted solute remains mostly isotropic, resulting in weak or absent solute signals. The region of anisotropic water may also remain the same as a clean water surface, resulting in little-to-no change in SFG/SHG spectra compared to pure water. The depletion of solute near the surface is thermodynamically relevant, and would result in an increase in surface tension. In case C, the region of refractive index change is larger than the region where excess concentration of the soluble surfactant exists. This leads to probing of molecules via RAS that do not contribute thermodynamically to the decreased surface tension. For SFG/SHG, it is difficult to predict which molecules will be anisotropic in this situation, and produce spectral signals. Some of the solute molecules, appear above the water, will almost certainly possess some degree of anisotropy. The water could be more isotropic in this situation, resulting in less signal, although it depends strongly on the interactions between the water and the solute. It is possible in this case that the region of changing water density would be nearly completely isotropic, resulting in little-to-no water signal. While these differences appear relatively minor, they can be particularly important for interpreting changes in signal, and comparing results obtained with different spectroscopic techniques, and thermodynamic properties.

IRRAS and vibrational-SFG (V-SFG) utilize IR frequency light to examine vibrational states of molecules. The selection rules are slightly different for vibrational transitions that are observable. For IRRAS, the same selection rules apply as for normal IR spectroscopy; the vibration in question must result in a change in the diploe moment of the molecule. For V-SFG, transitions must have a change in dipole moment as well as a change in polarizability in order to be observable.[11] In other words, vibrations must be both observable to linear IR spectroscopy and Raman scattering. More complex polarized

experiments are possible with SFG, dubbed chiral SFG, that can be performed for V-SFG as well. These experiments produce interesting results, although clear interpretations are often difficult.[12]

An analogous technique to IRRAS, which has received less attention, is Ultra Violet-Visible Reflection Absorption Spectroscopy (UVRAS).[13–22] It operates on the same principle as unpolarized IRRAS, where the selectivity comes from the fact that light will only reflect where the refractive index is changing, i.e. in the interfacial region. There are several advantages for UVRAS compared to IRRAS.[13] First, absorptions of gas phase water are less problematic, although they do limit the useful range of the technique in the deep UV (absorbing <185 nm).[23] This also means that PM-UVRAS is less advantageous than PM-IRRAS. Second, brighter broad-band light sources are available in the UV and visible spectral regions than in the IR. Third, the absorption cross sections, for a given molecule, which are allowed transitions are generally several orders of magnitude higher in the UV and visible compared to the IR. Considering only these facts, it is difficult to see why UVRAS is not a more popular technique.

Considering the techniques that are available to examine the aggregation state and partitioning of material at the water-air or water-phospholipid interface, I have chosen to pursue a combination of IRRAS and UVRAS to gather complementary data. As aggregates of aromatic compounds are formed, changes to vibrational modes are expected, although they could be relatively small. Electronic states, responsible for the absorption in the UV and visible regions of the spectrum, are also expected to change with many types of aggregation. For conjugated π systems, such as aromatic rings, aggregation often occurs through stacking of π orbitals. Depending on the geometry, this generally results in either a blue-shift or a red-shift of the absorption spectrum, known as H aggregation or J aggregation, respectively. These considerations underline the RAS approach developed in this work.

7.2 Methods, Results, and Discussion

IRRAS data was collected using a home-built system, and is illustrated in Figure 7.2. Illumination from the external port on a Bruker Tensor 27 FTIR was focused into a purge box using a calcium fluoride lens. The purge box contained a small Langmuir trough for sample deposition and control, and a liquid

nitrogen cooled MCT detector for light collection. Two gold flat mirrors were used, one to deflect the IR beam into the water surface at ~60° from surface normal, and another to deflect the reflected beam into the detector at a matching angle. A gold 90° off axis parabolic mirror was used to focus incident light into the sensitive area of the detector. The purge box is fed by a constant flow of dry, CO_2 scrubbed air.
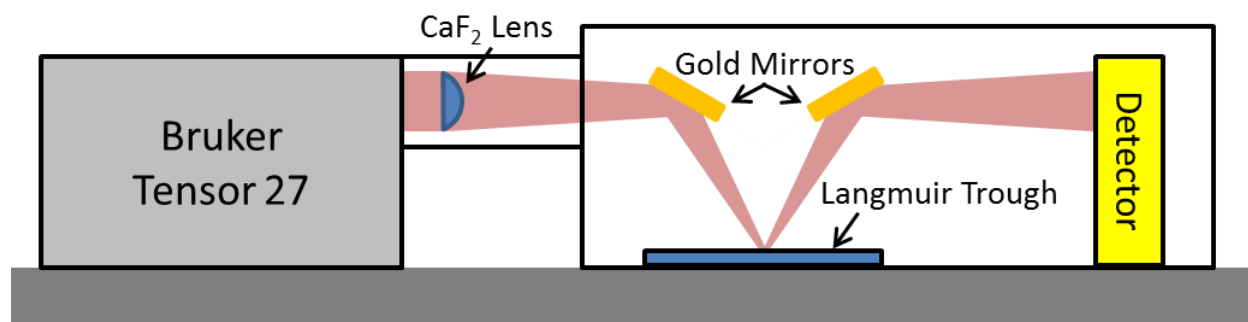

Figure 7.2: Schematic of the home built IRRAS systems, with IR light beam shown in pink.

In order to collect high quality spectra, several aspects of the procedure were found to be critical. Because this is not a PM-IRRAS, vapor phase water lines tend to make a strong appearance in the spectrum. In order to remove these lines, background spectra needed to be collected under similar conditions to sample spectra. Because changing the aqueous sample necessitates the removal of the purge box lid, there is some time dependence to the relative humidity inside the purge box. In order to account for this, blanks are taken sequentially immediately following lid closure, averaging scans continuously for 10 minute intervals. Sample scans are taken using the same procedure, and are compared against the corresponding blank spectrum in order to generate a reflected-absorption spectrum. Because of small deviations in relative humidity, there is still some residual water signal in these spectra, however. This is further reduced using the built-in atmospheric compensation function in OPUS, the software running the FTIR instrument. This requires an experimental spectrum of gas phase water, with similar scan parameters, as an input.

Interpretation of actual spectra, while in some ways is simpler than for non-linear techniques, is not straight forward due to the combination of absorption and reflection processes. Several works have explored the relationships between absorption intensities, changes in refractive index as a function of

depth, polarization, and orientations of interfacial molecules.[24–26] The quantity that is generally probed in these systems is reflected absorption (RA), which is defined as

$$RA = -log\left(\frac{R}{R_0}\right)$$

Where R is the sample reflected intensity and R_0 is the background reflected intensity. It is not uncommon for peaks associated with a new layer of material on top of the interface to appear as negative reflected absorption, depending on the angle of incidence, the polarization, and the molecular orientation. That is, the addition of absorbing species at the interface can result in enhanced reflection of light near absorptive transitions. While this is counterintuitive, it is well supported by both theory and experiment,[24,26–30] and arises from the fact that the entire complex refractive index is probed at the interface. For the unpolarized IRRAS used in these experiments the angle of incidence is ~80°, the behavior is dominated by S polarized light (due to higher interfacial reflectivity), and results in negative reflected absorption from interfacial species.

IRRAS spectra were collected using this scan procedure to obtain spectra for solutions of water and 2.5 or 100 mM Phe, with or without the addition of a 70 $\mathring{A}^2$/molecule film of dipalmitoylphosphatidylcholine (DPPC). Spectra for DPPC and DPPC with 2.5 mM Phe are shown in Figure 7.3 below. Assignments of spectral features of DPPC were based on known FTIR features in solid DPPC, or similar compounds. There is an additional peak present for the 2.5 mM Phe subphase, which grows in over time. This peak is tentatively assigned to Phe, as it also appears with 2.5 mM Phe in the absence of DPPC (Figure 7.4), although there are some complicating factors.
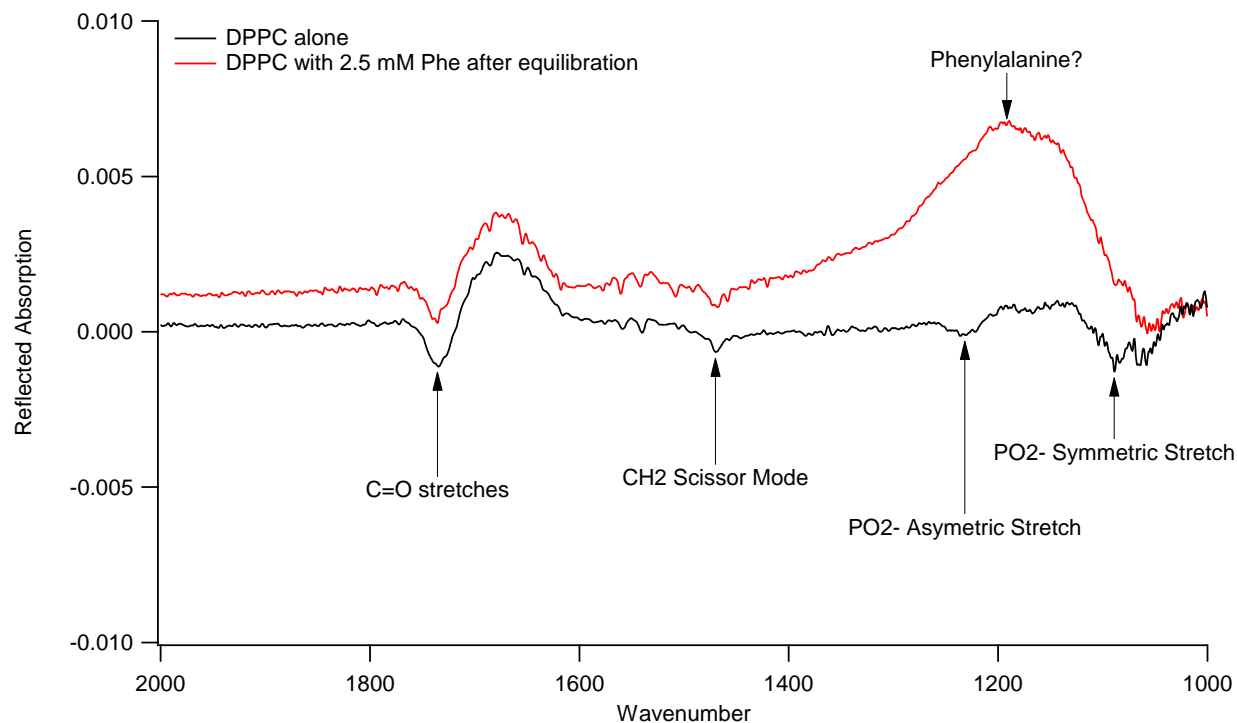
Figure 7.3: IRRAS spectrum of DPPC on clean water as well as 2.5 mM Phe subphases. Tentative peak assignments are indicated.

One issue with the assignment of the ~1200 cm^{-1} peak to Phe is that it also sometimes appears in experiments with pure aqueous subphases. The magnitude of the changes is significantly less, which leads to the possibility that it is due to contamination. In this case it seems likely that it is self-contamination with Phe that is not easily removed from the trough surface. If this were true, then the assignment as Phe would still be correct. It is difficult to say conclusively, however, without performing more experiments. The second problem shown in Figure 7.4 is the differences in Phe spectra between 2.5 and 100 mM. The feature at ~1200 cm^{-1} is perhaps present in the 100 mM sample, although is seems to be particularly low intensity compared with the other, more characteristic peaks that are shared by solid Phe. It is possible that this peak is characteristic of Phe aggregates, however, and may not appear strongly in solid Phe samples. Because of these issues, the results of the IRRAS studies could not be interpreted unambiguously. This is at least partly due to the difficulty in assigning vibrational peaks, especially in the region where the Phe signal appears, which is often the result of collective motions.[31]
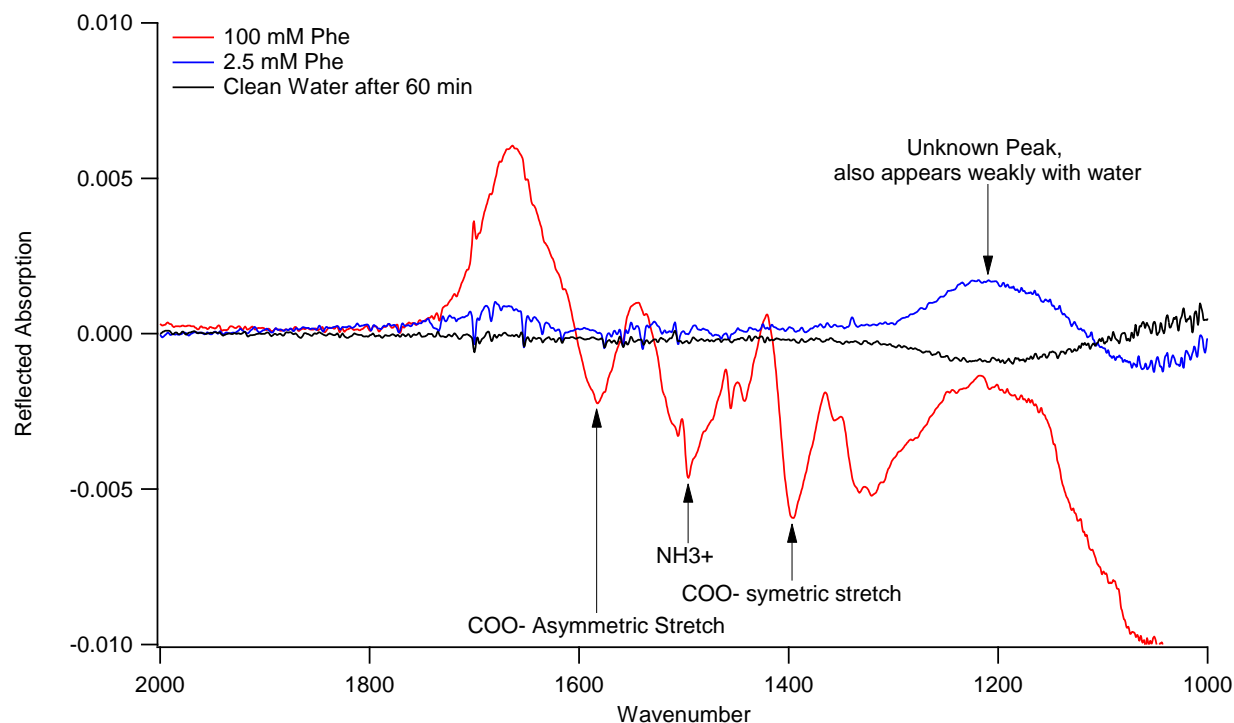
Figure 7.4: IRRAS spectra of 0, 2.5, and 100 mM Phe at identical time points after deposition. The residual peak from water is potentially due to Phe contamination.

In order to provide complementary information to the IRRAS spectra, the construction of a UVRAS was undertaken. Previous attempts at recording UVRAS data are reported in the literature, and changes in reflectance between bare water and dye covered surfaces are on the order of 0.5% reflectance.[14,15] Because of the low differences in intensities that are expected, a successful UVRAS would need a sensitivity greater than 0.1% reflectance. This did not initially seem like a difficult requirement, although several issues were uncovered during the construction of the instrument.

The initial construction utilized a Horiba iHR550 UV-visible spectrometer with a UV-sensitized Synapse CCD detector. The lightsource was an EnergetIQ EQ-99 laser driven Xe plasma lamp. It uses an IR laser to sustain a Xe plasma, rather than a conventional electric current. This allows for a very small spot size ~100 µm across, and a hotter plasma, which extends the emission further into the UV spectral region. The small source size is optically advantageous, and allows for almost all of the emitted light to be captured and re-focused down to a microscopic size. The initial setup for the UVRAS was similar to the existing IRRAS, with a few important differences. The purge box was initially not deemed necessary,

because the relative humidity was not expected to alter the spectrum over the range investigated. An aluminum 90° off-axis parabolic mirror was used to collimate the light coming from the EQ-99. The CCD used was very sensitive but, as a trade-off, it is relatively slow. Consequently, integration times needed to be at least ~100 ms, so high intensity light saturates the detector even at the shortest integration time possible. This, unfortunately, doesn't allow for taking advantage of the high light intensity from the EQ-99 light source. It also requires the addition of an iris into the system and the removal of the focusing lens in order to decrease the light intensity.

Using this setup spectra could be collected, although the sensitivity was too low to observe absorbing molecules at the water surface. Visible vibration at the water surface was apparent, and resulted in movement of the incident beam on the spectrometer entrance. This resulted in considerable noise in the collected spectrum, and ultimately reduced the sensitivity of the UVRAS. In order to vibrationally isolate the sample, several steps were attempted. First, sorbothane feet were attached to the bottom of the breadboard supporting the sample and optics. This did not result in a noticeable change in the vibration of the water surface. This is at least some indication that the vibration is due to low frequency modes in the table that are not easily isolated. Further isolation was attempted using a suspension system. A steel disc about 6" diameter and 0.5" thick was suspended from lab scaffolding bars about 1.5' high arranged in a square about 9" from the center of the platform. Initially thin, plastic coated wire was used to suspend the disc. The disc was then used as a sample platform. This setup is depicted in Figure 7.5, and provided excellent isolation of horizontal vibrations, and results in a noticeable decrease in the ripples at the water sample surface.
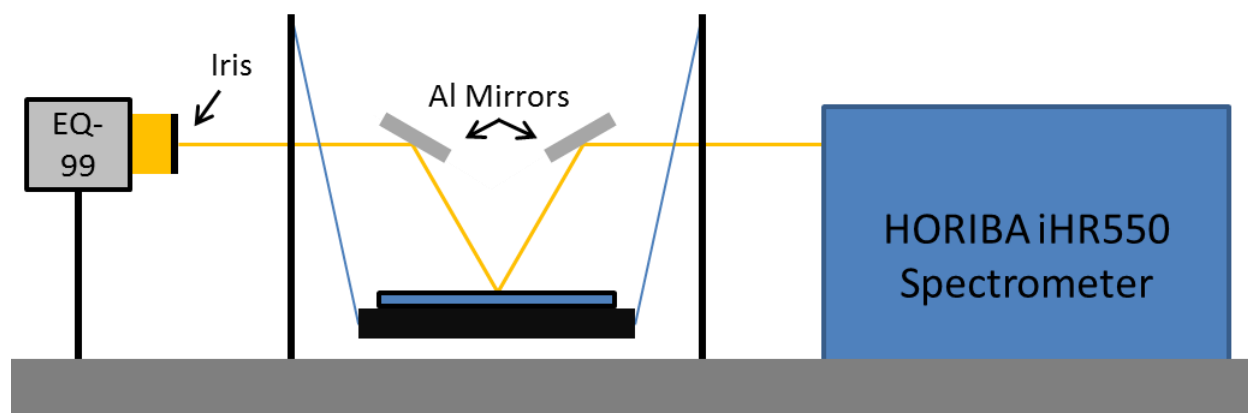
Figure 7.5: Attempted UVRAS setup, including the suspension system for vibration isolation of the liquid sample.

With this system it became apparent, however, that there was too much drift over time in the intensity of collected spectra. This could be due to several factors which were investigated, with steps taken to correct them. First, it could be due to the evaporation of water, and subsequent change in water level, over time. This would change the position of the incident beam on the spectrometer, and could be responsible for the change in intensity. To test for this, the aqueous solution was replaced with a flat mirror, and the drift was still significant. Second, it could be due to stretching of the suspension system during operation. The suspension cables were replaced with braided steel cables, and no difference was observed. This does not rule out stretching completely, although some change would be expected. Third, it could be due to internal changes in the CCD. This would be an inherent issue with the spectrometer, and is difficult to diagnose.
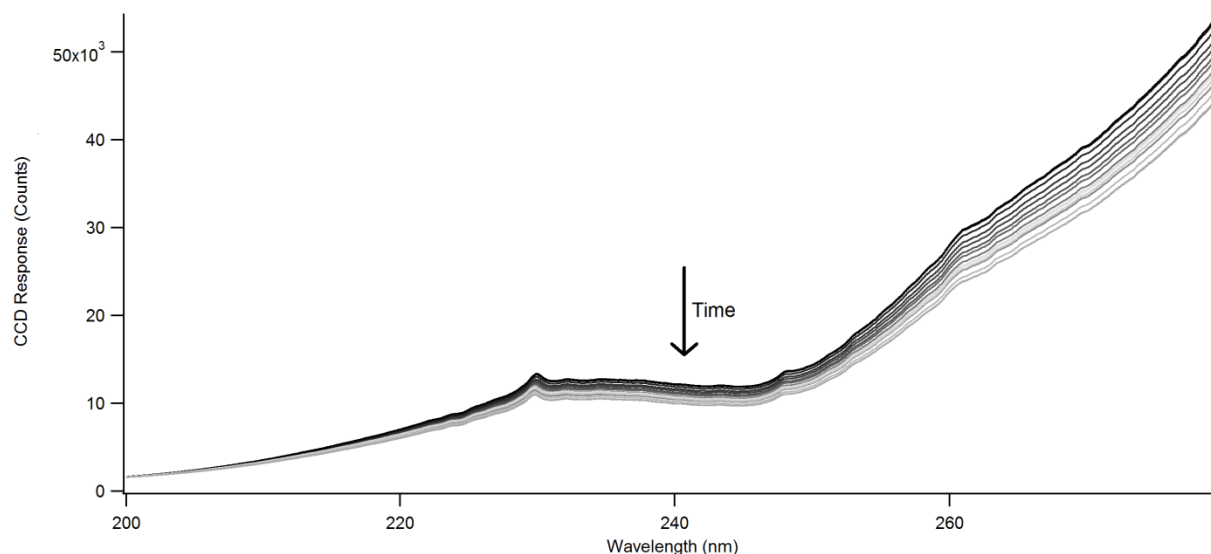
Figure 7.6: Drift in CCD signal over time when the suspension system was in use. Spectra were taken with a mirror in place of the sample, using the Horiba UVRAS setup and a suspension vibration isolating sample platform.

Because of the potential issues with the CCD reliability, as well as the mismatch between CCD sensitivity and lightsource intensity, I chose to adapt this system to a different spectrometer. The spectrometer I used was a refurbished Jobin Yvon (JY) spectrometer with a grating blazed at 210 nm, for efficient use in the UV and VUV regions of the spectrum. For a detector, a Hamamatsu H1146-09 photomultiplier tube (PMT) detector was used. This detector was solar-blind, i.e. insensitive to visible light, which simplified its construction. PMTs are high sensitivity detectors that are advantageous due to their variable gain settings, making them useful across a wide range of incident light intensities. The setup for this instrument was similar to the setup for the UVRAS with the Horiba spectrometer, and is depicted in Figure 7.6. The main difference was that the new setup allowed for utilization of the high intensity light from the EQ-99, due to the high variable gain of the PMT as well as the low bandwidth of light hitting the PMT (compared to the broadband detection of a CCD). This setup was sensitive further into the UV, with the spectrum limited by the absorption of oxygen and ozone. In order to examine deeper UV features, a plastic purgable enclosure was constructed, and was flushed with pure nitrogen originating inside the lamp housing and the spectrometer casing. This allowed for spectral collection in slightly lower

wavelength regions, although the absorption due to water vapor is not much lower, and is impossible to eliminate when using aqueous samples.

This new setup lowered the detection limit considerably, although some of the same issues remained. The experiment was first attempted without the suspension isolating platform, but this system ultimately proved too noisy to accurately record spectra of surface materials. The JY UVRAS setup was then tested with the suspension isolations system. It seemed to encounter the same problem as the UVRAS setup with the Horiba spectrometer; spectral drift over time dominates the uncertainty in measured spectra (Figure 7.7).
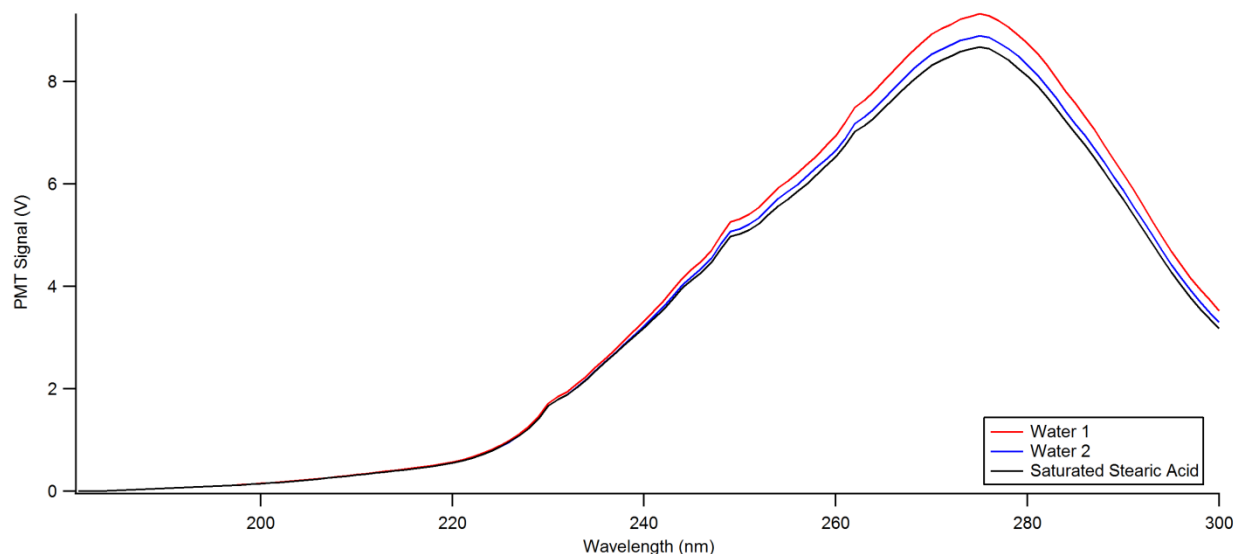
Figure 7.7: UVRAS intensity spectra of water and water with a stearic acid film. The variation in spectra over time is large compared to the differences that are observed with surface-active species.

Because of the drift that appears to be induced by the suspension system, alternative equipment for isolating from vibrations was sought. The type of system that appeared the most promising is active vibrational isolation. In these types of systems, vibrations are monitored in the supported platform, and piezoelectric actuators are utilized to produce identical vibrations of opposite phase. This works well for removing low and medium frequency vibrations, and is generally combined with a passive isolator system for removal of high frequency vibrations. These combined systems have very low resonant frequencies, and only small amplifications in vibrations at resonance. They are also advantageous in that they have

very good special stability, which could make isolating only the sample and not the surrounding optics viable. For the UVRAS instrumentation however, an isolation system was purchased from Herzan that should be capable of isolating the entire UVRAS instrument. This system had not arrived at the time of writing, however.

Although there were difficulties in building the UVRAS, nothing was uncovered that was fundamentally problematic. Vibrational isolation and positional stability become much more important for UVRAS instrumentation than IRRAS. This is likely perhaps due to the lower wavelength IR light being less sensitive to surface roughness.

7.3 Conclusions

The IRRAS studies of Phe and DPPC gave promising results. A peak grows in over time that is nearly identical for 2.5 mM Phe as well as 2.5 mM Phe with 70 $Å^2$/molecule DPPC. Unfortunately, this peak can also be seen weakly with pure water, although this is likely due to contamination from Phe iteslf. More problematic is that this peak, around 1200 cm^{-1} cannot readily be assigned to any peak from the bulk state Phe spectrum. This is potentially due to some sort of aggregate structure, although the surface reflection spectrum alone is not conclusive.

UVRAS studies were attempted to compliment the IRRAS studies, although they proved challenging due to the high sensitivity to environmental conditions. In particular, vibrations caused ripples at the water surface and reduced signal-to-noise ratios in reflected-absorption spectra. Attempts to vibrationally isolate the sample using a suspension system reduced the water surface vibrations, however they appeared to induce signal drift in the system that was not easily corrected. An active vibration isolation system was chosen to address these issues, and will hopefully result in a working UVRAS in the near future.

Once a functioning instrument is constructed, many intriguing problems can readily be examined with this technique, including Phe and related aromatic groups. This technique is not limited to those

cases, and the combination of VUV sensitivity and surface sensitivity expand the possible systems to many molecules containing double bonded functional groups, including acids, ketones, and unsaturated carbons.

7.4 Materials

Phenylalanine (99%, Alfa Aesar), stearic acid (99% Sigma Aldrich), and Chloroform (≥99.8%, Sigma Aldrich) were used without further purification.

Bibliography

(1)   Griffith, E. C.; Perkins, R. J.; Telesford, D.-M.; Adams, E. M.; Cwiklik, L.; Allen, H. C.; Roeselová, M.; Vaida, V. Interaction of L-Phenylalanine with a Phospholipid Monolayer at the Water–Air Interface. *J. Phys. Chem. B* **2015**, *119* (29), 9038–9048.

(2)   Perkins, R. J.; Kukharchuk, A.; Delcroix, P.; Shoemaker, R. K.; Roeselová, M.; Cwiklik, L.; Vaida, V. The Partitioning of Small Aromatic Molecules to Air–Water and Phospholipid Interfaces Mediated by Non-Hydrophobic Interactions. *J. Phys. Chem. B* **2016**, *120* (30), 7408–7422.

(3)   Hanley, W. B. Adult Phenylketonuria. *Am. J. Med.* **2004**, *117* (8), 590–595.

(4)   Adler-Abramovich, L.; Vaks, L.; Carny, O.; Trudler, D.; Magno, A.; Caflisch, A.; Frenkel, D.; Gazit, E. Phenylalanine Assembly into Toxic Fibrils Suggests Amyloid Etiology in Phenylketonuria. *Nat Chem Biol* **2012**, *8* (8), 701–706.

(5)   Duffy, D. C.; Davies, P. B.; Bain, C. D.; Ward, R. N.; Creeth, A. M. Sum Frequency Vibrational Spectroscopy of the Solid-Liquid Interface; 1995; Vol. 2547, pp 342–351.

(6)   Eisenthal, K. B. Liquid Interfaces Probed by Second-Harmonic and Sum-Frequency Spectroscopy. *Chem. Rev.* **1996**, *96* (4), 1343–1360.

(7)   Jubb, A. M.; Hua, W.; Allen, H. C. Environmental Chemistry at Vapor/Water Interfaces: Insights from Vibrational Sum Frequency Generation Spectroscopy. *Annu. Rev. Phys. Chem.* **2012**, *63* (1), 107–130.

(8)   Ma, G.; Allen, H. C. New Insights into Lung Surfactant Monolayers Using Vibrational Sum Frequency Generation Spectroscopy. *Photochem. Photobiol.* **2006**, *82* (6), 1517–1529.

(9)   Geissler, P. L. Water Interfaces, Solvation, and Spectroscopy. *Annu. Rev. Phys. Chem.* **2013**, *64* (1), 317–337.

(10)   Noah-Vanhoucke, J.; Smith, J. D.; Geissler, P. L. Statistical Mechanics of Sum Frequency Generation Spectroscopy for the Liquid–vapor Interface of Dilute Aqueous Salt Solutions. *Chem. Phys. Lett.* **2009**, *470* (1), 21–27.

(11)   Noah-Vanhoucke, J.; Smith, J. D.; Geissler, P. L. Toward a Simple Molecular Understanding of Sum Frequency Generation at Air−Water Interfaces. *J. Phys. Chem. B* **2009**, *113* (13), 4065–4074.

(12)   Yan, E. C. Y.; Fu, L.; Wang, Z.; Liu, W. Biological Macromolecules at Interfaces Probed by Chiral Vibrational Sum Frequency Generation Spectroscopy. *Chem. Rev.* **2014**, *114* (17), 8471–8498.

(13)   Rubia-Payá, C.; de Miguel, G.; Martín-Romero, M. T.; Giner-Casares, J. J.; Camacho, L. UV–Vis Reflection–Absorption Spectroscopy at Air–liquid Interfaces. *Adv. Colloid Interface Sci.* **2015**, *225*, 134–145.

(14)   Martín, S.; Haro, M.; López, M. C.; Royo, F. M.; Cea, P. Charge Transfer Complex Formation at the Air–water Interface "in Situ" Studied by Means of UV–vis Reflection Spectroscopy. *Surf. Sci.* **2006**, *600* (15), 3045–3051.

(15)   Grüniger, H.; Möbius, D.; Meyer, H. Enhanced Light Reflection by Dye Monolayers at the Air–water Interface. *J. Chem. Phys.* **1983**, *79* (8), 3701–3710.

(16)   Moriya, Y.; Hasegawa, T.; Okada, T.; Ogawa, N.; Kawai, E.; Abe, K.; Ogasawara, M.; Kato, S.; Nakata, S. Analysis of Gibbs Monolayer Adsorbed at the Toluene/Water Interface by UV−Visible Partial Internal Reflection Spectrometry. *Anal. Chem.* **2006**, *78* (22), 7850–7856.

(17)   Ahuja, R. C.; Caruso, P. L.; Moebius, D.; Wildburg, G.; Ringsdorf, H.; Philp, D.; Stoddart, J. F.; Preece, J. A. Molecular Organization via Ionic Interactions at Interfaces. 1. Monolayers and LB Films of Cyclic Bisbipyridinium Tetracations and Dimyristoylphosphatidic Acid. *Langmuir* **1993**, *9* (6), 1534–1544.

(18)   Giner-Casares, J. J.; de Miguel, G.; Pérez-Morales, M.; Martín-Romero, M. T.; Camacho, L.; Muñoz, E. Effect of the Molecular Methylene Blue Aggregation on the Mesoscopic Domain Morphology in Mixed Monolayers with Dimyristoyl−Phosphatidic Acid. *J. Phys. Chem. C* **2009**, *113* (14), 5711–5720.

(19)   Selektor, S. L.; Raitman, O. A.; Silant'eva, D. A.; Ivanova, N. V.; Yonusauskas, G.; Lukovskaya, E. V.; Batat, P.; Arslanov, V. V. Control of Photochemical Properties of Monolayers and Langmuir-Blodgett Films of Amphiphilic Chromoionophores. *Prot. Met. Phys. Chem. Surf.* **2011**, *47* (4), 484–493.

(20)   Porteu, F.; Palacin, S.; Ruaudel-Teixier, A.; Barraud, A. Supermolecular Engineering at the Air-Water Interface: Spatially Controlled Formation of Heterodimers from Amphiphilic Porphyrins and Porphyrazines through Specific Molecular Recognition. *J. Phys. Chem.* **1991**, *95* (19), 7438–7447.

(21)   Bohanon, T. M.; Caruso, P.-L.; Denzinger, S.; Fink, R.; Möbius, D.; Paulus, W.; Preece, J. A.; Ringsdorf, H.; Schollmeyer, D. Molecular Recognition-Induced Function and Competitive Replacement by Hydrogen-Bonding Interactions: Amphiphilic Barbituric Acid Derivatives, 2,4,6-Triaminopyrimidine, and Related Structures at the Air−Water Interface. *Langmuir* **1999**, *15* (1), 174–184.

(22)   González-Delgado, A. M.; Giner-Casares, J. J.; Brezesinski, G.; Regnouf-de-Vains, J.-B.; Camacho, L. Langmuir Monolayers of an Inclusion Complex Formed by a New Calixarene Derivative and Fullerene. *Langmuir* **2012**, *28* (33), 12114–12121.

(23)   Gürtler, P.; Saile, V.; Koch, E. E. Rydberg Series in the Absorption Spectra of H2O and D2O in the Vacuum Ultraviolet. *Chem. Phys. Lett.* **1977**, *51* (2), 386–391.

(24)   Mendelsohn, R.; Brauner, J. W.; Gericke, A. External Infrared Reflection Absorption Spectrometry of Monolayer Films at the Air-Water Interface. *Annu. Rev. Phys. Chem.* **1995**, *46* (1), 305–334.

(25)   Tachibana, K.; Shirafuji, T.; Muraishi, S. Construction and Performance of a Fourier-Transform Infrared Phase-Modulated Ellipsometer for In-Process Surface Diagnostics. *Jpn. J. Appl. Phys.* **1996**, *35* (6R), 3652.

(26)   Gericke, A.; Michailov, A. V.; Hühnerfuss, H. Polarized External Infrared Reflection-Absorption Spectrometry at the Air/Water Interface: Comparison of Experimental and Theoretical Results for Different Angles of Incidence. *Vib. Spectrosc.* **1993**, *4* (3), 335–348.

(27)   Gericke, A.; Mendelsohn, R. Partial Chain Deuteration as an IRRAS Probe of Conformational Order of Different Regions in Hexadecanoic Acid Monolayers at the Air/Water Interface. *Langmuir* **1996**, *12* (3), 758–762.

(28)   Sarangi, N. K.; Ramesh, N.; Patnaik, A. Structure and Dynamics of H2O Vis-á-Vis Phenylalanine Recognition at a DPPC Lipid Membrane via Interfacial H-Bond Types: Insights from Polarized FT-IRRAS and ADMP Simulations. *J. Chem. Phys.* **2015**, *142* (2), 024702.

(29)   Cai, P.; Flach, C. R.; Mendelsohn, R. An Infrared Reflection−Absorption Spectroscopy Study of the Secondary Structure in (KL4)4K, a Therapeutic Agent for Respiratory Distress Syndrome, in Aqueous Monolayers with Phospholipids†. *Biochemistry (Mosc.)* **2003**, *42* (31), 9446–9452.

(30)   Mitchell, M. L.; Dluhy, R. A. Understanding The Interfacial Structure Of Aqueous Phospholipid Monolayer Films Via External Reflection FT-IR Spectroscopy.; 1989; Vol. 1145, pp 255–256.

(31)   Rijs, A. M.; Compagnon, I.; Oomens, J.; Hannam, J. S.; Leigh, D. A.; Buma, W. J. Stiff, and Sticky in the Right Places: Binding Interactions in Isolated Mechanically Interlocked Molecules Probed by Mid-Infrared Spectroscopy. *J. Am. Chem. Soc.* **2009**, *131* (7), 2428–2429.

Chapter 8: Chemical Equilibria and Kinetics in Aqueous Solutions of Zymonic Acid

Adapted with permission from Perkins, R. J.; Shoemaker, R. K.; Carpenter, B. K.; Vaida, V. Chemical Equilibria and Kinetics in Aqueous Solutions of Zymonic Acid. *J. Phys. Chem. A* **2016**, *120* (51), 10096–10107. Copyright 2016 American Chemical Society. The original article can be accessed at http://pubs.acs.org/doi/abs/10.1021/acs.jpca.6b10526.

8.1 Introduction

Pyruvic acid is a ubiquitous molecule in biology, where it takes an essential place at the core of metabolism for all life. It intersects anabolic and catabolic pathways that occur both aerobically and anaerobically, earning it a special place as a metabolite in both modern[1] and ancient life.[2,3] Additionally, it is an important molecule in the environment, particularly in the Earth's atmosphere,[4–13] and has even been found in carbonaceous meteorites.[14] In the atmosphere, formation of pyruvic acid oligomers or other high molecular weight compounds can be important for aerosol formation and processing.[15–17] The reactivity of pyruvic acid is important in these systems, and many studies have been carried out in an attempt to characterize reactive pathways involving pyruvic acid.[18–35] In many recent studies, however, the spontaneous dimerization of pyruvic acid is overlooked. It results in the formation of parapyruvic acid (γ-methyl-γ-hydroxy-α-ketoglutarate) along with its lactone, zymonic acid (α-keto-γ-valerolactone-γ-carboxylic acid). This "decomposition" was observed along with the first isolations of pyruvic acid by Berzelius in 1835,[36,37] according to Wolff who, building on previous work,[38–41] produced the first correct structures and reasonable formation mechanisms around 1900.[42–44] Further investigations analyze the mechanism of formation as well as the structure of larger pyruvic acid polymers.[45–48]

Later studies are split between work examining metal catalysis,[49–52] and biological processes.[53–74] Zymonic acid was identified as a metabolite in yeast,[53] only to be shown to be a contaminant from pyruvic acid used and an incorrect structure was first reported.[54,55] A number of other papers have discussed the detection or role of parapyruvic and zymonic acid in various biological contexts, including

detections from living tissues and interactions with enzymes.[56–74] Interestingly, parapyruvic acid has been observed in meteorites alongside pyruvic acid,[14] and discussed in the context of the origin of life.[75] There are several papers discussing the spontaneous formation of zymonic and parapyruvic acids from pyruvic acid under different conditions, and suggest that these molecules exist as contaminants in other experiments.[55,76–79] Because these dimerization products[*] are formed relatively easily, it is somewhat unclear whether previous detections of zymonic and parapyruvic acids are artifacts of the analytical techniques that are used.

The interconversion between the different forms of zymonic, parapyruvic, and pyruvic acids are especially interesting in aqueous solution, and are necessary to elucidate for a full understanding of the aqueous phase chemistry of pyruvic acid. In this work, structural identification of different tautomers and hydrates of zymonic acid is performed using several different NMR techniques. At equilibrium under low pH conditions, we detect and assign five different forms of pyruvic acid dimers in solution, and investigate the mechanisms of their interconversion. Our higher resolution NMR work across a broader pH range allows for the differentiation of quickly exchanging species that were assigned to single components in most previous works.[49–79] We report identification and characterization of the pyruvic acid chemical dimerization products, followed by a study of the kinetics of interconversion. Finally, potential mechanisms are discussed for the novel interconversions that are observed.

8.2 Experimental Section

8.2.1 Purification: Crude zymonic acid was isolated from ~25 mL of pyruvic acid (Sigma-Aldrich, 98%) that had been stored at 4°C for several months by distillation. Distillation was carried out at 70°C and 400 mTorr for several hours, until the bulk of the pyruvic acid was removed. Upon completion of distillation, several grams of a viscous yellow liquid remained that smelled strongly of caramel. Upon cooling, this yellow substance became extremely viscous, and was a sticky, glassy solid at 4°C. This substance was

---

[*] For convenience, in this work we will refer to all the six carbon molecules we observe as pyruvic acid dimerization products, even though they appear to be produced through a variety of hydration and isomerization reactions. Included in this category are zymonic acid and parapyruvic acid.

identified as mainly zymonic acid via NMR and will be referred to as "crude zymonic acid", with approximately 10-20% pyruvic acid remaining and several unidentified impurities. 125 mg of crude zymonic acid was dissolved in approximately 1 mL ethyl acetate (Mallinckrodt ≥99.5%), and then exposed to 0.5 mmHg vacuum for several hours. About 450 mg ethyl acetate remained and the sample became very viscous. The ethyl acetate was then extracted with excess hexanes (Sigma-Aldrich, ≥99%) facilitated by water bath sonication. Hexane supernatant was discarded, and vacuum was applied to remove residual solvent. This process was repeated several times in order to obtain an off-white sticky powder.

8.2.2 NMR:

Proton, COSY, HMBC, and HSQC spectra were obtained at 23°C using a Varian INOVA-500 NMR spectrometer operating at 499.60 MHz for ^{1}H observation. To perform NMR with 1H detection in aqueous solution, WET solvent suppression was used to eliminate >99% of the H2O signal.[111] In all cases (1D and 2D), 1H detection experiments were performed using an optimized WET water suppression as the initial preparation step of the NMR pulse sequence. The two-dimensional gradient-selected heteronuclear single-bond correlation spectrum using matched adiabatic pulses (2D-gHSQCad) experiments were performed with matched adiabatic sweeps for coherence transfer, corresponding to a central 13C-1H J-value of 146 Hz.[112] Gradient-selected heteronuclear multiple bond correlation using adiabatic pulses (gHMBCad) experiments were optimized for a long-range ^{13}C-^{1}H coupling constant of 8.0 Hz. Gradient-selected homonuclear correlation spectroscopy (gCOSY) was performed with two 90° pulses and variable evolution time between them.

Temperature dependent spectra were acquired using a Varian/Agilent VNMRS/DD2 800 MHz NMR operating at 798.6 mHz for ^{1}H detection.

Solid-state ^{13}C CPMAS NMR experiments were performed using a Varian INOVA-400 NMR spectrometer operating at 400.16 MHz for ^{1}H observation. The probe used in these experiments is a Varian 2-channel 4 mm CPMAS probe, modified with a new spinning module and coil designed and

constructed by Revolution NMR, LLC in Fort Collins, CO. This probe utilizes Zirconia "pencil" style rotors and is capable of spinning 4 mm rotors stably at spinning frequencies up to 18 kHz. ^{13}C CPMAS experiments were performed using a 3.3 μs ^{1}H 90° pulse, employing ramped cross-polarization with a spin-lock field centered at a magnitude 67 kHz. The contact time used was 4.0 ms, optimized for maximum polarization transfer with minimal signal loss due to $T_{1\rho}$ relaxation. A delay of 3.0 s was employed to allow for ^{1}H relaxation between scans. Broadband TPPM (time-proportional phase modulation) ^{1}H decoupling was applied during signal acquisition, utilizing a CW decoupling power of 75 kHz. MAS (magic angle spinning) was performed at 13.1 kHz.

8.2.3 FTIR: Fourier transform infrared spectroscopy was performed using a Bruker Tensor 27 spectrometer for crude samples, and a Thermo-Nicolet Avatar 360 spectrometer for powder samples. Crude samples were prepared by spreading crude zymonic acid on NaCl windows, and were scanned with 1 cm^{-1} resolution averaged over 100 scans. Powder samples were mixed with KBr (>99% Sigma-Aldrich) and pressed into transparent discs using a pellet press. These samples were scanned with 1 cm^{-1} resolution and averaged over 64 scans.

8.2.4 UV-VIS: Purified zymonic acid was mixed with 18.2 MΩ water and immediately scanned using a Varian (Agilent) Cary 5000 spectrometer with a 0.1 s average time, 1 nm data interval, and a 0.5 nm spectral band width. Scans were taken periodically and tracked by the time elapsed since zymonic dissolution.

8.2.5 Kinetic Fit: NMR kinetic data was first analyzed in MestReNova v10.0.2-15465 by fitting assigned peaks to generalized Lorentzian line shapes, and extracting relative peak areas from the fit areas for each timestep. The kinetic data was modeled in MATLAB R2016a (9.0.0.341360) using a full set of differential equations for all reaction pathways described. Rate constants were simultaneously optimized by minimizing uncertainty-weighted deviation of the fit from the experimental data using the built-in constrained optimization function fmincon. Error estimates for rate constants were generated by

randomizing input kinetic data as a Gaussian distribution within experimental uncertainty, and refitting, generating a statistical pool of rate constants. Average values are not reported because the statistical pools are, for many rate constants, highly non-Gaussian.

8.3 Results and Discussion:

8.3.1 Purification and Identification:

Pyruvic acid is the simplest alpha keto acid and, like most ketones, can convert between the ketone, enol, and geminal diol forms in aqueous solution.[49,80] For pyruvic acid the ketone and geminal diol forms are thermodynamically favored in water, and constitute the bulk of pyruvic acid with the ratio between them depending on solution conditions (pH, concentration, salt, temperature). Parapyruvic acid, likewise, is a keto acid, and exists dominantly as either a ketone or geminal diol. Unlike pyruvic acid, it can undergo an intramolecular esterification reaction, resulting in the formation of a lactone. The lactone additionally has a ketone functionality, and can exist in solution as a mixture of the ketone, geminal diol, and enol forms. The lactone enol of parapyruvic acid has been referred to as zymonic acid.

Zymonic acid appears to form spontaneously in pure liquid pyruvic acid samples or in aqueous solutions, likely through an aldol addition reaction.[78] This means that even very well purified pyruvic acid will spontaneously convert to zymonic acid over time under normal storage conditions. In fact, several grams of crude zymonic acid were isolated via distillation from approximately 25 mL of pyruvic acid that had been stored at 4°C for several months (see Methods for details). Further purification of zymonic acid was carried out in dry, aprotic solvents in order to preserve the purity and prevent the formation of hydrates, and ultimately resulted in a sticky, off-white powder which will be referred to as "purified zymonic acid". Zymonic acid, both in crude and purified forms, smells strongly of caramel and is hygroscopic as well as solvoscopic.

NMR spectra of purified compounds were first taken in deuterated dimethyl sulfoxide (DMSO-d_6). The proton spectrum is shown in Figure 8.1.
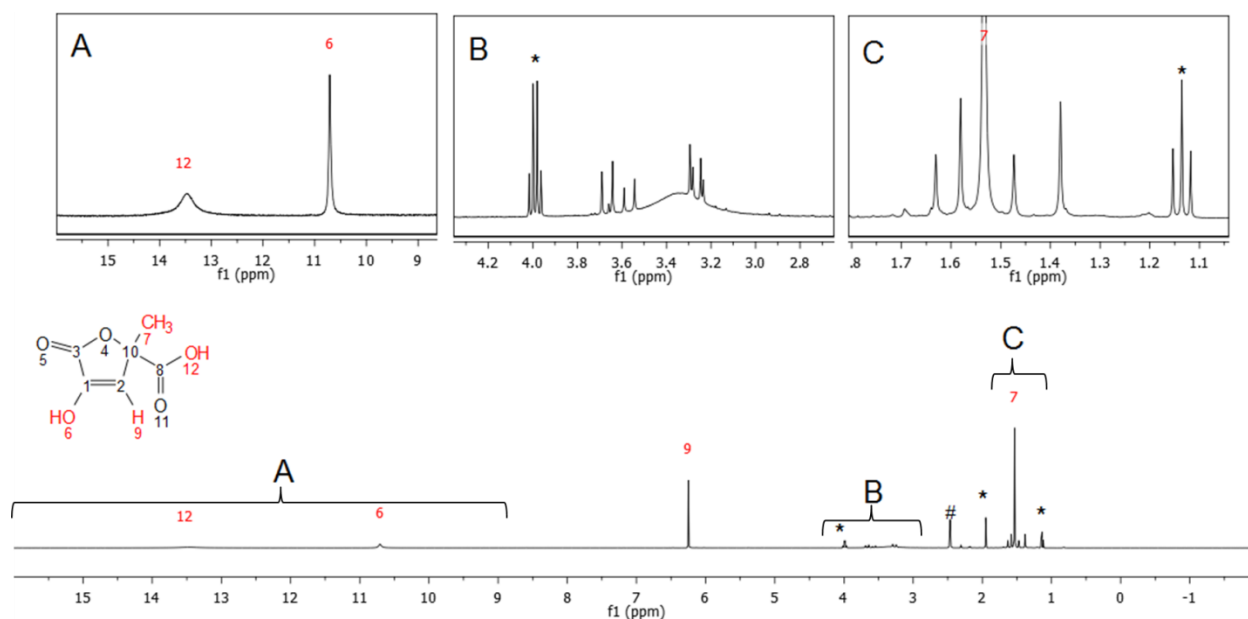
Figure 8.1: 400 MHz Proton NMR spectrum of purified zymonic acid in DMSO-d₆ (bottom), with expanded spectral regions (top). Peaks numbered in red correlate with H atoms in the zymonic acid structure shown. * indicates ethyl acetate impurity and # indicates un-deuterated DMSO. In box B the broad peak at 3.35 ppm is water impurity due to the DMSO-d₆.

While the singlet peak at 6.25 ppm is strongly indicative of the enol form of this molecule and great care has been taken to avoid water contamination during purification, further evidence is required in order to rule out the corresponding molecule that has been hydrolyzed to create the open chain form. The open form would have an additional alcohol group as well as another acid group that should be visible in this spectrum. The broadness from peak 12 is likely due to exchange of the acid proton with water contamination in the DMSO, where peak 6, the enol proton, is not exchanging as quickly. This makes it unlikely that both peaks 12 and 6 are associated with carboxylic acids. It could be possible, although unlikely, for two carboxylic acid peaks to overlap, and perhaps for the alcohol peak to overlap with the peak from water contamination. The ratios of the peaks $H^{12} : H^6 : H^9 : H^7$ are 1.17 : 1.06 : 1.00 : 2.92, which are in much better agreement for the closed form than the open one, however. Carbon 13 NMR spectra were taken for both the sample in DMSO-d₆ as well as the solid. Both spectra agree well with the structure of the closed enol form (Figure A4.12 in Appendix 4).

NMR spectra were also taken in 10% deuterated water solutions, and are shown in Figure 8.2. Assignments were made through the use of a combination of NMR spectroscopies (COSY, HMBC, and HSQC see Figures A4.1-A4.11 in Appendix 4). To a lesser extent trends in chemical shift were used to differentiate between very similar molecules. For example, differentiating between the set of peaks assigned to the ketone and diol molecules was done by referencing the region in the carbon spectrum where geminal diols are generally found. Five different species zymonic species are detected in equilibrium with each other in water, and will be referred to as zymonic closed enol (ZCE), zymonic closed ketone (ZCK), zymonic open ketone (ZOK, aka parapyruvic acid), zymonic closed diol (ZCD) and zymonic open diol (ZOD). The nomenclature closed and open here refers to the cyclic and acyclic forms, respectively.
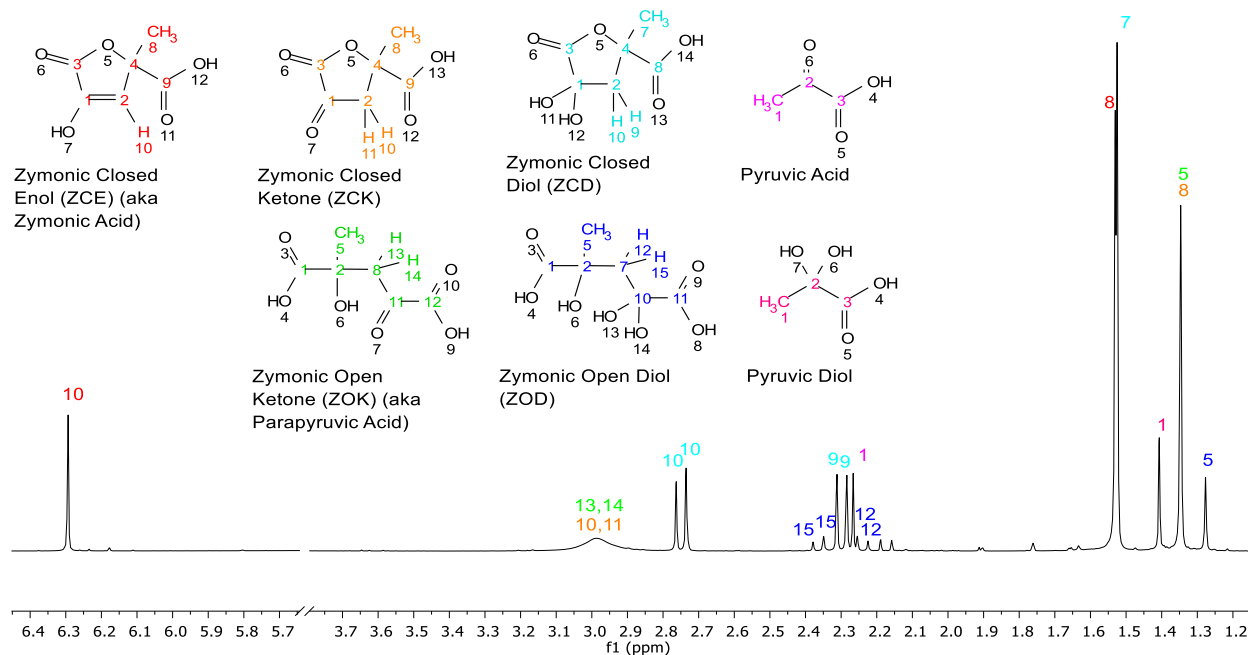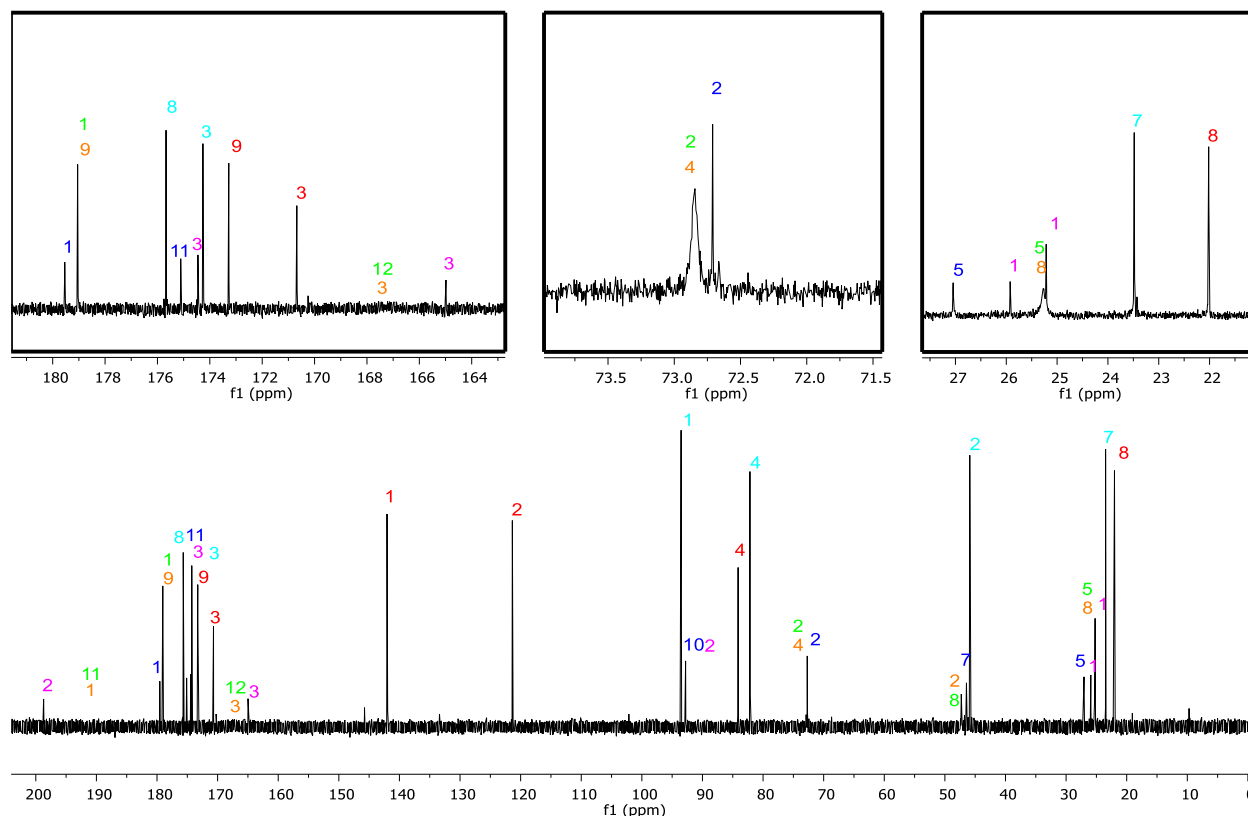
Figure 8.2: 500 MHz Proton (top) and carbon (bottom) NMR of zymonic acid in 10% deuterated water using WET water suppression, with their corresponding structures. Peaks are labeled with the color and number corresponding to a carbon or group of equivalent hydrogens in the corresponding structures. The carbon NMR spectrum has been zoomed in regions with overlapping peaks. Assignments of ZCK carbon 3 and ZOK carbon 12 are tentative, as they are expected to be very broad but somewhere in the region depicted.

One compound that is expected from this chemistry, but not assigned in Figure 8.2, is the aldol condensation product of pyruvic acid. This product would be ZOK (parapyruvic acid) with, using the atom labels found in Figure 8.2, OH 6 and H 13 or 14 removed via dehydration, with a double bond appearing between carbons 2 and 8. The peaks at approximately 146 and 134 ppm in the carbon spectrum may be due to this aldol condensation product, but due to their relatively low abundance and lack of correlation in the 2D NMR spectra, a concrete assignment is not possible here.

There are several broad features in the spectra in Figure 8.2, which are associated with the two ketone forms of zymonic acid, ZOK and ZCK. These arise due to an exchange between the closed and open ring ketone forms, which appears to be in the intermediate exchange regime where chemical

exchange occurs on the NMR timescale. Broader peaks are associated with atoms that are closest to the oxygens involved in ring formation. Peak width due to chemical exchange falls into several regimes based on the ratio of the exchange rate to the difference in resonance frequency of the exchanging species. When the exchange is very slow relative to the frequency difference, very little broadening occurs. As the exchange rate increases, the peaks associated with the exchanging species become increasingly broad and averaged until the coalescence point is reached, and faster exchange results in sharper peaks. The coalescence point occurs when the exchange rate $k_c = \pi \Delta \upsilon / \sqrt{2}$ where $\Delta \upsilon$ is the frequency difference between the exchanging species. The observation that the peaks are broader where the largest chemical changes are occurring suggests that all the observed peaks are at or above the coalescence point. This was investigated further as a function of temperature and pH (Figure 8.3).
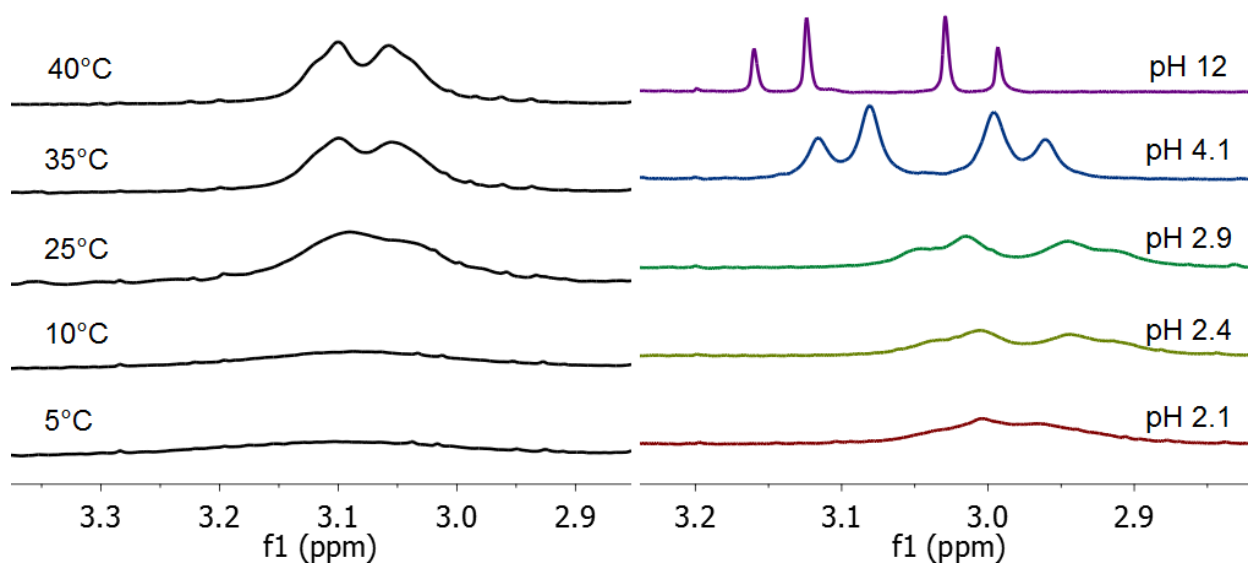
Figure 8.3: Comparison of CH₂ ketone proton NMR peaks as a function of temperature at unadjusted pH of 2.1 (left) and as a function of pH at 23°C (right). The temperature dependent NMR spectra (left) were taken on an 800 MHz instrument, while the pH dependent spectra (right) were taken on a 500 MHz instrument.

The peaks in Figure 8.3 become sharper as temperature increases, clearly indicating that the CH₂ peak for ZOK/ZCK species are above coalescence, or close to the coalescence temperature at 5°C. This also results in broader peaks at 25°C in the 800 MHz spectra compared to the 500 MHz spectra. The fact

that the peaks become sharper with increasing pH indicates that the rate of exchange is increasing as a function of pH. This also indicates that the sharp peaks attributed to parapyruvic acid (ZOK here) in previous works are in fact due to two species in fast exchange, ZOK and ZCK. We approximate that this exchange rate is on the sub-second timescale in all cases as a very conservative estimate. Unfortunately, it is difficult to quantify the exchange rate without knowing the frequency difference between the exchanging species. This is generally measured in the slow exchange limit, but is inaccessible for this system in water as it would require temperatures below the freezing point or the addition of large quantities of strong acid which become problematic both due to reactivity and for the measurement of comparable spectra. While problematic, it is also extremely interesting that relatively fast exchange between ZOK and ZCK occurs across all pH and temperature conditions for liquid water at ambient pressure.

With these forms of zymonic acid identified, infrared spectra were taken of the zymonic acid ZCE form both as the crude product and the purified powder (Figure 8.4). The crude product includes a significant amount of pyruvic acid, which may be acting as a solvent. The initial spectrum obtained, therefore, has a large pyruvic acid absorption. The pyruvic acid absorption is subtracted using the known spectrum for pyruvic acid.[81] Because the quantity of pyruvic acid was not well characterized in the crude product (and changes over time), subtraction was carried out in order to eliminate the peak at 1350 cm^{-1} that is due to pyruvic acid and in a reasonably clear region of the zymonic acid spectrum. This procedure is supported by the fact that the second spectrum, taken of purified powder in a KBr pellet, does not exhibit the peak at 1350 cm^{-1}. The IR spectra are very similar between the subtracted crude product and the purified product, further suggesting that the crude product exists in the ZCE structure. The peak at 1660 cm^{-1} is likely the C=C enol stretch, lending additonal support to this assignment.
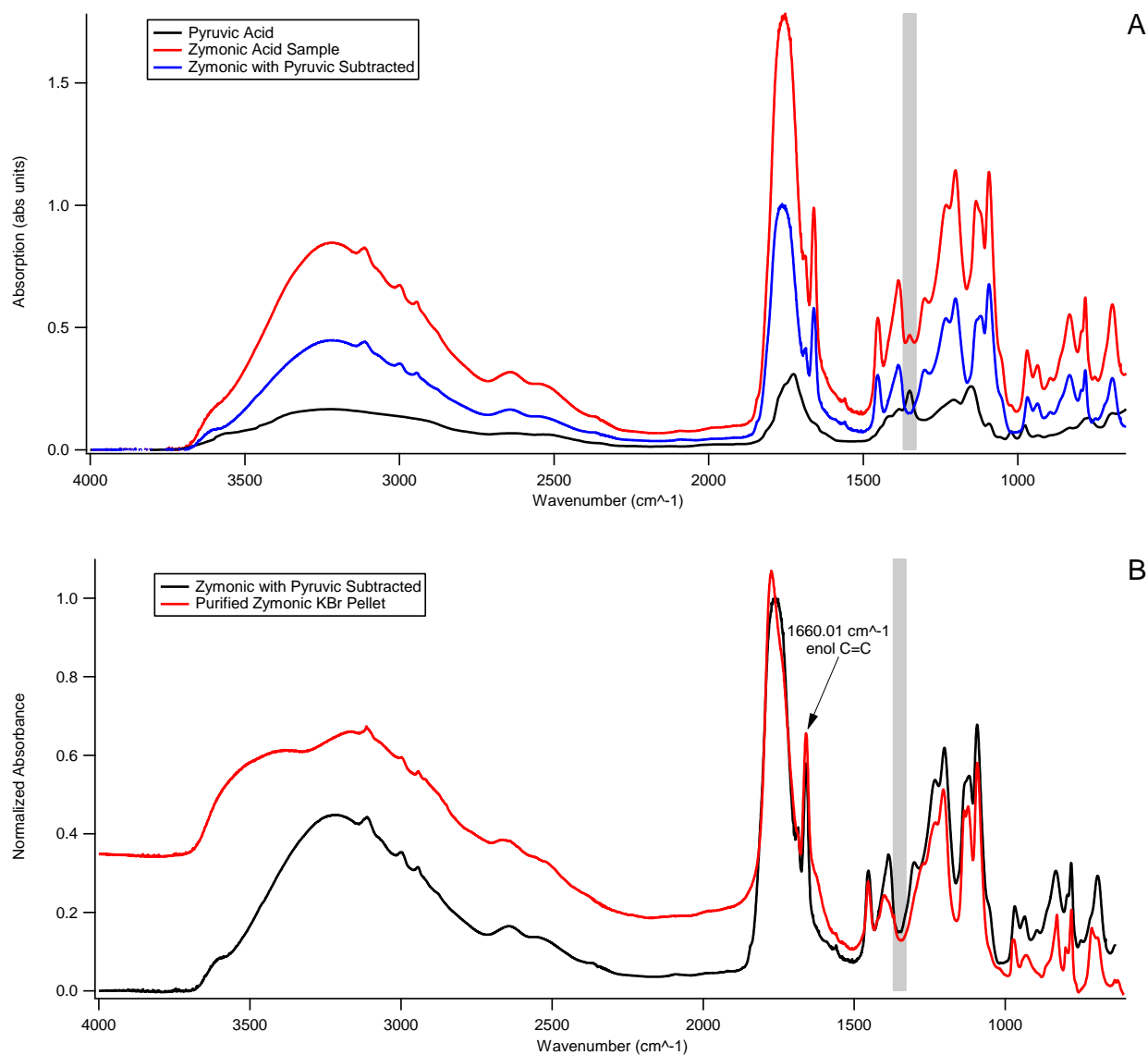
Figure 8.4: Infrared spectra of: A) crude zymonic acid spread on a NaCl window (red), pyruvic acid[82] (black), and zymonic acid with the pyruvic acid contamination subtracted. B) comparison of zymonic closed enol (ZCE) spectra taken in A) and a spectrum of purified zymonic acid in a KBr pellet. The grey region highlights the area where the pyruvic acid peak is subtracted away.

8.3.2 Aqueous Interconversions:

With the structures well identified, the interconversions between the different forms in aqueous solution were investigated. Because the solid form is almost entirely the closed enol initially, conversion to the other forms can be monitored using NMR after mixing with 90% water, 10% D_2O (Figure 8.5). Immediately following mixing, there is a decrease in the enol form, and a corresponding increase in the

closed diol form. Quasi-equilibrium appears to be reached around 25 minutes after mixing, with about 62% closed diol and 35% enol, with less than 5% total other forms. At longer times, the enol and closed diol forms decrease concurrently as the ketone and open diol forms grow in. The short time data suggest that a transformation from the enol directly to the closed diol form is occurring, which would correlate with the regioselective addition of water across the enol double bond. This is further evidenced by quickly decreasing UV absorption as a function of time immediately following mixing (Figure A4.13 in Appendix 4).
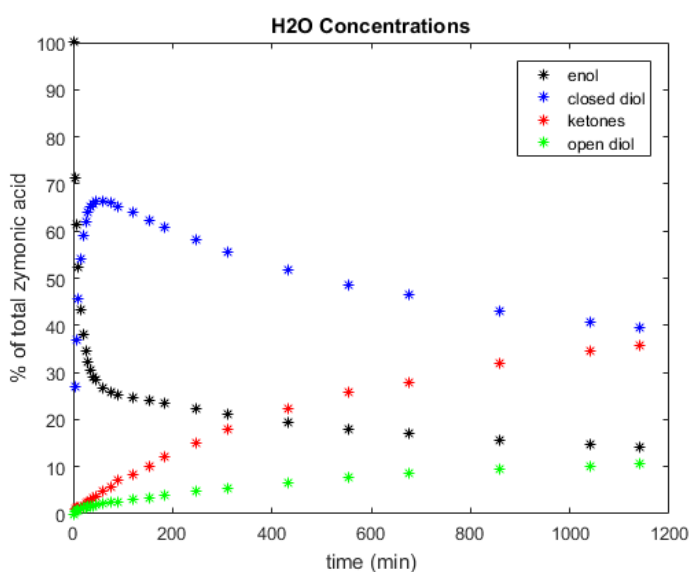
Figure 8.5: Changes in zymonic acid structures after mixing with 90% water 10% D_2O measured in situ with NMR.

Additional information can be gained by monitoring mixing with 100% D_2O, because the carbons alpha to a ketone group can exchange upon reaction from a ketone to an enol. The methyl hydrogens, however, do not exchange. This allows simultaneous observation of the change in relative abundance of zymonic species, and the deuteration of each species (Figure 8.6).
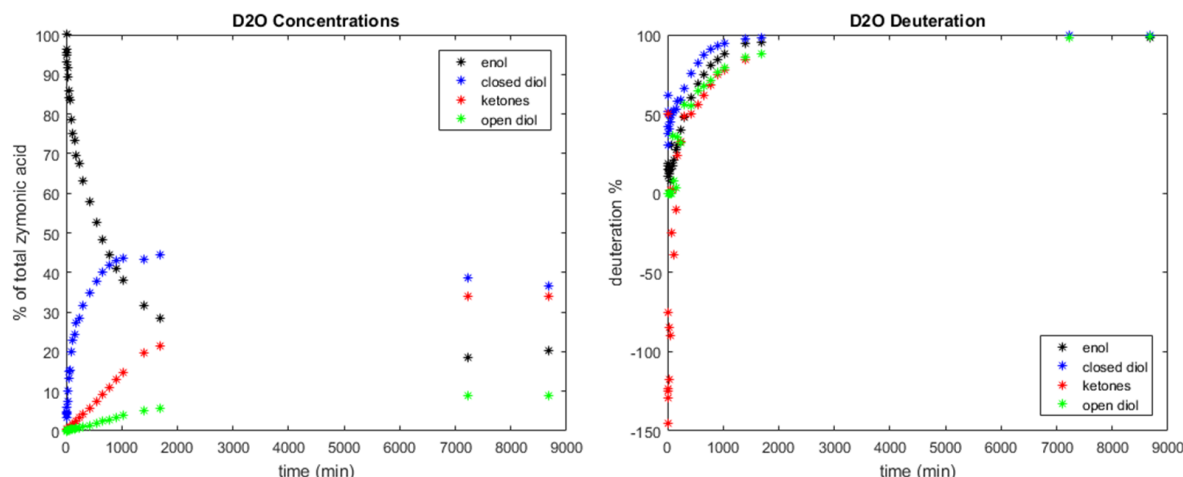
Figure 8.6: change in zymonic acid structure (left) and deuteration (right) after mixing with 100% D₂O.

The same trend is observed, with much slower rates of transformation. The slowing of rates is at least partially due to a kinetic isotope effect, as most of the transformations between zymonic species involve hydrogen or deuterium movement. The equilibrium ratios between species are shifted slightly in D$_2$O as well, which is not unexpected given the drastic changes to the kinetics. The deuteration percentages calculated for low time points are clearly erroneous for species that have very low abundance, the ketone and the open diol. Because the deuteration kinetics will depend on both forward and backwards reaction rates, fitting this data should allow for their extraction. First, a full kinetic fit was performed using a relatively simple model allowing for exchange between most species, shown in Scheme 8.1.

k_1

$+H_2O$

$-H_2O$ Zymonic Closed Enol (ZCE)
(a.k.a. Zymonic Acid)

k_2

H transfer

CH₃ ... OH ... O ... HO ... H (Zymonic Closed Enol structure)

Zymonic Closed Diol (ZCD)

k_3

$-H_2O$

$+H_2O$

Zymonic Closed Ketone (ZCK)

k_4

$-H_2O$ $+H_2O$

$-H_2O$ $+H_2O$

k_5

$-H_2O$

$+H_2O$

Zymonic Open Diol (ZOD)

Zymonic Open Ketone (ZOK)
(a.k.a. Parapyruvic Acid)
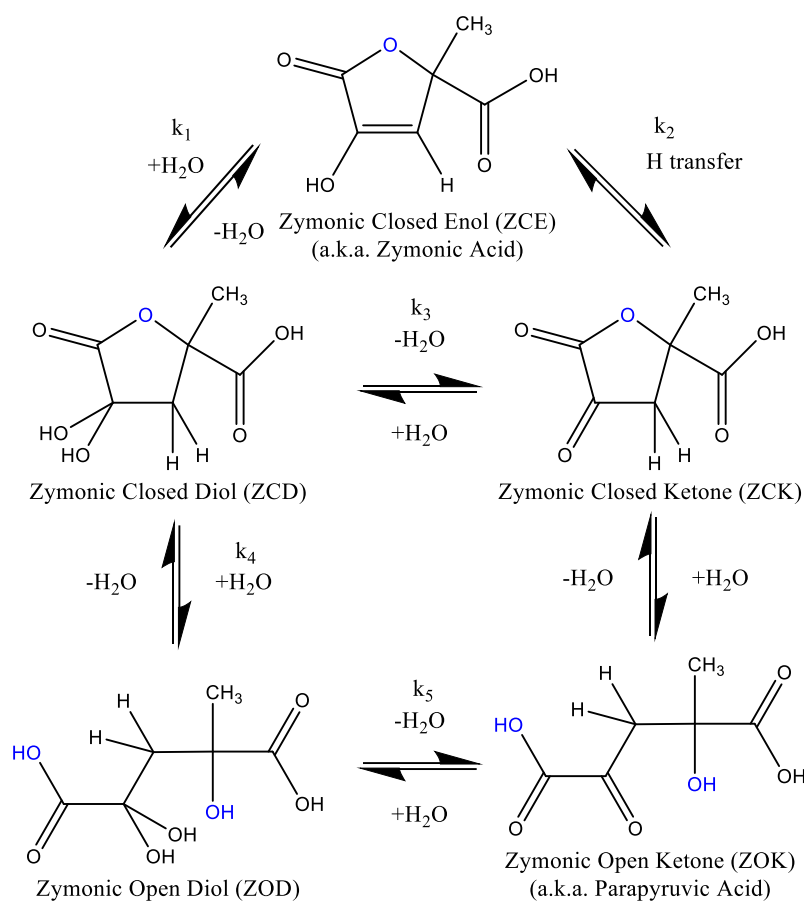
Scheme 8.1: Schematic of the simple kinetic model for the observed conversion of zymonic acid structures in aqueous solution. Rate constants for the conversion in water are shown, with the closest arrow indicating the forward direction. Oxygens/OHs involved in ring formation are highlighted in blue.

Using this kinetic scheme to fit only the water data works well, but there is not enough information to successfully fit both forward and backwards rate constants with a high degree of certainty. When considering the deuteration experiment, however, there are a few observations that necessitate modification of this simple scheme. The peaks from the ZCD methylene protons (labeled as 9 and 10 in light blue in Figure 8.2) exhibit a geminal splitting due to the chiral center on the adjacent quaternary carbon (labeled as 4 in light blue in Figure 8.2). These peaks are associated with two different isomers, one with the acid group syn to the hydrogen, and one anti (10 and 9 in light blue in Figure 8.2). While it is tempting to assign the downfield peaks as the syn conformation, this simple analysis is often misleading. When one of the methylene hydrogens is replaced with a deuterium, the geminal coupling becomes much weaker, resulting in a single resolvable peak associated with the syn or anti conformations of ZCD. For the D_2O mixing experiment, the only methylene peaks that are observed for the ZCD and ZOD appear as singlets, indicating a minimum of 50% deuteration for these species (see Figure A4.14 in Appendix 4). This is expected given the initial ZCE form requires the addition of a water molecule in order to transition into any of the other forms. The more interesting observation, however, is that the syn and anti ZCD peaks do not grow in at the same rate. Although the

peaks have not been assigned to a one conformer or the other, there is certainly a stereoselective mechanism at work. This may be due to intramolecular acid catalysis, which has previously been described for different molecular systems.[83–85]

The D_2O mixing data can be fit simultaneously with the water mixing data to the following scheme:
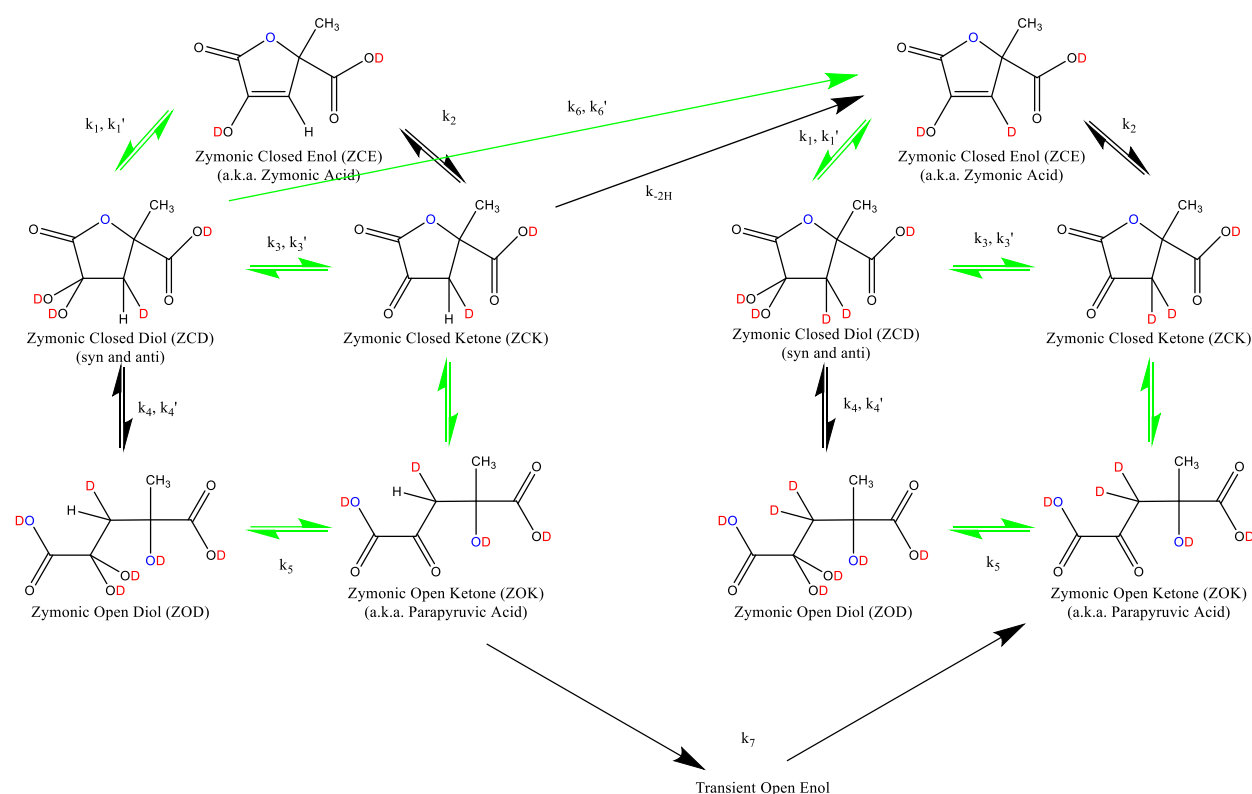
Scheme 8.2: Interconversion between zymonic acid forms and resulting deuteration for experiments mixing with 100% D_2O. Reaction rate constants are associated with the arrow closest to them being the forward direction. Identically numbered rate constants that are differentiated by priming (i.e. k_1 and k_1') are for reaction rates of different stereoisomers. Rate constant k_{-2H} is the rate constant for ZCK to ZCE observed in the water mixing experiment, and effectively couples the systems together. Steps k_6, k_6', k_7, and k_{-2H} are all expected to be effectively irreversible due to the very low abundance of H_2O in solution. Arrows in green indicate the dominant pathways.

It should be noted, that the rate constants in Scheme 8.2, labeled k_1-k_7, all involve the movement of deuterium instead of hydrogen. Because of this, these rate constants are not expected to be the same as the corresponding rate constants in water, that involve movement of hydrogens. k_{-2H} is the exception to

this, because it involves the loss of a hydrogen to the solvent, and should be identical to the k_{-2} in Scheme 8.2. The fits agree very well with the experimental data. Fits and rate constants are shown in Figure 8.7.
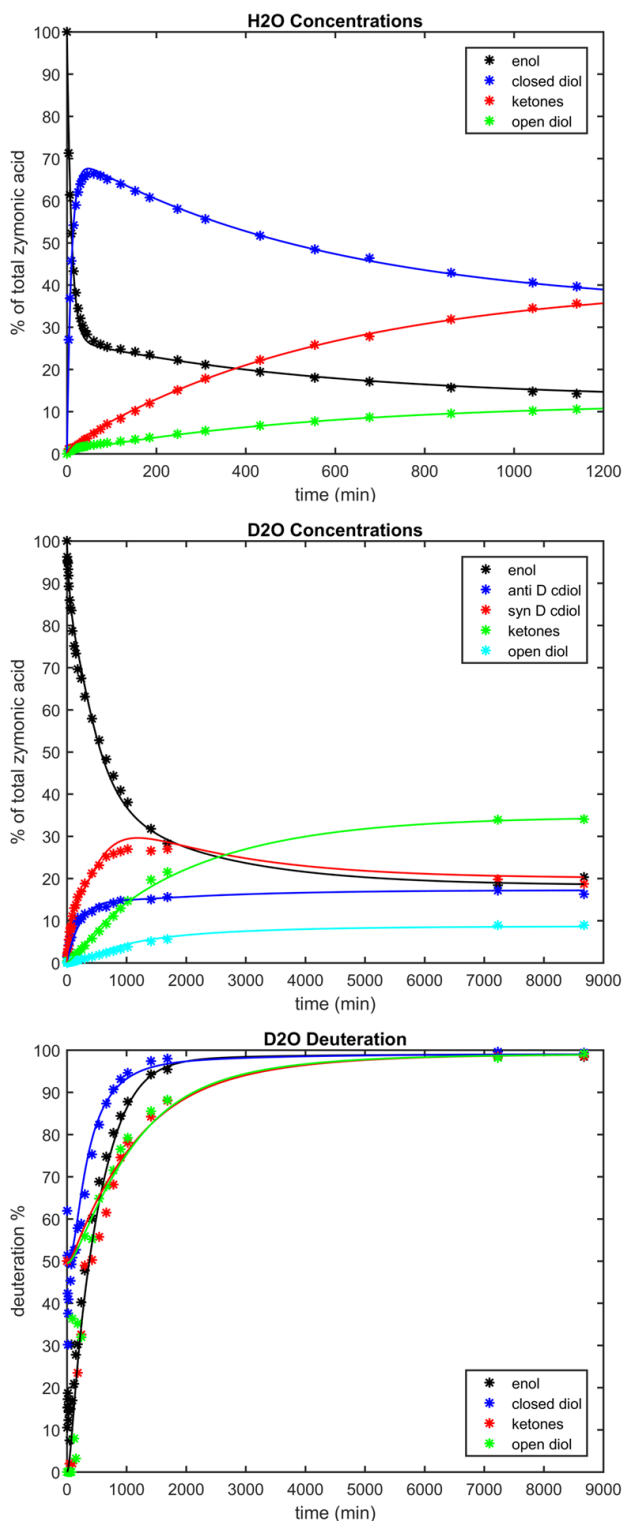
|	lower bound (min^{-1})	upper bound (min^{-1})
k_{w1}	6.98x 10^{-02}	7.19 x 10^{-02}
k_{w-1}	2.69 x 10^{-02}	2.83 x 10^{-02}
k_{w2}	5.47 x 10^{-11}	1.57 x 10^{-06}
k_{w-2}	1.68 x 10^{-09}	9.44 x 10^{-04}
k_{w3}	2.38 x 10^{-03}	3.22 x 10^{-03}
k_{w-3}	4.36 x 10^{-05}	3.41 x 10^{-04}
k_{w4}	5.02 x 10^{-09}	3.97 x 10^{-04}
k_{w-4}	8.94 x 10^{-05}	3.45 x 10^{-03}
k_{w5}	9.58 x 10^{-02}	1.53 x 10^{-01}
k_{w-5}	3.20 x 10^{-01}	4.99 x 10^{-01}
k_{d1}	6.42 x 10^{-04}	8.27 x 10^{-04}
k_{d-1}	1.13 x 10^{-10}	7.26 x 10^{-04}
k_{d1}'	2.85 x 10^{-03}	3.09 x 10^{-03}
k_{d-1}'	2.97 x 10^{-03}	3.56 x 10^{-03}
k_{d2}	5.90 x 10^{-12}	2.50 x 10^{-04}
k_{d-2}	1.20 x 10^{-13}	7.07 x 10^{-09}
k_{d3}	3.49 x 10^{-04}	1.96 x 10^{-03}
k_{d-3}	2.62 x 10^{-10}	9.30 x 10^{-04}
k_{d3}'	8.97 x 10^{-14}	6.09 x 10^{-09}
k_{d-3}'	7.62 x 10^{-13}	1.32 x 10^{-05}
k_{d4}	3.44 x 10^{-04}	7.87 x 10^{-04}
k_{d-4}	5.10 x 10^{-12}	3.37 x 10^{-03}
k_{d4}'	2.26 x 10^{-13}	1.61 x 10^{-08}
k_{d-4}'	4.17 x 10^{-04}	1.83 x 10^{-03}
k_{d5}	4.24 x 10^{-11}	1.20 x 10^{-03}
k_{d-5}	1.30 x 10^{-05}	1.28 x 10^{-03}
k_{d6}	6.64 x 10^{-04}	1.83 x 10^{-03}
k_{d6}'	1.33 x 10^{-02}	1.46 x 10^{-02}
k_{d7}	1.53 x 10^{-13}	1.03 x 10^{-08}

Figure 8.7: Left: experimental data (markers) and calculated fits (lines) for relative abundance of different zymonic acid forms over time for ~0.1 mM solutions in water and D₂O, as well as the deuteration of each species over time in D₂O. Right: Calculated forward and backwards rate constants for each reaction shown in Scheme 8.2, with k_w's and k_d's indicating reaction rates in water and D₂O, respectively. The range of each value is the 95% confidence interval calculated through bootstrap resampling. Shading in red indicates values that had not converged well after 2145 resamples, with bound changes greater than 5% with the addition of 100 resample values to the statistical pool. The cell shaded in blue is at the upper bound for the fit, and may be even larger.

While many of these reaction rates are likely to depend on the solution pH, and therefore concentration of zymonic acid, there is interesting mechanistic information present from this data under one set of conditions. Rather than the conventional ketone-enol tautomerism, the enol reacts relatively quickly with water to form the geminal diol (as ZCD). The reverse reaction from ZCD to ZCE happens readily as well. The "conventional" reaction mechanism for an enol under acidic conditions that could lead to the formation of diol is shown in Scheme 8.3. This mechanism takes advantage of intramolecular acid catalysis to activate the enol.[83–85]
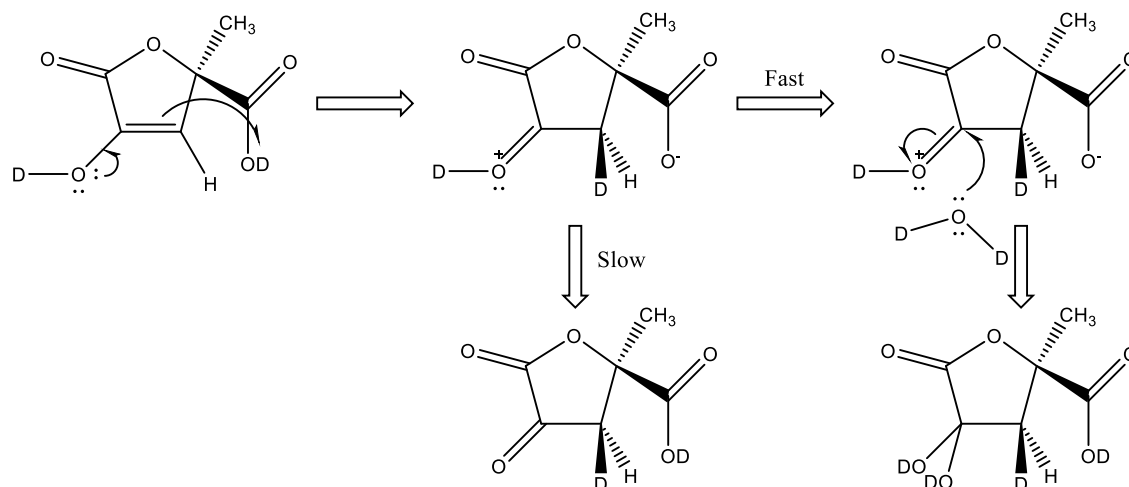
Scheme 8.3: "Conventional" reaction mechanism based on acid catalyzed enol chemistry that would result in the formation of ZCD from ZCE, and the required relative rates of reaction at the branch point in order to match experimental data.

At the branch point shown in Scheme 8.3, in order to match the experimental observation that the diol is formed preferentially over the ketone, it is required in this mechanism that the nucleophilic attack by water occurs much more quickly than the deprotonation of the ketone. This is something that is very difficult to justify, as it requires either an energetic barrier to deprotonation or for water to be an

exceptionally strong nucleophile in this situation. Neither of these requirements seem likely, so the mechanism shown in Scheme 8.3 is unlikely to occur, but why? There does not seem to be an obvious reason why the conventional chemistry should be forbidden.

There is a stark contrast between the reaction rates for the ring forming/opening reactions of the ketones and diols. The conversion between the closed and open ketone forms is by far the fastest reaction observed, with a rate constant in the sub-second range, rather than minutes or hours. The rate constant for the opening on the cyclic geminal diol (ZCD to ZOD) directly is at least 6 orders of magnitude slower. The formation of the lactone ring is expected to proceed via an esterification reaction, which involves the protonation of the carboxylic carbonyl oxygen, followed by nucleophilic attack on the carbonyl carbon by a hydroxyl group. In contrast to this conventional reaction mechanism, however, this reaction proceeds faster for the zymonic ketones under increasingly basic conditions, as evidenced by the movement further from coalescence and into the fast exchange regime for the CH_2 resonances in Figure 8.3 discussed earlier. This is extremely unusual, as it constitutes a base catalyzed esterification reaction, which is commonly accepted not to occur. While it is unclear what mechanisms explain the interesting chemistry that is occurring, they certainly are not the standard, expected mechanisms. There is, however, compelling evidence that these transitions between ZCE and ZCD as well as ZCK and ZOK are occurring, and the later rate increases with increasing pH.

8.4 Conclusions

In this work, zymonic acid was isolated, purified, and identified as a single component system as a solid or dissolved in DMSO. In aqueous solution, however, it is a complex, interconverting, multi-component system. One and two dimensional NMR measurements were carried out and supplemented by pH, field, and temperature dependent NMR studies. These measurements were used to assign all the major components observed in aqueous solution, as well as gather kinetic data for their interconversion in water and D_2O. The fastest interconversion appears to be between the cyclic and acyclic ketone forms of zymonic acid (ZCK and ZOK) on the sub-second timescale. This rate of interconversion increases with

increasing pH, which has caused the mixture of these two substances to be misidentified as a single substance in previous literature.[49–79] The slower kinetic interconversions in water indicate the direct transition from an enol to a geminal diol (ZCE to ZCD), without a ketone intermediate. A kinetic fit was performed that reinforces the validity of this observation. Two reaction paths are observed that contrast established mechanistic literature. To our knowledge this is the first time that either a base catalyzed esterification or a direct enol to geminal diol hydration has been observed. We have not proposed mechanisms for this unconventional chemistry.

The existence of these compounds may be important to current or past biology as contaminants, or possibly metabolites. There is evidence that in modern biology there are enzymes that catalyze the conversion of zymonic acid (likely an open chain form) to pyruvic acid.[64,65,67,70] This may arise due to structural similarities to native substrates, although there have been reports of inhibition of the tricarboxylic acid (TCA) cycle,[60,61] as well as anti-malarial effects of zymonic acid.[59] Other detections of zymonic acid, usually in the ZOK form or the transaminated amino acid derivative, have been made in various biological systems.[57,58,71,72] It is unclear exactly what role zymonic acid plays in these systems, but the coexistence between different structural forms in aqueous solutions that we clarify will be vital to understanding its behavior.

In atmospheric chemistry, these pyruvic dimers may also play a role in aerosol processing or formation, especially given their observed extreme hygroscopicity. Aerosol particles having an important impact on human health as well as climate, where they impact radiative forcing and act as condensation nuclei. Secondary organic aerosols (SOA) are formed in the atmosphere through gas or condensed phase reactions that often produce low volatility oligomers.[9,17,86–93] Aqueous phases provide effective and interesting reaction environments for organic oligomer formation, and contribute to the SOA budget.[93–100] The aqueous phase reactions that are most studied are oxidation by ozone[10] or hydroxyl radical,[101–105] as well as photochemical reactions.[35,98,106–110] The ability of pyruvic acid to dimerize may be a particularly relevant dark reaction for SOA formation, due to the properties of the dimers examined here.

Supporting Information Available in Appendix 4: 2D NMR spectra, solid state NMR spectra, UV-visible absorbance spectra, raw NMR FIDs, and tabulated kinetic and FTIR data.

Bibliography:

(1)   Voet, D.; Voet, J. G. *Biochemistry*, 4th Edition Binder Ready Version edition.; Wiley: Hoboken, NJ, 2010.

(2)   Griffith, E. C.; Shoemaker, R. K.; Vaida, V. Sunlight-Initiated Chemistry of Aqueous Pyruvic Acid: Building Complexity in the Origin of Life. *Orig. Life Evol. Biospheres* **2013**, *43* (4–5), 341–352.

(3)   Cody, G. D.; Boctor, N. Z.; Filley, T. R.; Hazen, R. M.; Scott, J. H.; Sharma, A.; Yoder, H. S. Primordial Carbonylated Iron-Sulfur Compounds and the Synthesis of Pyruvate. *Science* **2000**, *289* (5483), 1337–1340.

(4)   Kawamura, K. Identification of C2-C10 Omega-Oxocarboxylic Acids, Pyruvic Acid, and C2-C3 Alpha-Dicarbonyls in Wet Precipitation and Aerosol Samples by Capillary GC and GC/MS. *Anal. Chem.* **1993**, *65* (23), 3505–3511.

(5)   Sempére, R.; Kawamura, K. Comparative Distributions of Dicarboxylic Acids and Related Polar Compounds in Snow, Rain and Aerosols from Urban Atmosphere. *Atmos. Environ.* **1994**, *28* (3), 449–459.

(6)   Kawamura, K.; Kasukabe, H.; Barrie, L. A. Source and Reaction Pathways of Dicarboxylic Acids, Ketoacids and Dicarbonyls in Arctic Aerosols: One Year of Observations. *Atmos. Environ.* **1996**, *30* (10–11), 1709–1722.

(7)   Fu, P.; Zhuang, G.; Sun, Y.; Wang, Q.; Chen, J.; Ren, L.; Yang, F.; Wang, Z.; Pan, X.; Li, X.; et al. Molecular Markers of Biomass Burning, Fungal Spores and Biogenic SOA in the Taklimakan Desert Aerosols. *Atmos. Environ.* **2016**, *130*, 64–73.

(8)   Brooks Avery Jr., G.; Willey, J. D.; Kieber, R. J. Diurnal Variations in Major Rainwater Components at a Coastal Site in North Carolina. *Atmos. Environ.* **2001**, *35* (23), 3927–3933.

(9)   Altieri, K. E.; Carlton, A. G.; Lim, H.-J.; Turpin, B. J.; Seitzinger, S. P. Evidence for Oligomer Formation in Clouds: Reactions of Isoprene Oxidation Products. *Environ. Sci. Technol.* **2006**, *40* (16), 4956–4960.

(10)   Nguyen, T. B.; Bateman, A. P.; Bones, D. L.; Nizkorodov, S. A.; Laskin, J.; Laskin, A. High-Resolution Mass Spectrometry Analysis of Secondary Organic Aerosol Generated by Ozonolysis of Isoprene. *Atmos. Environ.* **2010**, *44* (8), 1032–1042.

(11)   Veres, P. R.; Roberts, J. M.; Cochran, A. K.; Gilman, J. B.; Kuster, W. C.; Holloway, J. S.; Graus, M.; Flynn, J.; Lefer, B.; Warneke, C.; et al. Evidence of Rapid Production of Organic Acids in an Urban Air Mass. *Geophys. Res. Lett.* **2011**, *38* (17), L17807.

(12)   Warneck, P. Multi-Phase Chemistry of C2 and C3 Organic Compounds in the Marine Atmosphere. *J. Atmospheric Chem.* **2005**, *51* (2), 119–159.

(13)   Guenther, A. Biological and Chemical Diversity of Biogenic Volatile Organic Emissions into the Atmosphere. *ISRN Atmospheric Sci.* **2013**, *2013*, 1–27.

(14)   Cooper, G.; Reed, C.; Nguyen, D.; Carter, M.; Wang, Y. Detection and Formation Scenario of Citric Acid, Pyruvic Acid, and Other Possible Metabolism Precursors in Carbonaceous Meteorites. *Proc. Natl. Acad. Sci.* **2011**, *108* (34), 14015–14020.

(15)   Charlson, R. J.; Seinfeld, J. H.; Nenes, A.; Kulmala, M.; Laaksonen, A.; Facchini, M. C. Reshaping the Theory of Cloud Formation. *Science* **2001**, *292* (5524), 2025–2026.

(16)   Ellison, G. B.; Tuck, A. F.; Vaida, V. Atmospheric Processing of Organic Aerosols. *J. Geophys. Res. Atmospheres* **1999**, *104* (D9), 11633–11641.

(17)   Donaldson, D. J.; Vaida, V. The Influence of Organic Films at the Air−Aqueous Boundary on Atmospheric Processes. *Chem. Rev.* **2006**, *106* (4), 1445–1461.

(18)   Vesley, G. F.; Leermakers, P. A. The Photochemistry of α-Keto Acids and α-Keto Esters. III. Photolysis of Pyruvic Acid in the Vapor Phase. *J. Phys. Chem.* **1964**, *68* (8), 2364–2366.

(19)   Closs, G. L.; Miller, R. J. Photoreduction and Photodecarboxylation of Pyruvic Acid. Applications of CIDNP to Mechanistic Photochemistry. *J. Am. Chem. Soc.* **1978**, *100* (11), 3483–3494.

(20)   Colberg, M. R.; Watkins, R. J.; Krogh, O. D. Vibrationally Excited Carbon Dioxide Produced by Infrared Multiphoton Pyrolysis. *J. Phys. Chem.* **1984**, *88* (13), 2817–2821.

(21)   Yamamoto, S.; Back, R. A. The Photolysis and Thermal Decomposition of Pyruvic Acid in the Gas Phase. *Can. J. Chem.* **1985**, *63* (2), 549–554.

(22)   Taylor, R. The Mechanism of Thermal Eliminations Part XXIII: [1] The Thermal Decomposition of Pyruvic Acid. *Int. J. Chem. Kinet.* **1987**, *19* (8), 709–713.

(23)   Saito, K.; Sasaki, G.; Okada, K.; Tanaka, S. Unimolecular Decomposition of Pyruvic Acid: An Experimental and Theoretical Study. *J. Phys. Chem.* **1994**, *98* (14), 3756–3761.

(24)   Stefan, M. I.; Bolton, J. R. Reinvestigation of the Acetone Degradation Mechanism in Dilute Aqueous Solution by the UV/H2O2 Process. *Environ. Sci. Technol.* **1999**, *33* (6), 870–873.

(25)   Mellouki, A.; Mu, Y. On the Atmospheric Degradation of Pyruvic Acid in the Gas Phase. *J. Photochem. Photobiol. Chem.* **2003**, *157* (2–3), 295–300.

(26)   Carlton, A. G.; Turpin, B. J.; Lim, H.-J.; Altieri, K. E.; Seitzinger, S. Link between Isoprene and Secondary Organic Aerosol (SOA): Pyruvic Acid Oxidation Yields Low Volatility Organic Acids in Clouds. *Geophys. Res. Lett.* **2006**, *33* (6), L06822.

(27) Takahashi, K.; Plath, K. L.; Skodje, R. T.; Vaida, V. Dynamics of Vibrational Overtone Excited Pyruvic Acid in the Gas Phase: Line Broadening through Hydrogen-Atom Chattering. *J. Phys. Chem. A* **2008**, *112* (32), 7321–7331.

(28) Plath, K. L.; Takahashi, K.; Skodje, R. T.; Vaida, V. Fundamental and Overtone Vibrational Spectra of Gas-Phase Pyruvic Acid. *J. Phys. Chem. A* **2009**, *113* (26), 7294–7303.

(29) Rincón, A. G.; Guzmán, M. I.; Hoffmann, M. R.; Colussi, A. J. Optical Absorptivity versus Molecular Composition of Model Organic Aerosol Matter. *J. Phys. Chem. A* **2009**, *113* (39), 10512–10520.

(30) Larsen, M. C.; Vaida, V. Near Infrared Photochemistry of Pyruvic Acid in Aqueous Solution. *J. Phys. Chem. A* **2012**, *116* (24), 5840–5846.

(31) Reed Harris, A. E.; Ervens, B.; Shoemaker, R. K.; Kroll, J. A.; Rapf, R. J.; Griffith, E. C.; Monod, A.; Vaida, V. Photochemical Kinetics of Pyruvic Acid in Aqueous Solution. *J. Phys. Chem. A* **2014**, *118* (37), 8505–8516.

(32) da Silva, G. Decomposition of Pyruvic Acid on the Ground State Potential Energy Surface. *J. Phys. Chem. A* **2015**.

(33) Asmus, C.; Mozziconacci, O.; Schöneich, C. Low-Temperature NMR Characterization of Reaction of Sodium Pyruvate with Hydrogen Peroxide. *J. Phys. Chem. A* **2015**, *119* (6), 966–977.

(34) Lopalco, A.; Dalwadi, G.; Niu, S.; Schowen, R. L.; Douglas, J.; Stella, V. J. Mechanism of Decarboxylation of Pyruvic Acid in the Presence of Hydrogen Peroxide. *J. Pharm. Sci.* **2016**, *105* (2), 705–713.

(35) Griffith, E. C.; Carpenter, B. K.; Shoemaker, R. K.; Vaida, V. Photochemistry of Aqueous Pyruvic Acid. *Proc. Natl. Acad. Sci.* **2013**, 201303206.

(36) Berzelius, J. J. Ueber Die Destillationsproducte Der Traubensäure. *Ann. Phys.* **1835**, *112* (9), 1–29.

(37) Berzelius, J. J. On Dry Distilled Racemic Acid. *Acta Chem. Scand.* **1960**, *14*, 1677–1680.

(38) Völckel, C. Ueber Die Producte Der Destillation Der Weinsäure. *Justus Liebigs Ann. Chem.* **1854**, *89* (1), 57–76.

(39) Finck, C. Ueber Die Zersetzung Der Brenztraubensäure Durch Barythydrat. *Justus Liebigs Ann. Chem.* **1862**, *122* (2), 182–191.

(40) Böttinger, C. Beitrag Zur Kenntniss Der Brenztraubensäure. *Justus Liebigs Ann. Chem.* **1877**, *188* (3), 293–342.

(41) Serda, R. *Beiträge Zur Kenntniss Der Pyrotritarsäure.*; Strassburg, 1889.

(42) Wolff, L. I. Ueber Die Synthese Der Uvitinsäure Aus Brenztraubensäure. *Justus Liebigs Ann. Chem.* **1899**, *305* (2), 125–153.

(43) Wolff, L. II. Ueber Die Parabrenztraubensäure. *Justus Liebigs Ann. Chem.* **1899**, *305* (2), 154–165.

(44)   Wolff, L. Ueber Ein Neues Condensationsproduct Der Brenztraubensäure. *Justus Liebigs Ann. Chem.* **1901**, *317* (1), 1–22.

(45)   de Jong, A. W. K. Les Transformations Des Sels de L'acide Pyruvique. *Recl. Trav. Chim. Pays-Bas Belg.* **1901**, *20* (10), 365–387.

(46)   Wille, F. Die Synthese Der 1,4-Diketoadipinsäure Und Ihre Biologische Bedeutung. *Justus Liebigs Ann. Chem.* **1939**, *538* (1), 237–260.

(47)   Waldmann, E.; Prey, V.; Jelinek, F. Zur Kenntnis der Brenztraubensäure. *Monatshefte Für Chem. Verwandte Teile Anderer Wiss.* **1954**, *85* (4), 872–881.

(48)   Prey, V.; Waldmann, E.; Berbalk, H. Zur Kenntnis der Brenztraubensäure. *Monatshefte Für Chem. Verwandte Teile Anderer Wiss.* **1955**, *86* (3), 408–413.

(49)   Leussing, D.; Stanfield, C. K. A Nuclear Magnetic Resonance Study of Aqueous Pyruvate-Glycinate-Zinc(II) and Related Systems. *J. Am. Chem. Soc.* **1964**, *86* (14), 2805–2810.

(50)   Tallman, D. E.; Leussing, D. L. Pyruvate Dimerization Catalyzed by nickel(II) and zinc(II). I. Equilibrium with nickel(II) and zinc(II). *J. Am. Chem. Soc.* **1969**, *91* (23), 6253–6256.

(51)   Tallman, D. E.; Leussing, D. L. Pyruvate Dimerization Catalyzed by nickel(II) and zinc(II). II. Kinetics. *J. Am. Chem. Soc.* **1969**, *91* (23), 6256–6262.

(52)   Lin, H.-L.; Yu, Y.-O.; Jwo, J.-J. Kinetic Study of the Ce(III)-, Mn(II)-, or Ferroin-Catalyzed Belousov-Zhabotinsky Reaction with Pyruvic Acid. *Int. J. Chem. Kinet.* **2000**, *32* (7), 408–418.

(53)   Stodola, F. H.; Shotwell, O. L.; Lockwood, L. B. Zymonic Acid, a New Metabolic Product of Some Yeasts Grown in Aerated Culture. I. Structure Studies2. *J. Am. Chem. Soc.* **1952**, *74* (21), 5415–5418.

(54)   Bloomer, J. L.; Gross, M. A. Biosynthesis of Zymonic Acid in Trichosporon Capitatum. *J. Chem. Soc. Chem. Commun.* **1970**, No. 2, 73–74.

(55)   Bloomer, J. L.; Gross, M. A.; Kappler, F. E.; Pandey, G. N. Identity of "zymonic Acid" with a Pyruvate Derivative. *J. Chem. Soc. Chem. Commun.* **1970**, No. 16, 1030a–1030a.

(56)   Krebs, H. A.; Johnson, W. A. Acetopyruvic Acid (Alphagamma-Diketovaleric Acid) as an Intermediate Metabolite in Animal Tissues. *Biochem. J.* **1937**, *31* (5), 772–779.

(57)   Virtanen, A. I.; Berg, A.-M.; Risberg, E.; Lamm, O. New Aminodicarboxylic Acids and Corresponding Alpha-Keto Acids in Phyllitis Scolopendrium. *Acta Chem. Scand.* **1955**, *9*, 553–554.

(58)   Grobbelaar, N.; Pollard, J. K.; Steward, F. C. New Soluble Nitrogen Compounds (Amino- and Imino-Acids and Amides) in Plants. *Nature* **1955**, *175* (4460), 703–708.

(59)   Trager, W.; Singer, I. An Antimalarial Effect in Vitro of Parapyruvic Acid. *Exp. Biol. Med.* **1955**, *90* (2), 539–542.

(60)   Montgomery, C. M.; Webb, J. L. Detection of a New Inhibitor of the Tricarboxylic Acid Cycle. *Science* **1954**, *120* (3125), 843–844.

(61) Montgomery, C. M.; Webb, J. L. Metabolic Studies on Heart Mitochondria II. the Inhibitory Action of Parapyruvate on the Tricarboxylic Acid Cycle. *J. Biol. Chem.* **1956**, *221* (1), 359–368.

(62) Montgomery, C. M.; Webb, J. L. Metabolic Studies on Heart Mitochondria I. the Operation of the Normal Tricarboxylic Acid Cycle in the Oxidation of Pyruvate. *J. Biol. Chem.* **1956**, *221* (1), 347–358.

(63) Stradner, A.; Sedgwick, H.; Cardinaux, F.; Poon, W. C. K.; Egelhaaf, S. U.; Schurtenberger, P. Equilibrium Cluster Formation in Concentrated Protein Solutions and Colloids. *Nature* **2004**, *432* (7016), 492–495.

(64) Marcus, A.; Shannon, L. M. γ-Methyl-γ-Hydroxy-α-Ketoglutaric Aldolase II. STUDIES WITH PYRUVATE-C14. *J. Biol. Chem.* **1962**, *237* (11), 3348–3353.

(65) Shannon, L. M.; Marcus, A. γ-Methyl-γ-Hydroxy-α-Ketoglutaric Aldolase I. PURIFICATION AND PROPERTIES. *J. Biol. Chem.* **1962**, *237* (11), 3342–3347.

(66) Kobes, R. D.; E.Dekker, E. Variant Properties of Bovine Liver 2-Keto-4-Hydroxyglutarate Aldolase; Its β-Decarboxylase Activity, Lack of Substrate Stereospecificity, and Structural Requirements for Binding Substrate Analogs. *Biochim. Biophys. Acta BBA - Enzymol.* **1971**, *250* (1), 238–250.

(67) Tack, B. F.; Chapman, P. J.; Dagley, S. Purification and Properties of 4-Hydroxy-4-Methyl-2-Oxoglutarate Aldolase. *J. Biol. Chem.* **1972**, *247* (20), 6444–6449.

(68) Herbert, J. D.; Coulson, R. A.; Hernandez, T.; Ehrensvärd, G. A Carbonic Anhydrase Requirement for the Synthesis of Glutamine from Pyruvate in the Chameleon. *Biochem. Biophys. Res. Commun.* **1975**, *65* (3), 1054–1060.

(69) Maruyama, K. Enzymes Responsible for Degradation of 4-Oxalmesaconic Acid in *Pseudomonas Ochraceae*. *J. Biochem. (Tokyo)* **1983**, *93* (2), 567–574.

(70) Ohyama, T.; Hoshino, T.; Ikarashi, T. Isolation and Structure of a New Organic Acid Accumulated in Tulip Plant (Tulipa Gesneriand). *Soil Sci. Plant Nutr.* **1988**, *34* (1), 75–86.

(71) Winter, H. C.; Dekker, E. E. Specificity of Aspartate Aminotransferases from Leguminous Plants for 4-Substituted Glutamic Acids. *Plant Physiol.* **1989**, *89* (4), 1122–1128.

(72) Maruyama, K. Purification and Properties of 4-Hydroxy-4-Methyl-2-Oxoglutarate Aldolase from *Pseudomonas Ochraceae* Grown on Phthalate. *J. Biochem. (Tokyo)* **1990**, *108* (2), 327–333.

(73) Hélaine, V.; Rossi, J.; Gefflaut, T.; Alaux, S.; Bolte, J. Synthesis of 4,4-Disubstituted L-Glutamic Acids by Enzymatic Transamination. *Adv. Synth. Catal.* **2001**, *343* (6–7), 692–697.

(74) Xian, M.; Alaux, S.; Sagot, E.; Gefflaut, T. Chemoenzymatic Synthesis of Glutamic Acid Analogues: Substrate Specificity and Synthetic Applications of Branched Chain Aminotransferase from Escherichia Coli. *J. Org. Chem.* **2007**, *72* (20), 7560–7566.

(75) Novikov, Y.; Copley, S. D. Reactivity Landscape of Pyruvate under Simulated Hydrothermal Vent Conditions. *Proc. Natl. Acad. Sci.* **2013**, *110* (33), 13283–13288.

(76)   Goldfine, H. The Formation of γ-Hydroxy-γ-Methylglutamic Acid from a Common Impurity in Pyruvic Acid. *Biochim. Biophys. Acta* **1960**, *40*, 557–559.

(77)   Buldain, G.; Santos, C. D. L.; Frydman, B. Carbon-13 Nuclear Magnetic Resonance Spectra of the Hydrate, Keto and Enol Forms of Oxalacetic Acid. *Magn. Reson. Chem.* **1985**, *23* (6), 478–481.

(78)   Margolis, S. A.; Coxon, B. Identification and Quantitation of the Impurities in Sodium Pyruvate. *Anal. Chem.* **1986**, *58* (12), 2504–2510.

(79)   Fell, L. M.; Francis, J. T.; Holmes, J. L.; Terlouw, J. K. The Intriguing Behaviour of (Ionized) Oxalacetic Acid Investigated by Tandem Mass Spectrometry. *Int. J. Mass Spectrom. Ion Process.* **1997**, *165*, 179–194.

(80)   Pocker, Y.; Meany, J. E.; Nist, B. J.; Zadorojny, C. Reversible Hydration of Pyruvic Acid. I. Equilibrium Studies. *J. Phys. Chem.* **1969**, *73* (9), 2879–2882.

(81)   NIST Mass Spec Data Center, S.E. Stein, director. Infrared Spectra. In *NIST Chemistry WebBook, NIST Standard Reference Database Number 69*; P.J. Linstrom, W.G. Mallard, Eds.; National Institute of Standards and Technology: Gaithersburg MD, 20899.

(82)   *The Coblentz Society Desk Book of Infrared Spectra, Second Edition*; C.D. Carver, Ed.; The Coblentz Society: Kirkwood, MO, 1982.

(83)   Kirby, A. J.; Meyer, G. Intramolecular Catalysis by the Ionised Carboxy-Group of the Hydrolysis of Enol Esters, and of the General Acid Catalysed Ketonisation of the Enols Produced. *J. Chem. Soc. Perkin Trans. 2* **1972**, No. 10, 1446.

(84)   Kirby, A. J.; O'Carroll, F. Highly Efficient Intramolecular General Acid Catalysis of Enol Ether Hydrolysis, with Rapid Proton Transfer to Carbon. *J. Chem. Soc. Perkin Trans. 2* **1994**, No. 4, 649.

(85)   Kirby, A. J.; Williams, N. H. Efficient Intramolecular General Acid Catalysis of Enol Ether Hydrolysis. Hydrogen-Bonding Stabilisation of the Transition State for Proton Transfer to Carbon. *J. Chem. Soc. Perkin Trans. 2* **1994**, No. 4, 643.

(86)   Finlayson-Pitts, B. J. Reactions at Surfaces in the Atmosphere: Integration of Experiments and Theory as Necessary (but Not Necessarily Sufficient) for Predicting the Physical Chemistry of Aerosols. *Phys. Chem. Chem. Phys.* **2009**, *11*, 7760–7779.

(87)   Martins-Costa, M. T. C.; Anglada, J. M.; Francisco, J. S.; Ruiz-Lopez, M. F. Reactivity of Volatile Organic Compounds at the Surface of a Water Droplet. *J. Am. Chem. Soc.* **2012**, *134*, 11821–11827.

(88)   Rudich, Y.; Donahue, N. M.; Mentel, T. F. Aging of Organic Aerosol: Bridging the Gap between Laboratory and Field Studies. *Annu. Rev. Phys. Chem.* **2007**, *58*, 321–352.

(89)   Carlton, A. G.; Wiedinmyer, C.; Kroll, J. H. A Review of Secondary Organic Aerosol (SOA) Formation from Isoprene. *Atmospheric Chem. Phys.* **2009**, *9*, 4987–5005.

(90)   Thornton, D. C. O.; Brooks, S. D.; Chen, J. Protein and Carbohydrate Exopolymer Particles in the Sea Surface Microlayer (SML). *Aquat. Microbiol.* **2016**, 135.

(91)   McNeill, V. F. Aqueous Organic Chemistry in the Atmosphere: Sources and Chemical Processing of Organic Aerosols. *Environ. Sci. Technol.* **2015**, *49* (3), 1237–1244.

(92)   Ebben, C. J.; Strick, B. F.; Upshur, M. A.; Chase, H. M.; Achtyl, J. L.; Thomson, R. J.; Geiger, F. M. Towards the Identification of Molecular Constituents Associated with the Surfaces of Isoprene-Derived Secondary Organic Aerosol (SOA) Particles. *Atmos Chem Phys* **2014**, *14* (5), 2303–2314.

(93)   Lienhard, D. M.; Bones, D. L.; Zuend, A.; Krieger, U. K.; Reid, J. P.; Peter, T. Measurements of Thermodynamic and Optical Properties of Selected Aqueous Organic and Organic–Inorganic Mixtures of Atmospheric Relevance. *J. Phys. Chem. A* **2012**, *116* (40), 9954–9968.

(94)   Herrmann, H.; Tilgner, A.; Barzaghi, P.; Majdik, Z.; Gligorovski, S.; Poulain, L.; Monod, A. Towards a More Detailed Description of Tropospheric Aqueous Phase Organic Chemistry: CAPRAM 3.0. *Atmos. Environ.* **2005**, *39*, 4351–4363.

(95)   Epstein, S. A.; Nizkorodov, S. A. A Comparison of the Chemical Sinks of Atmospheric Organics in the Gas and Aqueous Phase. *Atmospheric Chem. Phys.* **2012**, *12*, 8205–8222.

(96)   Bregonzio-Rozier, L.; Giorio, C.; Siekmann, F.; Pangui, E.; Morales, S. B.; Temime-Roussel, B.; Gratien, A.; Michoud, V.; Cazaunau, M.; DeWitt, H. L.; et al. Secondary Organic Aerosol Formation from Isoprene Photooxidation during Cloud Condensation-Evaporation Cycles. *Atmospheric Chem. Phys.* **2016**, *16*, 1747–1760.

(97)   Galloway, M. M.; Powelson, M. H.; Sedehi, N.; Wood, S. E.; Millage, K. D.; Kononenko, J. A.; Rynaski, A. D.; De Haan, D. O. Secondary Organic Aerosol Formation during Evaporation of Droplets Containing Atmospheric Aldehydes, Amines, and Ammonium Sulfate. *Environ. Sci. Technol.* **2014**, *48* (24), 14417–14425.

(98)   Sun, Y. L.; Zhang, Q.; Anastasio, C.; Sun, J. Insights into Secondary Organic Aerosol Formed via Aqueous-Phase Reactions of Phenolic Compounds Based on High Resolution Mass Spectrometry. *Atmos Chem Phys* **2010**, *10* (10), 4809–4822.

(99)   Bones, D. L.; Reid, J. P.; Lienhard, D. M.; Krieger, U. K. Comparing the Mechanism of Water Condensation and Evaporation in Glassy Aerosol. *Proc. Natl. Acad. Sci.* **2012**, *109* (29), 11613–11618.

(100)   Avzianova, E.; Brooks, S. D. Raman Spectroscopy of Glyoxal Oligomers in Aqueous Solutions. *Spectrochim. Acta. A. Mol. Biomol. Spectrosc.* **2013**, *101*, 40–48.

(101)   Ervens, B.; Sorooshian, A.; Lim, Y. B.; Turpin, B. J. Key Parameters Controlling OH-Initiated Formation of Secondary Organic Aerosol in the Aqueous Phase (aqSOA). *J. Geophys. Res.-Atmospheres* **2014**, *119*, 3997–4016.

(102)   Monod, A.; Poulain, L.; Grubert, S.; Voisin, D.; Wortham, H. Kinetics of OH-Initiated Oxidation of Oxygenated Organic Compounds in the Aqueous Phase: New Rate Constants, Structure-Activity Relationships and Atmospheric Implications. *Atmos. Environ.* **2005**, *39*, 7667–7688.

(103)   Lim, Y. B.; Tan, Y.; Turpin, B. J. Chemical Insights, Explicit Chemistry, and Yields of Secondary Organic Aerosol from OH Radical Oxidation of Methylglyoxal and Glyoxal in the Aqueous Phase. *Atmospheric Chem. Phys.* **2013**, *13*, 8651–8667.

(104) Claeys, M.; Graham, B.; Vas, G.; Wang, W.; Vermeylen, R.; Pashynska, V.; Cafmeyer, J.; Guyon, P.; Andreae, M. O.; Artaxo, P.; et al. Formation of Secondary Organic Aerosols through Photooxidation of Isoprene. *Science* **2004**, *303*, 1173–1176.

(105) Kroll, J. H.; Lim, C. Y.; Kessler, S. H.; Wilson, K. R. Heterogeneous Oxidation of Atmospheric Organic Aerosol: Kinetics of Changes to the Amount and Oxidation State of Particle-Phase Organic Carbon. *J. Phys. Chem. A* **2015**, *119*, 10767–10783.

(106) Fu, H.; Ciuraru, R.; Dupart, Y.; Passananti, M.; Tinel, L.; Rossignol, S.; Perrier, S.; Donaldson, D. J.; Chen, J.; George, C. Photosensitized Production of Atmospherically Reactive Organic Compounds at the Air/Aqueous Interface. *J. Am. Chem. Soc.* **2015**, *137* (26), 8348–8351.

(107) Guzman, M. I.; Colussi, A. J.; Hoffmann, M. R. Photoinduced Oligomerization of Aqueous Pyruvic Acid. *J. Phys. Chem. A* **2006**, *110*, 3619–3626.

(108) George, C.; Ammann, M.; D'Anna, B.; Donaldson, D. J.; Nizkorodov, S. A. Heterogeneous Photochemistry in the Atmosphere. *Chem. Rev.* **2015**, *115* (10), 4218–4258.

(109) Rossignol, S.; Aregahegn, K. Z.; Tinel, L.; Fine, L.; Nozière, B.; George, C. Glyoxal Induced Atmospheric Photosensitized Chemistry Leading to Organic Aerosol Growth. *Environ. Sci. Technol.* **2014**, *48* (6), 3218–3227.

(110) Bateman, A. P.; Nizkorodov, S. A.; Laskin, J.; Laskin, A. Photolytic Processing of Secondary Organic Aerosols Dissolved in Cloud Droplets. *Phys. Chem. Chem. Phys.* **2011**, *13* (26), 12199–12212.

(111) Ogg, R. J.; Kingsley, P. B.; Taylor, J. S. WET, a T1- and B1-Insensitive Water-Suppression Method for in Vivo Localized 1H NMR Spectroscopy. *J. Magn. Reson. B* **1994**, *104* (1), 1–10.

(112) Boyer, R. D.; Johnson, R.; Krishnamurthy, K. Compensation of Refocusing Inefficiency with Synchronized Inversion Sweep (CRISIS) in Multiplicity-Edited HSQC. *J. Magn. Reson.* **2003**, *165* (2), 253–259.

Chapter 9: Mechanistic Description of Photochemical Oligomer Formation from Aqueous Pyruvic Acid

9.1 Introduction

Atmospheric aerosols are known to contribute to pollution-related smog and haze, affecting visibility and human health;[1, 2] in addition, they have considerable influence over the global radiative budget.[3-10] The impact of atmospheric aerosols on radiative forcing is currently the largest source of uncertainty in climate models, with significant contributions to the accumulated error occurring from the effort to quantify secondary organic aerosol (SOA).[11] SOA, particles generated in the atmosphere through the oxidation of volatile organic compounds (VOCs), are the major contributor to aerosol mass in remote areas.[8, 12, 13] Recent work suggests that oligomers formed from aqueous phase photochemistry of small organics may contribute significantly to the formation and development of SOA.[8, 9, 14-22] Therefore, the generation of such molecular complexity via multiphase chemistry is critical in the understanding of the formation of SOA.

The chemistry governing the formation of SOA from small organics is inherently complex, involving interwoven networks of reactions between many species. As we show, even a single, simple three-carbon molecule can yield surprisingly rich chemistry. Here we examine the aqueous phase photochemistry of a model species, pyruvic acid, under acidic, anaerobic conditions, suggesting a new identification and mechanistic pathway for observed oligomeric species. By developing mechanistically the potential reactive pathways for aqueous pyruvic acid, we may add to the understanding of its possible photochemical fates in the natural environment.

Pyruvic acid, a key oxidation product of isoprene in the environment,[23-25] is found in both the gas and aqueous phases in the atmosphere.[23, 26-34] The simplest of the α-keto acids, pyruvic acid has also been used

as a proxy for atmospheric α-dicarbonyls.[24, 25, 28, 35] Pyruvic acid absorbs light in the near-UV from the solar photon flux reaching the surface of the Earth and is oxidized relatively slowly by H_2O_2 and the hydroxyl radical (OH).[36-40] Consequently, the main atmospheric sink for pyruvic acid is direct photolysis; in the aqueous phase, this photochemistry has been linked to oligomer formation and the production of SOA.[21, 37, 41-45]

While a seemingly simple, three-carbon molecule, pyruvic acid's reactivity is extremely diverse and dependent on reaction conditions. Its chemistry spans a wide variety of processes and environmental conditions, including gas and aqueous photochemistry,[37, 42-60] multiphase photochemistry,[61] oxidation by H_2O_2 and hydroxyl radicals,[25, 36, 38-40] thermal decomposition,[62-64] and multiphoton pyrolysis.[65] Pyruvic acid is also known to spontaneously oligomerize in aqueous solution or as a pure liquid, even in the dark, forming a variety dimer species that include zymonic acid and parapyruvic acid.[66]

The photochemical pathways available to pyruvic acid are strongly phase dependent. In the gas phase, absorption of a UV photon (λ_{max} ~350 nm) promotes ground state pyruvic acid to the first excited singlet state (S_1, $^1(n, \pi^*)$), whereupon it decomposes, forming CO_2 and acetaldehyde, with additional minor products.[36, 48, 54, 55, 57-59, 67, 68] However, the species produced by this gas phase photochemistry can be affected by changing the buffer gas, total pressure, and composition.[58] Different photochemical pathways become accessible in the aqueous phase than in gas phase[41, 43-45, 56, 60] because interactions with water affect pyruvic acid's electronic structure, changing its photophysical and photochemical mechanisms. The λ_{max} of the S_1, $^1(n, \pi^*)$, state shifts to the blue (λ_{max} ~320 nm) such that, following excitation, intersystem crossing and internal conversion to the T_1, $^3(n, \pi^*)$ state occurs, subsequently generating organic radicals. These radicals then react further, often recombining to generate oligomeric species.

Recent work on the aqueous photochemistry of pyruvic acid has exposed its extreme sensitivity to the environment: the rate of decomposition and resulting products are dependent on both the concentration of pyruvic acid and on the atmospheric composition.[37, 61] This sensitivity to reaction conditions likely explains some of the discrepancies in the literature about some minor photoproducts;[37, 41-45, 69, 70] however, there is broad agreement that the major aqueous photochemical pathways generate more complex

oligomeric species,[37, 42, 43] including covalently bonded dimers and trimers[71] of pyruvic acid. In this work, we structurally characterize oligomeric species and propose a new mechanistic pathway by which these oligomers are photochemically formed through reactions with reactive intermediate species.

9.2 Experimental

Pyruvic acid (98%, Sigma-Aldrich) was distilled twice under reduced pressure (< 1 Torr) while heating gently (< 55 °C) and diluted with 18.2 MΩ water (3 ppb TOC) to make solutions of 10, 1, and 0.5 mM concentration. For each 100 mL volume solution, 10 mL of the solution was saved as a pre-irradiation control, and the remaining 90 mL of solution were illuminated for 5 hours in a temperature-stabilized water bath at 4 °C with a 450 W Xe arc lamp (Newport). The lower concentration solutions (1 mM and 0.5 mM) were also irradiated with the water bath held at 20 °C. There was no difference in observed products based on water bath temperature. Unless otherwise specified, all solutions were purged with N_2 to displace dissolved O_2, beginning one hour prior to the start of irradiation and continuing for the duration of the experiment. Oxygen-depleted conditions are known to favor formation of the oligomeric species under study here,[37] allowing for easier analysis and identification of products at relatively low reaction concentrations. The irradiated solutions were allowed to come to room temperature before any further analysis was conducted.

The solutions were used without adjustment from their natural pH, meaning all photochemical experiments were conducted under acidic conditions. There is a slight variance in the pH of the solutions as a function of the concentration of pyruvic acid, increasing with decreasing concentration. The pH of the 10 mM pyruvic acid solutions was ~2.4 and rises to approximately 3.5 for the 0.5 mM pre-irradiation solutions.

The Xe arc lamp used was not filtered, meaning that its output extends into the UV to about 220 nm as shown in Figure A5.1 in Appendix 5. Because of the extended light in the UV, under our experimental conditions, it is likely some excitation to the S_2, $^1(\pi, \pi^*)$, state in addition to the S_1 state also occurs. However, as is common with excitation to higher excited states,[72] [73] it is likely that the system in the S_2 rapidly undergoes internal conversion to the lower S_1 state before following the same photochemical

pathway of intersystem crossing and internal conversion to the reactive T_1 state. The photochemical products observed here using with the unfiltered Xe arc lamp are in good agreement with the previous results generated with a filtered Xe arc lamp with wavelengths $\lambda < 300$ nm removed from the spectrum.[37] In the latter case, the radiation provided can excite the S_1 but not the S_2 state, suggesting the same reactive photochemical pathway is preserved. The rate of photochemistry is, however, increased when the light is not filtered, as would be expected when more photons are present. These observations are consistent with those in the literature, which have shown, for example, that the photochemistry of nonanoic acid in aqueous solution using a filtered Xe arc lamp is observed to slow but not result in significantly different products than when not filtered.[74]

9.2.1 Electronic Structure Calculations: Calculations with the composite CBS-QB3 model[75] and using the Gaussian 09 suite of programs[76] were conducted on the relative barriers to H-atom abstraction from the methyl and carboxyl groups of pyruvic acid S_0 by pyruvic acid T_1, $^3(n,\pi^*)$. The calculations suggested that the activation enthalpy for the former is only 1.47 kcal/mol greater than that for the latter. Details are provided in the Appendix 5.

9.2.2 UV-Vis Spectroscopy: Pre- and post-irradiation solutions of the oxoacids were scanned using a Varian (Agilent) Cary 5000 spectrometer with a 0.1 s average time, 0.5 nm data interval, and a 0.5 nm spectral bandwidth.

9.2.3 NMR Analysis: NMR experiments were obtained at 23 °C using a Varian INOVA-500 NMR spectrometer operating at 499.60 MHz for ^{1}H detection. To perform experiments in aqueous solution, an optimized WET solvent suppression pulse sequence was used to eliminate >99% of the H_2O signal.[77]

9.2.4 Mass Spectrometry Analysis: High resolution mass spectrometry was performed on a Waters Synapt G2 HDMS mass spectrometer using electrospray ionization operated in negative mode. Instrument parameters remained constant, and were as follows: analyzer, resolution mode; capillary voltage, 1.5 kV; source temperature, 80 °C; sampling cone, 30 V; extraction cone, 5 V; source gas flow, 0.00 mL/min; desolvation temperature, 150 °C; cone gas flow, 0.0 L/h; desolvation gas flow, 500.0 L/h.

Instrument parameters were chosen to minimize the potential for in-source fragmentation and reactions due to ionization. Under the ionization conditions used here, we observe both [M-H]$^-$ and singly charged adduct ions for the analytes of interest. The adducts identified are formed from two or more deprotonated organic species coordinated to a metal ion, yielding a non-covalent adduct ion with a net charge of -1. In the pyruvic acid solutions, especially before irradiation, we observe adduct ions consisting of multiple deprotonated pyruvic acid molecules coordinated with a positive counterion, usually Na$^+$ or Ca^{2+} at quite high intensities, as shown in Table A5.1 and Figure A5.2 in Appendix 5. To minimize the presence of adduct ions, all photochemical experiments were conducted in 18.2 MΩ water without the addition of salt and any such metal ions are assumed to be only present in trace quantities.

The ESI$^-$ mass spectrometry analysis conducted here is not designed to be absolutely quantitative. As expected, we observe [M-H]$^-$ ions for a number of species with observed intensities varying considerably due to variations in ionization efficiency for these analyte mixtures. We applied a conservative intensity threshold of 10^4 counts for analyte identification to avoid incorrect ion assignments to noise peaks; the noise threshold is about 1000 counts. For comparative purposes, categories of signal intensity are defined as follows: "strong" ions display intensities greater than 10^6 counts, "medium" ions display intensities greater than 10^5 counts, and "weak" ions display intensities greater that 10^4 counts for the monoisotopic ion in all cases. It is important to note that these intensity categories do not necessarily correlate directly to absolute analyte concentrations and are used for relative comparisons only.

9.3 Results and Discussion

The aqueous chemistry of pyruvic acid is generally defined by the formation of oligomeric species, under both light and dark conditions. The aqueous phase photochemistry of pyruvic acid has been studied previously in the literature[41, 43-45, 56, 60, 61] and is known to generate a surprisingly complex mixture of observed photoproducts, many of which have been assigned following the literature mechanism.[37, 43] Here, studying the aqueous phase photochemistry of pyruvic acid with high-resolution negative mode electrospray ionization mass spectrometry (ESI$^-$ MS), we are able to suggest a new structural

identification for oligomeric photoproducts. The new mechanistic pathway we suggest for these products is informed by a recent investigation of the dark oligomerization processes of pyruvic acid,[66] as well as recent results examining the multiphase photochemistry of pyruvic acid in an environmental simulation chamber.[61]

9.3.1 Pre-Irradiation Solutions and Dark Processes

The generation of covalently-bonded dimers of pyruvic acid in the dark has been known since the 19th century;[78-80] nevertheless, these dark processes have been largely ignored by the modern literature. Recently, however, it has been demonstrated that pyruvic acid, either pure or in aqueous solution, will spontaneously dimerize, likely through an aldol addition reaction.[66] The dimerization products include parapyruvic acid and zymonic acid, the lactone enol form of parapyruvic acid (see Scheme 9.2 for structures). In aqueous solution, there is an equilibrium between pyruvic acid, parapyruvic acid, zymonic acid, and their tautomers and hydrates, which depends on the concentration and pH of the solution.[66]

When studying the photochemical products generated by pyruvic acid, it is necessary to consider whether the oligomerization processes that take place in the dark may be contributing to the identified products. However, such dark oligomerization processes do not occur on a timescale that competes with the observed photochemistry. As observed in the MS spectra, the rate of formation of these dimerization products in pure, distilled pyruvic acid stored 4 °C occurs over the course of weeks. As shown by NMR analysis in Figure A5.3 in Appendix 5, there is very little contamination present in the 10 mM aqueous solutions before irradiation, with conservative estimates placing an upper limit on zymonic acid of < 0.1%. As mentioned above, the equilibrium between pyruvic acid and the various forms of parapyruvic and zymonic acid shifts as a function of concentration. In the dilute aqueous solutions under which photochemistry was conducted here, the equilibrium favors the reformation of monomeric pyruvic acid from dimerization products that may have been formed in the pure pyruvic acid. The kinetics of this shift are slow, but they provide reassurance that further dark dimerization products are not formed fast enough to influence either the light-initiated chemistry or analysis in these experiments.

Although the overall concentration of the pyruvic acid dimers formed by dark reactions is low in our

pre-irradiation samples, the presence of zymonic acid species is detectable by our ESI⁻ MS analysis. There are six species derived from zymonic acid, including parapyruvic acid, that exist in aqueous solution.[66] Because these are closely related tautomers and enols, the chemical formulas of these species overlap. For example, using ESI⁻ MS we detect an ion with an average experimental *m/z* for [M-H]⁻ of 175.0239, which suggests the molecular formula $C_6H_8O_6$. This likely represents both parapyruvic acid and the closed ring form of the zymonic acid diol. Of the equilibrium species of zymonic acid in aqueous solution, these structures are the favored species.[66] In our analysis of the MS data (see Table 9.1 and Table A5.1 in Appendix 5), we applied a conservative intensity threshold of 10^4 counts for analyte identifications to avoid incorrect ion assignments to noise peaks (see Experimental Section for more detail). The ions that correspond to parapyruvic acid and the closed zymonic diol are consistently observed above this threshold for the 10 mM pyruvic acid solutions before irradiation. Ions corresponding to the other zymonic acid species were observed occasionally at the threshold of intensity, but were not consistently observed above the intensity cutoff we implemented. At the lower pyruvic acid solution concentrations (e.g. 1 mM and 0.5 mM), ions from zymonic acid are not generally observed in the mass spectra above the threshold. It is not surprising that the presence of zymonic acid is not observable at low concentrations of pyruvic acid; an already very low concentration of the contaminant is spread over multiple equilibrium structures, making it less likely that it would rise above our conservative threshold for detection.

Parapyruvic acid and other zymonic acid derivatives are not generally observed in the post-irradiation solutions with intensities that rise above our threshold for detection. The lack of signal from parapyruvic acid in the ESI-MS of post-irradiation solutions suggests that most of it has been consumed during the photochemical experiments. This is not surprising because parapyruvic acid is itself an α-keto acid and therefore photoactive. Similarly, if any parapyruvic acid was generated photochemically during the course of irradiation, it may not be detected in the post-irradiation samples. This raises the possibility that these species might also be synthesized photochemically and act as reactive oligomeric intermediate species whose further chemistry contributes to the observed photoproducts in the light-initiated chemistry

of pyruvic acid, as is discussed in detail below. The recent observation of zymonic acid as a photoproduct generated from the irradiation of multiphase pyruvic acid under atmospherically-relevant conditions in environmental simulation chamber studies[61] lends credence to the photochemical formation and subsequent photochemistry of parapyruvic acid that may take place in aqueous solution.

Table 9.1. Select Compiled Pyruvic Acid Photochemistry ESI⁻ MS Data[a]

Assigned Formula [M-H]⁻	Assigned Structure	Average Experimental m/z[b]	Theoretical m/z	Mass Diff. (ppm)	Pre-Irradiation	Post-Irradiation
Pre-Irradiation Species						
$C_3H_3O_3$	Pyruvic Acid	87.0091 ± 0.0005	87.0082	10.8	Strong	Strong
$C_3H_5O_4$	2,2-Dihydroxy-propanoic Acid (Pyruvic Diol)	105.0190 ± 0.0007	105.0188	2.3	Weak	Below Threshold
$C_6H_7O_6$	Parapyruvic Acid[c]	175.0243 ± 0.0004	175.0243	0.21	Weak	Below Threshold
Key Photochemical Products						
$C_4H_7O_2$	Acetoin	87.0454 ± 0.0007	87.0446	8.7	Below Threshold	Medium
$C_3H_5O_3$	Lactic Acid	89.0239 ± 0.0003	89.0239	0.45	Below Threshold	Weak
$C_5H_7O_4$	Acetolactic Acid	131.0354 ± 0.001	131.0345	6.6	Below Threshold	Medium
$C_7H_{11}O_5$	DMOHA[d]	175.0617 ± 0.0006	175.0607	5.5	Below Threshold	Strong
$C_6H_9O_6$	Dimethyltartaric Acid	177.0409 ± 0.0005	177.0400	5.0	Below Threshold	Strong
$C_8H_{11}O_7$	CDMOHA[e]	219.0512 ± 0.0009	219.0505	3.2	Below Threshold	Medium

[a]Chemical formulas are assigned as the ionized [M-H]⁻ species, structures are assigned as the neutral species. [b]The experimental m/z is the observed average across experiments, and the uncertainty given is the 95% confidence interval. [c]The peak assigned to parapyruvic acid likely also has contributions from the closed ring form of zymonic acid diol as well.[d]DMOHA = 2,4-dihydroxy-2-methyl-5-oxohexanoic acid [e]CDMOHA = 4-carboxy-2,4-dihydroxy-2-methyl-5-oxohexanoic acid

9.3.2 Photochemical Oligomerization Processes

As mentioned above, photochemistry in aqueous solution begins upon absorption of a photon by the α-keto acid in the near UV. The absorption maximum of this transition occurs for pyruvic acid at a

wavelength of ~320 nm (Figure A5.1 in Appendix 5). In aqueous solution, the ketone group of pyruvic acid can be hydrated to form a geminal diol, 2,2,dihydroxypropanoic acid, (2,2-DHPA).[81-84] Unlike the ketone form, the geminal diol conformer does not absorb light within the solar spectrum. Many α-dicarbonyl species undergo almost complete hydration to the diol form in aqueous solution, where catalysis by water, acid, or base lowers the relatively high reaction barriers.[85-87] Pyruvic acid retains significant amounts of the ketonic functionality. The extent of hydration is both pH- and temperature-dependent,[82, 88] but, at 298 K, aqueous pyruvic acid generally exists as ~40% in the keto and ~60% in the diol form.[37, 42, 83, 84] However, this ratio is concentration dependent as well. For the 10 mM solutions of pyruvic acid investigated here, the ratio is closer to 50% keto and 50% diol (Figure A5.3 in Appendix 5). This ratio shifts during the photochemical experiments to slightly favor the keto form, which is likely due to the coupled effects of the depletion of pyruvic acid and subsequent slight decrease in acidity of the solution. All photochemical experiments were conducted without adjusting the solutions from their natural pH. The pH of the solution is increased slightly as the concentration of pyruvic acid is lowered. For the 0.5 mM pre-irradiation solutions, the pH is approximately 3.5, compared to ~2.4 for 10 mM solutions. At this lower concentration and higher pH, the amount of pyruvic acid in the keto conformer increases to about 75% (Figure A5.4 in Appendix 5).

While all photochemical experiments were conducted under acidic conditions, the pH of the solutions are near the effective pK_a for pyruvic acid solutions of 2.49,[89] implying the protonation state of pyruvic acid is important to consider. This literature value is an effective pK_a because the keto and diol conformers have different, individual pK_a values, of 2.18 and 3.6, respectively.[82] Under our reaction conditions, then, more than 50% of the keto form of pyruvic acid is in its anionic form, pyruvate for all concentrations, which reduces the number of photoactive protonated species in solution.

Regardless of the exact ratio of keto and diol conformer and their respective protonation states, the presence of significant amounts of protonated keto conformer in aqueous solution means that photochemistry is still a major reactive pathway under such conditions. However, interactions with the solvent shift the accessible electronic states for aqueous pyruvic acid, which favors photochemical

mechanisms in the aqueous phase that follow different pathways than in the gas phase, as shown in Scheme 9.1.

In the aqueous phase, chemistry occurs from the T_1, $^3(n, \pi^*)$, state (Reaction 1 in Scheme 9.1). As has been shown previously in the literature, the excited T_1 state can abstract a hydrogen from the carboxyl group of another pyruvic acid molecule and decarboxylates to form two radical species (Reaction 2 in Scheme 9.1), one with hydroxyl acid functionality, $CH_3\dot{C}(OH)CO_2H$, denoted as HA• and one with geminal diol functionality, $CH_3\dot{C}(OH)_2$, denoted as GD•.[37, 43] The hydrogen abstraction from another pyruvic acid molecule can either occur from the keto form of the molecule or from its geminal diol form, 2,2-DHPA, though abstraction from the diol is favored energetically.[43] Because 10 mM pyruvic acid under our reaction conditions is approximately 50% in the diol form, it is likely that abstraction from the diol is the major pathway. It has also been suggested that proton-coupled electron transfer can also occur,[42, 60] which would generate the same reactive radicals from the T_1 excited state of pyruvic acid.
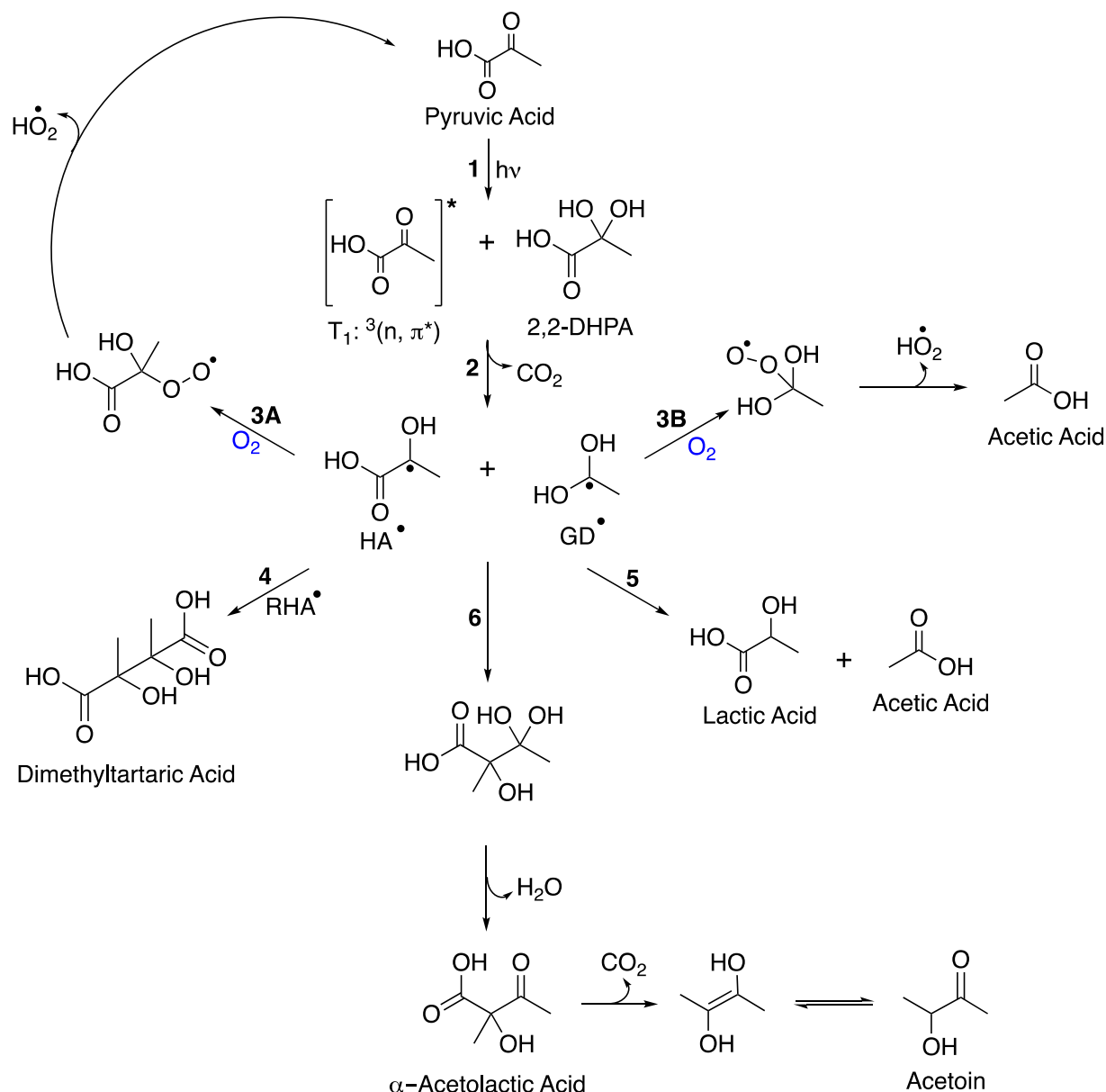
Scheme 9.1. *Aqueous photochemical pathways for pyruvic acid.*[37, 43]

The HA• and GD• radicals that are formed following hydrogen abstraction from the carboxyl group of either pyruvic acid or 2,2-DHPA, then go on to react further following a number of pathways, which are summarized in Scheme 9.1[37, 43] with MS results given in Table 9.1. The branching ratio of the pathways, and therefore the yields of the generated species, is influenced by the environmental conditions under which the aqueous photochemistry is conducted. Under our reaction conditions, at 10 mM concentration under a nitrogen atmosphere, approximately 90% of the pyruvic acid is consumed during five hours of irradiation (Figure A5.3 in Appendix 5).

As is consistent with the previous literature, the main products observed from the aqueous phase photochemistry of pyruvic acid are oligomeric species, such as dimethyltartaric acid (DMTA), following Reaction 4 of Scheme 9.1. DMTA is formed by the recombination of two HA• radicals.[42, 43] For this recombination to happen, the HA• radicals must be able to escape from the initial solvent cage surrounding the generated HA• and GD• radicals in order to encounter a second HA• radical. Because these radicals must both undergo cage escape and encounter one another in dilute solution to form dimethyltartaric acid, HA• radicals must be relatively long-lived species. This observation is consistent with the stabilization of HA• by the captodative effect, enabled by the presence of both electron-donating and electron-withdrawing groups.[90]

DMTA is not the only observed oligomeric product species. Previous ^{1}H NMR studies have observed a number of oligomeric photoproducts that remain unidentified.[37, 43] Additionally, MS analyses consistently observe an oligomeric photoproduct ion that that is detected with similar intensity to DMTA and likely represents the chemical formula $C_7H_{12}O_5$.[37, 42] The formation of this product cannot be explained following the mechanisms described in Scheme 9.1. It has been suggested previously that this species may be one of two possible structures, 2-(hydroxyethanyloxy)-2-carboxy-3oxobutane or 2-(3-oxobutan-2-yloxy)-2-hydroxypropanoic acid.[42, 70] Here, we propose that this product may be produced by further photochemistry of reactive oligomeric intermediates generated during photolysis with pyruvic acid.

The previously known mechanism for pyruvic acid aqueous photochemistry generates HA• and GD• following hydrogen abstraction from the carboxyl group of pyruvic acid or 2,2-DHPA.[43] Using electronic structure calculations, we examined the possibility of hydrogen abstraction from the methyl group rather than the carboxyl group of a neutral pyruvic acid molecule, which, at the CBS-QB3 level, show that methyl hydrogen abstraction has a transition state that is 1.47 kcal/mol higher in enthalpy than that for abstraction from the carboxyl hydrogen. This is a small difference in energy that is close to the likely error in the method, suggesting that hydrogen abstraction from the methyl group is likely competitive with hydrogen abstraction from the carboxyl group of pyruvic acid. Abstraction from the methyl group

may be further favored because, for all pyruvic acid concentrations under our reaction conditions, more than 50% of the keto form of pyruvic acid (pK_a = 2.18)[82] is in its anionic form, pyruvate. Photochemistry under high pH conditions (pH = 6.1), where most of the pyruvic acid is deprotonated, has been observed to be considerably slower than under more acidic conditions,[44] suggesting that hydrogen abstraction from the carboxyl group is indeed favored. However, for deprotonated pyruvate molecules only the methyl group is available for abstraction. While perhaps not the major location of abstraction, it is likely some abstraction from the methyl group of pyruvic acid occurs during the photochemical experiments (Reaction 1 of Scheme 9.2), yielding two radicals, HA• and one with oxoacid functionality, $\dot{C}H_2C(O)CO_2H$, denoted as OA•. It is worth noting that it is unlikely that proton-coupled electron transfer could generate the OA• radical.

The recombination of HA• and OA• (Reaction 2 of Scheme 9.2) generates parapyruvic acid, suggesting that it is a dimer of pyruvic acid that can be generated photochemically, in addition to dark oligomerization processes.[66] Each radical pair generated by hydrogen abstraction at the methyl group (Reaction 1 of Scheme 9.2) will have an overall net triplet characteristic, meaning that intra-cage geminate recombination to form parapyruvic acid will not occur. Instead, either intersystem crossing back to the singlet state or cage escape must take place before the radicals can react further, either of which is possible. The relative probability of these two possibilities, however, is difficult to predict.
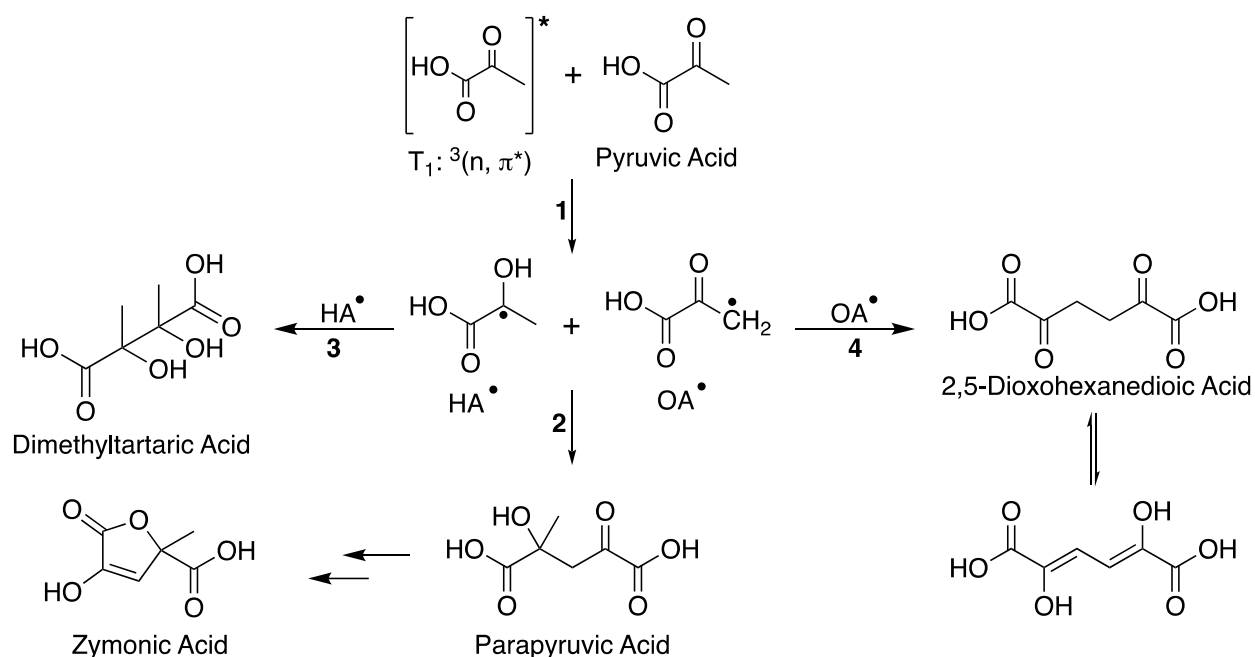
Scheme 9.2. *Photochemical generation of parapyruvic acid via hydrogen abstraction from the methyl group of pyruvic acid.*

If intersystem crossing back to the singlet state was the dominant pathway, one would expect only to see the recombination product between HA• and OA•, generating parapyruvic acid. In the case of the radicals undergoing cage escape, the recombination product of each radical with itself would also be observed, in addition to the cross product between radicals. As is discussed above, the recombination of two HA• radicals generates DMTA, which is shown in Reaction 4 of Scheme 9.1 and in Reaction 3 of Scheme 9.2. The recombination of two OA• radicals would generate the dioxoacid compound shown by Reaction 4 of Scheme 9.2. This dioxoacid, 2,5 dioxohexanedioic acid (DOHDA, $C_6H_6O_6$), would likely exist in equilibrium with its enol form, though we do not observe such a peak in the MS data. However, the absence of detection does not mean that this species is not formed. OA•, unlike HA•, is not stabilized by the captodative effect, so its lifetime would be expected to be somewhat shorter. It is also less likely to encounter another OA• radical after undergoing cage escape because, while the energetics are not prohibitive, hydrogen abstraction from the methyl group of pyruvic acid is less likely than from the carboxyl group and thus OA• concentrations are expected to be small. Additionally, the keto form of DOHDA will be in equilibrium with the enol form of the acid in aqueous solution. Both the keto and enol forms of DOHDA are likely to be themselves photoactive: the keto form has two α-keto acid groups and

the enol form has a conjugated double bond system. This means that any DOHDA that might be generated during illumination may go on to react, further depleting its concentration in the post-irradiation solution and limiting our ability to detect it. It is possible that such reactions can account for some of the minor photoproducts that we currently have not identified.

Because we do not observe DOHDA in the MS data, we are unable to conclusively state whether intersystem crossing back to the singlet state or cage escape is the favored mechanistic pathway. We tentatively favor cage escape as the more likely path by which HA• and OA• may react with each other to form parapyruvic acid. Our reasons are twofold. First, because it provides another mechanistic pathway by which DMTA, a product observed in high concentrations, can be formed, and, secondly, because cage escape has been demonstrated to occur for both HA• and GD•, as shown in Scheme 9.1.

Regardless of the path by which recombination of HA• and OA• occurs, it seems likely that parapyruvic acid is formed photochemically during the course of the illumination of pyruvic acid. This reactivity will reduce its concentration in solution, and is likely the main reason it is not detected in the post-irradiation MS data with an intensity above the threshold we implement here. Parapyruvic acid, itself an α-keto acid, has the same reactive functionality as pyruvic acid, and is, therefore, capable of undergoing the same photochemistry as pyruvic acid, as shown in Scheme 9.3. Therefore, any trace parapyruvic acid in the initial pre-irradiation solution, as well as any generated photochemically, can also be excited by near-UV photons. An excited parapyruvic acid molecule may then abstract a hydrogen from either a pyruvic acid or 2,2-DHPA molecule, which would be followed by decarboxylation as in the pathway originally shown in Reaction 2 of Scheme 9.1.

This generates both the familiar GD• and a parapyruvic radical, $CO_2HC(CH_3)OH\dot{C}(OH)CO_2H$ denoted as PPA•, shown in Reaction 1 of Scheme 9.3. These two radical species can then combine, following Reaction 2 and 3 of Scheme 9.3, generating 4-carboxy-2,4-dihydroxy 2-methyl-5-oxohexanoic acid (CDMOHA) and, following decarboxylation (Reaction 4 of Scheme 9.3), 2,4-dihydroxy-2-methyl-5-oxohexanoic acid (DMOHA). CDMOHA has a chemical formula of $C_8H_{12}O_7$ and we observe, correspondingly, a species in the MS data with an average experimental m/z for [M-H]$^-$ of 219.0517.

DMOHA's chemical formula is $C_7H_{12}O_5$. . We posit that the oligomeric photoproduct that is detected in the MS data with a high intensity, both here and in the literature,[37, 42] can be assigned to DMOHA and explained by the photochemical mechanism given in Scheme 9.3.

These structures, CDMOHA and DMOHA, are consistent with the MS results presented here and the known chemistry of pyruvic acid and zymonic acid.[37, 43, 66] The mechanistic pathway presented in Scheme 9.3 is further supported because it directly parallels one of the accepted mechanistic pathways for aqueous pyruvic acid photochemistry in the literature.[43, 45] As shown by Reaction 6 of Scheme 9.1, the recombination of the HA• and GD• radicals followed by the subsequent dehydration to form α-acetolactic acid, which then decarboxylates to form acetoin.[43] Consistent with this mechanism, we observe a species with an accurate mass corresponding to the chemical formula $C_5H_8O_4$, which is mostly likely acetolactic acid. Acetolactic acid, as a β-keto acid, will thermally decarboxylate into acetoin under ambient temperature conditions in aqueous solution. The rate of this decomposition is both pH and temperature dependent, increasing as temperature is raised and pH is lowered.[91] The time required for complete decarboxylation of aqueous acetolactic acid at 20 °C ranges from a few hours at a pH of 1.0[42] to two weeks at a pH of 4.65.[92] For our reaction conditions that are not buffered or pH adjusted (dependent on pyruvic acid concentration, pH ~2.4 for 10 mM pre-irradiation solutions), it is reasonable to expect that acetolactic acid generated photochemically would be partially decarboxylated, allowing us to observe both acetolactic acid and acetoin during post-irradiation analysis.
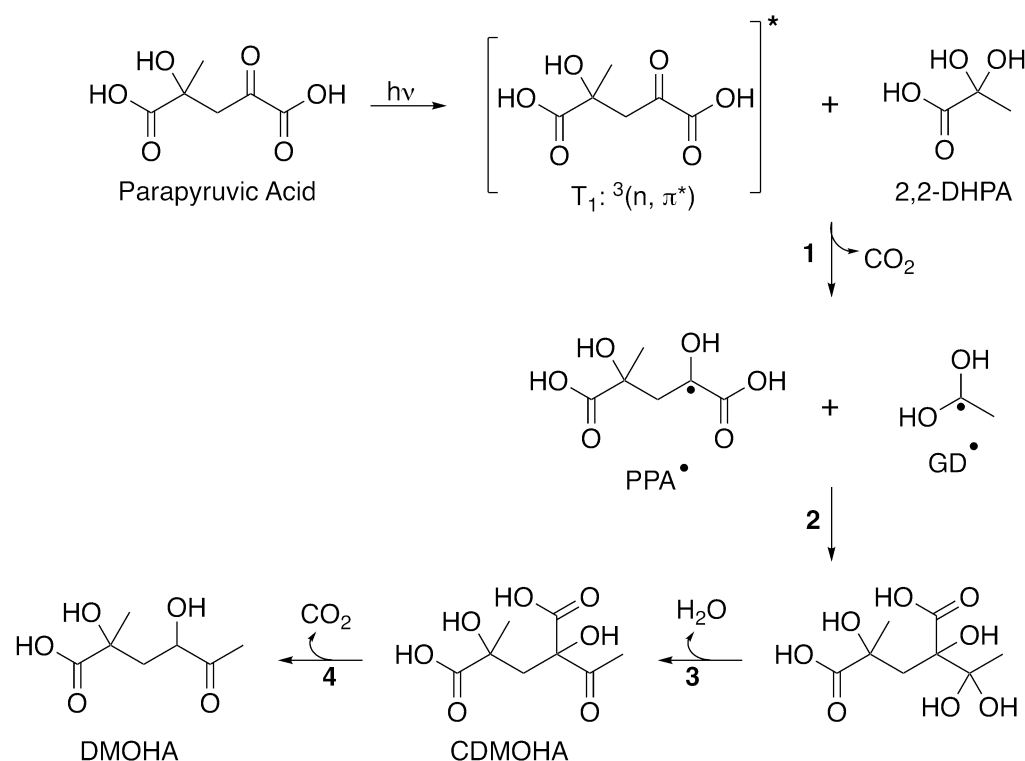
Scheme 9.3. *Photochemistry of parapyruvic acid to generate trimer species.*

Acetoin has been widely reported in the literature as a known product of the aqueous photochemistry of pyruvic acid.[37, 41, 43-45] It is readily apparent that the pathway presented in Scheme 9.3 is wholly analogous to the pathway presented by Reaction 6 of Scheme 9.1, where the intermediate species, CDMOHA, corresponds to acetolactic acid and DMOHA corresponds to acetoin. Griffith et al. (2013) unambiguously identified acetoin as a minor product by COSY NMR.[43] Here we identify acetoin as a photoproduct using ESI⁻ MS as well (Table 9.1).

The observation of acetoin as a product of the aqueous photochemistry of pyruvic acid has been a point of contention in the literature.[42, 43, 69, 70] This discrepancy likely stems in part from the fact that acetoin is not a primary photoproduct, but, is instead formed from the thermal decarboxylation from a larger oligomer generated by radical-radical recombination. Indeed, several of the observed photoproducts of the light-initiated chemistry of pyruvic acid are not directly formed from the simple recombination of pyruvic acid-derived radicals. Rather, species that are generated by these initial recombination processes, such as 2-methyl-2,3,3-trihydroxybutanoic acid, go on to further react, forming

species such as acetolactic acid and acetoin, as shown in Reaction 6 of Scheme 9.1. Such species can decompose into smaller product species, as is observed in the dehydration reactions that form acetolactic acid and CDMOHA and the decarboxylation reactions that form acetoin and DMOHA. But oligomeric intermediates can also react to generate larger oligomeric species, as is observed when parapyruvic acid, a dimer of pyruvic acid, is photochemically excited and reacts with another pyruvic acid molecule, ultimately generating DMOHA, a trimer of pyruvic acid. The generation and subsequent reactions of intermediate species, especially oligomeric intermediates, is not always appreciated. Because of this reactivity, both an increase in molecular complexity by the generation of oligomeric species and the generation of a complex mixture of molecules within the solution are observed. These interconnected reactions mean that even the three-carbon pyruvic acid generates a diverse library of products upon irradiation in aqueous solution. The combination of the reaction pathways outlined in Schemes 9.1 through 9.3, can explain the majority of the photochemical products observed in the MS data. This includes both acetic acid and lactic acid as shown in Reaction 5 of Scheme 9.1. Acetic acid has been observed by NMR previously[43] and is readily seen in the NMR of the experiments conducted here (Figures A5.3 and A5.4 in Appendix 5). Lactic acid was conclusively identified as a photoproduct by COSY and DOSY NMR.[43] Here, for the first time here we have observed the formation of lactic acid in the MS data as well (Table 9.1). However, there remain a number of minor photoproducts, we observe several of which have not been previously reported in the literature and that have not yet been identified. For completeness, we report the detailed MS data in Table A5.1 in Appendix 5.

That the observed chemistry is so rich, even at very low pyruvic acid concentrations (from 0.5 mM to 10 mM), is perhaps surprising. We are able to detect more minor photoproducts in the 10 mM post-irradiation solutions in the MS, which is likely due to the lower concentration of products formed in solutions with lower initial pyruvic acid concentrations, as we used the same ionization parameters for all MS analyses. The main oligomeric products, including DMTA and DMOHA, are observed in the 0.5 mM post-irradiation solutions. The formation of these products requires that two radicals escape their initial solvent cage, encounter each other, and recombine before they are quenched. Even the initial generation

of these radicals requires that a photoexcited species encounter another molecule in solution before quenching. Under more dilute conditions, the chance of such encounters occurring decreases. A kinetics analysis of the aqueous pyruvic acid photochemistry under anaerobic conditions found that the rates of depletion of pyruvic acid were roughly equivalent between 100 mM and 20 mM solutions,[37] suggesting both these concentrations are above this dilute limit. While a formal investigation of the kinetics of photolysis as a function of concentration was outside the scope of this study, the observed consumption of pyruvic acid in the NMR after five hours of photolysis is lower for the low concentration solutions, as would be expected for radical-driven chemistry. For the solutions of 0.5 mM, the depletion of pyruvic acid was observed by NMR to be closer to 50% (Figure A5.4 in Appendix 5), compared to the roughly 90% depletion observed for the 10 mM solutions. This observed decrease in reactivity is likely due to a combination of factors, all stemming from the low concentrations of pyruvic acid used. As mentioned above, in the 0.5 mM solutions, pyruvic acid exists primarily as the keto conformer and the higher pH of the solution (~3.5) means that more exists as pyruvate, both of which likely slow reaction compared to the 10 mM solutions. In the low concentration limit, it would also be expected that the probability of two species encountering each other before quenching decreases to essentially zero and only unimolecular homolysis products would be observed. It has previously been suggested that the transition from bimolecular to unimolecular processes would occur for solutions around 10 mM pyruvic acid.[42, 60] Here, however, we demonstrate that under our reaction conditions bimolecular processes still readily occur even in very dilute solutions.

It is important to consider the implications of the reaction conditions used here, as the aqueous photochemistry of pyruvic acid is extremely sensitive to its environmental surroundings. This sensitivity helps explain differences between reported products in the literature.[37, 41-45, 69, 70] As shown in Scheme 9.1, a number of pathways exist for the further reactions of HA• and GD• to give the observed photoproducts. The branching ratio of these pathways is influenced by the environmental conditions under which the aqueous photochemistry is conducted. For example, it has been shown that the composition of the atmosphere under which the photochemistry is conducted can strongly influence this branching ratio.[37]

Reactions 3A and 3B of Scheme 9.1 involve the reaction of the radical species with oxygen. Reaction 3A is a pathway by which pyruvic acid is regenerated, therefore slowing the kinetics of pyruvic photolysis.[37] Reaction 3B forms acetic acid. In the high oxygen concentration limit, obtained by bubbling pure O_2 through the photolysis reactor, the branching ratio is such that only acetic acid is observed as a photoproduct using NMR (Figure A5.5 in Appendix 5). Here, we are reliant on our combined, complementary NMR and ESI⁻ MS analyses: while acetic acid is formed and readily observed by NMR, it is not seen in the MS. Acetic acid is difficult to observe by the ESI⁻ MS used here, likely because, as a small molecule, it is toward the low mass range of our instrument, and the signal and mass accuracy of the instrument decrease as ion m/z is decreased. Even at 100 mM concentration, acetic acid is observed only weakly in the ESI⁻ MS, as shown in Figure A5.6 in Appendix 5. It is not surprising that we do not observe it as a photoproduct in the MS when the concentration is much lower.

The effect to the branching ratio of the photochemical pathways under a pure O_2 atmosphere is extreme, but it serves as an example highlighting the differences in observable products created by different reaction conditions. In environments that are not saturated with O_2, the familiar oligomeric species discussed above are readily formed. In oxygen-limited conditions, these oligomers are the major observable products. Because we were interested primarily in these oligomeric species, we chose to conduct our photochemical experiments under a nitrogen atmosphere in order to maximize our ability to observe such species at low concentrations. Under conditions free of dissolved O_2 Reaction 3 of Scheme 9.1 is effectively removed, and lifetimes of excited state pyruvic acid are effectively increased by removing the quenching effects of O_2. The oxygen-limited conditions may account for the persistence of biomolecular photochemical processes even at very dilute concentrations in the experiments reported here.

While the branching ratio observed for reactions under oxygen-depleted conditions is not directly comparable to those that might occur in the natural environment, the products observed and the mechanistic insight behind their formation provide us with a better understanding of the complexity of reactions that occur in the natural environment. Biasing the branching ratio toward oligomeric species for

laboratory studies simply aids in the ability to analyze the resultant products at low concentrations, it does not change the nature of the species generated. Oxygen-limited conditions may additionally be relevant for certain systems found in the natural environment as well. Irradiation of pyruvic acid in the bulk aqueous phase open to air has been shown to deplete oxygen from the reaction vessel.[37, 93] Atmospheric aerosols in the modern atmosphere are unlikely to be depleted in oxygen, but even under conditions where dissolved O_2 is not depleted reactions to form oligomers are still active.[37, 93]

The observation that the formation of more complex, oligomeric species is favored under anoxic conditions does raise intriguing possibilities for the relevance of this chemistry in the ancient, prebiotic environment. Unlike the modern atmosphere, the prebiotic atmosphere contained very little O_2 and ozone, allowing more UV light to reach the troposphere and Earth's surface.[94, 95] Aqueous photochemistry of pyruvic acid has been shown to be competitive with hydroxyl radical reaction in the modern environment.[37] The absence of oxygen in the prebiotic atmosphere suggests that the photochemistry of carbonyl-containing compounds is expected be an even more significant process on the ancient Earth than it is today, given that far less OH radical would have been available in prebiotic environments. The generation of oligomers under prebiotically-relevant conditions demonstrates that pyruvic acid can harness sunlight and convert it into usable chemical energy stored in complex, reactive molecules. In addition to being an important atmospheric species, pyruvic acid is also at the center of metabolism,[96-100] and it has been suggested that its photochemistry may have driven protometabolic cycles.[95, 99-101]

9.4 Conclusions

In this work, the aqueous phase photochemistry of pyruvic acid was investigated at low concentrations under an anaerobic, N_2 atmosphere. Even in very dilute solutions with low concentrations of pyruvic acid, covalently-bonded dimers and trimers are formed from the recombination of photochemically-generated radical species. We have shown that it is energetically possible for an excited pyruvic acid molecule to abstract a hydrogen from the methyl hydrogen group of another pyruvic acid molecule in addition to hydrogen abstraction from the carboxyl group. This generates a new radical, OA•,

which can recombine with HA• to form parapyruvic acid, a dimer of pyruvic acid known to be generated via dark oligomerization processes.[66]

Several of the observed species in the post-irradiation solutions are not primary photoproducts of pyruvic acid but are, rather, generated from the further reactions of oligomeric intermediates. Such intermediate species can decompose by dehydration or decarboxylation, but they can also undergo further photochemical reactions to generate larger molecules. We have proposed that parapyruvic acid, itself an α-keto acid, when photoexcited follows the same photochemical pathways as pyruvic acid, cross-reacting with pyruvic acid to form 2,4-dihydroxy-2-methyl-5-oxohexanoic acid, a trimer of pyruvic acid.

Pyruvic acid's photochemistry is known to be incredibly sensitive to environmental conditions, with completely different reaction pathways available in the aqueous phase than in the gas phase. Within the aqueous phase, the composition of dissolved gases in solution has a strong influence on the branching ratio of these pathways. This network of reactions yields a diverse library of photoproducts even when considering only a simple model system of a single species. This highlights that the formation of SOA from the aqueous chemistry of small organics under atmospheric conditions is reliant on a Gordian Knot of interwoven networks of reactions between many species. However, while a complex mixture of products is generated from the aqueous photochemistry of pyruvic acid, the mechanisms governing their formation are robust and self-consistent, suggesting that by understanding in detail the photochemistry of model species, mechanistic motifs may be found across classes of molecules that help untangle the reactive behavior of more complex mixtures of species.

Acknowledgments

Supporting Information in Appendix 5: Additional UV-vis, NMR, and high resolution ESI mass spectra are included in the supporting information, along with detailed tables of the mass spectrometry analysis and electronic structure calculation data.

Bibliography

(1)   Perraud, V.; Bruns, E. A.; Ezell, M. J.; Johnson, S. N.; Yu, Y.; Alexander, M. L.; Zelenyuk, A.; Imre, D.; Chang, W. L.; Dabdub, D., et al., Nonequilibrium atmospheric secondary organic aerosol formation and growth. *Proc. Natl. Acad. Sci.* **2012,** *109* (8), 2836-2841.

(2)   Harrison, R. M.; Yin, J., Particulate matter in the atmosphere: Which particle properties are important for its effects on health? *Sci. Total Environ.* **2000,** *249* (1), 85-101.

(3)   Finlayson-Pitts, B. J.; Pitts, J. N., *Chemistry of the upper and lower atmosphere*. Academic Press: San Diego, 1999.

(4)   Hinds, W. C., *Aerosol technology : Properties, behavior, and measurement of airborne particles*. 2nd ed.; Wiley: New York, 1999.

(5)   Ervens, B., Modeling the processing of aerosol and trace gases in clouds and fogs. *Chem Rev* **2015,** *115* (10), 4157-4198.

(6)   Lohmann, U.; Feichter, J., Global indirect aerosol effects: A review. *Atmo. Chem. Phys.* **2005,** *5*, 715-737.

(7)   Hansen, J.; Sato, M.; Ruedy, R., Radiative forcing and climate response. *J. Geophys. Res. Atmos.* **1997,** *102* (D6), 6831-6864.

(8)   Hallquist, M.; Wenger, J. C.; Baltensperger, U.; Rudich, Y.; Simpson, D.; Claeys, M.; Dommen, J.; Donahue, N. M.; George, C.; Goldstein, A. H., et al., The formation, properties and impact of secondary organic aerosol: Current and emerging issues. *Atmos. Chem. Phys.* **2009,** *9* (14), 5155-5236.

(9)   Ervens, B.; Turpin, B. J.; Weber, R. J., Secondary aerosol formation in cloud droplets and aqueous particles (aqsoa): A review of laboratory, field and model studies. *Atmo. Chem. Phys.* **2011,** *11* (21), 11069-11102.

(10)   Seinfeld, J. H.; Pandis, S. N., *Atmospheric chemistry and physics: From air pollution to climate change*. John Wiley & Sons, Inc.: New York, 1998.

(11)   Boucher, O.; Randall, D.; Artaxo, P.; Bretherton, C.; Feingold, G.; Forster, P.; Kerminen, V. M.; Kondo, Y.; Liao, H.; Lohmann, U., et al., Clouds and aerosols. In *Climate change 2013: The physical science basis. Contribution of working group i to the fifth assessment report of the intergovernmental panel on climate change*, Stocker, T. F.; Qin, D.; Plattner, G. K.; Tignor, M.; Allen, S. K.; Boschung, J.; Nauels, A.; Xia, Y.; Bex, V.; Midgley, P. M., Eds. Cambridge Univ. Press, : Cambridge, U.K. and New York, NY, USA, 2013; pp 465-570.

(12)   Heald, C. L.; Jacob, D. J.; Park, R. J.; Russell, L. M.; Huebert, B. J.; Seinfeld, J. H.; Liao, H.; Weber, R. J., A large organic aerosol source in the free troposphere missing from current models. *Geophys. Res. Lett.* **2005,** *32* (18), L18809.

(13)   Jimenez, J. L.; Canagaratna, M. R.; Donahue, N. M.; Prevot, A. S. H.; Zhang, Q.; Kroll, J. H.; DeCarlo, P. F.; Allan, J. D.; Coe, H.; Ng, N. L., et al., Evolution of organic aerosols in the atmosphere. *Science* **2009,** *326* (5959), 1525-1529.

(14)   Carlton, A. G.; Wiedinmyer, C.; Kroll, J. H., A review of secondary organic aerosol (soa) formation from isoprene. *Atmo. Chem. Phys.* **2009,** *9* (14), 4987-5005.

(15)   Monod, A.; Carlier, P., Impact of clouds on the tropospheric ozone budget: Direct effect of multiphase photochemistry of soluble organic compounds. *Atmos. Environ.* **1999,** *33* (27), 4431-4446.

(16)   Kroll, J. H.; Ng, N. L.; Murphy, S. M.; Flagan, R. C.; Seinfeld, J. H., Secondary organic aerosol formation from isoprene photooxidation. *Environ. Sci. Technol.* **2006,** *40* (6), 1869-1877.

(17)   Claeys, M.; Graham, B.; Vas, G.; Wang, W.; Vermeylen, R.; Pashynska, V.; Cafmeyer, J.; Guyon, P.; Andreae, M. O.; Artaxo, P., Formation of secondary organic aerosols through photooxidation of isoprene. *Science* **2004,** *303* (5661), 1173-1176.

(18)   Kroll, J. H.; Ng, N. L.; Murphy, S. M.; Flagan, R. C.; Seinfeld, J. H., Secondary organic aerosol formation from isoprene photooxidation under high-nox conditions. *Geophys. Res. Lett.* **2005,** *32* (18), L18808.

(19)   Brégonzio-Rozier, L.; Giorio, C.; Siekmann, F.; Pangui, E.; Morales, S.; Temime-Roussel, B.; Gratien, A.; Michoud, V.; Cazaunau, M.; DeWitt, H., Secondary organic aerosol formation from isoprene photooxidation during cloud condensation–evaporation cycles. *Atmo. Chem. Phys.* **2016,** *16* (3), 1747-1760.

(20)   George, C.; Ammann, M.; D'Anna, B.; Donaldson, D. J.; Nizkorodov, S. A., Heterogeneous photochemistry in the atmosphere. *Chem. Rev.* **2015,** *115* (10), 4218-4258.

(21)   Boris, A. J.; Desyaterik, Y.; Collett, J. L., How do components of real cloud water affect aqueous pyruvate oxidation? *Atmospheric Research* **2014,** *143*, 95-106.

(22)   Vaida, V., Spectroscopy of photoreactive systems: Implications for atmospheric chemistry. *J. Phys. Chem. A* **2009,** *113*, 5-18.

(23)   Altieri, K. E.; Carlton, A. G.; Lim, H.-J.; Turpin, B. J.; Seitzinger, S. P., Evidence for oligomer formation in clouds: Reactions of isoprene oxidation products. *Environ. Sci. Technol.* **2006,** *40* (16), 4956-4960.

(24)   Ervens, B.; Carlton, A. G.; Turpin, B. J.; Altieri, K. E.; Kreidenweis, S. M.; Feingold, G., Secondary organic aerosol yields from cloud-processing of isoprene oxidation products. *Geophys. Res. Lett.* **2008,** *35* (2), L02816.

(25)   Carlton, A. G.; Turpin, B. J.; Lim, H.-J.; Altieri, K. E.; Seitzinger, S., Link between isoprene and secondary organic aerosol (soa): Pyruvic acid oxidation yields low volatility organic acids in clouds. *Geophys. Res. Lett.* **2006,** *33*, L06822.

(26)   Kawamura, K.; Kasukabe, H.; Barrie, L. A., Source and reaction pathways of dicarboxylic acids, ketoacids and dicarbonyls in arctic aerosols: One year of observations. *Atmos. Environ.* **1996,** *30* (10-11), 1709-1722.

(27)   Sempere, R.; Kawamura, K., Comparative distributions of dicarboxylic acids and related polar compounds in snow, rain, and aerosols from urban atmosphere. *Atmos. Environ.* **1994,** *28* (3), 449-459.

(28) Nguyen, T. B.; Bateman, A. P.; Bones, D. L.; Nizkorodov, S. A.; Laskin, J.; Laskin, A., High-resolution mass spectrometry analysis of secondary organic aerosol generated by ozonolysis of isoprene. *Atmos. Environ.* **2010,** *44* (8), 1032-1042.

(29) Veres, P. R.; Roberts, J. M.; Cochran, A. K.; Gilman, J. B.; Kuster, W. C.; Holloway, J. S.; Graus, M.; Flynn, J.; Lefer, B.; Warneke, C., et al., Evidence of rapid production of organic acids in an urban air mass. *Geophys. Res. Lett.* **2011,** *38*, L17807.

(30) Warneck, P., Multi-phase chemistry of c-2 and c-3 organic compounds in the marine atmosphere. *Journal of Atmospheric Chemistry* **2005,** *51* (2), 119-159.

(31) Andreae, M. O.; Talbot, R. W.; Li, S. M., Atmospheric measurements of pyruvic and formic acid. *J. Geophys. Res. Atmos.* **1987,** *92* (D6), 6635-6641.

(32) Ho, K.; Lee, S.; Cao, J.; Kawamura, K.; Watanabe, T.; Cheng, Y.; Chow, J. C., Dicarboxylic acids, ketocarboxylic acids and dicarbonyls in the urban roadside area of hong kong. *Atmos. Environ.* **2006,** *40* (17), 3030-3040.

(33) Talbot, R.; Andreae, M.; Berresheim, H.; Jacob, D. J.; Beecher, K., Sources and sinks of formic, acetic, and pyruvic acids over central amazonia: 2. Wet season. *J. Geophys. Res. Atmos.* **1990,** *95* (D10), 16799-16811.

(34) Veres, P.; Roberts, J. M.; Burling, I. R.; Warneke, C.; de Gouw, J.; Yokelson, R. J., Measurements of gas-phase inorganic and organic acids from biomass fires by negative-ion proton-transfer chemical-ionization mass spectrometry. *J. Geophys. Res. Atmos.* **2010,** *115* (D23), D23302.

(35) Kawamura, K.; Kasukabe, H.; Barrie, L. A., Secondary formation of water-soluble organic acids and alpha-dicarbonyls and their contributions to total carbon and water-soluble organic carbon: Photochemical aging of organic aerosols in the arctic spring. *J. Geophys. Res. Atmos.* **2010,** *115*, D21306.

(36) Mellouki, A.; Mu, Y. J., On the atmospheric degradation of pyruvic acid in the gas phase. *J. Photochem. Photobiol., A* **2003,** *157* (2-3), 295-300.

(37) Reed Harris, A. E.; Ervens, B.; Shoemaker, R. K.; Kroll, J. A.; Rapf, R. J.; Griffith, E. C.; Monod, A.; Vaida, V., Photochemical kinetics of pyruvic acid in aqueous solution. *J. Phys. Chem. A* **2014,** *118* (37), 8505-8516.

(38) Lopalco, A.; Dalwadi, G.; Niu, S.; Schowen, R. L.; Douglas, J.; Stella, V. J., Mechanism of decarboxylation of pyruvic acid in the presence of hydrogen peroxide. *J. Pharm. Sci.* **2016,** *105* (2), 705-713.

(39) Stefan, M. I.; Bolton, J. R., Reinvestigation of the acetone degradation mechanism in dilute aqueous solution by the uv/h2o2 process. *Environ. Sci. Technol.* **1999,** *33* (6), 870-873.

(40) Schöne, L.; Herrmann, H., Kinetic measurements of the reactivity of hydrogen peroxide and ozone towards small atmospherically relevant aldehydes, ketones and organic acids in aqueous solutions. *Atmo. Chem. Phys.* **2014,** *14* (9), 4503.

(41) Leermakers, P. A.; Vesley, G. F., Photochemistry of alpha-keto acids and alpha-keto esters. 1. Photolysis of pyruvic acid and benzoylformic acid. *J. Am. Chem. Soc.* **1963,** *85* (23), 3776-3779.

(42) Guzman, M. I.; Colussi, A. J.; Hoffmann, M. R., Photoinduced oligomerization of aqueous pyruvic acid. *J. Phys. Chem. A* **2006,** *110* (10), 3619-3626.

(43) Griffith, E. C.; Carpenter, B. K.; Shoemaker, R. K.; Vaida, V., Photochemistry of aqueous pyruvic acid. *Proc. Natl. Acad. Sci.* **2013,** *110* (29), 11714-11719.

(44) Leermakers, P. A.; Vesley, G. F., Photolysis of pyruvic acid in solution. *J. Org. Chem.* **1963,** *28* (4), 1160-1161.

(45) Closs, G. L.; Miller, R. J., Photo-reduction and photodecarbosylation of pyruvic acid - applications of cidnp to mechanistic photochemistry. *J. Am. Chem. Soc.* **1978,** *100* (11), 3483-3494.

(46) Hall, G. E.; Muckerman, J. T.; Preses, J. M.; Weston, R. E.; Flynn, G. W., Time-resolved ftir studies of the photodissociation of pyruvic-acid at 193 nm. *Chem. Phys. Lett.* **1992,** *193* (1-3), 77-83.

(47) Rincon, A. G.; Guzman, M. I.; Hoffmann, M. R.; Colussi, A. J., Optical absorptivity versus molecular composition of model organic aerosol matter. *J. Phys. Chem. A* **2009,** *113* (39), 10512-10520.

(48) Vesley, G. F.; Leermakers, P. A., Photochemistry of alpha-keto acids and alpha-keto esters .3. Photolysis of pyruvic acid in vapor phase. *J. Phys. Chem.* **1964,** *68* (8), 2364-2366.

(49) Dhanya, S.; Maity, D. K.; Upadhyaya, H. P.; Kumar, A.; Naik, P. D.; Saini, R. D., Dynamics of oh formation in photodissociation of pyruvic acid at 193 nm. *J. Chem. Phys.* **2003,** *118* (22), 10093-10100.

(50) Oneill, J. A.; Kreutz, T. G.; Flynn, G. W., Ir diode-laser study of vibrational-energy distribution in co2 produced by uv excimer laser photofragmentation of pyruvic-acid. *J. Chem. Phys.* **1987,** *87* (8), 4598-4605.

(51) Wood, C. F.; Oneill, J. A.; Flynn, G. W., Infrared diode-laser probes of photofragmentation products - bending excitation in co2 produced by excimer laser photolysis of pyruvic-acid. *Chem. Phys. Lett.* **1984,** *109* (4), 317-323.

(52) Berges, M. G.; Warneck, P., Product quantum yields for the 350 nm photodecomposition of pyruvic acid in air. *Ber. Bunsen-Ges. Phys. Chem* **1992,** *96* (3), 413-416.

(53) Grosjean, D., Atmospheric reactions of pyruvic-acid. *Atmos. Environ.* **1983,** *17* (11), 2379-2382.

(54) Yamamoto, S.; Back, R. A., The photolysis and thermal decomposition of pyruvic acid in the gas phase. *Can. J. Chem.* **1985,** *63* (2), 549-554.

(55) Plath, K. L.; Takahashi, K.; Skodje, R. T.; Vaida, V., Fundamental and overtone vibrational spectra of gas-phase pyruvic acid. *J. Phys. Chem. A* **2009,** *113*, 7294-7303.

(56) Larsen, M. C.; Vaida, V., Near infrared photochemistry of pyruvic acid in aqueous solution. *J. Phys. Chem. A* **2012,** *116*, 5840-5846.

(57)   Takahashi, K.; Plath, K. L.; Skodje, R. T.; Vaida, V., Dynamics of vibrational overtone excited pyruvic acid in the gas phase: Line broadening through hydrogen-atom chattering. *J. Phys. Chem. A* **2008,** *112* (32), 7321-7331.

(58)   Reed Harris, A. E.; Doussin, J.-F.; Carpenter, B. K.; Vaida, V., Gas-phase photolysis of pyruvic acid: The effect of pressure on reaction rates and products. *J. Phys. Chem. A* **2016,** *120* (51), 10123-10133.

(59)   Chang, X.-P.; Fang, Q.; Cui, G., Mechanistic photodecarboxylation of pyruvic acid: Excited-state proton transfer and three-state intersection. *J. Chem. Phys.* **2014,** *141* (15), 154311.

(60)   Davidson, R. S.; Goodwin, D.; De Violet, P. F., The mechanism of the photo-induced decarboxylation of pyruvic acid in solution. *Chem. Phys. Lett.* **1981,** *78* (3), 471-474.

(61)   Reed Harris, A. E.; Pajunoja, A.; Cazaunau, M.; Gratien, A.; Pangui, E.; Monod, A.; Griffith, E. C.; Virtanen, A.; Doussin, J. F.; Vaida, V., Multiphase photochemistry of pyruvic acid under atmospheric conditions. *J. Phys. Chem. A* **2017**, In Press, DOI: 10.1021/acs.jpca.7b01107.

(62)   Saito, K.; Sasaki, G.; Okada, K.; Tanaka, S., Unimolecular decomposition of pyruvic acid - an experimental and theoretical study. *J. Phys. Chem.* **1994,** *98* (14), 3756-3761.

(63)   Taylor, R., The mechanism of thermal eliminations xxiii: [1] the thermal-decomposition of pyruvic-acid. *Int. J. Chem. Kinet.* **1987,** *19* (8), 709-713.

(64)   da Silva, G., Decomposition of pyruvic acid on the ground-state potential energy surface. *J. Phys. Chem. A* **2015,** *120* (2), 276–283.

(65)   Colberg, M. R.; Watkins, R. J.; Krogh, O. D., Vibrationally excited carbon-dioxide produced by infrared multiphoton pyrolysis. *J. Phys. Chem.* **1984,** *88* (13), 2817-2821.

(66)   Perkins, R. J.; Shoemaker, R. K.; Carpenter, B. K.; Vaida, V., Chemical equilibria and kinetics in aqueous solutions of zymonic acid. *J. Phys. Chem. A* **2016,** *120* (51), 10096-10107.

(67)   Horowitz, A.; Meller, R.; Moortgat, G. K., The uv–vis absorption cross sections of the α-dicarbonyl compounds: Pyruvic acid, biacetyl and glyoxal. *J. Photochem. Photobiol., A* **2001,** *146* (1), 19-27.

(68)   Schreiner, P. R.; Reisenauer, H. P.; Ley, D.; Gerbig, D.; Wu, C.-H.; Allen, W. D., Methylhydroxycarbene: Tunneling control of a chemical reaction. *Science* **2011,** *332* (6035), 1300-1303.

(69)   Griffith, E. C.; Carpenter, B. K.; Shoemaker, R. K.; Vaida, V., Reply to eugene et al.: Photochemistry of aqueous pyruvic acid. *Proc. Natl. Acad. Sci.* **2013,** *110* (46), E4276-E4276.

(70)   Eugene, A. J.; Xia, S.-S.; Guzman, M. I., Negative production of acetoin in the photochemistry of aqueous pyruvic acid. *Proc. Natl. Acad. Sci.* **2013,** *110* (46), E4274-E4275.

(71)   If not specified the terms "dimer" and "trimer" are used here to refer to covalently-bonded oligomeric species, rather than non-covalently associated species.

(72)   Leermakers, P. A.; Vesley, G. F., Organic photochemistry and the excited state. *J. Chem. Educ* **1964,** *41* (10), 535.

(73)   Turro, N. J.; Ramamurthy, V.; Scaiano, J. C., *Modern molecular photochemistry of organic molecules*. University Science Books: Sausalito, California, 2010.

(74)   Rossignol, S.; Tinel, L.; Bianco, A.; Passananti, M.; Brigante, M.; Donaldson, D. J.; George, C., Atmospheric photochemistry at a fatty acid–coated air-water interface. *Science* **2016,** *353* (6300), 699-702.

(75)   Montgomery, J. A.; Frisch, M. J.; Ochterski, J. W.; Petersson, G. A., A complete basis set model chemistry. Vi. Use of density functional geometries and frequencies. *J. Chem. Phys.* **1999,** *110* (6), 2822-2827.

(76)   Frisch, M. J.; Trucks, G. W.; Schlegel, H. B.; Scuseria, G. E.; Robb, M. A.; Cheeseman, J. R.; Scalmani, G.; Barone, V.; Petersson, G. A.; Nakatsuji, H., et al. *Gaussian 09, revision d.01*, Gaussian, Inc.: Wallingford, CT, 2016.

(77)   Ogg, R. J.; Kingsley, R.; Taylor, J. S., Wet, a t 1-and b 1-insensitive water-suppression method for in vivo localized 1 h nmr spectroscopy. *Journal of Magnetic Resonance, Series B* **1994,** *104* (1), 1-10.

(78)   Wolff, L., Ueber ein neues condensationsproduct der brenztraubensäure. *Justus Liebigs Ann. Chem.* **1901,** *317* (1), 1–22.

(79)   Prey, V.; Waldmann, E.; Berbalk, H., Zur kenntnis der brenztraubensäure. *Monatshefte für Chemie und verwandte Teile anderer Wissenschaften* **1955,** *86* (3), 408-413.

(80)   Wolff, L., Ii. Ueber die parabrenztraubensäure. *Justus Liebigs Ann Chem* **1899,** *305* (2), 154-165.

(81)   Schnitzler, E. G.; Seifert, N. A.; Ghosh, S.; Thomas, J.; Xu, Y.; Jäger, W., Hydration of the simplest α-keto acid: A rotational spectroscopic and ab initio study of the pyruvic acid–water complex. *Phys. Chem. Chem. Phys.* **2017,** *19* 4440-4446.

(82)   Pocker, Y.; Meany, J. E.; Nist, B. J.; Zadorojny, C., Reversible hydration of pyruvic acid. I. Equilibrium studies. *J. Phys. Chem.* **1969,** *73* (9), 2879-2882.

(83)   Buschmann, H. J.; Dutkiewicz, E.; Knoche, W., The reversible hydration of carbonyl compounds in aqueous solution.2. The kinetics of the keto gen-diol transition. *Ber. Bunsen-Ges. Phys. Chem* **1982,** *86*, 129-134.

(84)   Buschmann, H. J.; Füldner, H. H.; Knoche, W., The reversible hydration of carbonyl compounds in aqueous solution. Part i, the keto/gem-diol equilibrium. *Ber. Bunsen-Ges. Phys. Chem* **1980,** *84* (1), 41-44.

(85)   Vaida, V., Perspective: Water cluster mediated atmospheric chemistry. *J. Chem. Phys.* **2011,** *135* (2), Art. Nr. 020901.

(86)   Kumar, M.; Francisco, J. S., The role of catalysis in alkanediol decomposition: Implications for general detection of alkanediols and their formation in the atmosphere. *J. Phys. Chem. A* **2015,** *119* (38), 9821-9833.

(87)   Kramer, Z. C.; Takahashi, H.; Vaida, V.; Skodje, R. T., Will water act as a photocatalyst for cluster phase chemical reactions? Vibrational overtone-induced dehydration reaction of methanediol. *J. Chem. Phys.* **2012,** *136*, 164302.

(88)   Maroń, M. K.; Takahashi, K.; Shoemaker, R. K.; Vaida, V., Hydration of pyruvic acid to its geminal-diol, 2, 2-dihydroxypropanoic acid, in a water-restricted environment. *Chem. Phys. Lett.* **2011,** *513* (4), 184-190.

(89)   Pedersen, K. J., The dissociation constants of pyruvic and oxaloacetic acid. *Acta Chem. Scand.* **1952,** *6* (2), 243-256.

(90)   Viehe, H. G.; Janousek, Z.; Merenyi, R.; Stella, L., The captodative effect. *Acc. Chem. Res.* **1985,** *18* (5), 148-154.

(91)   Ronkainen, P.; Brummer, S.; Suomalainen, H., Diacetyl and formic acid as decomposition products of 2-acetolactic acid. *Acta Chem. Scand.* **1970,** *24* (9), 3404-3406.

(92)   De Man, J., The formation of diacetyl and acetoin from α-acetolactic acid. *Recl. Trav. Chim. Pays-Bas* **1959,** *78* (7), 480-486.

(93)   Renard, P.; Reed Harris, A. E.; Rapf, R. J.; Rainer, S.; Demelas, C.; Coulomb, B.; Quivet, E.; Vaida, V.; Monod, A., Aqueous phase oligomerization of methyl vinyl ketone by atmospheric radical reactions. *J. Phys. Chem. C* **2014,** *118*, 29421-29430.

(94)   Ranjan, S.; Sasselov, D. D., Influence of the uv environment on the synthesis of prebiotic molecules. *Astrobio.* **2016,** *16* (1), 68-88.

(95)   Rapf, R. J.; Vaida, V., Sunlight as an energetic driver in the synthesis of molecules necessary for life. *Phys. Chem. Chem. Phys.* **2016,** *18* (30), 20067-20084.

(96)   Cooper, G.; Reed, C.; Nguyen, D.; Carter, M.; Wang, Y., Detection and formation scenario of citric acid, pyruvic acid, and other possible metabolism precursors in carbonaceous meteorites. *Proc. Natl. Acad. Sci.* **2011,** *108* (34), 14015-14020.

(97)   Voet, D.; Voet, J. G., *Biochemistry*. 4 ed.; John Wiley and Sons, Inc: Hoboken, NJ, 2011.

(98)   Cody, G. D.; Boctor, N. Z.; Filley, T. R.; Hazen, R. M.; Scott, J. H.; Sharma, A.; Yoder, H. S., Primordial carbonylated iron-sulfur compounds and the synthesis of pyruvate. *Science* **2000,** *289* (5483), 1337 -1340.

(99)   Griffith, E. C.; Shoemaker, R. K.; Vaida, V., Sunlight-initiated chemistry of aqueous pyruvic acid: Building complexity in the origin of life. *Origins Life Evol. Biosphere* **2013,** *43*, 341-352.

(100) Guzman, M. I.; Martin, S. T., Prebiotic metabolism: Production by mineral photoelectrochemistry of alpha-ketocarboxylic acids in the reductive tricarboxylic acid cycle. *Astrobio.* **2009,** *9* (9), 833-842.

(101) Shapiro, R., Small molecule interactions were central to the origin of life. *Q. Rev. Bio.* **2006,** *81* (2), 105-125.

Chapter 10: Zymonic Acid as a Prebiotic Sugar Analogue

10.1 Introduction

Sugars, as a class of molecule, are an essential component of modern life. Due to their critical incorporation into the structures of DNA and RNA, the synthesis of sugars and their incorporation into nucleosides have attracted attention in prebiotic chemistry. In life, however, sugars play roles beyond information storage, including metabolism, energy storage, and physical structuring. In this work we examine the ability of a prebiotically relevant sugar-like molecule, zymonic acid, to fill the roles played by modern sugars in a prebiotic, enzyme-free setting.

In studies of prebiotic chemical evolution, it is common to examine chemical systems and their functions in modern life, in order to understand the necessary roles similar chemical systems must have played during the emergence of life. For the case of sugars, however, this is not so simple, because of the plethora of functions that sugars appear to serve in modern biology, including roles in energy storage, other metabolic processes, and maintaining structure. In some cases, this is further complicated because we still lack complete understanding of several of these roles.

Sugars are most commonly thought of as metabolites. Metabolism, broadly speaking, is the process by which life generates all of the molecules required for continued survival. Metabolic processes can be split into two classes, catabolic and anabolic processes. In catabolism, sugars (as well as other molecules) are converted to lower energy waste products to simultaneously create useful high energy molecules, such as adenosine triphosphate (ATP) from adenosine monophosphate (AMP). In anabolism, high energy molecules like ATP are consumed (or rather converted to AMP) in order to drive reactions up-hill in energy and create useful products. Sugars are modified anabolically to make useful small molecules, such as nucleosides like adenosine. A related cellular use of sugars is for energy storage, which often involves assembly into sugar polymers (polysaccharides) such as starch or glycogen, in order to regulate both resource usage and osmotic pressure. Different sugar polymers can have other functional roles in cells, although these have been far less studied than their amino acid polymer (protein) analogues.

Common examples are structural components made largely of polysaccharides, such as cellulose or chitin. Sugars also make up the structural backbones of the informational polymers DNA and RNA. A role of sugars that has begun receiving a great deal of attention in biology is the modification of proteins, to form amino acid sugar copolymers known as glycoproteins. Glycoproteins seem to occupy the same types of roles as unmodified proteins, and can range from structures consisting mostly of amino acids, to structures that are mainly polysaccharides. Sugar groups attached to lipids can be important membrane components and have a role in several types of signaling processes as well. In short, sugars appear to be used in nearly all, if not all, aspects of modern cellular life.

Despite the prevalence of sugars in so many areas of life, the prebiotic interest in sugars has largely focused on the synthesis of ribose and, subsequently, RNA. RNA has gained a great deal of attention due to its ability to act both as an informational polymer and a catalyst. Some RNA polymer sequences, known as ribozymes, possess autocatalytic activity, or ability to catalyze the formation of other RNA polymers.[1,2] It is commonly hypothesized that RNA was an essential component of early life.[3] The sugar ribose is a critical component of RNA, and forms the polymer backbone along with phosphate linking groups. There has been work showing the formation of a mixture of sugars, including ribose, from the so-called formose reactions. Starting with glycolaldehyde, which can be formed prebiotically,[4,5] the reaction proceeds with the addition of formaldehyde and calcium hydroxide to reach very high pH.[6,7] This reaction proceeds further, quickly degrading the sugars, although this can be prevented by the addition of a borate mineral.[8] There is some evidence that this reaction could occur under hydrothermal vent conditions at less extreme pH;[8–10] however, formose reactions in prebiotic contexts have been subject to criticism due to low yields, the relative instability of ribose, and the scarcity of the required reaction conditions prebiotically.[11–16] Some work has been done that partially addresses these issues, using additional catalysts[17] or photochemical initiation,[12] but many problems remain.

While auto-catalytic RNA is likely to be an important component of early life, and the synthesis of ribose is clearly a key step, limiting the study of prebiotic sugars solely to ribose is too narrow given

the variety of roles that sugars occupy in modern life. Another factor, which likely contributes to the relatively limited scope of investigations of sugars is their restrictive formal definition based on structure rather than function. In modern life, carbohydrates (sugars and sugar polymers) are defined as having approximately the chemical formula of $C_nH_{2n}O_n$, where $n \geq 3$.[18] This definition is problematic even for modern sugars like deoxyribose, a critical component of DNA, and sucrose which do not meet the chemical formula requirement, and exceptions are made for these molecules. The formulaic definition comes from the stoichiometry of photosynthetic sugar generation, and may not be particularly relevant for prebiotic or early biotic sugar analogues, which are expected to be generated through different processes. In order to broaden the breadth of our studies, we will turn away from the formal definition of sugars and investigate sugar analogues that are able to fill the functional roles of sugars in modern life.

Perhaps the most essential roles of sugars in life are as metabolites and energy reservoirs, although there are not obvious reasons to discard their role as a structural building block across the many materials and subsystems used in modern life. The roles in metabolism and energy storage lead to further questions, of course, about what kind of metabolism might exist in prebiotic or early biotic systems. The core function of metabolism is to make molecules that are useful to the survival or replication of an organism or prebiotic chemical assembly. This is often accomplished through coupled processes that consume energy, and those that release energy. In modern life, these processes are viewed as being coupled, but distinct. Catabolic processes degrade complex molecules in order to produce high energy driver molecules (like ATP), and these can separately be used to drive anabolic processes that produce useful, complex molecules. Several prebiotic reactions have been proposed for various steps required to make ATP.[19–23] Because ribose is incorporated into the structure of ATP, synthesis of ATP face the same criticisms of prebiotic ribose generation in addition to criticisms of further reactions and conditions.[15,24,25] As a result, ATP is unlikely to be a viable high energy molecule to drive prebiotic or early biotic metabolism. Instead, alternative molecules that are essentially capable of filling the role of ATP could be used. These types of molecules have been referred to as driver molecules. Driver molecule schemes have

been discussed in detail elsewhere,[26–28] and essentially allow for chemical energy transduction as demonstrated in Figure 10.1. The role of the driver molecule is essentially the same role as that of ATP in modern life and serves to utilize an external source of energy to make a wide variety of products.
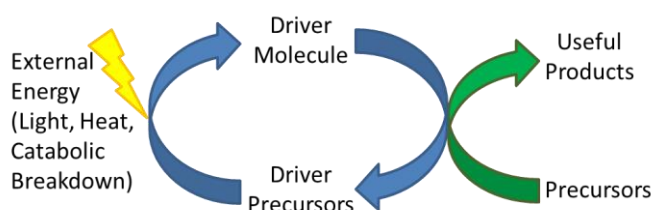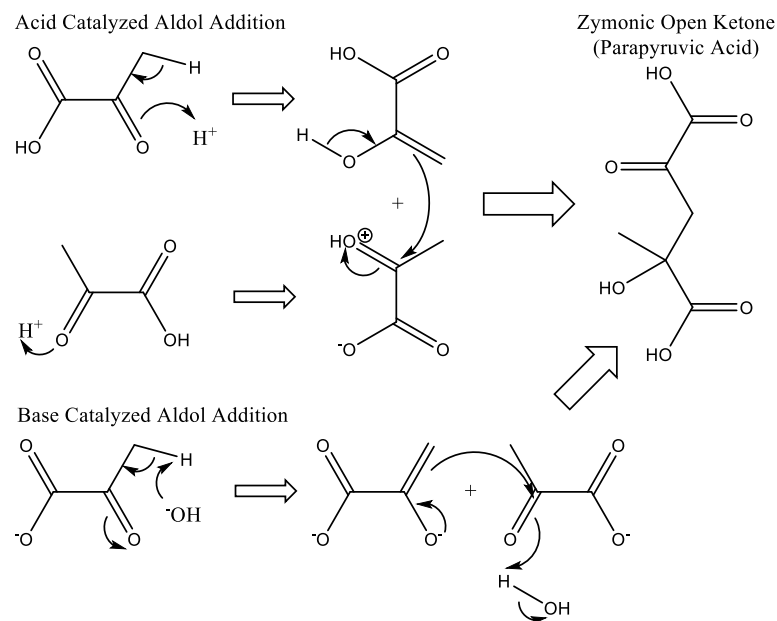

Figure 10.1: A schematic of driver molecules harnessing external energy sources and subsequently driving useful reactions.

One particularly promising candidate as a metabolic driver molecule is pyruvic acid. Pyruvic acid has advantages in this role due to its central location in the metabolism of all modern life, its prebiotic relevance,[29–33] and its ability to harness solar radiation to undergo photochemical reactions and consequently generate complex organic molecules, an important piece of metabolism.[30,32,34] With this view of metabolism, a key requirement of a sugar analogue would be its ability to be formed from a driver molecule, like pyruvic acid, as well as break down into the same driver molecule. It is also important that this cyclic conversion is possible under relatively mild conditions or with simple and abundant catalysts, due to the absence of enzymes in prebiotic scenarios.

Another primary role of sugars in modern life is energy storage. In order to survive in times of low energy intake, previously acquired energy must be stored in a form that can be converted back to the driver molecule relatively easily. In the longer term, modern sugars are stored as polymers, such as starch or glycogen, which helps reduce osmotic pressure inside cells compared to monomer sugar storage. It would clearly be advantageous for our sugar analogue to be able to polymerize for this reason. Many of the other roles of sugars involve polymerization reactions as well, both to form structural components, or informational polymers.

To summarize, we are interested in identifying prebiotic sugar analogues, with the requirement that they can both be produced from, and converted to, a metabolic driver molecule, such as pyruvic acid. It would also be advantageous for these sugar analogues to be able to fill other roles of sugars in modern life, namely reacting to form other useful molecules, particularly useful polymers. There are likely a variety of candidates for prebiotic sugars, largely depending on which driver molecule is used, but in this work we present one interesting candidate for a pyruvic acid driver system: zymonic acid.

Scheme 10.1: Acid and Base Catalyzed reaction mechanisms for the formation of the open ketone form of zymonic acid (parapyruvic acid) from pyruvic acid.

Zymonic acid is a six carbon molecule that forms spontaneously from pyruvic acid, both as a pure liquid or an aqueous solution. The rate of formation of zymonic acid from pyruvic acid appears to increase with increasing pH, or in the presence of several divalent cations.[35–41] There is also some evidence that the rate of formation increases at very low pH as well, which is consistent with the proposed aldol addition mechanism shown in Scheme 10.1.[35–39] The ability of zymonic acid, or the readily interconvertible parapyruvic acid, to form spontaneously from pyruvic acid gives it a clear prebiotic relevance. It has even been found in meteorites alongside pyruvic acid,[32] and under simulated hydrothermal vent conditions.[42] Because zymonic acid is so closely related to pyruvic acid, a modern and potential prebiotic metabolite, it has a direct link to metabolism in either case. In fact, zymonic acid appears to bind analogously to α-ketoglutarate in several enzymes.[43–45] Zymonic acid can be degraded in water in order to regenerate pyruvic acid,[46] allowing for simple, prebiotically relevant conversions both ways between pyruvic and zymonic acids.

10.2 Results

Our recent work[46] has shown several interesting properties of this molecule that are relevant to the story at hand. In aqueous solution it exists in equilibrium between at least five different forms (Figure 10.2), as well as pyruvic acid. Among these five forms, three are closed-ring and two are open-chain. There is some resemblance to the closed-ring and open-chain coexistence that is observed in modern sugars, although in zymonic acid the ringed forms are lactones rather than hemiacetals or hemiketals. The chemical polymorphism* both current sugars and zymonic acid exhibit (Figure 10.2) may contribute to the ability to fill some of the many roles associated with sugars in modern biology. This polymorphism in solution is also entropically favorable and, along with the high O:C ratio of all the forms, contributes to the favorable interactions with water that is a hallmark of sugars. The ratios between the different forms of ribose or zymonic acid in solution will vary depending on the solution conditions (concentration, pH, temperature, etc.). The variety of chemical forms in solution cause different reactive pathways to be accessible. This allows for both more ways to create these sugar-like molecules, as well as more ways for them to react anabolically and catabolically.

---

* For the purposes of this paper, we define chemical polymorphism to mean the ability of a compound to exist as a mixture of different chemical structures at equilibrium (especially in aqueous solution). It is simplest to refer to the mixture of chemicals as a single compound due to the inseparable nature of the mixture.

	Zymonic	D-Ribose
Open-Chain		
Closed-Ring		
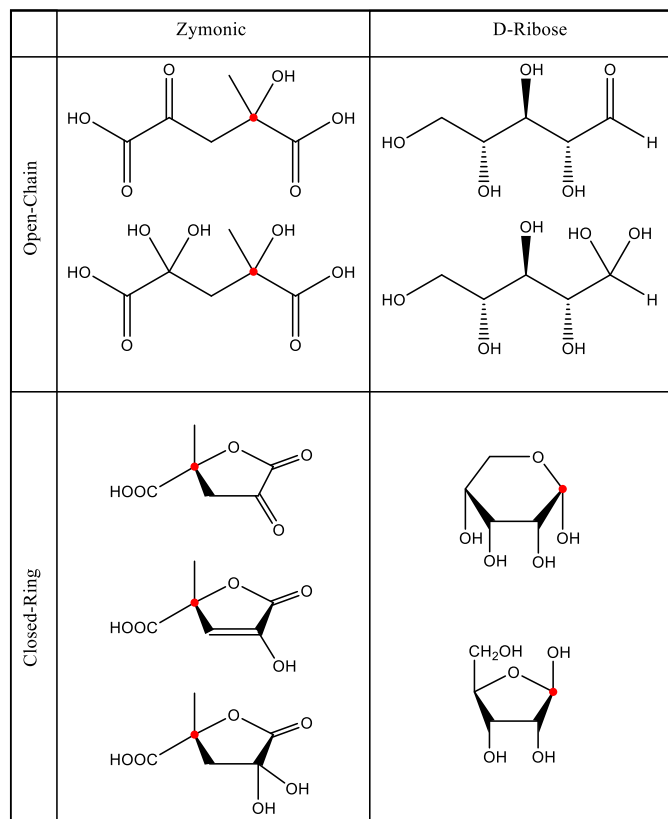
Figure 10.2: Structures that zymonic acid and ribose adopt in solution, illustrating the polymorphic nature of these compounds. Zymonic acid forms, from top to bottom are named as: open ketone (parapyruvic acid), open diol, closed ketone, closed enol, closed diol. Red dots indicate chiral centers with either handedness being possible for these sites. Ribose has additional chiral centers that are not marked in this manner, because differing chirality changes the common name for the sugar (e.g. D- or L- arabinose, lyxose, and xylose).

It is worth noting the chirality of the structures shown in Figure 10.2. Life today is generally homochiral in its use of sugars and amino acids, and the evolution of homochirality is a matter of considerable interest. While an in depth discussion of chirality is beyond the scope of this work, the similarities between zymonic acid and modern chiral sugars are intriguing. Sugars are often distinguished by their chirality in several ways. For example, stereoisomers of sugars are often given different common names, such as aldopentose, whose epimers are ribose, lyxose, arabanose, and xylose, all differing only by the relative positions of the chiral centers. Each epimer can be further distinguished by their handedness, into D- and L- enantiomers. Zymonic acid contains a single chiral center, and, therefore, also exists as a pair of enantiomers. While zymonic acid as synthesized under our reaction conditions will be produced as a racemic mixture, it has been shown that under certain reaction conditions the selective formation of one enantiomer over another can be favored for similar sugars.[10,47–50]

Zymonic acid clearly is structurally similar to sugars, such as ribose. However, the efficacy of zymonic acid as a sugar analogue within a protometabolic setting is dependent on the nature of its conversion from pyruvic acid. To a large extent its usefulness depends on the ratio of pyruvic acid to

zymonic acid at equilibrium. Using aqueous NMR techniques over time, we examine the ratios of zymonic and pyruvic acid over time. In order to increase the transferability of these studies, equilibrium thermodynamic relationships are used. In this case two pyruvic acid molecules are used to make one zymonic acid molecule, which results in an equilibrium ratio that is dependent on the concentration of pyruvic acid in the system, with higher concentrations of pyruvic acid favoring zymonic acid formation, as illustrated in equation 1.

(Equation 1) $\qquad$ $K_{eq} = \frac{[pyruvic]^2}{[zymonic]}$ $\qquad$ $\frac{[pyruvic]}{[zymonic]} = \frac{K_{eq}}{[pyruvic]}$

Equilibrium constants do not change directly as a function of pyruvic acid concentration, however they will depend on the solution pH (which can change with pyruvic acid concentration) and generally other factors such as solution salt content and temperature. Measuring equilibrium constants for this system unfortunately becomes complicated for several reasons. First, equilibrium is achieved very slowly, on the order of several months. Second, the different zymonic species have different pK_a values and even different numbers of acid groups than the initial pyruvic acid. This leads to a change in pH over time, often resulting in a drastically different equilibrium pH than the starting pH. For example, when adding ¾ equivalence of NaOH to 100 mM pyruvic acid, the pH begins at approximately 3.5 and ends up at 12.5 after ~40 days (see Figures A6.1-A6.3 and Table A6.1 in Appendix 6). Third, near equilibrium, especially under basic conditions, a plethora of unidentified species are observed both by nuclear magnetic resonance (NMR) and negative ion electrospray ionization mass spectrometry (ESI⁻ MS) measurements (see Figures A6.4 and A6.5 and Table A6.1 in Appendix 6).

While exact quantification of equilibrium constants is extremely difficult for the reasons listed above, more approximate approaches can still be useful. For 100 mM samples of pure, doubly distilled pyruvic acid, the ratio of pyruvic acid to zymonic acid is approximately 200:1 under unadjusted, acidic conditions. For basic conditions however, the ratio shifts in favor of zymonic acid at approximately 1:4 if not more (Figures A6.1, A6.2 and Table A6.1 in Appendix 6). Under high pH conditions, it can be

difficult to quantify the amount of pyruvic acid in the NMR because of the high density of peaks. We have conservatively estimated the concentration of zymonic acid, using the upper limit for pyruvic acid; therefore, it is likely that the formation of zymonic acid may be even more favored. 100 mM pyruvic acid is a quite high concentration for most prebiotic scenarios, however. In order to estimate the ratio of pyruvic acid to zymonic acid at lower concentrations, we can use the same idea shown in equation 1. If the concentration of pyruvic acid is decreased from 100 to 10 mM, the equilibrium ratio of pyruvic acid to zymonic acid should increase by a factor of 10, yielding an estimated 2000:1 ratio of pyruvic to zymonic at low pH, and a 5:2 ratio at high pH. Decreasing the concentration further to 1 mM, we expect approximately a 20000:1 ratio at low pH and a 25:1 ratio at high pH. Even with these conservative estimates for zymonic acid availabilities, there is reason to believe that zymonic acid is a prebiotically relevant species across a wide range of pyruvic acid concentrations under basic conditions, while free pyruvic acid is much more favored under acidic conditions.

The aldol addition reaction that creates parapyruvic acid (which quickly equilibrates with other zymonic species in aqueous solution) is known to proceed further, creating larger pyruvic acid polymers as well.[39] These products can be observed in polymerized pyruvic acid that was isolated from pure pyruvic acid. Peaks associated with larger pyruvic polymers are observed using ESI⁻ MS and shown in Figure 10.3. Several zymonic acid species can be identified in 100 mM aqueous pyruvic acid under acidic conditions after 90 days via ESI⁻ MS (Figure A6.4 in Appendix 6). Larger polymer species are not observed, however, due to the nature of ESI⁻ MS measurements this does not preclude their formation. ESI⁻ MS measurements are not inherently quantitative, due to the dependence of ionization processes on not only a given analyte, but also the composition of the solution and the ESI parameters.[51]
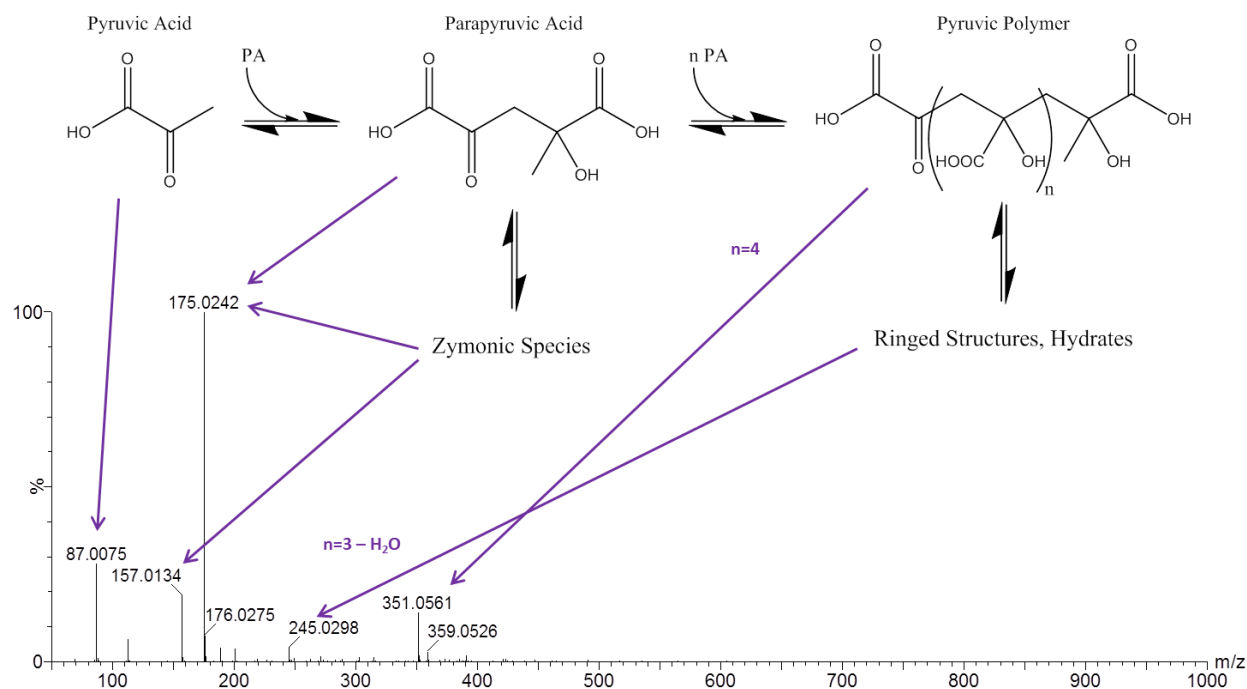
Figure 10.3: ESI⁻ MS data for polymerized pyruvic acid, with peaks indicating the existence of larger polymers, along with a general reaction scheme for the formation of zymonic acid and larger pyruvic acid polymers.

Under basic conditions, however, a wide variety of unidentified polymers are formed from 100 mM pyruvic acid solutions. The conclusive identification of these polymers has proven difficult, due to the large variety of species that are observed. Some of the species observed in the mass spectrum may be Na^+ ion adducts as well because of the addition of NaOH, further complicates the identification of detected species. After 90 days of room temperature equilibration, polymers with masses of 800 daltons or larger are observed for pyruvic acid neutralized with 1 equivalent of NaOH (Figure A6.5 in Appendix 6). These masses correspond to polymeric species composed of >9 pyruvic acid monomers. It is unclear, however, what the structures of these polymers are, and what chemical mechanisms lead to their formation. The chemistry under basic conditions may proceed through the identified zymonic acid species, but may also differ significantly from the acidic chemistry, even for low molecular weights. The diversity observed in the polymeric species, is however consistent with the polymorphic nature of zymonic acid: polymerization of a mixture of 5 species has many more accessible reactive pathways than a single species might.

An important aspect of biological polymers is their ability to degrade back into their monomeric units. For proteins, this allows for recycling and modification after synthesis. For informational polymers, this allows for repair and recycling. For sugar polymers this allows for regeneration of sugar monomers, which is crucial for their role of energy storage. Zymonic acid and the larger polymers that we observe appear to spontaneously reconvert to pyruvic acid under acidic conditions. High pH polymerized sample was re-acidified using concentrated hydrochloric acid to pH 2.6, the approximate pH of the original pyruvic acid solution, and after 26 days NMR spectra were recorded. The original solution had less than 2% of the organic H incorporated into pyruvic acid, while the acidified solution contained between 16 and 34% (Figure A6.6 in Appendix 6). The higher end of this range is more plausible for reasons discussed in the Appendix 6. The observed increase in signal is large enough that the direct conversion of zymonic acid back to pyruvic acid cannot account for the full amount of pyruvic acid recovered alone, implying that the other polymeric species are likely being converted back into pyruvic acid under acidic conditions.

10.3 Discussion

Zymonic acid clearly fulfills our simple requirements for a prebiotic sugar analogue. First, it can be directly formed from pyruvic acid, our example driver molecule. This occurs in aqueous solution at a reasonable rate for relatively concentrated pyruvic acid (100 mM) under both basic and acidic conditions. This concentration may be too high to be reasonably found in an environment like an ocean, it is perhaps not entirely unreasonable for an atmospheric aerosol. While, it is observed that pyruvic acid is favored over zymonic acid under more dilute conditions, the equilibrium is such that relatively large quantities of zymonic acid will still be present under dilute, basic conditions. Second, zymonic acid can also be converted back to pyruvic acid in solution, especially under acidic conditions. Acidification of aqueous samples containing zymonic acid resulted in the regeneration of pyruvic acid. These properties allow zymonic acid to form reactive pathways between pyruvic acid and other species, in a manner that mimics simple catabolic and anabolic pathways.

While these basic requirements are not particularly stringent, there are a number of additional features to the zymonic acid system that make it an appealing candidate for a prebiotic or early biotic sugar analogue. The most obvious property is its ability to polymerize under simple basic conditions. Many of the key functions of sugars in modern life require polymeric forms, such as information storage (RNA and DNA), cell structural components (cellulose and chitin), or energy storage reservoirs (starches and glycogen). Large sugar polymers are also present in some glycoproteins. Prebiotic chemical assemblies or even early life might not require sugars to fill these roles, but modern life clearly does. If the observed polymers are capable of playing the part of sugar polymers, it is advantageous not only due to the desirability of defined structure, information, and energy storage in maintaining a robust chemical assembly or early lifeform, but also because it provides a direct evolutionary link between early life and modern life. While it remains to be seen how well the observed polymers would be able to fill these roles, the diversity in spontaneously generated polymers increases the likelihood that functional polymers could be generated.

Another potentially advantageous property of this pyruvic acid and zymonic acid polymer system is its dependence on environmental conditions. High pH conditions favor the formation of zymonic acid and polymeric species, while low pH conditions favor free pyruvic acid. This allows for a range of different ratios of these species under various environmental conditions, allowing for room for optimization. Along with proper material transport, it also allows for establishment of a steady state, out of equilibrium system, a hallmark of life. This is possible, in principle, because of the shift in energetics as a function of pH. Molecules that were at equilibrium at high pH, when transported to an area of lower pH, become relatively higher in energy, and no longer in equilibrium. Areas where pH gradients exist are not uncommon in the environment and include hydrothermal vents and ocean/aerosol systems, which have been proposed to be of great importance in prebiotic chemistry.[29,52–56]

For the generation of out of equilibrium systems, perhaps an even more useful property of zymonic and pyruvic acids, is their ability to absorb light. Pyruvic acid and zymonic acid have UV

absorption features ($\lambda_{max, \ pyruvic}$ ~320 nm,[57] $\lambda_{max, \ zymonic}$ ~240 nm[46]) that would be capable of absorbing wavelengths of light that are accessible on the prebiotic Earth.[29,30,58] This allows for photochemical reactions to take place, potentially including reactions that result in higher energy products. Previous investigations of the photochemistry of pyruvic acid have shown the formation of complex reaction products,[30,59–62] including some products that are metabolic intermediates in modern life.[30] Very recent work also suggests that pyruvic acid can react photochemically to form zymonic acid. In bulk aqueous phase, photochemically generated parapyruvic acid serves as a reactive intermediate, leading to larger oligomeric products.[63] Under atmospherically relevant conditions, gas phase zymonic acid has been observed from the multiphase photochemistry of pyruvic acid.[62] Alkyl α-keto acids with longer carbon chains appear to react similarly to pyruvic acid, with an intermediate reminiscent of zymonic acid.[64] In a broader sense, the absorption of light allows for direct addition of energy to a chemical system. This additional energy allows for the creation of higher energy, useful compounds and, potentially, the maintenance or propagation of a non-equilibrium system. The absorption of light is the major driving force behind most of modern life, through photosynthetic organisms and their subsequent consumption by other organisms.

In addition to energy capture, an important element in maintaining an out of equilibrium system is catalytic control. The ability of chemical pathways to be activated or deactivated based on environmental conditions has the potential to create more robust chemical systems. For example, when a pathway becomes very thermodynamically favorably, it could be advantageous to slow the kinetics to prevent a loss of energy through that path. Zymonic acid formation has been shown to be catalyzed by metal ions, like Zn(II) and Ni(II).[40] As discussed previously, basic conditions seem to favor polymer formation, while acidic conditions favor zymonic acid monomers and pyruvic acid itself. Changing pH conditions from basic to acidic could result in kinetically trapped zymonic acid and polymers, but the addition of Zn(II) to the system would lower the kinetic barrier and allow for conversion back to free pyruvic acid. This is essentially a very basic regulatory response, where a signal (in this case Zn(II)) results in a chemical

change (generation of pyruvic acid). The use of Zn(II) in particular is appealing due both to its abundance in modern biology, as well as its plausible prebiotic relevance.[65] Interestingly, zymonic acid metal catalyzed systems have been shown to display oscillating, out of equilibrium chemical changes under certain conditions.[66]

Thermodynamically, the reactions that compose life are a balancing act between stability and reactivity. In modern life, this balance is shifted toward more stable chemical systems. In order to compensate for the added molecular stability, catalytic enzymes are utilized, which lower reaction barriers. This allows reactions to proceed that would otherwise not occur on reasonable timescales. This scheme has additional advantages due to the directed nature of enzymatic catalysis, promoting only a narrow range of substrates and reactions. While some degree of catalytic control may be available to prebiotic or early biotic systems, it will necessarily be less specific than the enzymatic control in modern life. Therefore, prebiotically the balance would be shifted such that more reactive chemical components are favored. Zymonic acid is more reactive than a modern sugar, as evidenced by its observed reactions in simple aqueous solutions. Because of this enhanced reactivity, zymonic acid is an intriguing sugar analogue for prebiotic chemical systems.

10.4 Conclusions

While the prebiotic chemistry of sugars has often focused on the generation of modern, strictly-defined sugars like ribose, we instead have examined more broadly the roles that sugar analogues would need to fill in prebiotic or early biotic systems. Perhaps the most important functions of sugars in life are as metabolites and energy storage reservoirs. In order to maintain this function prebiotically, it is essential that a prebiotic sugar analogue is capable of both generating, and being generated from, a prebiotically-plausible high-energy driver molecule. Further roles of sugars often involve the covalent bonding of sugar molecules to: proteins in the case of glycoproteins; lipids in the case of glycolipids; nucleosides in the case of informational polymers; and other sugars in the case of polysaccharides. While these complex

structures may not be essential to prebiotic or early living systems, it appears that the adaptability and reactivity of sugars are important to their function.

We proposed that zymonic acid is a promising candidate for a prebiotic sugar analogue, using a pyruvic acid driver molecule system. We have demonstrated its prebiotic plausibility, as well as its robust connection to pyruvic acid. It can spontaneously convert to and from pyruvic acid with relatively slow uncatalyzed rates, and the equilibrium constant between pyruvic acid and zymonic acid depends on concentration and pH. Zymonic acid displays favorable water interactions and chemical polymorphism in solution, similar to modern sugars. This likely contributes to its reactivity and its ability to polymerize. Demonstration of these reactions is a necessary first step towards harnessing them in a prebiotic or early biotic system. Furthermore, the capture of additional energy by zymonic acid is made possible via photochemistry. The ability of zymonic acid to take part in simple regulatory schemes was also discussed, relying on a combination of divalent metal catalysis and conditional dependence. This is exemplified with the establishment of out of equilibrium, oscillating chemical systems.[66] While zymonic acid is almost certainly not the only molecule capable of filling the roles of sugars in prebiotic or early biotic scenarios, it is an interesting and promising example molecule worthy of further investigation.

10.5 Materials and Methods

Pyruvic acid was purchased from Sigma-Aldrich (98%) and was distilled prior to use to remove zymonic acid and polymer products. Distillation was carried out at temperatures under 55 °C and pressures under 1 Torr. Distilled pyruvic acid was stored at 4 °C and used within one month of distillation. Zymonic acid was isolated and purified as previously described.[46] Briefly: crude zymonic acid was isolated from pyruvic acid (Sigma-Aldrich, 98%), that had been stored at 4 °C for several months, via distillation. It was further purified by washing with dry ethyl acetate (Mallinckrodt, ≥99.5%) and hexanes (Sigma-Aldrich, ≥99%). Where water was used it was deionized water with 18.2 MΩ/cm resistivity and 3 ppb total oxidizable carbon (TOC).

NMR: [1]H spectra were collected with a Varian INOVA-500 NMR spectrometer operating at 499.60 MHz. Samples were prepared in water, held at 23 °C, and an optimized WET solvent suppression sequence was used to remove >99% of the water signal.[67]

MS: Negative ion electrospray mass spectra were collected on a Waters Synapt G2 HDMS mass spectrometer. Instrument parameters were the following: analyzer, resolution mode; capillary voltage, 1.5 kV; source temperature, 80 °C; sampling cone, 30 V; extraction cone, 5 V; source gas flow, 0.00 mL/min; desolvation temperature, 150 °C; cone gas flow, 0.0 L/h; desolvation gas flow, 500.0 L/h.

Bibliography:

(1)   Zaug, A. J.; Cech, T. R. The Intervening Sequence RNA of Tetrahymena Is an Enzyme. *Science* **1986**, *231* (4737), 470–475.

(2)   Cech, T. R. A Model for the RNA-Catalyzed Replication of RNA. *Proc. Natl. Acad. Sci.* **1986**, *83* (12), 4360–4363.

(3)   Robertson, M. P.; Joyce, G. F. The Origins of the RNA World. *Cold Spring Harb. Perspect. Biol.* **2012**, *4* (5).

(4)   Ritson, D.; Sutherland, J. D. Prebiotic Synthesis of Simple Sugars by Photoredox Systems Chemistry. *Nat. Chem.* **2012**, *4* (11), 895–899.

(5)   Ritson, D. J.; Sutherland, J. D. Synthesis of Aldehydic Ribonucleotide and Amino Acid Precursors by Photoredox Chemistry. *Angew. Chem. Int. Ed.* **2013**, *52* (22), 5845–5847.

(6)   Butlerow, A. Bildung Einer Zuckerartigen Substanz Durch Synthese. *Justus Liebigs Ann. Chem.* **1861**, *120*, 295–298.

(7)   Breslow, R. On the Mechanism of the Formose Reaction. *Tetrahedron Lett.* **1959**, *1* (21), 22–26.

(8)   Ricardo, A.; Carrigan, M. A.; Olcott, A. N.; Benner, S. A. Borate Minerals Stabilize Ribose. *Science* **2004**, *303* (5655), 196–196.

(9)   Cleaves II, H. J. The Prebiotic Geochemistry of Formaldehyde. *Precambrian Res.* **2008**, *164* (3–4), 111–118.

(10)   Toxvaerd, S. The Role of Carbohydrates at the Origin of Homochirality in Biosystems. *Orig. Life Evol. Biospheres* **2013**, *43* (4–5), 391–409.

(11)   Shapiro, R. Prebiotic Ribose Synthesis: A Critical Analysis. *Orig. Life Evol. Biosph.* **1988**, *18* (1–2), 71–85.

(12)   Schwartz, A. W.; Graaf, R. M. de. The Prebiotic Synthesis of Carbohydrates: A Reassessment. *J. Mol. Evol.* **1993**, *36* (2), 101–106.

(13)   Pestunova, O.; Simonov, A.; Snytnikov, V.; Stoyanovsky, V.; Parmon, V. Putative Mechanism of the Sugar Formation on Prebiotic Earth Initiated by UV-Radiation. *Adv. Space Res.* **2005**, *36* (2), 214–219.

(14)   Cafferty, B. J.; Hud, N. V. Abiotic Synthesis of RNA in Water: A Common Goal of Prebiotic Chemistry and Bottom-up Synthetic Biology. *Curr. Opin. Chem. Biol.* **2014**, *22*, 146–157.

(15)   Orgel, L. E. Prebiotic Chemistry and the Origin of the RNA World. *Crit. Rev. Biochem. Mol. Biol.* **2004**, *39* (2), 99–123.

(16)   Kawamura, K.; Maurel, M.-C. Walking over 4 Gya: Chemical Evolution from Photochemistry to Mineral and Organic Chemistries Leading to an RNA World. *Orig. Life Evol. Biospheres* **2017**, 1–16.

(17)   Weber, A. L. Prebiotic Sugar Synthesis: Hexose and Hydroxy Acid Synthesis from Glyceraldehyde Catalyzed by Iron(III) Hydroxide Oxide. *J. Mol. Evol.* **1992**, *35* (1), 1–6.

(18)   Voet, D.; Voet, J. G. *Biochemistry*, 4th Edition Binder Ready Version edition.; Wiley: Hoboken, NJ, 2010.

(19)   Yamagata, Y. Prebiotic Formation of ADP and ATP from AMP, Calcium Phosphates and Cyanate in Aqueous Solution. *Orig. Life Evol. Biosph.* **1999**, *29* (5), 511–520.

(20)   Levy, M.; Miller, S. L.; Brinton, K.; Bada, J. L. Prebiotic Synthesis of Adenine and Amino Acids Under Europa-like Conditions. *Icarus* **2000**, *145* (2), 609–613.

(21)   Saladino, R.; Crestini, C.; Costanzo, G.; Negri, R.; Di Mauro, E. A Possible Prebiotic Synthesis of Purine, Adenine, Cytosine, and 4(3H)-Pyrimidinone from Formamide: Implications for the Origin of Life. *Bioorg. Med. Chem.* **2001**, *9* (5), 1249–1253.

(22)   Oró, J. Synthesis of Adenine from Ammonium Cyanide. *Biochem. Biophys. Res. Commun.* **1960**, *2* (6), 407–412.

(23)   Voet, A. B.; Schwartz, A. W. Prebiotic Adenine Synthesis from HCN—Evidence for a Newly Discovered Major Pathway. *Bioorganic Chem.* **1983**, *12* (1), 8–17.

(24)   Shapiro, R. The Prebiotic Role of Adenine: A Critical Analysis. *Orig. Life Evol. Biosph.* **1995**, *25* (1–3), 83–98.

(25)   Orgel, L. E. Prebiotic Adenine Revisited: Eutectics and Photochemistry. *Orig. Life Evol. Biosph.* **2004**, *34* (4), 361–369.

(26)   Eakin, R. E. An Approach to the Evolution of Metabolism. *Proc. Natl. Acad. Sci.* **1963**, *49* (3), 360–366.

(27)   Fry, I. *Emergence of Life on Earth: A Historical and Scientific Overview*, 1 edition.; Rutgers University Press, 2000.

(28)   Shapiro, R. Small Molecule Interactions Were Central to the Origin of Life. *Q. Rev. Biol.* **2006**, *81* (2), 105–126.

(29)   Rapf, R. J.; Vaida, V. Sunlight as an Energetic Driver in the Synthesis of Molecules Necessary for Life. *Phys. Chem. Chem. Phys.* **2016**.

(30)   Griffith, E. C.; Shoemaker, R. K.; Vaida, V. Sunlight-Initiated Chemistry of Aqueous Pyruvic Acid: Building Complexity in the Origin of Life. *Orig. Life Evol. Biospheres* **2013**, *43* (4–5), 341–352.

(31)   Hazen, R. M.; Deamer, D. W. Hydrothermal Reactions of Pyruvic Acid: Synthesis, Selection, and Self-Assembly of Amphiphilic Molecules. *Orig. Life Evol. Biospheres* **2007**, *37* (2), 143–152.

(32)   Cooper, G.; Reed, C.; Nguyen, D.; Carter, M.; Wang, Y. Detection and Formation Scenario of Citric Acid, Pyruvic Acid, and Other Possible Metabolism Precursors in Carbonaceous Meteorites. *Proc. Natl. Acad. Sci.* **2011**, *108* (34), 14015–14020.

(33)   Pizzarello, S.; Lahav, M. On the Emergence of Biochemical Homochirality: An Elusive Beginning. *Orig. Life Evol. Biospheres* **2009**, *40* (1), 1–2.

(34)   Guzman, M. I.; Martin, S. T. Photo-Production of Lactate from Glyoxylate: How Minerals Can Facilitate Energy Storage in a Prebiotic World. *Chem. Commun.* **2010**, *46* (13), 2265–2267.

(35)   Wolff, L. Ueber Ein Neues Condensationsproduct Der Brenztraubensäure. *Justus Liebigs Ann. Chem.* **1901**, *317* (1), 1–22.

(36)   Wolff, L. I. Ueber Die Synthese Der Uvitinsäure Aus Brenztraubensäure. *Justus Liebigs Ann. Chem.* **1899**, *305* (2), 125–153.

(37)   Wolff, L. II. Ueber Die Parabrenztraubensäure. *Justus Liebigs Ann. Chem.* **1899**, *305* (2), 154–165.

(38)   de Jong, A. W. K. Les Transformations Des Sels de l'acide Pyruvique. *Recl. Trav. Chim. Pays-Bas Belg.* **1901**, *20* (10), 365–387.

(39)   Prey, V.; Waldmann, E.; Berbalk, H. Zur Kenntnis der Brenztraubensäure. *Monatshefte Für Chem. Verwandte Teile Anderer Wiss.* **1955**, *86* (3), 408–413.

(40)   Tallman, D. E.; Leussing, D. L. Pyruvate Dimerization Catalyzed by Nickel(II) and Zinc(II). II. Kinetics. *J. Am. Chem. Soc.* **1969**, *91* (23), 6256–6262.

(41)   Tallman, D. E.; Leussing, D. L. Pyruvate Dimerization Catalyzed by Nickel(II) and Zinc(II). I. Equilibrium with Nickel(II) and Zinc(II). *J. Am. Chem. Soc.* **1969**, *91* (23), 6253–6256.

(42)   Novikov, Y.; Copley, S. D. Reactivity Landscape of Pyruvate under Simulated Hydrothermal Vent Conditions. *Proc. Natl. Acad. Sci.* **2013**, *110* (33), 13283–13288.

(43)   Montgomery, C. M.; Webb, J. L. Detection of a New Inhibitor of the Tricarboxylic Acid Cycle. *Science* **1954**, *120* (3125), 843–844.

(44)   Montgomery, C. M.; Webb, J. L. Metabolic Studies on Heart Mitochondria II. the Inhibitory Action of Parapyruvate on the Tricarboxylic Acid Cycle. *J. Biol. Chem.* **1956**, *221* (1), 359–368.

(45)   Marcus, A.; Shannon, L. M. γ-Methyl-γ-Hydroxy-α-Ketoglutaric Aldolase II. STUDIES WITH PYRUVATE-C14. *J. Biol. Chem.* **1962**, *237* (11), 3348–3353.

(46) Perkins, R. J.; Shoemaker, R. K.; Carpenter, B. K.; Vaida, V. Chemical Equilibria and Kinetics in Aqueous Solutions of Zymonic Acid. *J. Phys. Chem. A* **2016**, *120* (51), 10096–10107.

(47) Cooper, G.; Rios, A. C. Enantiomer Excesses of Rare and Common Sugar Derivatives in Carbonaceous Meteorites. *Proc. Natl. Acad. Sci.* **2016**, *113* (24), E3322–E3331.

(48) Dong, H.; Ignés-Mullol, J.; Claret, J.; Pérez, L.; Pinazo, A.; Sagués, F. Interfacial Chiral Selection by Bulk Species. *Chem. – Eur. J.* **2014**, *20* (24), 7396–7401.

(49) Toxvaerd, S. Origin of Homochirality in Biosystems. *Int. J. Mol. Sci.* **2009**, *10* (3), 1290–1299.

(50) Pizzarello, S.; Weber, A. L. Stereoselective Syntheses of Pentose Sugars Under Realistic Prebiotic Conditions. *Orig. Life Evol. Biospheres* **2009**, *40* (1), 3–10.

(51) Cech, N. B.; Enke, C. G. Practical Implications of Some Recent Studies in Electrospray Ionization Fundamentals. *Mass Spectrom. Rev.* **2001**, *20* (6), 362–387.

(52) Hazen, R. M.; Sverjensky, D. A. Mineral Surfaces, Geochemical Complexities, and the Origins of Life. *Cold Spring Harb. Perspect. Biol.* **2010**, *2* (5), a002162.

(53) Russell, M. J.; Nitschke, W.; Branscomb, E. The Inevitable Journey to Being. *Phil Trans R Soc B* **2013**, *368* (1622), 20120254.

(54) Dobson, C. M.; Ellison, G. B.; Tuck, A. F.; Vaida, V. Atmospheric Aerosols as Prebiotic Chemical Reactors. *Proc. Natl. Acad. Sci. U. S. A.* **2000**, *97* (22), 11864–11868.

(55) Donaldson, D. J.; Tervahattu, H.; Tuck, A. F.; Vaida, V. Organic Aerosols and the Origin of Life: An Hypothesis. *Orig. Life Evol. Biosph.* **2004**, *34* (1–2), 57–67.

(56) Griffith, E. C.; Tuck, A. F.; Vaida, V. Ocean-Atmosphere Interactions in the Emergence of Complexity in Simple Chemical Systems. *Acc. Chem. Res.* **2012**, *45*, 2106–2113.

(57) Griffith, E. C.; Carpenter, B. K.; Shoemaker, R. K.; Vaida, V. Photochemistry of Aqueous Pyruvic Acid. *Proc. Natl. Acad. Sci.* **2013**, 201303206.

(58) Rugheimer, S.; Segura, A.; Kaltenegger, L.; Sasselov, D. UV Surface Environment of Earth-like Planets Orbiting FGKM Stars Through Geological Evolution. *Astrophys. J.* **2015**, *806* (1), 137.

(59) Reed Harris, A. E.; Ervens, B.; Shoemaker, R. K.; Kroll, J. A.; Rapf, R. J.; Griffith, E. C.; Monod, A.; Vaida, V. Photochemical Kinetics of Pyruvic Acid in Aqueous Solution. *J. Phys. Chem. A* **2014**, *118* (37), 8505–8516.

(60) Renard, P.; Reed Harris, A. E.; Rapf, R. J.; Ravier, S.; Demelas, C.; Coulomb, B.; Quivet, E.; Vaida, V.; Monod, A. Aqueous Phase Oligomerization of Methyl Vinyl Ketone by Atmospheric Radical Reactions. *J. Phys. Chem. C* **2014**, *118* (50), 29421–29430.

(61) Guzman, M. I.; Colussi, A. J.; Hoffmann, M. R. Photoinduced Oligomerization of Aqueous Pyruvic Acid. *J. Phys. Chem. A* **2006**, *110*, 3619–3626.

(62) Reed Harris, A. E.; Pajunoja, A.; Cazaunau, M.; Gratien, A.; Pangui, E.; Monod, A.; Griffith, E. C.; Virtanen, A.; Doussin, J.-F.; Vaida, V. Multiphase Photochemistry of Pyruvic Acid under Atmospheric Conditions. *J. Phys. Chem. A* **2017**.

(63)   Rapf, R. J.; Perkins, R. J.; Carpenter, B. K.; Vaida, V. Mechanistic Description of Photochemical Oligomer Formation from Aqueous Pyruvic Acid. *J. Phys. Chem. A* **2017**.

(64)   Rapf, R. J.; Perkins, R. J.; Yang, H.; Miyake, G. M.; Carpenter, B. K.; Vaida, V. Photochemical Synthesis of Oligomeric Amphiphiles from Alkyl Oxoacids in Aqueous Environments. *J. Am. Chem. Soc.* **2017**, *139* (20), 6946–6959.

(65)   Hazen, R. M. Paleomineralogy of the Hadean Eon: A Preliminary Species List. *Am. J. Sci.* **2013**, *313* (9), 807–843.

(66)   Lin, H.-L.; Yu, Y.-O.; Jwo, J.-J. Kinetic Study of the Ce(III)-, Mn(II)-, or Ferroin-Catalyzed Belousov-Zhabotinsky Reaction with Pyruvic Acid. *Int. J. Chem. Kinet.* **2000**, *32* (7), 408–418.

(67)   Ogg, R. J.; Kingsley, P. B.; Taylor, J. S. WET, a T1- and B1-Insensitive Water-Suppression Method for in Vivo Localized 1H NMR Spectroscopy. *J. Magn. Reson. B* **1994**, *104* (1), 1–10.

Chapter 11: Concluding Remarks

Throughout this manuscript there has been a focus on the partitioning of material to aqueous interfacial regions. The driving forces behind partitioning and the consequences of such partitioning were investigated. The consequences of surface partitioning were shown to be particularly important in Chapters 3, 5, and 6, which discussed the genetic disorder phenylketonuria (PKU). These studies conclude that the partitioning of phenylalanine (Phe) into interfacial regions changes the morphology and interfacial tension of a model cell membrane (Chapter 3 and 5), and leads to an increase in the permeability of the membrane (Chapter 6). This provides a plausible molecular-level mechanism for the cellular damage associated with untreated PKU.

In these systems, surface partitioning was driven by a complex mixture of forces. An investigation of a series of molecules structurally similar to Phe was undertaken in chapter 5 to elucidate these. Despite the structural similarities of the molecules in the series, contrasting solution and surface behavior were observed. The solution and interfacial properties also diverged from what would be predicted by a simple hydrophobic framework. It was ultimately concluded that interactions between aromatic species were the dominant factors controlling the observed behavior, due largely to interfacial clustering. This illustrated an important point about surface partitioning: as with any consideration of phase partitioning, the energetics of all available phases must be considered. Theories of hydrophobicity can be used to predict the interactions between dissolved species and water with reasonable success. However, they fail to adequately predict the energetics of material in the interfacial phase and do not attempt to predict the energy of material in a pure or very solute rich phase (in the case of precipitate formation, liquid-liquid phase separation, etc.). Because of this, hydrophobic theories can only be predictive of surface partitioning to the extent that pure and interfacial phase energetics are not changing within a series, or the changes are insignificant compared to the aqueous energetics.

Theories of hydrophobicity are often further confounded by the term "hydrophobicity" being used in very different ways. It could be said that a material is hydrophobic due to its preferential partitioning

into octanol out of water. Or it could be hydrophobic because it has low solubility in water. Or it could be hydrophobic because it disrupts the hydrogen bonding network of water. Or it partitions to an interfacial region. In some cases these properties are related, but the underlying thermodynamic quantities that govern them are generally not the same. So while a molecule may be "hydrophobic" based on one property that does not guarantee that it will act "hydrophobically" when considering other properties.

Beyond developing a more nuanced understanding of the factors that can drive surface partitioning, I have also shown that partitioned material can affect the properties of the interface. By examining the interfacial aggregation of Phe, I was able to not only explain its partitioning behavior, but also to explain the effect Phe has on other interfacial species, such as model membrane systems. While it is commonly accepted that the interfacial structure dictates the behavior of insoluble surfactants, this idea has not often been applied to soluble ones. The interfacial aggregation of Phe appears to explain the changes in membrane permeability discussed in Chapter 6, while phenylacetic acid, which was shown to partition to the surface in Chapter 5 but did not alter membrane permeability.

Water plays important roles not only as a solvent, but also as a reactive species, as the studies in Chapter 4, 8, 9 and 10 document. In Chapter 4, hydrolysis reactions were examined and in Chapters 8-10 aldol-addition reactions, lactone ring formations, and reactions transforming ketone, enol, and geminal diol functional groups were investigated. In all of these reactions water plays a critical role as a reactant, a product, and/or a catalyst. The pH of an aqueous solution, while often thought of as simply the amount of added acid or base, can also be considered a measure of the reactivity of water in a given solution. The unique reactivity of water is particularly important given its ubiquity in the natural environment and biology, governing in many cases the equilibria and kinetics of networks of reactions.

Aqueous interactions are inseparable from so many aspects of chemistry and life. Much progress has been made in understanding water, but there is much more work to do. Through this dissertation and

the associated works, I hope to have contributed to a deeper understanding of the complex, fascinating, and essential material that is water.

Bibliography

Adams, E. M., & Allen, H. C. (2013). Palmitic Acid on Salt Subphases and in Mixed Monolayers of Cerebrosides: Application to Atmospheric Aerosol Chemistry. *Atmosphere*, *4*(4), 315–336. https://doi.org/10.3390/atmos4040315

Adler-Abramovich, L., Vaks, L., Carny, O., Trudler, D., Magno, A., Caflisch, A., Frenkel, D., & Gazit, E. (2012). Phenylalanine assembly into toxic fibrils suggests amyloid etiology in phenylketonuria. *Nat Chem Biol*, *8*(8), 701–706. https://doi.org/10.1038/nchembio.1002

Advanced Chemistry Development (ACD/Labs) Software. (n.d.). (Version 11.02).

Ahuja, R. C., Caruso, P. L., Moebius, D., Wildburg, G., Ringsdorf, H., Philp, D., Stoddart, J. F., & Preece, J. A. (1993). Molecular organization via ionic interactions at interfaces. 1. Monolayers and LB films of cyclic bisbipyridinium tetracations and dimyristoylphosphatidic acid. *Langmuir*, *9*(6), 1534–1544. https://doi.org/10.1021/la00030a019

Albert, A. (1984). *The Determination of Ionization Constants : A Laboratory Manual* (3rd ed.). New York: Chapman and Hall. Retrieved from http://trove.nla.gov.au/work/8286316?selectedversion=NBD3143139

Altieri, K. E., Carlton, A. G., Lim, H.-J., Turpin, B. J., & Seitzinger, S. P. (2006). Evidence for Oligomer Formation in Clouds: Reactions of Isoprene Oxidation Products. *Environmental Science & Technology*, *40*(16), 4956–4960. https://doi.org/10.1021/es052170n

Andreae, M. O., Talbot, R. W., & Li, S. M. (1987). Atmospheric Measurements of Pyruvic and Formic-Acid. *Journal of Geophysical Research: Atmospheres*, *92*, 6635–6641. https://doi.org/DOI 10.1029/JD092iD06p06635

Andrews, C. T., & Elcock, A. H. (2013). Molecular Dynamics Simulations of Highly Crowded Amino Acid Solutions: Comparisons of Eight Different Force Field Combinations with Experiment and with Each Other. *Journal of Chemical Theory and Computation*, *9*(10), 4585–4602. https://doi.org/10.1021/ct400371h

Ariza, A., Richard, D. J., White, M. F., & Bond, C. S. (2005). Conformational flexibility revealed by the crystal structure of a crenarchaeal RadA. *Nucleic Acids Research*, *33*(5), 1465–1473. https://doi.org/10.1093/nar/gki288

Avdeef, A., Box, K. J., Comer, J. E., Hibbert, C., & Tam, K. Y. (1998). pH-metric logP 10. Determination of liposomal membrane-water partition coefficients of ionizable drugs. *Pharmaceutical Research*, *15*(2), 209–215.

Barnes, G. T., Lawrie, G. A., & Walker, K. (1998). Equilibrium Penetration of Monolayers. 9. A Comparison of Treatments for Analyzing Surface-Pressure−Area Data. *Langmuir*, *14*(8), 2148–2154. https://doi.org/10.1021/la970201p

Bayly, C. I., Cieplak, P., Cornell, W., & Kollman, P. A. (1993). A well-behaved electrostatic potential based method using charge restraints for deriving atomic charges: the RESP model. *The Journal of Physical Chemistry*, *97*(40), 10269–10280. https://doi.org/10.1021/j100142a004

Berges, M. G., & Warneck, P. (1992). Product quantum yields for the 350 nm photodecomposition of pyruvic acid in air. *Berichte Der Bunsengesellschaft Für Physikalische Chemie*, *96*(3), 413–416.

Berkowitz, M. L., Bostick, D. L., & Pandit, S. (2006). Aqueous Solutions next to Phospholipid Membrane Surfaces: Insights from Simulations. *Chemical Reviews*, *106*(4), 1527–1539. https://doi.org/10.1021/cr0403638

Berzelius, J. J. (1835). Ueber die Destillationsproducte der Traubensäure. *Annalen Der Physik*, *112*(9), 1–29. https://doi.org/10.1002/andp.18351120902

Berzelius, J. J. (1960). On Dry Distilled Racemic Acid. *Acta Chemica Scandinavica*, *14*, 1677–1680. https://doi.org/10.3891/acta.chem.scand.14-1677

Björneholm, O., Hansen, M. H., Hodgson, A., Liu, L.-M., Limmer, D. T., Michaelides, A., Pedevilla, P., Rossmeisl, J., Shen, H., Tocci, G., Tyrode, E., Walz, M.-M., Werner, J., & Bluhm, H. (2016). Water at Interfaces. *Chemical Reviews*. https://doi.org/10.1021/acs.chemrev.6b00045

Blodgett, K. B. (1935). Films Built by Depositing Successive Monomolecular Layers on a Solid Surface. *Journal of the American Chemical Society*, *57*(6), 1007–1022. https://doi.org/10.1021/ja01309a011

Bloomer, J. L., & Gross, M. A. (1970). Biosynthesis of zymonic acid in trichosporon capitatum. *Journal of the Chemical Society D: Chemical Communications*, (2), 73–74. https://doi.org/10.1039/C29700000073

Bloomer, J. L., Gross, M. A., Kappler, F. E., & Pandey, G. N. (1970). Identity of "zymonic acid" with a pyruvate derivative. *Journal of the Chemical Society D: Chemical Communications*, (16), 1030a–1030a. https://doi.org/10.1039/C2970001030A

Bohanon, T. M., Caruso, P.-L., Denzinger, S., Fink, R., Möbius, D., Paulus, W., Preece, J. A., Ringsdorf, H., & Schollmeyer, D. (1999). Molecular Recognition-Induced Function and Competitive Replacement by Hydrogen-Bonding Interactions: Amphiphilic Barbituric Acid Derivatives, 2,4,6-Triaminopyrimidine, and Related Structures at the Air−Water Interface. *Langmuir*, *15*(1), 174–184. https://doi.org/10.1021/la980348w

Boris, A. J., Desyaterik, Y., & Collett, J. L. (2014). How do components of real cloud water affect aqueous pyruvate oxidation? *Atmospheric Research*, *143*, 95–106. https://doi.org/Doi 10.1016/J.Atmosres.2014.02.004

Böttinger, C. (1877). Beitrag zur Kenntniss der Brenztraubensäure. *Justus Liebigs Annalen Der Chemie*, *188*(3), 293–342. https://doi.org/10.1002/jlac.18771880305

Boucher, O., Randall, D., Artaxo, P., Bretherton, C., Feingold, G., Forster, P., Kerminen, V. M., Kondo, Y., Liao, H., Lohmann, U., Rasch, P., Satheesh, S. K., Sherwood, S., Stevens, B., & Zhang, X. Y. (2013). Clouds and aerosols. In T. F. Stocker, D. Qin, G. K. Plattner, M. Tignor, S. K. Allen, J. Boschung, A. Nauels, Y. Xia, V. Bex, & P. M. Midgley (Eds.), *Climate Change 2013: The Physical Science Basis. Contribution of Working Group I to the Fifth Assessment Report of the Intergovernmental Panel on Climate Change* (pp. 465–570). Cambridge, U.K. and New York, NY, USA: Cambridge Univ. Press,. https://doi.org/10.1017/CBO9781107415324.016

Boyer, R. D., Johnson, R., & Krishnamurthy, K. (2003). Compensation of refocusing inefficiency with synchronized inversion sweep (CRISIS) in multiplicity-edited HSQC. *Journal of Magnetic Resonance*, *165*(2), 253–259. https://doi.org/10.1016/j.jmr.2003.08.009

Brégonzio-Rozier, L., Giorio, C., Siekmann, F., Pangui, E., Morales, S., Temime-Roussel, B., Gratien, A., Michoud, V., Cazaunau, M., & DeWitt, H. (2016). Secondary organic aerosol formation from

isoprene photooxidation during cloud condensation–evaporation cycles. *Atmospheric Chemistry and Physics*, *16*(3), 1747–1760.

Breslow, R. (1959). On the mechanism of the formose reaction. *Tetrahedron Letters*, *1*(21), 22–26. https://doi.org/10.1016/S0040-4039(01)99487-0

Brockman, H. (1999). Lipid monolayers: why use half a membrane to characterize protein-membrane interactions? *Current Opinion in Structural Biology*, *9*(4), 438–443. https://doi.org/10.1016/S0959-440X(99)80061-X

Brooks Avery Jr., G., Willey, J. D., & Kieber, R. J. (2001). Diurnal variations in major rainwater components at a coastal site in North Carolina. *Atmospheric Environment*, *35*(23), 3927–3933. https://doi.org/10.1016/S1352-2310(01)00202-3

Buldain, G., Santos, C. D. L., & Frydman, B. (1985). Carbon-13 nuclear magnetic resonance spectra of the hydrate, keto and enol forms of oxalacetic acid. *Magnetic Resonance in Chemistry*, *23*(6), 478–481. https://doi.org/10.1002/mrc.1260230615

Buschmann, H., Füldner, H., & Knoche, W. (1980). The Reversible Hydration of Carbonyl Compounds in Aqueous Solution. Part I, The Keto/Gem-diol Equilibrium. *Berichte Der Bunsengesellschaft Für Physikalische Chemie*, *84*(1), 41–44.

Buschmann, H. J., Dutkiewicz, E., & Knoche, W. (1982). The reversible hydration of carbonyl compounds in aqueous solution.2. The kinetics of the keto gen-diol transition. *Berichte Der Bunsen-Gesellschaft Physical Chemistry Chemical Physics*, *86*, 129–134.

Bussi, G., Donadio, D., & Parrinello, M. (2007). Canonical sampling through velocity-rescaling. *The Journal of Chemical Physics*, *126*(1), 014101. https://doi.org/10.1063/1.2408420

Butlerow, A. (1861). Bildung einer zuckerartigen Substanz durch Synthese. *Justus Liebigs Annalen Der Chemie*, *120*, 295–298.

Cafferty, B. J., & Hud, N. V. (2014). Abiotic synthesis of RNA in water: a common goal of prebiotic chemistry and bottom-up synthetic biology. *Current Opinion in Chemical Biology*, *22*, 146–157. https://doi.org/10.1016/j.cbpa.2014.09.015

Carlton, A. G., Turpin, B. J., Lim, H.-J., Altieri, K. E., & Seitzinger, S. (2006). Link between isoprene and secondary organic aerosol (SOA): Pyruvic acid oxidation yields low volatility organic acids in clouds. *Geophysical Research Letters*, *33*(6), L06822. https://doi.org/10.1029/2005GL025374

Carlton, A. G., Wiedinmyer, C., & Kroll, J. H. (2009). A review of Secondary Organic Aerosol (SOA) formation from isoprene. *Atmospheric Chemistry and Physics*, *9*, 4987–5005.

C.D. Carver (Ed.). (1982). *The Coblentz Society Desk Book of Infrared Spectra, Second Edition*. Kirkwood, MO: The Coblentz Society. Retrieved from http://webbook.nist.gov/cgi/cbook.cgi?ID=C127173&Units=SI&Type=IR-SPEC&Index=1#IR-SPEC

Cech, N. B., & Enke, C. G. (2001). Practical implications of some recent studies in electrospray ionization fundamentals. *Mass Spectrometry Reviews*, *20*(6), 362–387. https://doi.org/10.1002/mas.10008

Cech, T. R. (1986). A model for the RNA-catalyzed replication of RNA. *Proceedings of the National Academy of Sciences*, *83*(12), 4360–4363.

Chandler, D. (2002). Hydrophobicity: Two faces of water. *Nature*, *417*(6888), 491–491. https://doi.org/10.1038/417491a

Chang, X. P., Fang, Q., & Cui, G. L. (2014). Mechanistic photodecarboxylation of pyruvic acid: Excited-state proton transfer and three-state intersection. *Journal of Chemical Physics*, *141*, 154311. https://doi.org/Artn 154311 10.1063/1.4898085

Charlson, R. J. (2001). ATMOSPHERIC SCIENCE: Reshaping the Theory of Cloud Formation. *Science*, *292*(5524), 2025–2026. https://doi.org/10.1126/science.1060096

Chastang, J. C. (1983). Oblique Viewing Attachment For Microscope. *Proceedings of the SPIE*, *399*, 239–245. https://doi.org/10.1117/12.935437

CHAU, P.-L., & HARDWICK, A. J. (1998). A new order parameter for tetrahedral configurations. *Molecular Physics*, *93*(3), 511–518. https://doi.org/10.1080/002689798169195

Chen, P. Y., Pearce, D., & Verkman, A. S. (1988). Membrane water and solute permeability determined quantitatively by self-quenching of an entrapped fluorophore. *Biochemistry*, *27*(15), 5713–5718. https://doi.org/10.1021/bi00415a048

Chen, X., & Allen, H. C. (2009). Interactions of Dimethylsulfoxide with a Dipalmitoylphosphatidylcholine Monolayer Studied by Vibrational Sum Frequency Generation†. *The Journal of Physical Chemistry A*, *113*(45), 12655–12662. https://doi.org/10.1021/jp905066w

Chen, X., Huang, Z., Hua, W., Castada, H., & Allen, H. C. (2010). Reorganization and Caging of DPPC, DPPE, DPPG, and DPPS Monolayers Caused by Dimethylsulfoxide Observed Using Brewster Angle Microscopy. *Langmuir*, *26*(24), 18902–18908. https://doi.org/10.1021/la102842a

Choo-Smith, L.-P., Garzon-Rodriguez, W., Glabe, C. G., & Surewicz, W. K. (1997). Acceleration of Amyloid Fibril Formation by Specific Binding of Aβ-(1–40) Peptide to Ganglioside-containing Membrane Vesicles. *Journal of Biological Chemistry*, *272*(37), 22987–22990. https://doi.org/10.1074/jbc.272.37.22987

Claeys, M., Graham, B., Vas, G., Wang, W., Vermeylen, R., Pashynska, V., Cafmeyer, J., Guyon, P., Andreae, M. O., Artaxo, P., & Maenhaut, W. (2004). Formation of secondary organic aerosols through photooxidation of isoprene. *Science*, *303*, 1173–1176. https://doi.org/10.1126/science.1092805

Cleary, M. A., Walter, J. H., Wraith, J. E., White, F., Tyler, K., & Jenkins, J. P. (1995). Magnetic resonance imaging in phenylketonuria: reversal of cerebral white matter change. *The Journal of Pediatrics*, *127*(2), 251–255.

Cleaves II, H. J. (2008). The prebiotic geochemistry of formaldehyde. *Precambrian Research*, *164*(3–4), 111–118. https://doi.org/10.1016/j.precamres.2008.04.002

Closs, G. L., & Miller, R. J. (1978). Photoreduction and photodecarboxylation of pyruvic acid. Applications of CIDNP to mechanistic photochemistry. *Journal of the American Chemical Society*, *100*(11), 3483–3494. https://doi.org/10.1021/ja00479a033

Cody, G. D., Boctor, N. Z., Filley, T. R., Hazen, R. M., Scott, J. H., Sharma, A., & Yoder, H. S. (2000). Primordial Carbonylated Iron-Sulfur Compounds and the Synthesis of Pyruvate. *Science*, *289*(5483), 1337–1340. https://doi.org/10.1126/science.289.5483.1337

Cohen Stuart, M. A., Wegh, R. A. J., Kroon, J. M., & Sudhölter, E. J. R. (1996). Design and Testing of a Low-Cost and Compact Brewster Angle Microscope. *Langmuir*, *12*(11), 2863–2865. https://doi.org/10.1021/la9507592

Colberg, M. R., Watkins, R. J., & Krogh, O. D. (1984). Vibrationally excited carbon dioxide produced by infrared multiphoton pyrolysis. *The Journal of Physical Chemistry*, *88*(13), 2817–2821. https://doi.org/10.1021/j150657a030

Connell, M. A., Bowyer, P. J., Adam Bone, P., Davis, A. L., Swanson, A. G., Nilsson, M., & Morris, G. A. (2009). Improving the accuracy of pulsed field gradient NMR diffusion experiments: Correction for gradient non-uniformity. *Journal of Magnetic Resonance*, *198*(1), 121–131. https://doi.org/10.1016/j.jmr.2009.01.025

Cooper, G., Reed, C., Nguyen, D., Carter, M., & Wang, Y. (2011). Detection and formation scenario of citric acid, pyruvic acid, and other possible metabolism precursors in carbonaceous meteorites. *Proceedings of the National Academy of Sciences*, *108*(34), 14015–14020. https://doi.org/10.1073/pnas.1105715108

Coutinho, A., Loura, L. M. S., & Prieto, M. (2011). FRET studies of lipid-protein aggregates related to amyloid-like fibers. *Journal of Neurochemistry*, *116*(5), 696–701. https://doi.org/10.1111/j.1471-4159.2010.07000.x

Creuwels, L. A., van Golde, L. M., & Haagsman, H. P. (1997). The pulmonary surfactant system: biochemical and clinical aspects. *Lung*, *175*(1), 1–39.

da Silva, G. (2015). Decomposition of Pyruvic Acid on the Ground State Potential Energy Surface. *The Journal of Physical Chemistry A*. https://doi.org/10.1021/acs.jpca.5b10078

Darden, T., York, D., & Pedersen, L. (1993). Particle mesh Ewald: An N·log(N) method for Ewald sums in large systems. *The Journal of Chemical Physics*, *98*(12), 10089–10092. https://doi.org/10.1063/1.464397

Davidson, R. S., Goodwin, D., & De Violet, P. F. (1981). The mechanism of the photo-induced decarboxylatton of pyruvic acid in solution. *Chemical Physics Letters*, *78*(3), 471–474. https://doi.org/10.1016/0009-2614(81)85239-6

de Jong, A. W. K. (1901). Les transformations des sels de l'acide pyruvique. *Recueil Des Travaux Chimiques Des Pays-Bas et de La Belgique*, *20*(10), 365–387. https://doi.org/10.1002/recl.19010201005

De Man, J. (1959). The formation of diacetyl and acetoin from α-acetolactic acid. *Recueil Des Travaux Chimiques Des Pays-Bas*, *78*(7), 480–486.

Dhanya, S., Maity, D. K., Upadhyaya, H. P., Kumar, A., Naik, P. D., & Saini, R. D. (2003). Dynamics of OH formation in photodissociation of pyruvic acid at 193 nm. *Journal of Chemical Physics*, *118*, 10093–10100. https://doi.org/10.1063/1.1572133

Do, T. D., de Almeida, N. E. C., LaPointe, N. E., Chamas, A., Feinstein, S. C., & Bowers, M. T. (2016). Amino Acid Metaclusters: Implications of Growth Trends on Peptide Self-Assembly and Structure. *Analytical Chemistry*, *88*(1), 868–876. https://doi.org/10.1021/acs.analchem.5b03454

Do, T. D., Kincannon, W. M., & Bowers, M. T. (2015). Phenylalanine Oligomers and Fibrils: The Mechanism of Assembly and the Importance of Tetramers and Counterions. *Journal of the American Chemical Society*, *137*(32), 10080–10083. https://doi.org/10.1021/jacs.5b05482

Dobson, C. M., Ellison, G. B., Tuck, A. F., & Vaida, V. (2000). Atmospheric aerosols as prebiotic chemical reactors. *Proceedings of the National Academy of Sciences of the United States of America*, *97*(22), 11864–11868.

Dołowy, K. (1979). Effect of interfacial tension and curvature of charged lipid bilayer-polylysine complexes. *Bioelectrochemistry and Bioenergetics*, *6*(2), 305–307. https://doi.org/10.1016/0302-4598(79)87015-4

Domagal-Goldman, S. D., Wright, K. E., Adamala, K., Arina de la Rubia, L., Bond, J., Dartnell, L. R., Goldman, A. D., Lynch, K., Naud, M.-E., Paulino-Lima, I. G., Singer, K., Walter-Antonio, M., Abrevaya, X. C., Anderson, R., Arney, G., Atri, D., Azúa-Bustos, A., … Wong, T. (2016). The Astrobiology Primer v2.0. *Astrobiology*, *16*(8), 561–653. https://doi.org/10.1089/ast.2015.1460

Domene, C., Vemparala, S., Klein, M. L., Vénien-Bryan, C., & Doyle, D. A. (2006). Role of Aromatic Localization in the Gating Process of a Potassium Channel. *Biophysical Journal*, *90*(1), L01–L03. https://doi.org/10.1529/biophysj.105.072116

Donaldson, D. J., Tervahattu, H., Tuck, A. F., & Vaida, V. (2004). Organic Aerosols and the Origin of Life: An Hypothesis. *Origins of Life and Evolution of the Biosphere*, *34*(1–2), 57–67. https://doi.org/10.1023/B:ORIG.0000009828.40846.b3

Donaldson, D. J., & Vaida, V. (2006). The Influence of Organic Films at the Air–Aqueous Boundary on Atmospheric Processes. *Chemical Reviews*, *106*(4), 1445–1461. https://doi.org/10.1021/cr040367c

Duan, Y., Wu, C., Chowdhury, S., Lee, M. C., Xiong, G., Zhang, W., Yang, R., Cieplak, P., Luo, R., Lee, T., Caldwell, J., Wang, J., & Kollman, P. (2003). A point-charge force field for molecular mechanics simulations of proteins based on condensed-phase quantum mechanical calculations. *Journal of Computational Chemistry*, *24*(16), 1999–2012. https://doi.org/10.1002/jcc.10349

Duffy, D. C., Davies, P. B., Bain, C. D., Ward, R. N., & Creeth, A. M. (1995). Sum frequency vibrational spectroscopy of the solid-liquid interface (Vol. 2547, pp. 342–351). https://doi.org/10.1117/12.221487

Duncan, S. L., & Larson, R. G. (2008). Comparing Experimental and Simulated Pressure-Area Isotherms for DPPC. *Biophysical Journal*, *94*(8), 2965–2986. https://doi.org/10.1529/biophysj.107.114215

Dyson, H. J., & Wright, P. E. (2005). Intrinsically unstructured proteins and their functions. *Nature Reviews. Molecular Cell Biology*, *6*(3), 197–208. https://doi.org/10.1038/nrm1589

Eakin, R. E. (1963). An Approach to the Evolution of Metabolism. *Proceedings of the National Academy of Sciences*, *49*(3), 360–366.

Eaves, J. D., Tokmakoff, A., & Geissler, P. L. (2005). Electric Field Fluctuations Drive Vibrational Dephasing in Water. *The Journal of Physical Chemistry A*, *109*(42), 9424–9436. https://doi.org/10.1021/jp051364m

Ebben, C. J., Strick, B. F., Upshur, M. A., Chase, H. M., Achtyl, J. L., Thomson, R. J., & Geiger, F. M. (2014). Towards the identification of molecular constituents associated with the surfaces of

isoprene-derived secondary organic aerosol (SOA) particles. *Atmos. Chem. Phys.*, *14*(5), 2303–2314. https://doi.org/10.5194/acp-14-2303-2014

Eisenthal, K. B. (1996). Liquid Interfaces Probed by Second-Harmonic and Sum-Frequency Spectroscopy. *Chemical Reviews*, *96*(4), 1343–1360. https://doi.org/10.1021/cr9502211

Ellison, G. B., Tuck, A. F., & Vaida, V. (1999). Atmospheric processing of organic aerosols. *Journal of Geophysical Research: Atmospheres*, *104*(D9), 11633–11641. https://doi.org/10.1029/1999JD900073

Ervens, B. (2015). Modeling the Processing of Aerosol and Trace Gases in Clouds and Fogs. *Chemical Reviews*, *115*, 4157–4198. https://doi.org/10.1021/cr5005887

Ervens, B., Carlton, A. G., Turpin, B. J., Altieri, K. E., Kreidenweis, S. M., & Feingold, G. (2008). Secondary organic aerosol yields from cloud-processing of isoprene oxidation products. *Geophysical Research Letters*, *35*, L02816. https://doi.org/Artn L02816 10.1029/2007gl031828

Ervens, B., Sorooshian, A., Lim, Y. B., & Turpin, B. J. (2014). Key parameters controlling OH-initiated formation of secondary organic aerosol in the aqueous phase (aqSOA). *Journal of Geophysical Research-Atmospheres*, *119*, 3997–4016. https://doi.org/10.1002/2013jd021021

Ervens, B., Turpin, B. J., & Weber, R. J. (2011). Secondary aerosol formation in cloud droplets and aqueous particles (aqSOA): a review of laboratory, field and model studies. *Atmospheric Chemistry and Physics*, *11*(21), 11069–11102.

Estrada-López, E. D., Murce, E., P. Franca, M. P., & S. Pimentel, A. (2017). Prednisolone adsorption on lung surfactant models: insights on the formation of nanoaggregates, monolayer collapse and prednisolone spreading. *RSC Advances*, *7*(9), 5272–5281. https://doi.org/10.1039/C6RA28422A

Eugene, A. J., Xia, S.-S., & Guzman, M. I. (2013). Negative production of acetoin in the photochemistry of aqueous pyruvic acid. *Proceedings of the National Academy of Sciences*, *110*(46), E4274–E4275. https://doi.org/10.1073/pnas.1313991110

Feitelson, J. (1964). On the Mechanism of Fluorescence Quenching. Tyrosine and Similar Compounds. *The Journal of Physical Chemistry*, *68*(2), 391–397. https://doi.org/10.1021/j100784a033

Fell, L. M., Francis, J. T., Holmes, J. L., & Terlouw, J. K. (1997). The intriguing behaviour of (ionized) oxalacetic acid investigated by tandem mass spectrometry. *International Journal of Mass Spectrometry and Ion Processes*, *165*, 179–194. https://doi.org/10.1016/S0168-1176(97)00174-2

Finck, C. (1862). Ueber die Zersetzung der Brenztraubensäure durch Barythydrat. *Justus Liebigs Annalen Der Chemie*, *122*(2), 182–191. https://doi.org/10.1002/jlac.18621220204

Finlayson-Pitts, B. J. (2009). Reactions at surfaces in the atmosphere: integration of experiments and theory as necessary (but not necessarily sufficient) for predicting the physical chemistry of aerosols. *Physical Chemistry Chemical Physics*, *11*, 7760–7779. https://doi.org/10.1039/b906540g

Finlayson-Pitts, B. J., & Pitts, J. N. (1999). *Chemistry of the Upper and Lower Atmosphere*. San Diego: Academic Press.

Freitas, R. A. (1999). *Nanomedicine, Volume I: Basic Capabilities* (1 edition). Austin, TX: CRC Press.

Frisch, M. J. ;, Trucks, G. W. ;, Schlegel, H. B. ;, Scuseria, G. E. ;, Robb, M. A. ;, Cheeseman, J. R. ;, Scalmani, G. ;, Barone, V. ., Petersson, G. A. ;, Nakatsuji, H. ;, Li, X. . C., M. ;, Marenich, A. ;, Bloino, J. ;, Janesko, B. G. ;, Gomperts, R. ;, Mennucci, B. ;, Hratchian, H. P. ;, … Fox, D. J. (2016). *Gaussian 09, Revision D.01*. Wallingford, CT: Gaussian, Inc.

Frisch, M., Trucks, G., Schlegel, H., Scuseria, G., Robb, M., Cheeseman, J., Scalmani, G., Barone, V., Mennucci, B., Petersson, G., Nakatsuji, H., Caricato, M., Li, X., Hratchian, H., Izmaylov, A., Bloino, J., Zheng, G., … Fox, D. (2009). *Gaussian 09*.

Fry, I. (2000). *Emergence of Life on Earth: A Historical and Scientific Overview* (1 edition). Rutgers University Press.

Fu, L., Ma, G., & Yan, E. C. Y. (2010). In Situ Misfolding of Human Islet Amyloid Polypeptide at Interfaces Probed by Vibrational Sum Frequency Generation. *Journal of the American Chemical Society*, *132*(15), 5405–5412. https://doi.org/10.1021/ja909546b

Fu, P., Zhuang, G., Sun, Y., Wang, Q., Chen, J., Ren, L., Yang, F., Wang, Z., Pan, X., Li, X., & Kawamura, K. (2016). Molecular markers of biomass burning, fungal spores and biogenic SOA in the Taklimakan desert aerosols. *Atmospheric Environment*, *130*, 64–73. https://doi.org/10.1016/j.atmosenv.2015.10.087

Gaines, G. L. (1966). Thermodynamic relationships for mixed insoluble monolayers. *Journal of Colloid and Interface Science*, *21*(3), 315–319. https://doi.org/10.1016/0095-8522(66)90015-8

Gaines, G. L. (1982). The thermodynamic equation of state for insoluble monolayers. *Journal of Colloid and Interface Science*, *85*(1), 16–18. https://doi.org/10.1016/0021-9797(82)90230-2

Gallo, P., Amann-Winkel, K., Angell, C. A., Anisimov, M. A., Caupin, F., Chakravarty, C., Lascaris, E., Loerting, T., Panagiotopoulos, A. Z., Russo, J., Sellberg, J. A., Stanley, H. E., Tanaka, H., Vega, C., Xu, L., & Pettersson, L. G. M. (2016). Water: A Tale of Two Liquids. *Chemical Reviews*, *116*(13), 7463–7500. https://doi.org/10.1021/acs.chemrev.5b00750

Gazit, E. (2002). A possible role for π-stacking in the self-assembly of amyloid fibrils. *The FASEB Journal*, *16*(1), 77–83. https://doi.org/10.1096/fj.01-0442hyp

Geissler, P. L. (2013). Water Interfaces, Solvation, and Spectroscopy. *Annual Review of Physical Chemistry*, *64*(1), 317–337. https://doi.org/10.1146/annurev-physchem-040412-110153

George, C., Ammann, M., D'Anna, B., Donaldson, D. J., & Nizkorodov, S. A. (2015). Heterogeneous Photochemistry in the Atmosphere. *Chemical Reviews*, *115*(10), 4218–4258. https://doi.org/10.1021/cr500648z

Gericke, A., Michailov, A. V., & Hühnerfuss, H. (1993). Polarized external infrared reflection-absorption spectrometry at the air/water interface: Comparison of experimental and theoretical results for different angles of incidence. *Vibrational Spectroscopy*, *4*(3), 335–348. https://doi.org/10.1016/0924-2031(93)80007-3

German, H. W., Uyaver, S., & Hansmann, U. H. E. (2015). Self-Assembly of Phenylalanine-Based Molecules. *The Journal of Physical Chemistry A*, *119*(9), 1609–1615. https://doi.org/10.1021/jp5077388

Gibbs, J. W., Bumstead, H. A., & Name, R. G. V. (1906). *Thermodynamics*. Longmans, Green and Company.

Giner-Casares, J. J., de Miguel, G., Pérez-Morales, M., Martín-Romero, M. T., Camacho, L., & Muñoz, E. (2009). Effect of the Molecular Methylene Blue Aggregation on the Mesoscopic Domain Morphology in Mixed Monolayers with Dimyristoyl−Phosphatidic Acid. *The Journal of Physical Chemistry C*, *113*(14), 5711–5720. https://doi.org/10.1021/jp810935x

Giraudeau, P., Silvestre, V., & Akoka, S. (2015). Optimizing water suppression for quantitative NMR-based metabolomics: a tutorial review. *Metabolomics*, *11*(5), 1041–1055. https://doi.org/10.1007/s11306-015-0794-7

Gobrogge, C. A., Blanchard, H. S., & Walker, R. A. (2017). Temperature-Dependent Partitioning of Coumarin 152 in Phosphatidylcholine Lipid Bilayers. *The Journal of Physical Chemistry B*, *121*(16), 4061–4070. https://doi.org/10.1021/acs.jpcb.6b10893

Goldfine, H. (1960). The formation of γ-hydroxy-γ-methylglutamic acid from a common impurity in pyruvic acid. *Biochimica et Biophysica Acta*, *40*, 557–559. https://doi.org/10.1016/0006-3002(60)91407-4

González-Delgado, A. M., Giner-Casares, J. J., Brezesinski, G., Regnouf-de-Vains, J.-B., & Camacho, L. (2012). Langmuir Monolayers of an Inclusion Complex Formed by a New Calixarene Derivative and Fullerene. *Langmuir*, *28*(33), 12114–12121. https://doi.org/10.1021/la302440g

Gorbenko, G. P., & Kinnunen, P. K. J. (2006). The role of lipid-protein interactions in amyloid-type protein fibril formation. *Chemistry and Physics of Lipids*, *141*(1–2), 72–82. https://doi.org/10.1016/j.chemphyslip.2006.02.006

Görbitz, C. H. (2001). Nanotube formation by hydrophobic dipeptides. *Chemistry (Weinheim an Der Bergstrasse, Germany)*, *7*(23), 5153–5159.

Gracin, S., & Rasmuson, A. (2002). Solubility of Phenylacetic Acid, p-Hydroxyphenylacetic Acid, p-Aminophenylacetic Acid, p-Hydroxybenzoic Acid, and Ibuprofen in Pure Solvents. *Journal of Chemical and Engineering Data*, *47*(6), 1379–1383.

Griffith, E. C., Carpenter, B. K., Shoemaker, R. K., & Vaida, V. (2013). Photochemistry of Aqueous Pyruvic Acid. *Proceedings of the National Academy of Sciences of the United States of America*, *110*(29), 11714–11719. https://doi.org/10.1073/pnas.1303206110

Griffith, E. C., Perkins, R. J., Telesford, D.-M., Adams, E. M., Cwiklik, L., Allen, H. C., Roeselová, M., & Vaida, V. (2015). Interaction of l-Phenylalanine with a Phospholipid Monolayer at the Water–Air Interface. *The Journal of Physical Chemistry B*, *119*(29), 9038–9048. https://doi.org/10.1021/jp508473w

Griffith, E. C., Shoemaker, R. K., & Vaida, V. (2013). Sunlight-initiated Chemistry of Aqueous Pyruvic Acid: Building Complexity in the Origin of Life. *Origins of Life and Evolution of Biospheres*, *43*(4–5), 341–352. https://doi.org/10.1007/s11084-013-9349-y

Griffith, E. C., Tuck, A. F., & Vaida, V. (2012). Ocean-Atmosphere Interactions in the Emergence of Complexity in Simple Chemical Systems. *Accounts of Chemical Research*, *45*, 2106–2113. https://doi.org/10.1021/ar300027q

Griffith, E. C., & Vaida, V. (2012). In situ observation of peptide bond formation at the water–air interface. *Proceedings of the National Academy of Sciences*, *109*(39), 15697–15701. https://doi.org/10.1073/pnas.1210029109

Grobbelaar, N., Pollard, J. K., & Steward, F. C. (1955). New Soluble Nitrogen Compounds (Amino- and Imino-Acids and Amides) in Plants. *Nature*, *175*(4460), 703–708. https://doi.org/10.1038/175703a0

Grosjean, D. (1983). Atmospheric Reactions of Pyruvic Acid. *Atmospheric Environment*, *17*, 2379–2382. https://doi.org/Doi 10.1016/0004-6981(83)90242-1

Gruner, S. M., Lenk, R. P., Janoff, A. S., & Ostro, N. J. (1985). Novel multilayered lipid vesicles: comparison of physical characteristics of multilamellar liposomes and stable plurilamellar vesicles. *Biochemistry*, *24*(12), 2833–2842. https://doi.org/10.1021/bi00333a004

Grüniger, H., Möbius, D., & Meyer, H. (1983). Enhanced light reflection by dye monolayers at the air–water interface. *The Journal of Chemical Physics*, *79*(8), 3701–3710. https://doi.org/10.1063/1.446290

Guenther, A. (2013). Biological and Chemical Diversity of Biogenic Volatile Organic Emissions into the Atmosphere. *ISRN Atmospheric Sciences*, *2013*, 1–27. https://doi.org/10.1155/2013/786290

Guggenheim, E. A. (1945). Statistical thermodynamics of the surface of a regular solution. *Transactions of the Faraday Society*, *41*(0), 150–156. https://doi.org/10.1039/TF9454100150

Guggenheim, E. A., & Adam, N. K. (1933). The Thermodynamics of Adsorption at the Surface of Solutions. *Proceedings of the Royal Society of London A: Mathematical, Physical and Engineering Sciences*, *139*(837), 218–236. https://doi.org/10.1098/rspa.1933.0015

Guo, C., Luo, Y., Zhou, R., & Wei, G. (2012). Probing the self-assembly mechanism of diphenylalanine-based peptide nanovesicles and nanotubes. *ACS Nano*, *6*(5), 3907–3918. https://doi.org/10.1021/nn300015g

Gürtler, P., Saile, V., & Koch, E. E. (1977). Rydberg series in the absorption spectra of H2O and D2O in the vacuum ultraviolet. *Chemical Physics Letters*, *51*(2), 386–391. https://doi.org/10.1016/0009-2614(77)80427-2

Guzmán, M. I., Colussi, A. J., & Hoffmann, M. R. (2006). Photoinduced Oligomerization of Aqueous Pyruvic Acid. *The Journal of Physical Chemistry A*, *110*(10), 3619–3626. https://doi.org/10.1021/jp056097z

Guzman, M. I., & Martin, S. T. (2009). Prebiotic Metabolism: Production by Mineral Photoelectrochemistry of alpha-Ketocarboxylic Acids in the Reductive Tricarboxylic Acid Cycle. *Astrobiology*, *9*(9), 833–842. https://doi.org/10.1089/ast.2009.0356

Guzman, M. I., & Martin, S. T. (2010). Photo-production of lactate from glyoxylate: how minerals can facilitate energy storage in a prebiotic world. *Chemical Communications*, *46*(13), 2265–2267. https://doi.org/10.1039/B924179E

Hąc-Wydro, K., & Dynarowicz-Łątka, P. (2008). Biomedical applications of the Langmuir monolayer technique. *Annales UMCS, Chemistry*, *63*, 47–60. https://doi.org/10.2478/v10063-008-0027-2

Hall, G. E., Muckerman, J. T., Preses, J. M., Weston, R. E., & Flynn, G. W. (1992). Time-Resolved FTIR Studies of the Photodissociation of Pyruvic-Acid at 193 nm. *Chemical Physics Letters*, *193*, 77–83. https://doi.org/Doi 10.1016/0009-2614(92)85685-4

Hallquist, M., Wenger, J. C., Baltensperger, U., Rudich, Y., Simpson, D., Claeys, M., Dommen, J., Donahue, N. M., George, C., Goldstein, A. H., Hamilton, J. F., Herrmann, H., Hoffmann, T.,

Iinuma, Y., Jang, M., Jenkin, M. E., Jimenez, J. L., … Wildt, J. (2009). The formation, properties and impact of secondary organic aerosol: current and emerging issues. *Atmos. Chem. Phys.*, *9*(14), 5155–5236. https://doi.org/10.5194/acp-9-5155-2009

Hanley, W. B. (2004). Adult phenylketonuria. *The American Journal of Medicine*, *117*(8), 590–595. https://doi.org/10.1016/j.amjmed.2004.03.042

Hansen, J., Sato, M., & Ruedy, R. (1997). Radiative forcing and climate response. *Journal of Geophysical Research-Atmospheres*, *102*, 6831–6864. https://doi.org/Doi 10.1029/96jd03436

Harrison, R. M., & Yin, J. (2000). Particulate matter in the atmosphere: which particle properties are important for its effects on health? *Science of the Total Environment*, *249*(1), 85–101.

Haynes, W. M. (Ed.). (2015). *CRC Handbook of Chemistry and Physics, 96th Edition* (96 edition). Boca Raton, FL: CRC Press.

Hazen, R. M. (2013). Paleomineralogy of the Hadean Eon: A preliminary species list. *American Journal of Science*, *313*(9), 807–843. https://doi.org/10.2475/09.2013.01

Hazen, R. M., & Deamer, D. W. (2007). Hydrothermal Reactions of Pyruvic Acid: Synthesis, Selection, and Self-Assembly of Amphiphilic Molecules. *Origins of Life and Evolution of Biospheres*, *37*(2), 143–152. https://doi.org/10.1007/s11084-006-9027-4

Hazen, R. M., & Sverjensky, D. A. (2010). Mineral Surfaces, Geochemical Complexities, and the Origins of Life. *Cold Spring Harbor Perspectives in Biology*, *2*(5), a002162. https://doi.org/10.1101/cshperspect.a002162

Heald, C. L., Jacob, D. J., Park, R. J., Russell, L. M., Huebert, B. J., Seinfeld, J. H., Liao, H., & Weber, R. J. (2005). A large organic aerosol source in the free troposphere missing from current models. *Geophysical Research Letters*, *32*(18), L18809. https://doi.org/10.1029/2005gl023831

Hess, B., Bekker, H., Berendsen, H. J. C., & Fraaije, J. G. E. M. (1997). LINCS: A linear constraint solver for molecular simulations. *Journal of Computational Chemistry*, *18*(12), 1463–1472. https://doi.org/10.1002/(SICI)1096-987X(199709)18:12<1463::AID-JCC4>3.0.CO;2-H

Hess, B., Kutzner, C., van der Spoel, D., & Lindahl, E. (2008). GROMACS 4: Algorithms for Highly Efficient, Load-Balanced, and Scalable Molecular Simulation. *Journal of Chemical Theory and Computation*, *4*(3), 435–447. https://doi.org/10.1021/ct700301q

Hinds, W. C. (1999). *Aerosol technology : properties, behavior, and measurement of airborne particles* (2nd ed.). New York: Wiley.

Ho, K. F., Lee, S. C., Cao, J. J., Kawamura, K., Watanabe, T., Cheng, Y., & Chow, J. C. (2006). Dicarboxylic acids, ketocarboxylic acids and dicarbonyls in the urban roadside area of Hong Kong. *Atmospheric Environment*, *40*, 3030–3040. https://doi.org/10.1016/j.atmosenv.2005.11.069

Ho, R. J. Y., Schmetz, M., & Deamer, D. W. (1987). Nonenzymatic hydrolysis of phosphatidylcholine prepared as liposomes and mixed micelles. *Lipids*, *22*(3), 156–158. https://doi.org/10.1007/BF02537295

Hockney, R. W., Goel, S. P., & Eastwood, J. W. (1974). Quiet high-resolution computer models of a plasma. *Journal of Computational Physics*, *14*(2), 148–158. https://doi.org/10.1016/0021-9991(74)90010-2

Hong, H., Park, S., Flores Jiménez, R. H., Rinehart, D., & Tamm, L. K. (2007). Role of Aromatic Side Chains in the Folding and Thermodynamic Stability of Integral Membrane Proteins. *Journal of the American Chemical Society*, *129*(26), 8320–8327. https://doi.org/10.1021/ja068849o

Hoover, null. (1985). Canonical dynamics: Equilibrium phase-space distributions. *Physical Review. A, General Physics*, *31*(3), 1695–1697.

Horowitz, A., Meller, R., & Moortgat, G. K. (2001). The UV–VIS absorption cross sections of the α-dicarbonyl compounds: pyruvic acid, biacetyl and glyoxal. *Journal of Photochemistry and Photobiology A*, *146*(1), 19–27.

Huber, R. (1979). Conformational flexibility and its functional significance in some protein molecules. *Trends in Biochemical Sciences*, *4*(12), 271–276. https://doi.org/10.1016/0968-0004(79)90298-6

Humphrey, W., Dalke, A., & Schulten, K. (1996). VMD: Visual molecular dynamics. *Journal of Molecular Graphics*, *14*(1), 33–38. https://doi.org/10.1016/0263-7855(96)00018-5

Ickenstein, L. M., Sandström, M. C., Mayer, L. D., & Edwards, K. (2006). Effects of phospholipid hydrolysis on the aggregate structure in DPPC/DSPE-PEG2000 liposome preparations after gel to liquid crystalline phase transition. *Biochimica et Biophysica Acta (BBA) - Biomembranes*, *1758*(2), 171–180. https://doi.org/10.1016/j.bbamem.2006.02.016

Jämbeck, J. P. M., & Lyubartsev, A. P. (2012a). An Extension and Further Validation of an All-Atomistic Force Field for Biological Membranes. *Journal of Chemical Theory and Computation*, *8*(8), 2938–2948. https://doi.org/10.1021/ct300342n

Jämbeck, J. P. M., & Lyubartsev, A. P. (2012b). Derivation and Systematic Validation of a Refined All-Atom Force Field for Phosphatidylcholine Lipids. *The Journal of Physical Chemistry B*, *116*(10), 3164–3179. https://doi.org/10.1021/jp212503e

Jerschow, A., & Müller, N. (1997). Suppression of Convection Artifacts in Stimulated-Echo Diffusion Experiments. Double-Stimulated-Echo Experiments. *Journal of Magnetic Resonance*, *125*(2), 372–375. https://doi.org/10.1006/jmre.1997.1123

Jimenez, J. L., Canagaratna, M. R., Donahue, N. M., Prevot, A. S. H., Zhang, Q., Kroll, J. H., DeCarlo, P. F., Allan, J. D., Coe, H., Ng, N. L., Aiken, A. C., Docherty, K. S., Ulbrich, I. M., Grieshop, A. P., Robinson, A. L., Duplissy, J., Smith, J. D., … Worsnop, D. R. (2009). Evolution of Organic Aerosols in the Atmosphere. *Science*, *326*, 1525–1529. https://doi.org/10.1126/science.1180353

Jubb, A. M., Hua, W., & Allen, H. C. (2012). Environmental Chemistry at Vapor/Water Interfaces: Insights from Vibrational Sum Frequency Generation Spectroscopy. *Annual Review of Physical Chemistry*, *63*(1), 107–130. https://doi.org/10.1146/annurev-physchem-032511-143811

Kalimeri, M., Rahaman, O., Melchionna, S., & Sterpone, F. (2013). How Conformational Flexibility Stabilizes the Hyperthermophilic Elongation Factor G-Domain. *The Journal of Physical Chemistry B*, *117*(44), 13775–13785. https://doi.org/10.1021/jp407078z

Kawamura, K. (1993). Identification of C2-C10 omega-oxocarboxylic acids, pyruvic acid, and C2-C3 alpha-dicarbonyls in wet precipitation and aerosol samples by capillary GC and GC/MS. *Analytical Chemistry*, *65*(23), 3505–3511. https://doi.org/10.1021/ac00071a030

Kawamura, K., Kasukabe, H., & Barrie, L. A. (1996). Source and reaction pathways of dicarboxylic acids, ketoacids and dicarbonyls in arctic aerosols: One year of observations. *Atmospheric Environment*, *30*(10–11), 1709–1722. https://doi.org/10.1016/1352-2310(95)00395-9

Kawamura, K., Kasukabe, H., & Barrie, L. A. (2010). Secondary formation of water-soluble organic acids and alpha-dicarbonyls and their contributions to total carbon and water-soluble organic carbon: Photochemical aging of organic aerosols in the Arctic spring. *Journal of Geophysical Research-Atmospheres*, *115*, D21306. https://doi.org/Artn D21306 10.1029/2010jd014299

Kawamura, K., & Maurel, M.-C. (2017). Walking over 4 Gya: Chemical Evolution from Photochemistry to Mineral and Organic Chemistries Leading to an RNA World. *Origins of Life and Evolution of Biospheres*, 1–16. https://doi.org/10.1007/s11084-017-9537-2

Kelkar, D. A., & Chattopadhyay, A. (2006). Membrane interfacial localization of aromatic amino acids and membrane protein function. *Journal of Biosciences*, *31*(3), 297–302.

Kensil, C. R., & Dennis, E. A. (1981). Alkaline hydrolysis of phospholipids in model membranes and the dependence on their state of aggregation. *Biochemistry*, *20*(21), 6079–6085. https://doi.org/10.1021/bi00524a025

King, J. L., & Jukes, T. H. (1969). Non-Darwinian evolution. *Science (New York, N.Y.)*, *164*(3881), 788–798.

Kirby, A. J., & Meyer, G. (1972). Intramolecular catalysis by the ionised carboxy-group of the hydrolysis of enol esters, and of the general acid catalysed ketonisation of the enols produced. *Journal of the Chemical Society, Perkin Transactions 2*, (10), 1446. https://doi.org/10.1039/p29720001446

Kirby, A. J., & O'Carroll, F. (1994). Highly efficient intramolecular general acid catalysis of enol ether hydrolysis, with rapid proton transfer to carbon. *Journal of the Chemical Society, Perkin Transactions 2*, (4), 649. https://doi.org/10.1039/p29940000649

Kirby, A. J., & Williams, N. H. (1994). Efficient intramolecular general acid catalysis of enol ether hydrolysis. Hydrogen-bonding stabilisation of the transition state for proton transfer to carbon. *Journal of the Chemical Society, Perkin Transactions 2*, (4), 643. https://doi.org/10.1039/p29940000643

Klopfer, K. J., & Vanderlick, T. K. (1996). Isotherms of Dipalmitoylphosphatidylcholine (DPPC) Monolayers: Features Revealed and Features Obscured. *Journal of Colloid and Interface Science*, *182*(1), 220–229. https://doi.org/10.1006/jcis.1996.0454

Knecht, V., Müller, M., Bonn, M., Marrink, S.-J., & Mark, A. E. (2005). Simulation studies of pore and domain formation in a phospholipid monolayer. *The Journal of Chemical Physics*, *122*(2), 024704. https://doi.org/10.1063/1.1825992

Knight, J. D., & Miranker, A. D. (2004). Phospholipid catalysis of diabetic amyloid assembly. *Journal of Molecular Biology*, *341*(5), 1175–1187. https://doi.org/10.1016/j.jmb.2004.06.086

Koller, J. E., & Washburn, E. R. (1954). The Diffusion of Phenylacetic Acid in Water as Measured by Changes of Surface Tension. *Journal of the American Chemical Society*, *76*(9), 2562–2565. https://doi.org/10.1021/ja01638a077

Koonin, E. V., & Novozhilov, A. S. (2009). Origin and evolution of the genetic code: The universal enigma. *IUBMB Life*, *61*(2), 99–111. https://doi.org/10.1002/iub.146

Kramer, Z. C., Takahashi, H., Vaida, V., & Skodje, R. T. (2012). Will water act as a photocatalyst for cluster phase chemical reactions? Vibrational overtone-induced dehydration reaction of methanediol. *Journal of Chemical Physics*, *136*, 164302.

Kroll, J. H., Lim, C. Y., Kessler, S. H., & Wilson, K. R. (2015). Heterogeneous Oxidation of Atmospheric Organic Aerosol: Kinetics of Changes to the Amount and Oxidation State of Particle-Phase Organic Carbon. *Journal of Physical Chemistry A*, *119*, 10767–10783. https://doi.org/10.1021/acs.jpca.5b06946

Kroll, J. H., Ng, N. L., Murphy, S. M., Flagan, R. C., & Seinfeld, J. H. (2005). Secondary organic aerosol formation from isoprene photooxidation under high-NOx conditions. *Geophysical Research Letters*, *32*(18), L18808.

Kroll, J. H., Ng, N. L., Murphy, S. M., Flagan, R. C., & Seinfeld, J. H. (2006). Secondary Organic Aerosol Formation from Isoprene Photooxidation. *Environmental Science and Technology*, *40*(6), 1869–1877. https://doi.org/10.1021/es0524301

Krzyściak, W. (2011). Activity of Selected Aromatic Amino Acids in Biological Systems. *Acta Biochimica Polonica*, *58*(4), 461–466.

Kumar, M., & Francisco, J. S. (2015). The Role of Catalysis in Alkanediol Decomposition: Implications for General Detection of Alkanediols and Their Formation in the Atmosphere. *Journal of Physical Chemistry A*, *119*(38), 9821–9833.

Langmuir, I. (1917). THE CONSTITUTION AND FUNDAMENTAL PROPERTIES OF SOLIDS AND LIQUIDS. II. LIQUIDS.1. *Journal of the American Chemical Society*, *39*(9), 1848–1906. https://doi.org/10.1021/ja02254a006

Larsen, M. C., & Vaida, V. (2012). Near Infrared Photochemistry of Pyruvic Acid in Aqueous Solution. *The Journal of Physical Chemistry A*, *116*(24), 5840–5846. https://doi.org/10.1021/jp2087972

Lazcano, A., & Miller, S. L. (1996). The Origin and Early Evolution of Life: Prebiotic Chemistry, the Pre-RNA World, and Time. *Cell*, *85*(6), 793–798. https://doi.org/10.1016/S0092-8674(00)81263-5

Lee, H.-J., Choi, C., & Lee, S.-J. (2002). Membrane-bound α-Synuclein Has a High Aggregation Propensity and the Ability to Seed the Aggregation of the Cytosolic Form. *Journal of Biological Chemistry*, *277*(1), 671–678. https://doi.org/10.1074/jbc.M107045200

Lee, M. C., & Duan, Y. (2004). Distinguish protein decoys by using a scoring function based on a new AMBER force field, short molecular dynamics simulations, and the generalized born solvent model. *Proteins*, *55*(3), 620–634. https://doi.org/10.1002/prot.10470

Leermakers, P. A., & Vesley, G. F. (1963a). Photochemistry of Alpha-Keto Acids and Alpha-Keto Esters .1. Photolysis of Pyruvic Acid and Benzoylformic Acid. *Journal of the American Chemical Society*, *85*, 3776-. https://doi.org/DOI 10.1021/ja00906a013

Leermakers, P. A., & Vesley, G. F. (1963b). Photolysis of Pyruvic Acid in Solution. *Journal of Organic Chemistry*, *28*, 1160-.

Leermakers, P. A., & Vesley, G. F. (1964). Organic photochemistry and the excited state. *J. Chem. Educ*, *41*(10), 535.

Leussing, D., & Stanfield, C. K. (1964). A Nuclear Magnetic Resonance Study of Aqueous Pyruvate-Glycinate-Zinc(II) and Related Systems. *Journal of the American Chemical Society*, *86*(14), 2805–2810. https://doi.org/10.1021/ja01068a011

Levy, M., Miller, S. L., Brinton, K., & Bada, J. L. (2000). Prebiotic Synthesis of Adenine and Amino Acids Under Europa-like Conditions. *Icarus*, *145*(2), 609–613. https://doi.org/10.1006/icar.2000.6365

Lheveder, C., Hénon, S., Mercier, R., Tissot, G., Fournet, P., & Meunier, J. (1998). A new Brewster angle microscope. *Review of Scientific Instruments*, *69*(3), 1446–1450. https://doi.org/10.1063/1.1148779

Li, P. X., Li, Z. X., Shen, H.-H., Thomas, R. K., Penfold, J., & Lu, J. R. (2013). Application of the Gibbs Equation to the Adsorption of Nonionic Surfactants and Polymers at the Air–Water Interface: Comparison with Surface Excesses Determined Directly using Neutron Reflectivity. *Langmuir*, *29*(30), 9324–9334. https://doi.org/10.1021/la4018344

Lienhard, D. M., Bones, D. L., Zuend, A., Krieger, U. K., Reid, J. P., & Peter, T. (2012). Measurements of Thermodynamic and Optical Properties of Selected Aqueous Organic and Organic–Inorganic Mixtures of Atmospheric Relevance. *The Journal of Physical Chemistry A*, *116*(40), 9954–9968. https://doi.org/10.1021/jp3055872

Lim, Y. B., Tan, Y., & Turpin, B. J. (2013). Chemical insights, explicit chemistry, and yields of secondary organic aerosol from OH radical oxidation of methylglyoxal and glyoxal in the aqueous phase. *Atmospheric Chemistry and Physics*, *13*, 8651–8667. https://doi.org/10.5194/acp-13-8651-2013

Lin, H.-L., Yu, Y.-O., & Jwo, J.-J. (2000). Kinetic study of the Ce(III)-, Mn(II)-, or ferroin-catalyzed Belousov-Zhabotinsky reaction with pyruvic acid. *International Journal of Chemical Kinetics*, *32*(7), 408–418. https://doi.org/10.1002/(SICI)1097-4601(2000)32:7<408::AID-KIN3>3.0.CO;2-7

Lohmann, U., & Feichter, J. (2005). Global indirect aerosol effects: a review. *Atmospheric Chemistry and Physics*, *5*, 715–737.

Lopalco, A., Dalwadi, G., Niu, S., Schowen, R. L., Douglas, J., & Stella, V. J. (2016). Mechanism of Decarboxylation of Pyruvic Acid in the Presence of Hydrogen Peroxide. *Journal of Pharmaceutical Sciences*, *105*(2), 705–713. https://doi.org/10.1002/jps.24653

López-Montero, I., Vélez, M., & Devaux, P. F. (2007). Surface tension induced by sphingomyelin to ceramide conversion in lipid membranes. *Biochimica Et Biophysica Acta*, *1768*(3), 553–561. https://doi.org/10.1016/j.bbamem.2007.01.001

Lu, Y., & Freeland, S. (2006). On the evolution of the standard amino-acid alphabet. *Genome Biology*, *7*, 102. https://doi.org/10.1186/gb-2006-7-1-102

Luria, M. (1972). Fluorescence Quenching in Benzene Vapor. *Israel Journal of Chemistry*, *10*(3), 721–724. https://doi.org/10.1002/ijch.197200071

Ma, G., & Allen, H. C. (2006a). DPPC Langmuir Monolayer at the Air−Water Interface: Probing the Tail and Head Groups by Vibrational Sum Frequency Generation Spectroscopy. *Langmuir*, *22*(12), 5341–5349. https://doi.org/10.1021/la0535227

Ma, G., & Allen, H. C. (2006b). New insights into lung surfactant monolayers using vibrational sum frequency generation spectroscopy. *Photochemistry and Photobiology*, *82*(6), 1517–1529. https://doi.org/10.1562/2006-06-30-IR-958

MacCallum, J. L., Bennett, W. F. D., & Tieleman, D. P. (2008). Distribution of amino acids in a lipid bilayer from computer simulations. *Biophysical Journal*, *94*(9), 3393–3404. https://doi.org/10.1529/biophysj.107.112805

Magalhães, N. S. S., de Oliveira, H. M., & Baszkin, A. (1996). Motomura's modified equation for surfactant penetration into spread monolayers. *Colloids and Surfaces A: Physicochemical and Engineering Aspects*, *118*(1–2), 63–73. https://doi.org/10.1016/0927-7757(96)03712-0

Maget-Dana, R. (1999). The monolayer technique: a potent tool for studying the interfacial properties of antimicrobial and membrane-lytic peptides and their interactions with lipid membranes. *Biochimica et Biophysica Acta (BBA) - Biomembranes*, *1462*(1–2), 109–140. https://doi.org/10.1016/S0005-2736(99)00203-5

Maibaum, L., Dinner, A. R., & Chandler, D. (2004). Micelle Formation and the Hydrophobic Effect†. *The Journal of Physical Chemistry B*, *108*(21), 6778–6781. https://doi.org/10.1021/jp037487t

Makin, O. S., Atkins, E., Sikorski, P., Johansson, J., & Serpell, L. C. (2005). Molecular basis for amyloid fibril formation and stability. *Proceedings of the National Academy of Sciences of the United States of America*, *102*(2), 315–320. https://doi.org/10.1073/pnas.0406847102

Mandal, S. M., Chakraborty, D., & Dey, S. (2010). Phenolic acids act as signaling molecules in plant-microbe symbioses. *Plant Signaling & Behavior*, *5*(4), 359–368.

Marcus, A., & Shannon, L. M. (1962). γ-Methyl-γ-hydroxy-α-ketoglutaric Aldolase II. STUDIES WITH PYRUVATE-C14. *Journal of Biological Chemistry*, *237*(11), 3348–3353.

Margolis, S. A., & Coxon, B. (1986). Identification and quantitation of the impurities in sodium pyruvate. *Analytical Chemistry*, *58*(12), 2504–2510. https://doi.org/10.1021/ac00125a033

Maroń, M. K., Takahashi, K., Shoemaker, R. K., & Vaida, V. (2011). Hydration of pyruvic acid to its geminal-diol, 2,2-dihydroxypropanoic acid, in a water-restricted environment. *Chemical Physics Letters*, *513*(4–6), 184–190. https://doi.org/10.1016/j.cplett.2011.07.090

Marshall, K. E., Morris, K. L., Charlton, D., O'Reilly, N., Lewis, L., Walden, H., & Serpell, L. C. (2011). Hydrophobic, Aromatic, and Electrostatic Interactions Play a Central Role in Amyloid Fibril Formation and Stability. *Biochemistry*, *50*(12), 2061–2071. https://doi.org/10.1021/bi101936c

Martín, S., Haro, M., López, M. C., Royo, F. M., & Cea, P. (2006). Charge transfer complex formation at the air–water interface "in situ" studied by means of UV–vis reflection spectroscopy. *Surface Science*, *600*(15), 3045–3051. https://doi.org/10.1016/j.susc.2006.05.050

Martins-Costa, M. T. C., Anglada, J. M., Francisco, J. S., & Ruiz-Lopez, M. F. (2012). Reactivity of Volatile Organic Compounds at the Surface of a Water Droplet. *Journal of the American Chemical Society*, *134*, 11821–11827. https://doi.org/Doi 10.1021/Ja304971e

Maruyama, K. (1990). Purification and Properties of 4-Hydroxy-4-Methyl-2-Oxoglutarate Aldolase from *Pseudomonas ochraceae* Grown on Phthalate. *The Journal of Biochemistry*, *108*(2), 327–333.

Matsumoto, M., Saito, S., & Ohmine, I. (2002). Molecular dynamics simulation of the ice nucleation and growth process leading to water freezing. *Nature*, *416*(6879), 409–413. https://doi.org/10.1038/416409a

McConlogue, C. W., Malamud, D., & Vanderlick, T. K. (1998). Interaction of DPPC monolayers with soluble surfactants: electrostatic effects of membrane perturbants. *Biochimica et Biophysica Acta (BBA) - Biomembranes*, *1372*(1), 124–134. https://doi.org/10.1016/S0005-2736(98)00052-2

McConlogue, C. W., & Vanderlick, T. K. (1997). A Close Look at Domain Formation in DPPC Monolayers. *Langmuir*, *13*(26), 7158–7164. https://doi.org/10.1021/la970898e

McGregor, M. A., & Barnes, G. T. (1974). The equilibrium penetration of monolayers. *Journal of Colloid and Interface Science*, *49*(3), 362–367. https://doi.org/10.1016/0021-9797(74)90380-4

McNeill, V. F. (2015). Aqueous Organic Chemistry in the Atmosphere: Sources and Chemical Processing of Organic Aerosols. *Environmental Science & Technology*, *49*(3), 1237–1244. https://doi.org/10.1021/es5043707

Mellouki, A., & Mu, Y. (2003). On the atmospheric degradation of pyruvic acid in the gas phase. *Journal of Photochemistry and Photobiology A: Chemistry*, *157*(2–3), 295–300. https://doi.org/10.1016/S1010-6030(03)00070-4

Mendelsohn, R., Brauner, J. W., & Gericke, A. (1995). External Infrared Reflection Absorption Spectrometry of Monolayer Films at the Air-Water Interface. *Annual Review of Physical Chemistry*, *46*(1), 305–334. https://doi.org/10.1146/annurev.pc.46.100195.001513

Meunier, J. (2000). Why a Brewster angle microscope? *Colloids and Surfaces A: Physicochemical and Engineering Aspects*, *171*(1–3), 33–40. https://doi.org/10.1016/S0927-7757(99)00555-5

Miura, T., & Seki, K. (2015). Diffusion Influenced Adsorption Kinetics. *The Journal of Physical Chemistry B*, *119*(34), 10954–10961. https://doi.org/10.1021/acs.jpcb.5b00580

Monod, A., & Carlier, P. (1999). Impact of clouds on the tropospheric ozone budget: Direct effect of multiphase photochemistry of soluble organic compounds. *Atmospheric Environment*, *33*(27), 4431–4446.

Monod, A., Poulain, L., Grubert, S., Voisin, D., & Wortham, H. (2005). Kinetics of OH-initiated oxidation of oxygenated organic compounds in the aqueous phase: new rate constants, structure-activity relationships and atmospheric implications. *Atmospheric Environment*, *39*, 7667–7688. https://doi.org/10.1016/j.atmosenv.2005.03.019

Montgomery, C. M., & Webb, J. L. (1954). Detection of a New Inhibitor of the Tricarboxylic Acid Cycle. *Science*, *120*(3125), 843–844. https://doi.org/10.1126/science.120.3125.843

Montgomery, C. M., & Webb, J. L. (1956). Metabolic Studies on Heart Mitochondria II. the Inhibitory Action of Parapyruvate on the Tricarboxylic Acid Cycle. *Journal of Biological Chemistry*, *221*(1), 359–368.

Montgomery, J. A., Frisch, M. J., Ochterski, J. W., & Petersson, G. A. (1999). A complete basis set model chemistry. VI. Use of density functional geometries and frequencies. *Journal of Chemical Physics*, *110*(6), 2822–2827. https://doi.org/10.1063/1.477924

Moriya, Y., Hasegawa, T., Okada, T., Ogawa, N., Kawai, E., Abe, K., Ogasawara, M., Kato, S., & Nakata, S. (2006). Analysis of Gibbs Monolayer Adsorbed at the Toluene/Water Interface by

UV−Visible Partial Internal Reflection Spectrometry. *Analytical Chemistry*, *78*(22), 7850–7856. https://doi.org/10.1021/ac061501r

Morriss-Andrews, A., Brown, F. L. H., & Shea, J.-E. (2014). A Coarse-Grained Model for Peptide Aggregation on a Membrane Surface. *The Journal of Physical Chemistry B*, *118*(28), 8420–8432. https://doi.org/10.1021/jp502871m

Motomura, K. (1974). Thermodynamics of multicomponent monolayers. I. General formulation. *Journal of Colloid and Interface Science*, *48*(2), 307–318. https://doi.org/10.1016/0021-9797(74)90165-9

Motomura, K., Hayami, Y., Aratono, M., & Matuura, R. (1982). Thermodynamics of multicomponent monolayers: IV. Monolayer penetration. *Journal of Colloid and Interface Science*, *87*(2), 333–338. https://doi.org/10.1016/0021-9797(82)90330-7

Motomura, K., Yoshino, S., Fujii, K., & Matuura, R. (1977). Thermodynamics of multicomponent monolayers. *Journal of Colloid and Interface Science*, *60*(1), 87–95. https://doi.org/10.1016/0021-9797(77)90258-2

Nagarajan, S., Schuler, E. E., Ma, K., Kindt, J. T., & Dyer, R. B. (2012). Dynamics of the Gel to Fluid Phase Transformation in Unilamellar DPPC Vesicles. *The Journal of Physical Chemistry. B*, *116*(46), 13749–13756. https://doi.org/10.1021/jp309832u

Needham, T. E., Paruta, A. N., & Gerraughty, R. J. (1971). Solubility of amino acids in pure solvent systems. *Journal of Pharmaceutical Sciences*, *60*(4), 565–567. https://doi.org/10.1002/jps.2600600410

Nemes, P., Schlosser, G., & Vékey, K. (2005). Amino acid cluster formation studied by electrospray ionization mass spectrometry. *Journal of Mass Spectrometry*, *40*(1), 43–49. https://doi.org/10.1002/jms.771

Ng, C. L., Waterman, D. G., Koonin, E. V., Walters, A. D., Chong, J. P., Isupov, M. N., Lebedev, A. A., Bunka, D. H., Stockley, P. G., Ortiz-Lombardía, M., & Antson, A. A. (2009). Conformational flexibility and molecular interactions of an archaeal homologue of the Shwachman-Bodian-Diamond syndrome protein. *BMC Structural Biology*, *9*, 32. https://doi.org/10.1186/1472-6807-9-32

Nguyen, T. B., Bateman, A. P., Bones, D. L., Nizkorodov, S. A., Laskin, J., & Laskin, A. (2010). High-resolution mass spectrometry analysis of secondary organic aerosol generated by ozonolysis of isoprene. *Atmospheric Environment*, *44*(8), 1032–1042. https://doi.org/10.1016/j.atmosenv.2009.12.019

NIST Mass Spec Data Center, S.E. Stein, director. (n.d.). Infrared Spectra. In P.J. Linstrom & W.G. Mallard (Eds.), *NIST Chemistry WebBook, NIST Standard Reference Database Number 69*. Gaithersburg MD, 20899: National Institute of Standards and Technology. Retrieved from http://webbook.nist.gov/cgi/cbook.cgi?ID=C127173&Units=SI&Type=IR-SPEC&Index=1#IR-SPEC

Noah-Vanhoucke, J., Smith, J. D., & Geissler, P. L. (2009a). Statistical mechanics of sum frequency generation spectroscopy for the liquid–vapor interface of dilute aqueous salt solutions. *Chemical Physics Letters*, *470*(1), 21–27. https://doi.org/10.1016/j.cplett.2009.01.028

Noah-Vanhoucke, J., Smith, J. D., & Geissler, P. L. (2009b). Toward a Simple Molecular Understanding of Sum Frequency Generation at Air−Water Interfaces. *The Journal of Physical Chemistry B*, *113*(13), 4065–4074. https://doi.org/10.1021/jp805928h

Nosé, S. (1984). A molecular dynamics method for simulations in the canonical ensemble. *Molecular Physics*, *52*(2), 255–268. https://doi.org/10.1080/00268978400101201

Noüy, P. L. (1919). A NEW APPARATUS FOR MEASURING SURFACE TENSION. *The Journal of General Physiology*, *1*(5), 521–524.

Novikov, Y., & Copley, S. D. (2013). Reactivity landscape of pyruvate under simulated hydrothermal vent conditions. *Proceedings of the National Academy of Sciences*, *110*(33), 13283–13288. https://doi.org/10.1073/pnas.1304923110

Ogg, R. J., Kingsley, P. B., & Taylor, J. S. (1994). WET, a T1- and B1-insensitive water-suppression method for in vivo localized 1H NMR spectroscopy. *Journal of Magnetic Resonance. Series B*, *104*(1), 1–10.

Ogg, R. J., Kingsley, R., & Taylor, J. S. (1994). WET, a T 1-and B 1-insensitive water-suppression method for in vivo localized 1 H NMR spectroscopy. *Journal of Magnetic Resonance, Series B*, *104*(1), 1–10.

Ohki, S., & Ohki, C. B. (1976). Monolayers at the oil/water interface as a proper model for bilayer membranes. *Journal of Theoretical Biology*, *62*(2), 389–407. https://doi.org/10.1016/0022-5193(76)90126-0

Ohyama, T., Hoshino, T., & Ikarashi, T. (1988). Isolation and structure of a new organic acid accumulated in tulip plant (Tulipa gesneriand). *Soil Science and Plant Nutrition*, *34*(1), 75–86. https://doi.org/10.1080/00380768.1988.10415581

Oneill, J. A., Kreutz, T. G., & Flynn, G. W. (1987). IR Diode-Laser Study of Vibrational-Energy Distribution in CO2 Produced by UV Excimer Laser Photofragmentation of Pyruvic-Acid. *Journal of Chemical Physics*, *87*(8), 4598–4605. https://doi.org/10.1063/1.453711

Orgel, L. E. (2004a). Prebiotic Adenine Revisited: Eutectics and Photochemistry. *Origins of Life and Evolution of the Biosphere*, *34*(4), 361–369. https://doi.org/10.1023/B:ORIG.0000029882.52156.c2

Orgel, L. E. (2004b). Prebiotic Chemistry and the Origin of the RNA World. *Critical Reviews in Biochemistry and Molecular Biology*, *39*(2), 99–123. https://doi.org/10.1080/10409230490460765

Oró, J. (1960). Synthesis of adenine from ammonium cyanide. *Biochemical and Biophysical Research Communications*, *2*(6), 407–412. https://doi.org/10.1016/0006-291X(60)90138-8

Panda, A. K., Nag, K., Harbottle, R. R., Possmayer, F., & Petersen, N. O. (2004). Thermodynamic studies on mixed molecular langmuir films: Part 2. Mutual mixing of DPPC and bovine lung surfactant extract with long-chain fatty acids. *Colloids and Surfaces A: Physicochemical and Engineering Aspects*, *247*(1–3), 9–17. https://doi.org/10.1016/j.colsurfa.2004.07.008

Pandey, R., Swamy, K. V., Pandey, Rachna, Swamy, K V, & Khetmalas, M. B. (2013). Indole: A novel signaling molecule and its applications. *Indian Journal of Biotechnology*, *12*(3), 297–310.

Pedersen, K. J. (1952). The dissociation constants of pyruvic and oxaloacetic acid. *Acta Chemica Scandinavica*, *6*(2), 243–256.

Peetla, C., Stine, A., & Labhasetwar, V. (2009). Biophysical Interactions with Model Lipid Membranes: Applications in Drug Discovery and Drug Delivery. *Molecular Pharmaceutics*, *6*(5), 1264–1276. https://doi.org/10.1021/mp9000662

Perkins, R. J., Kukharchuk, A., Delcroix, P., Shoemaker, R. K., Roeselová, M., Cwiklik, L., & Vaida, V. (2016). The Partitioning of Small Aromatic Molecules to Air–Water and Phospholipid Interfaces Mediated by Non-Hydrophobic Interactions. *The Journal of Physical Chemistry B*, *120*(30), 7408–7422. https://doi.org/10.1021/acs.jpcb.6b05084

Perkins, R. J., Shoemaker, R. K., Carpenter, B. K., & Vaida, V. (2016). Chemical Equilibria and Kinetics in Aqueous Solutions of Zymonic Acid. *The Journal of Physical Chemistry A*, *120*(51), 10096–10107. https://doi.org/10.1021/acs.jpca.6b10526

Perraud, V., Bruns, E. A., Ezell, M. J., Johnson, S. N., Yu, Y., Alexander, M. L., Zelenyuk, A., Imre, D., Chang, W. L., Dabdub, D., Pankow, J. F., & Finlayson-Pitts, B. (2012). Nonequilibrium atmospheric secondary organic aerosol formation and growth. *Proceedings of the National Academy of Sciences of the United States of America*, *109*(8), 2836–2841.

Pestunova, O., Simonov, A., Snytnikov, V., Stoyanovsky, V., & Parmon, V. (2005). Putative mechanism of the sugar formation on prebiotic Earth initiated by UV-radiation. *Advances in Space Research*, *36*(2), 214–219. https://doi.org/10.1016/j.asr.2005.02.049

Pethica, B. A. (1955). The thermodynamics of monolayer penetration at constant area. Part 1. *Transactions of the Faraday Society*, *51*(0), 1402–1411. https://doi.org/10.1039/TF9555101402

Petrache, H. I., Dodd, S. W., & Brown, M. F. (2000). Area per lipid and acyl length distributions in fluid phosphatidylcholines determined by (2)H NMR spectroscopy. *Biophysical Journal*, *79*(6), 3172–3192.

Pizzarello, S., & Lahav, M. (2009). On the Emergence of Biochemical Homochirality: An Elusive Beginning. *Origins of Life and Evolution of Biospheres*, *40*(1), 1–2. https://doi.org/10.1007/s11084-009-9182-5

Plath, K. L., Takahashi, K., Skodje, R. T., & Vaida, V. (2009). Fundamental and Overtone Vibrational Spectra of Gas-Phase Pyruvic Acid. *The Journal of Physical Chemistry A*, *113*(26), 7294–7303. https://doi.org/10.1021/jp810687t

Pockels, A. (1892). On the Relative Conamination of the Water-Surface by Equal Quantities of Different Substances. *Nature*, (46), 418–419. https://doi.org/10.1038/046418e0

Pocker, Y., Meany, J. E., Nist, B. J., & Zadorojny, C. (1969). Reversible hydration of pyruvic acid. I. Equilibrium studies. *The Journal of Physical Chemistry*, *73*(9), 2879–2882. https://doi.org/10.1021/j100843a015

Porteu, F., Palacin, S., Ruaudel-Teixier, A., & Barraud, A. (1991). Supermolecular engineering at the air-water interface: spatially controlled formation of heterodimers from amphiphilic porphyrins and porphyrazines through specific molecular recognition. *The Journal of Physical Chemistry*, *95*(19), 7438–7447. https://doi.org/10.1021/j100172a060

Prey, V., Waldmann, E., & Berbalk, H. (1955). Zur Kenntnis der Brenztraubensäure. *Monatshefte für Chemie und verwandte Teile anderer Wissenschaften*, *86*(3), 408–413. https://doi.org/10.1007/BF00903624

Ranjan, S., & Sasselov, D. D. (2016). Influence of the UV Environment on the Synthesis of Prebiotic Molecules. *Astrobiology*, *16*(1), 68–88.

Rapf, R. J., Perkins, R. J., Carpenter, B. K., & Vaida, V. (2017). Mechanistic Description of Photochemical Oligomer Formation from Aqueous Pyruvic Acid. *The Journal of Physical Chemistry A*, *121*(22), 4272–4282. https://doi.org/10.1021/acs.jpca.7b03310

Rapf, R. J., Perkins, R. J., Yang, H., Miyake, G. M., Carpenter, B. K., & Vaida, V. (2017). Photochemical Synthesis of Oligomeric Amphiphiles from Alkyl Oxoacids in Aqueous Environments. *Journal of the American Chemical Society*, *139*(20), 6946–6959. https://doi.org/10.1021/jacs.7b01707

Rapf, R. J., & Vaida, V. (2016). Sunlight as an energetic driver in the synthesis of molecules necessary for life. *Physical Chemistry Chemical Physics*, *18*(30), 20067–20084. https://doi.org/10.1039/C6CP00980H

Reed Harris, A. E., Doussin, J.-F., Carpenter, B. K., & Vaida, V. (2016). Gas-Phase Photolysis of Pyruvic Acid: The Effect of Pressure on Reaction Rates and Products. *Journal of Physical Chemistry A*, *120*(51), 10123–10133. https://doi.org/10.1021/acs.jpca.6b09058

Reed Harris, A. E., Ervens, B., Shoemaker, R. K., Kroll, J. A., Rapf, R. J., Griffith, E. C., Monod, A., & Vaida, V. (2014). Photochemical Kinetics of Pyruvic Acid in Aqueous Solution. *The Journal of Physical Chemistry A*, *118*(37), 8505–8516. https://doi.org/10.1021/jp502186q

Reed Harris, A. E., Pajunoja, A., Cazaunau, M., Gratien, A., Pangui, E., Monod, A., Griffith, E. C., Virtanen, A., Doussin, J.-F., & Vaida, V. (2017). Multiphase Photochemistry of Pyruvic Acid under Atmospheric Conditions. *The Journal of Physical Chemistry A*. https://doi.org/10.1021/acs.jpca.7b01107

Reiner, J. E., Jahn, A., Stavis, S. M., Culbertson, M. J., Vreeland, W. N., Burden, D. L., Geist, J., & Gaitan, M. (2010). Accurate Optical Analysis of Single-Molecule Entrapment in Nanoscale Vesicles. *Analytical Chemistry*, *82*(1), 180–188. https://doi.org/10.1021/ac901698v

Renard, P., Reed Harris, A. E., Rapf, R. J., Ravier, S., Demelas, C., Coulomb, B., Quivet, E., Vaida, V., & Monod, A. (2014). Aqueous Phase Oligomerization of Methyl Vinyl Ketone by Atmospheric Radical Reactions. *The Journal of Physical Chemistry C*, *118*(50), 29421–29430. https://doi.org/10.1021/jp5065598

Ricardo, A., Carrigan, M. A., Olcott, A. N., & Benner, S. A. (2004). Borate Minerals Stabilize Ribose. *Science*, *303*(5655), 196–196. https://doi.org/10.1126/science.1092464

Rijs, A. M., Compagnon, I., Oomens, J., Hannam, J. S., Leigh, D. A., & Buma, W. J. (2009). Stiff, and Sticky in the Right Places: Binding Interactions in Isolated Mechanically Interlocked Molecules Probed by Mid-Infrared Spectroscopy. *Journal of the American Chemical Society*, *131*(7), 2428–2429. https://doi.org/10.1021/ja808788c

Rincón, A. G., Guzmán, M. I., Hoffmann, M. R., & Colussi, A. J. (2009). Optical Absorptivity versus Molecular Composition of Model Organic Aerosol Matter. *The Journal of Physical Chemistry A*, *113*(39), 10512–10520. https://doi.org/10.1021/jp904644n

Rissanou, A. N., Georgilis, E., Kasotakis, E., Mitraki, A., & Harmandaris, V. (2013). Effect of Solvent on the Self-Assembly of Dialanine and Diphenylalanine Peptides. *The Journal of Physical Chemistry B*, *117*(15), 3962–3975. https://doi.org/10.1021/jp311795b

Ritson, D. J., & Sutherland, J. D. (2013). Synthesis of Aldehydic Ribonucleotide and Amino Acid Precursors by Photoredox Chemistry. *Angewandte Chemie International Edition*, *52*(22), 5845–5847. https://doi.org/10.1002/anie.201300321

Ritson, D., & Sutherland, J. D. (2012). Prebiotic synthesis of simple sugars by photoredox systems chemistry. *Nature Chemistry*, *4*(11), 895–899. https://doi.org/10.1038/nchem.1467

Robertson, M. P., & Joyce, G. F. (2012). The Origins of the RNA World. *Cold Spring Harbor Perspectives in Biology*, *4*(5). https://doi.org/10.1101/cshperspect.a003608

Ronkainen, P., Brummer, S., & Suomalainen, H. (1970). Diacetyl and formic acid as decomposition products of 2-acetolactic acid. *Acta Chemica Scandinavica*, *24*(9), 3404–3406. https://doi.org/10.3891/acta.chem.scand.24-3404

Rontu, N., & Vaida, V. (2007). Miscibility of Perfluorododecanoic Acid with Organic Acids at the Air−Water Interface. *The Journal of Physical Chemistry C*, *111*(27), 9975–9980. https://doi.org/10.1021/jp0718395

Rosa, A. S., Cutro, A. C., Frías, M. A., & Disalvo, E. A. (2015). Interaction of Phenylalanine with DPPC Model Membranes: More Than a Hydrophobic Interaction. *The Journal of Physical Chemistry B*. https://doi.org/10.1021/acs.jpcb.5b08490

Rossignol, S., Tinel, L., Bianco, A., Passananti, M., Brigante, M., Donaldson, D. J., & George, C. (2016). Atmospheric photochemistry at a fatty acid–coated air-water interface. *Science*, *353*(6300), 699–702.

Rubia-Payá, C., de Miguel, G., Martín-Romero, M. T., Giner-Casares, J. J., & Camacho, L. (2015). UV–Vis Reflection–Absorption Spectroscopy at air–liquid interfaces. *Advances in Colloid and Interface Science*, *225*, 134–145. https://doi.org/10.1016/j.cis.2015.08.012

Rudich, Y., Donahue, N. M., & Mentel, T. F. (2007). Aging of organic aerosol: Bridging the gap between laboratory and field studies. *Annual Review of Physical Chemistry*, *58*, 321–352. https://doi.org/10.1146/annurev.physchem.58.032806.104432

Rugheimer, S., Segura, A., Kaltenegger, L., & Sasselov, D. (2015). UV Surface Environment of Earth-like Planets Orbiting FGKM Stars Through Geological Evolution. *The Astrophysical Journal*, *806*(1), 137. https://doi.org/10.1088/0004-637X/806/1/137

Russell, M. J., Nitschke, W., & Branscomb, E. (2013). The inevitable journey to being. *Phil. Trans. R. Soc. B*, *368*(1622), 20120254. https://doi.org/10.1098/rstb.2012.0254

Sacerdote, M. G., & Szostak, J. W. (2005). Semipermeable lipid bilayers exhibit diastereoselectivity favoring ribose. *Proceedings of the National Academy of Sciences*, *102*(17), 6004–6008. https://doi.org/10.1073/pnas.0408440102

Saito, H., & Shinoda, W. (2011). Cholesterol Effect on Water Permeability through DPPC and PSM Lipid Bilayers: A Molecular Dynamics Study. *The Journal of Physical Chemistry B*, *115*(51), 15241–15250. https://doi.org/10.1021/jp201611p

Saito, K., Sasaki, G., Okada, K., & Tanaka, S. (1994). Unimolecular Decomposition of Pyruvic Acid: An Experimental and Theoretical Study. *The Journal of Physical Chemistry*, *98*(14), 3756–3761. https://doi.org/10.1021/j100065a034

Saladino, R., Crestini, C., Costanzo, G., Negri, R., & Di Mauro, E. (2001). A possible prebiotic synthesis of purine, adenine, cytosine, and 4(3H)-pyrimidinone from formamide: implications for the origin of life. *Bioorganic & Medicinal Chemistry*, *9*(5), 1249–1253. https://doi.org/10.1016/S0968-0896(00)00340-0

Sampaio, J. L., Gerl, M. J., Klose, C., Ejsing, C. S., Beug, H., Simons, K., & Shevchenko, A. (2011). Membrane lipidome of an epithelial cell line. *Proceedings of the National Academy of Sciences*, *108*(5), 1903–1907. https://doi.org/10.1073/pnas.1019267108

Santana, M., Ribeiro, M. P. A., Leite, G. A., Giordano, R. L. C., Giordano, R. C., & Mattedi, S. (2010). Solid–liquid equilibrium of substrates and products of the enzymatic synthesis of ampicillin. *AIChE Journal*, *56*(6), 1578–1583. https://doi.org/10.1002/aic.12082

Schindler, H., & Seelig, J. (1975). Deuterium order parameters in relation to thermodynamic properties of a phospholipid bilayer. Statistical mechanical interpretation. *Biochemistry*, *14*(11), 2283–2287. https://doi.org/10.1021/bi00682a001

Schnitzler, E. G., Seifert, N. A., Ghosh, S., Thomas, J., Xu, Y., & Jäger, W. (2017). Hydration of the simplest α-keto acid: a rotational spectroscopic and ab initio study of the pyruvic acid–water complex. *Physical Chemistry Chemical Physics*, *19*, 4440–4446.

Schöne, L., & Herrmann, H. (2014). Kinetic measurements of the reactivity of hydrogen peroxide and ozone towards small atmospherically relevant aldehydes, ketones and organic acids in aqueous solutions. *Atmospheric Chemistry and Physics*, *14*(9), 4503.

Schreiner, P. R., Reisenauer, H. P., Ley, D., Gerbig, D., Wu, C.-H., & Allen, W. D. (2011). Methylhydroxycarbene: Tunneling Control of a Chemical Reaction. *Science*, *332*(6035), 1300–1303. https://doi.org/10.1126/science.1203761

Schwartz, A. W., & Graaf, R. M. de. (1993). The prebiotic synthesis of carbohydrates: A reassessment. *Journal of Molecular Evolution*, *36*(2), 101–106. https://doi.org/10.1007/BF00166245

Seinfeld, J. H., & Pandis, S. N. (1998). *Atmospheric Chemistry and Physics: From Air Pollution to Climate Change*. New York: John Wiley & Sons, Inc.

Selektor, S. L., Raitman, O. A., Silant'eva, D. A., Ivanova, N. V., Yonusauskas, G., Lukovskaya, E. V., Batat, P., & Arslanov, V. V. (2011). Control of photochemical properties of monolayers and Langmuir-Blodgett films of amphiphilic chromoionophores. *Protection of Metals and Physical Chemistry of Surfaces*, *47*(4), 484–493. https://doi.org/10.1134/S2070205111040174

Sempére, R., & Kawamura, K. (1994). Comparative distributions of dicarboxylic acids and related polar compounds in snow, rain and aerosols from urban atmosphere. *Atmospheric Environment*, *28*(3), 449–459. https://doi.org/10.1016/1352-2310(94)90123-6

Seoane, R., Miñones, J., Conde, O., Miñones, J., Casas, M., & Iribarnegaray, E. (2000). Thermodynamic and Brewster Angle Microscopy Studies of Fatty Acid/Cholesterol Mixtures at the Air/Water Interface. *The Journal of Physical Chemistry B*, *104*(32), 7735–7744. https://doi.org/10.1021/jp001133+

Serda, R. (1889). *Beiträge zur Kenntniss der Pyrotritarsäure.* J.H.E. Heitz, Strassburg. Retrieved from http://hdl.handle.net/2027/uc1.$b622150

Shannon, L. M., & Marcus, A. (1962). γ-Methyl-γ-hydroxy-α-ketoglutaric Aldolase I. PURIFICATION AND PROPERTIES. *Journal of Biological Chemistry*, *237*(11), 3342–3347.

Shapiro, R. (1988). Prebiotic ribose synthesis: A critical analysis. *Origins of Life and Evolution of the Biosphere*, *18*(1–2), 71–85. https://doi.org/10.1007/BF01808782

Shapiro, R. (1995). The prebiotic role of adenine: A critical analysis. *Origins of Life and Evolution of the Biosphere*, *25*(1–3), 83–98. https://doi.org/10.1007/BF01581575

Shapiro, R. (2006). Small Molecule Interactions were Central to the Origin of Life. *The Quarterly Review of Biology*, *81*(2), 105–126. https://doi.org/10.1086/506024

Shen, Y., Si, W., Erbakan, M., Decker, K., Zorzi, R. D., Saboe, P. O., Kang, Y. J., Majd, S., Butler, P. J., Walz, T., Aksimentiev, A., Hou, J., & Kumar, M. (2015). Highly permeable artificial water channels that can self-assemble into two-dimensional arrays. *Proceedings of the National Academy of Sciences*, *112*(32), 9810–9815. https://doi.org/10.1073/pnas.1508575112

Shultz, M. J., Bisson, P., & Vu, T. H. (2014). Insights into hydrogen bonding via ice interfaces and isolated water. *The Journal of Chemical Physics*, *141*(18), 18C521. https://doi.org/10.1063/1.4896603

Singh, A., Kaur, S., Kaur, J., & Singh, P. (2014). Transformation of gas-phase amino acid clusters to dipeptides: a nice approach to demonstrate the formation of prebiotic peptides. *Rapid Communications in Mass Spectrometry*, *28*(18), 2019–2023. https://doi.org/10.1002/rcm.6985

Singh, P., Brar, S. K., Bajaj, M., Narang, N., Mithu, V. S., Katare, O. P., Wangoo, N., & Sharma, R. K. (2017). Self-assembly of aromatic α-amino acids into amyloid inspired nano/micro scaled architects. *Materials Science and Engineering: C*, *72*, 590–600. https://doi.org/10.1016/j.msec.2016.11.117

Singh, V., Rai, R. K., Arora, A., Sinha, N., & Thakur, A. K. (2014). Therapeutic implication of L-phenylalanine aggregation mechanism and its modulation by D-phenylalanine in phenylketonuria. *Scientific Reports*, *4*, 3875.

Sobell, H. M., Tsai, C.-C., Jain, S. C., & Sakore, T. D. (1978). Conformational Flexibility in DNA Structure and Its Implications in Understanding the Organization of DNA in Chromatin. *Philosophical Transactions of the Royal Society of London. Series B, Biological Sciences*, *283*(997), 295–298.

Stefan, M. I., & Bolton, J. R. (1999). Reinvestigation of the Acetone Degradation Mechanism in Dilute Aqueous Solution by the UV/H2O2 Process. *Environmental Science & Technology*, *33*(6), 870–873. https://doi.org/10.1021/es9808548

Sterling, H. J., Cassou, C. A., Trnka, M. J., Burlingame, A. L., Krantz, B. A., & Williams, E. R. (2011). The role of conformational flexibility on protein supercharging in native electrospray ionization. *Physical Chemistry Chemical Physics*, *13*(41), 18288–18296. https://doi.org/10.1039/C1CP20277D

Stodola, F. H., Shotwell, O. L., & Lockwood, L. B. (1952). Zymonic Acid, a New Metabolic Product of Some Yeasts Grown in Aerated Culture. I. Structure Studies2. *Journal of the American Chemical Society*, *74*(21), 5415–5418. https://doi.org/10.1021/ja01141a057

Stroobant, P., & Kaback, H. R. (1979). Reconstitution of ubiquinone-linked functions in membrane vesicles from a double quinone mutant of Escherichia coli. *Biochemistry*, *18*(1), 226–231. https://doi.org/10.1021/bi00568a035

Sun, B., & Chiu, D. T. (2005). Determination of the Encapsulation Efficiency of Individual Vesicles Using Single-Vesicle Photolysis and Confocal Single-Molecule Detection. *Analytical Chemistry*, *77*(9), 2770–2776. https://doi.org/10.1021/ac048439n

Szymczyk, K. (2012). Composition of Multicomponent Surfactant Systems at the Water–Air Interface. *Journal of Surfactants and Detergents*, *15*(5), 647–656. https://doi.org/10.1007/s11743-012-1336-1

Tachibana, K., Shirafuji, T., & Muraishi, S. (1996). Construction and Performance of a Fourier-Transform Infrared Phase-Modulated Ellipsometer for In-Process Surface Diagnostics. *Japanese Journal of Applied Physics*, *35*(6R), 3652. https://doi.org/10.1143/JJAP.35.3652

Tack, B. F., Chapman, P. J., & Dagley, S. (1972). Purification and Properties of 4-Hydroxy-4-methyl-2-oxoglutarate Aldolase. *Journal of Biological Chemistry*, *247*(20), 6444–6449.

Takahashi, K., Plath, K. L., Skodje, R. T., & Vaida, V. (2008). Dynamics of Vibrational Overtone Excited Pyruvic Acid in the Gas Phase: Line Broadening through Hydrogen-Atom Chattering. *The Journal of Physical Chemistry A*, *112*(32), 7321–7331. https://doi.org/10.1021/jp803225c

Takats, Z., Nanita, S. C., Cooks, R. G., Schlosser, G., & Vekey, K. (2003). Amino Acid Clusters Formed by Sonic Spray Ionization. *Analytical Chemistry*, *75*(6), 1514–1523. https://doi.org/10.1021/ac0260793

Talbot, R. W., Andreae, M. O., Berresheim, H., Jacob, D. J., & Beecher, K. M. (1990). Sources and Sinks of Formic, Acetic, and Pyruvic Acids over Central Amazonia 2. Wet Season. *Journal of Geophysical Research-Atmospheres*, *95*, 16799–16811. https://doi.org/DOI 10.1029/JD095iD10p16799

Tallman, D. E., & Leussing, D. L. (1969a). Pyruvate dimerization catalyzed by nickel(II) and zinc(II). I. Equilibrium with nickel(II) and zinc(II). *Journal of the American Chemical Society*, *91*(23), 6253–6256. https://doi.org/10.1021/ja01051a011

Tallman, D. E., & Leussing, D. L. (1969b). Pyruvate dimerization catalyzed by nickel(II) and zinc(II). II. Kinetics. *Journal of the American Chemical Society*, *91*(23), 6256–6262. https://doi.org/10.1021/ja01051a012

Tamamis, P., Adler-Abramovich, L., Reches, M., Marshall, K., Sikorski, P., Serpell, L., Gazit, E., & Archontis, G. (2009). Self-assembly of phenylalanine oligopeptides: insights from experiments and simulations. *Biophysical Journal*, *96*(12), 5020–5029. https://doi.org/10.1016/j.bpj.2009.03.026

Taylor, R. (1987). The mechanism of thermal eliminations part XXIII: [1] The thermal decomposition of pyruvic acid. *International Journal of Chemical Kinetics*, *19*(8), 709–713. https://doi.org/10.1002/kin.550190804

Thompson, A. J., Tillotson, S., Smith, I., Kendall, B., Moore, S. G., & Brenton, D. P. (1993). Brain MRI changes in phenylketonuria. Associations with dietary status. *Brain: A Journal of Neurology*, *116 (Pt 4)*, 811–821.

Thompson, K. C., Jones, S. H., Rennie, A. R., King, M. D., Ward, A. D., Hughes, B. R., Lucas, C. O. M., Campbell, R. A., & Hughes, A. V. (2013). Degradation and Rearrangement of a Lung Surfactant Lipid at the Air–Water Interface during Exposure to the Pollutant Gas Ozone. *Langmuir*, *29*(14), 4594–4602. https://doi.org/10.1021/la304312y

Thornton, D. C. O., Brooks, S. D., & Chen, J. (2016). Protein and Carbohydrate Exopolymer Particles in the Sea Surface Microlayer (SML). *Aquatic Microbiology*, 135. https://doi.org/10.3389/fmars.2016.00135

Tinel, L., Rossignol, S., Ciuraru, R., Dumas, S., & George, C. (2016). Photosensitized reactions initiated by 6-carboxypterin: singlet and triplet reactivity. *Phys. Chem. Chem. Phys.*, *18*(25), 17105–17115. https://doi.org/10.1039/C6CP03119F

Tomasi, J., Mennucci, B., & Cancès, E. (1999). The IEF version of the PCM solvation method: an overview of a new method addressed to study molecular solutes at the QM ab initio level. *Journal of Molecular Structure: THEOCHEM*, *464*(1), 211–226. https://doi.org/10.1016/S0166-1280(98)00553-3

Tompa, P. (2002). Intrinsically unstructured proteins. *Trends in Biochemical Sciences*, *27*(10), 527–533.

Toxvaerd, S. (2013). The Role of Carbohydrates at the Origin of Homochirality in Biosystems. *Origins of Life and Evolution of Biospheres*, *43*(4–5), 391–409. https://doi.org/10.1007/s11084-013-9342-5

Trager, W., & Singer, I. (1955). An Antimalarial Effect in vitro of Parapyruvic Acid. *Experimental Biology and Medicine*, *90*(2), 539–542. https://doi.org/10.3181/00379727-90-22093

Trifonov, E. N. (2000). Consensus temporal order of amino acids and evolution of the triplet code. *Gene*, *261*(1), 139–151. https://doi.org/10.1016/S0378-1119(00)00476-5

Tsoneva, Y., Jonker, H. R. A., Wagner, M., Tadjer, A., Lelle, M., Peneva, K., & Ivanova, A. (2015). Molecular Structure and Pronounced Conformational Flexibility of Doxorubicin in Free and Conjugated State within a Drug–Peptide Compound. *The Journal of Physical Chemistry B*, *119*(7), 3001–3013. https://doi.org/10.1021/jp509320q

Tu, P., Yao, Y., Li, Y., & Liu, B. (2009). Conformational flexibility of phycocyanobilin: Monte-Carlo and DFT study. *Journal of Molecular Structure: THEOCHEM*, *894*(1–3), 9–13. https://doi.org/10.1016/j.theochem.2008.09.034

Tuckermann, R. (2007). Surface tension of aqueous solutions of water-soluble organic and inorganic compounds. *Atmospheric Environment*, *41*(29), 6265–6275. https://doi.org/10.1016/j.atmosenv.2007.03.051

Turro, N. J., Ramamurthy, V., & Scaiano, J. C. (2010). *Modern Molecular Photochemistry of Organic Molecules*. Sausalito, California: University Science Books.

Uversky, V. N. (2002). Natively unfolded proteins: a point where biology waits for physics. *Protein Science: A Publication of the Protein Society*, *11*(4), 739–756. https://doi.org/10.1110/ps.4210102

Vaida, V. (2009). Spectroscopy of Photoreactive Systems: Implications for Atmospheric Chemistry. *Journal of Physical Chemistry A*, *113*, 5–18. https://doi.org/10.1021/jp806365r

Vaida, V. (2011). Perspective: Water cluster mediated atmospheric chemistry. *The Journal of Chemical Physics*, *135*(2), 020901. https://doi.org/10.1063/1.3608919

Vaida, V. (2016). Atmospheric radical chemistry revisited Sunlight may directly drive previously unknown organic reactions at environmental surfaces. *Science*, *353*, 650–650. https://doi.org/10.1126/science.aah4111

van Kan, E. J. M., Demel, R. A., van der Bent, A., & de Kruijff, B. (2003). The role of the abundant phenylalanines in the mode of action of the antimicrobial peptide clavanin. *Biochimica et Biophysica Acta (BBA) - Biomembranes*, *1615*(1–2), 84–92. https://doi.org/10.1016/S0005-2736(03)00233-5

Varughese, S., Hoser, A. A., Jarzembska, K. N., Pedireddi, V. R., & Woźniak, K. (2015). Positional Isomerism and Conformational Flexibility Directed Structural Variations in the Molecular Complexes of Dihydroxybenzoic Acids. *Crystal Growth & Design*, *15*(8), 3832–3841. https://doi.org/10.1021/acs.cgd.5b00471

Vega, C., & Miguel, E. de. (2007). Surface tension of the most popular models of water by using the test-area simulation method. *The Journal of Chemical Physics*, *126*(15), 154707. https://doi.org/10.1063/1.2715577

Veres, P. R., Roberts, J. M., Cochran, A. K., Gilman, J. B., Kuster, W. C., Holloway, J. S., Graus, M., Flynn, J., Lefer, B., Warneke, C., & de Gouw, J. (2011). Evidence of rapid production of organic acids in an urban air mass. *Geophysical Research Letters*, *38*(17), L17807. https://doi.org/10.1029/2011GL048420

Veres, P., Roberts, J. M., Burling, I. R., Warneke, C., de Gouw, J., & Yokelson, R. J. (2010). Measurements of gas-phase inorganic and organic acids from biomass fires by negative-ion proton-transfer chemical-ionization mass spectrometry. *Journal of Geophysical Research: Atmospheres*, *115*(D23), D23302.

Vesley, G. F., & Leermakers, P. A. (1964). The Photochemistry of α-Keto Acids and α-Keto Esters. III. Photolysis of Pyruvic Acid in the Vapor Phase. *The Journal of Physical Chemistry*, *68*(8), 2364–2366. https://doi.org/10.1021/j100790a507

Viehe, H. G., Janousek, Z., Merenyi, R., & Stella, L. (1985). The captodative effect. *Accounts of Chemical Research*, *18*(5), 148–154.

Virtanen, A. I., Berg, A.-M., Risberg, E., & Lamm, O. (1955). New Aminodicarboxylic Acids and Corresponding alpha-Keto Acids in Phyllitis scolopendrium. *Acta Chemica Scandinavica*, *9*, 553–554. https://doi.org/10.3891/acta.chem.scand.09-0553

Voet, A. B., & Schwartz, A. W. (1983). Prebiotic adenine synthesis from HCN—Evidence for a newly discovered major pathway. *Bioorganic Chemistry*, *12*(1), 8–17. https://doi.org/10.1016/0045-2068(83)90003-2

Voet, D., & Voet, J. G. (2010). *Biochemistry* (4th Edition Binder Ready Version edition). Hoboken, NJ: Wiley.

Völckel, C. (1854). Ueber die Producte der Destillation der Weinsäure. *Justus Liebigs Annalen Der Chemie*, *89*(1), 57–76. https://doi.org/10.1002/jlac.18540890105

Waldmann, E., Prey, V., & Jelinek, F. (1954). Zur Kenntnis der Brenztraubensäure. *Monatshefte für Chemie und verwandte Teile anderer Wissenschaften*, *85*(4), 872–881. https://doi.org/10.1007/BF00898714

Walter, J. H., White, F., Wraith, J. E., Jenkins, J. P., & Wilson, B. P. M. (1997). Complete reversal of moderate/severe brain MRI abnormalities in a patient with classical phenylketonuria. *Journal of Inherited Metabolic Disease*, *20*(3), 367–369. https://doi.org/10.1023/A:1005330012574

Wang, J., Wang, W., Kollman, P. A., & Case, D. A. (2006). Automatic atom type and bond type perception in molecular mechanical calculations. *Journal of Molecular Graphics and Modelling*, *25*(2), 247–260. https://doi.org/10.1016/j.jmgm.2005.12.005

Wang, J., Wolf, R. M., Caldwell, J. W., Kollman, P. A., & Case, D. A. (2004). Development and testing of a general amber force field. *Journal of Computational Chemistry*, *25*(9), 1157–1174. https://doi.org/10.1002/jcc.20035

Warneck, P. (2005). Multi-Phase Chemistry of C2 and C3 Organic Compounds in the Marine Atmosphere. *Journal of Atmospheric Chemistry*, *51*(2), 119–159. https://doi.org/10.1007/s10874-005-5984-7

Weber, A. L. (1992). Prebiotic sugar synthesis: Hexose and hydroxy acid synthesis from glyceraldehyde catalyzed by iron(III) hydroxide oxide. *Journal of Molecular Evolution*, *35*(1), 1–6. https://doi.org/10.1007/BF00160255

White, S. H., & Wimley, W. C. (1998). Hydrophobic interactions of peptides with membrane interfaces. *Biochimica et Biophysica Acta (BBA) - Reviews on Biomembranes*, *1376*(3), 339–352. https://doi.org/10.1016/S0304-4157(98)00021-5

Wilce, M. C. J., Aguilar, M.-I., & Hearn, M. T. W. (1995). Physicochemical Basis of Amino Acid Hydrophobicity Scales: Evaluation of Four New Scales of Amino Acid Hydrophobicity Coefficients Derived from RP-HPLC of Peptides. *Analytical Chemistry*, *67*(7), 1210–1219. https://doi.org/10.1021/ac00103a012

Wille, F. (1939). Die Synthese der 1,4-Diketoadipinsäure und ihre biologische Bedeutung. *Justus Liebigs Annalen Der Chemie*, *538*(1), 237–260. https://doi.org/10.1002/jlac.19395380114

Williams, R. A., Mamotte, C. D., & Burnett, J. R. (2008). Phenylketonuria: An Inborn Error of Phenylalanine Metabolism. *The Clinical Biochemist Reviews*, *29*(1), 31–41.

Wilson Jr., E. B., Decius, J. C., & Cross, P. C. (1980). *Molecular Vibrations: The Theory of Infrared and Raman Vibrational Spectra* (Revised ed. edition). New York: Dover Publications.

Winter, H. C., & Dekker, E. E. (1989). Specificity of Aspartate Aminotransferases from Leguminous Plants for 4-Substituted Glutamic Acids. *Plant Physiology*, *89*(4), 1122–1128. https://doi.org/10.1104/pp.89.4.1122

Wolff, L. (1899a). I. Ueber die Synthese der Uvitinsäure aus Brenztraubensäure. *Justus Liebigs Annalen Der Chemie*, *305*(2), 125–153. https://doi.org/10.1002/jlac.18993050202

Wolff, L. (1899b). II. Ueber die Parabrenztraubensäure. *Justus Liebigs Annalen Der Chemie*, *305*(2), 154–165. https://doi.org/10.1002/jlac.18993050203

Wolff, L. (1901). Ueber ein neues Condensationsproduct der Brenztraubensäure. *Justus Liebigs Annalen Der Chemie*, *317*(1), 1–22. https://doi.org/10.1002/jlac.19013170102

Wong, J. T.-F. (2005). Coevolution theory of the genetic code at age thirty. *BioEssays*, *27*(4), 416–425. https://doi.org/10.1002/bies.20208

Wood, C. F., Oneill, J. A., & Flynn, G. W. (1984). Infrared Diode-Laser Probes of Photofragmentation Products - Bending Excitation in CO2 Produced by Excimer Laser Photolysis of Pyruvic-Acid. *Chemical Physics Letters*, *109*(4), 317–323. https://doi.org/10.1016/0009-2614(84)85593-1

Xiang, T.-X., & Anderson, B. D. (1998). Phase structures of binary lipid bilayers as revealed by permeability of small molecules. *Biochimica et Biophysica Acta (BBA) - Biomembranes*, *1370*(1), 64–76. https://doi.org/10.1016/S0005-2736(97)00244-7

Xiang, T.-X., Xu, Y.-H., & Anderson, B. D. (1998). The Barrier Domain for Solute Permeation Varies With Lipid Bilayer Phase Structure. *The Journal of Membrane Biology*, *165*(1), 77–90. https://doi.org/10.1007/s002329900422

Xu, H., Li, P. X., Ma, K., Thomas, R. K., Penfold, J., & Lu, J. R. (2013). Limitations in the Application of the Gibbs Equation to Anionic Surfactants at the Air/Water Surface: Sodium Dodecylsulfate and Sodium Dodecylmonooxyethylenesulfate Above and Below the CMC. *Langmuir*, *29*(30), 9335–9351. https://doi.org/10.1021/la401835d

Xu, X., Costa, A., & Burgess, D. J. (2012). Protein Encapsulation in Unilamellar Liposomes: High Encapsulation Efficiency and A Novel Technique to Assess Lipid-Protein Interaction. *Pharmaceutical Research*, *29*(7), 1919–1931. https://doi.org/10.1007/s11095-012-0720-x

Yamagata, Y. (1999). Prebiotic Formation of ADP and ATP from AMP, Calcium Phosphates and Cyanate in Aqueous Solution. *Origins of Life and Evolution of the Biosphere*, *29*(5), 511–520. https://doi.org/10.1023/A:1006672232730

Yamamoto, S., & Back, R. A. (1985). The Photolysis and Thermal Decomposition of Pyruvic Acid in the Gas Phase. *Canadian Journal of Chemistry*, *63*(2), 549–554. https://doi.org/10.1139/v85-089

Yan, E. C. Y., Fu, L., Wang, Z., & Liu, W. (2014). Biological Macromolecules at Interfaces Probed by Chiral Vibrational Sum Frequency Generation Spectroscopy. *Chemical Reviews*, *114*(17), 8471–8498. https://doi.org/10.1021/cr4006044

Zaug, A. J., & Cech, T. R. (1986). The intervening sequence RNA of Tetrahymena is an enzyme. *Science (New York, N.Y.)*, *231*(4737), 470–475.

Zhang, C., Su, M., He, Y., Zhao, X., Fang, P., Ribbe, A. E., Jiang, W., & Mao, C. (2008). Conformational flexibility facilitates self-assembly of complex DNA nanostructures. *Proceedings of the National Academy of Sciences*, *105*(31), 10665–10669. https://doi.org/10.1073/pnas.0803841105

Zhou, X., Fan, J., Li, N., Du, Z., Ying, H., Wu, J., Xiong, J., & Bai, J. (2012). Solubility of l-phenylalanine in water and different binary mixtures from 288.15 to 318.15 K. *Fluid Phase Equilibria*, *316*, 26–33. https://doi.org/10.1016/j.fluid.2011.08.029

Zhuang, X., Ha, T., Kim, H. D., Centner, T., Labeit, S., & Chu, S. (2000). Fluorescence quenching: A tool for single-molecule protein-folding study. *Proceedings of the National Academy of Sciences*, *97*(26), 14241–14244. https://doi.org/10.1073/pnas.97.26.14241

Zuo, Y. Y., Veldhuizen, R. A. W., Neumann, A. W., Petersen, N. O., & Possmayer, F. (2008). Current perspectives in pulmonary surfactant — Inhibition, enhancement and evaluation. *Biochimica et Biophysica Acta (BBA) - Biomembranes*, *1778*(10), 1947–1977. https://doi.org/10.1016/j.bbamem.2008.03.021

Appendix 1: Supporting Information for Chapter 3

Methods

Brewster Angle Microscopy – BAM images shown in Figure A1.6 were collected on a BAM instrument similar to the one described in the main text with slight alterations: a 17 mW p-polarized 633 nm illumination source (Research Electro-Optics), a Nikon 20x infinity corrected super long working distance objective, and a back illuminated anti-reflective CCD (Andor model DV412-BV)

MD Simulation Insertion Procedure – The following procedure was used to create the initial configuration for the simulations of aqueous solution of L-phenylalanine (Phe) between two monolayers of DPPC. A pre-equilibrated system consisting of a water slab (6876 water molecules) with a DPPC monolayer (64 DPPC molecules) on either air-water interface was visualized in VMD and used as the starting configuration. The dimensions of the entire periodic box were 6.69 x 6.69 x 28 nm. The middle portion of the water slab, i.e., a 2 nm-thick slice containing only water molecules, was removed, leaving the two solvated DPPC monolayers and a void between them (System A, Figure A1.1).
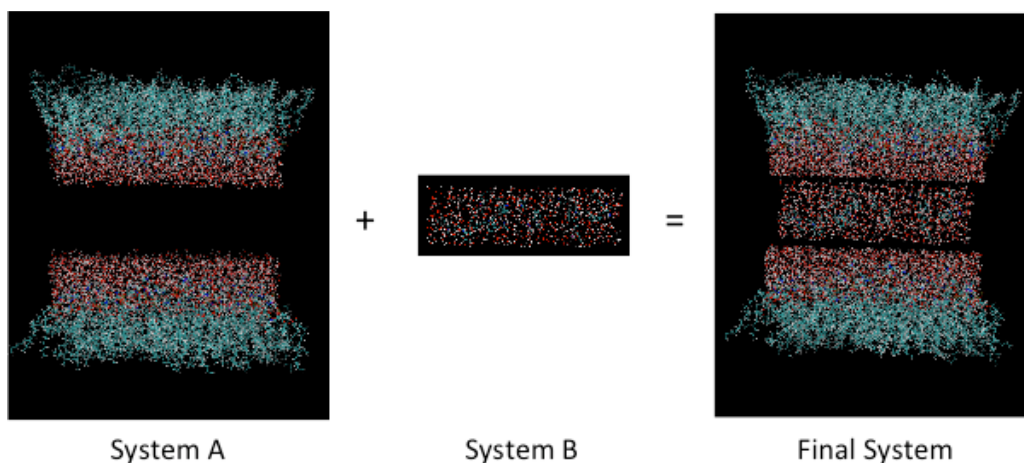
Figure A1.1: Snapshots during insertion procedure.

Using GROMACS, a 6 x 6 x 1.75 nm box (i.e., of slightly smaller size than the void in System A) was generated, containing the desired number of Phe molecules. The molecules were positioned randomly within the box in such a way as to avoid overlap between them, and subsequently solvated with water (System B, Figure A1.1).   Both systems were then combined by inserting the box of solvated Phe molecules between the two hydrated monolayers of DPPC and centering it within the void. The resulting configuration is shown in Figure A1.1. Finally, a short energy minimization was performed with GROMACS to prevent close contacts between atoms, followed by a 10ns equilibration NVT run at T=310 K. Any void space remaining in the system after the insertion of the box of Phe solution between the two DPPC monolayers was quickly eliminated within the first few tens of picoseconds of the simulation run.
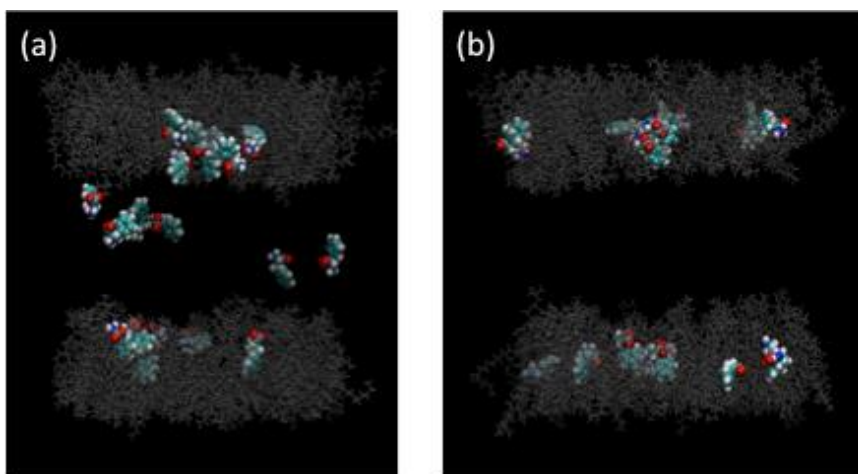
Figure A1.2: Snapshot after 20 ns of simulation of (a) zwitterionic Phe and (b) neutral Phe, DPPC system. DPPC molecules are shown in gray and water molecules are removed for clarity.
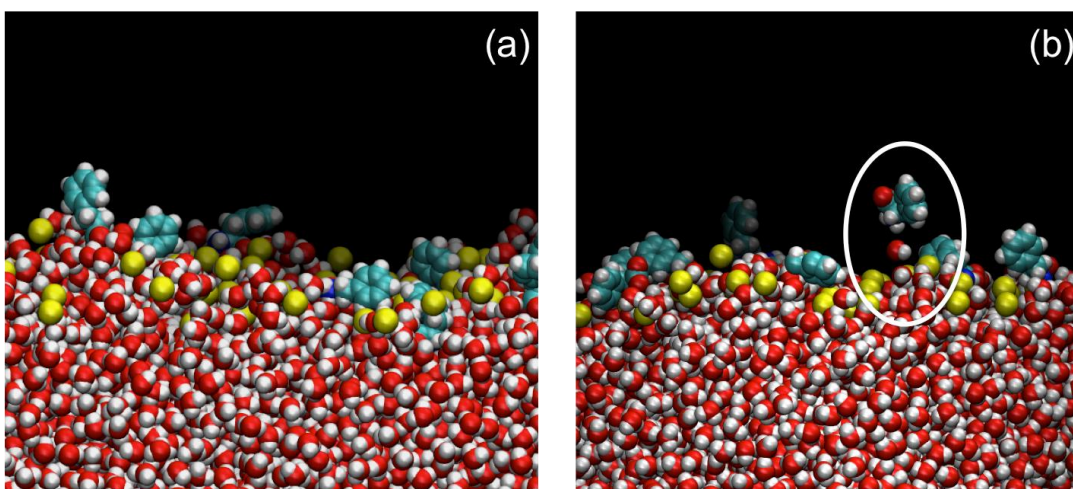
Figure A1.3: Snapshot from zwitterionic (a) and neutral (b) Phe within the DPPC film (only C2 atom from DPPC molecules are shown for clarity) illustrating occasional dehydration of neutral Phe molecules within film (indicated by white circle) but consistent solvation of headgroups of zwitterionic Phe throughout the simulations.
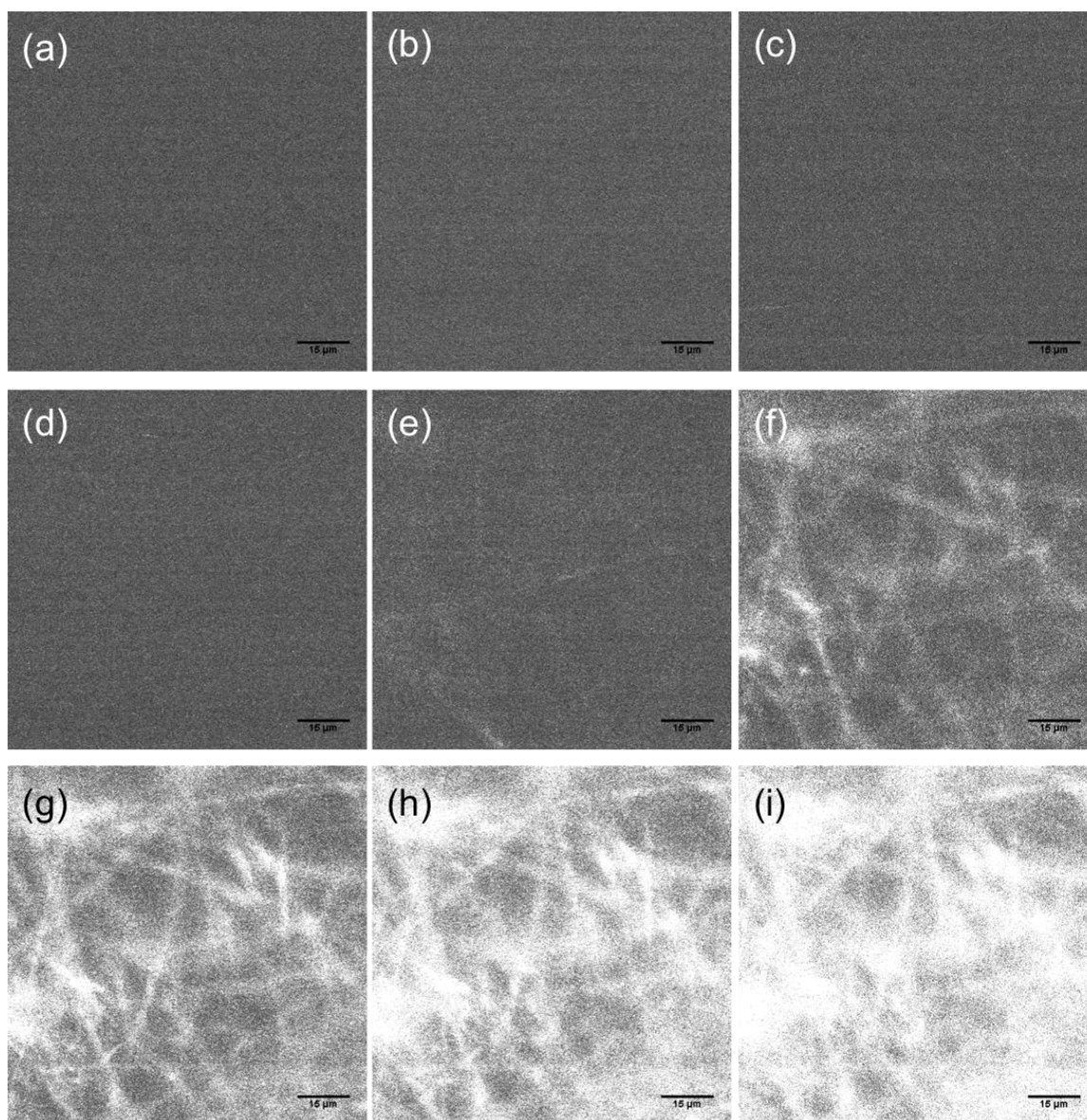
Figure A1.4: Confocal microscope images over time during drying out of 120 mM Phe solution forming fibrils.   The images are taken at the following times after deposition: (a) 1 minute, (b) 7 minutes, (c) 8 minutes, (d) 8.5 minutes, (e) 9 minutes, (f) 9.5 minutes, (g) 10 minutes, (h) 10.5 minutes, (i) 11 minutes. Scale bars represent 15 μm.
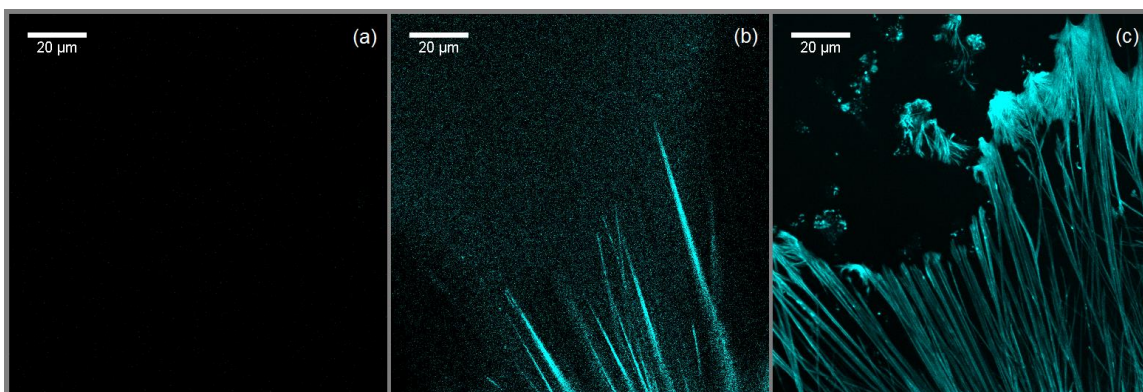
Figure A1.5: *Confocal microscope images of 2.5 mM Phe solution (a) immediately after deposition on slide, (b) fibrils forming in solution as the drop dries and shrinks and (c) dried fibrils in better focus. Scale bar represents 20 μm.*
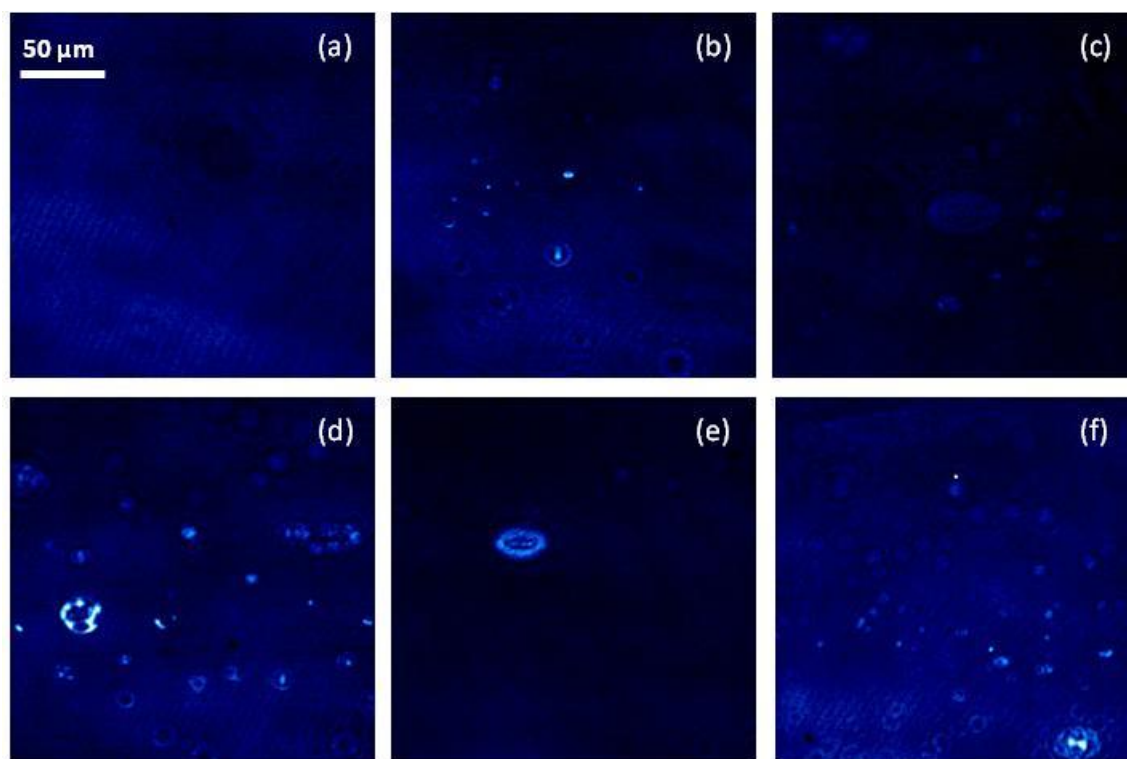
Figure A1.6: BAM images of 2.5, 10 and 20 mM Phe only aggregates at the bare water surface (a) and (b) 2.5mM Phe at 0 and 16500 s, (c) and (d) 10 mM Phe at 0 and 16500 s, (e) and (f) 20 mM Phe at 0 and 16500s. Scale bar represents 50μm.
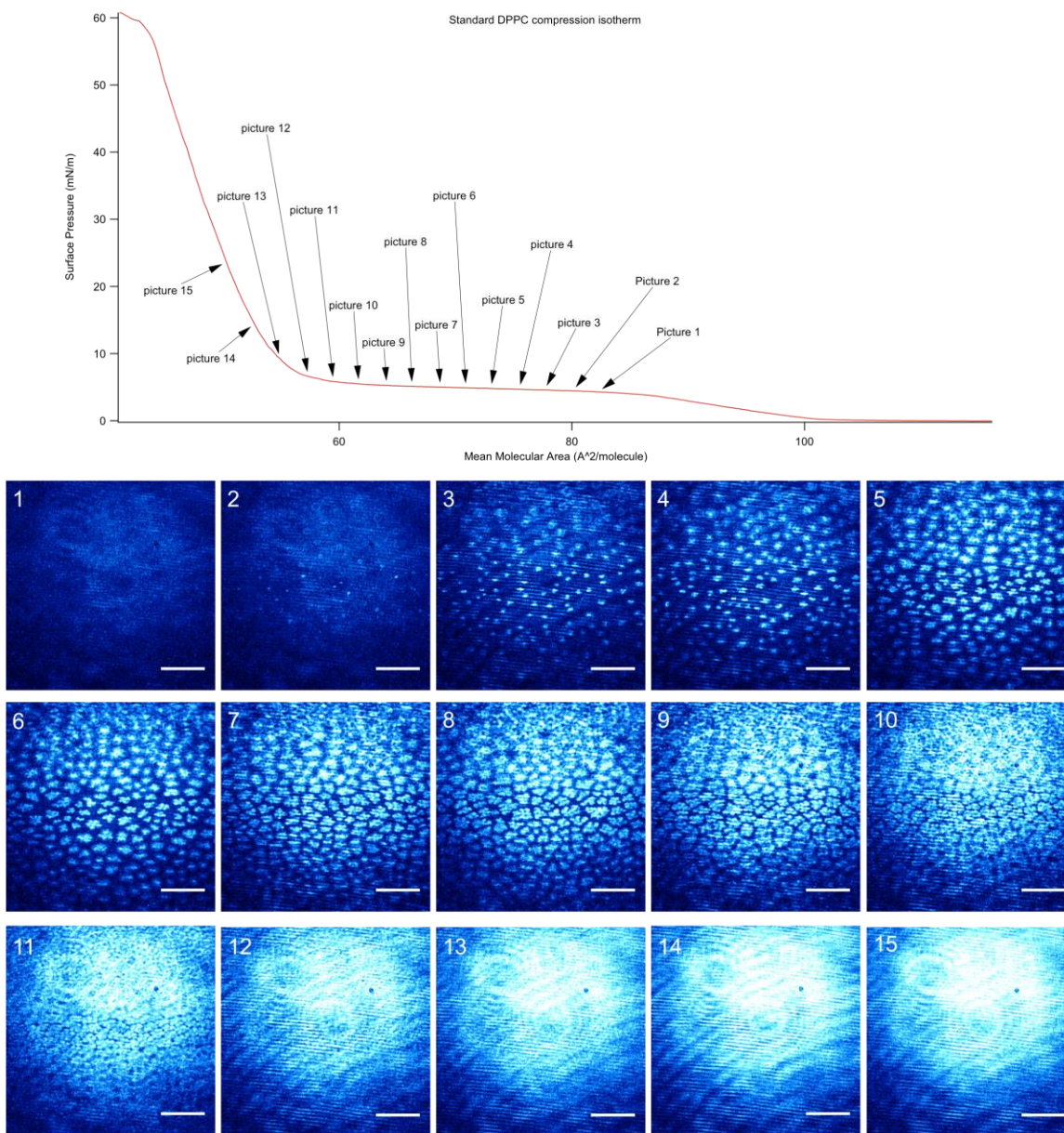
Figure A1.7: Isotherm of DPPC deposited on water with corresponding BAM images in different phases throughout its isotherm as indicated.
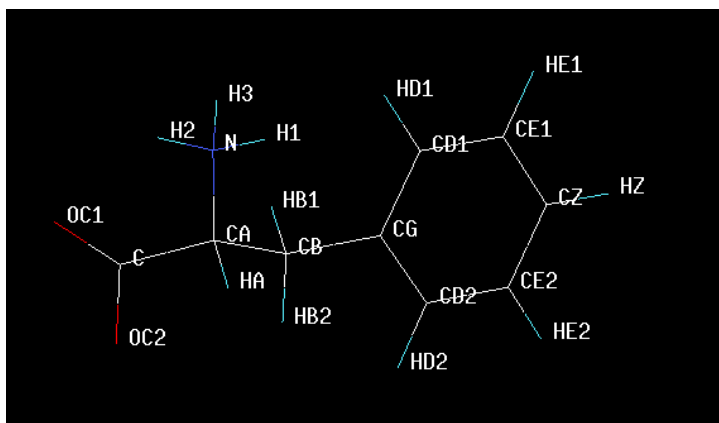
Figure A1.8. Atom names for zwitterionic Phe

Table A1.1: Atomic types and charges for zwitterionic Phe. Atom names correspond to Figure A1.8.

Atom name	Amber ff03 atom type	Charge
N	N3	-0.335478
H1	H	0.266212
H2	H	0.266212
H3	H	0.266212
CA	CT	0.003747
HA	HP	0.098054
CB	CT	-0.369740
HB1	HC	0.127679
HB2	HC	0.169801
CG	CA	0.237468
CD1	CA	-0.209531
HD1	HA	0.129611
CE1	CA	-0.122457
HE1	HA	0.131357
CZ	CA	-0.129696
HZ	HA	0.128047
CE2	CA	-0.122457
HE2	HA	0.131357
CD2	CA	-0.209531
HD2	HA	0.129611
C	C	0.678048
OC1	O2	-0.632264
OC2	O2	-0.632264
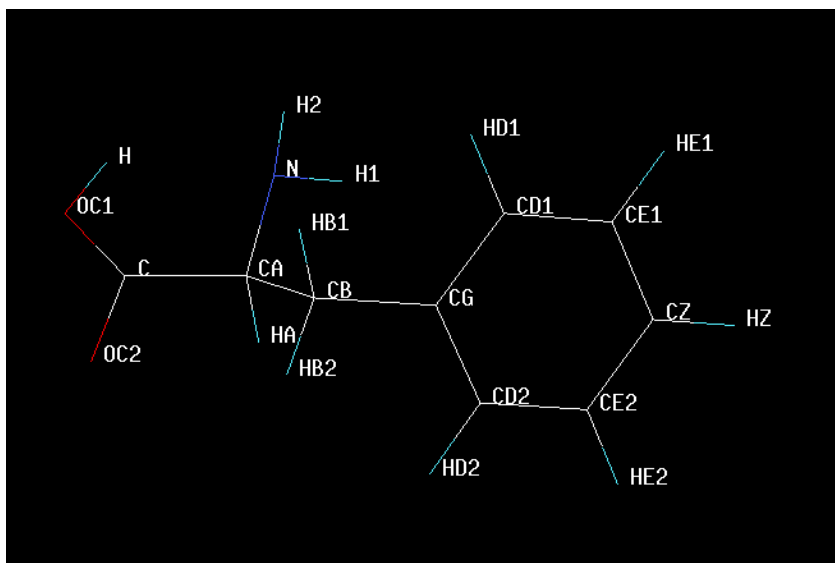
Figure A1.9. Atom names for neutral Phe

Table A1.2: Atomic types and charges for neutral Phe. Atom names correspond to Figure A1.9.

Atom name	Amber ff03 atom type	Charge
N	N3	-0.841199
H1	H	0.326533
H2	H	0.326533
CA	CT	0.238852
HA	HP	0.025766
CB	CT	-0.257047
HB1	HC	0.083838
HB2	HC	0.057174
CG	CA	0.171940
CD1	CA	-0.169748
HD1	HA	0.108205
CE1	CA	-0.117582
HE1	HA	0.121796
CZ	CA	-0.122945
HZ	HA	0.119201
CE2	CA	-0.117582
HE2	HA	0.121796
CD2	CA	-0.169748
HD2	HA	0.108205
C	C	0.550381
OC1	OH	-0.484507
OC2	O	-0.431490
H	HO	0.351627

Appendix 2: Supporting Information for Chapter 5

A2.1 Adsorption Isotherms to Bare Water
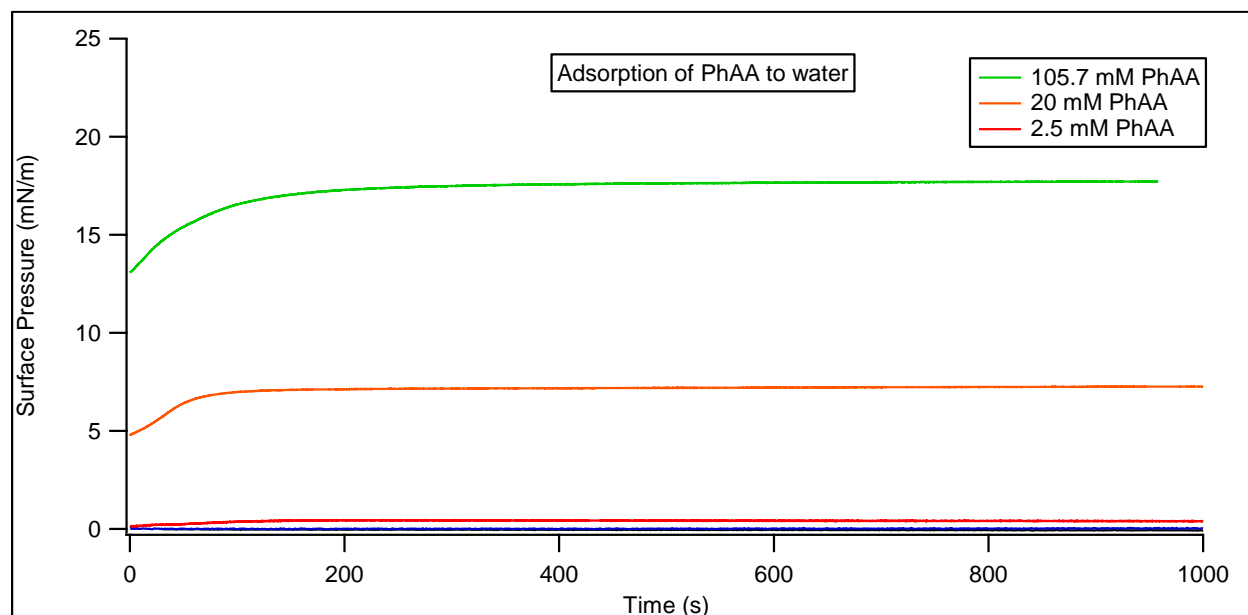
Figure A2.1: Adsorption of PhAA to water as a function of concentration.

Raw data is shown in red, and was collected as described in the experimental section of the main paper. Average traces are shown in black and were obtained by averaging the shown raw data in Igor Pro using the Average Waves function. Point by point standard deviations were generated using the same tool, and used to calculate uncertanties averaged over a given time period.
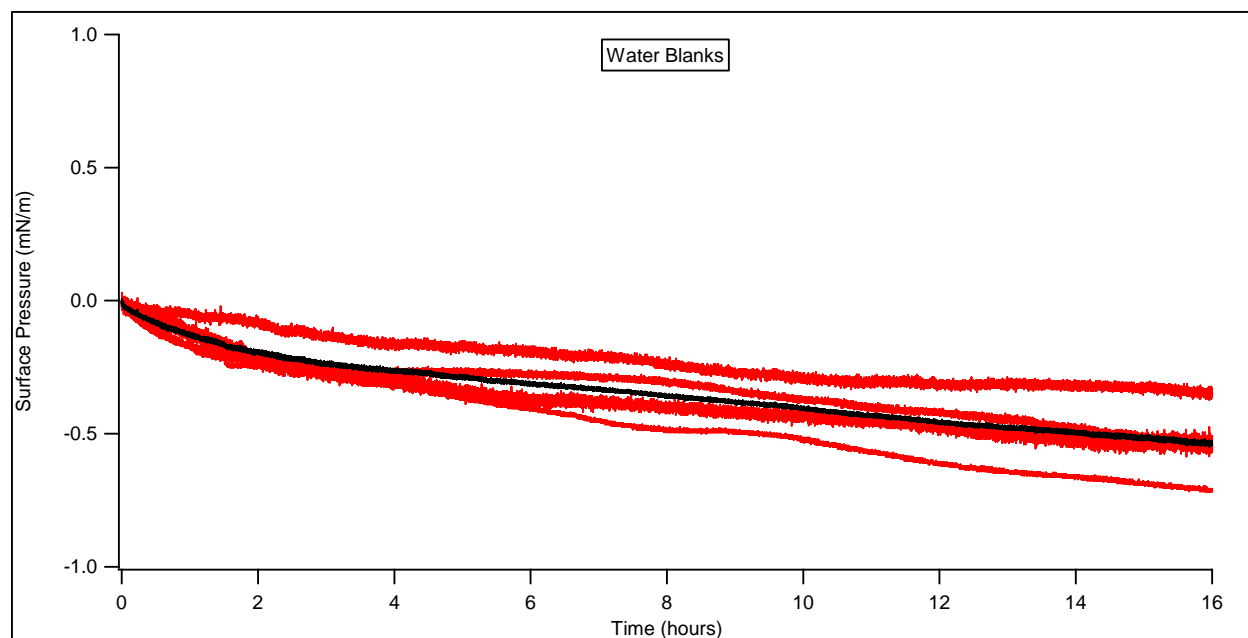
Figure A2.2: Change in surface pressure over time for a pure water (18.2 mΩ, 3 ppb total oxadizable

carbon).
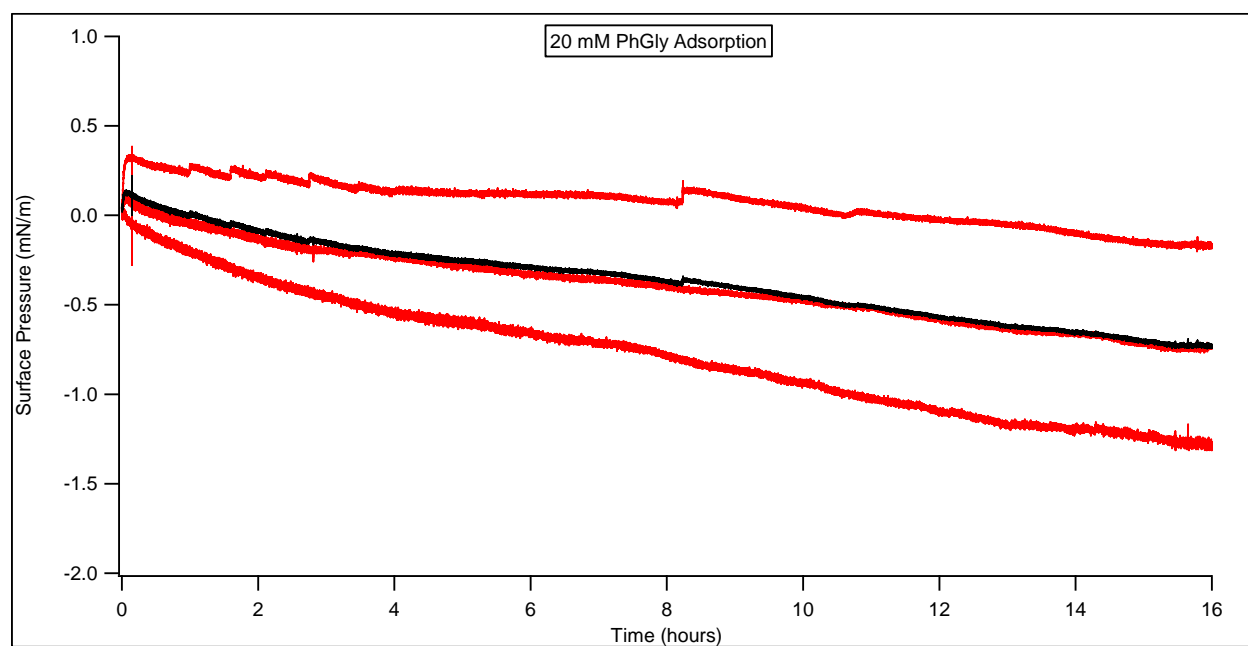
Figure A2.3: Adsorption isotherm for 20 mM PhGly solution over time.
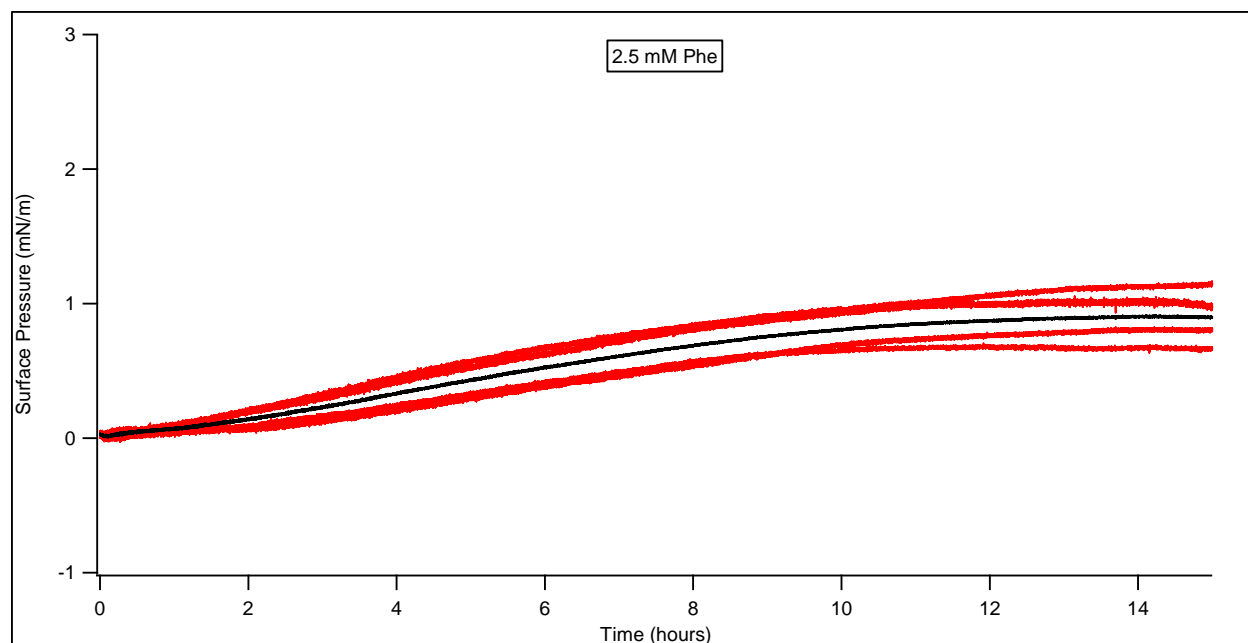
Figure A2.4: Adsorption isotherm of 2.5 mM Phe over time.
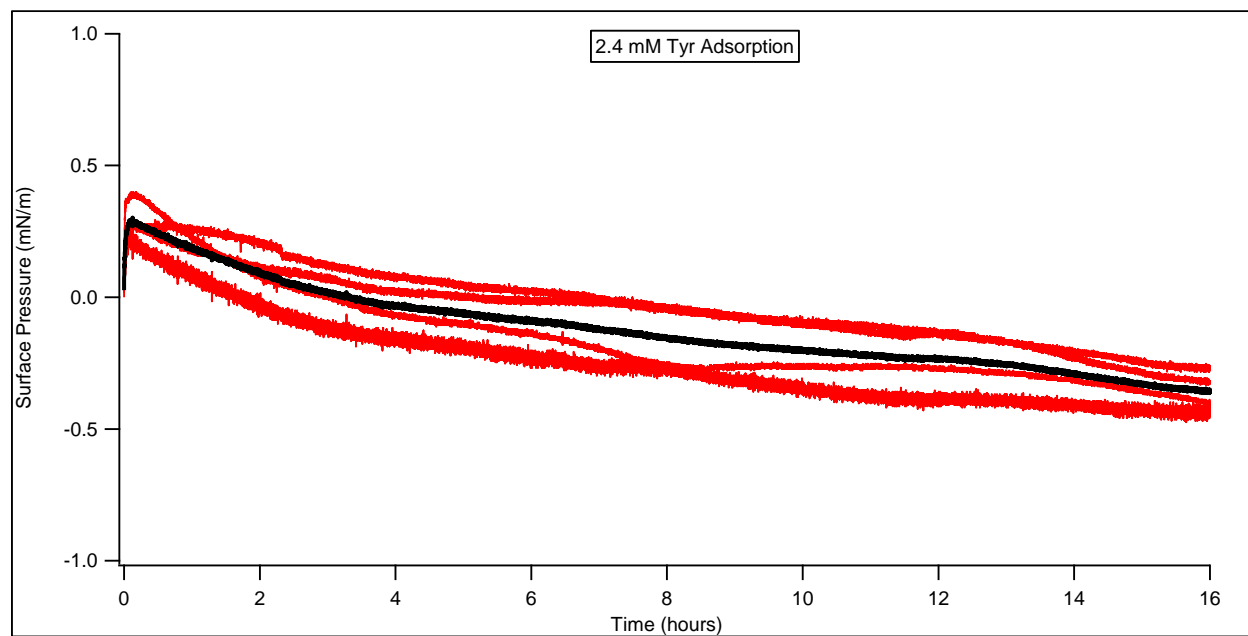
Figure   A2.5:   Adsorption   isotherms   for   2.4   mM   Tyr   over   time.

Average isotherm data was corrected for water evaporation by subtracting the average water adsorption isotherm from the average adsorption isotherm for each soluble surfactant.
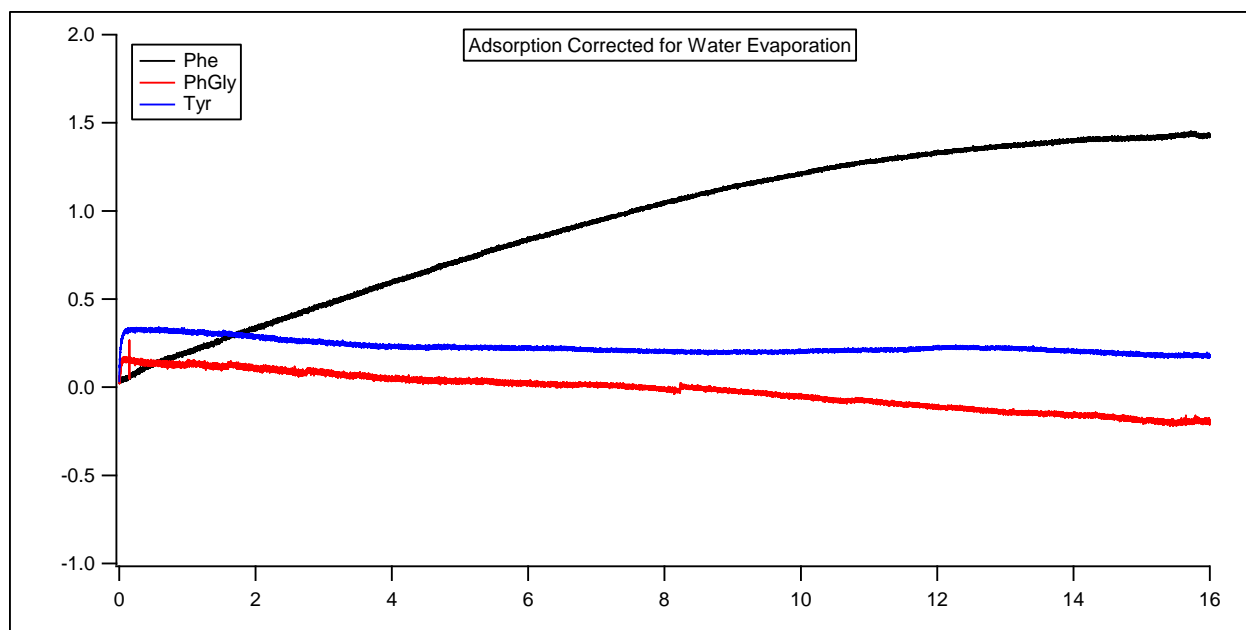
Figure A2.6: Water corrected average adsorption isotherms for Phe, PhGly, and Tyr.

DPPC adsorption isotherms were averaged in the same way. Mean molecular area was estimated for each film immediately following the acquisition of the adsorption isotherm by compressing the film and assuming a characteristic condensed phase was pressent at the surface pressure of 40 mN/m. This approach is assumed to be valid based on the observation that most film contaminants are removed at high surface pressures, including Phe and PhAA. This process is outlined for one DPPC run below, but was identical for all runs. Calibrations are shown on individual traces.
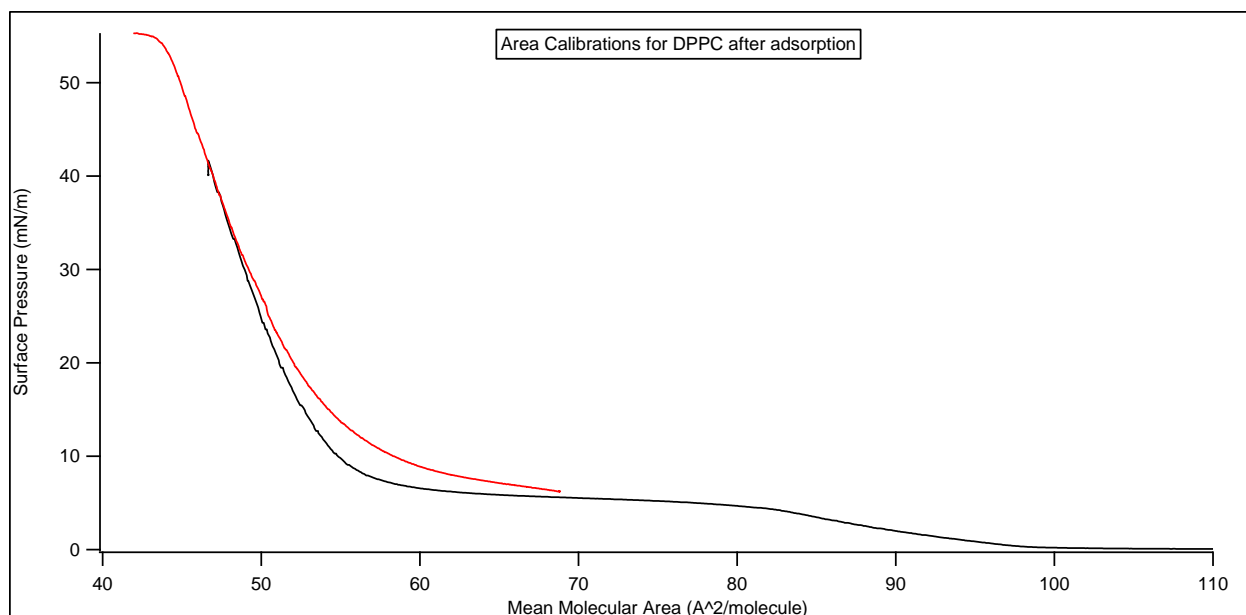
Figure A2.7: Example DPPC area calibration after an adsorption experiment was performed. The black trace is a standard DPPC compression isotherm, and the red trace is a compression isotherm after adsorption data was collected.
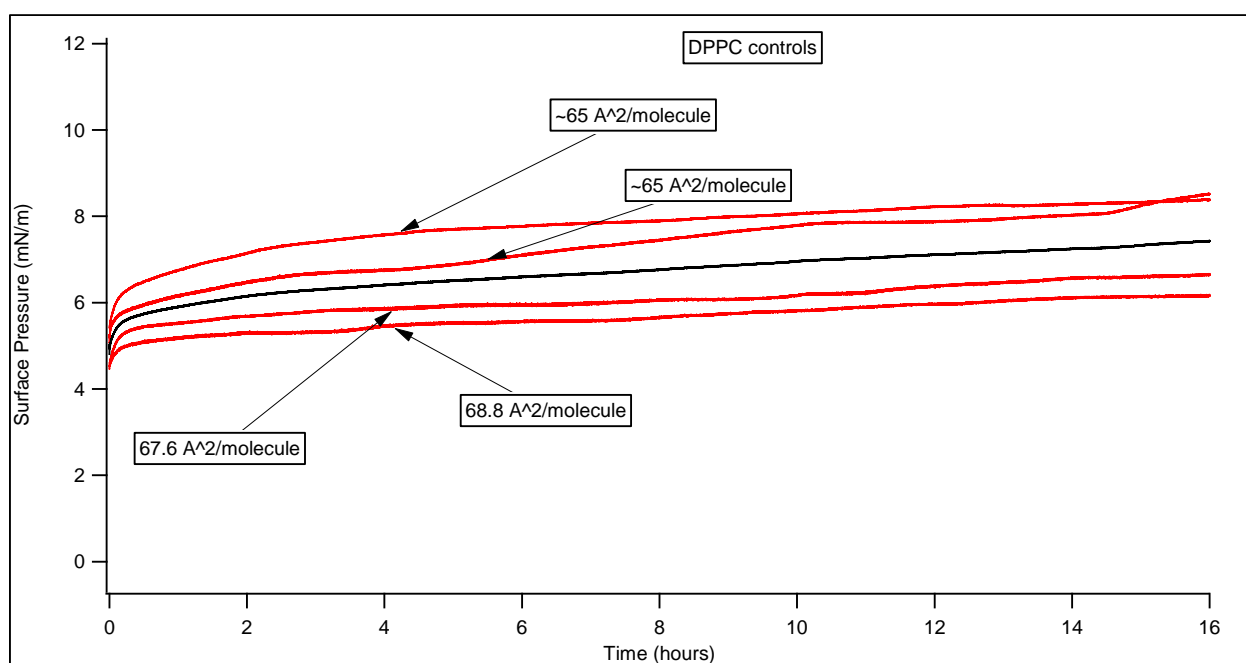
Figure A2.8: DPPC surface pressure over time.
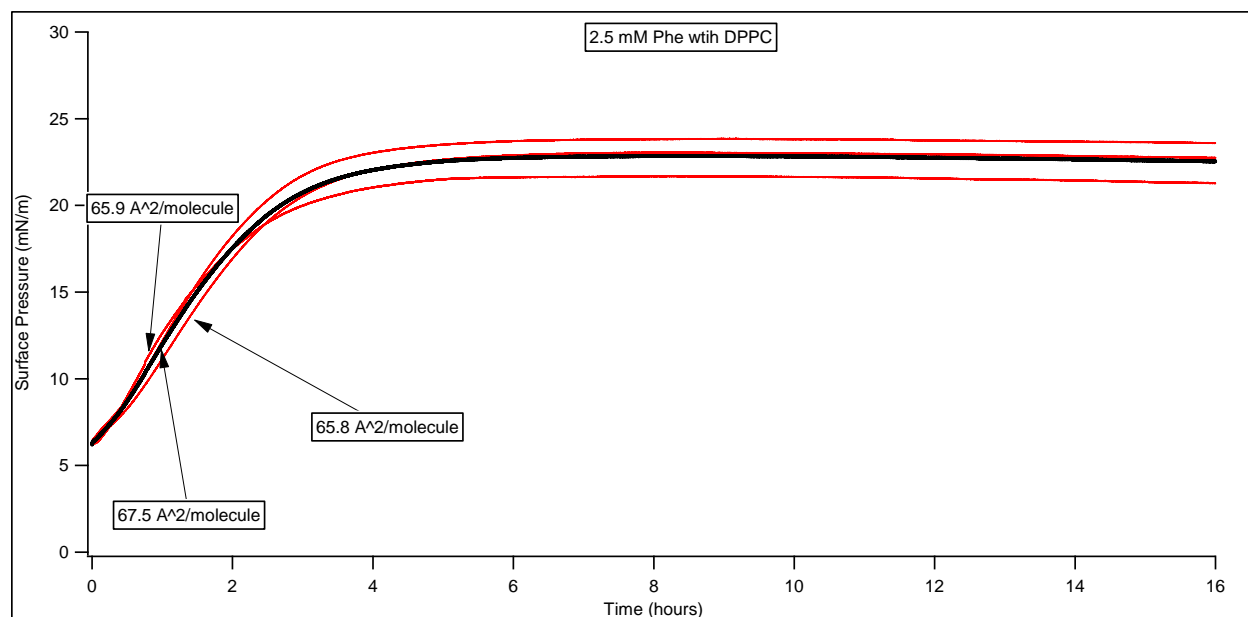
Figure A2.9: 2.5 mM Phe adsorbption isotherms in the pressence of a DPPC film. Individual traces are labeled with the calculated mean molecular area of DPPC after adsorption.
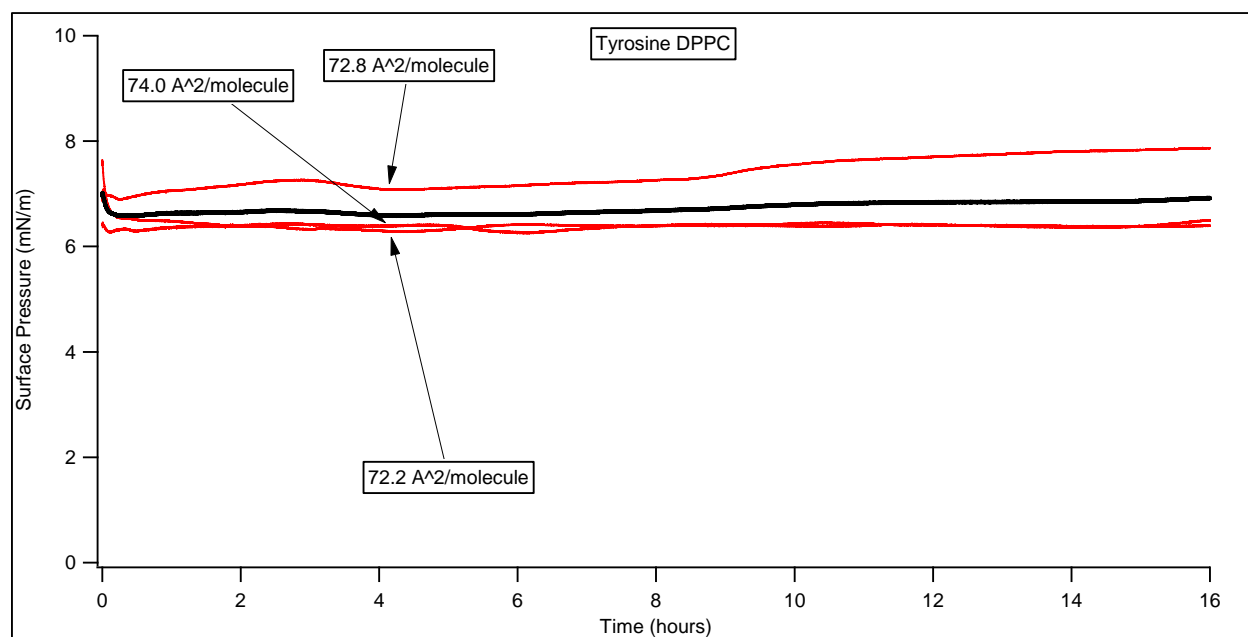
Figure A2.10: 2.4 mM Tyr adsorbption isotherms in the pressence of a DPPC film. Individual traces are labeled with the calculated mean molecular area of DPPC after adsorption.
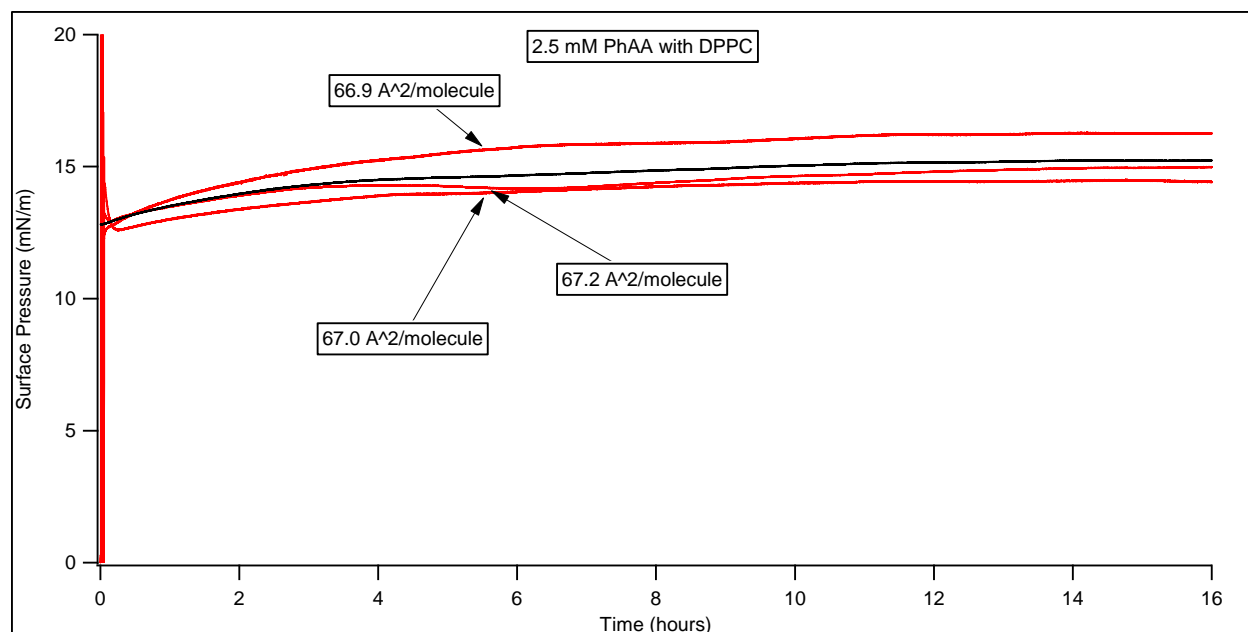
Figure A2.11: 2.5 mM PhAA adsorbption isotherms in the pressence of a DPPC film. Individual traces are labeled with the calculated mean molecular area of DPPC after adsorption.
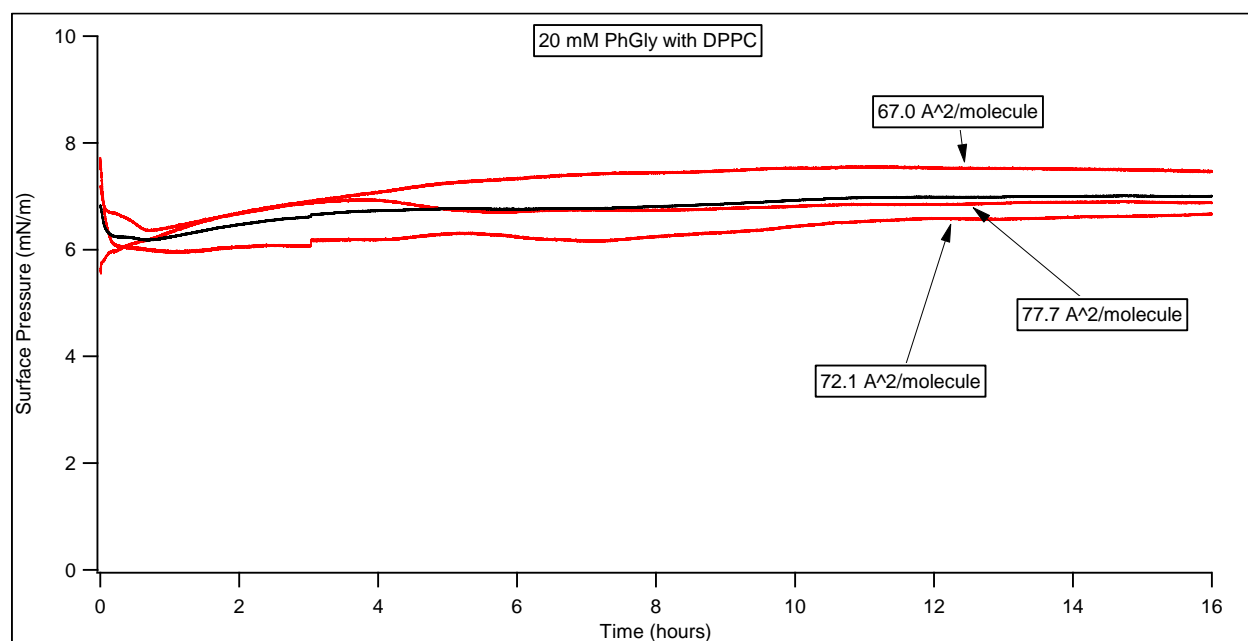
Figure A2.12: 20 mM PhGly adsorbption isotherms in the pressence of a DPPC film. Individual traces are labeled with the calculated mean molecular area of DPPC after adsorption.

Phe equilibrations times were estimated using evaporation corrected isotherms shown below in supplimental figure 12.
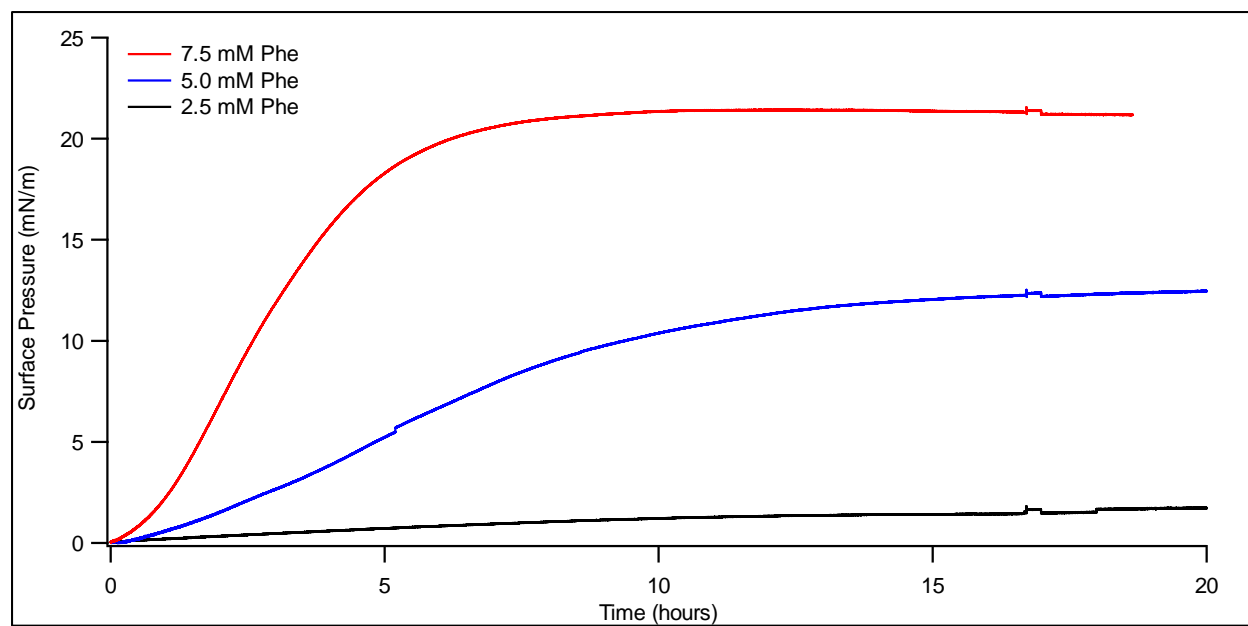
Figure A2.13: Adsorption isotherms of Phe as a function of concentration, corrected for water evaporation.

A2.2 NMR Diffusion (DOSY) Results

100 mMolar Phenylalanine:

HOD, D = 16.8 x10⁻¹⁰ m²/Sec

Phe, D = 5.0x10⁻¹⁰ m²/Sec

100 μMolar Phenylalanine:

HOD, D = 17.2 x10⁻¹⁰ m²/Sec

Phe, D = 5.2x10⁻¹⁰ m²/Sec
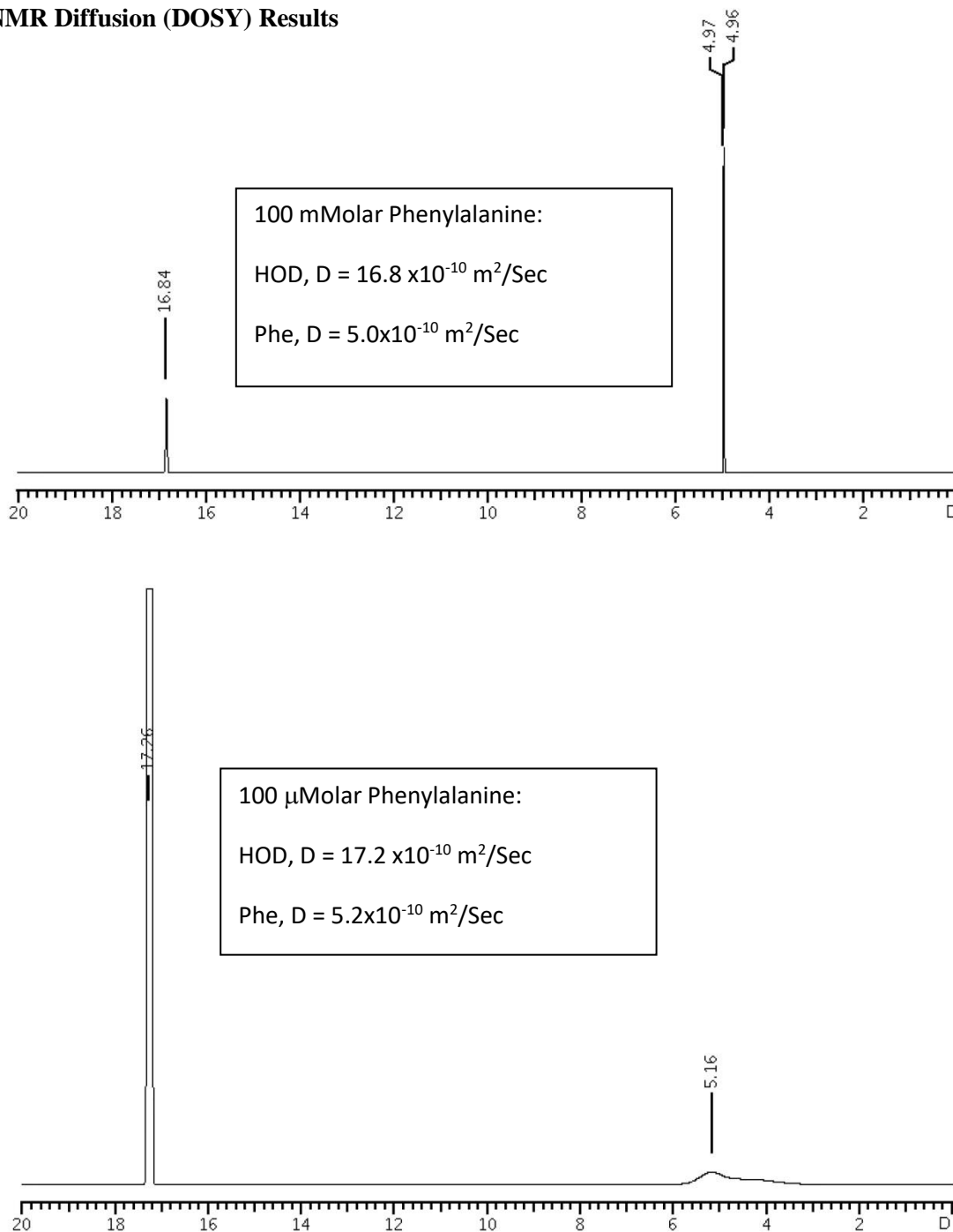
Figure A2.14: Projections of the Diffusion Dimension of DOSY NMR experiments from 100 mM (top) and 100 μM (bottom) Phe samples. The peak near 5 is the diffusion constant calculated for Phe and the peak near 17 is the calculated diffusion constant for HOD (singly deuterated water). The ratio of $D_{(HOD)}:D_{(Phe)}$ is 3.4 ±0.1 for both, indicating that the small change in $D_{(Phe)}$ is due to the change in solution viscosity with increasing Phe concentration. The larger error in $D_{(Phe)}$ at 100 μM is due to lower Signal:Noise after 18 hours of acquisition time.

A2.3 Electrospray Ionization Mass Spec. Results

5 V Electrospray Data - % of Monomer					
AA/cluster size	1	2	3	4	5
Phe	100.000	10.000	0.644		
PhGly	100.000	6.204	1.491		
PhAA	100.000	6.148	0.131		
Tyr	100.000	80.405	42.793	16.441	4.572
50 V Electrospray Data - % of Monomer					
AA/cluster size	1	2	3	4	5
Phe	100.000	11.908	0.540		
PhGly	100.000	50.776	4.346		
PhAA	100.000	48.537	32.846		
Tyr	100.000	34.217	11.826	4.609	2.048

Table A2.1: Electrospray Ionization Clustering Data for 1 mM solutions of each amino acid in a 1:1 mixture of water and methanol, Ionized at 5 volts and 50 volts. PhAA displays the least clustering under 5 V ionization conditions, but the most clustering at 50 V.

A2.4 Simulation Details
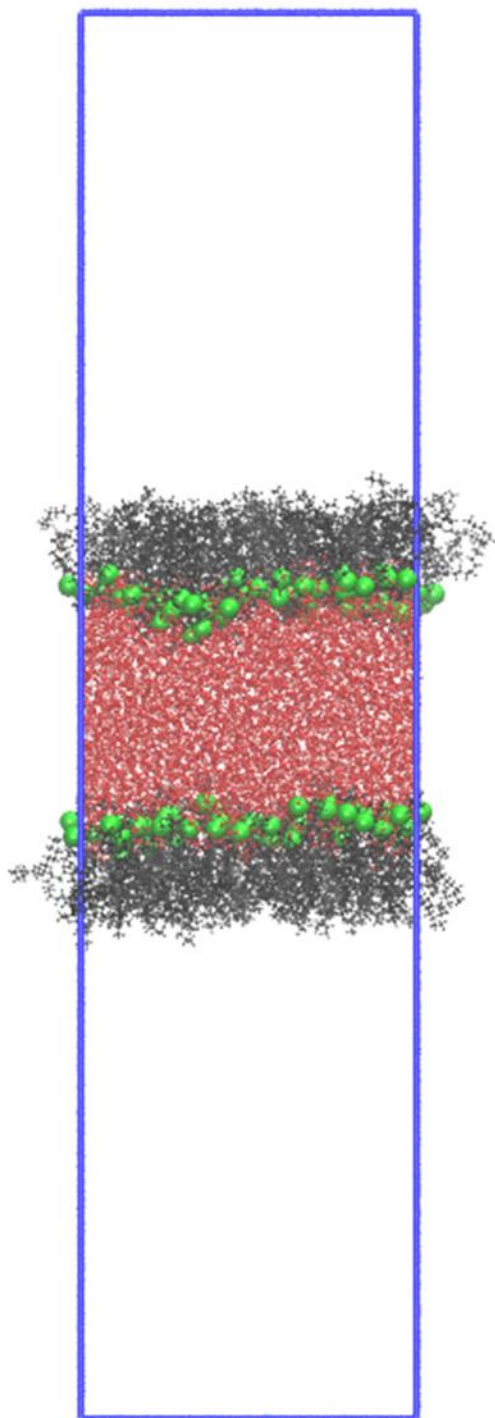
Figure A2.15: Schematic representation of the simulation box. A side view in the direction parallel to the water-air interface is shown. A slab of water (red) is placed in the middle of the periodic box (blue) hence forming two water-air interfaces. In DPPC-containing systems both interfaces are covered by DPPC molecules (black for acyl chains and green for phosphorus atoms of headgroups).
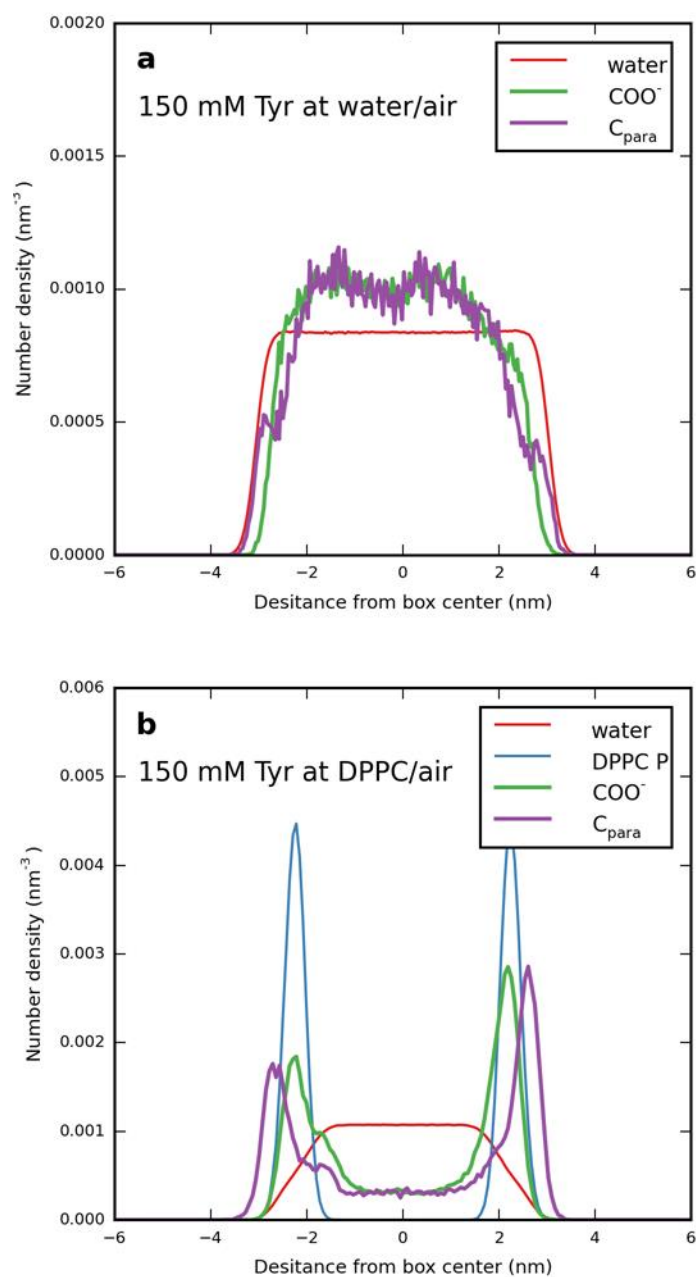
Figure A2.16. Density profiles for 150 mM Tyrosine at air-water (a) and air-DPPC-water (b) interfaces.

Appendix 3: Supporting Information for Chapter 6

Permeability Coefficient Fitting Procedure

Fitting procedures were carried out as described elsewhere,[1] although some details were not clear in the literature explanations. For the sake of clarity and completeness, the entire fitting procedure will be described here. The raw fluorescence data for each ribose addition was first normalized and corrected by the normalized buffer addition data. Normalization occurred so that the average value of the last 10 seconds of fluorescence data was one. This was then scaled to fit with the empirical emissivity equation discussed in Chapter 6, such that the calcein concentration could be determined from the fluorescence data. This was constrained so that the last 10 seconds of data produced approximately a 0.018 mM calcein concentration. This calcein concentration was then used to calculate a volume fraction as a function of time, such that during the last 10 seconds of data the volume fraction averaged to one. This volume fraction was the experimental data that the fit was compared to.

The fitting of the experimental data was performed in a stepwise fashion. It is assumed for these calculations that the movement of water across the membrane is much faster than the movement of solute. This manifests itself in the assumptions that no solute has crossed the membrane at time 0, and that the vesicles are assumed to be at osmotic equilibrium. The volume fraction at each timestep was calculated as the fraction of the internal concentration of osmolyte divided by the external concentration of osmolyte. The concentrations used took into account all ions in the case of dissociative species. External osmolyte concentrations were assumed to be constant, as the encapsulated volume of the vesicles was less than 1.5% of the solution volume. For the initial timestep there was assumed to be no ribose inside the vesicle. For each timestep the movement of osmolyte across the membrane was calculated using the equation

$$\frac{dN_s}{dt} = P_s * A * (c_s^{in} - c_s^{out})$$

where N_s is the number of moles of ribose inside the vesicle, P_s is the permeability coefficient of the membrane to ribose, A is the exposed surface area of a single vesicle, and c_s is the concentration of ribose either inside or outside the vesicle, as indicated by the superscript. In order for the units on dN_s/dt to be in moles/s, surface area was expressed in dm^2, permeability coefficient was expressed in dm/s, and concentrations were given in moles/L. For subsequent timesteps, dN_s/dt was added to the number of moles of ribose encapsulated by the vesicle, and c_s^{in} was adjusted accordingly. This fitting technique left a single free parameter for evaluation, P_s, which was then fit using a least square minimization comparing the experimental and theoretical volume fractions at each time point. Individual traces were all fit using this method, and average values and standard deviations of the mean were then calculated.

Bibliography

(1)   Sacerdote, M. G.; Szostak, J. W. Semipermeable Lipid Bilayers Exhibit Diastereoselectivity Favoring Ribose. *Proc. Natl. Acad. Sci.* **2005**, *102* (17), 6004–6008.

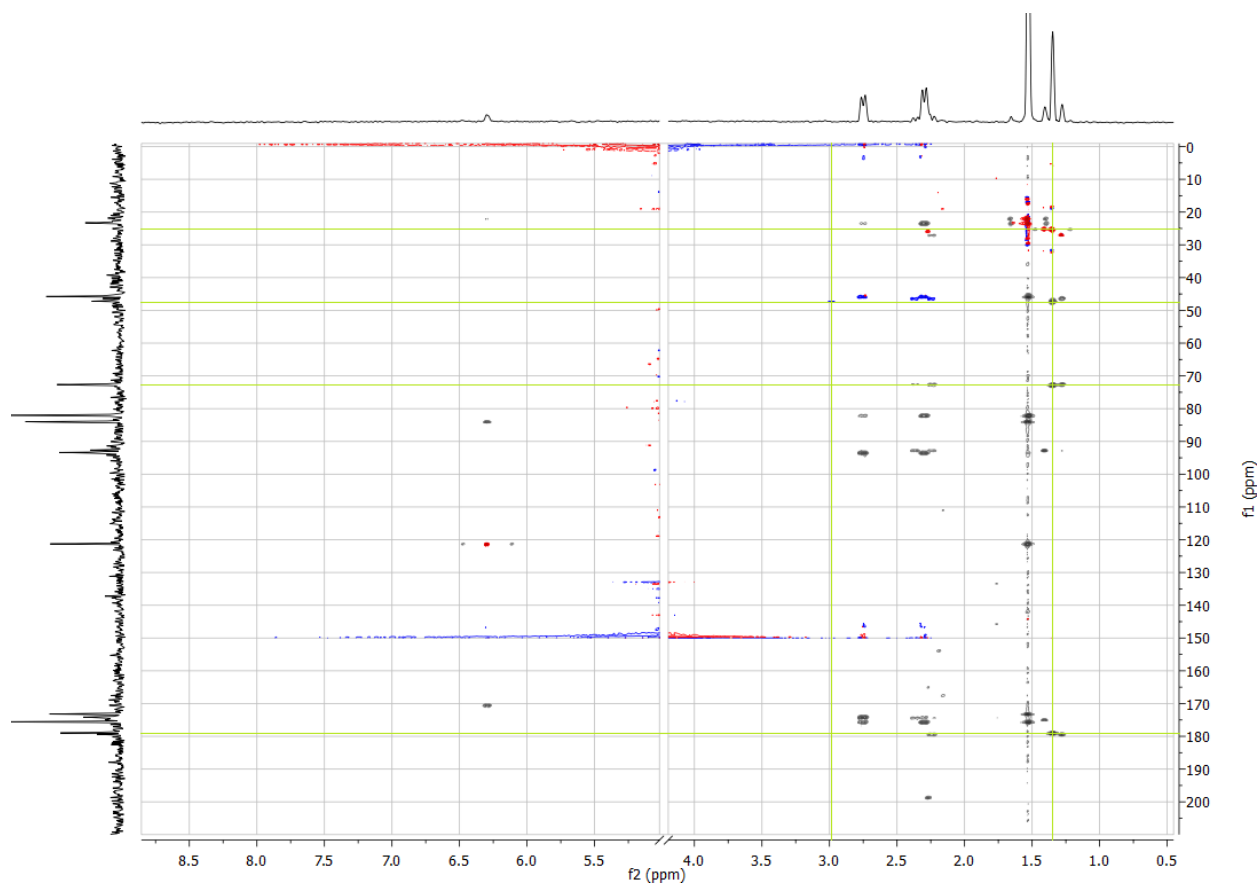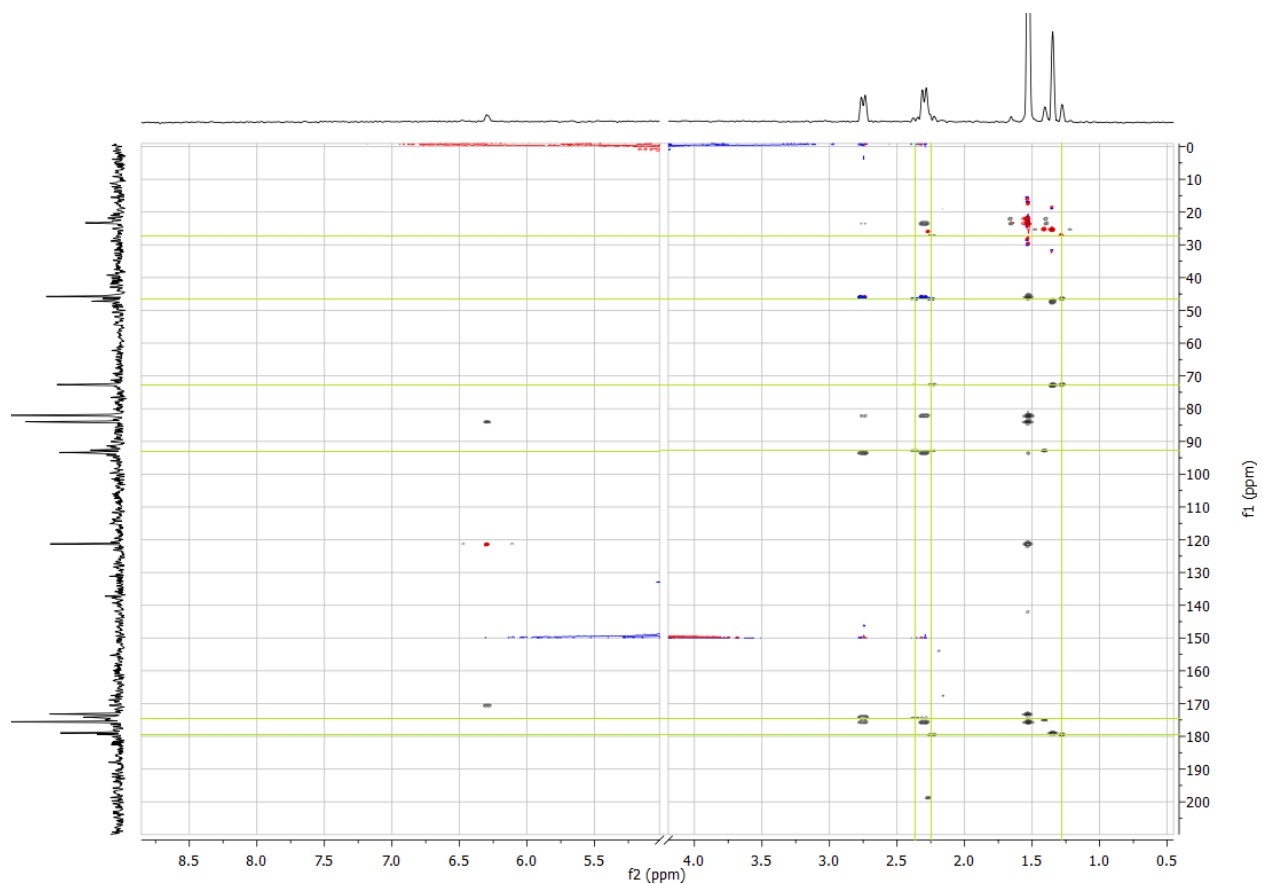# Appendix 4: Supporting Information for Chapter 8
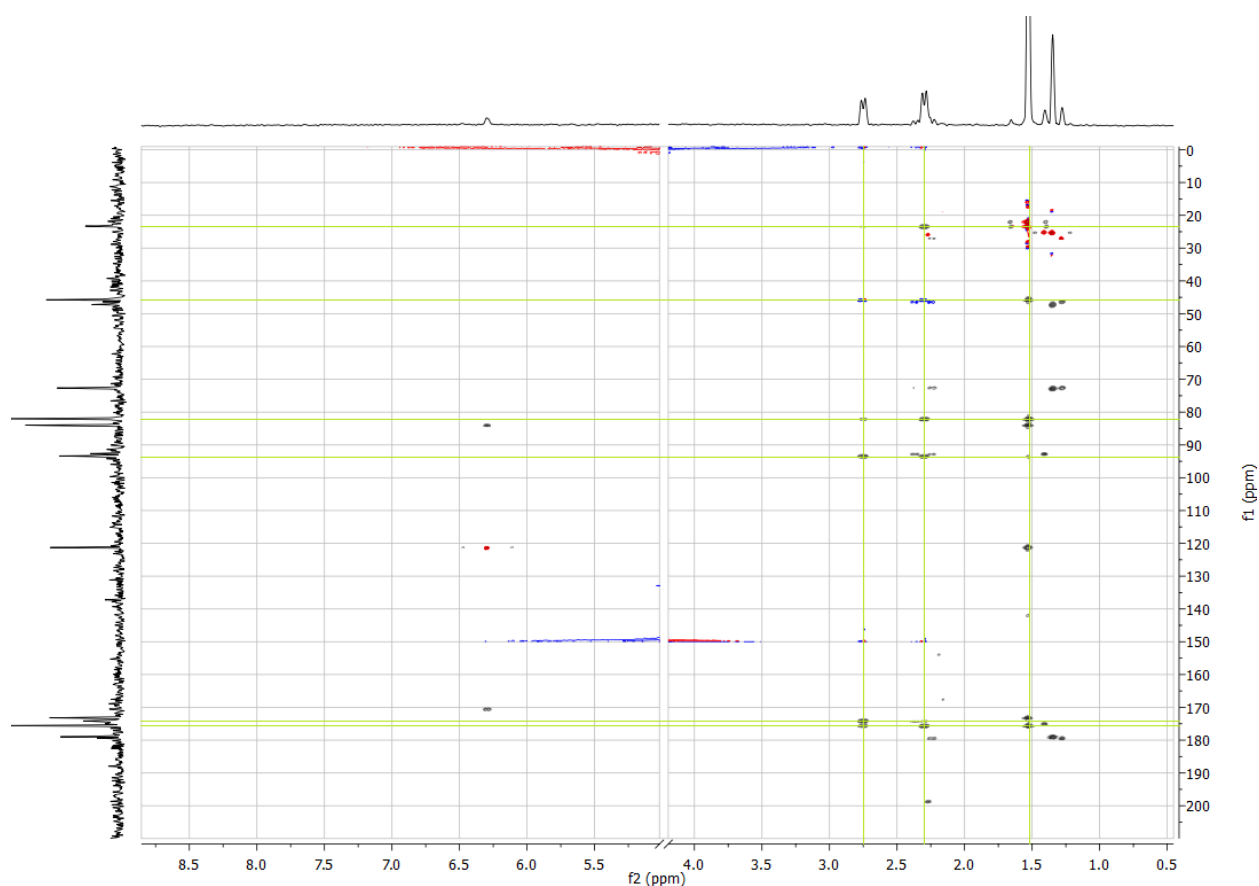
Figure A4.1: HMBC with overlapped HSQC spectra. F1 axis shows carbon chemical shifts and f2 axis shows proton chemical shifts. Water peak has been removed for clarity. HSQC peaks appear blue for CH₂ group and red for CH or CH₃ groups. Peaks associated with the closed diol form of zymonic acid (ZCD) are shown with green lines.
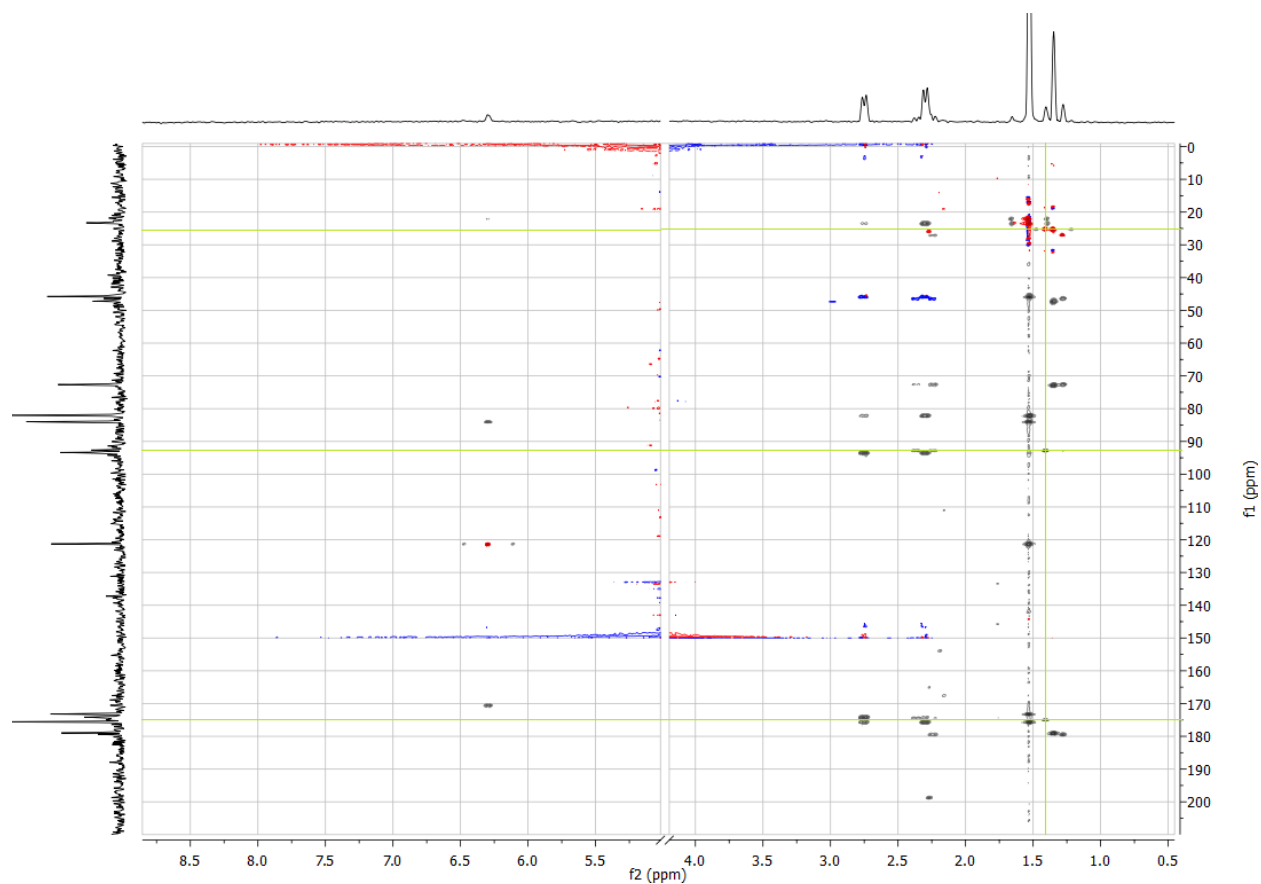
Figure A4.2: HMBC with overlapped HSQC spectra. F1 axis shows carbon chemical shifts and f2 axis shows proton chemical shifts. Water peak has been removed for clarity. HSQC peaks appear blue for CH₂ group and red for CH or CH₃ groups. Peaks associated with the closed enol form of zymonic acid (ZCE) are shown with green lines.
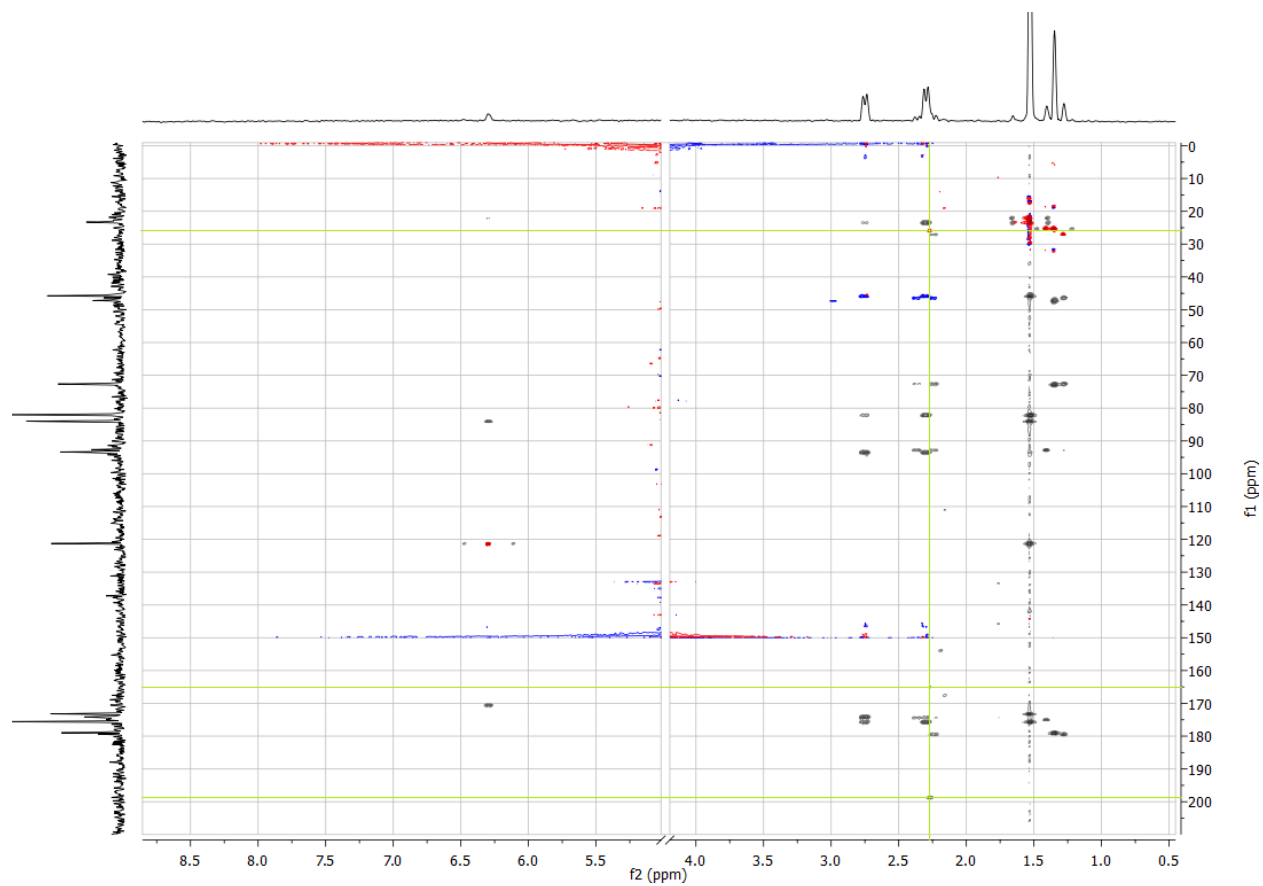
Figure A4.3: HMBC with overlapped HSQC spectra. F1 axis shows carbon chemical shifts and f2 axis shows proton chemical shifts. Water peak has been removed for clarity. HSQC peaks appear blue for CH₂ group and red for CH or CH₃ groups. Peaks associated with the ketone forms of zymonic acid (ZCK and ZOK) are shown with green lines. They are indistinguishable due to relatively quick exchange between the two species in solution. This also leads to broad peaks from nuclei close to the exchange site, which are difficult to observe.

Figure A4.4: HMBC with overlapped HSQC spectra. F1 axis shows carbon chemical shifts and f2 axis shows proton chemical shifts. Water peak has been removed for clarity. HSQC peaks appear blue for CH₂ group and red for CH or CH₃ groups. Peaks associated with the open diol form of zymonic acid (ZOD) are shown with green lines.

Figure A4.5: HMBC with overlapped HSQC spectra. F1 axis shows carbon chemical shifts and f2 axis shows proton chemical shifts. Water peak has been removed for clarity. HSQC peaks appear blue for CH_2 group and red for CH or CH_3 groups. Peaks associated with the diol form of pyruvic acid are shown with green lines.
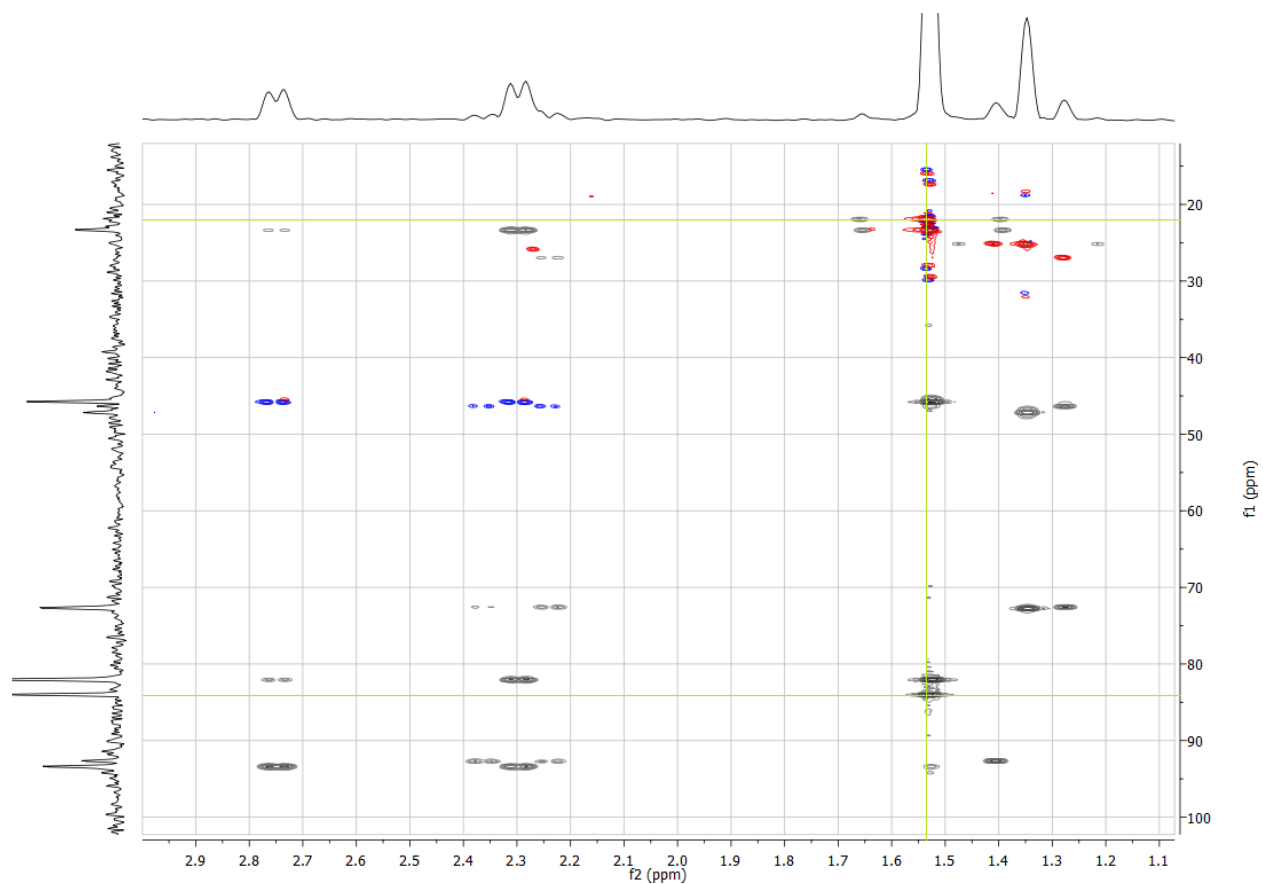
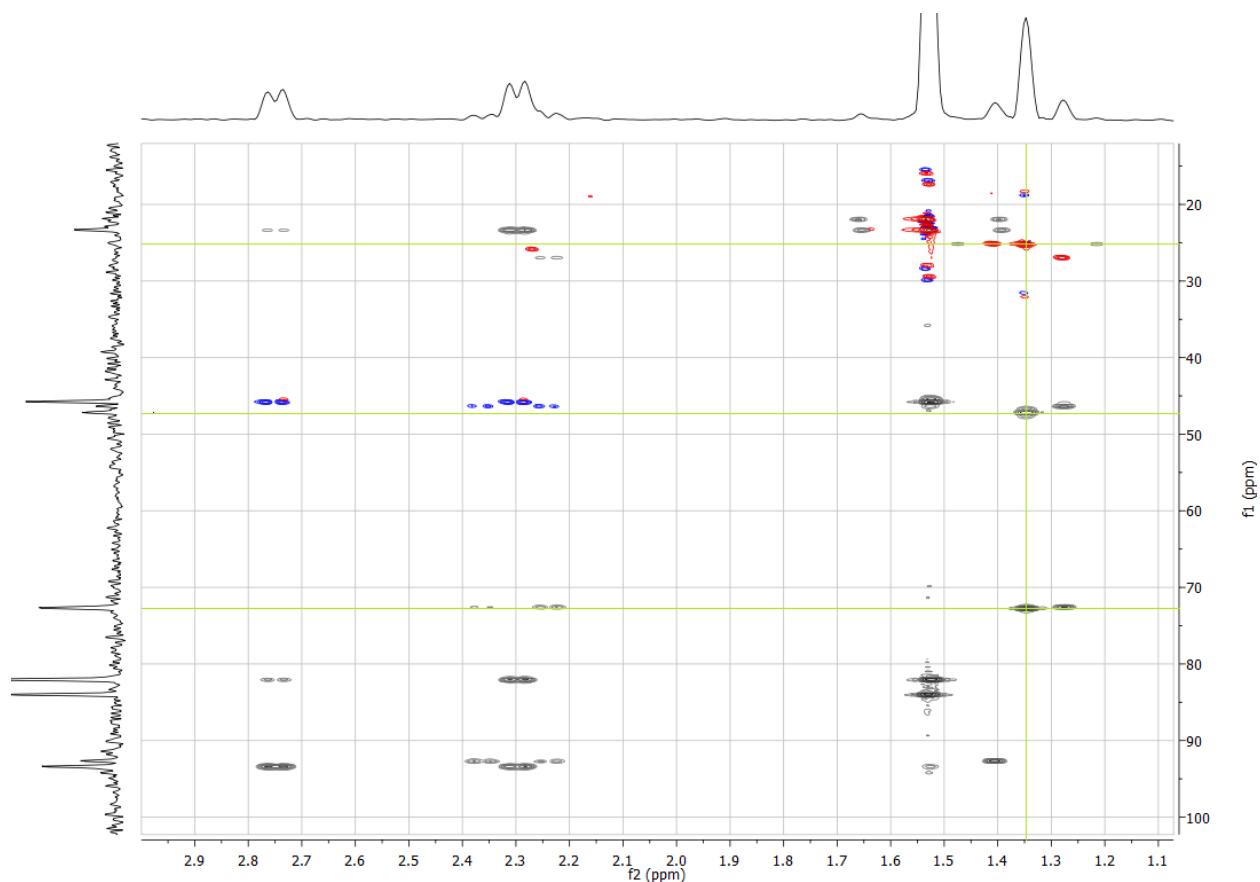*Figure A4.6: HMBC with overlapped HSQC spectra. F1 axis shows carbon chemical shifts and f2 axis shows proton chemical shifts. Water peak has been removed for clarity. HSQC peaks appear blue for CH₂ group and red for CH or CH₃ groups. Peaks associated with the ketone form of pyruvic acid are shown with green lines.*

Figure A4.7: Zoomed in view of HMBC with overlapped HSQC spectra. F1 axis shows carbon chemical shifts and f2 axis shows proton chemical shifts. Water peak has been removed for clarity. HSQC peaks appear blue for CH₂ group and red for CH or CH₃ groups. Peaks associated with the closed enol form of zymonic acid (ZCE) are shown with green lines.
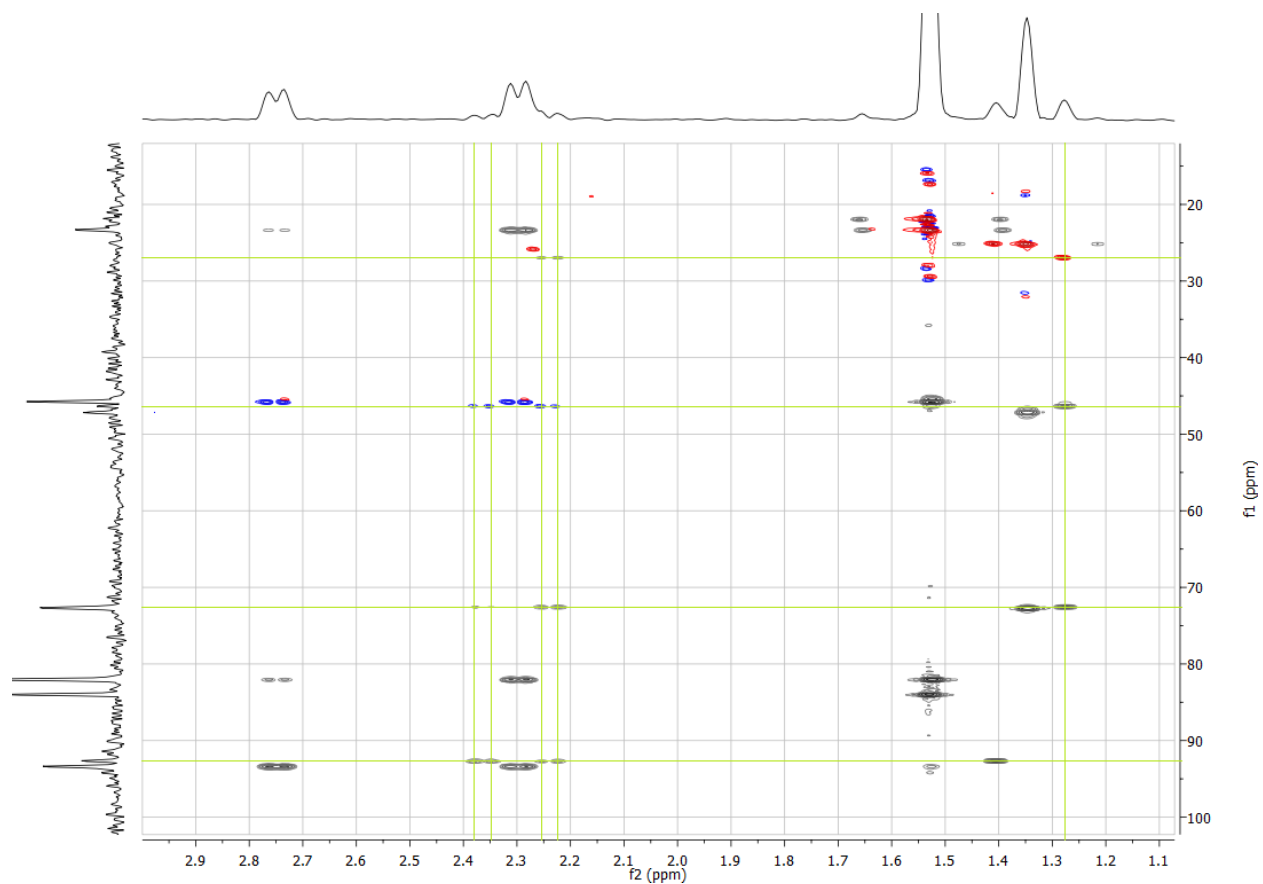
Figure A4.8: Zoomed in view of HMBC with overlapped HSQC spectra. F1 axis shows carbon chemical shifts and f2 axis shows proton chemical shifts. Water peak has been removed for clarity. HSQC peaks appear blue for CH$_2$ group and red for CH or CH$_3$ groups. Peaks associated with the ketone forms of zymonic acid (ZCK and ZOK) are shown with green lines. They are indistinguishable due to relatively quick exchange between the two species in solution. This also leads to broad peaks from nuclei close to the exchange site, which are difficult to observe.

Figure A4.9: Zoomed in view of HMBC with overlapped HSQC spectra. F1 axis shows carbon chemical shifts and f2 axis shows proton chemical shifts. Water peak has been removed for clarity. HSQC peaks appear blue for CH₂ group and red for CH or CH₃ groups. Peaks associated with the open diol form of zymonic acid (ZOD) are shown with green lines.
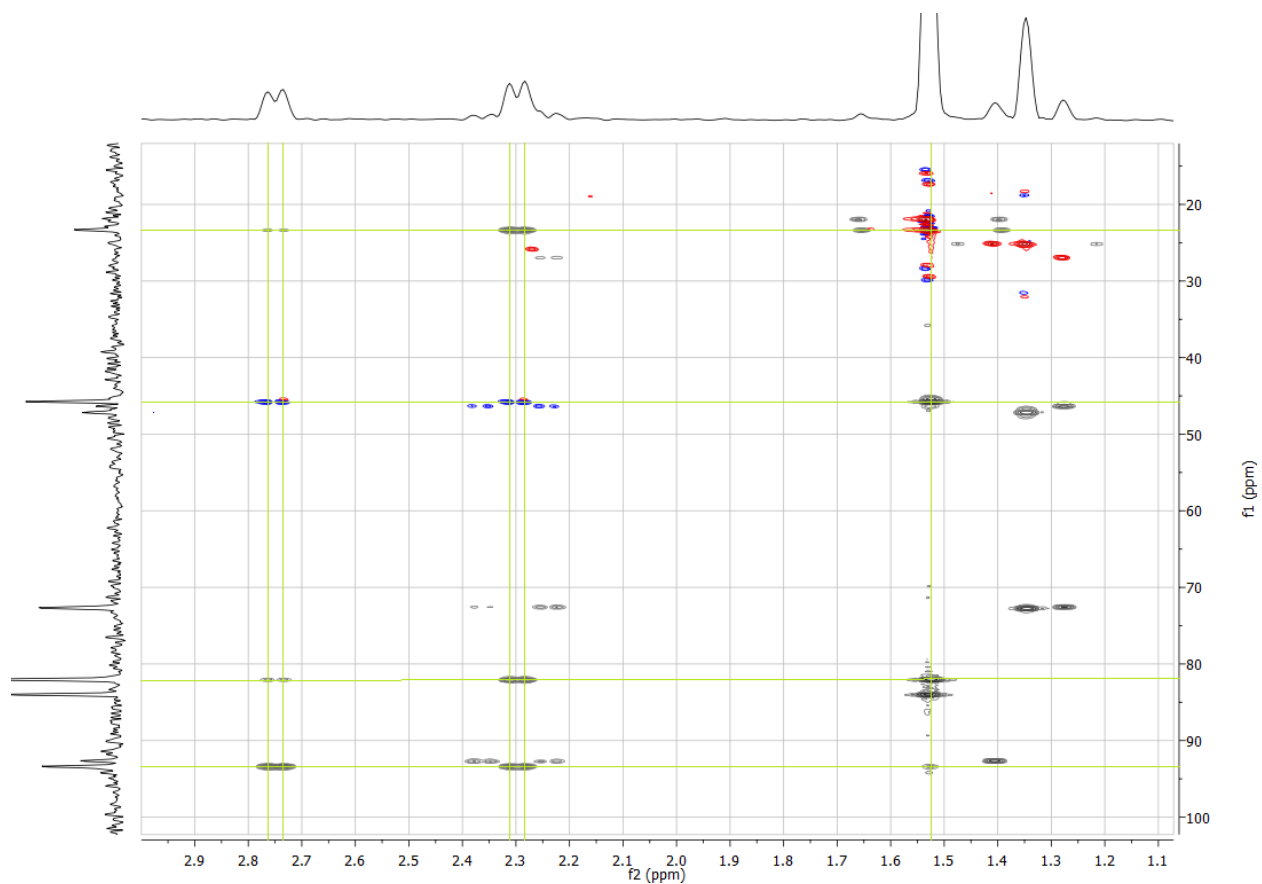
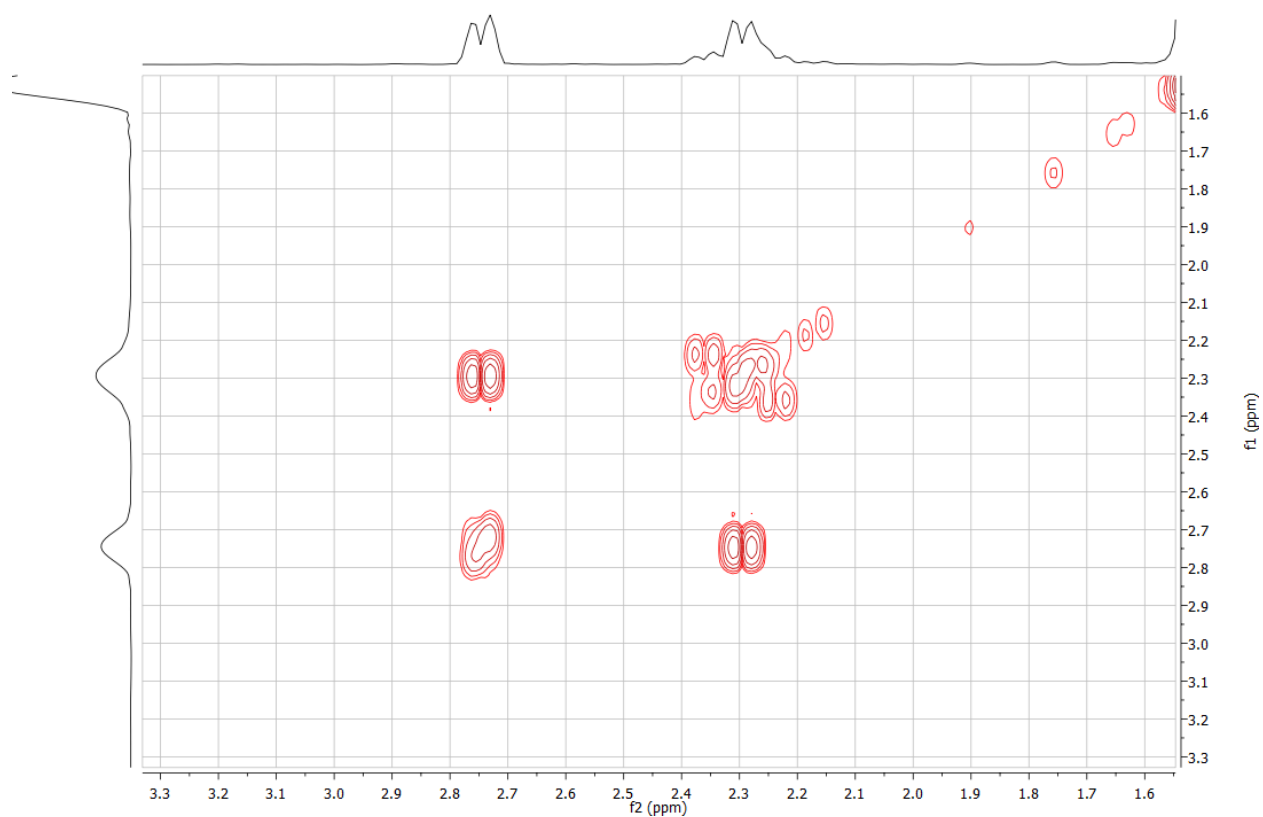*Figure A4.10: Zoomed in view of HMBC with overlapped HSQC spectra. F1 axis shows carbon chemical shifts and f2 axis shows proton chemical shifts. Water peak has been removed for clarity. HSQC peaks appear blue for CH₂ group and red for CH or CH₃ groups. Peaks associated with the closed diol form of zymonic acid (ZCD) are shown with green lines.*

Figure A4.11: COSY spectra showing correlation between the sets of zymonic closed diol (ZCD) peaks, and the sets of zymonic open diol (ZOD) peaks. Both axes are proton chemical shift.
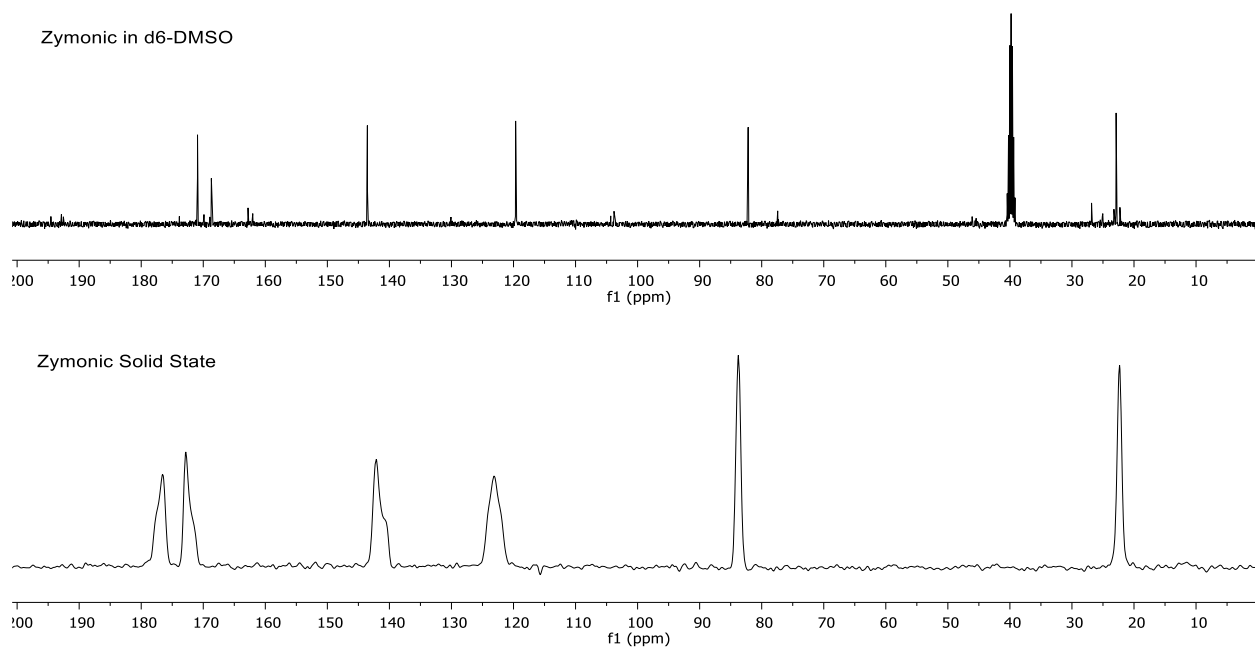
Figure A4.12: *^{13}C NMR of crude zymonic acid in d6-DMSO and purified zymonic acid powder using optimized CPMAS.*
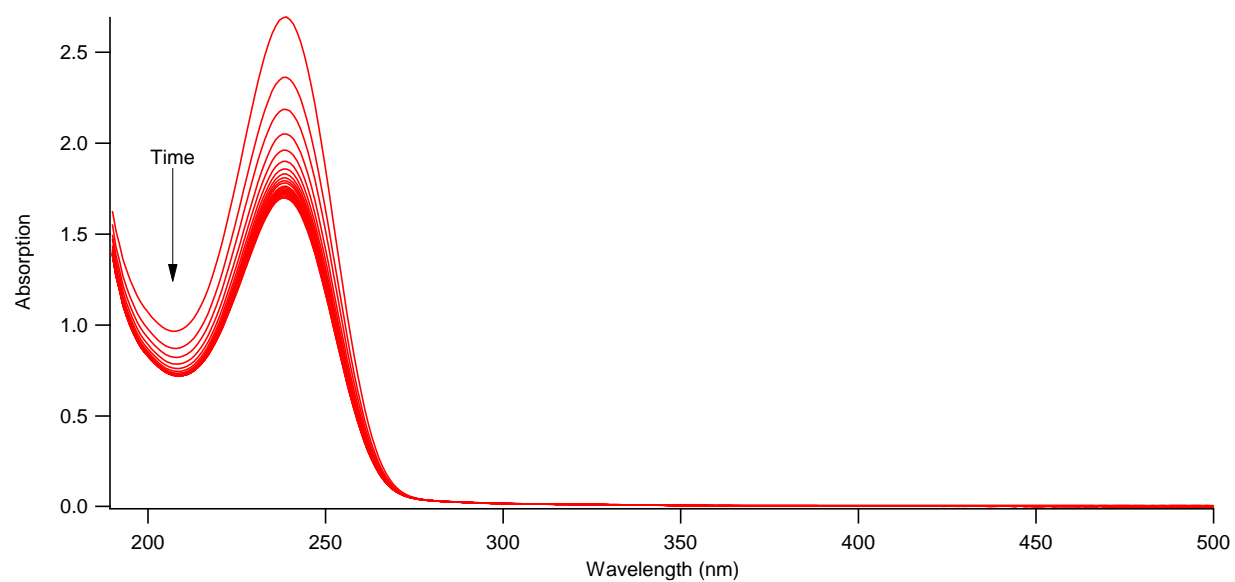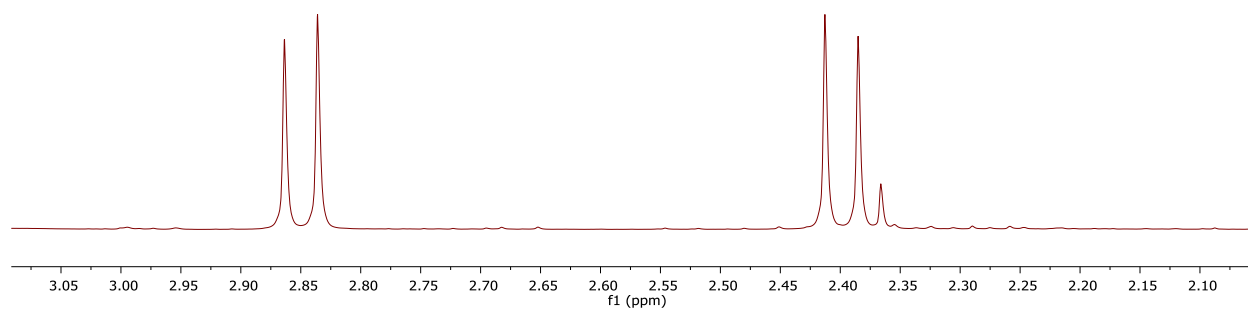

Figure A4.13: *The UV absorption of 5 mM zymonic acid upon mixing with water. Intensity decreases with time, traces are approximately 10 minutes apart.*
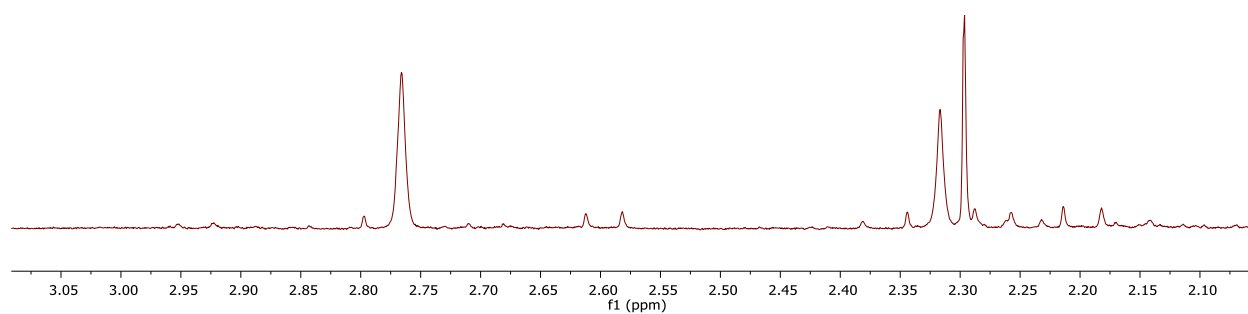
Zymonic Water Mixing

Zymonic D2O Mixing

Figure A4.14: NMR spectra of ZCD CH$_2$ peaks in both water (top) and D$_2$O (bottom). In D$_2$O the geminal splitting is much weaker in D$_2$O, where the methylene is partially deuterated, and is observed as a slight broadening rather than a splitting.

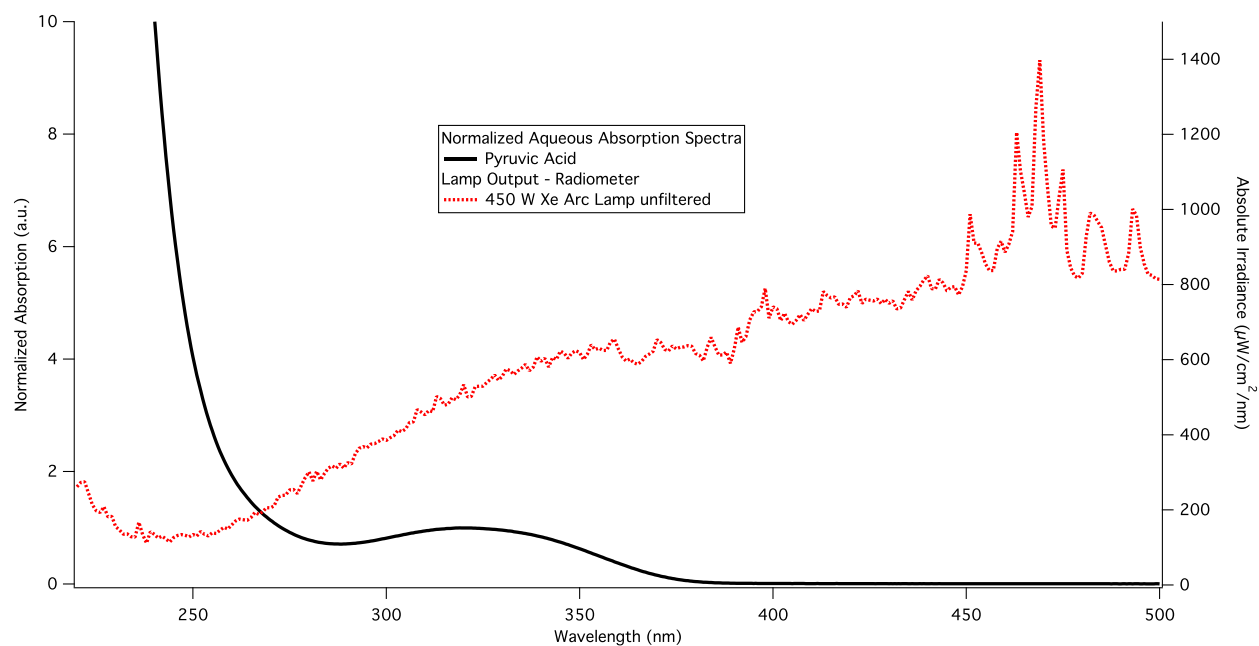# Appendix 5: Supporting Information for Chapter 9

Figure A5.1: Normalized aqueous absorption spectrum of pyruvic acid (black) overlaid with the spectral output of the unfiltered 450 W Xe arc lamp used for photolysis (dashed red).
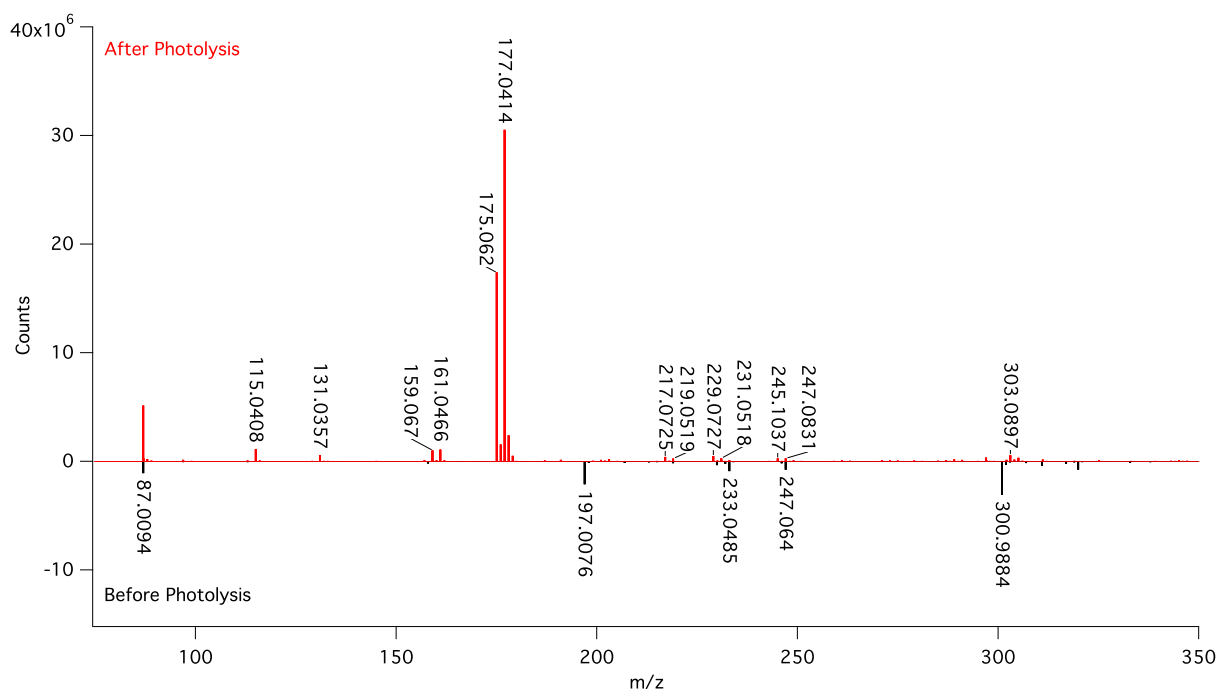
Figure A5.2: Representative high resolution ESI⁻ MS of 10 mM pyruvic acid before (black, counts multiplied by -1 for ease of presentation) and after (red) 5 hours of photolysis under N₂.

Table A5.1: Pyruvic Acid Photolysis Detailed ESI⁻ MS Results

Assigned Formula [M-H]-	Assigned Structure	Avg Exp. m/z	Theor. m/z	Mass Diff. (ppm)	Exp. Nat. Abun	Avg. Nat. Abun	Pre-Photolysis	Post-Photolysis
$C_3H_3O_3$	Pyruvic Acid	87.0091 ± 0.0005	87.0082	10.8			Strong	Strong
		88.0124 ± 0.0004	88.0116	9.2	3.2%	3.8%		
$C_4H_7O_2$	Acetoin	87.0454 ± 0.0007	87.0446	8.7			Below Threshold	Medium
		88.0487 ± 0.0009	88.0480	7.8	4.3%	5.7%		
$C_3H_5O_3$	Lactic Acid	89.0239 ± 0.0003	89.0239	0.45			Below Threshold	Weak
$C_3H_5O_4$	2,2-DHPA	105.0190 ± 0.0007	105.0188	2.3			Weak	Below Threshold
$C_5H_7O_3$	Unassigned	115.0404 ± 0.0008	115.0395	8.1			Below Threshold	Medium
		116.0434 ± 0.0008	116.0429	4.6	5.4%	6.1%		
$C_5H_7O_4$	Acetolactic Acid	131.0354 ± 0.001	131.0345	6.6			Below Threshold	Medium
		132.0383 ± 0.0008	132.0378	3.7	5.4%	6.4%		
$C_6H_7O_5$	Unassigned	159.0300 ± 0.001	159.0294	3.5			Below Threshold	Medium

		160.0335 ± 0.0008	160.0327	5.1	6.5%	7.8%		
$C_7H_{11}O_4$	Unassigned	159.0666 ± 0.0007	159.0658	5.0			Below Threshold	Medium
		160.0695 ± 0.0007	160.0691	2.3	7.6%	8.9%		
$C_6H_9O_6$	Unassigned	161.0457 ± 0.001	161.0450	4.3			Below Threshold	Medium
		162.0487 ± 0.001	162.0484	2.1	6.5%	8.0%		
$C_6H_7O_6$	Parapyruvic Acid*	175.0243 ± 0.0004	175.0243	0.21			Weak	Below Threshold
$C_7H_{11}O_5$	DMOHA	175.0617 ± 0.0006	175.0607	5.5			Below Threshold	Strong
		176.0650 ± 0.0006	176.0640	5.5	7.6%	8.5%		
$C_6H_9O_6$	Dimethyl-tartaric Acid	177.0409 ± 0.0005	177.0400	5.0			Below Threshold	Strong
		178.0443 ± 0.001	178.0433	5.7	6.5%	7.6%		
$C_6H_6O_6Na$	Na Adduct of 2 PA-	197.0072 ± 0.0004	197.0062	5.2			Strong	Weak
		198.0102 ± 0.0005	198.0096	2.8	6.5%	7.3%		
Unidentified		217.0724 ± 0.0006					Below Threshold	Medium
		218.0757 ± 0.001				10.4%		
$C_8H_{11}O_7$	CDMOHA	219.0512 ± 0.0009	219.0505	3.2			Below Threshold	Medium
		220.0546 ± 0.0006	220.0539	3.3	8.7%	9.7%		
$C_{10}H_{13}O_6$	Unassigned	229.0717 ± 0.001	229.0713	1.7			Below Threshold	Medium
		230.0754 ± 0.001	230.0746	3.4	10.8%	11.7%		
$C_9H_{11}O_7$	Unassigned	231.0511 ± 0.001	231.0505	2.7			Below Threshold	Medium
		232.0544 ± 0.0008	232.0539	2.1	9.7%	11.5%		
$C_{10}H_{15}O_6$	Unassigned	231.0874 ± 0.0007	231.0869	2.3			Below Threshold	Medium
		232.0909 ± 0.002	232.0903	2.6	10.8%	11.5%		
Unidentified		233.0474 ± 0.0007					Medium for 10 mM PA, B.T. at low conc	Below Threshold

		234.0513 ± 0.0008				8.6%		
Unidentified		247.0635 ± 0.0005					Medium for 10 mM PA, B.T. at low conc	Below Threshold
		248.0684 ± 0.0009				11.1%		
C$_{10}$H$_{14}$O$_8$Na	Na Adduct of 2 Acetolactates	285.0597 ± 0.0007	285.0587	3.6			Below Threshold	Medium
		286.0622 ± 0.0009	286.0620	0.82	10.8%	11.8%		
C$_9$H$_{12}$O$_9$Na	Na Adduct of PA- and DMTA-	287.0391 ± 0.0006	287.0380	3.8			Below Threshold	Weak
C$_9$H$_9$O$_9$Ca	Ca Adduct of 3 PA-	300.9883 ± 0.0005	300.9873	3.3			Strong	Below Threshold
		301.9918 ± 0.0005	301.9907	3.7	9.7%	10.7%		
Unidentified		303.0899 ± 0.003					Below Threshold	Medium
		304.0821 ± 0.002				25.0%		
C$_9$H$_9$O$_9$Na$_2$	Na Adduct of 3 PA-	307.0052 ± 0.0006	307.0043	3.1			Medium	Below Threshold
		308.0086 ± 0.001	308.0076	3.2	9.7%	10.8%		

Notes: Chemical formulas are assigned as the ionized [M-H]$^-$ species, structures are assigned as the neutral species. The experimental *m/z* is the observed average across experiments, and the uncertainty given is the 95% confidence interval
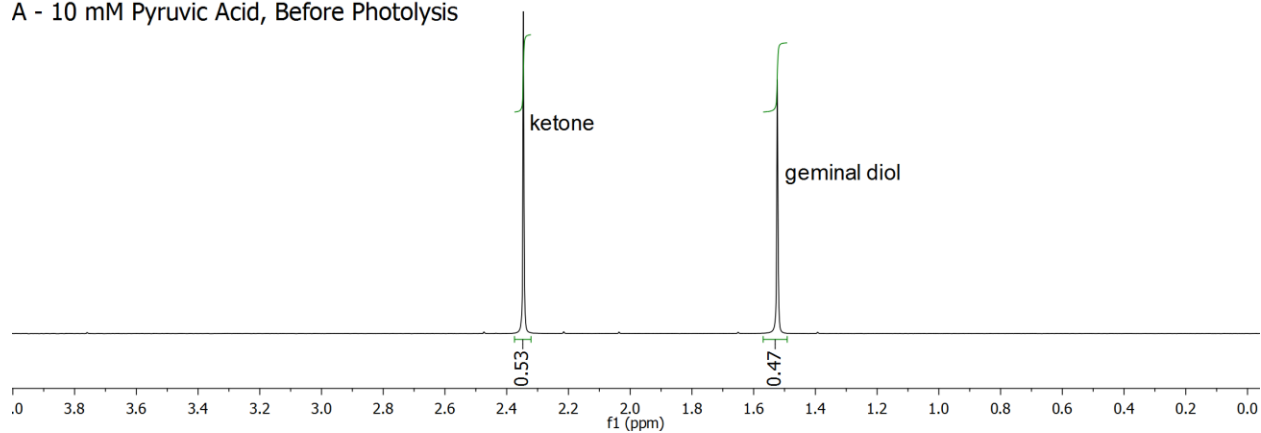
2,2-DHPA = 2,2-Dihydroxypropanoic Acid, diol of pyruvic acid

DMOHA = 2,4-dihydroxy-2-methyl-5-oxohexanoic acid

CDMOHA = 4-carboxy-2,4-dihydroxy 2-methyl-5-oxohexanoic acid

*The peak assigned to parapyruvic acid likely also has contributions from the closed ring form of the zymonic acid diol as well.
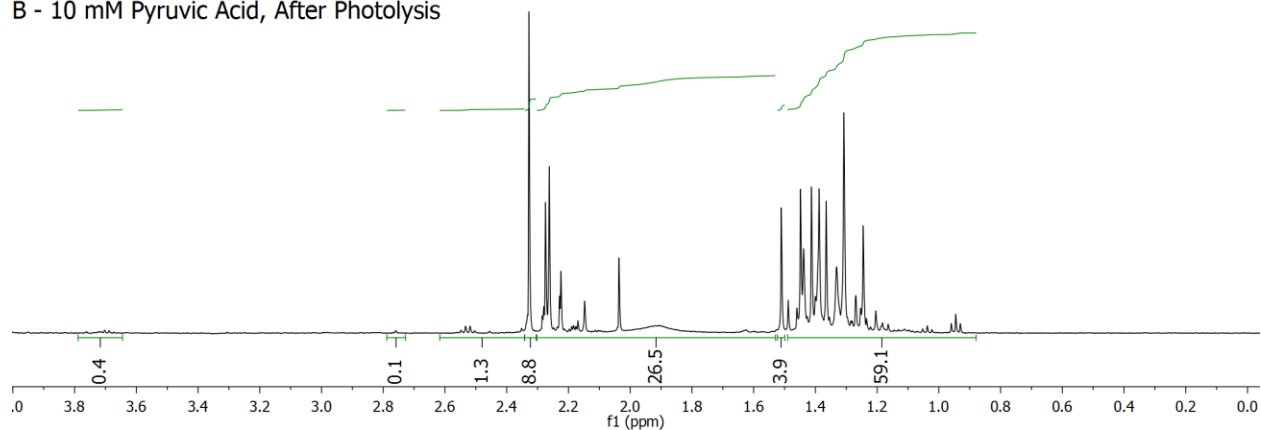
A - 10 mM Pyruvic Acid, Before Photolysis

ketone

geminal diol

0.53

0.47

.0   3.8   3.6   3.4   3.2   3.0   2.8   2.6   2.4   2.2   2.0   1.8   1.6   1.4   1.2   1.0   0.8   0.6   0.4   0.2   0.0
f1 (ppm)

B - 10 mM Pyruvic Acid, After Photolysis

0.4   0.1   1.3   8.8   26.5   3.9   59.1

.0   3.8   3.6   3.4   3.2   3.0   2.8   2.6   2.4   2.2   2.0   1.8   1.6   1.4   1.2   1.0   0.8   0.6   0.4   0.2   0.0
f1 (ppm)

Figure A5.3: ^{1}H NMR spectra of 10 mM pyruvic acid in aqueous solution before (A) and after (B) 5 hours of photolysis under N_2.

A- 0.5 mM Pyruvic Acid Before Photolysis

B - 0.5 mM Pyruvic Acid After Photolysis

Figure A5.4: ^1H NMR spectra of 0.5 mM pyruvic acid in aqueous solution before (A) and after (B) 5 hours of photolysis under N_2.
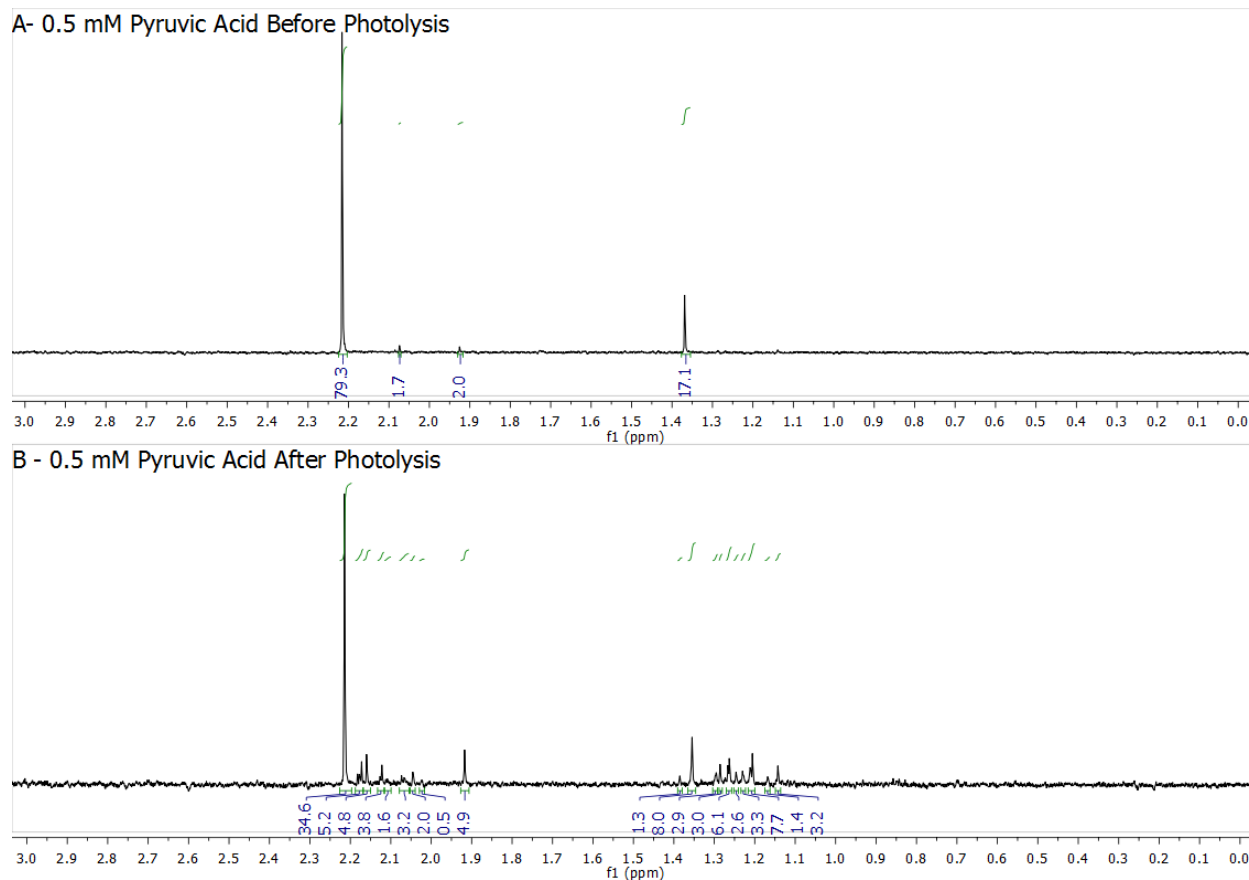
Pyruvic Acid Oxygen Saturated Prephotolysis
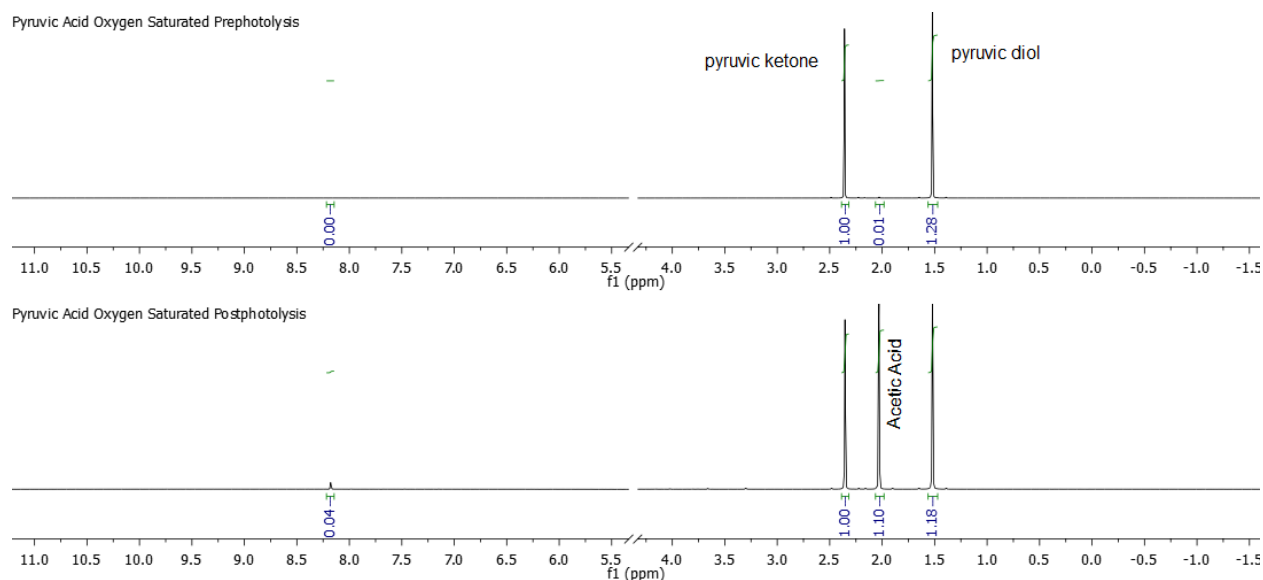

Pyruvic Acid Oxygen Saturated Postphotolysis

Figure A5.5: ^1H NMR of 50 mM pyruvic acid bubbled O_2 through pre (A) and post (B) photolysis for 5 hours.
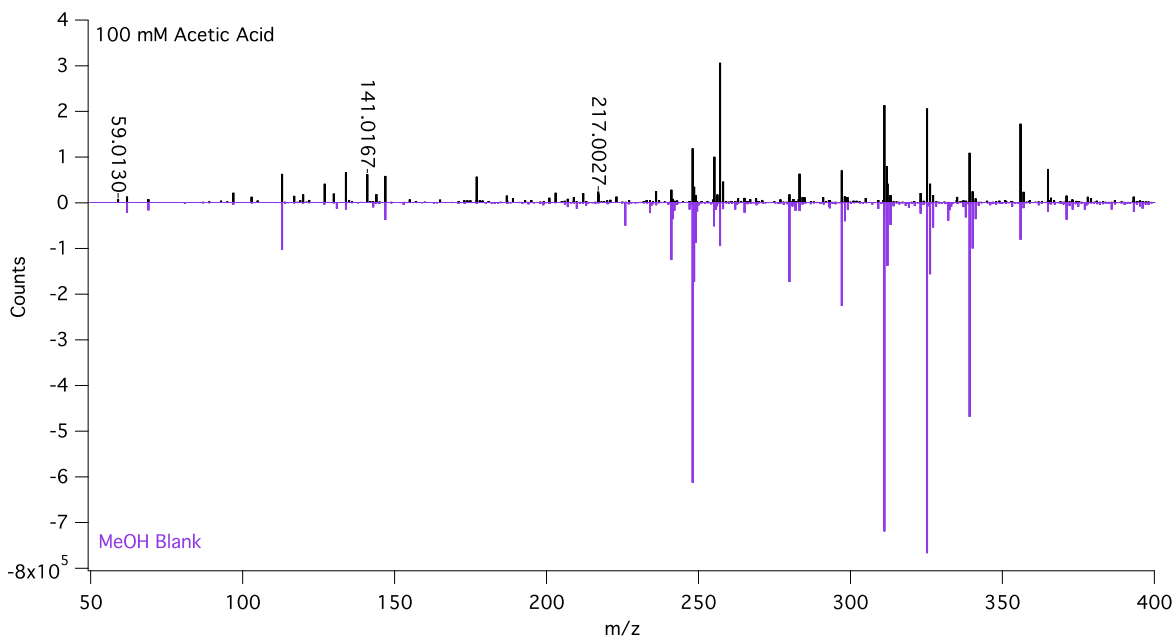
Figure A5.6: ESI⁻ MS spectrum of 100 mM acetic acid in aqueous solution (black) compared to a methanol blank spectrum (purple, counts multiplied by -1 for ease of presentation). Labeled peaks are contributions from acetic acid species: m/z of 59.0130 corresponds to acetic acid with [M-H]- of $C_2H_3O_2$, m/z of 141.0167 corresponds to an adduct of 2 AA- and Na with [M-H]- of $C_4H_6O_4Na$, and m/z of 217.0027 corresponds to an adduct of 3 AA- and Ca with [M-H]- of $C_6H_9O_6Ca$. The intensity of the [M-H]- of $C_2H_3O_2$ is 8500 counts, below the threshold for detection of 10^4 counts

Electronic Structure Calculations

Electronic structure calculations were carried out using the Gaussian 09 suite of programs.[1]

Structures, harmonic vibrational frequencies and relative energies of key species are listed below. In

these data, pyruvic acid is abbreviated to PA.

PA:
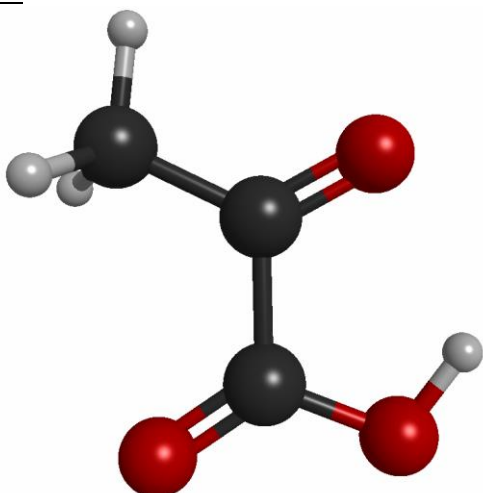
Cartesian coordinates (Å)
C 0.034160 -0.819768   0.000000
C 0.000000   0.732114   0.000000
C -1.347214   1.382920   0.000000
8 1.279980 -1.299496   0.000000
8 -0.956240 -1.496486   0.000000
8 1.060650   1.318808   0.000000
H 1.874420 -0.525975   0.000000
H -1.916469   1.052931   0.873522
H -1.916469   1.052931 -0.873522
H -1.238283   2.465917   0.000000

Harmonic vibrational frequencies (cm^{-1})
83.8394	117.7387	254.8581
395.2006	395.4936	528.5184
609.5732	692.9043	744.1031
768.6280	978.4885	1032.9526
1155.9124	1247.8606	1384.4770
1404.4158	1455.4593	1455.8380
1787.9132	1856.7344	3043.1418
3097.8811	3154.2496	3635.3368

CBS-QB3 Enthalpy =   -341.936157
CBS-QB3 Free Energy =   -341.973527

PA hydrate:
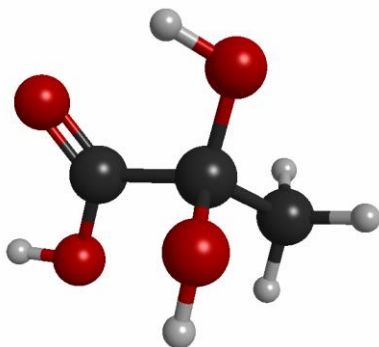
Cartesian coordinates (Å)
C 1.273168 -0.935158 -0.917408
C 0.606774   0.059692   0.022598
C -0.933379   0.095813 -0.091693
O -1.483641 -1.133247 -0.007763
O -1.576610   1.109590 -0.173325
O 1.104389   1.320142 -0.244508
O 0.881422 -0.247149   1.395513
H 1.061921 -0.678324 -1.957233
H 0.926011 -1.951547 -0.726400
H 2.349959 -0.881180 -0.751046
H -2.446333 -1.018910 -0.014645
H 0.440144   1.961833   0.042736

H 0.584442 -1.148636   1.566269

Harmonic vibrational frequencies (cm⁻¹)

76.0546	215.3682	228.5325
247.0093	306.2063	348.6522
372.4174	439.1277	457.3947
553.9270	613.8161	622.5400
746.7703	785.3789	906.5089
981.1738	1104.6774	1130.7022
1150.9057	1183.7499	1335.4466
1372.7120	1408.6863	1441.5613
1485.1754	1495.7887	1829.8608
3048.2403	3122.6593	3131.4084
3749.2229	3762.5423	3813.2324

CBS-QB3 Enthalpy =   -418.280082
CBS-QB3 Free Energy =   -418.320302

PA $^3(n,\pi^*)$:
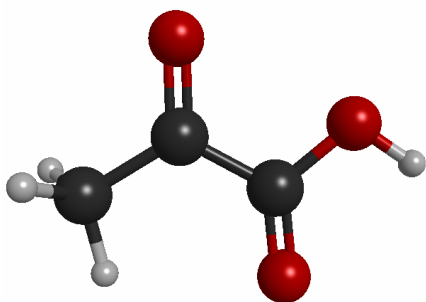
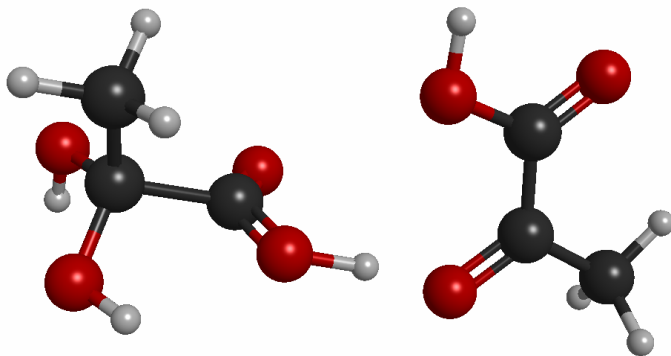

Cartesian coordinates (Å)

C -1.798715 -0.741322   0.004418
C -0.654931   0.236256   0.002499
C 0.721080 -0.233310 -0.002630
O 1.614247   0.790849 -0.003678
O 1.048941 -1.409516 -0.005760
O -0.898972   1.493174   0.005299
H -1.362585 -1.741604   0.000230
H -2.428809 -0.604848 -0.879273
H -2.421961 -0.609388   0.893655
H 2.495018   0.390041 -0.007221

Harmonic vibrational frequencies (cm⁻¹)

121.2752	137.9882	237.3834
304.6244	349.4645	494.9044
510.4565	551.6879	672.1335
760.7918	997.8989	1023.5836
1096.9460	1193.7874	1312.8923
1366.9864	1404.5718	1456.4856
1484.4932	1687.3367	3020.7945
3080.0122	3122.4437	3779.1842

CBS-QB3 Enthalpy =   -341.826031
CBS-QB3 Free Energy =   -341.864614

TS for carboxyl H abstraction by PA $^3(n,\pi^*)$ from PA hydrate:

Cartesian coordinates (Å)
C 2.800327   1.406403 -0.720301
C 2.836586   0.046753 -0.028523
C 1.267592 -0.335194   0.368650
O 0.638764 -0.631155 -0.713251
O 0.922089 -0.298102   1.516805
O 3.617452   0.134884   1.087400
O 3.294251 -0.999635 -0.830331
H 2.441600   2.166508 -0.025435
H 2.149190   1.374987 -1.592650
H 3.820181   1.648686 -1.025353
H -0.435641 -0.873824 -0.546849
H 3.749353 -0.752270   1.446169
H 2.610364 -1.193065 -1.486392
C -3.977811 -1.293947   0.128181
C -2.678999 -0.578331 -0.101206
C -2.645260   0.863278 -0.025238
O -1.414346   1.403486 -0.287277
O -1.641149 -1.306709 -0.372683
O -3.608390   1.577150   0.240629
H -4.263251 -1.866311 -0.760415
H -4.749855 -0.557653   0.354280
H -3.882979 -1.998735   0.960164
H -1.522934   2.358553 -0.183230

Harmonic vibrational frequencies (cm^{-1})
| 1240.6198 i	16.5306	25.5419
30.3583	48.8855	81.6529
116.9839	135.7395	142.7778
189.7970	213.5987	248.4666
271.2628	287.9578	331.5223
333.1700	369.8086	392.9335
453.9141	482.5846	486.4255

508.8635	537.3021	553.6180
611.9103	671.7600	684.2402
739.9204	772.8003	816.0652
891.4512	995.8263	1012.5864
1024.0202	1062.5575	1074.3474
1120.6430	1189.9916	1206.9051
1251.6433	1304.4739	1340.8561
1352.8995	1379.6657	1385.5570
1408.7800	1420.9538	1441.3219
1461.1230	1477.3299	1488.7723
1492.9893	1650.7463	1811.7382
3017.4158	3052.3906	3068.8851
3123.4765	3130.8573	3148.6064
3773.5144	3787.5544	3793.4924

CBS-QB3 Enthalpy =   -760.099260
CBS-QB3 Free Energy =   -760.162415

TS for carboxyl H abstraction by PA $^3(n,\pi^*)$ from PA :
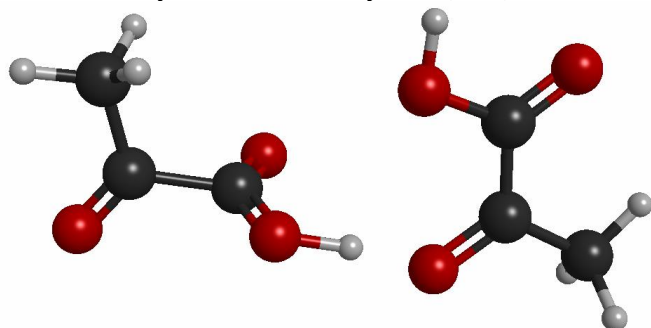
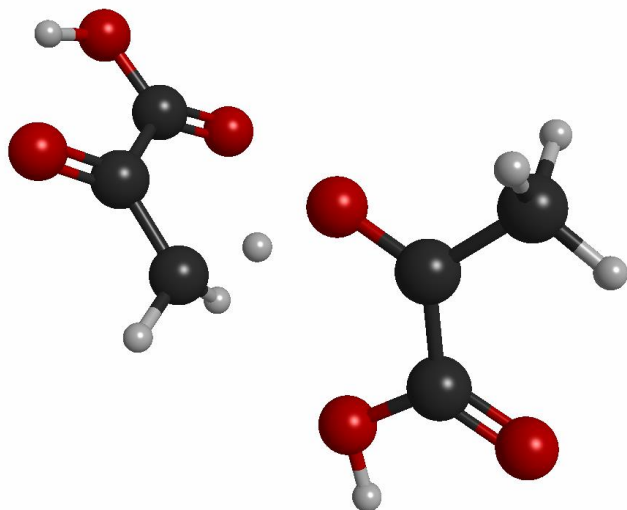Cartesian coordinates (Å)
C 3.404311   1.396762 -0.200482
C 3.128410 -0.076164 -0.042116
C 1.599465 -0.405691   0.295560
O 0.960302 -0.665563 -0.779677
O 1.283052 -0.341258   1.455786
O 3.921334 -0.963242 -0.100220
H 3.115436   1.906110   0.722481
H 2.781711   1.789484 -1.008462
H 4.460349   1.555051 -0.414204
H -0.107332 -0.889686 -0.603776
C -3.662708 -1.266452   0.119349
C -2.357124 -0.564469 -0.117525
C -2.305892   0.876419 -0.036473
O -1.069735   1.403761 -0.303658
O -1.331482 -1.303686 -0.400552
O -3.258699   1.600405   0.236841
H -3.964240 -1.826942 -0.771317
H -4.421655 -0.520809   0.359087
H -3.567970 -1.979092   0.944385
H -1.173241   2.360116 -0.206234

Harmonic vibrational frequencies (cm^{-1})

1034.7831 *i*	15.4481	24.9043
32.5512	45.5231	86.7453
118.4899	130.6904	139.7377
143.9975	180.7595	251.6982
272.9477	323.2696	330.7457
386.8692	480.0062	500.4593
551.8803	568.1733	582.6234
671.4655	679.1343	747.5658
776.0841	836.4713	959.3660
1016.0554	1023.8538	1040.8493
1075.3872	1127.5872	1197.1736
1242.4167	1322.4547	1348.5967
1367.0532	1379.1259	1409.1716
1446.0842	1458.6965	1460.0598
1462.7280	1493.6329	1654.5224
1807.0418	1852.3072	3018.6929
3042.1999	3071.5721	3111.6069
3123.4433	3151.9024	3786.5970

CBS-QB3 Enthalpy =   -683.753641
CBS-QB3 Free Energy =   -683.814877

<u>TS for methyl H abstraction by PA $^3(n,\pi^*)$ from PA :</u>

Cartesian coordinates (Å)
C 0.825906 -1.173778 -0.290637
C 2.108314 -0.501105 -0.548912
C 2.791008   0.205522   0.650672
C -2.058076   0.710656 -0.189550
C -2.768344 -0.492354   0.172389
C -2.794962   2.011807 -0.310778
O 3.954091   0.765056   0.314900
O 2.655793 -0.445788 -1.634980
O 2.309674   0.239070   1.748231
O -0.765892   0.810018 -0.446948

O -3.966795 -0.535167   0.401989
O -1.981748 -1.611458   0.237820
H 4.085859   0.594088 -0.635906
H -0.018115 -0.220012 -0.339478
H 0.682501 -1.540163   0.720860
H -2.578095 -2.329441   0.491281
H -2.696345   2.420981 -1.320944
H -2.393831   2.749386   0.391046
H -3.845968   1.826062 -0.089502
H 0.499933 -1.839221 -1.084561

Harmonic vibrational frequencies (cm^{-1})

1690.0654 *i*	20.4813	27.4160
47.9518	64.1793	104.6072
118.0349	127.7731	140.1583
265.1953	267.9460	297.5273
323.9717	385.2770	420.2217
467.4828	502.9604	514.0147
542.8307	557.8030	618.1232
640.8311	689.6989	702.0478
768.6052	773.5904	791.3612
993.6530	996.1024	1027.6056
1031.4541	1085.0669	1140.9796
1156.5052	1217.9294	1239.0260
1281.8132	1314.6072	1382.9747
1390.5332	1430.8236	1439.8276
1462.1088	1499.0927	1702.2079
1721.5104	1854.1654	3021.3375
3074.0896	3124.5329	3131.5366
3223.4705	3645.0287	3785.0789

CBS-QB3 Enthalpy =   -683.751297
CBS-QB3 Free Energy =   -683.809982

Bibliography
(1)   Frisch, M. J.; Trucks, G. W.; Schlegel, H. B.; Scuseria, G. E.; Robb, M. A.; Cheeseman, J. R.; Scalmani, G.; Barone, V.; Petersson, G. A.; Nakatsuji, H., et al. *Gaussian 09, revision d.01*, Gaussian, Inc.: Wallingford, CT, 2016.

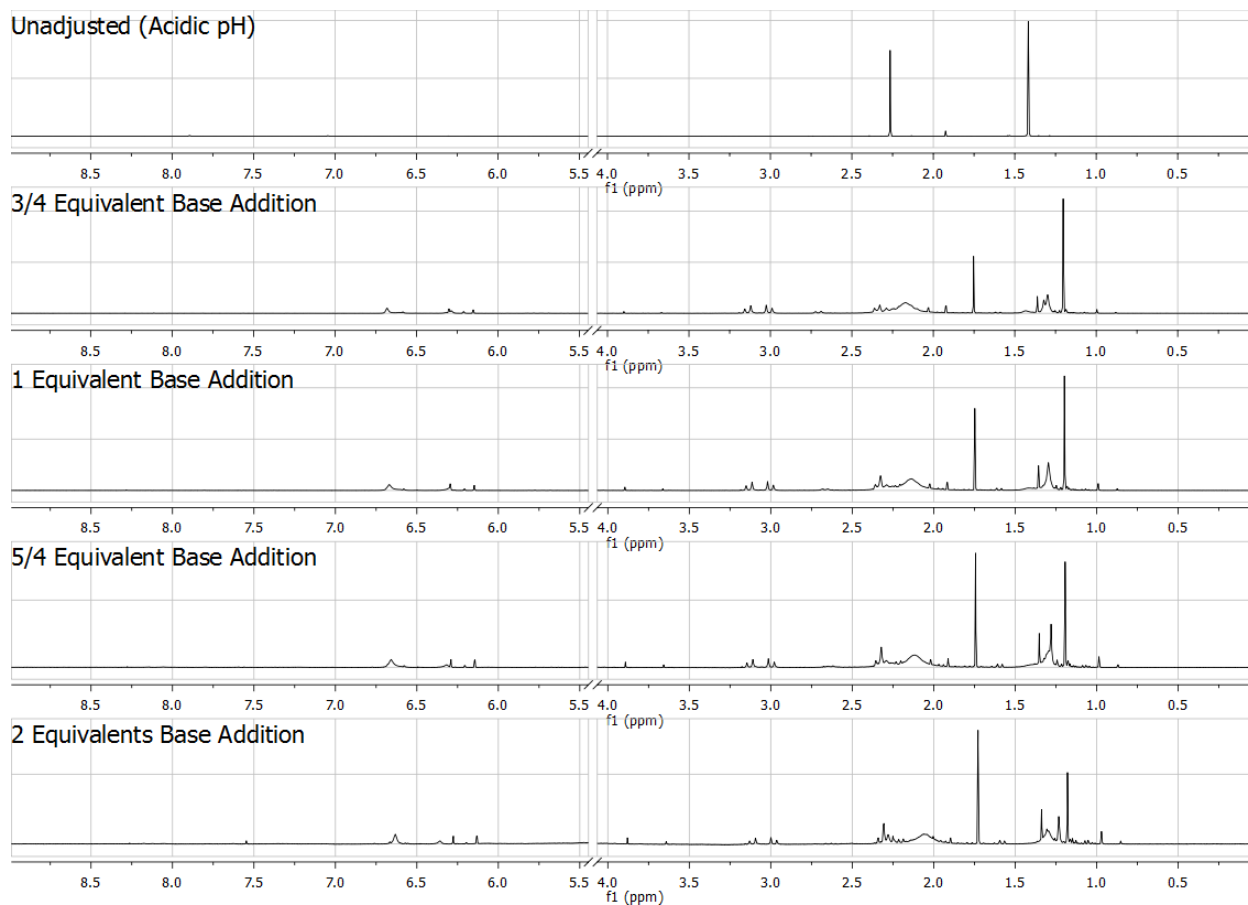# Appendix 6: Supporting Information for Chapter 10

Figure A6.1: NMR of 100 mM aqueous pyruvic acid samples after 41 days at room temperature in the dark. The majority of peaks are unassigned. The broad features that are observed are likely due to either diverse populations of similar species, or species undergoing chemical exchange on a timescale similar to that of the NMR measurement.
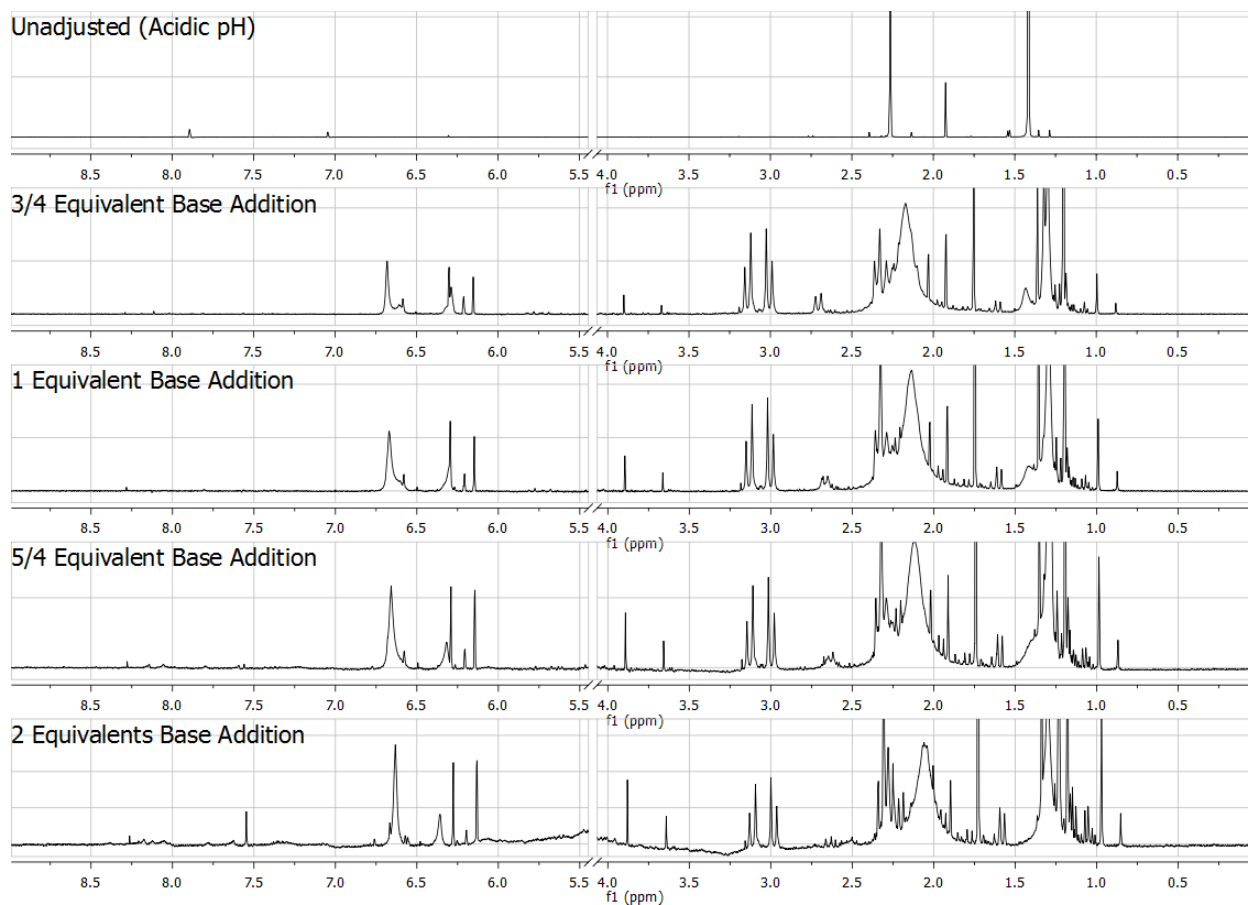
Figure A6.2: Zoomed in NMR of 100 mM aqueous pyruvic acid samples after 41 days at room temperature in the dark. The majority of peaks are unassigned. The broad features that are observed are likely due to either diverse populations of similar species, or species undergoing chemical exchange on a timescale similar to that of the NMR measurement.

The change in base content of the samples can alter the chemical shift values of the compounds under study. pH dependent NMR measurements of purified zymonic acid were used to help assign several peaks, and are shown in Figure A6.3.
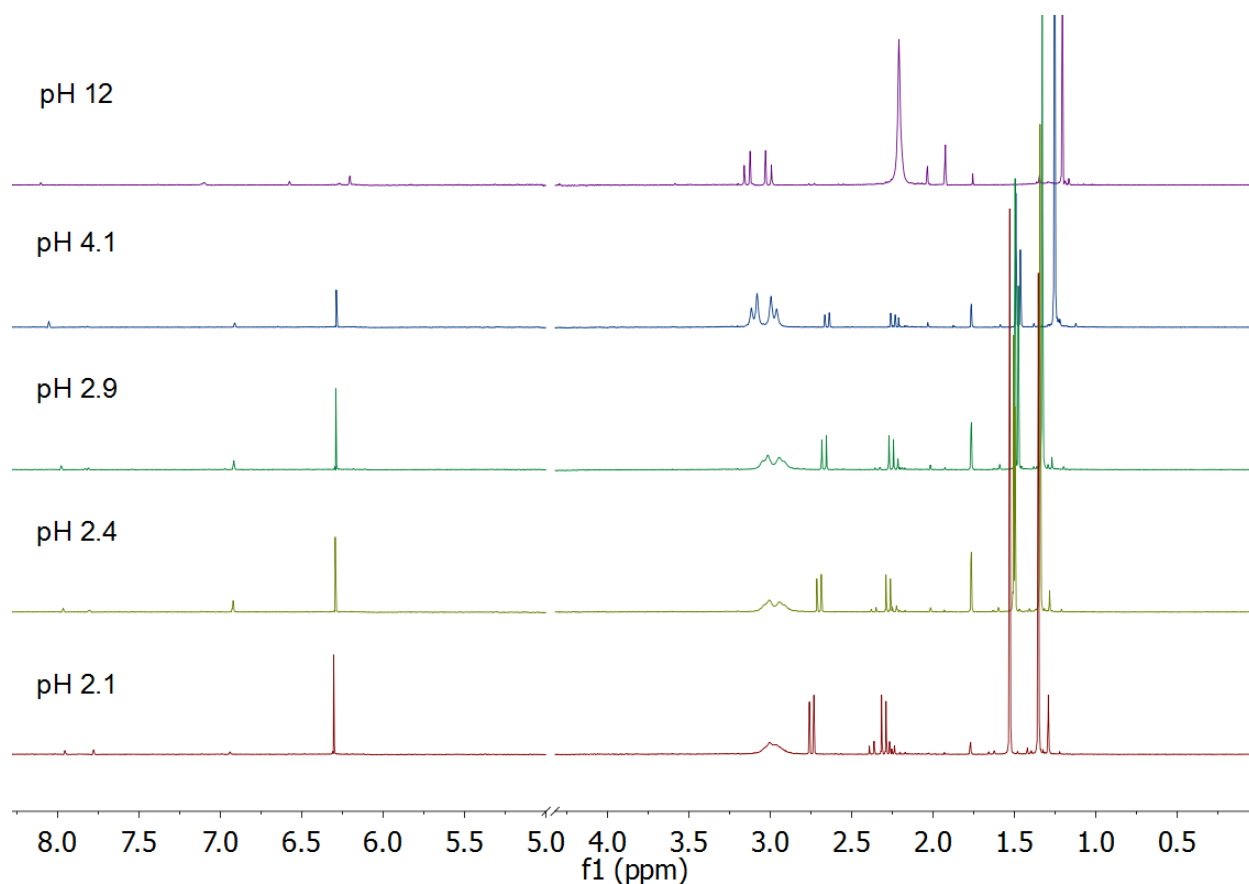
Figure A6.3: pH dependent ^1H NMR spectra of zymonic acid species. For details about specific assignments see Perkins et al 2016.[1]

Compound\Base Equivalence	0	3/4	1	5/4	2
Pyruvic Acid (3H)	93.95	<2*	<2*	<2*	<2*
Zymonic Ketones (5H)	0.375	18.56	14.15	11.09	8.32
Zymonic Closed Enol (4H)	0.28	3.4	2.56	2.56	2.76
Unassigned	5.395	78.04	83.29	86.35	88.92

Table A6.1: Assignments of chemical components based on NMR data for 100 mM pyruvic acid solutions after 41 days in the dark at room temperature. Quantities of each compound are given as a % of the total proton signal. Because the number of protons on each species is not the same, these are not relative concentrations. Relative concentrations could be easily calculated for known species, but not unassigned ones. The number of protons associated with each species is listed in parentheses. *Pyruvic acid is likely present in all samples, but cannot be definitively identified due to the high density of peaks in the spectral region that it appears. It is unlikely that it constitutes more than a few percent of the solution, however.
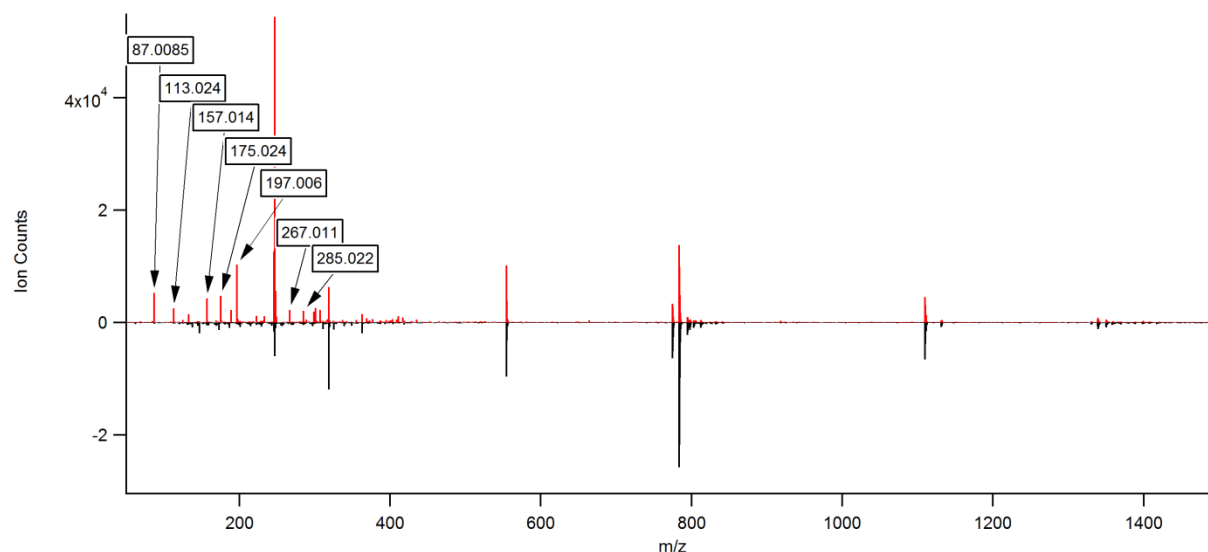
Figure A6.4: ESI⁻ MS data for 100 mM pyruvic acid after 90 days. Sample was diluted 10x with water and then mixed 1:1 with methanol immediately prior to the acquisition of spectra. The top (red) trace is for the sample, and the bottom (black) trace is a blank using only 1:1 methanol. Qualitatively similar spectra were recorded after 41 days. Species appearing in the blank trace are likely contaminants.

Labeled species have been identified, from left to right as: 87.0085 - pyruvic acid; 113.024 - decarboxylated zymonic acid closed enol; 157.014 - zymonic acid closed enol; 175.124 - parapyruvic acid; 197.006 - the adduct of 2 pyruvic acids and one sodium; 267.011 – adduct of pyruvic acid, zymonic closed enol, and sodium; 285.022 adduct of pyruvic acid, parapyruvic acid, and sodium.
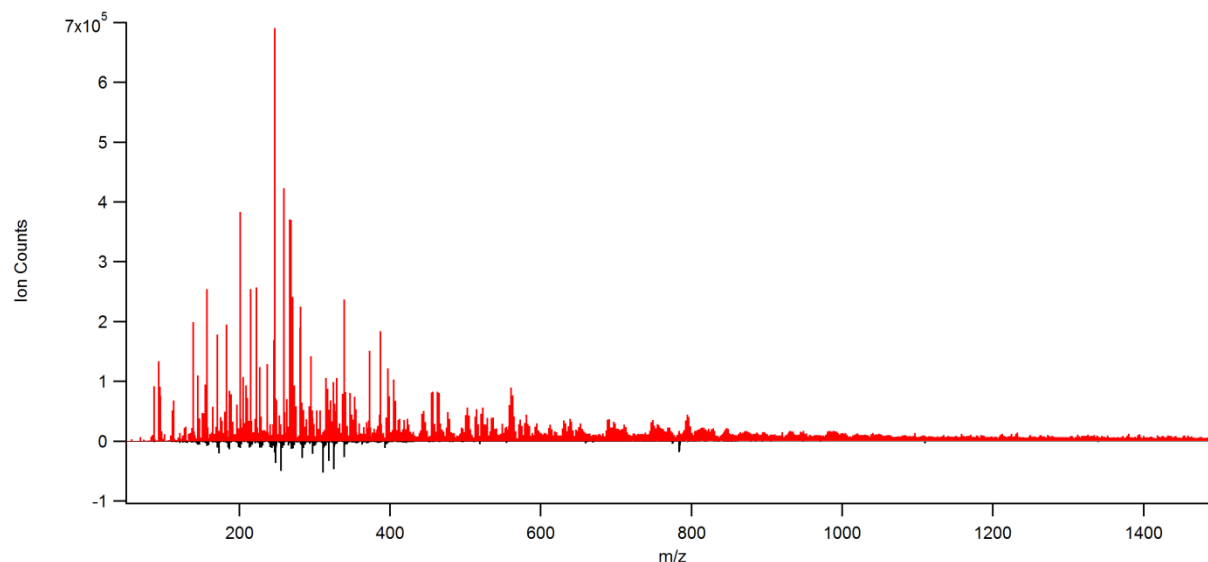

Figure A6.5: ESI⁻ MS data for 100 mM pyruvic acid with the addition of 1 equivalent of NaOH, after equilibrating at room temperature for 90 days.

Several hours prior to acquisition, the sample was acidified by dropwise addition of HCl until pH was approximately 2. Sample was diluted 10x with water and then mixed 1:1 with methanol immediately prior to the acquisition of spectra. The top (red) trace is for the sample, and the bottom (black) trace is a blank using only 1:1 methanol. Qualitatively similar spectra were recorded after 41 days, but additional control experiments were collected at later times. The only assigned products are pyruvic acid, and minor peaks corresponding with adducts of pyruvic acid and sodium.
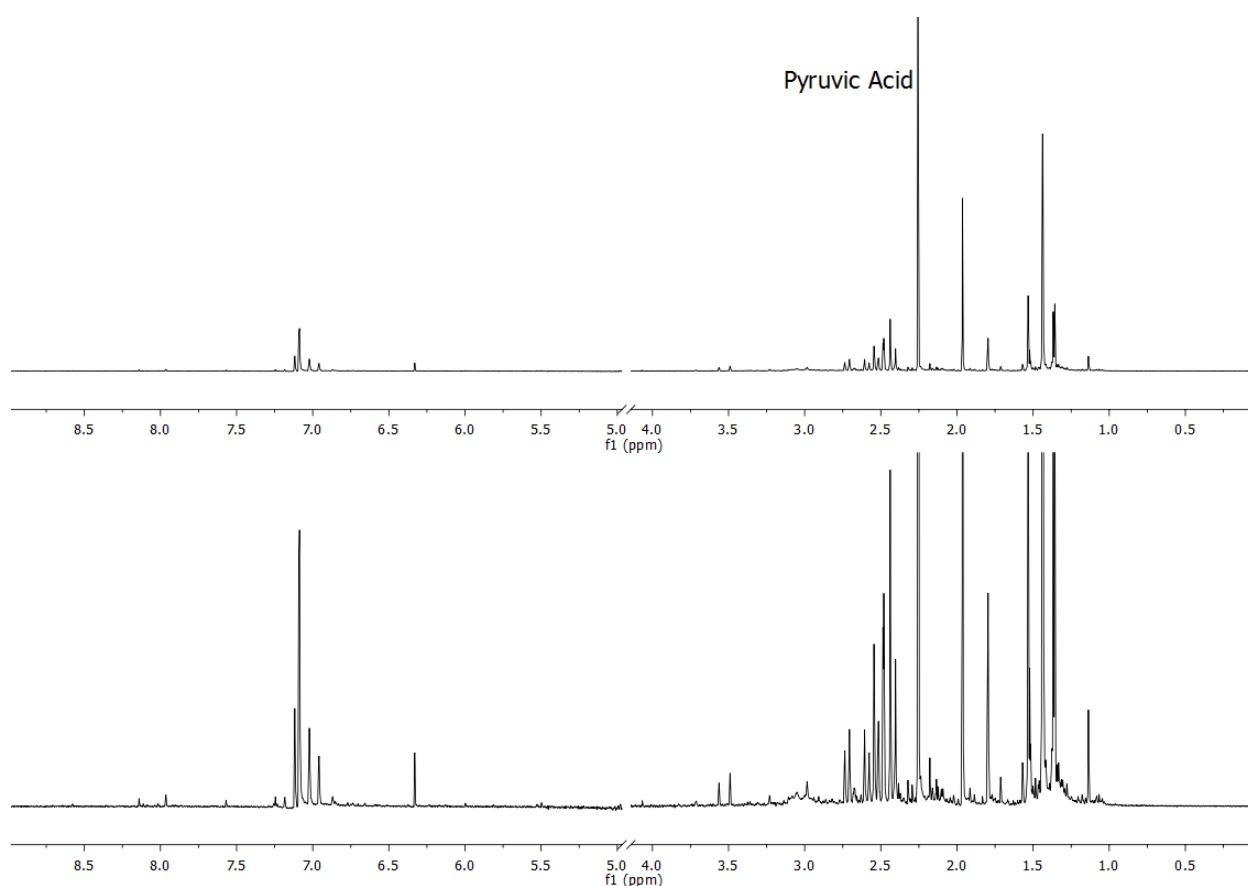

Figure A6.6: 100 mM pyruvic acid sample neutralized with 1 equivalent NaOH that was allowed to sit at room temperature in the dark for 90 days before being acidified to pH 2.6 with HCl. This NMR spectrum was collected 26 days after acidification. Pyruvic acid was regenerated, and constitutes between 16 and 34% of the total ^1H signal, a significant increase from <2% under basic conditions.

The uncertainty in the pyruvic acid quantity is due to overlapping peaks in the 1.4 region where the signal from the pyruvic acid geminal diol appears at low pH. The ratio of pyruvic acid ketone and

geminal diol forms depends on many factors, but in this concentration and pH range, is often more diol

than ketone.[2] This suggests that the higher end of the range is more likely.

Bibliography

(1) Perkins, R. J.; Shoemaker, R. K.; Carpenter, B. K.; Vaida, V. Chemical Equilibria and Kinetics in Aqueous Solutions of Zymonic Acid. *J. Phys. Chem. A* **2016**, *120* (51), 10096–10107.

(2) Reed Harris, A. E.; Ervens, B.; Shoemaker, R. K.; Kroll, J. A.; Rapf, R. J.; Griffith, E. C.; Monod, A.; Vaida, V. Photochemical Kinetics of Pyruvic Acid in Aqueous Solution. *J. Phys. Chem. A* **2014**, *118* (37), 8505–8516.